Multiparametric characterisation of peripheral immunity in recipients of checkpoint immunotherapy across a large patient cohort

Chelsea Alice Taylor

Supervisor Dr Benjamin P. Fairfax
Cosupervisor Prof Mark R. Middleton

A thesis presented for the degree of
Doctor of Philosophy





Department of Oncology
Balliol College
University of Oxford
February 2022

Abstract

Immune checkpoint blockade (ICB) has revolutionised the treatment of metastatic melanoma (MM) which was historically resistant to conventional therapies, yet only a minority of patients experience durable clinical benefit. Dissecting peripheral immune responses to ICB may discern predictive markers of clinical outcome. However, infection with human cytomegalovirus (CMV) can have profound effects on immunity and the extent to which this affects the peripheral immune response to ICB is unclear. Using an agnostic transcriptomic and cytometric assessment of peripheral immune ICB responses across a large cohort of MM patients, I identify dynamic changes in immune composition, activation and adaptive immune cell repertoires. I also determine the contribution of CMV to these changes and describe predictors of clinical outcome.

Firstly, I identify $CD8^+$ T-cells as being the most responsive cell type to ICB treatment and that responses in other peripheral blood mononuclear cell subsets are secondary to $CD8^+$ T-cell ICB response. Next, I find that only B-cell proportion and subset composition are sensitive to ICB treatment. This includes a transient depletion of B-cells and an induction of antibody-secreting cells which associate with clinical outcome. I then characterise these changes and determine that these ICB-mediated effects are largely dependent on $CD8^+$ T-cell activation and production of B-cell chemoattractant CXCL13. Finally, I describe the effects of ICB and CMV on corresponding B-cell receptor and T-cell receptor repertoires. Significantly, I find that B-cells undergo accelerated class switch recombination and somatic hypermutation following ICB, whilst MAIT cells are depleted and associate with clinical outcome. Although CMV infection is a major determinant of MAIT cell changes following ICB, all other identified ICB-mediated effects are independent of CMV serostatus.

In this thesis I present novel findings surrounding B-cell and T-cell responses to ICB treatment and identify predictive markers which may have clinical utility in monitoring patient treatment responses as well as guiding treatment stratification. My observations demonstrate that the response to ICB is multifaceted, involving a coordinated interaction between different cell subsets, driven by $CD8^+$ T-cells. Notably, B-cells cannot be assumed to play a bystander role and my work highlights the importance of B-cell:$CD8^+$ T-cell interactions in the response to ICB and long-term clinical benefit.

Pour mon grenouille et mon favori de tout...

Acknowledgements

Without any doubt, this has been the easiest section of this thesis to write.

I'd firstly like to thank Dr Benjamin Fairfax and Prof Mark Middleton for taking me on as their student and giving me the freedom to guide my own research. Thank you also to the EPSRC, Department of Oncology and Balliol College for awarding me a joint studentship that has given me this opportunity. These thanks extend to all the patients and blood donors that have kindly donated blood over the years making this work possible.

I also undoubtedly need to thank all of my colleagues, past and present, who have helped review this thesis and keep me sane during late nights in the lab. In particular, thank you to my angels Piyush, Orion, Alba, Ros, Rob, Surya, Elsita and Isar.

Thank you also to my fellow Balliolites, Stefania, Lois, Laura and Caitlin, who have made my short time in Oxford so memorable.

I'd like to thank my family for all their support, but especially Georgie who was always there during the stressful times and at hand to go through any drafts.

I would also like to thank my new French family from across the Channel who have supported me over the years.

Above all, I would like to thank Will for his undying support across my academic career and for always giving me the confidence to believe in myself and go for it.

Declaration

I declare that this work is my own except where it is explicitly stated in author contributions.

In light of the SARS-CoV-2 global pandemic, my DPhil was massively impacted with several months of not being able to go into the lab or at limited working capacity. However, I used this time to develop my bioinformatic skills and became involved in the COvid-19 Multi-omics Blood ATlas (COMBAT) Consortium, investigating differences in the TCR repertoire in patients of varying disease severity. This work serves as a large data resource that will aid further investigations into understanding the impact of the SARS-CoV-2 virus on human immune health.

Publications

1. Taylor C.A. (2022) "IL7 genetic variation and toxicity to immune checkpoint blockade in patients with melanoma". In: *Nature Medicine*. DOI:10.1038/s41591-022-02095-5

2. COvid-19 Multi-omics Blood ATlas (COMBAT) Consortium. (2022) "A blood atlas of COVID-19 defines hallmarks of disease severity and specificity". In: *Cell*. DOI: 10.1016/ j.cell.2022.01.012

3. Peng, Y. (2022). "Immunodominant $NP_{105\text{-}113}$ B*0702 cytotoxic response controls viral replication and is associated with less severe COVID-19 disease". In: *Nature Immunology*. DOI: 10.1038/s41590-021-01084-z.

4. Beatson, R.E. (2021). "TGF-β1 potentiates Vγ9Vδ2 T-cell adoptive immunotherapy of cancer". In: *Cell Reports Medicine*. DOI: 10.1016/j.xcrm.2021.100473.

5. Watson, R.A. (2021). "Immune checkpoint blockade sensitivity and progression-free survival associates with baseline CD8 + T cell clone size and cytotoxicity". In: *Science Immunology*. DOI: 10.1126/sciimmunol.abj8825.

6. Ye, W. (2021). "Checkpoint-blocker-induced autoimmunity is associated with favourable outcome in metastatic melanoma and distinct T-cell expression profiles". In: *British Journal of Cancer*. DOI: 10.1038/s41416-021-01310-3.

7. Fairfax, B.P. (2020). "Peripheral CD8+ T cell characteristics associated with durable responses to immune checkpoint blockade in patients with metastatic melanoma". In: *Nature Medicine*. DOI:10.1038/s41591-019-0734-6.

8. Al-Mossawi, H. (2019). "Context-specific regulation of surface and soluble IL7R expression by an autoimmune risk allele". In: *Nature Communications*. DOI: 10.1038/s41467-019-12393-1.

Contents

1 Introduction **1**

1.1 Melanoma . . . 1
1.1.1 Overview . . . 1
1.1.2 Melanomagenesis . . . 1
1.1.2.1 Mutagenesis . . . 1
1.1.2.2 Common mutations . . . 2
1.1.3 Immune involvement . . . 4
1.1.3.1 Overview . . . 4
1.1.3.2 Elimination . . . 4
1.1.3.3 Equilibrium . . . 7
1.1.3.4 Escape . . . 7
1.1.4 Standard of care . . . 9
1.1.4.1 Overview . . . 9
1.1.4.2 Targeted therapies . . . 10
1.1.4.3 Immunotherapy . . . 10
1.2 Immune checkpoint blockade . . . 11
1.2.1 Immune checkpoint proteins . . . 11
1.2.1.1 CTLA-4 signalling . . . 11
1.2.1.2 PD-1/PD-L1 signalling . . . 11
1.2.2 Current ICB treatment strategies . . . 13
1.2.3 Mechanism of action . . . 13
1.2.3.1 CTLA-4 blockade . . . 13
1.2.3.2 PD-1/PD-L1 blockade . . . 14
1.3 Predictive markers of immune checkpoint blockade . . . 15
1.3.1 Development of immune-related adverse events . . . 15
1.3.2 Features of the tumour . . . 15
1.3.2.1 Overview . . . 15
1.3.2.2 Tumour mutational burden . . . 15
1.3.2.3 Mutations in immune-related genes . . . 16
1.3.2.4 MHC diversity . . . 17
1.3.2.5 Summary . . . 18
1.3.3 Immunosuppression . . . 18
1.3.3.1 Overview . . . 18
1.3.3.2 Tregs . . . 18
1.3.3.3 Myeloid cells . . . 18
1.3.3.4 Neutrophils . . . 19
1.3.3.5 PD-L1 . . . 19
1.3.3.6 Immune checkpoints . . . 20
1.3.4 Lymphocytes . . . 20

1.3.4.1 T-cells . . . 20
1.3.4.2 Unconventional T-cells . . . 22
1.3.4.3 B-cells . . . 24
1.3.5 CMV . . . 25
1.4 Summary . . . 25
1.5 Aims . . . 27

2 Materials and Methods **28**
2.1 Patient cohort . . . 28
2.1.1 Samples . . . 28
2.1.2 Clinical outcome data . . . 29
2.2 Blood processing . . . 29
2.2.1 Ficoll density gradient centrifugation . . . 29
2.2.2 Plasma collection . . . 30
2.2.3 Peripheral blood mononuclear cell isolation . . . 30
2.2.4 Magnetic-activated cell sorting . . . 30
2.3 Transcriptomic analysis . . . 31
2.3.1 Bulk RNAseq . . . 31
2.3.1.1 RNA extraction . . . 31
2.3.1.2 Library preparation . . . 31
2.3.1.3 Sequencing . . . 31
2.3.1.4 Upstream data processing . . . 32
2.3.1.5 Differential gene expression . . . 32
2.3.1.6 Pathway analysis . . . 33
2.3.1.7 BCR/TCR mapping . . . 33
2.3.2 Investigating BCR/TCR repertoires . . . 34
2.3.2.1 BCR/TCR usage . . . 34
2.3.2.2 Unconventional T-cell percentages . . . 34
2.3.2.3 Clonality indices . . . 34
2.3.2.4 Mutation rate . . . 35
2.3.2.5 Clonal dynamics . . . 35
2.3.2.6 Identifying and tracking known TCR clones . . . 35
2.3.3 Single cell RNAseq . . . 35
2.3.3.1 Sample preparation . . . 35
2.3.3.2 Sequencing . . . 36
2.3.3.3 Upstream data processing . . . 36
2.3.3.4 Quality control . . . 36
2.3.3.5 Downstream data processing . . . 36
2.3.3.6 Clustering analysis . . . 36
2.3.3.7 Cluster annotation . . . 37
2.3.3.8 Generating B-cell subset scores from bulk RNAseq data 37
2.3.3.9 BCR analysis . . . 37
2.4 qPCR analysis . . . 38
2.4.1 Primer design . . . 38
2.4.2 *MiXCR* validation . . . 38
2.4.3 qPCR reaction . . . 38
2.5 Cell culture . . . 38
2.5.1 Tumour cell lines . . . 38

2.5.2 MAIT cell stimulations and culture . . . 40
2.5.3 T-cell activation and culture . . . 41
2.5.3.1 $CD8^+$/MAIT/γδ T-cell isolation and activation . . . 41
2.5.3.2 T-cell-melanoma cocultures . . . 42
2.5.4 Cell and cytokine assays . . . 42
2.5.4.1 Cytotoxicity assay . . . 42
2.5.4.2 ELISA analysis . . . 43
2.6 Flow cytometry analysis . . . 43
2.7 Data analysis . . . 46
2.7.1 Bioinformatic analysis . . . 46
2.7.2 Statistical analysis . . . 46

3 T-cells **47**
3.1 Summary . . . 47
3.1.1 Background . . . 47
3.1.2 Aims . . . 48
3.1.3 Experimental Approach . . . 48
3.2 Results . . . 49
3.2.1 Changes in PBMC composition and activation in response to ICB 49
3.2.1.1 cICB treatment leads to B-cell lymphopenia . . . 49
3.2.1.2 ICB-induced changes are unaffected by CMV serostatus 50
3.2.1.3 PD-1 loss observed in T-cells acts as a marker of efficient PD-1 blockade . . . 53
3.2.1.4 ICB induces T-cell activation within conventional subsets 55
3.2.2 Characterising the effect of melanoma on the $CD8^+$ T-cell transcriptome . . . 58
3.2.2.1 Age, sex and library RNA input contribute to RNAseq data variation . . . 58
3.2.2.2 T-cells are more proliferative in melanoma . . . 59
3.2.2.3 CMV infection is associated with distinct $CD8^+$ T-cell expression . . . 61
3.2.2.4 CMV serostatus doesn't influence the differential expression observed between healthy donor and melanoma patient $CD8^+$ T-cells . . . 62
3.2.3 Describing the $CD8^+$ T-cell ICB transcriptomic response . . . 63
3.2.3.1 $CD8^+$ T-cells have the strongest response to ICB . . . 63
3.2.3.2 $CD8^+$ T-cells become activated and proliferate in response to ICB . . . 65
3.2.3.3 cICB has larger effects on $CD8^+$ T-cell expression than sICB . . . 67
3.2.3.4 *TOX2*, *MKI67* and ICB binding are important for the $CD8^+$ T-cell ICB response . . . 69
3.2.3.5 $CD8^+$ T-cell ICB activation drives response in other cell types . . . 70
3.3 Conclusions . . . 75
3.4 Supporting Information . . . 77
3.5 Author Contributions . . . 88

4 B-cells **89**
4.1 Summary . . . 89
4.1.1 Background . . . 89
4.1.2 Aims . . . 90
4.1.3 Experimental Approach . . . 90
4.2 Results . . . 90
4.2.1 Phenotypic changes in B-cells following ICB treatment . . . 90
4.2.1.1 Dynamic changes in B-cell percentage and subset composition following cICB . . . 90
4.2.1.2 cICB induces potent B-cell activation . . . 94
4.2.1.3 B-cell loss is associated with changes in B-cell subsets and activation . . . 94
4.2.2 Dissecting the effects of melanoma and ICB on the peripheral B-cell transcriptome . . . 95
4.2.2.1 Age, sex and library RNA input contribute to RNAseq data variation . . . 95
4.2.2.2 Peripheral B-cells are highly activated in melanoma . . . 97
4.2.2.3 cICB induces transient transcriptomic changes in B-cells at C2 . . . 98
4.2.3 Deconvoluting B-cell subset scores from bulk RNAseq data . . . 99
4.2.3.1 Defining peripheral B-cell clusters . . . 99
4.2.3.2 Generating subset scores from bulk RNAseq data . . . 105
4.2.4 Contribution of monocytes, T-cells and NK cells to the B-cell ICB response . . . 108
4.2.4.1 $CD8^+$ T-cell activation confers B-cell response to cICB . 108
4.2.4.2 $CD8^+$ T-cell induction of *CXCL13* predicts B-cell changes to cICB . . . 112
4.3 Conclusions . . . 116
4.4 Supporting Information . . . 118
4.5 Author Contributions . . . 121

5 Adaptive immune cell repertoires **122**
5.1 Summary . . . 122
5.1.1 Background . . . 122
5.1.2 Aims . . . 123
5.1.3 Experimental Approach . . . 123
5.2 Results . . . 124
5.2.1 Comparison between peripheral BCR and TCR repertoires . . . 124
5.2.1.1 Summary of BCR and TCR repertoires . . . 124
5.2.1.2 *MiXCR* validation . . . 125
5.2.1.3 The BCR repertoire is more diverse than the TCR repertoire 127
5.2.2 CMV has profound effects on the $CD8^+$ T-cell TCR repertoire . . . 130
5.2.2.1 CMV infection reduces TCR diversity . . . 130
5.2.2.2 Peripheral MAIT cells are depleted in CMV^+ individuals 132
5.2.2.3 MAIT cells are depleted in SARS-CoV-2 infection . . . 136
5.2.2.4 MAIT cells associate with TCR diversity . . . 137
5.2.2.5 MAIT cell-associated genes are downregulated in $CD8^+$ T-cells in CMV^+ patients . . . 139

5.2.2.6 MAIT cell activation associates with cytotoxicity score in CMV$^+$ individuals . . . 141
5.2.2.7 CMV-associated features correlate with CMV-specific clone proportion . . . 143
5.2.3 Melanoma-associated BCR/TCR profiles . . . 145
5.2.3.1 No effect of melanoma on overall BCR and TCR clonality 145
5.2.3.2 Switched BCR clones are larger in melanoma . . . 146
5.2.3.3 Melanoma induces differential TCR usage . . . 148
5.2.4 The effect of ICB treatment on BCR and TCR repertoires . . . 149
5.2.4.1 ICB treatment has no effect on overall BCR and TCR diversity . . . 149
5.2.4.2 cICB induces CSR and SHM in BCR clones . . . 151
5.2.4.3 cICB induces a loss in circulating MAIT cells . . . 155
5.2.4.4 MAIT cells demonstrate cytotoxicity against melanoma cell lines . . . 160
5.2.5 Clonal dynamics . . . 167
5.2.5.1 Large clones at baseline persist following ICB treatment 167
5.2.5.2 Greater clonal changes are observed following cICB treatment . . . 168
5.2.5.3 BCR clonal expansion resolves at later time-points . . . 172
5.2.5.4 Expanding BCR clones are predominantly switched . . . 172
5.2.5.5 TCR clonal expansion resolves at later time-points . . . 174
5.2.5.6 MAIT cells are enriched in involuting clones after cICB . 176
5.2.5.7 BCR changes in response to ICB may be secondary to CD8$^+$ T-cell changes . . . 179
5.3 Conclusions . . . 181
5.4 Supporting Information . . . 184
5.5 Author Contributions . . . 214

6 Discussion **215**
6.1 CMV . . . 215
6.2 Metastatic melanoma . . . 217
6.3 ICB . . . 218
6.4 Summary of ICB mechanism of action . . . 222
6.5 Concluding remarks . . . 223

List of Figures

1.1 Melanoma has the highest tumour mutational burden of any cancer type 2
1.2 Mutations in Ras/Raf/MEK/ERK and PI3K/Akt pathways are enriched in melanoma . . . 3
1.3 The hallmarks of cancer . . . 8

2.1 Calculating fold change and relative expression from qPCR data . . . 40
2.2 Calculating cytotoxicity from MTT assays . . . 42
2.3 Calculating cytotoxicity from WST-8 assays . . . 43
2.4 Calculating antibody staining index . . . 44

3.1 B-cells are depleted at C2 . . . 49
3.2 Non-B-cell subsets remain stable at C2 . . . 50
3.3 T-cells are expanded in CMV$^+$ individuals . . . 51
3.4 CD8$^+$ T-cells form the majority of T-cells in CMV$^+$ individuals . . . 51
3.5 CMV infection results in an inflated Temra population . . . 52
3.6 MAIT cells are depleted in CMV$^+$ individuals . . . 53
3.7 CMV does not determine PBMC changes at C2 . . . 53
3.8 PD-1 is highly expressed by T-cells and successfully blocked at C2 . . . 54
3.9 Loss of surface PD-1 in T-cells is related to ICB binding . . . 55
3.10 cICB induces greater activation in T-cells than sICB . . . 56
3.11 ICB activation is limited to conventional T-cell subsets . . . 57
3.12 CD8$^+$ T-cell RNAseq sample summary . . . 58
3.13 Scree plot of early CD8$^+$ T-cell principal components . . . 59
3.14 Early principal components correlate with library RNA input, age and sex 60
3.15 Differential CD8$^+$ T-cell expression in metastatic melanoma . . . 61
3.16 CMV infection alters CD8$^+$ T-cell expression . . . 62
3.17 CMV does not contribute to the differential expression of CD8$^+$ T-cells observed in melanoma . . . 63
3.18 T-cells express the highest levels of *CTLA4* and *PDCD1* . . . 64
3.19 CD8$^+$ T-cells have the greatest transcriptomic response to ICB . . . 65
3.20 Induction of cell cycle-associated genes by CD8$^+$ T-cells at C2 . . . 66
3.21 ICB has no effect on the CD8$^+$ T-cell response to stimulation . . . 67
3.22 cICB induces similar genes to sICB, but to a higher magnitude . . . 68
3.23 Expression of CD8$^+$ T-cell *TOX2* and *MKI67* is associated with CD8$^+$ T-cell ICB response . . . 69
3.24 Direct ICB binding correlates with CD8$^+$ T-cell ICB response . . . 70
3.25 CD8$^+$ T-cell ICB response is important for activation in other cell types 71
3.26 CD8$^+$ T-cell ICB response is not dependent on activation in other subsets 72
3.27 CD14$^+$ monocyte, CD19$^+$ B-cell and NK cell expression of interferon-stimulated genes associates with the CD8$^+$ T-cell ICB response 74

3.28 Comparison of genes upregulated at C2 between different PBMC subsets 74
S3.1 Panel B1 flow cytometry gating strategy of PBMC subsets 77
S3.2 tSNE of panel B1 PBMC flow cytometry data 78
S3.3 B-cells are depleted after cICB 78
S3.4 Panel T2 flow cytometry gating strategy of T-cells 79
S3.5 Panel M3 flow cytometry gating strategy of T-cells 79
S3.6 No changes observed in non-B-cell subsets at C2 regardless of treatment type 80
S3.7 CMV inflates the Temra population for both $CD4^+$ and $CD8^+$ T-cells . 81
S3.8 PBMC subsets associated with CMV do not correlate with anti-CMV IgG antibody titre 82
S3.9 CMV has no effect on subset changes in response to ICB 83
S3.10 CMV does not associate with clinical outcome 84
S3.11 More IgG4 detected on $CD8^+$ T-cells following cICB 85
S3.12 Both $CD4^+$ and $CD8^+$T-cells become activated in response to ICB . . . 85
S3.13 Double positive $CD4^+$ $CD8^+$ T-cells are enriched for unconventional T-cells 86
S3.14 Principal component analysis of PBMC RNAseq samples 87
S3.15 Library RNA input associates with early principal components for all PBMC types 87
S3.16 T-cell response to stimulation is unaffected by ICB regardless of treatment type 88

4.1 cICB induces B-cell lymphopenia 91
4.2 Patients with low B-cell percentage have longer survival 92
4.3 cICB promotes ASC differentiation 93
4.4 cICB upregulates markers of B-cell activation 94
4.5 B-cell decline correlates with B-cell differentiation and activation 95
4.6 B-cell RNAseq sample summary 96
4.7 Scree plot of early $CD19^+$ B-cell principal components and association with sex 96
4.8 Early $CD19^+$ B-cell principal components correlate with library RNA input, age and sex 97
4.9 Peripheral B-cells are activated in melanoma 98
4.10 cICB induces expression changes in peripheral B-cells 101
4.11 Single cell feature summary 101
4.12 Determining the optimal number of principal components for analysis . 102
4.13 Determining optimal resolution using Clustree analysis 103
4.14 $CD19^+$ B-cell Seurat cluster annotations 104
4.15 Final $CD19^+$ B-cell cluster annotations 105
4.16 Validating $CD19^+$ B-cell subset deconvolution from bulk RNAseq data 105
4.17 Deconvoluted $CD19^+$ B-cell subset scores show an increase in ASC score following cICB treatment 106
4.18 Subset annotation from public single cell B-cell datasets 107
4.19 ASC scores generated using online datasets are increased following cICB 107
4.20 ASC induction prolongs survival 108
4.21 Baseline T-cell PD-1 expression associates with B-cell ICB response . . 109
4.22 B-cell expression of interferon-associated genes correlates with cICB response 110

4.23 $CD8^+$ T-cell gene expression determines B-cell cICB response 111
4.24 $CD8^+$ T-cell activation associates with B-cell cICB response 111
4.25 B-cell ICB score correlates with B-cell loss and ASC induction 112
4.26 *CXCL13* is induced by $CD8^+$ T-cells in melanoma 113
4.27 $CD8^+$ T-cells induce *CXCL13* at C2 114
4.28 CXCL13 correlates with the peripheral B-cell depletion observed after cICB 115
S4.1 Panel B5 B-cell subset flow gating strategy 118
S4.2 cICB causes B-cell depletion in the periphery 119
S4.3 B-cell tSNE clustering of panel B5 flow cytometry data 119
S4.4 Antibody panel B5 identifies B-cell subsets and validates peripheral B-cell depletion 120
S4.5 Induction of CXCL10 at C2 following cICB associates with peripheral T-cell depletion 121
S4.6 Single cell B-cell clusters and marker expression 121

5.1 Summarised BCR/TCR CDR3 amino acid sequences 125
5.2 *MiXCR*-aligned TCR data corresponds with qPCR and flow cytometry analyses 126
5.3 *MiXCR* IGHC alignment correlates with flow cytometry ASC percentage 126
5.4 The BCR repertoire displays greater diversity than the $CD8^+$ T-cell TCR repertoire 128
5.5 The TCR repertoire is made up of more large clones than the BCR repertoire 129
5.6 BCR clones are more synonymous than TCR clones 129
5.7 BCR clones have longer CDR3 nucleotide sequences and more mutations than TCR clones 130
5.8 CMV serostatus associates with enlarged TCR clones 131
5.9 $CD8^+$ T-cells are more clonal in CMV^+ individuals 132
5.10 CMV^+ individuals have more large T-cell clones 133
5.11 CMV infection induces differential TCR usage 134
5.12 Peripheral MAIT cells are depleted in CMV^+ individuals 135
5.13 CMV increases γδ T-cell clonal unevenness 136
5.14 Peripheral MAIT cells are depleted in SARS-CoV-2 infection 137
5.15 $CD8^+$ MAIT cell percentage associates with NK cells and T-cell differentiation 138
5.16 Unconventional T-cells associate with TCR diversity and clonal unevenness 138
5.17 $CD8^+$ T-cell genes associated with MAIT and γδ T-cells 139
5.18 MAIT cell-associated genes are downregulated in CMV^+ individuals . . 140
5.19 Unconventional T-cells associate with overall $CD8^+$ T-cell cytotoxicity score 141
5.20 MAIT cell activation correlates with overall $CD8^+$ T-cell cytotoxicity score 142
5.21 MAIT cells are more activated in CMV^+ individuals 142
5.22 The association of MAIT cell activation with MAIT cell percentage and $CD8^+$ T-cell cytotoxicity score is dependent on CMV serostatus 143
5.23 CMV-specific and CMV-associated clones are found more highly expressed by CMV^+ patients 144
5.24 Carriage of CMV-specific clones correlates with CMV-associated factors 145

5.25 No difference in BCR/TCR clone number or size in melanoma patients 146
5.26 Differential BCR usage in melanoma patients 147
5.27 Switched BCR clones are larger in melanoma patients 148
5.28 Differential TCR usage in melanoma patients 149
5.29 BCR and TCR average clone number and size are unaffected by ICB treatment 150
5.30 Patients with low TCR clonality at C4 have favourable outcomes 151
5.31 cICB induces differential BCR gene expression 152
5.32 Increased CSR is observed at C2 following cICB treatment 154
5.33 cICB increases the BCR mutation rate at C2 154
5.34 ICB-induced CSR associates with the $CD8^+$ T-cell ICB response 155
5.35 MAIT cell-associated TCR genes are downregulated following cICB treatment 156
5.36 MAIT cells are depleted following cICB treatment 157
5.37 MAIT cell-associated genes are downregulated after cICB treatment . . 158
5.38 MAIT cell percentage inversely correlates with plasma CXCL10 159
5.39 $TRAJ33^+$ MAIT cell loss associates with $CD8^+$ T-cell ICB response, but not $CD19^+$ B-cell ICB response 160
5.40 MAIT cell loss associates with an increase in cytotoxicity score at C2 . 161
5.41 MAIT cells demonstrate antimelanoma cytotoxicity 162
5.42 Culture with T-cell expander beads improves melanoma-specific cytotoxicity 163
5.43 Expression of cytolytic MAIT cytokines associates with melanoma cytotoxicity 163
5.44 MAIT cells contribute to antimelanoma cytotoxicity 165
5.45 Maintenance of peripheral MAIT cell populations at C4 associates with survival 166
5.46 The majority of baseline BCR and TCR clones by CDR3 nucleotide sequence are lost following ICB treatment 167
5.47 Most large clones at baseline persist after ICB treatment 168
5.48 ICB induces changes in BCR and TCR clone proportions 170
5.49 cICB induces more clonal changes in BCR and TCR clones than sICB treatment 170
5.50 Patients with a higher level of novel TCR clones at C2 have enhanced survival 171
5.51 Significantly expanding BCR clones are reduced at later time-points . . 172
5.52 Expanding BCR clones are predominantly switched and highly mutated 173
5.53 Most novel BCR clones at C2 are switched 174
5.54 Significantly expanding TCR clones are reduced at later time-points . . 175
5.55 Differential TCR usage of expanding clones 176
5.56 MAIT cell clones are enriched in involuting TCR clones following cICB 177
5.57 Cancer-specific and CMV-specific clones are unaffected by ICB and persist as large clones 179
5.58 B-cell and $CD8^+$ T-cell ICB responses are linked 180
S5.1 BCR/TCR contamination is minimal 184
S5.2 The BCR is expressed more highly than the TCR 184
S5.3 Switched BCR clones express a higher level of BCR 185

S5.4 *MiXCR* IGHC alignment correlates with flow cytometry plasma cell percentage . . . 185
S5.5 Library RNA input associates with the number of BCR and TCR reads detected . . . 186
S5.6 The top BCR clones constitute a lower proportion of the repertoire than the top TCR clones . . . 186
S5.7 Interchain variation in BCR and TCR diversity . . . 187
S5.8 BCR and TCR mutations are differentially enriched by gene segment, chain and isotype . . . 188
S5.9 BCR light chain usage is unaffected in CMV^+ patients . . . 189
S5.10 CMV infection has no effect on IGHC usage . . . 189
S5.11 CMV has no impact on BCR mutation rate . . . 190
S5.12 MAIT cell TCR and CD161 are downregulated in response to TCR-mediated activation . . . 190
S5.13 MAIT cell TCR and CD161 downregulation associate with activation . . . 191
S5.14 CMV has no effect on MAIT cell response to stimulation . . . 192
S5.15 CMV-specific and CMV-associated clones are more highly expressed by CMV^+ patients according to HLA type . . . 194
S5.16 More TCR clones of size 0.1-0.5% are found in melanoma . . . 194
S5.17 No differences are observed in BCR or TCR diversity indexes between healthy donors and melanoma patients . . . 195
S5.18 BCR light chain usage is unaffected in melanoma . . . 196
S5.19 Melanoma has no effect on BCR mutation rate . . . 196
S5.20 No differences in unconventional T-cell composition are observed in melanoma . . . 197
S5.21 ICB has no effect on BCR and TCR clone number and size at C4 . . . 198
S5.22 ICB has no effect on BCR or TCR clone proportion regardless of size . . . 199
S5.23 No differences in BCR or TCR diversity indexes are detected after ICB treatment . . . 200
S5.24 ICB treatment has no effect on BCR light chain usage . . . 201
S5.25 A higher induction of switched BCR clones is observed following cICB treatment . . . 201
S5.26 Changes in IGHC usage resolve by C4 . . . 202
S5.27 ICB increases the mutation rate in BCR clones regardless of chain . . . 203
S5.28 MAIT cell-associated TCR genes remain depleted at C4, but resolve by later time-points following cICB treatment . . . 203
S5.29 cICB maintains MAIT cell depletion at C4 with MAIT cell loss restricted to CMV^- patients . . . 204
S5.30 cICB has no effect on MAIT cell diversity indexes . . . 205
S5.31 ICB treatment has no effect on the MAIT cell response to stimulation . . . 206
S5.32 Expanded T-cells have broad cytotoxicity against melanoma cell lines . . . 207
S5.33 MAIT cells have antimelanoma cytotoxic potential against a variety of melanoma cell lines . . . 208
S5.34 The majority of baseline BCR and TCR clones by CDR3 amino acid sequence are lost following ICB treatment . . . 209
S5.35 ICB induces greater changes in BCR light chain clones . . . 209
S5.36 The healthy donor TCR repertoire remains largely stable over the course of three weeks . . . 210

S5.37 Clonal changes in the TCR repertoire following ICB treatment exceed background fluctuations . . . 210
S5.38 cICB induces greater clonal changes in the TCR repertoire than sICB at C4 . . . 211
S5.39 Significantly involuted BCR clones after ICB treatment resolve at later time-points . . . 211
S5.40 No difference is observed in CSR in clones persisting at C4 . . . 212
S5.41 Significantly involuted TCR clones after ICB treatment resolve at later time-points . . . 213

6.1 Working model of ICB response . . . 224

List of Tables

1.1 Inhibitory immune checkpoint proteins . . . 9

2.1 Sample cohort . . . 29
2.2 Summary of MM patient clinical outcomes . . . 29
2.3 Summary of bulk RNAseq samples . . . 32
2.4 qPCR primer list . . . 39
2.5 qPCR cycling stages . . . 40
2.6 Melanoma cell line ExPASy characterisation . . . 40
2.7 Flow cytometry antibody summary . . . 45

5.1 BCR clonal summary for $CD19^+$ B-cell samples . . . 124
5.2 TCR clonal summary for $CD8^+$ T-cell samples . . . 124

Abbreviations

Abbreviation	Term
5-OP-RU	5-(2-oxopropylideneamino)-6-d-ribitylaminouracil
A2AR	Adenosine A2A receptor
Ac-6-FP	Acetyl-6-formylpterin
ADCC	Antibody-dependent cellular cytotoxicity
ADCP	Antibody-dependent cellular phagocytosis
ADP	Adenosine diphosphate
AF647	Alexa Fluor® 647
AF700	Alexa Fluor® 700
AID	Activation-induced cytidine deaminase
AIRE	Autoimmune regulator protein
AMP	Adenosine monophosphate
APC	Allophycocyanin
APC/Cy7	Allophycocyanin/Cyanine7 tandem fluorophore
ASC	Antibody-secreting cell including plasmablasts and plasma cells
ATP	Adenosine triphosphate
β-ME	Beta-mercaptoethanol
BCR	B-cell receptor
Bmem	Memory B-cell
Bn	Naïve B-cell
bp	Base pairs
BTLA	B- and T-lymphocyte attenuator (CD272)
Btr	Transitional B-cell
BV421	Brilliant Violet 421™
BV510	Brilliant Violet 510™
BV605	Brilliant Violet 605™
BV650	Brilliant Violet 650™
BV711	Brilliant Violet 711™
BV785	Brilliant Violet 785™
C gene segment	Constant gene segment
C1	Cycle 1 (day 0)
C2	Cycle 2 (day 21)
C4	Cycle 4 (day 63)
CC	Critical SARS-CoV-2 infection
CD	Cluster of differentiation
cDNA	Complementary DNA
CDR	Complementarity determining region
cICB	Combination ICB

Abbreviation	Term
CM	Mild SARS-CoV-2 infection
CMV	Human cytomegalovirus
CO_2	Carbon dioxide
CRC	Colorectal cancer
CS	Severe SARS-CoV-2 infection
CSiN	Cauchy-Schwarz index of neoantigens
CSR	Class switch recombination
CTCAE	National Cancer Institute common terminology criteria for adverse events
CTLA-4	Cytotoxic T-lymphocyte-associated protein 4 (CD152)
CXCL	C-X-C motif ligand
D gene segment	Diversity gene segment
D10 Media	DMEM, 10% FBS, 2mM L-Glut, 100U/ml P/S
DC	Dendritic cell
DEG	Differentially expressed gene
DMEM	Dulbecco's Modified Eagle's Medium
DMSO	Dimethyl sulphoxide
DN	Double negative $CD27^-$ IgD^- B-cell or $CD4^-$ $CD8^-$ T-cell
DNA	Deoxyribonucleic acid
DP	Double positive $CD4^+$ $CD8^+$ T-cell
dsDNA	Double stranded DNA
EDTA	Ethylenediaminetetraacetic acid
ELISA	Enzyme-linked immunosorbent assay
FBS	Heat-inactivated foetal bovine serum
FC	Fold change
FITC	Fluorescein isothiocyanate
FMO	Fluorescence minus one
FSC-A	Forward scatter by area
GBP	Guanylate binding protein
GC	Guanine/Cytosine
GEX	Whole gene expression
GITR	Glucocorticoid-induced TNFR-related protein (CD357)
GOBP	Gene ontology biological processes
GZMB	Granzyme B
HBSS	Hank's balanced salt solution
HD	Healthy donor
HEPES	4-(2-hydroxyethyl)-1-piperazineethanesulphonic acid
HIV	Human immunodeficiency virus
HLA	Human leukocyte antigen
HNSCC	Head and neck squamous cell carcinoma
HOBIT	Homolog of Blimp-1 in T-cells (*ZNF683*)
HVEM	Herpesvirus entry mediator (CD270)
ICB	Immune checkpoint blockade
ICOS	Inducible T-cell costimulator (CD278)
IFN	Interferon
IGH	BCR heavy chain
IGHC	BCR heavy chain constant gene

Abbreviation	Term
IGHD	BCR heavy chain diversity gene
IGHJ	BCR heavy chain joining gene
IGHV	BCR heavy chain variable gene
IGK	BCR-κ light chain
IGKC	BCR-κ light chain constant gene
IGKJ	BCR-κ light chain joining gene
IGKV	BCR-κ light chain variable gene
IGL	BCR-λ light chain
IGLC	BCR-λ light chain constant gene
IGLJ	BCR-λ light chain joining gene
IGLV	BCR-λ light chain variable gene
IL	Interleukin
iNKT	Type I invariant natural killer T-cell
Iono	Ionomycin
irAE	Immune-related adverse event
irRECIST.1.1	Immune-related response evaluation criteria in solid tumors v1.1
ITAM	Immunoreceptor tyrosine-based activation motif
ITIM	Immunoreceptor tyrosine-based inhibitory motif
ITSM	Immunoreceptor tyrosine-based switch motif
J gene segment	Joining gene segment
Kb	Kilobases
L-Glut	L-Glutamine solution
LAG-3	Lymphocyte-activation gene 3 (CD223)
LPS	Lipopolysaccharide
MACS	Magnetic-activated bead sorting
MACS buffer	50ml HBSS, 0.5% FBS, 2mM EDTA
MAIT cell	Mucosal-associated invariant T-cell
Mb	Megabase
MC1R	Melanocortin 1 receptor
MDSC	Myeloid-derived suppressor cell
MFI	Median fluorescence intensity
MHC	Major histocompatibility complex
MM	Metastatic melanoma
MMR	Mismatch repair
MR1	Major histocompatibility complex, class I-related
MSI	Microsatellite instability
MTT	3-(4,5-Dimethylthiazol-2-yl)-2,5-Diphenyltetrazolium Bromide
NAD(P)H	Nitrite reductase
Near-IR	Near-infrared
NER	Nucleotide excision repair
NET	Neutrophil extracellular trap
NICE	National Institute for Health and Care Excellence
NIHR	National Institute for Health Research
NK cells	Natural killer cells
NKT cells	Natural killer T-cells
ns	Not significant
NSCLC	Non-small cell lung cancer

Abbreviation	Term
OS	Overall survival
P/S	Penicillin/Streptomycin
padj	Adjusted p-value
PBMC	Peripheral blood mononuclear cell
PBMCs-MAITs	MAIT cell-depleted PBMCs
PC	Principal component
PCA	Principal component analysis
PCR	Polymerase chain reaction
PD-1	Programmed cell death protein 1 (CD279, *PDCD1*)
PD-L1	Programme death ligand 1 (B7-H1, *CD274*)
PD-L2	Programme death ligand 2 (B7-H2, *PDCD1LG2*)
PE	Phycoerythrin
PE/Cy7	Phycoerythrin/Cyanine7 tandem fluorophore
PE/Dazzle 594	Phycoerythrin/Dazzle^{TM} 594 tandem fluorophore
PE-Vio770	Phycoerythrin/Violet® 770 tandem fluorophore
PFS	Progression-free survival
PMA	Phorbol myristate acetate
PMA/IONO	Phorbol myristate acetate and Ionomycin
pMHC	Peptide/MHC complex
qPCR	Quantitative PCR
R5 Media	RPMI 1640, 10% FBS, 5% human AB serum, 2mM L-Glut, 100U/ml P/S, 15mM HEPES, 0.1mM NEAA, 1mM sodium pyruvate, 50µM β-ME
R10 Media	RPMI 1640, 10% FBS, 2mM L-Glut, 100U/ml P/S
RCC	Renal cell carcinoma
RLT buffer	Buffer RLT Plus supplemented with either 2M Dithiothreitol or 0.143M β-mercaptoethanol
RNA	Ribonucleic acid
RNAseq	RNA sequencing
RORγT	Retinoid-related orphan receptor (*RORC*)
ROS	Reactive oxygen species
RPMI	Roswell Park Memorial Institute
rSD	Relative standard deviation
SARS-CoV-2	Severe acute respiratory syndrome coronavirus 2
SD	Standard deviation
SHM	Somatic hypermutation
sICB	Single agent ICB
SM	Switched memory B-cell
SSC-A	Side scatter by area
SSC-H	Side scatter by height
Staining buffer	5% FBS, 95% HBSS
TAM	Tumour-associated macrophage
Tcm	Central memory T-cell
TCR	T-cell receptor
Tem	Effector memory T-cell
Temra	Effector memory T-cell re-expressing CD45RA
Tfh	Follicular helper T-cell

Abbreviation	Term
TIGIT	T-cell immunoreceptor with Ig and ITIM domains
TIL	Tumour-infiltrating lymphocyte
TIM-3	T-cell immunoglobulin and mucin-domain containing-3 (CD366, *HAVCR2*)
TLR	Toll-like receptor
TLS	Tertiary lymphoid structure
TMB	Tumour mutational burden
TME	Tumour microenvironment
Tn	Naïve T-cell
TNF	Tumour necrosis factor
Tr	Transitional B-cell
TRA	TCR-α chain
TRAC	TCR-α chain constant gene
TRAJ	TCR-α chain joining gene
TRAV	TCR-α chain variable gene
TRB	TCR-β chain
TRBC	TCR-β chain constant gene
TRBD	TCR-β chain diversity gene
TRBJ	TCR-β chain joining gene
TRBV	TCR-β chain variable gene
TRD	TCR-δ chain
TRDC	TCR-δ chain constant gene
TRDD	TCR-δ chain diversity gene
TRDJ	TCR-δ chain joining gene
TRDV	TCR-δ chain variable gene
Treg	Regulatory T-cell
TRG	TCR-γ chain
TRGC	TCR-γ chain constant gene
TRGJ	TCR-γ chain joining gene
TRGV	TCR-γ chain variable gene
tSNE	t-distributed stochastic neighbor embedding
U/ml	Units per millilitre
UCC	Urothelial cell carcinoma
UCSC	University of California, Santa Cruz
UMAP	Uniform manifold approximation and projection
UMI	Unique molecular identifier
USM	Unswitched memory B-cell
UT	Untreated
UV	Ultraviolet
V gene segment	Variable gene segment
VEGF	Vascular endothelial growth factor
VISTA	V-domain Ig suppressor of T-cell activation (B7-H5)
WST-8	2-(2-methoxy-4-nitrophenyl)-3-(4-nitrophenyl)-5-(2,4-disulphophenyl)-2H -tetrazolium,monosodium salt

Chapter 1

Introduction

1.1 Melanoma

1.1.1 Overview

Cutaneous melanoma arises from the neoplastic transformation of melanocytes and is the most aggressive form of skin cancer, representing the fifth most prevalent cancer in the UK[1]. In most cases, melanoma development is linked to ultraviolet (UV) exposure which induces DNA damage, oxidative stress and inflammation, all of which stimulate melanomagenesis. Melanoma is typically removed via surgical excision and has high survival rates with 87.4% of people surviving ten years following diagnosis (2013-2017)[1]. However, unresectable and metastatic disease has been historically difficult to treat due to low sensitivity to chemotherapy and radiotherapy[2–6].

1.1.2 Melanomagenesis

1.1.2.1 Mutagenesis

Melanoma has the highest mutation rate of any cancer with up to 100 mutations detected per Mb[7,8] (Figure 1.1). However, the mutation rate in melanoma is highly variable and depends on the origin of the primary tumour and the types of genes mutated.

Tumours in sun-exposed areas are typically reflective of chronic UV exposure and are characterised by a higher number of mutations. UV radiation is broadly categorised into three subtypes based on wavelength including UV-A (315nm-400nm), UV-B (280nm-315nm) and UV-C (100nm–280nm). UV radiation induces two major types of mutagenic DNA lesion including cyclobutane pyrimidine dimers and 6-4 photoproducts which form between adjacent pyrimidines[9]. The formation of these products ultimately interferes with DNA structure and alters transcription. Such lesions are targeted for removal by nucleotide excision repair (NER)[10], however, dysregulation of NER-associated genes can inhibit this process and ultimately increase the risk of melanoma. Xeroderma pigmentosum, a disease which causes extreme sensitivity to UV radiation, arises from genetic defects in NER and is associated with a 1,000-fold increased risk of skin cancer[11]. Accordingly, insufficient repair of skin cancer-associated mutations may be the cause of subsequent melanomagenesis[12,13].

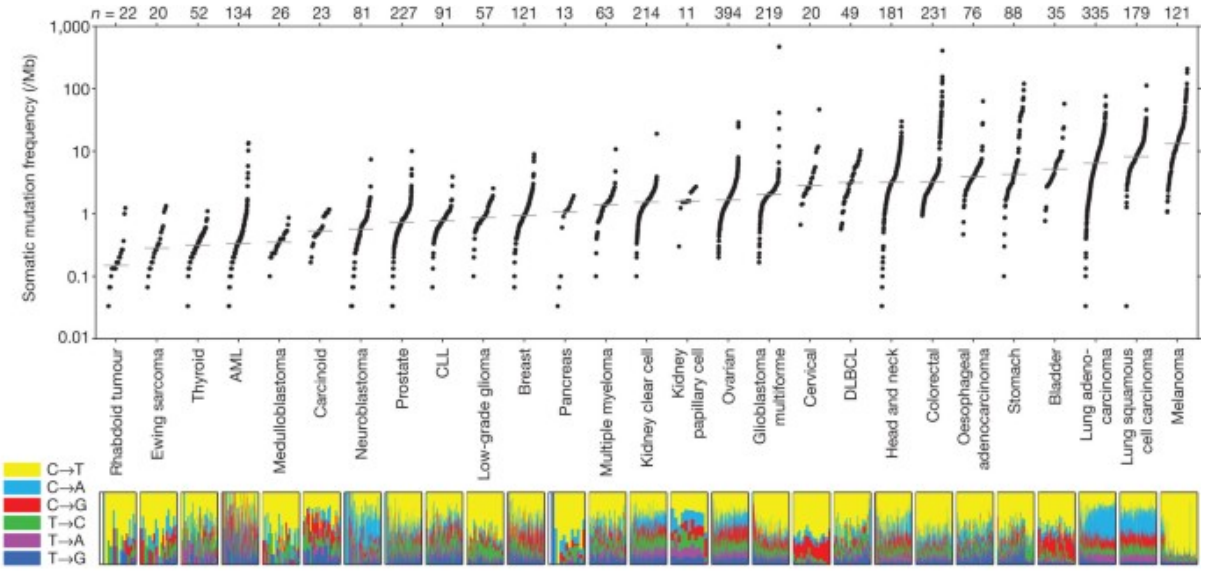


Figure 1.1 Melanoma has the highest tumour mutational burden of any cancer type
Somatic mutation frequency per megabase (Mb) and mutation-associated nucleotide substitutions are compared between different tumour types. Sample sizes are displayed above. Figure is taken from Lawrence *et al.* (2013)[7].

These mutagenic DNA lesions are produced much more efficiently by UV-B and UV-C wavelengths than UV-A, with production of cyclobutane pyrimidine dimers responsible for 85% of mutations induced by UV-B radiation[14]. Whilst UV-B and UV-C radiation are highly absorbed by DNA, and thus able to induce direct DNA damage, UV-A is poorly absorbed. However, UV-A radiation has the capacity to induce reactive oxygen species (ROS), oxidative DNA damage and strand breaks, resulting in generation of 8-oxo-7,8-dihydro-2'-deoxyguanosine oxidative DNA lesions[15–17]. The effects of UV-A radiation are hence dependent on oxygen, oxidases and endogenous photosensitisers which induce protumourigenic ROS including H_2O_2[18,19]. As a result, whilst UV-B and UV-C can cause immediate DNA damage, the effects of UV-A are delayed and occur indirectly through the generation of ROS and subsequent inflammation[20].

1.1.2.2 Common mutations

Melanoma is characterised by a preponderance of UV-associated C->T transition mutations (Figure 1.1) which are found in 46% of driver mutations[7,8,21]. Genetic drivers of melanoma include genes associated with proliferation (*BRAF*, *NRAS*, *NF1*), cell growth (*PTEN*, *KIT*), apoptosis (*TP53*) and the cell cycle (*CDKN2A*, *TERT*)[21–31]. Interestingly, many of these genes are enriched within both Ras/Raf/MEK/ERK and PI3K/Akt pathways, with these somatic mutations inducing signalling via mitogenic pathways (Figure 1.2).

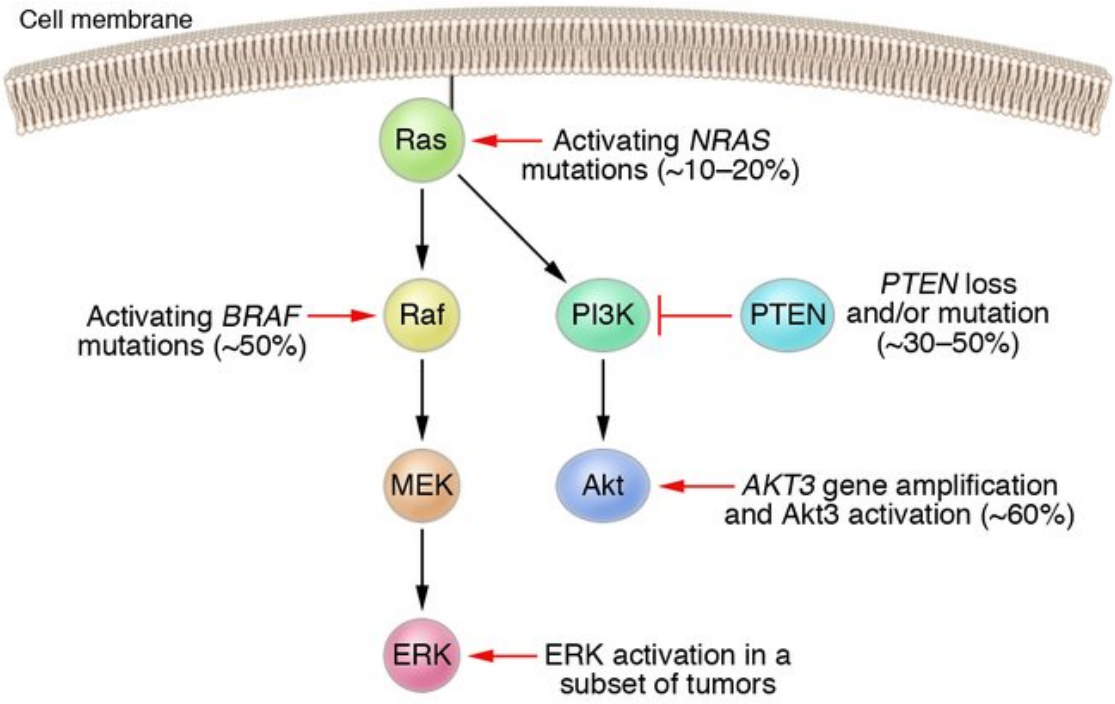


Figure 1.2 Mutations in Ras/Raf/MEK/ERK and PI3K/Akt pathways are enriched in melanoma The signalling cascades for Ras/Raf/MEK/ERK and PI3K/Akt pathways are visualised. Melanoma-associated mutations are highlighted per pathway member with percentage representing the percentage of melanoma cases in which these mutations occur. Figure is taken from Chudnovsky *et al.* (2005)[32].

Genes associated with proliferative activity are frequently mutated in melanoma. Common melanoma driver mutations limit suppressor genes, notably *NF1* which functions to inhibit Ras activation through its GTPase activity. Loss-of-function mutations in *NF1* are the third most commonly identified somatic mutation in melanoma and result in constitutive N-ras activation and downstream signalling[25,33]. Activating missense mutations in *NRAS* represent the second most commonly detected mutation in melanoma, present in 15-30% of cases[25,28,34,35]. These mutations prolong GTP binding and thus N-ras GTPase activity[36]. Upon activation, N-ras then goes on to activate the kinase B-Raf which has an essential role in MEK phosphorylation and subsequent MAPK activation[26]. Activating missense mutations in *BRAF* are the most commonly detected mutation in melanoma, present in 39-66% of malignant melanomas[25,27]. The majority of *BRAF* mutations typically involve substitution of valine at $BRAF^{V600}$ for glutamic acid ($BRAF^{V600E}$)[27,37], altering the conformation of B-Raf such that it is constitutively active[38]. $BRAF^{V600E}$ and *NRAS* mutations, occurring in 52-73% and 15-30% of melanoma cases respectively, are mutually exclusive[27,28,37,39,40]. Whereas, about half of tumours with wild type *NRAS* or *BRAF* are *NF1* mutants[25].

Melanomas secondary to chronic UV exposure are typically characterised by a high tumour mutational burden, however, melanomas occurring in less sun-exposed sites often arise at a younger age, have a lower mutational load and are associated with $BRAF^{V600E}$ mutations. Whilst most melanoma cases are associated with UV exposure, the rest are related to non-UV-induced somatic mutations or genetic predisposition. Genome-wide association studies have led to the identification of several genomic loci that are associated with melanoma susceptibility[41–45]. In particular, mutations within the gene encoding

melanocortin 1 receptor (MC1R), which determines skin pigmentation, are found to increase the chance of cutaneous melanoma by 40%[41,43,46]. As a result, individuals with a fair complexion are more genetically predisposed to melanoma.

In addition, patients with germline mutations in *CDKN2A* are associated with a 65-fold increased risk of melanoma, developing melanoma 15 years earlier than average[47–49]. Furthermore, *CDKN2A*-mutation carriers had worse survival than melanoma patients with wild type *CDKN2A*[47,48]. *CDKN2A* is a tumour suppressor gene that regulates cell cycle mediator CDK4, important for downstream MAPK activity, and hence tumour growth. Germline mutations in *CDK4* and *TERT* are also thought to predispose to melanoma, although these mutations are rare[50–52].

1.1.3 Immune involvement

1.1.3.1 Overview

Somatic mutations, crucial for cancer development, can result in the formation of novel proteins, referred to as neoantigens, which may be recognised as "foreign" by the immune system. Strikingly, numerous observations of spontaneous melanoma regression have been made over the years and are attributed to successful immune recognition and enhanced cytotoxicity[53–58]. The substantial mutational burden of melanoma makes it a highly immunogenic tumour due to enhanced expression of novel epitopes and subsequent immune recognition. Consequently, melanoma is associated with extensive immune cell infiltration and is considered an "immune-warm" tumour. Correspondingly, the presence of tumour-infiltrating lymphocytes (TILs) within melanoma tissue is associated with reduced tumour progression, lymph node involvement and metastasis, where TILs have been found to have direct cytotoxic effects on autologous tumours[59–67]. This relationship between immunosurveillance and tumour immunogenicity, known as cancer immunoediting, is categorised into three stages: elimination, equilibrium and escape[68].

1.1.3.2 Elimination

Within the elimination phase, both innate and adaptive immune systems detect and eradicate cancerous cells during early melanoma development before it is even clinically detectable. Production of inflammatory cytokines by melanoma cells and associated stroma firstly recruits cells of the innate immune system including neutrophils, macrophages and NK cells. These innate immune cells are able to eliminate melanoma cells through phagocytosis, degranulation, antibody-dependent cellular cytotoxicity (ADCC) and production of cytotoxic molecules including IFN-γ, TNF-α and ROS, to name a few.

During phagocytosis, cancer cells are internalised by phagocytic cells into a phagosome which then fuses with a lysosome to create a phagolysosome. Within these phagolysosomes, degranulation results in the release of digestive enzymes and ROS to induce respiratory burst and break down the cancer cell. Similarly, cells may release these antimicrobial peptides and ROS extracellularly to exert damage.

Innate immune cells are also able to mediate ADCC of cancer cells through expression of Fc receptors which bind the Fc portion of antibodies. This is important for recognition of antibody-opsonised antigen and eliciting anticancer responses through Fc receptor signalling and subsequent production of cytolytic molecules.

Neutrophils form the majority of granulocytes and migrate to tumours, predominantly in response to IL-8 (CXCL8) gradients. Although neutrophils are generally considered to be protumourigenic due to their immunosuppressive effects, they have also been shown to have roles in antitumour immunity[69]. Neutrophils help eradicate cancer cells through ADCC, phagocytosis, degranulation and production of neutrophil extracellular traps (NETs)[70–72]. Chromatin fibres coated with antimicrobial peptides, known as NETs, can be extruded through a process known as NETosis and have been found to trap melanoma cells, limit tumour growth and metastasis[72]. The importance of neutrophils is also highlighted in cancer patients receiving antibody therapies, whereby neutrophil-mediated ADCC, antibody-dependent cellular phagocytosis (ADCP) and trogocytosis of cancer cells[73–75] are found to enhance tumour killing[76–78].

Macrophages are derived from monocyte differentiation and typically reside within the tissue. M1 macrophages are activated in response to IFN-γ and exert most of their anticancer effects through direct ADCP of cancer cells[79,80]. However, macrophages also have a role in antigen presentation[80–82] and cytokine production. This includes secretion of proinflammatory cytokines IL-6, TNF-α and IL-12 which activate NK cells and polarise T-cell differentiation.

NK cells are a class of innate lymphoid cell able to mount rapid immune responses due to their ability to detect cancer in the absence of activation, antibodies and MHC, hence coining them "Natural Killer cells". NK cells are typically activated in response to antibody-opsonised antigen, stress-induced ligands, MHC downregulation or proinflammatory cytokines including IL-12, IL-15 and IL-18. The majority of NK cells express Fc receptors, allowing them to induce profound ADCC, and have been observed to enhance antibody therapies for cancer via this mechanism[76]. The extent of NK cell function is determined by the balance of activating and inhibitory receptor signalling. Whereas activating receptors (natural cytotoxicity receptors and Fc receptors) detect tumour-associated stress-induced ligands, including ULBPs and MICA/MICB, or antibody-opsonised tumour, inhibitory receptors (killer-cell immunoglobulin-like receptors) recognise MHCI. Thus, in instances of immune evasion in which cancer cells downregulate MHCI to avoid T-cell detection, there is less signalling by inhibitory receptors and the balance is tipped in favour of activation. NK cells are then able to elicit their effector function, primarily through secretion of cytolytic molecules including IFN-γ, TNF-α as well as perforin and granzymes which are stored in cytotoxic granules. IFN-γ is important for macrophage activation, MHC upregulation and T-cell differentiation, activation and proliferation, whereas, TNF-α induces inflammation. Perforin and granzymes induce apoptosis, with perforin creating pores in target cell membranes to facilitate diffusion of granzymes which in turn, activate caspases and subsequent apoptosis of target cells. Together, secretion of these highly cytolytic molecules results in melanoma cell lysis.

Dendritic cells (DCs) are professional antigen presenting cells that sample tumour debris and present processed antigen. In doing this, DCs bridge the gap between innate and adaptive immune systems in which they migrate to draining lymph nodes or secondary lymphoid organs where they activate B-cells and T-cells. Here, DCs present antigen to T-cells through T-cell receptor (TCR)/MHC interactions and provide the necessary costimulatory signals and cytokines required to stimulate differentiation into effector cells. However, follicular DCs, residing in the B-cell areas of lymphoid tissue, are involved in B-cell recruitment, organisation of germinal centres and trapping opsonised antigen through complement and Fc receptors for subsequent presentation. A higher

DC density is associated with greater infiltration of activated T-cells and as a result, a reduced melanoma thickness[83].

B-cells form part of the adaptive immune system and are responsible for antibody production, T-cell activation and antigen presentation. Naïve B-cells are found within lymphoid organs, which receive a supply of tumour-associated antigen via the lymphatic system, and are able to detect native antigen through either expression of pattern recognition receptors or their B-cell receptor (BCR). However, antigen-stimulated B-cells require costimulatory signals from T-cells in order to become fully activated. Antigen-experienced B-cells and follicular helper T-cells (Tfh) proceed to migrate to the B-cell-T-cell zone border in lymphoid tissue where B-cells present antigen to cognate T-cells via MHCII. This binding is stabilised through CD40-CD40L interactions and in turn, stimulates IL-4 and IL-21 production by Tfh which provide the necessary costimulatory signals for B-cells. As a consequence, B-cells become activated and differentiate into effector cells, namely memory B-cells or antibody-secreting cells including plasmablasts and plasma cells. Antibodies are essential for the humoral immune response and elicit their effects through neutralisation or opsonisation of antigen which stimulate ADCC, ADCP and complement activation.

Upon cross-signalling, B-cells may differentiate outside of the lymphoid follicles via the extrafollicular response into short-lived plasma cells which produce low-affinity antibodies, mostly of class IgM, and circulate the blood for rapid responses. Alternatively, B-cells may enter germinal centre reactions. Within germinal centres, B-cells undergo rapid proliferation and antibody diversification, allowing production of many types of antibody with greater affinity for their targets. Here, activation-induced cytidine deaminase (AID) is upregulated by B-cells inducing somatic hypermutation (SHM) and class switch recombination (CSR). BCR antigen affinity is enhanced through a mechanism called affinity maturation, a process to select B-cells that have acquired favourable BCR mutations which enhance antigen affinity. Through the action of AID, SHM involves insertion of random mutations into variable segments in both BCR heavy and light chains which either increase or decrease antigen affinity. BCR clones with enhanced antigen affinity receive survival signals and are subsequently selected for. AID also induces CSR which only affects the BCR heavy chain. CSR involves fusion of the variable heavy gene with another heavy chain isotype constant region resulting in Fc replacement. This process occurs without any change in epitope recognition, only effector function. Together, SHM and CSR increase antibody diversification through enhanced BCR antigen affinity and effector function respectively. However, in addition to antibody production, B-cells also have a crucial role in antigen presentation, cytokine production and T-cell activation.

T-cells also belong to the adaptive immune system and are essential in B-cell activation, tumour cytotoxicity and cytokine production. T-cells are largely grouped into two different subtypes based on expression of CD4 or CD8 glycoproteins. $CD4^+$ T-cells are appropriately referred to as helper T-cells owing to their involvement in B-cell, $CD8^+$ T-cell and macrophage activation. $CD4^+$ T-cells are further distinguished into different subsets based on the specific cytokines they produce and hence, effector function. $CD8^+$ T-cells, alternatively known as cytotoxic T-cells, are important for eliciting potent tumour killing. This killing is direct and highly specific owing to expression of the highly variable TCR. In conventional T-cells, the TCR recognises melanoma-associated peptidic antigens through TCR/MHC interactions, but require costimulatory signals in order to become fully activated. Following delivery of the appropriate costimulation and cytokine

signals, T-cells become activated and infiltrate the tumour site where they are responsible for a large proportion of the cytotoxicity observed. This cytotoxicity is predominantly mediated through production of IFN-γ, perforin and granzymes, similar to NK cells.

However, unconventional T-cells such as MAITs, iNKTs and γδ T-cells are able to respond to nonpeptidic antigen in the absence of MHC. This facilitates a more rapid, innate-like response in which the cells are also responsive to proinflammatory cytokines, such as IL-12, IL-15 and IL-18, akin to NK cells.

1.1.3.3 Equilibrium

Surviving melanoma cells that are not eliminated are able to progress into a proposed equilibrium stage[68]. This stage is characterised by a fine balance between effector and immunosuppressive activity. Here, melanoma cells acquire the ability to recruit immunosuppressive cells including regulatory T-cells (Tregs) and myeloid-derived suppressor cells (MDSCs) via production of VEGF, IL-10 and TGF-β[84], as well as to induce polarisation of tumour-associated macrophages (TAMs) into an anti-inflammatory, protumourigenic M2-like phenotype. M2 macrophages arise in response to IL-4 and IL-13 and secrete immunosuppressive cytokines IL-10 and TGF-β. Cancers maintained in equilibrium are typically characterised by high levels of effector $CD8^+$ T-cells and NK cells, but low levels of immunosuppressive Tregs, MDSCs and M2-like TAMs[85].

1.1.3.4 Escape

The escape phase represents a period of evolution where mutations that may enable immune escape can be selected for. Similarly, the immune system may become less effective due to age or concomitant infection. The end result is that immunoresistant melanoma variants emerge which have reduced immunogenicity and establish a tumour microenvironment (TME) through recruitment of immunosuppressive cells. The balance is thus shifted in favour of immunosuppression with protumourigenic effects. As a result, immune evasion is considered one of the major hallmarks of cancer[86] (Figure 1.3).

Although melanoma is marked as an "immune-warm" tumour, melanoma has developed several mechanisms of efficiently avoiding immune cell detection and subsequent destruction. One such mechanism is downregulation of antigen processing and presentation machinery. Various melanoma cell lines have accrued simultaneous frameshift mutations in both *TAP1* and *HLA-A*, resulting in reduced antigen processing and loss of surface MHCI expression, hence abrogating cytotoxic T-cell recognition and antitumour responses[87]. Loss of MHCI expression is similarly observed in melanoma patient tumour samples[88]. Furthermore, loss of immunogenic melanoma markers, including melanocyte differentiation and cancer-testis antigens, is frequently observed in melanoma patients[88]. Loss of either MHCI or melanoma-associated antigens is associated with rapid disease progression[88,89].

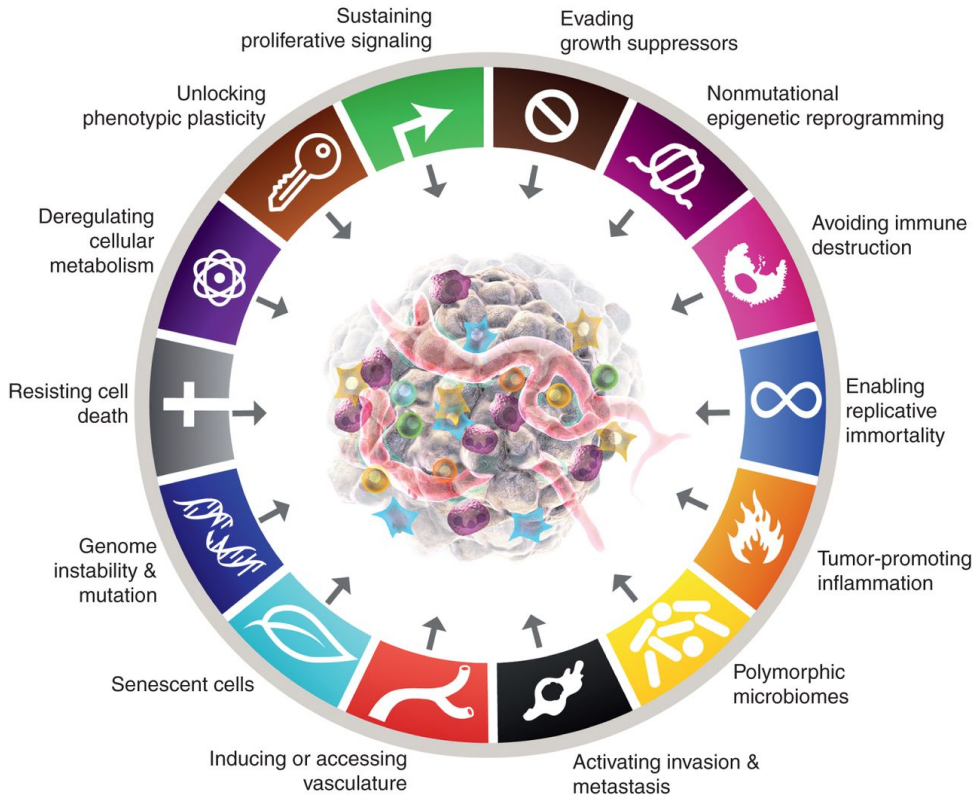


Figure 1.3 The hallmarks of cancer
The 14 hallmarks important for tumourigenesis are depicted. Figure is taken from Hanahan *et al.* (2022)[86].

A further mechanism of melanoma immune evasion is recruitment of immunosuppressive cells. Tregs are highly enriched within melanoma, where they restrict T-cell function through the production of immunosuppressive cytokines including IL-10, TGF-β and IL-35[90,91]. A higher level of immunosupressive Tregs in melanoma associates with disease recurrence, whereas depletion is shown to improve response[92–94]. Similarly, melanoma can induce transformation of myeloid cells into MDSCs and subsequent enrichment within the tumour. MDSCs elicit their immunosuppressive action on NK cells and T-cells through production of nitric oxide, ROS, TGF-β and arginase-1. Although MDSCs represent a minority of cells in healthy donors, they are found to be elevated in advanced melanoma, along with having greater suppressive activity[95]. This enhanced immunosuppression is associated with Treg recruitment and poorer survival[95–97]. In addition to MDSC and Treg recruitment, polarisation of proinflammatory M1-like macrophages into immunosuppressive protumourigenic M2-like TAMs is observed in melanoma and is associated with disease progression[98]. Finally, recruitment of neutrophils to tumour sites induces protumourigenic effects via their capacity for T-cell suppression[99]. Immunosuppression limits T-cell function with loss of either TNFR1 or IFN-γ signalling by neoantigen-specific T-cells sufficient to remove melanoma cells from a state of dormancy and induce disease progression[100].

In addition to recruitment of immunosuppressive cells, melanoma cells and TME-associated cells also acquire the ability to express inhibitory immune checkpoint ligands. Expression of these proteins limits T-cell activation and antitumour responses through binding cognate inhibitory immune checkpoint proteins which are predominantly expressed by activated T-cells. Immune checkpoints are in place to regulate the

immune system and ensure appropriate activation to avoid developing autoimmunity. The extent of lymphocyte activation is determined by the balance of stimulatory and inhibitory immune checkpoints. This includes phosphorylation of either immunoreceptor tyrosine-based activation motifs (ITAMs), immunoreceptor tyrosine-based inhibitory motifs (ITIMs) or immunoreceptor tyrosine-based switch motifs (ITSMs) which are present in several immune checkpoint proteins.

Stimulatory immune checkpoints include markers of costimulation, such as CD27, CD28, CD40, ICOS, OX40 and 4-1BB, which act as essential secondary signals in adaptive immune responses. Conversely, inhibitory immune checkpoints (Table 1.1) are crucial in producing a negative feedback loop upon recognition of self-antigen or in cases of chronic infection and disease[101–112]. Many cancers are able to hijack this process and shield themselves from immune attack through upregulation of inhibitory immune checkpoint ligands, which dampen any further antitumour immune responses. Cancer cells, associated stroma and immune infiltrate frequently upregulate immune regulatory molecules, which primarily dampen T-cell activation and cytotoxicity, thereby limiting antitumour activity in the context of effective immunorecognition. These checkpoints are thought to have evolved to control T-cell responses to viral infections and play key roles in regulating peripheral tolerance.

Immune checkpoint	**Ligand(s)**
CTLA-4 (Cytotoxic T-Lymphocyte-Associated protein 4, CD152)	CD80/CD86
PD-1 (Programmed cell death protein, CD279)	PD-L1/PD-L2
LAG-3 (Lymphocyte Activation Gene-3, CD223)	MHCII
TIM-3 (T-cell Immunoglobulin domain and Mucin domain 3, CD366)	Galectin-9/HMGB1
TIGIT (T cell immunoreceptor with Ig and ITIM domains)	CD112/CD155
BTLA (B- and T-lymphocyte attenuator, CD272)	HVEM
VISTA (V-domain Ig suppressor of T cell activation, B7-H5)	Unknown
CD39 (Ectonucleoside triphosphate diphosphohydrolase-1, ENTPD1)	ADP/ATP
CD73 (5'-nucleotidase)	AMP
A2AR (Adenosine A2A receptor)	Adenosine

Table 1.1 Inhibitory immune checkpoint proteins
Table showing known inhibitory immune checkpoint proteins and cognate ligands.

1.1.4 Standard of care

1.1.4.1 Overview

Treatment of early stage melanoma involves excision of the primary tumour, with an excision margin, and possibly also sentinel lymph nodes. Surgery has a high success rate, however, unresectable and metastatic melanoma (MM) have poor response to standard chemotherapy and radiotherapy regimens[2–6], with a historic median survival of just five months from diagnosis for stage IV MM patients[113]. For many years, dacarbazine, an alkylating agent, was the only chemotherapeutic agent approved for use in MM patients, but had no evidence that it prolonged survival[2–4]. Consequently, targeted therapies offered new opportunities for the treatment of advanced or metastatic disease.

1.1.4.2 Targeted therapies

Due to the high proportion of melanoma patients expressing $BRAF^{V600}$ mutations, molecular inhibitors of BRAF were developed to limit BRAF activity and downstream MAPK pathway activation. Vemurafenib and dabrafenib are potent BRAF inhibitors and were found to improve survival compared to dacarbazine[114–116].

However, limited therapeutic options were available for $BRAF^{V600}$ mutation negative MM patients. Furthermore, those who received B-Raf inhibitor treatment did not exhibit durable responses[114–117]. This may be explained by development of B-Raf inhibitor resistance including generation of further *BRAF* mutations and downstream *MEK1/2* mutations that enable activation in the absence of B-Raf signalling[118–127]. Nevertheless, B-Raf inhibitors remain a viable first line treatment for $BRAF^{V600}$ mutation positive unresectable or metastatic melanoma[128–130].

1.1.4.3 Immunotherapy

Due to the extensive immune involvement in melanoma, immune regulation has long been investigated as an alternative avenue of treatment to reduce immunosuppression and ultimately, boost T-cell responses. First, the utility of proinflammatory IFN-α2b and T-cell growth factor IL-2 was examined in MM patients. The use of IFN-α2b or IL-2 demonstrated modest improvements in survival, but responses were limited, short-lasting and accompanied by substantial toxicity[131–136].

Melanoma is characterised by increased neoantigen expression, including melanoma differentiation (tyrosinase, gp100, MART-1) and cancer-testis (MAGE proteins, NY-ESO-1) antigens, which are found to be highly shared between different melanomas[137]. In particular, melanoma differentiation antigens are expressed by most melanomas regardless of disease stage[137] and thus the prospect of a viable cancer vaccine was investigated. HLA-A*02-restricted immunodominant gp100 peptides were administered to HLA-A*02-expressing MM patients, along with IL-2, and revealed that coadministration of gp100 with IL-2 improved survival compared to IL-2 administered alone, and that vaccination associated with objective responses for several patients[138–140]. Similarly, several HLA-A*02-expressing patients treated with either MART-1 or MAGE-3 peptides had objective responses in which neoantigen-specific T-cells had enhanced cytotoxic capacity[141,142]. While cancer vaccines appear promising, response rates remain low with patient eligibility being dependent on HLA type. Furthermore, tumours have demonstrated an ability to downregulate neoantigen expression[88], thus making vaccination often ineffective.

Due to high expression of immune checkpoints by both melanoma and immune cell infiltrates, monoclonal antibodies were developed to block immune checkpoint function, thus reinvigorating T-cell antitumour responses. The introduction of immune checkpoint blockade (ICB) revolutionised the treatment of MM, significantly improving survival outcomes, regardless of *BRAF* mutation status and HLA type[143].

1.2 Immune checkpoint blockade

1.2.1 Immune checkpoint proteins

1.2.1.1 CTLA-4 signalling

CTLA-4 was first discovered during a mouse T-cell cDNA library study and was found to be highly expressed by activated T-cells[144]. CTLA-4 was subsequently identified as one of the first inhibitory immune checkpoints to be essential for controlling immune cell activation and maintaining homeostasis. *CTLA4* deficient mice rapidly develop lymphoproliferative disease, with severe multiorgan inflammation, and die prematurely, highlighting the importance of CTLA-4 in limiting autoimmunity[145,146]. CTLA-4 is upregulated by T-cells upon activation[101,105,144] and is trafficked from intracellular stores to the cell surface before being rapidly internalised[147–149]. CTLA-4 is closely related to costimulatory protein CD28 and is situated proximal to the *CD28* gene locus, adopting a similar structure[150,151]. Similarly, CTLA-4 is able to bind costimulatory receptors CD80 (B7-1) and CD86 (B7-2) on antigen presenting cells, but with greater affinity and avidity than CD28 as CTLA-4 homodimers are bivalent, but CD28 homodimers are monovalent[152,153].

However, CTLA-4 functions antagonistically and instead suppresses T-cell proliferation upon signalling[101,105]. CTLA-4 thereby reduces CD80/CD86 bioavailability, acting to competitively inhibit CD28-mediated costimulation and promote an anergic-like state in T-cells. In addition, CTLA-4 induces transendocytosis of CD80 and CD86 prior to degradation to limit interaction with any other cells[154]. Unlike CD28-CD80/CD86 interactions, CTLA-4 instead delivers an inhibitory signal upon ligation. This further limits T-cell activation through recruitment of phosphatases[155–157], which act to dephosphorylate tyrosine residues on ITAMs, and ultimately attenuate AP-1, NFAT and NKχB activity which are necessary for T-cell activation[158,159]. CTLA-4 is also constitutively expressed by Tregs and is essential for expression of *FOXP3* and immunosuppressive function[160–165].

1.2.1.2 PD-1/PD-L1 signalling

Soon after the discovery of CTLA-4, PD-1 was isolated and found to be upregulated during activation-induced T-cell death[166]. PD-1 was identified as another immune checkpoint and a further member of the CD28/CTLA-4 family of T-cell regulators. Similarly, PD-1 was found to be instrumental in limiting the development of autoimmunity. *PDCD1* deficient mice develop autoimmunity, including arthritis, glomerulonephritis and cardiomyopathy, as well as having augmented T-cell proliferation[167,168]. However, PD-1 depletion does not result in premature death as with CTLA-4 depletion[167,168]. In keeping with its name, PD-1 controls programmed cell death and promotes apoptosis of T-cells as a mechanism of self-tolerance. Although PD-1 can be expressed by multiple immune cell subsets, it is most highly expressed by T-cells where it acts as a defining marker of T-cell activation and exhaustion, dampening anticancer responses[106].

The intracellular tail of PD-1 is composed of an ITIM at the *N*-terminus and an ITSM at the *C*-terminus. Phosphorylation of PD-1 ITIM and ITSM functions in contrast to ITAM phosphorylation that occurs within BCR/CD79 and TCR/CD3 complexes. Instead, PD-1 forms docking sites for inhibitory phosphatases SHP-1

(ITIM) and SHP-2 (ITIM, ITSM) with PD-1/SHP-2 interaction sustained by Lck[169–174]. Simultaneous BCR/TCR and PD-1 signalling induces SHP-1 and SHP-2 recruitment to these sites. Here, these enzymes dephosphorylate the ITAMs present within BCR/CD79 and TCR/CD3 complexes as well as costimulatory marker CD28 and effector molecules ZAP70, Syk and PI3K which are important for eliciting downstream BCR/TCR signalling[169–171,173]. As a result, PD-1 ligation limits activation of downstream PI3K/Akt, PKCϑ and Ras/Raf/MEK/ERK pathways which are necessary for propagating BCR/TCR signals[170,175]. Lck is important for CD4/CD8 coreceptor recruitment to TCR and aids recognition of peptide/MHC (pMHC) complexes. Because Lck is important for stabilising PD-1/SHP-2 interactions, recruitment of Lck to the TCR is inhibited, disrupting CD4/CD8 accumulation and interfering with TCR-pMHC interaction time and subsequently, impeding antigen recognition[171,176,177]. Moreover, PD-1 signalling downregulates TCR through Cbl-mediated degradation and further limits TCR-pMHC recognition[178].

Engagement of PD-1 with its ligands, either PD-L1 (B7-H1, *CD274*) or PD-L2 (B7-H2, *PDCD1LG2*), initiates this PD-1 signalling cascade. PD-L1 and PD-L2 are expressed by both haematopoietic and nonhaematopoietic cells including antigen presenting cells, heart and lung tissue[172,173]. Specifically, conventional DCs upregulate *PDL1* during antigen presentation and in response to LPS and IFN-γ stimulation[172,173,179]. This occurs predominantly through JAK2 activation and subsequent STAT3 and STAT5 phosphorylation which are able to enhance the *PDL1* promoter directly and upregulate expression[180–183]. However, additional mechanisms of *PDL1* upregulation have also been described[182,184–188].

In addition to *PDL1* upregulation, IFN-γ also induces expression of costimulatory molecules CD80 and CD86 which interact *in cis* with PD-L1 on the surface of antigen presenting cells[172,173,179,189,190]. PD-L1/CD80 heterodimers maintain the ability to stimulate CD28 on T-cells, although to a lesser extent, but lose the potential for CTLA-4 binding which requires homodimeric CD80 for interaction and hence limits the extent of CTLA-4-mediated CD80 transendocytosis and inhibition[176,189]. Simultaneous blockade of CTLA-4 may therefore have additive effects. Due to their high affinity, PD-L1 typically exists in heterodimeric form with CD80. Increased expression of CD80 during immune activation results in PD-L1 saturation and ultimately the inability to bind PD-1, hence propagating important costimulatory signals[176,189,190]. Conversely, an excess of PD-L1 during chronic stimulation overcomes this blockade and is able to bind to its cognate receptor PD-1[189,190]. A higher ratio of PD-L1:CD80 in DCs has previously been identified in several cancers including non-small cell lung cancer (NSCLC) and renal cell carcinoma (RCC) within both the blood and tumour, limiting T-cell costimulation and antitumour responses[176].

Expression of both PD-L1 and PD-L2 is often increased in cancer and historically confers worse survival, especially for high PD-L1 expression[191–197]. *PDL1* is frequently upregulated in cancer as a mechanism of immune evasion, expressed by immune cells or by the tumour itself, and is suggestive of immunosensitivity. Overall, upregulation of *PDL1* is commonly detected in cancer and saturates CD80 binding. This liberates PD-L1 enabling it to bind PD-1 which is similarly upregulated in cancer by T-cells. Activation of PD-1 recruits inhibitory phosphatases which reduce BCR/TCR signalling, CD4/CD8 recruitment and costimulation. This is in addition to TCR downmodulation and inhibition of T-cell proliferation, IL-2 and IFN-γ production, but enhanced IL-10 production[172–175,178].

1.2.2 Current ICB treatment strategies

From the perspective of therapeutic intervention, immune checkpoint proteins represent modifiable determinants of the immune response to cancer. To combat the immunosuppression elicited by immune checkpoint proteins in cancer, humanised monoclonal antibodies were designed to specifically target inhibitory immune checkpoint proteins and reinvigorate immune cell activation. The introduction of ICB has revolutionised the treatment of cancer, particularly for MM, NSCLC, RCC and urothelial cell carcinoma (UCC), which have been historically resistant to conventional therapies and are highly immunogenic.

The foremost ICB being ipilimumab, an IgG1 antibody targeted against CTLA-4, was the first ICB to demonstrate improved overall survival (OS) for MM patients in phase III trials as compared to gp100 vaccination[198]. This was shortly followed by the development of anti-PD-1 IgG4 antibodies, including pembrolizumab and nivolumab, which demonstrated enhanced survival compared to chemotherapy and ipilimumab in phase III trials[199–205].

However, a combination of both ipilimumab and nivolumab (cICB) was shown to have superior outcomes for MM patients compared to single agent (sICB) ipilimumab and nivolumab in phase III trials[143,203–205]. As a result, use of single agent ipilimumab has been largely replaced by cICB and is primarily administered in tandem with the anti-PD-1 antibody nivolumab as combination treatment with NICE approval for advanced melanoma[206].

The other major class of ICB targets the ligand for PD-1 directly, namely PD-L1, with the IgG1 monoclonals durvalumab, atezolizumab and avelumab being the most commonly used. These drugs have mainly found use in the treatment of NSCLC, UCC and Merkel cell carcinoma.

1.2.3 Mechanism of action

1.2.3.1 CTLA-4 blockade

Chronic TCR stimulation in cancer often results in elevated CTLA-4 expression by antitumour cytotoxic T-cells and is accompanied by high tumour infiltration of Tregs. CTLA-4 blockade reverses T-cell exhaustion, inducing a more activated state, likely facilitated by CTLA-4 lysosomal degradation and enhanced CD28-CD80/CD86 costimulation, which as a result, is partnered with increased T-cell cytotoxic function, proliferation and IL-2 production[207,208]. In addition to increased CD28 costimulation, CTLA-4 blockade also increases expression of costimulatory molecule ICOS by T-cells in the blood, tumour and surrounding tissue[209–212]. Although ICOS is induced by all T-cell types, it is upregulated to the highest magnitude by $CD4^+$ T-cells and is associated with increased T-cell activation[209–213].

Additionally, CTLA-4 blockade is associated with intratumoural Treg depletion. IgG1 and IgG2 antibodies potently induce ADCC and may explain the loss of $CTLA\text{-}4^+$ Tregs that is observed after CTLA-4 blockade using IgG1 or IgG2 antibodies[214,215]. These effects are not dependent on complement, FasL/TRAIL, NK cells or $CD8^+$ T-cells, but are rather mediated through recognition by nonclassical monocytes through FcγRIII (CD16) for IgG1 or FcγRII (CD32) for IgG2[214–216]. The importance of FcγR chains in the anti-CTLA-4 response is highlighted in Fc receptor γ-chain and Fc-receptor knockout mice which show neither Treg depletion nor clinical benefit of CTLA-4 blockade[217,218].

The reduction in intratumoural Tregs observed is also accompanied by increased $CD8^+$ T-cell tumour infiltration and enhanced survival in MM patients, likely due to a reduction in immunosuppression and restoration of T-cell function, and may represent a further mechanism of the anti-CTLA-4 response[215]. This suggests that the benefit of CTLA-4 blockade is largely based on increased $CD4^+$ T-cell activation, Treg depletion, $CD8^+$ T-cell tumour infiltration and overall enhanced T-cell function.

1.2.3.2 PD-1/PD-L1 blockade

Targeting the PD-1/PD-L1 axis inhibits PD-1 signalling and associated immunosuppression which reinvigorates T-cells to become less exhausted, but more functional and proliferative[208,212,219]. Specifically, PD-1^+ cells are found to be the majority of proliferating T-cells in the periphery and tumour after PD-1 blockade[219,220]. Furthermore, PD-1/PD-L1 blockade is accompanied by enhanced NK cell and T-cell infiltration into the tumour and subsequent cytotoxicity[182].

The same benefit of PD-1 blockade is not observed for PD-1^+ Tregs where treatment enhances Treg activation, as demonstrated by *GITR* and *ICOS* upregulation, and thus immunosuppressive activity[221]. PD-1^{hi} Tregs lose the ability to suppress effector T-cells and so revival of function can limit any benefit observed from reinvigorating conventional T-cells[222]. The balance of PD-1 in conventional T-cells and Tregs may ultimately determine overall sensitivity to PD-1/PD-L1 blockade.

IgG4 antibodies, used in PD-1 blockade, are only capable of inducing weak ADCC and so do not result in the depletion of target cells following anti-PD-1 treatment.

DCs, in particular, are instrumental for anti-PD-L1 efficacy, in which removal of DCs or specific depletion of PD-L1 in DCs reduces anti-PD-L1 responses[176,179,223]. Blocking PD-L1 on DCs relieves CD80 sequestration by PD-L1, enhancing CD28/CD80 costimulation and hence T-cell priming[176]. The benefit of both PD-1 and PD-L1 blockade is dependent on expression of CD80/CD86 and is enhanced by CD28, CD40, Flt3L and TLR3 stimulation, which promote DC activation, T-cell costimulation and subsequent T-cell responses[223–226]. These effects are dependent on DCs and T-cells and are associated with T-cell expansion, infiltration into the tumour and IFN-γ production[223–226].

The benefit of DCs is not limited to enhanced T-cell priming, but also for T-cell recruitment. Delivery of CCL4 into tumours enhances DC accumulation and is accompanied by increased $CD8^+$ T-cell infiltration[227]. This effect is dependent on DC CXCL9 production and $CD8^+$ T-cell CXCR3 expression[227]. Although CXCR3 is not required for T-cell infiltration into tumours, it has an essential role in the T-cell response to anti-PD-1[228]. PD-1 blockade stimulates production of CXCR3 ligands CXCL9, CXCL10 and CXCL11 by DCs which govern T-cell proliferation and cytotoxicity, including the production of IFN-γ, TNF-α and GZMB[228]. Secretion of CXCR3 ligands in tumours sensitises them to anti-PD-1 treatment, potentially through enhanced DC-T-cell interactions and subsequent T-cell activation in the TME[228].

The benefit of PD-1/PD-L1 blockade is therefore explained by reduced T-cell exhaustion, enhanced T-cell priming, proliferation and cytokine production.

1.3 Predictive markers of immune checkpoint blockade

ICB has significantly improved survival outcomes for a variety of cancer types, however durable responses are only observed in a minority of patients. Furthermore, a large proportion of these individuals experience severe immune-mediated toxicities. Knowledge of the determinants and correlates of this is vital to the development of novel candidates and therapeutic stratification.

1.3.1 Development of immune-related adverse events

Aside from the development of resistance, the major treatment limitation of ICB is its propensity to cause immune-related adverse events (irAEs), including more severe grade 3-4 toxicities. This is a particular concern for those receiving combination CTLA-4/PD-1 blockade where irAEs are observed in more than half of MM patients and are thought to be mediated through TNF-α and IL-6 signalling[204,229,230]. Strikingly, irAE occurrence is associated with enhanced ICB response, improved disease control and survival, regardless of cancer type and ICB treatment type, likely illustrating immune reawakening[200,231–248]. Furthermore, within patients who develop irAEs, those who experience multiple types have longer OS compared to those with just one[233].

Interestingly, knockdown of *AIRE*, important in elimination of self-reactive TCR clones, was found to improve survival following CTLA-4 blockade in mice using murine models of melanoma[249]. This is thought to be explained by an expanded pool of melanoma-reactive TCR clones that are typically deleted during thymic education. Although ICB doesn't increase thymic output[250], it may reduce the stringency of TCR selection and rescue T-cell clones from elimination. This would increase the repertoire of TCR clones that survive and hence the diversity and capacity for neoantigen recognition. However, this would also result in increased survival of self-reactive clones and may explain the association between irAE development and ICB response. In favour of this theory, patients who develop irAEs in response to ipilimumab treatment also experience simultaneous TCR diversification and ICB response[251].

1.3.2 Features of the tumour

1.3.2.1 Overview

Tumour-intrinsic factors are the most studied and understood determinants of ICB response. The frequency that neoantigen formation occurs varies according to cancer type and the predominant mutational process. There is similar disparity among proteins with their propensity for immunorecognition and this is influenced by the host's HLA type which is crucial in antigen presentation.

1.3.2.2 Tumour mutational burden

Notably, tumours with a high mutation rate, including MM, NSCLC and UCC[7,8], demonstrate high sensitivity to ICB. A high tumour mutational burden (TMB) represents an important predictor of ICB efficacy for several cancer types, including MM, NSCLC, UCC, head and neck squamous cell carcinoma (HNSCC) and colorectal cancer (CRC)[197,252–265]. The benefit of high TMB likely derives from an increased chance of

neoantigen formation and a subsequently higher propensity to be recognised by cytotoxic T-cells[8,263–265]. Correspondingly, a high neoantigen load is associated with enhanced tumour recognition, TCR diversity and ICB response[197,253,255,259,266–269]. Supporting this, the association within MM patients is confined to patients with cutaneous disease and is not observed for occult, acral or mucosal subtypes[262]. This is likely reflective of mutational origin in which UV-exposed cutaneous MM has probably incurred more mutations. In accordance, melanomas with UV mutation signatures have enhanced survival after PD-1 blockade which is attributed to enhanced T-cell infiltration into the tumour and T-cell proliferation[270]. Similarly, mutations within DNA repair pathway members also associate with improved survival[253,265].

In order to generate neoantigens, cancer-associated mutations must occur within coding genes, be translated and produce distinct antigen. Accordingly, a high frequency of nonsynonymous mutations, specifically within coding genes, have greater predictive power than overall TMB[252]. Furthermore, carriage of mutations resistant to nonsense-mediated decay elimination is also essential for T-cell recognition and ICB response, owing to maintenance of neoantigen translation[271]. Although nonsynonymous mutations are associated with enhanced survival after ICB treatment, mutations resulting in more variable antigens are able to mount greater ICB responses. A higher burden of frameshift mutations and transversions, as opposed to transitions, is found to correlate with clinical benefit, likely due to changes in reading frame and purine/pyrimidine conversion, producing more variable, highly immunogenic neoantigens[253,272,273]. However, deletions and mutations responsible for loss of heterozygosity are associated with shorter survival, thus highlighting the importance of neoantigen diversity[265]. However, neoantigens must maintain high affinity for HLA in order to be detected. High HLA neoantigen binding affinity is associated with ICB response, demonstrating that it is not just the quantity and variability of neoantigens, but also the potential for inducing antitumour responses[197].

Whilst a high TMB is associated with clinical benefit at a macroscopic level, a high intratumoural diversity, characterised by the presence of multiple subclonal populations with divergent mutational profiles, can lead to islands of resistance[263,269]. This means that although an immune response may be generated by subclonal mutations, the response is limited to the cancer cells bearing those particular mutations[263,269]. Correspondingly, a higher proportion of clonal neoantigens and lower tumour heterogeneity is associated with prolonged survival following ICB[262–264,269]. Additionally, contraction of tumour cell clones is observed in patients with prolonged OS and progression-free survival (PFS)[264]. This is further demonstrated using the Cauchy-Schwarz index of neoantigens (CSiN) which scores tumours by estimating the frequency of neoantigen-encoding clonal mutations, determined by the variant allele frequency, the number of predicted neoantigens and the respective HLA binding affinity[274]. After taking these factors into consideration, a high CSiN score is found to have greater predictive power of ICB response than neoantigen load and neoantigen fitness across several cohorts and cancer types[274].

1.3.2.3 Mutations in immune-related genes

Highly mutated tumours with low tumour heterogeneity associate with clinical benefit from ICB-mediated immune cell reinvigoration, likely due to increased neoantigen production and subsequent immune recognition. However, this effect is context-specific in which genomic alterations within immune-related genes can instead dampen ICB response and act as a mechanism of immune evasion. Thus, in addition to mutational load, type,

clonality and HLA binding affinity, the specific genes in which mutations occur may also determine ICB response.

Tumours derived from patients who demonstrate an initial response to ICB followed by rapid progression frequently incur mutations, deletions and loss of heterozygosity in *B2M*. This includes an altogether absence of surface MHCI expression, which associates with a reduction in B-cell and T-cell infiltration into the tumour at the time of progression[275–278]. Alterations in *B2M* occur in 29.4% of MM patients experiencing disease progression and associates with worse survival[276]. Moreover, depletion of *B2M* in murine models of lung cancer is sufficient to induce resistance to anti-PD-1 therapy[275]. Similarly, a patient with lung adenocarcinoma on a course of nivolumab treatment was found to rapidly progress after acquiring a homozygous deletion in *HLA-B*[279], demonstrating the importance of preserving antigen presentation for ICB-mediated effects. Conversely, overexpression of immunoproteasome subunits results in a broader peptide repertoire presented and enhanced tumour regression, suggesting a crucial role for neoantigen detection[280]. Accordingly, high expression of *B2M*, *TAP1*, *TAP2* and immunoproteasome components in the tumour associate with enhanced survival in MM patients[280,281].

In addition to antigen presentation, preservation of IFN-γ signalling is essential for T-cell effector function and subsequent ICB benefit[262]. Despite having a high TMB, MM patients who develop loss of function mutations in *JAK1* and *JAK2* or copy number mutations in IFN-γ pathway genes have a poor response to PD-1 blockade and rapidly progress[263,277,282,283]. Conversely, amplifications in *PDL1* and *PDCD1LG2* or chromosomal alterations of the 9p24.1 locus, encompassing both *PDL1*, *PDCD1LG2* and *JAK2* loci, sensitise cancers cells to ICB treatment[284,285].

In order to identify genes important for $CD8^+$ T-cell effector function and ICB efficacy, CRISPR-Cas9-based gene knockdown has been used in melanoma cells as an unbiased method. This revealed that depletion of neoantigens (*NY-ESO1*, *MLANA*), antigen presentation (*HLA-A*, *B2M*, *TAP1*, *TAPBP*, *PSMB5*) and IFN-γ signalling (*IFNGR1*, *IFNGR2*, *JAK1*, *STAT1*, *PDL1*, *APLNR*) dampens $CD8^+$ T-cell effector function, cytotoxicity and induces resistance to anti-PD-1[281,286]. On the contrary, depletion of *PTPN2*, involved in dampening antigen presentation and IFN-γ signalling, sensitises melanoma cells to ICB-mediated killing[286].

1.3.2.4 MHC diversity

Supporting the importance of tumour surveillance mechanisms in ICB response, maximal heterozygosity at MHCI and MHCII loci as well as a higher evolutionary divergence, calculated using the Grantham distance in peptide-binding domains, associates with enhanced OS in MM patients[252,287,288]. This holds true even within fully heterozygous patients and implies that a greater capacity to detect neoantigens is important in ICB response[288]. Additionally, high HLA diversity is accompanied by an increased number of neopeptides and associates with tumour TCR diversity[288].

Specific HLA types also associate with survival, including HLA-A*01[265] and HLA-B*44[287] which associate with prolonged OS, but also HLA-A*03[289] and HLA-B*15:01[287] which confer worse survival. However, these specific associations are inconsistent between different cancer types[265] and may be dependent on the type of mutation and subsequent neoantigen expression.

1.3.2.5 Summary

Efficient cancer cell elimination relies on the recognition of neoantigens by the immune system. Cancers with a high TMB, particularly those with a high carriage of nonsynonymous mutations within coding genes, have an increased capacity for neoantigen formation and experience greater response to ICB. However, responses are limited in patients with high tumour heterogeneity owing to subclonal mutations and the requirement for detection of multiple subclones. Although a high tumour mutational load is associated with enhanced survival, mutations that occur within antigen processing, presentation or IFN-γ signalling genes instead limit ICB response due to reduced neoantigen detection and immune cell response. Furthermore, a patient's propensity to detect such mutations, including HLA heterogeneity and diversity, may limit neoantigen detection and thus any benefit derived from ICB treatment.

1.3.3 Immunosuppression

1.3.3.1 Overview

While tumours may be highly immunogenic, the extent of antitumour activity is limited by the surrounding immunosuppressive TME as well as by upregulation of distinct inhibitory immune checkpoints as compensation.

1.3.3.2 Tregs

Tregs have a crucial role in maintaining homeostasis and limiting T-cell activation. Importantly, Treg infiltration into the tumour associates with enhanced T-cell suppression, but also recruitment of MDSCs[290,291]. High Treg counts are associated with worse survival following ICB treatment[214,292–294]. However, Treg depletion or suppression through multiple mechanisms overcomes resistance to ICB and results in increased $CD8^+$ T-cell infiltration into the tumour as well as increased production of IFN-γ and GZMB[217,218,292,295–298].

CTLA-4 expression is highly expressed by Tregs and may represent a major target of CTLA-4 blockade[215]. Part of the efficacy of CTLA-4 blockade is associated with Treg depletion through ADCC, mediated by nonclassical monocytes[214–217,299]. Strikingly, the benefit of Treg suppression and depletion is not observed in Fc common gamma chain or Fc-receptor knockout mice and suggests that the benefit of CTLA-4 blockade derives from ADCC of Tregs[217,218].

1.3.3.3 Myeloid cells

Myeloid cells, including monocytes, MDSCs and TAMs, are typically considered to be associated with poorer responses to ICB treatment. Correspondingly, targeting IDO, CSF1R or PI3Kγ, enriched within myeloid cells, enhances T-cell responses and restores ICB sensitivity[290,291,300,301]. Interestingly, myeloid cells have the capacity for expression of both PD-1 and PD-L1, which play an important role in myeloid programming, and are thus targetable by both PD-1 and PD-L1 inhibitors. Specific ablation of PD-1 within myeloid cells results in reduced MDSCs, enhanced T-cell function and improved survival[302].

MDSCs are also responsible for immunosuppression within both the blood and tumour. A lower MDSC count associates with favourable clinical outcome following

ICB treatment[292,303–306]. Through production of IL-10, MDSCs not only elicit immunosuppressive activity on T-cells, but also stimulate Treg development and recruitment[304]. Furthermore, targeting of the CCR2/CCL2 axis, necessary for MDSC tumour recruitment, is associated with an increase in TIL infiltration, activation, IFN-γ production and enhanced survival following ICB treatment[259,307]. Moreover, suppression of the MDSC-inducing IL-1 signalling pathway reduces MDSCs, PD-L1 expression and improves ICB response owing to enhanced tumour-specific immunity[308]. In a similar fashion to Tregs, MDSCs thus represent a major obstacle to ICB response through their immunosuppressive activity.

Tumour-associated macrophages are largely composed of M1-like and M2-like TAMs, which are considered to be antitumourigenic and protumourigenic respectively. TAMs typically exhibit polarisation towards a protumourigenic M2 phenotype. Interestingly, some macrophages are able to express PD-1 and undergo polarisation into immunosuppressive M2-like TAMs upon PD-L1 ligation[309]. Conversely, repolarisation into a proinflammatory M1-like state includes a reduction in TGF-β, arginase-1, IL-1β, IL-10 and IL-6 expression[214,310–313]. This phenotypic shift is associated with a reduction in tumour-associated MDSCs and Tregs, but enhanced DC responses, including production of key T-cell recruiting chemokines CXCL9, CXCL10, CXCL11[214,310–313]. Consequently, this associates with enhanced T-cell activation, tumour infiltration and production of cytolytic factors which ultimately sensitises typically ICB-resistant tumours to treatment[214,310,311,313]. Alternatively, targeting of TAM-associated molecules (TREM2 or PI3kγ) also enhances ICB responses[312,314]. Accordingly, a smaller TAM population is associated with improved outcomes following ICB treatment[264].

As a whole, myeloid cells also have capacity to limit ICB responses. This includes dynamic myeloid reprogramming to increase MDSC tumour infiltration, inflammation and polarisation of TAMs into an immunosuppressive state. Together, these cells are able to efficiently dampen antitumour responses.

1.3.3.4 Neutrophils

In addition to Tregs, MDSCs and TAMs, tumour-associated neutrophils are also predominantly protumourigenic, with capacity for T-cell suppression, and are considered one of the most predictive cells of tumour progression across several cancer types[99]. Peripheral neutrophils are also predictive of patient outcomes to ICB treatment. Specifically, a high neutrophil count or neutrophil:lymphocyte ratio associates with poorer survival in several cancer types following ICB treatment and is associated with reduced $CD8^+$ T-cell tumour infiltration[256,303,305,315–325].

Furthermore, the role of IL-8, a potent neutrophil chemoattractant, is also associated with cancer progression following ICB treatment[326–328]. Unsurprisingly, IL-8 levels correspond with neutrophil tumour infiltration, but also inversely correlate with T-cell infiltration as well as antigen presentation and IFN-γ signatures[326,327].

Neutrophils are typically considered to be detrimental to ICB responses, regardless of localisation, secondary to their immunosuppressive characteristics.

1.3.3.5 PD-L1

High PD-L1 expression is a marker of PD-1 activity and therefore associates with enhanced response to PD-1/PD-L1 blockade[329–335]. Consequently, PD-L1 demonstrates utility in a clinical setting to predict outcomes and stratify treatment[336–339], although not

in melanoma. Whilst a level exists, patients without PD-L1 expression in the primary tumour may still derive benefit.

High PD-L1 expression in the TME also correlates with improved survival outcomes[231,340–347]. Importantly, PD-L1 expression by DCs attenuates T-cell activation, which are reinvigorated following PD-1/PD-L1 blockade[179]. Surprisingly, T-cells are also able to express PD-L1 and can bind PD-1 on neighbouring T-cells, preventing further T-cell activation and inducing an anergic-like state which associates with disease progression[309,340]. PD-L1$^+$ T-cells have also been shown to stimulate macrophage polarisation into an immunosuppressive M2-like state through ligation with macrophage PD-1[309].

The benefit of PD-1/PD-L1 blockade is also demonstrated by PD-L1 depletion. PD-L1 depletion may be achieved through STAT3 inhibition or treatment with rapamycin, which suppresses Akt/mTOR signalling and thus PD-L1 upregulation. PD-L1 suppression through these methods associates with an enhanced antitumour response[183,184].

1.3.3.6 Immune checkpoints

The benefit of ICB is largely dependent on T-cell responses and thus, the balance of stimulatory to inhibitory immune checkpoints may determine treatment response.

High T-cell expression of stimulatory immune checkpoints including ICOS, 4-1BB and OX40 associates with enhanced survival[67,209,211,219,340]. These may act as markers of successful costimulation and hence, T-cell priming.

Although ICB relieves the immunosuppression delivered by CTLA-4 and/or PD-1 signalling, upregulation of further inhibitory immune checkpoints may act to compensate immunosuppression. The majority of tumour-associated CD8$^+$ T-cells simultaneously express multiple immune checkpoints, including CTLA-4, PD-1, TIGIT, TIM-3 and CD39,[348] and thus blockade of just CTLA-4 and/or PD-1 may be insufficient to completely alleviate T-cell suppression. Accordingly, nonresponding patients have been found to have elevated expression of LAG3, CD39, TIM-3, CD73, A2aR, B7-H3 and B7-H4, all of which have been associated with limiting T-cell infiltration, activation and function[278,293,297,304,325,349–357]. However, simultaneous targeting of inhibitory immune checkpoints further improves CD8$^+$ T-cell responses and ultimately survival[278,306,358,359].

1.3.4 Lymphocytes

The benefit of ICB likely derives from immune reinvigoration and subsequently heightened antitumour responses. Increases in peripheral lymphocyte counts are found to be favourable and may represent the enhanced T-cell proliferation that is induced by ICB and hence treatment sensitivity[292,293,324,325,334,360,361].

1.3.4.1 T-cells

Cytotoxic CD8$^+$ T-cells are essential for efficient tumour eradication through direct tumour recognition and subsequent cytotoxicity which govern antitumour responses. Elevated CD8$^+$ T-cell tumour infiltration is associated with enhanced tumour cell lysis and enhanced clinical benefit with ICB treatment[214,215,264,331,334,335,362–364]. Exemplifying the importance of CD8$^+$ T-cell infiltration is the association of DC signatures and the CXCR3-CXCL9/CXCL10/CXCL11 axis, involved in the recruitment and activation of cytotoxic T-cells, with enhanced ICB response[67,176,223,227,228,261,320,343,365–367]. Subsequent

T-cell priming, T-cell activation and IFN-γ signalling also associate with clinical benefit[197,258,264,343,359,363].

T-cell activity is also dependent on T-cell differentiation state as this shapes cell function. Interestingly, ICB treatment is associated with a depletion in naïve and central memory $CD8^+$ T-cell subsets, but a concurrent increase in mitotic and effector memory $CD8^+$ T-cells[208]. Higher levels of memory $CD8^+$ T-cells, especially effector memory T-cells, are associated with ICB response and form the majority of proliferating cells[208,219,250,351,359,368,369]. On the other hand, higher carriage of antigen-inexperienced naïve $CD8^+$ T-cells is associated with disease progression[351,368,369]. Effector T-cells are able to elicit rapid effector function and are the most responsive subset to ICB[208]. Tumour-specific T-cells typically adopt an effector-like phenotype, persist long-term and are more prevalent in responding patients[294,348,369,370]. Strikingly, almost all large peripheral T-cell clones (>0.5% of the TCR repertoire) are found to have an effector phenotype[208]. These effector cells demonstrate the highest TCR clonality of any T-cell subtype and are accompanied by profound cytotoxic potential, which may be explained by the presence of expanded tumour-specific T-cell clones[208,250].

However, the cytotoxic potential of T-cells is only unlocked upon successful antigen recognition. In support of this, Fairfax *et al.* (2020)[371] describe TCR signalling as an important predictor of clinical outcome, after performing pathway enrichment analysis of differentially expressed peripheral $CD8^+$ T-cell transcripts between responding and nonresponding patients following ICB[371]. More specifically, differential TCR usage is observed between responding and nonresponding patients, perhaps reflecting carriage of specific V(D)J segments within tumour-specific clones[371]. Furthermore, expanding peripheral T-cell clones align with those previously demonstrated to be melanoma-reactive[371]. These data highlight a potentially important role of the TCR repertoire in determining ICB responses.

Within the tumour, T-cell expansion and an increase in clonal unevenness is associated with enhanced survival and may represent expansion of tumour-specific T-cell clones[252,264,265,335,372–376]. However, the predictive capacity of TCR clonality and diversity within the periphery is limited with different studies reporting contradictory results. While some studies have reported peripheral T-cell expansion, clonality and TCR convergence as being favourable[331,372,377,378], others have demonstrated that responding patients have higher TCR diversity[250,251,363,379] or even detect no effect at all[370,371,378,380]. However, the true association may be context-dependent and limited to clones of a specific nature rather than as a whole.

Chronic activation of T-cells within the tumour often predisposes them to an exhausted and dysfunctional phenotype which limits antitumour activity. However, this can be rescued by circulating T-cell clones[372,381]. Many clones expressed within the tumour are also detected in the blood, especially large clones, in which the clonal proportion in the tumour correlates with that in the blood[250,348,370,372,373]. These shared clones accommodate clonally related CDR3 sequences which diversify after ICB in responders[250]. Correspondingly, TCR diversity of peripheral T-cells associates with the number of novel clonotypes detected in the tumour and further suggests that these clones may have originated from the periphery[372,373].

ICB treatment induces proliferation of novel clonotypes and a subsequent increase in diversity of the proliferating clone pool[250]. Proliferating peripheral T-cell clones identified in cell-free DNA at baseline are also clonally related to one another, suggesting recognition of a common antigen[250]. This reduction in clonal relatedness is limited to responding

patients and implies that it is these proliferating, reactivated clones that replace those in the tumour[250]. TCR diversification of these proliferating clones associates with a loss in tumour subclonal mutations and neoantigens, indicative of antitumour response, and may be due to the increased capacity for neoantigen recognition that is translated into the tumour[264]. Although the benefit of overall TCR diversity in the periphery is dubious, the TCR diversity of proliferating clones and those shared with the tumour might be more important in determining response.

Furthermore, Fairfax *et al.* (2020) have identified that it is large peripheral clones, specifically those representing ≥0.5% of TRA and TRB repertoires, that are associated with ICB response[371]. This supports previous data which shows that maintenance of large clones is important[380]. This number of large clones correlates with levels of circulating effector memory T-cells and prolonged PFS and OS[371]. A follow-up study from Watson *et al.* (2021), demonstrates that patients with a combination of high large clone count and cytotoxicity have the best survival[208].

These data show that whilst the effect of overall TCR diversity in the periphery is not clear, large proliferating cytotoxic clones that replenish the tumour might be most important in understanding antitumour responses. More importantly, these data highlight a potentially important role of peripheral T-cells in predicting ICB response.

1.3.4.2 Unconventional T-cells

Whilst the role of cytotoxic T-cells in facilitating antitumourigenic clinical responses has been well described, whether these effects extend to unconventional T cells is largely unknown. Unconventional T-cells are defined by the expression of an invariant TCR and include mucosal-associated invariant T-cells (MAIT cells), invariant natural killer T-cells (iNKT cells) and γδ T-cells. These unconventional T-cells are appropriately named due to their innate-like phenotype, high conservation across different individuals and are thought to bridge the gap between innate and adaptive immunity. In stark contrast to conventional T-cells, these invariant T-cells do not recognise peptidic antigen and are MHC-unrestricted. Furthermore, unconventional T-cells are able to respond to proinflammatory cytokines in a similar manner to NK cells and form an innateness gradient, where their expression lies somewhere between T-cells and NK cells[382]. Despite having features of adaptive immunity, unconventional T-cells mount rapid response against antigen and may respond to antigen independently of their TCR, similar to innate immune cells.

Strikingly, CD161 (*KLRB1*), highly expressed by unconventional T-cells, has previously been reported as one of the strongest predictive markers of clinical response in tumours[99,383]. Additionally, $CD56^+$ T-cells, predominantly composed of unconventional T-cells, associate with response to PD-1 blockade[384]. As such, unconventional T-cells may have important antitumour roles and ultimately determine ICB response.

Whilst the majority of T-cells express αβ TCRs, a small proportion are defined by carriage of γδ TCRs. Although γδ T-cells only represent <5% of peripheral T-cells, they are found to be highly enriched within mucosal tissue with an important role in maintaining homeostasis. Whilst the mode of γδ T-cell antigen recognition is relatively poorly described, γδ T-cells are thought to be able to sense stress-induced molecules expressed by cancer through butyrophilin-like molecules[385–388]. On the whole, γδ T-cells have been found to be favourable in cancer, representing one of the most important cell types for survival[99,389]. However, despite displaying capacity for IFN-γ production and

cytotoxicity, γδ T-cells have also been found to be protumourigenic through production of IL-17[390]. As such, the presence of certain γδ T-cells has been associated with disease progression after ICB[351,391]. Understanding the particular role that γδ T-cells play in melanoma and ICB responses may therefore be of relevance.

INKT cells form the majority of natural killer T-cells and are identified by coexpression of TRAV10, TRAJ18 and TRBV25-1. INKT cells recognise glycolipid antigens, including GalCer, presented by nonpolymorphic CD1d on antigen presenting cells. Interestingly, iNKT cell activation has been demonstrated to kill inhibitory TAMs and limit MDSC immunosuppressive activity[392]. That being the case, higher occurrence of NKT cells in general has been found to be beneficial for ICB response[351]. However, the impact of cancer and ICB on iNKT cells is yet to be elucidated.

MAIT cells are so named due to carriage of a semi-invariant TRA chain and enrichment within the intestinal lamina propria and other mucosal tissues[393–395]. Specifically, MAIT cells are defined by carriage of TRAV1-2 with one of TRAJ12/TRAJ20/TRAJ33 and also accommodate a limited TRB repertoire, with biases towards TRBV6-1, TRBV6-4 and TRBV20-1 usage[393–396]. Interestingly, circulating MAIT cells are MHC-unrestricted and recognise nonpeptidic antigen presented by monomorphic MR1, which acts like a pattern recognition receptor for MAIT cells, facilitating rapid innate-like effector responses. MAIT cells are able to respond directly to a diverse array of bacterial species and yeasts through MR1 presentation and recognition of vitamin B metabolites[397–399]. This includes folate photodegradation product acetyl-6-FP (Ac-6-FP) which inhibits MAIT cell responses[400–402] as well as riboflavin synthesis intermediate 5-(2-oxopropylideneamino)-6-D-ribitylaminouracil (5-OP-RU) which serves as the most potent MR1 activating ligand currently described[403]. Although MAIT cells cannot recognise viruses directly through MR1 presentation, they are able to respond to viral infections independently of the TCR through monocyte-derived cytokines including IL-18 and type I IFNs[404]. Correspondingly, MAIT cells have been found to respond against dengue, influenza, hepatitis B, hepatitis C, HIV and SARS-CoV-2 infections, with enhanced activation and depletion observed within the periphery[404–417].

Whilst the role of MAIT cells in infectious disease has been extensively studied, the role that MAIT cells play in cancer is unclear. Interestingly, MAIT cells have been found to be depleted in cancer patients, but enriched at tumour sites, indicating migration to the tumour[418–424]. Strikingly, high MAIT cell count in the peripheral blood of melanoma patients associates with a favourable response to ICB[425–427]. Moreover, MAIT cells have been shown to respond directly to ICB including upregulation of cytolytic markers and may thus be involved in antitumour responses[425]. Although MAIT cells have demonstrated an ability to elicit anticancer cytotoxicity upon culture with activating ligand 5-OP-RU, whether MAIT cells can recognise cancer independently of vitamin B intermediate ligands is unknown. Given the recent description of an MR1-restricted T-cell clone eliciting broad antitumour cytotoxicity, it is interesting to speculate if MR1-restricted cells have an important function in cancer recognition[428].

Due to the high conservation of unconventional T-cells, as well as the differing associations they have with ICB treatment, unconventional T-cells may represent important predictive markers of ICB response.

1.3.4.3 B-cells

Although the role of T-cells in ICB responses has been described extensively, the corresponding effect of ICB on B-cells is less clear. High B-cell and plasma cell tumour infiltration is associated with clinical response to ICB for a multitude of cancers, and is found to increase T-cell infiltration through chemokine production and additionally, sustains antimelanoma responses[99,252,320,334,359,365,366,391,429–437]. However, the clinical benefit of B-cells has not been observed in all studies[364,438–440]. In a similar fashion to Tregs, IL-10-expressing regulatory B-cells, as well as inflammatory B-cells, are found to limit ICB response[434,439].

B-cells have an essential role in humoral immunity through expression of antibodies, which can recognise melanoma antigens directly and exert tumouricidal effects on melanoma through ADCP or ADCC[441]. Importantly, melanoma-specific antibodies against differentiation and cancer testis antigens have been identified, and are found to be preferentially enriched within responding patients[442]. Furthermore, high titres of switched antibodies, particularly of class IgG, are associated with enhanced survival after ICB[442,443]. These data implicate a role for antibody production in antitumour responses and ultimately, ICB response.

However, B-cells are also essential in mediating T-cell activation within lymphoid tissue. Although B-cells can be found within the tumour, they typically reside within draining lymph nodes and tertiary lymphoid structures (TLS's). TLS's are localised proximal to the tumour and are frequently identified in melanoma[444]. TLS's are ectopic lymphoid organs found within nonlymphoid tissue, including at tumour sites, and are important for initiating adaptive immune responses. TLS's are a complex structure of fibroblasts, follicular DCs, Tfh cells and high endothelial venules, which allow influx of B-cells and T-cells. These B-cells form highly structured B-cell follicles which contain germinal centres, whereas the T-cells localise to T-cell zones which are enriched for DCs. $CCR7^+$ T-cells and DCs are recruited to TLS's in response to secretion of CCR7 ligands, CCL19 and CCL21, while $CXCR5^+$ B-cells and Tfh cells are recruited by CXCL13. Here, B-cells and T-cells are exposed to antigen which induces migration to the B-cell/T-cell zone border, B-cell/T-cell interaction and subsequent differentiation into either effector B-cells or T-cells. B-cells may also undergo CSR and SHM within germinal centre reactions to further enhance antigen affinity through affinity maturation.

Intriguingly, ICB increases TLS formation at tumour sites in which TLS's represent an important predictor of ICB response for a variety of cancer types[363,366,430,435,445–448]. Moreover, induction of B-cell recruiter and marker of germinal centre activity, CXCL13, has similarly been observed following ICB treatment and demonstrates enhanced survival[261,343,363–365,376,449–451], whereas CXCL13 depletion in mice induces ICB resistance[365]. Supporting the theory that B-cell recruitment and subsequent TLS activity is important for antitumour T-cell responses, activated expanding $PD\text{-}1^{hi}$ TILs, tumour-specific T-cells and tumour-associated MAIT cells are found to express exceedingly high levels of CXCL13 which correlates with neoantigen load and induces B-cell recruitment[261,348,376,425,451–454]. $CD86^+$ B-cells accumulate within TLS's following ICB and demonstrate an essential role in providing costimulation to induce tumour-specific T-cell activation, proliferation, migration to tumour and T-cell composition[299,433,455,456]. Correspondingly, the presence of TLS-associated follicular Tregs, which inhibit both B-cell and T-cell activation, are found to limit ICB efficacy[457].

Interestingly, the clinical benefit of TLS's is dependent on expression of AID[445]. This

potentially uncovers a crucial role of secondary antibody diversification, including CSR and SHM, in ICB responses. Correspondingly, a higher level of switched memory B-cells and antibody-secreting cells are found in tumour-associated TLS's[366]. However, the impact on other B-cell subsets and the BCR repertoire is unknown. Whether an increase in CSR and SHM is observed following ICB treatment remains to be formally tested.

Although tumour-infiltrated and TLS-associated B-cells appear to have an essential role in T-cell activation and antitumour responses[455], the importance of peripheral B-cells is less clear. Das *et al.* (2018) explore the impact of ICB on peripheral B-cells and find a profound depletion following combination CTLA-4/PD-1 treatment, but not after single agent CTLA-4 or PD-1 blockade[458]. However, the reason behind these differences has not been established. The B-cell depletion associated with increased proliferation and plasma cells which might be indicative of increased germinal centre activity and hence the increase in TLS's observed[458]. Persistence of these plasma cells in the blood, especially those demonstrating CSR and SHM, has favourable outcomes in ICB response[459]. Whilst most studies have focused on tumour-associated B-cells, these data suggest a predictive role for peripheral B-cells.

1.3.5 CMV

In addition to cancer, the immune system is also heavily impacted by chronic infection including human cytomegalovirus (CMV). CMV is a ubiquitous β-herpesvirus (HHV-5) infecting 45-100% of the population depending on age, geography and socioeconomic status[460–463]. CMV typically results in chronic infection which remains latent, but can be reactivated throughout life. Although CMV is largely asymptomatic and subclinical in healthy adults, it can have severe consequences in infants and immunocompromised individuals, such as cancer patients, owing to persistent immune cell surveillance, subsequent dysfunction and immune senescence that is observed in infection. With most CMV genes found to be dispensable in production of infectious virus, it has been suggested that CMV dedicates most of its genes to immune evasion, including inhibition of antigen presentation, immune surveillance, cell function and subsequent NK cell and T-cell responses[464–472]. Persistence of CMV infection, along with expression of the plethora of CMV-associated immunoevasins, contributes to dynamic changes in both innate and adaptive immune systems.

CMV-specific $CD8^+$ T-cells are essential for infection control and are sustained in the periphery as large, activated expanded clones[473]. As a result, CMV^+ individuals associate with enhanced differentiation and reduced TCR diversity[371,474–482]. These CMV-specific clones grow with age, yet decrease in functionality and become exhausted[483].

Given the role of $CD8^+$ T-cells in ICB response, confounding effects of infection on the ICB response need to be identified.

1.4 Summary

This introduction has highlighted the extensive involvement of the immune system in melanoma and corresponding survival, as well as how ICB has improved clinical outcomes. However, response rates are still limited for MM patients, with only a minority experiencing durable clinical benefit and many patients developing toxicities. An extensive review of the literature has revealed several key features that determine ICB response.

Most importantly, the benefit of CTLA-4 and PD-1/PD-L1 blockade is determined by the extent of T-cell priming, activation, tumour infiltration and ultimately melanoma-directed cytotoxicity. This is in addition to B-cell recruitment and TLS activity which are important for directing T-cell responses.

Tumour-associated features have also been well described in predicting outcome. Most significantly, a high tumour mutational burden correlates with clinical benefit, owing to enhanced neoantigen load and tumour immunogenicity, which enhances immune reinvigoration. However, an immunosuppressive TME, including infiltration of Tregs, MDSCs, TAMs and neutrophils, limits the extent of this response and confers disease progression. This is in addition to compensation of diminished CTLA-4/PD-1/PD-L1 activity through upregulation of other inhibitory immune checkpoints, and thus suggests a role for simultaneously targeting multiple inhibitory immune checkpoints.

Given that ICB activity is predicated on host immune-based correlates, correlates within the immune system have proven to be robust predictors of response. Although T-cells are considered to be the principal target of ICB, recent data has also indicated an important role of B-cells and TLS activity in ICB response.

Most currently appreciated predictive markers rely on features of the tumour, including mutation rate, cellular composition and expression of PD-L1. However, tumour biopsies are invasive, time-consuming, risk local injury and insufficiently represent intratumoural heterogeneity. The use of a peripheral marker facilitates a more convenient approach to sample collection and provides the opportunity for frequent biopsies and longitudinal monitoring of ICB response. Additionally, tumours are repopulated by circulating T-cells and hence represent important determinants of ICB response. Thus, characterising predictive markers in the periphery is of great interest.

To date, several key areas remain unexplored. Although the benefit of ICB is thought to be mediated through T-cell activation, the effect on unconventional T-cells remains elusive, despite demonstrating anticancer activity and changes in expression following ICB treatment. Furthermore, although the mechanism of ICB action is well understood within T-cells, the effect on other non-T-cell immune cell subsets including B-cells, which can also express immune checkpoint targets, is unclear. Whether changes observed within peripheral immune subsets are secondary to T-cell responses is not known. Finally, owing to the significant polarising effects of CMV infection on T-cells, how CMV serostatus affects the propensity of ICB-mediated changes is uncertain.

1.5 Aims

The main aims of this thesis are to characterise the peripheral immune response to ICB treatment and identify any predictive markers of clinical outcome. In view of the importance lymphocytes have in mediating ICB responses, I explore ICB-associated peripheral T cell responses in Chapter three and B cell responses in Chapter four. Corresponding effects on BCR and TCR repertoires, including for unconventional T-cells, are subsequently described in Chapter five. I also investigate any effect of CMV infection in patients with melanoma and characterise how this affects immune-based responses to ICB. My key aims are highlighted below:

- What is the effect of ICB on peripheral immune cells?
- Are any of these effects dependent on treatment type?
- Does CMV serostatus determine ICB response?
- Are T-cells the main target of ICB?
- Are the effects of ICB consistent between conventional and unconventional T-cells?
- Are changes in peripheral immune subsets determined by T-cell response?
- Do any of these changes correspond to BCR and TCR repertoires?
- Can we use features from peripheral B-cells and T-cells to predict clinical outcome?

Chapter 2

Materials and Methods

2.1 Patient cohort

2.1.1 Samples

Peripheral blood samples were obtained from either healthy donors or MM patients over the course of ICB treatment (Table 2.1). Patients were recruited via the Oxford Radcliffe Biobank (Oxford Centre for Histopathology Research ethical approval numbers 16/A019 and 18/A064), whilst healthy control samples were collected via the Oxford Biobank (Research ethical approval number 06/Q1605/55), after providing written informed consent.

Patients were treated with either single agent pembrolizumab or nivolumab monoclonal anti-PD-1 antibodies (sICB) or a combination of ipilimumab and nivolumab (cICB), targeting both CTLA-4 and PD-1 simultaneously. Samples were collected immediately prior to commencement of ICB treatment (d0, C1), as well as before the second dose (d21, C2), fourth dose (d63, C4) and at later time-points when available. All patients received the NHS standard of care at the time with pembrolizumab administered once every three weeks and nivolumab every four weeks. Patients receiving cICB treatment received one dose every three weeks with cessation of ipilimumab after four doses followed by maintenance nivolumab treatment.

Factor	Healthy donors Number/Range, Average ±SD	Patients Number/Range, Average ±SD
Number	172	200
Age	21–76, 45 ±11	21–96, 64 ±14
Sex	105 F, 67 M	89 F, 111 M
CMV serostatus	7 CMV−, 7 CMV+, 158 unknown	88 CMV−, 82 CMV+, 30 unknown
Cycle	n/a	193 C1, 166 C2, 96 C3–C4, 14 C5–C10, 17 C11–C20, 15 C21–C30, 8 C30+
Treatment	n/a	100 ipilimumab/nivolumab, 85 pembrolizumab, 15 nivolumab
ICB	n/a	100 sICB, 100 cICB
Disease type	n/a	10 nonmetastatic, 190 metastatic
BRAF status	n/a	139 non−mutated BRAF, 53 mutated BRAF, 8 unknown
Melanoma subtype	n/a	113 epithelial, 8 mucosal, 6 uveal, 2 small cell, 1 amelanocytic, 70 unknown

Table 2.1

Table 2.1 (Previous page) Sample cohort
Summary of clinical features, where available, for both healthy donors and melanoma patients in the cohort. *CMV = human cytomegalovirus, ICB = immune checkpoint blockade, sICB = single agent anti-PD-1, cICB = combination anti-CTLA-4/PD-1, F = female, M = male, SD = standard deviation.*

2.1.2 Clinical outcome data

Patient clinical data, including disease progression and development of irAEs, was collected for the cohort (Table 2.2). Outcome data was generated using clinical or radiological data according to immune-related Response Evaluation Criteria in Solid Tumors v1.1 (irRECIST.1.1)[484]. As well as determining OS and PFS, patients were dichotomised according to progression status at either six or twelve months. Development of irAEs was identified as evidence of autoimmune toxicity occurring within three months of commencing ICB treatment, as per the National Cancer Institute Common Terminology Criteria for Adverse Events (CTCAE)[485]. Only patients who were still alive at three months were included in analysis. Kaplan-Meier curves were generated using *survival*[486], *survminer*[487] and *survMisc*[488] packages to compare OS and PFS.

Clinical outcome	sICB	cICB
Response at 6 months	40 NR, 60 R (60%)	38 NR, 62 R (62%)
Response at 12 months	41 NR, 59 R (59%)	46 NR, 48 R (51.1%)
Average months to progression ±sd	21.9 ±21.2	16.8 ±15.6
Average months to death ±sd	28.7 ±20.9	24.4 ±15.7
Presence of irAEs at 3 months	36 irAE–, 22 irAE+ (37.9%)	8 irAE–, 48 irAE+ (85.7%)

Table 2.2 Summary of MM patient clinical outcomes
MM patients were dichotomised into those with or without evidence of progression at six or twelve months. Percentages represent the percentage of patients without progression at the relevant time-point. Average months to progression and death are displayed along with standard deviation. Patients were also separated based on development of immune-related adverse events (irAEs) at three months for patients with available clinical data. Only those still alive at three months were included for irAE analysis. *NR = no response, R = response, sd = standard deviation.*

2.2 Blood processing

2.2.1 Ficoll density gradient centrifugation

30-50ml peripheral blood was collected from healthy donors or MM patients into Ethylenediaminetetraacetic acid (EDTA)-coated tubes (BD Vacutainer System). Samples were diluted 1/2 in Hank's Balanced Salt Solution (HBSS) without Phenol Red or Calcium (Lonza). Diluted blood was carefully layered onto 12.5ml Ficoll-Paque™ PLUS (GE Healthcare) into multiple 50ml Falcon tubes. Samples were then subjected to density centrifugation by centrifuging samples at 400G, with acceleration set as "slow" and deceleration set as "off", for 30 minutes at room temperature.

2.2.2 Plasma collection

Plasma was gently aspirated from the resulting top layer, taking care not to disturb the buffy coat. Plasma was then ultracentrifuged at 16,000G, with "max" acceleration and deceleration, for 20 minutes at 4°C, to remove any contaminating platelets, immune cells and cellular debris. Centrifuged plasma samples were kept at -80°C and used for CMV testing and ELISA analyses.

2.2.3 Peripheral blood mononuclear cell isolation

Peripheral blood mononuclear cells (PBMCs) were isolated from the buffy coat layer and placed into a 50ml Falcon tube. Samples were washed twice in cold HBSS and centrifuged at 300G for 10 minutes at 4°C, prior to counting via trypan blue (Merck) exclusion using a haemocytometer (Hausser Scientific). 3-10x10^6 PBMCs were resuspended in freezing media (90% foetal bovine serum (FBS, Gibco), 10% Dimethyl sulphoxide (DMSO, Merck)) per cryovial and kept in liquid nitrogen storage for subsequent flow cytometry analysis and cell culture. In addition, 1.25x10^6 PBMCs were lysed in 350µl RLT Plus buffer (Qiagen) supplemented with either 40mM Dithiothreitol (Merck) or 0.143M β-mercaptoethanol (β-ME, VWR), hereon referred to as RLT buffer, and stored at -80°C for subsequent qPCR analysis.

2.2.4 Magnetic-activated cell sorting

Magnetic-activated cell sorting (MACS) separation of remaining PBMCs was performed to isolate a combination of $CD8^+$ T-cells, $CD14^+$ monocytes, $CD19^+$ B-cells, $CD4^+$ naïve T-cells, $CD4^+$ memory T-cells and NK cells using microbeads (Miltenyi), applying either positive ($CD8^+$ T-cells, $CD14^+$ monocytes, $CD19^+$ B-cells) or negative ($CD4^+$ naïve T-cells, $CD4^+$ memory T-cells and NK cells) selection-based approaches. The number of cell selections performed per sample largely depended on the number of PBMCs isolated. However, typically for each sample, two positive selections were performed in parallel using leftover sample for two subsequent negative selections. MACS-based sorting was performed according to manufacturer instructions using MACS buffer (50ml HBSS, 0.5% FBS, 2mM EDTA (Merck)), MS columns (Miltenyi) and an OctoMACS magnet (Miltenyi). Samples were kept on ice throughout the protocol.

Firstly, positive selections were performed on remaining PBMCs. Samples were separated into two tubes, aiming for 10-20x10^6 cells per selection. Cells were resuspended in cold 80µl MACS buffer per 10^7 PBMCs. Next, 20µl microbeads were added per 10^7 PBMCs, mixed well and incubated for 15 minutes at 4°C. Cells were washed in 1ml MACS buffer and centrifuged at 300G for 10 minutes at 4°C to remove excess microbeads. Supernatants were discarded and samples were resuspended in 500µl MACS buffer. MS columns were first prewet with 500µl MACS buffer before samples were passed through. Columns were then washed three times with 500µl MACS buffer. These sample flow throughs were kept for subsequent negative selections. Magnetically-labelled cells were flushed out of columns in 1ml MACS buffer using the plunger provided.

Secondly, negative selections were performed using sample flow throughs from the preceding positive selections. Samples were centrifuged at 300G for 10 minutes at 4°C, prior to resuspension in 80µl MACS buffer per 10^7 PBMCs. 10µl biotin-antibody cocktails were then added to samples, mixed and incubated for 5 or 10 minutes at 4°C (NK cells/$CD4^+$ naïve cells or $CD4^+$ memory cells respectively). Following this incubation,

an extra 30µl MACS buffer was added, along with 20µl anti-biotin microbeads per 10^7 PBMCs. Samples were resuspended and incubated at 4°C for 10 or 15 minutes (NK cells/$CD4^+$ naïve cells or $CD4^+$ memory cells respectively). Volumes for NK cells and $CD4^+$ naïve cells were topped up to 500µl with MACS buffer before adding to prewet columns. Columns were then washed once with 500µl MACS buffer. Contrary to positive selections, target cells were collected directly from sample flow throughs. Alternatively, $CD4^+$ memory cells were washed in 1ml MACS buffer and centrifuged at 300G for 10 minutes at 4°C. Samples were resuspended in 500µl MACS buffer before applying to prewet columns. Samples were then washed with 500µl MACS buffer three times, collecting cells directly from sample flow throughs.

All isolated cell samples were counted using a Countess II FL Automated Cell Counter (Thermo Fisher Scientific) and trypan blue exclusion. Cells were then washed in HBSS and lysed in 350µl RLT buffer. Samples were stored at -80°C prior to RNA/DNA extraction and subsequent RNA sequencing (RNAseq). Alternatively, intact cells were used for 10x single cell sequencing.

2.3 Transcriptomic analysis

2.3.1 Bulk RNAseq

2.3.1.1 RNA extraction

Samples in RLT were thawed on ice and homogenised using QIAshredder columns (Qiagen). RNA was extracted using the AllPrep DNA/RNA/miRNA kit (Qiagen), adhering to manufacturer guidelines. RNA samples were treated with 10µl DNase I (2.73 Kunitz units/µl, Qiagen) for 20 minutes to minimise DNA contamination. RNA was eluted in 33µl of nuclease-free water, with concentration determined using a Qubit 4 fluorometer (Thermo Fisher Scientific) and corresponding Qubit reagents (Qubit RNA HS Assay kit, Thermo Fisher Scientific). RNA samples were subsequently stored at -80°C prior to RNAseq library preparation.

2.3.1.2 Library preparation

RNA samples were thawed on ice prior to mRNA isolation using the NEBNext® Poly(A) mRNA Magnetic Isolation Module kit (New England Biolabs) following standard protocol. Libraries were then generated using an input of between 100 and 1000ng of RNA using NEBNext® Ultra II Directional RNA Library Prep Kit for Illumina® (New England Biolabs) and SPRISelect™ beads (Beckman Coulter) for sample clean-up steps. Library dsDNA was quantified using a Qubit 4 fluorometer and high sensitivity dsDNA Qubit kits (Thermo Fisher Scientific). Libraries were also screened using the 2200 TapeStation system, TapeStation D1000 HS tapes and corresponding reagents (all Agilent Technologies).

2.3.1.3 Sequencing

Samples were sequenced across four batches on either an Illumina® HiSeq 4000 (75bp paired-end) or NovaSeq 6000 (150bp paired-end) at the Oxford Genome Centre (Wellcome Trust Centre for Human Genetics).

2.3.1.4 Upstream data processing

HISAT2[489,490] was used to align reads to the *Homo sapiens* GRCh38/hg38 genome build. *Bamtools*[491] was then implemented to filter out low quality reads by MAPQ score and *Picard*[492] was used to exclude any duplicate reads. *HTSeq*[493] was then used to generate final read count tables. *VerifyBamID* software[494] was applied to identify sample contamination in which 2.5% was accepted as a maximum. Table 2.3 displays the number of high quality transcriptomes generated per cell type and average number of reads per sample. The lower average read number observed for $CD19^+$ B-cell samples is attributed to sequencing batch.

Cell type	Number of transcriptomes	Average number of reads
CD8+ T-cells	504	35689800
CD19+ B-cells	308	17042568
CD14+ monocytes	284	37096016
NK cells	174	33381693
CD4+ naïve T-cells	69	33703467
CD4+ memory T-cells	26	36483560

Table 2.3 Summary of bulk RNAseq samples
Table showing the number of high quality transcriptomes generated and average number of reads per sample by cell type.

2.3.1.5 Differential gene expression

DESeq2[495] was used to normalise gene counts. First, a *DESeq2* object was created using "*DESeqDataSetFromMatrix(countData = Gene count data, colData = Sample metadata, design = ~ 1)*". Next, gene counts were normalised for library size and gene variations using "*estimateSizeFactors(DESeq2 object)*" and "*estimateDispersions(DESeq2 object)*" respectively. After estimating the gene dispersions, "*counts(DESeq2 object, normalised = TRUE)*" was applied to retrieve the counts data after dividing by the size factors. Data was then transformed to be approximately homoskedastic from the fitted dispersion-means using "*getVarianceStabilizedData(DESeq2 object)*". Lowly expressed genes with an average normalised count of $\leq$10 were excluded from analysis using "*rowMeans(Normalised gene counts) >10*". This created a matrix of normalised gene counts which was subsequently used for principal component analysis (PCA). Normalised gene counts were also used to generate gene expression scores by calculating the geometric mean of the most significantly associated genes for a specified condition. Genes used for generation of cytotoxicity score were obtained from previously published work[208]. The number of genes used per score is stated per figure.

PCA was performed using "*prcomp(Normalised gene counts, center = TRUE, scale = TRUE)*" from the default *stats* package[496]. Principal components (PCs) were tested for their association with any confounding variables such as age, sex and library RNA input. All of these variables were found to associate with PC values and were subsequently controlled for in differential gene expression analyses where appropriate.

Differential gene expression between different conditions was performed in a similar

manner to gene normalisation using *DESeq*2. Firstly, a *DESeq*2 object was created using "*DESeqDataSetFromMatrix(countData = Gene count data, colData = Sample metadata, design = ~ Confounding variables + Testing variable)*". Gene counts were normalised and transformed as before using "*estimateSizeFactors(DESeq2 object)*" and "*estimateDispersions(DESeq2 object)*" as well as removing genes with a normalised count ≤10 using "*rowMeans(Normalised gene counts) >10*". Next, a negative binomial generalised linear model was applied to test for significance of coefficients using "*nbinomWaldTest(DESeq2 object)*", adjusting for multiple testing using the Benjamini-Hochberg procedure. Gene enrichment scores were then extracted using "*results(DESeq2 object)*". Ensembl gene IDs were translated into gene names using "*getGenes(Ensembl gene IDs, fields = 'symbol')*" as part of the *mygene*[497] package. Genes differentially expressed between two variables were considered significant for $padj \leq 0.05$. For any pairwise comparisons e.g. for paired C1/C2 samples, patient ID was controlled to ensure a paired analysis.

For comparisons between different cell types or treatments, data was randomly subsampled to the same number of samples per comparison to ensure equivalent statistical power. This was performed using "*resample(data, size = Subsample number, replace = FALSE)*" using the *mosaic* package[498].

2.3.1.6 Pathway analysis

Pathway analysis was performed using genes found to be significantly upregulated within a certain condition using *clusterProfiler*[499,500] and *org.Hs.eg.db*[501] packages. Specifically, pathway enrichment of upregulated genes was analysed using "*enrichGO(Upregulated genes, universe = All genes, OrgDb = org.Hs.eg.db, ont = 'BP', pAdjustMethod = 'BH', qvalueCutoff = 0.05)*" to return GO enriched pathways using the *Homo sapiens* database, "Biological processes" subontology and Benjamini-Hochberg procedure, keeping only pathways with a significant enrichment of $padj \leq 0.05$. Outputs were simplified to remove redundant terms using "*simplify(GO object, cutoff = 0.7)*" to remove GO terms with a similarity score of ≥ 0.7. Alternatively, *fgsea*[502] was used for pathway enrichment of custom gene sets, including MAIT cell and γδ T-cell-associated genes. Analysis was performed using "*fgsea(pathways = Custom gene set, states = Ranked differentially expressed genes)*".

2.3.1.7 BCR/TCR mapping

MiXCR[503,504] was used to map BCR/TCR reads from bulk RNAseq fastq files to reference V, D, J and C genes and to detect clonotypes based on unique BCR/TCR nucleotide sequence, according to previously published protocols[371]. After filtering out contaminating BCR/TCR clones, as detected by BCR/TCR usage, an average of 108,744 BCR reads were detected per $CD19^+$ B-cell sample and 13,035 TCR reads per $CD8^+$ T-cell sample. Individual *MiXCR* output files were combined into two separate lists in an R environment for BCR and TCR files which were then analysed independently.

Complementarity determining regions (CDRs), including CDR1, CDR2 and CDR3, were identified by *MiXCR* for BCR and TCR clones. Summarised CDR3 amino acid sequences were calculated and visualised using *ggseqlogo*[505] for BCR and TCR clones of amino acid lengths 15 and 14 respectively. CDR3 synonymy was generated by calculating the difference in number of unique CDR3 clones by nucleotide and amino acid sequences and expressed as a percentage of total identified clones as a measure of clonal redundancy.

2.3.2 Investigating BCR/TCR repertoires

2.3.2.1 BCR/TCR usage

MiXCR output files contained annotated BCR/TCR genes per clone. Chains were then identified per clone based on expression of IGH/IGK/IGL or TRA/TRB/TRG/TRD gene segments for BCR and TCR samples respectively. Chain usage for TCR clones expressing TRAV/DV V gene elements, which may be expressed by either TRA or TRD clones, was determined by J gene segment usage. Carriage of both a TRAV/DV and TRAJ gene identified clones as being TRA, whereas carriage of a TRAV/DV and TRDJ gene identified clones as being TRD. Few clones containing TRAV/DV, TRDD and TRAJ elements were detected (an average 0.18% of TRA clones) and remained classified as a TRA clone despite expression of a TRD D gene.

BCR/TCR usage was then generated for each of V, D, J and C gene segments. Usage was calculated by unique BCR/TCR gene as the percentage of reads expressing a particular gene segment out of all reads from the relevant chain. BCR/TCR clonal usage was instead determined as the percentage of clones, rather than reads, expressing specific gene segments.

2.3.2.2 Unconventional T-cell percentages

MAIT cell percentage was predicted by calculating the percentage of TRA reads or clones carrying TRAV1-2 and one of either TRAJ12, TRAJ20 or TRAJ33. Similarly, iNKT cell percentage was determined by calculating the percentage of TRA reads or clones with TRAV10 recombined with TRAJ18. Finally, γδ T-cell percentage was calculated as the percentage of all TCR reads or clones expressing either a TRG or TRD chain.

2.3.2.3 Clonality indices

Owing to variation in sample read number, data was randomly subsampled to the same number of reads per sample to allow for fair comparison of clone and diversity indexes. Firstly, clones were uncounted using "*uncount(data, Clone count)*" from package *tidyr*[506] making each row a unique read. Next, clone or diversity measures were calculated on subsampled reads and iterated 1,000 times using "*do(1000) * resample(data, size = Subsample number, replace = TRUE)*" from the *mosaic* package[498], taking the average from the 1,000 iterations as final readings. Reads were subsampled to the lowest number of reads detected for a sample which was 4,471 for BCR samples and 1,496 for TCR samples. However, for interchain comparisons, data was subsampled to 1,028 or 100 reads for BCR and TCR chains respectively. B-cell samples were also downsampled to 1,496 reads for comparison with paired TCR samples.

Shannon diversity was used as a measure of clonal richness and was generated using "*diversity(Clone counts, index='shannon')*" as part of the vegan package[507,508]. Equivalent results were observed using the fossil package[509] and manual calculations. Secondly, clonal unevenness was measured using the Gini index, calculated using "*Gini(Clone counts)*" as part of the *DescTools* package[510]. In a similar manner, the average number of unique clones and average clonal proportion were calculated for BCR and TCR samples using this subsampling approach.

2.3.2.4 Mutation rate

Mutation rate was inferred in BCR and TCR samples, representative of junctional diversity as well as SHM in BCR clones. Information regarding base substitutions, insertions and deletions was extracted from *MiXCR* output files from "allVAlignments", "allDAlignments" and "allJAlignments" columns. The average number of mutations was calculated as the average number of substitutions, insertions and deletions per clone combined.

2.3.2.5 Clonal dynamics

In order to measure clonal dynamics, paired C1/C2 or C1/C4 samples were merged. Per patient, clone proportion, total clone number as well as the difference between the two was determined to generate a contingency table for Fisher's exact test analysis and was calculated using "*fisher.test(Contingency matrix)*" from the default *stats* package. This calculated a p-value for the enrichment of the clone in either cycle on a patient-specific basis. This p-value was adjusted by Bonferroni correction using "*p.adjust(p-values, method = 'bonferroni', n = length(Number of clones))*" from the *stats* package, correcting for the number of clones tested per individual. Percentage of expanding or contracting clones was calculated as the percentage of clones significantly increasing or decreasing at C2/C4 over the total number of clones identified. The percentage of novel clones was calculated as the percentage of significantly expanding clones that were not present at C1 over the total number of clones.

2.3.2.6 Identifying and tracking known TCR clones

CMV and cancer-associated TCR CDR3 amino acid sequences were extracted from VDJdb[511,512], McPAS[513] and TBAdb[514] databases. Only TCR clones with a reliability score of >0 from VDJdb were included for analysis. Any TCR clones with a CDR3 amino acid sequence aligning to these clones were hence identified as being CMV or cancer-reactive clones. The percentage of CMV/cancer-associated clones was calculated as the percentage of reads/clones aligning to these known CMV/cancer-associated clones by TCR chain.

2.3.3 Single cell RNAseq

2.3.3.1 Sample preparation

The 10x Chromium platform was used to generate single cell libraries for $CD19^+$ B-cells in two batches. In the first batch, 10x was performed on 12,000 $CD19^+$ B-cells derived from three healthy donors (4,000 cells per donor). Alternatively, 6,000 $CD19^+$ B-cells from one untreated MM patient were used for the 10x reaction in the second batch. Cells were put through the 10x Chromium controller, along with partitioning oil and gel beads, to tag each individual cell with a unique barcode. Libraries were subsequently generated using Chromium Single Cell 5' V(D)J Library kits v1 (10x Genomics) following manufacturer guidelines. In addition to whole gene expression (GEX) libraries, BCR-enriched libraries were prepared using nested polymerase chain reaction (PCR) enrichment, targeting BCR constant regions. Samples were visualised and quantified using a 2100 Bioanalyzer and associated reagents (both Agilent Technologies) at each stage of the protocol.

2.3.3.2 Sequencing

Both GEX and BCR libraries were sequenced together on an Illumina® NovaSeq 6000 with 150bp paired-end reads. Samples were sequenced so as to attain a minimum of 50,000 reads/cell for GEX libraries and 5,000 reads/cell for BCR libraries, as recommended by 10x Genomics.

2.3.3.3 Upstream data processing

Cell Ranger[515] was used to produce fastq files from Illumina® base call files, applying the command "*cellranger mkfastq*" to align GEX reads as well as demultiplexing each individual reaction. Commands "*cellranger count*" and "*cellranger aggr*" were then applied to fastq files to generate single cell feature counts and aggregate samples. Alternatively, "*cellranger vdj*" was used to align BCR reads from generated fastq files, outputting sample barcode, cell barcode, assembled clonotypes, chain usage and unique molecular identifier (UMI) number. Outliers and multiplets were removed using *scater*[516] and *scran*[517] packages respectively.

2.3.3.4 Quality control

Seurat[518–521] was used to analyse single cell data including quality control, data preparation and clustering. Firstly, a Seurat object was created using "*CreateSeuratObject(counts = Feature expression matrix, min.cells = 3, min.features = 200)*", keeping only cells with at least 200 unique genes and only genes that are expressed in at least 3 cells. By calculating the percentage of mitochondrial genes using "*PercentageFeatureSet(Seurat object, pattern = '∧MT-')*", cells expressing high levels of mitochondrial genes, likely representing dying cells and multiplets, were removed. After considering the high expression of mitochondria in B-cells[522,523] and the variation in percentage, cells with $\leq 1\%$ or $\geq 15\%$ mitochondrial genes were subsequently removed.

2.3.3.5 Downstream data processing

Data was then log normalised to control for cell sequencing depth, applying a scale factor of 10,000 using "*NormalizeData(Seurat object, normalization.method = 'LogNormalize', scale.factor = 10000)*". Next, "*FindVariableFeatures(Seurat object)*" was applied to detect the most variable genes using a mean variability plot. To control for batch effect, integration anchors were identified between the two Seurat objects, using "*FindIntegrationAnchors(object.list = list(Seurat objects))*", and were used to merge data, applying the function "*IntegrateData(anchorset = Immune anchors)*".

2.3.3.6 Clustering analysis

Data was then centred and scaled to give all genes the same range and prevent highly expressed genes from dominating downstream PCA analysis. This was performed using "*RunPCA(Seurat object, features = VariableFeatures(object = Seurat object))*". PCs significantly contributing to the explained data variance were determined using "*ElbowPlot(Seurat object, reduction = 'pca')*", "*JackStraw(Seurat object)*" and "*ScoreJackStraw(Seurat object, reduction = 'pca', do.plot = TRUE)*" to visualise the contribution of each PC to the standard variation of the data, as well as the significance of contribution for Elbow and Jack Straw plots respectively.

Next, data was subjected to "*FindNeighbors(Seurat object, reduction = 'pca', dims = 1:x)*" in order to generate a shared nearest neighbour graph using the k-nearest neighbour similarity measure per cell. This was performed on the data applying the optimal number of PCs (x) as determined by Elbow and JackStraw plots. "*FindClusters(Seurat object, resolution = y)*" facilitated unsupervised clustering of cells with optimal resolution (y) determined using clustering trees at varying resolutions as visualised by "*clustree(Seurat object)*" analysis using the *clustree* package[524]. Annotated cell clusters were visualised by uniform manifold approximation and projection (UMAP) plot. Public single cell B-cell data files were downloaded online and analysed in an identical manner[359,410,525].

2.3.3.7 Cluster annotation

Cell cluster annotation was aided by alignment with previously published datasets using *SingleR*[526]. Firstly, Seurat objects were transformed into readable objects using "*as.SingleCellExperiment(Seurat object)*". Next, single cell PBMC expression data from Monaco *et al.* (2019)[527] was read into R using "*MonacoImmuneData()*". Finally, "*SingleR(test = Seurat object, ref = MonacoImmuneData, labels = MonacoImmuneData subsets)*" was used to generate scores per Monaco Immune Data cell subset for all cells. Cells were subsequently assigned to the Monaco Immune Data cell subset with the highest score. Cells which aligned to non-B-cell subsets were subsequently removed.

2.3.3.8 Generating B-cell subset scores from bulk RNAseq data

"*FindAllMarkers(Seurat object)*" was used to identify the most significantly enriched genes per cell subset. The geometric mean of the top 20 enriched genes per subset was calculated for each bulk RNAseq $CD19^+$ B-cell sample using "*geometricmeanRow(Normalised gene counts)*" from the *compositions* package[528]. This generated subset expression scores for all subsets per sample, representing imputed subset proportion.

2.3.3.9 BCR analysis

Assembled BCR clones were merged with cell subset annotations by matching cell barcodes. B-cells were then dichotomised into either unswitched or switched B-cells based on IGHC usage for comparisons in switch status. BCR expression was determined as the number of BCR UMIs detected and normalised by the total number of sequenced reads per cell. This was also performed for single cell $CD8^+$ T-cell data derived from MM patients in the same cohort[208,371] to compare the level of BCR and TCR expression per cell.

2.4 qPCR analysis

2.4.1 Primer design

Primers (Invitrogen) were designed using NCBI Primer Blast[529] to selectively amplify target genes. More specifically, primers were designed to produce amplicons with a minimum length of 70bp and a maximum of 400bp for subsequent qPCR analysis. In order to reduce primer-dimer formation, but maintain target specificity, primers of length 20-23bp were chosen with ∼50% GC content and minimal self-complementarity score. The UCSC *in silico* PCR tool[530] was used to test for nonspecific amplification. Melt curves were performed to further optimise primer specificity and were visualised by agarose gel (3% UltraPure™ Agarose, Invitrogen).

2.4.2 *MiXCR* validation

MiXCR output data was validated by comparison with qPCR analysis of known growing and stable $CD8^+$ T-cell clones[371]. Primers were designed against expanding and stable $CD8^+$ T-cell clones at C2 for TRA and TRB chains identified from *MiXCR* data. Forward primers were targeted against CDR3 regions with reverse primers complementary to TRA or TRB constant regions (Table 2.4).

2.4.3 qPCR reaction

8µl of RNA from 1.25x10^6 PBMCs was reverse transcribed using the SuperScriptIII First-Strand Synthesis System (Thermo Fisher Scientific) to generate cDNA. 10µl PCR reactions were set up in triplicate using 4.2µl cDNA (4ng diluted in nuclease-free water), 5µl iTaq™ Universal SYBR® Green Supermix (BioRad) and 0.8µl 5µM primers (final concentration of 200nM each). qPCR analysis was performed using an Applied Biosystems 7500 Real-Time PCR machine (Thermo Fisher Scientific) for 40 cycles with cycling steps shown in Table 2.5.

Average Ct values were normalised to CD3E for TCR *MiXCR* validation to account for T-cell proportion of PBMCs. The delta-delta Ct method was implemented to calculate relative expression and fold change of genes between samples (Figure 2.1).

2.5 Cell culture

2.5.1 Tumour cell lines

All cancer cell lines used were derived from human melanoma cells and are described in Table 2.6 using information from ExPASy[531]. Cell lines were kindly donated by Valentine McCaulay with the exception of Mel-Juso and D10 which were provided by Victoria Woodcock. Cell lines were maintained in D10 media: Dulbecco's Modified Eagle's Medium (DMEM; Gibco) with 10% heat-inactivated FBS, 2mM L-Glutamine solution (L-Glut, Lonza) and 100U/ml Penicillin/Streptomycin (P/S, Lonza). Primary Normal Human Epidermal Melanocyte (PromoCell) controls were instead maintained in Melanocyte Growth Medium M2 supplemented with SupplementMix (PromoCell). Cells were incubated at 37°C in a humidified atmosphere of 5% CO_2.

Patient	Target	Clonal change (C1 to C2)	Forward primer	Reverse primer
n/a	CD3E	n/a	GCAGGCAAAGGGGACAAAAC	GCAGTGTTCTCCAGAGGGTC
37	TRA	Expanding	CCGTCTCAAACAATGACATGC	GGATTTAGAGTCTCTCAGCTGG
37	TRB	Expanding	CTTCAGGGGGCTATAGGACTG	GGGAGATCTCTGCTTCTGATGG
37	TRA	Stable	CTCTGAGGGACACAGGCTTTC	GGATTTAGAGTCTCTCAGCTGG
37	TRB	Stable	CCGCTTGGATGGACAGCTACG	GGGAGATCTCTGCTTCTGATGG
40	TRA	Expanding	CTTTGGCTTTCAGAAACTTGT	GCTGGTACACGGCAGGGTCAGG
40	TRB	Expanding	CTTTTCGCTTGAAAGCGAGAC	GGGAGATCTCTGCTTCTGATGG
40	TRA	Stable	CTGTCATGGATAGCAACTATC	GCTGGTACACGGCAGGGTCAGG
40	TRB	Stable	CAGCCCACAGGAAACCGACAC	GGGAGATCTCTGCTTCTGATGG
76	TRA	Expanding	GGGTGACATGTATAATGCAGG	GCTGGTACACGGCAGGGTCAGG
76	TRB	Expanding	GGGACAGGGATGGCGAATGAG	GGGAGATCTCTGCTTCTGATGG
76	TRA	Stable	ACCTTAGATAACTATGGTCAG	GCTGGTACACGGCAGGGTCAGG
76	TRB	Stable	CCAGCACTCTAGCGGGAGAAG	TGCTTCTGATGGCTCAAACAC
78	TRA	Expanding	GTATTACTAGCTATGGAAAGC	GCTGGTACACGGCAGGGTCAGG
78	TRB	Expanding	GCCGACCTAGAGACAGGGGCC	GGGAGATCTCTGCTTCTGATGG
78	TRA	Stable	TGCTGTGAGCCTCCTGACGGG	GGATTTAGAGTCTCTCAGCTGG
78	TRB	Stable	CAGCTTTGTGGTAGCTAGCGG	GGGAGATCTCTGCTTCTGATGG
79	TRA	Expanding	GAGAGAGGGCGATAGCAGCTA	GCTGGTACACGGCAGGGTCAGG
79	TRB	Expanding	GGGAACTAGCGGGGATCAATG	GGGAGATCTCTGCTTCTGATGG
79	TRA	Stable	AGAGAGGGCGATAGAGATGAC	GCTGGTACACGGCAGGGTCAGG
79	TRB	Stable	TCCGGACAGGGGGGGGAAACAC	GGGAGATCTCTGCTTCTGATGG
85	TRA	Expanding	GAGAGTGGCCCCACCTCTTGT	GGATTTAGAGTCTCTCAGCTGG
85	TRB	Expanding	CGGGGGGGGGGAACACTGAAG	TGCTTCTGATGGCTCAAACAC
85	TRA	Stable	CTGTCCCTTACAACTTCAACA	GCTGGTACACGGCAGGGTCAGG
85	TRB	Stable	GCGGGGGGTAAAGAGACCCAG	GGGAGATCTCTGCTTCTGATGG
90	TRA	Expanding	GCAAGTAGAAGGCCCGGTGGC	GGATTTAGAGTCTCTCAGCTGG
90	TRB	Expanding	CCAGCAGCTCGATCGGGACAT	TGCTTCTGATGGCTCAAACAC
90	TRA	Stable	GTGCTACTGACAGCTGGGGGA	GGATTTAGAGTCTCTCAGCTGG
90	TRB	Stable	GCAGTGAAGCGGGCACCTCCT	GGGAGATCTCTGCTTCTGATGG
91	TRA	Expanding	GCTTATAAGGAGGACGACTAC	GGATTTAGAGTCTCTCAGCTGG
91	TRB	Expanding	CGCCAGCCGGGGCGCGAACAC	GGGAGATCTCTGCTTCTGATGG
91	TRA	Stable	GCGGCGGATATGGAAACAAAC	GCTGGTACACGGCAGGGTCAGG
91	TRB	Stable	GCTTAGGGGGGGCCGCTTTCT	TGCTTCTGATGGCTCAAACAC
92	TRA	Expanding	GAAAGGCAACCAGGGAGGAAA	GGATTTAGAGTCTCTCAGCTGG
92	TRB	Expanding	GCCAAGACGAGGCCTACAACA	TGCTTCTGATGGCTCAAACAC
92	TRA	Stable	CCTGAGAGCCGCCTGGACCAG	GGATTTAGAGTCTCTCAGCTGG
92	TRB	Stable	CAGCTTAATTTTTGGTACAGG	GGGAGATCTCTGCTTCTGATGG
94	TRA	Expanding	CGGAGGGTAGCAACTATAAAC	GCTGGTACACGGCAGGGTCAGG
94	TRB	Expanding	CCAGCAGTCCTTCTACAGGTC	GGGAGATCTCTGCTTCTGATGG
94	TRA	Stable	GGGCCTAGTAATGCAGGCAAC	GCTGGTACACGGCAGGGTCAGG
94	TRB	Stable	GCAGCTCGAGCCCGGCAGGAG	TGCTTCTGATGGCTCAAACAC
96	TRA	Expanding	GCTCTGGAGGAATAATGCAGG	GGATTTAGAGTCTCTCAGCTGG
96	TRB	Expanding	GCCAGCAGTCCTCCCCCCTCC	TGCTTCTGATGGCTCAAACAC
96	TRA	Stable	GAGTTATTCAGGAAACACACC	GGATTTAGAGTCTCTCAGCTGG
96	TRB	Stable	CCAGCGGGGTCTACACCGGGG	TGCTTCTGATGGCTCAAACAC
99	TRA	Expanding	GCTGTGGGTGCCGGGGATGAC	GCTGGTACACGGCAGGGTCAGG
99	TRB	Expanding	GCCGGGACAGGGGGCCCTAAC	TGCTTCTGATGGCTCAAACAC
99	TRA	Stable	CCGTGAACTCGATTAACCAGG	GCTGGTACACGGCAGGGTCAGG
99	TRB	Stable	CCCGTCCTCGGCCACTGAAGC	TGCTTCTGATGGCTCAAACAC
100	TRA	Expanding	CGTGGGTGATAACAATGCCAG	GCTGGTACACGGCAGGGTCAGG
100	TRB	Expanding	GATTTTCAGCGGGGGGGCGGG	GGGAGATCTCTGCTTCTGATGG
100	TRA	Stable	GGCACAAATGCAGGCAACATG	GGATTTAGAGTCTCTCAGCTGG
100	TRB	Stable	GCCGGTCGGACACCGGGGAGC	GGGAGATCTCTGCTTCTGATGG

Table 2.4 qPCR primer list
Table of qPCR primers used to validate $MiXCR$ outputs including primers targeted against CD3E and specific TCR clones. Primers were designed against TRA and TRB clones shown to expand or remain stable at C2 per patient (n=13) from $MiXCR$ data. Both forward and reverse primers are displayed in the 5'-3' direction.

Stage	Temperature	Time
Holding	95°C	10m
Denaturation	95°C	15s
Primer annealing/elongation	63°C	60s
Cooling	4°C	...

Table 2.5 qPCR cycling stages
Cycling stages used for qPCR reactions are shown. *m = minutes, s = seconds.*

$$normalised\ Ct = average\ (sample\ repeats) - average(CD3E)$$
$$relative\ expression = 2^{normalisedCt}$$
$$fold\ change = 2^{-(normalised\ Ct\ (condition\ 1) - normalised\ Ct\ (condition\ 2))}$$

Figure 2.1 Calculating fold change and relative expression from qPCR data

Cell line	Sample type	Resource Identification Initiative (ExPASy)
501 Mel	Melanoma metastatic site, BRAF+	501−mel (RRID:CVCL_4633)
A375M	Amelanocytic metastatic melanoma, skin, BRAF+	A375−M (RRID:CVCL_B222)
A375P	Amelanocytic metastatic melanoma, skin, BRAF+	A375−P (RRID:CVCL_6233)
CHL1	Melanoma metastatic site, BRAF−	CHL−1 (RRID:CVCL_1122)
D10	Melanoma	D10 (RRID:CVCL_H945)
Malme 3M	Melanoma metastatic site, BRAF+	Malme−3M (RRID:CVCL_1438)
ME	Melanoma	ME1 (RRID:CVCL_L911)
Mel−Juso	Cutaneous melanoma, BRAF−	Mel JuSo (RRID:CVCL_1403)
Na8	Melanoma	NA8−MEL (RRID:CVCL_S599)
SKMEL2	Melanoma metastatic site, BRAF−	SK−MEL−2 (RRID:CVCL_0069)
SKMEL28	Cutaneous melanoma, BRAF+	SK−MEL−28 (RRID:CVCL_0526)
SKMEL29	Melanoma, BRAF+	SK−MEL−29 (RRID:CVCL_6031)

Table 2.6 Melanoma cell line ExPASy characterisation

2.5.2 MAIT cell stimulations and culture

Paired C1/C2/C4 PBMC samples were stimulated by MAIT cell-specific 5-OP-RU activating antigen or proinflammatory cytokines to understand the effect of ICB on MAIT cell activation. Frozen PBMC samples from liquid nitrogen storage were removed and quickly thawed in a water bath set to 37°C, prior to DMSO removal and resuspension

in R10 media: RPMI 1640 (Gibco) with 10% heat-inactivated FBS, 2mM L-Glut and 100U/ml P/S. 5x10^6 PBMCs were resuspended in 1ml R10 media and seeded into five wells (200µl each) of a tissue culture-treated 96-well U-bottom plate. Cells were subsequently stimulated with appropriate cytokines and/or antigens for 24 hours at 37°C in a humidified atmosphere of 5% CO_2 prior to flow cytometry analysis.

Unstimulated cells were cultured in R10 media alone and served as untreated (UT) controls. 5-OP-RU was kindly donated by Paul Klenerman and was added at a final concentration of 40nM to stimulate TCR-dependent activation. Alternatively, 50ng/ml IL-12 (PeproTech) and 50ng/ml IL-18 (Miltenyi) were added to induce TCR-independent activation. Otherwise, cells were supplemented with a cocktail of 5-OP-RU, IL-12 and IL-18 to investigate maximal activation of simultaneous TCR-mediated and non-TCR-mediated activation. A positive control of 10ng/ml phorbol myristate acetate (PMA, Thermo Fisher Scientific) and 0.66µM Ionomycin (Iono, Thermo Fisher Scientific) was also included. Experimental conditions and concentrations were selected based on previously published protocols[532]. Cells were treated with Brefeldin A solution (3µg/ml, eBioScience^{TM}) 4 hours prior to flow cytometry analysis to enable intracellular cytokine staining.

2.5.3 T-cell activation and culture

Frozen PBMCs were quickly thawed at 37°C in a water bath prior to centrifugation at 300G for 10 minutes at 4°C to efficiently remove DMSO from cells. Cells were resuspended in warmed R5 media (RPMI 1640, 10% FBS, 5% human AB serum (Merck), 2mM L-Glut, 100U/ml P/S, 15mM HEPES (Lonza), 0.1mM nonessential amino acids (Gibco), 1mM sodium pyruvate (Merck) and 50µM β-ME) and seeded at 1x10^6 cells/ml in tissue culture-treated T25 flasks. Cells were subsequently maintained at 37°C in a humidified atmosphere of 5% CO_2.

Upon thawing and resuspension in warmed R5 media, PBMCs were treated with anti-CD2/anti-CD3/anti-CD28 beads using the T-cell activation/expansion kit (Miltenyi) to enrich for T-cells. A volume of 2µl of beads per 1x10^6 PBMCs was determined to be optimal for T-cell growth. In addition, cells were supplemented with 100U/ml IL-2 (PeproTech) every 2/3 days. Cells were left to expand and outgrow the beads over the course of a week prior to cell isolation, tumour coculture and subsequent cytotoxicity analysis.

2.5.3.1 CD8$^+$/MAIT/γδ T-cell isolation and activation

Following T-cell expansion, either CD8$^+$, MAIT or γδ T-cells were isolated using MACS separation. First, any leftover anti-CD2/anti-CD3/anti-CD28 expander beads were removed by passing samples through MS columns on an OctoMACS magnet and keeping the sample flow through. Cells were then incubated with either CD8 microbeads (Miltenyi), 5-OP-RU-loaded MR1 tetramer-PE (NIHR) or pan γδ TCR PE antibody (BioLegend). CD8$^+$ T-cells were isolated as aforementioned in section 2.2.4. Following incubation with either 5-OP-RU-loaded MR1 tetramer-PE or pan γδ TCR PE antibody for 40 minutes, cells were washed to remove excess tetramer and antibody. Cells were then resuspended in 80µl MACS buffer per 10^7 cells and incubated with 20µl anti-PE microbeads (Miltenyi) per 10^7 cells for 15 minutes at 4°C. Cells were washed at 300G for 10 minutes at 4°C in MACS buffer prior to resuspension in 500µl MACS buffer. Samples

were then applied to prewet MS columns and washed three times with MACS buffer. MAIT cells/γδ T-cells were extracted by flushing columns with 1ml MACS buffer.

2.5.3.2 T-cell-melanoma cocultures

$2x10^4$ melanocyte controls or melanoma cells, derived from a range of melanoma cell lines (Table 2.6), were seeded per well into 96-well flat bottom tissue culture-treated plates in 100µl D10 media and left at 37°C in a humidified atmosphere of 5% CO_2 overnight. PBMCs or T-cells, including isolated $CD8^+$/MAIT/γδ T-cells, were then coincubated with melanoma cell lines the following day in 100µl R5 media. This is with the exception of control tumour monolayers in which 100µl of R5 media was added alone. Cocultures, including control tumour monolayers, were supplemented with 100U/ml IL-2 every 2/3 days. For some experimental conditions, blocking antibodies and cytokines were also added including anti-MR1 (BioLegend), anti-MHCI (BioLegend), IL-12 (50ng/ml, PeproTech), IL-15 (50ng/ml, Abcam) and IL-18 (50ng/ml, Miltenyi). Cells were added at a 1:1 effector:target ratio and cocultured for five days.

2.5.4 Cell and cytokine assays

2.5.4.1 Cytotoxicity assay

To quantify cell viability, MTT-based or WST-8-based colorimetric assays were used. Both methods rely upon reduction of tetrazolium salts into formazan crystals and subsequent solubilisation to produce a formazan dye, the colour intensity of which signifies cell viability.

Cytotoxicity was quantified via the MTT system using MTT. Yellow MTT tetrazolium salt is metabolised by NAD(P)H-dependent oxidoreductase enzymes in metabolically active cells into purple formazan crystals which are dissolved using a solubilisation solution. The absorbance is then read by a spectrophotometer at 550nm.

After the appropriate time of coculture, nonadherent PBMCs/T-cells were gently resuspended, taking care not to disturb tumour monolayers, and processed for flow cytometry analysis. Using the Cell Proliferation Kit I (Roche), 100µl MTT was added to remaining tumour monolayers in R5 media at a final concentration of 0.5mg/ml for 4 hours at 37°C in a humidified atmosphere of 5% CO_2 and protected from the light. 100µl of solubilisation solution was then added to solubilise formazan crystals and incubated overnight in the same conditions. Absorbance was read the following day using a SpectraMax M2e (Molecular devices) at 550nm as well as at 690nm for background normalisation. Cell cytotoxicity was calculated using the following calculation (see Figure 2.2).

$$Cytotoxicity = 100 - \left(\frac{(average\ absorbance\ at\ 550nm - average\ absorbance\ at\ 690nm)}{(average\ absorbance\ of\ tumour\ monolayer\ at\ 550nm - average\ absorbance\ of\ tumour\ monolayer\ at\ 690nm)} * 100\right)$$

Figure 2.2 Calculating cytotoxicity from MTT assays

Alternatively, the Cell Counting Kit (WST-8/CCK8) (Abcam) was used for more sensitive cytotoxicity measurements. This WST-8-based assay works in a similar way to the MTT assay in that when added to cells, mitochondrial dehydrogenases, in the presence of an electron carrier, reduce it into an orange formazan salt, which

is directly soluble in R5 media. Tumour cocultures were set up as before with supernatant containing the PBMCs/T-cells removed prior to addition of WST-8 (2-(2-methoxy-4-nitrophenyl)-3-(4-nitrophenyl)-5-(2,4-disulphophenyl)-2H-tetrazolium, monosodium salt). 100µl 10% WST-8 in R5 media was added to tumour monolayers for 3-4 hours in the dark at 37°C in a humidified atmosphere of 5% CO_2. WST-8 was also added to wells containing only R5 media as a blank control to normalise for background absorbance levels. Absorbance was then read using a SpectraMax M2e spectrophotometer at 460nm and cytotoxicity was determined using the following calculation (see Figure 2.3).

$$Cytotoxicity = 100 - \left(\frac{(average\ absorbance\ at\ 460nm - average\ absorbance\ of\ blank\ at\ 460nm)}{(average\ absorbance\ of\ tumour\ monolayer\ at\ 460nm - average\ absorbance\ of\ blank\ at\ 460nm)} * 100\right)$$

Figure 2.3 Calculating cytotoxicity from WST-8 assays

Cell coculture conditions were performed in duplicate/triplicate per condition with average normalised absorbance used for calculations.

2.5.4.2 ELISA analysis

Enzyme-linked immunosorbant assays (ELISAs) were used to quantify circulating plasma levels of CXCL10 and CXCL13 as well as determine CMV serostatus. Plasma samples were submitted to John Radcliffe hospital laboratories to detect anti-CMV IgG antibody titres, adhering to in-house methods.

CXCL10 and CXCL13 plasma protein levels were measured using ELISA MAX™ Deluxe Set Human CXCL10 (BioLegend) and human CXCL13 ELISA (Merck) kits respectively. To account for low expression and the initial dilution of blood in HBSS, a higher volume of plasma was added than recommended. Following optimisation, a volume of 250µl of plasma was determined to be favourable for detection. Samples were incubated in the precoated plate at room temperature with gentle shaking for 2.5-3 hours. Standards were added as per manufacturer instructions. Other than sample loading, protocols were carried out as recommended.

Absorbance levels for CXCL10 and CXCL13 ELISAs were read by a SpectraMax M2e spectrophotometer at 450nm and 570nm with absorbance values at 570nm subtracted from readings at 450nm for background normalisation. All samples were run in duplicate with average absorbance used for calculations. Standard curves were created using absorbance values from the standards. Four-parametric logistic regression was used to infer cytokine concentrations using the standard curve. Final cytokine concentrations were normalised using the appropriate dilution factor to take into account the dilution in HBSS during blood processing and the extra volume added to the plate.

2.6 Flow cytometry analysis

Flow cytometry analysis was performed across seven separate panels to investigate single cell protein expression within different PBMC subsets. Firstly, panel B1 was used to investigate PBMC composition using lineage and subset specific markers to identify any changes in proportion over the course of ICB treatment. T-cells were investigated more closely in panel T2 by examining T-cell CD4/CD8 composition, differentiation

status and unconventional T-cell proportions, including iNKT cells and γδ T-cells. In addition, MAIT cell percentage was quantified along with markers of T-cell activation in panel M3. More specifically, response to stimulation through both TCR-dependent and TCR-independent mechanisms (see section 2.5.2) was investigated in both MAIT cells and T-cells for panel M4 to quantify T-cell effector cytokine production and activation. Next, B-cell subset composition and activation was assessed in panel B5 to look for any dynamic changes occurring in B-cells following ICB treatment. Finally, both panels K6 and O7, performed by Orion Tong, were used to quantify Ki67 and IgG4/pembrolizumab staining in $CD8^+$ T-cells respectively.

Staining antibody concentrations were optimised using three distinct samples at three different dilutions including 1/25, 1/50 and 1/100. This is with the exception of near IR viability stain (1/500, 1/1000, 1/2000), tetramers (used at the recommended dilution of 1/200) and panel K6/O7 antibodies (performed by Orion Tong). Optimal staining concentration was determined by generating a stain index based on spread of the negative population, positive staining, median fluorescence intensity (MFI) and the difference between positive and negative populations (Figure 2.4). All primary antibodies used were reactive against human antigens.

$$Staining\ index = \frac{(MFI\ of\ positive\ population - MFI\ of\ negative\ population)}{(2\ x\ rSD\ of\ negative\ population)}$$

Figure 2.4 Calculating antibody staining index
MFI = Median fluorescence intensity, rSD = relative standard deviation.

Frozen PBMC samples were quickly thawed in a water bath set to 37°C before centrifugation at 400G for 10 minutes at 4°C and resuspension in HBSS to remove the DMSO. $1x10^6$ cells (or $3x10^6$ for panel B5) were aliquoted per 5ml FACS polystyrene tube (or per well of a 96-well U-bottom tissue culture-treated plate for panel M4), including fluorescence minus one (FMO) and isotype controls, and were washed in HBSS.

Fixable amine reactive viability dye was incubated with the cells at 1/1000 in HBSS for 30 minutes in the absence of FBS and kept at 4°C in the dark. Samples were then washed and costained with extracellular antibodies at the appropriate dilution (Table 2.7) in 50µl staining buffer (5% FBS, 95% HBSS) or brilliant stain buffer (for panel B5, BD BioSciences) for 30 minutes. Alternatively, cells were stained with either 5-OP-RU-loaded or Ac-6-FP-loaded MR1 tetramer at room temperature for 40 minutes for panel M3 prior to washing and incubation with surface antibodies. For panel O7, biotinylated IgG4 was cultured with paired C1/C2 samples prior to washing and subsequent incubation with fluorochrome-conjugated Streptavidin. However, for some C1 patient samples, cells were instead cultured first with pembrolizumab prior to subsequent IgG4 and Streptavidin staining. All cells were incubated with stains for 30 minutes at 4°C prior to washing with HBSS at each stage. Following surface antibody staining, cells were subsequently washed in HBSS to remove any unbound antibodies/tetramers and fixed in 100µl 2% formaldehyde (Merck) for 10 minutes prior to washing in HBSS.

For panel M4, which required intracellular cytokine staining, cells were permeabilised using 200µl 10% permeabilisation buffer (Invitrogen) for 10 minutes which was then washed off in more permeabilisation buffer. Samples were then incubated with intracellular antibodies in 50µl 10% permeabilisation buffer for 30 minutes at 4°C. Similarly, panel K6 required permeabilisation in order to detect intranuclear Ki67. Cells

were treated with 200µl Foxp3/Transcription Factor Fixation/Permeabilisation Reagent (eBioscience™) for 30 minutes in the dark at 4°C for intranuclear staining. Cells were then washed in permeabilisation buffer and cultured with anti-Ki67 in permeabilisation buffer for 30 minutes in the dark at 4°C prior to one final wash in permeabilisation buffer.

Finally, cells were resuspended in staining buffer prior to flow cytometry analysis into a single cell suspension.

Target/tetramer/stain	Fluorochrome	Clone	Dilution	Source	Panels
Live/Dead cell stain kit	Near-IR	n/a	1000	Thermo Fisher Scientific	B1, T2, M3, M4, B5, K6, O7
CD3	BV785	UCHT1	25	BioLegend	B1, T2, M3, M4
CD56	BV421	5.1H11	50	BioLegend	B1, T2
CD19	AF700	HIB19	50	BioLegend	B1
CD14	PE/Cy7	M5E2	50	BioLegend	B1
CD16	FITC	3G8	50	BioLegend	B1, B5
CD8α	BV510	RPA-T8	25	BioLegend	B1, T2, M3, M4, K6, O7
CD21	PE	Bu32	50	BioLegend	B1
MHCI	APC	W6/32	50	BioLegend	B1
PD1	BV650	EH12.2H7	50	BioLegend	B1, T2, M3, K6, O7
CD4	APC	RPA-T4	50	BioLegend	T2, M3
CD27	AF700	M-T271	50	BioLegend	T2
CD45RA	FITC	HI100	50	BD BioSciences	T2
Pan γδ TCR	PE	B1	50	BioLegend	T2
TCR Vα24-Jα18 (TRAV10-TRAJ18)	PE/Cy7	6B11	50	BioLegend	T2
5OPRU-loaded tetramer	PE	n/a	200	NIHR	M3
6FP-loaded tetramer	PE	n/a	200	NIHR	M3
CD38	AF700	HIT2	50	BioLegend	M3
HLADR	PE/Dazzle594	L243	50	BioLegend	M3
CD161	PE-Vio770	191B8	50	Miltenyi	M3, M4
CD69	FITC	FN50	50	BioLegend	M3, M4
GPR15	BV421	SA302A10	50	Biolegend	M3
Vα7.2 (TRAV1-2)	PE	3C10	50	BioLegend	M4
GZMB	AF700	GB11	50	BD BioSciences	M4
IFN-γ	BV421	4S.B3	25	BioLegend	M4
TNF-α	BV650	MAb11	25	BioLegend	M4
CD19	BUV395	SJ25C1	50	BD BioSciences	B5
CD3	FITC	UCHT1	25	BioLegend	B5, K6, O7
CD56	FITC	HCD56	50	BioLegend	B5
IgD	BV421	IA6-2	50	BioLegend	B5
CD27	APC	M-T271	25	BioLegend	B5
CD38	PE/Cy7	HB-7	50	BioLegend	B5
CD24	BV785	ML5	50	BioLegend	B5
CD138	PE	DL-101	50	BioLegend	B5
CD11c	BV605	3.9	50	BioLegend	B5
CD71	PE/Dazzle594	CY1G4	100	BioLegend	B5
Ki67	BV711	Ki-67	75	BioLegend	K6
Pembrolizumab	n/a	A1036-100	50	Biovision	O7
IgG4	Biotin	A-10663	200	Thermo Fisher Scientific	O7
Streptavidin	BV785	405429	250	BioLegend	O7

Table 2.7 Flow cytometry antibody summary
Table displaying details of antibodies, tetramers and stains used for flow cytometry analysis including antibody clone, fluorochrome conjugate, staining dilution, source and included panels. Fluorochromes are coloured by the detecting laser.

Each panel was analysed using the same flow cytometer each time to reduce any batch effects (BD Fortessa LSRII (B1/T2/M3/M4/B5), BD Fortessa X20 (K6/O7)) using FACS DIVA software. The LSRII autosampler 96-well plate attachment was used for panel M4. Compensation was performed for each run on fresh cells from the same batch.

Data was analysed using FlowJo software version v10s.7.1[533] only keeping high quality samples as determined by FlowJo. Due to the interindividual variation observed in FSC-A/SSC-A plots, samples were gated on a sample-wise basis. FMOs were included for markers with ambiguous gating including PD-1, CD38 and HLA-DR. Ac-6-FP-loaded tetramers were used as background controls for 5-OP-RU-loaded MR1 tetramer gating. Primary and secondary antibody alone controls were also included for panel O7. Samples were selected at random and data analysis was performed blinded to clinical outcome. All samples for each patient were run in the same batch.

2.7 Data analysis

2.7.1 Bioinformatic analysis

All downstream analysis was performed using R version 4.1.1 (2021-08-10) – "Kick Things"[496] on RStudio version 1.4.1717. The *tidyverse*[506] was used for data manipulation and plots were generated using *ggplot2*[534].

2.7.2 Statistical analysis

Statistical tests used are stated per figure legend. Spearman's rank correlation coefficient was applied for correlation analysis of continuous variables. Actual p-values were generated either manually or using *ggpubr*[535]. Wilcoxon signed-rank tests were used for comparison between discrete variables. The negative binomial generalised linear model with Benjamini-Hochberg procedure for multiple testing correction was used for differential gene expression analysis using *DESeq2*. Linear models were used to normalise for confounding variables using "lm(Dependent variable ~ Independent variable + Confounding variables, data)" from *stats*. Fisher's exact tests were used for comparing clone proportions before and after treatment using *stats*. Bonferroni correction was used to correct for multiple testing.

Chapter 3

T-cells

3.1 Summary

3.1.1 Background

In this chapter I explore the peripheral immune response to checkpoint blockade in terms of changes to cell subset proportions and expression. Understanding how cells respond to ICB in the periphery is of potential great importance and may associate with clinical outcome as well as guide patient treatment stratification. Initial findings in identifying $CD8^+$ T-cells as the primary target of ICB caused me to analyse these in depth and this is described here.

T-cells are a heterogeneous population of lymphocytes with a central role in adaptive immune responses including cytotoxicity and cytokine production. In particular, $CD8^+$ T-cells contribute to direct tumour cell lysis, predominantly induced upon recognition of cognate pMHC complexes. $CD8^+$ T-cells are reinvigorated following ICB treatment as evidenced by an increase in $Ki67^+$ $PD\text{-}1^+$ $CD8^+$ T-cells[219] and a reduction in suppression[536]. However, the degree to which the ICB response is orchestrated by $CD8^+$ T-cells, with the responses of other cells being secondary to this, is unclear. Indeed, there has been limited characterisation of non-T-cell responses in depth across large patient cohorts.

Whilst several studies have described the effect of ICB on intratumoural T-cells, predominantly through investigations into the TCR repertoire and protein expression using flow cytometry[221,250,376,381], its effect on the peripheral $CD8^+$ T-cell transcriptome is less understood and may provide insight into whether $CD8^+$ T-cell activation is necessary for response in other cell types.

CMV is a latent herpes virus shown to have marked effects on T-cell subsets and clonality[371,474–482], and therefore this was taken into account additionally. The effect of CMV on PBMC subset composition, as well as expression, was determined and hence any changes in response to ICB were compared between CMV^- and CMV^+ individuals to understand how CMV serostatus determines the extent of ICB response.

This chapter utilises transcriptomic and protein data, incorporating data derived from bulk RNAseq and flow cytometry analyses. Changes in PBMC composition in response to ICB treatment were monitored as well as any differences in the $CD8^+$ T-cell transcriptional profile following ICB treatment. Any differences due to type of treatment have also been elucidated. Finally, transcriptomic and phenotypic changes within non-T-cells have been investigated including the importance of T-cell activation

in these responses.

3.1.2 Aims

- How does ICB treatment affect PBMC composition?
- Are $CD8^+$ T-cells the primary target of ICB?
- How are peripheral $CD8^+$ T-cells affected by ICB and how does this vary between different treatment arms?
- Is the response of non-T-cell subsets to ICB dependent on $CD8^+$ T-cell activation?
- Are any of these effects modulated by CMV serostatus?

3.1.3 Experimental Approach

Peripheral blood samples were collected from 190 MM patients receiving ICB treatment, along with 10 nonmetastatic melanoma patients and 295 healthy donor controls. This included patients treated with sICB (anti-PD-1) or cICB (anti-CTLA-4/anti-PD-1) treatment. Samples were collected from patients immediately before the 1^{st} cycle of treatment (C1 samples), representing untreated controls, before the 2^{nd} dose of treatment having had one dose (C2 samples), as well as at other longitudinal time-points.

Ficoll density gradient centrifugation was performed on whole blood, extracting plasma and PBMCs which were used for ELISA or flow cytometry analysis and cell culture respectively. In addition, specific PBMC subsets, namely $CD8^+$ T-cells, $CD14^+$ monocytes, $CD19^+$ B-cells, NK cells, $CD4^+$ naïve T-cells and $CD4^+$ memory T-cells were isolated from PBMCs using magnetic-activated cell sorting. Isolated samples were lysed and prepared for bulk RNAseq, yielding 504 $CD8^+$ T-cell, 284 $CD14^+$ monocyte, 308 $CD19^+$ B-cell, 174 NK cell, 69 $CD4^+$ naïve T-cell and 26 $CD4^+$ memory T-cell high quality transcriptomes.

Flow cytometry was performed on thawed PBMC samples to quantify PBMC cell proportions, including specific monocyte, B-cell, NK cell and T-cell subsets, as well as markers of activation and ICB binding. Additionally, PBMCs were stimulated with PMA/Ionomycin for 24 hours prior to flow cytometry analysis of activation markers to investigate the effects of ICB treatment on response to activating stimuli.

*DESeq*2[495] was used to investigate differential expression using bulk RNAseq data. Firstly, expression was compared between healthy donor and untreated MM samples to understand changes in the transcriptome in response to cancer. Secondly, the degree to which CMV affects the transcriptome was determined through comparison of gene expression between CMV^- and CMV^+ individuals. Thirdly, any differences in expression between paired C1/C2 samples were explored to investigate changes induced by ICB treatment and how the magnitude varied by treatment type.

Plasma samples were submitted to John Radcliffe hospital laboratories to detect the presence of CMV-specific IgG antibodies and determine CMV serostatus. The impact of CMV serostatus was subsequently investigated on immunological changes observed in response to ICB.

3.2 Results

3.2.1 Changes in PBMC composition and activation in response to ICB

3.2.1.1 cICB treatment leads to B-cell lymphopenia

In order to appreciate the effect of ICB at the cellular level, flow cytometry was performed on thawed PBMC samples to quantify cell subsets. PBMC cell subset proportions were determined according to Figure S3.1. Monocytes and T-cells accounted for the vast majority of cells, representing an average of 39.07% (±18.00) and 35.44% (±15.49) of PBMCs respectively, followed by NK cells (11.49% ±7.67) and B-cells (5.84% ±4.15) (Figures 3.1a, S3.2). Remaining PBMCs comprised either lineage$^-$ cells or cells coexpressing different lineage markers.

Comparison of subset composition between paired C1/C2 samples revealed a depletion in B-cells at C2 (Figure 3.1b) which was only apparent following cICB treatment (Figures S3.3a, S3.3b). This B-cell depletion has previously been demonstrated following cICB, but not after sICB anti-CTLA-4 or anti-PD-1[458]. As a result, I focus upon the B-cell response to ICB in Chapter four. However, all other subsets remained largely stable regardless of treatment type (Figures 3.1b, S3.3a, S3.3b).

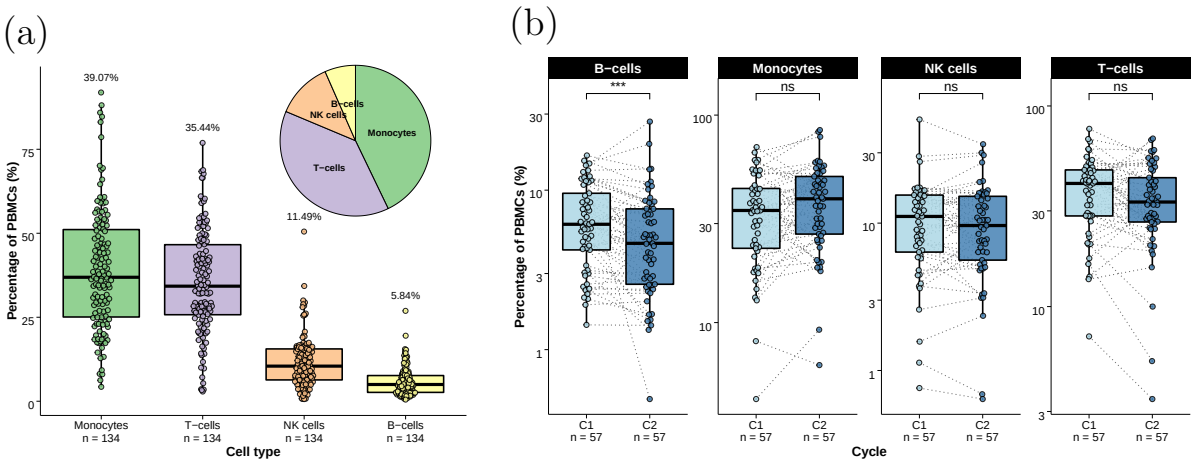


Figure 3.1 B-cells are depleted at C2
Flow cytometry was performed on 134 PBMC samples including 57 paired C1/C2 samples. **a)** Box plots showing the variation in PBMC percentage by subset in descending order with average percentage displayed above and a pie chart of cell proportions overlaid (n=134). **b)** Box plots comparing PBMC percentages between paired C1/C2 samples (n=57). Statistics were calculated using paired Wilcoxon signed-rank tests and adjusted using Bonferroni correction. Adjusted p $>$ 0.05 (ns), $p \leq 0.05$ (*), $p \leq 0.01$ (**), $p \leq 0.001$ (***), $p \leq 0.0001$ (****).

Non-B-cell PBMCs were further classified into previously defined subsets using flow cytometry (Figures S3.1, S3.4, S3.5). For monocytes these included classical, intermediate and nonclassical subsets based on CD14/CD16 expression. NK cells were subdivided based on relative expression of CD56, CD8 and CD16, including CD56$^{\text{bright}}$, CD56$^{\text{dim}}$, CD8$^+$ and CD16$^+$ subsets, which characterise different maturation and functional states[537–539]. Finally, T-cells were subsetted based on CD4/CD8 expression,

differentiation state using CD45RA and CD27, CD56 expression, as well as expression of invariant T-cell receptors, namely for MAIT cells, iNKT cells and γδ T-cells. All subsets were compared between paired C1/C2 samples and showed no difference regardless of treatment type (Figures 3.2, S3.6a, S3.6b).

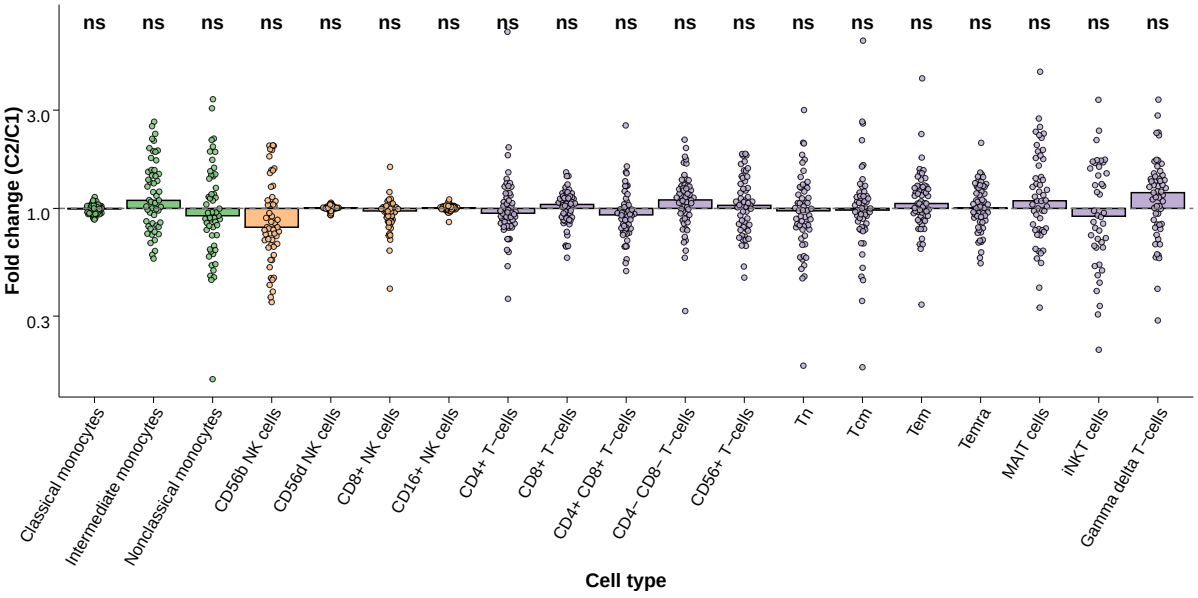


Figure 3.2 Non-B-cell subsets remain stable at C2
A total of three flow cytometry panels were performed to quantify PBMC cell subset proportions as well as specific subdivisions. Subset percentages are compared between paired C1/C2 samples (n=42-53) showing the fold change in the various subsets and level of significance of the change above each bar plot. Statistics were calculated using paired Wilcoxon signed-rank tests and adjusted using Bonferroni correction. Adjusted p > 0.05 (ns), $p \leq 0.05$ (*), $p \leq 0.01$ (**), $p \leq 0.001$ (***), $p \leq 0.0001$ (****). *CD56b = CD56^{bright}, CD56d = CD56^{dim}, Tn = Naïve T-cells, Tcm = Central memory T-cells, Tem = Effector memory T-cells, Temra = Effector memory T-cells reexpressing CD45RA.*

3.2.1.2 ICB-induced changes are unaffected by CMV serostatus

However, the impact of CMV infection within this cohort remained to be determined and may affect how cells respond to ICB. In this section I investigate whether the immunomodulatory effects of chronic CMV infection alter the amplitude or nature of the peripheral cellular response to ICB.

CMV serostatus was determined by ELISA, detecting the presence of anti-CMV IgG antibodies in patient plasma collected prior to ICB treatment. Due to the strong association of CMV infection with age[460–463], linear models were generated to compare PBMC composition whilst controlling for age.

Comparison between CMV$^-$ and CMV$^+$ samples (n=57 CMV$^-$, n=63 CMV$^+$) using flow cytometry data revealed a distinct shift in the NK:T-cell ratio (Figures 3.3a, 3.3b). CMV$^+$ individuals had an expanded T-cell population (CMV$^-$ 27.6% ±12.6, CMV$^+$ 42.3% ±14.5) and a diminished NK cell proportion (CMV$^-$ 14.5% ±9.0, CMV$^+$ 8.7% ±5.5), but no differences in monocytes or B-cells after adjusting for multiple testing.

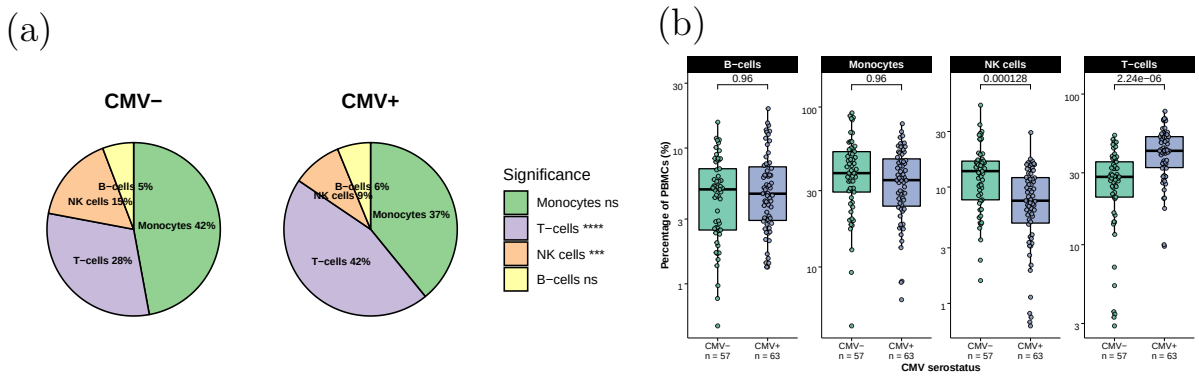


Figure 3.3 T-cells are expanded in CMV$^+$ individuals
Flow cytometry data of PBMC subset proportions are compared between CMV$^-$ (n=57) and CMV$^+$ (n=63) samples after controlling for age and are visualised by **a)** pie chart or **b)** box plot. Average subset percentage is highlighted per pie chart. Statistics were calculated using "lm(Cell subset percentage $\sim$ CMV serostatus + age, data)" and adjusted using Bonferroni correction. Adjusted p > 0.05 (ns), $p \leq 0.05$ (*), $p \leq 0.01$ (**), $p \leq 0.001$ (***), $p \leq 0.0001$ (****).

Despite the loss of NK cells observed in CMV$^+$ individuals, no differences in NK subset proportions were observed (data not shown). Conversely, circulating T-cell composition was markedly different. Firstly, upon comparing CD4/CD8 expression (n=59 CMV$^-$, n=64 CMV$^+$), an overrepresentation of CD8$^+$ T-cells (CMV$^-$ 40.6% ±14.5, CMV$^+$ 55.9% ±14.1) with a concomitant reduction in CD4$^+$ T-cells (CMV$^-$ 47.6% ±18.3, CMV$^+$ 35.0% ±14.2) was revealed (Figures 3.4a, 3.4b). An increase in double positive CD4$^+$ CD8$^+$ T-cells was also observed (CMV$^-$ 1.5% ±0.9, CMV$^+$ 2.9% ±2.8), albeit still representing a minority of T-cells.

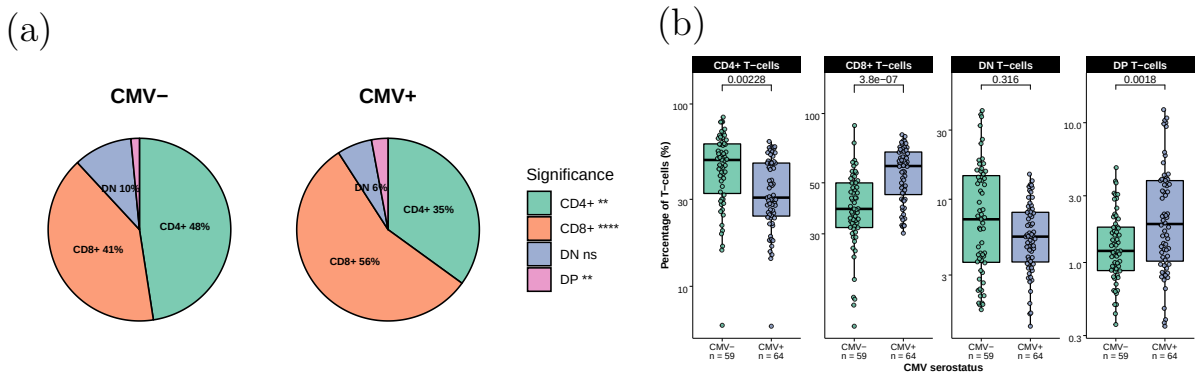


Figure 3.4 CD8$^+$ T-cells form the majority of T-cells in CMV$^+$ individuals
Flow cytometry data of T-cell CD4/CD8 expression is compared between CMV$^-$ (n=59) and CMV$^+$ (n=64) samples after controlling for age and are visualised by **a)** pie chart or **b)** box plot. Average subset percentage is highlighted per pie chart. Statistics were calculated using "lm(CD4/CD8 T-cell percentage $\sim$ CMV serostatus + age, data)" and adjusted using Bonferroni correction. Adjusted p > 0.05 (ns), $p \leq 0.05$ (*), $p \leq 0.01$ (**), $p \leq 0.001$ (***), $p \leq 0.0001$ (****). *DN = CD4$^-$ CD8$^-$*, *DP = CD4$^+$ CD8$^+$*.

Secondly, T-cell differentiation status was determined using CD45RA and CD27

expression from flow cytometry data (n=59 CMV$^-$, n=64 CMV$^+$) (Figure S3.4). A substantial two-fold increase in effector memory T-cells reexpressing CD45RA (Temras) was observed in CMV$^+$ compared to CMV$^-$ patients (CMV$^-$ 22.0% ±16.5, CMV$^+$ 46.4% ±20.6) (Figures 3.5a, 3.5b). As a consequence, a depletion was observed in both naïve (Tn) (CMV$^-$ 24.8% ±13.9, CMV$^+$ 13.9% ±10.0) and central memory (Tcm) T-cell (CMV$^-$ 29.9% ±13.0, CMV$^+$ 16.6% ±11.7) populations. Differences were observed in T-cell differentiation states for both CD4$^+$ and CD8$^+$ T-cells (Figures S3.7a, S3.7b, S3.7c, S3.7d). These findings reflect previous data that similarly show an association of CMV with a loss in Tn cells, but an increase in terminally differentiated cells, including Temra populations[474,476–482].

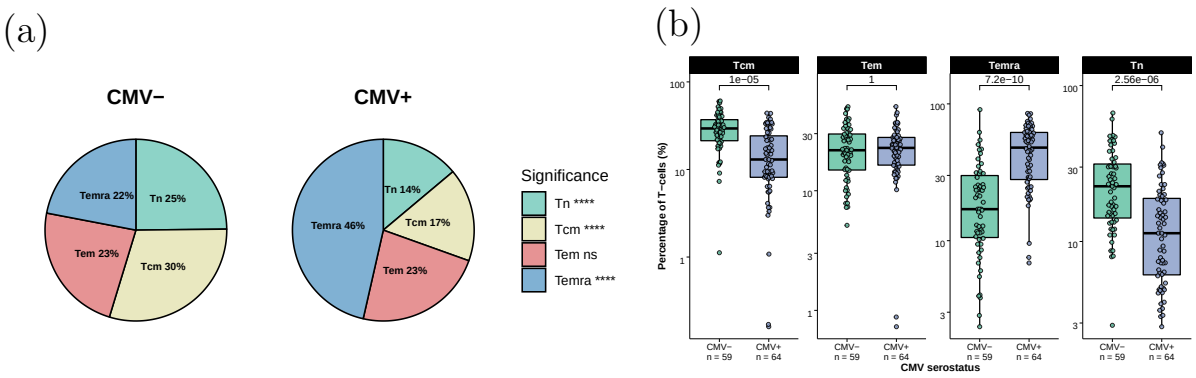


Figure 3.5 CMV infection results in an inflated Temra population
Flow cytometry data of T-cell differentiation subset composition is compared between CMV$^-$ (n=59) and CMV$^+$ (n=64) samples after controlling for age and are visualised by **a)** pie chart or **b)** box plot. Average subset percentage is highlighted per pie chart. Statistics were calculated using "lm(T-cell subset percentage ~ CMV serostatus + age, data)" and adjusted using Bonferroni correction. Adjusted p > 0.05 (ns), $p \leq 0.05$ (*), $p \leq 0.01$ (**), $p \leq 0.001$ (***), $p \leq 0.0001$ (****). *Tn = Naïve T-cells, Tcm = Central memory T-cells, Tem = Effector memory T-cells, Temra = Effector memory T-cells reexpressing CD45RA.*

The effects of CMV infection on unconventional T-cell proportions, including for MAIT cells, iNKT cells and γδ T-cells, were also investigated. Given the strong association between age and unconventional T-cell counts[540–546], linear models were similarly used to test the difference in proportions, controlling for age using $\log_{10}$ normalised counts. Although no significant differences were observed between CMV$^-$ and CMV$^+$ individuals for iNKT cells and γδ T-cells, a significant depletion in MAIT cells was detected (CMV$^-$ 2.45% ±2.97%, CMV$^+$ 0.99% ±1.19%) (Figure 3.6).

Despite such robust correlations of PBMC composition with CMV serostatus, no correlations were found with anti-CMV IgG antibody titre in CMV$^+$ individuals (Figure S3.8). This suggests that an increased CMV burden doesn't further regulate PBMC composition. However, with such profound differences observed in NK and T-cell proportions, paired C1/C2 samples were compared again, but this time by CMV serostatus (n=23 CMV$^-$, n=26 CMV$^+$) (Figures 3.7a, 3.7b). Regardless of CMV serostatus, a depletion in B-cell count was detected with no changes in monocytes, NK cells or T-cells observed. Further subsets were also compared with no discernible differences between CMV$^-$ and CMV$^+$ patients (Figures S3.9a, S3.9b). Similarly, CMV

serostatus was not found to associate with survival outcomes during ICB treatment (Figures S3.10a, S3.10b).

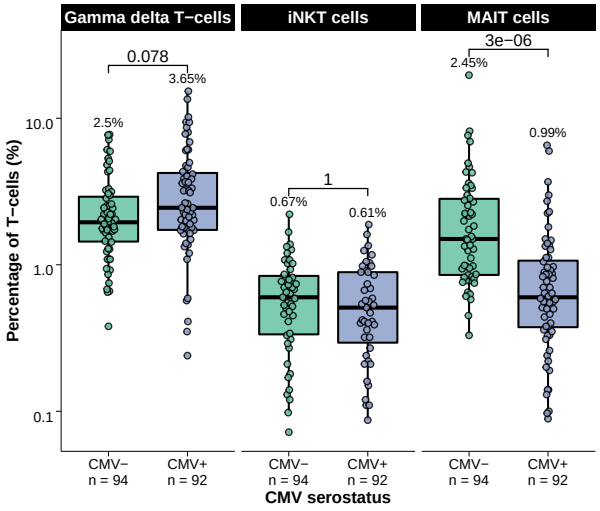


Figure 3.6 MAIT cells are depleted in CMV$^+$ individuals
Box plots comparing unconventional T-cell percentages between CMV$^-$ (n=94) and CMV$^+$ (n=92) samples. Average subset percentages are displayed above each box plot. Statistics were calculated using lm($\log_{10}$(Unconventional T-cell percentage) $\sim$ CMV serostatus + age, data) to control for age.

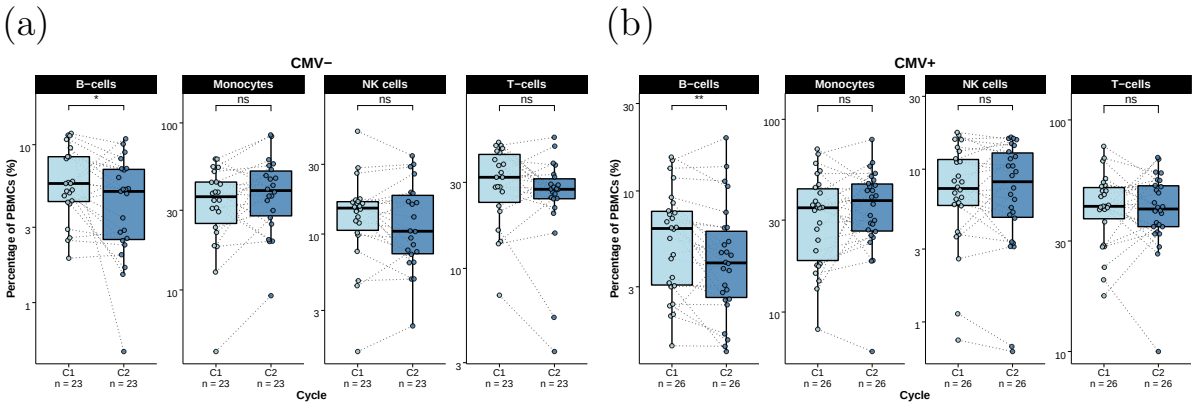


Figure 3.7 CMV does not determine PBMC changes at C2
Box plots comparing PBMC composition in paired C1/C2 samples in **a)** CMV$^-$ (n=23) and **b)** CMV$^+$ (n=26) patients. Statistics were calculated using paired Wilcoxon signed-rank tests and adjusted using Bonferroni correction. Adjusted p > 0.05 (ns), $p \leq 0.05$ (*), $p \leq 0.01$ (**), $p \leq 0.001$ (***), $p \leq 0.0001$ (****).

3.2.1.3 PD-1 loss observed in T-cells acts as a marker of efficient PD-1 blockade

In order to assess immune checkpoint blocker binding, PBMCs were stained with fluorochrome-conjugated anti-PD-1 antibodies since PD-1 should be blocked by both sICB and cICB therapies. First, surface PD-1 expression was measured in untreated

patient samples to identify expression per PBMC cell type and was found to be maximal in T-cells, followed by NK cells, B-cells and monocytes respectively (Figure 3.8a). Although no difference was observed in T-cell proportion following ICB, a loss in surface PD-1 expression was detected in T-cells at C2, but not in other PBMC cell subsets (Figure 3.8b). This depletion likely represents successful binding of anti-PD-1 ICB agents, in both sICB and cICB treatment arms, and hence subsequent blockade of anti-PD-1 flow cytometry staining antibodies. This indicates that ICB is directly targeting T-cells.

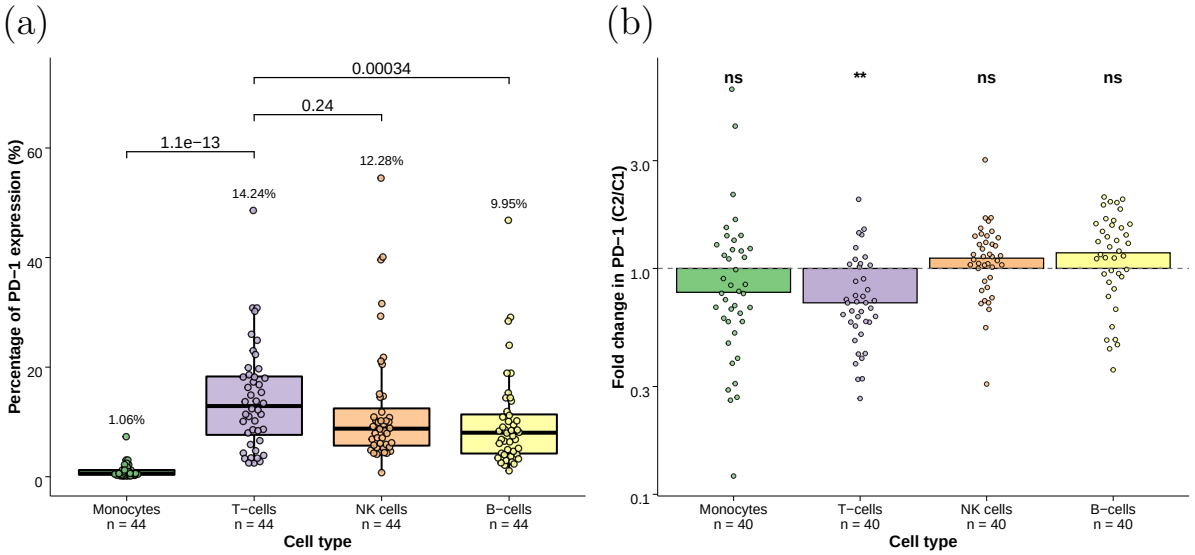


Figure 3.8 PD-1 is highly expressed by T-cells and successfully blocked at C2
a) PD-1 expression was measured by flow cytometry analysis and compared between different PBMC cell types in 44 untreated samples (C1). Average surface PD-1 expression is displayed above each box plot. **b)** The fold change in PD-1 expression is presented for 40 paired C1/C2 samples by lineage with statistical significance of any change displayed above each bar plot. Statistics were calculated using paired Wilcoxon signed-rank tests and adjusted using Bonferroni correction. Adjusted p $>$ 0.05 (ns), $p \leq 0.05$ (*), $p \leq 0.01$ (**), $p \leq 0.001$ (***), $p \leq 0.0001$ (****).

To ascertain if this loss in PD-1 was indeed a result of successful PD-1 blockade by ICB, untreated PBMC samples (C1) were cultured *in vitro* with pembrolizumab and subsequently stained with anti-IgG4 antibodies to detect pembrolizumab IgG4 antibody binding. IgG4 does not typically elicit ADCC nor is it highly expressed by B-cells, thus little to no background staining was detected in the absence of pembrolizumab (Figure 3.9a). Interestingly, pembrolizumab, as quantified by IgG4 staining, was only detected on T-cells with an absence of staining in B-cells, NK cells and monocytes (Figure 3.9a). Samples were concomitantly stained with fluorochrome-conjugated anti-PD-1 antibodies to confirm if the loss in PD-1 staining was associated with ICB binding. Analysis revealed that IgG4 binding was directly associated with a loss in PD-1 staining in T-cells after treatment with pembrolizumab (Figure 3.9b). Adopting a similar approach, flow cytometry was performed on paired C1/C2 samples, staining for both IgG4 and PD-1, which showed an increase in IgG4 staining at C2 that was observed alongside a reduction in PD-1, likely signifying ICB binding and subsequent PD-1 blockade (Figure 3.9c). Consequently, the loss in PD-1 staining observed at C2 is likely explained by the addition of pembrolizumab/nivolumab IgG4 antibodies.

Flow cytometry analysis was repeated for 41 paired C1/C2 samples using IgG4 staining as a surrogate of ICB binding for T-cells. Indeed, IgG4$^+$ T-cells were found to be induced at C2 after both sICB and cICB, likely representing successful binding of the pembrolizumab/nivolumab IgG4 antibody itself (Figure 3.9d). Surprisingly, the level of anti-PD-1 binding was found to be higher after cICB than sICB treatment and may signify a greater affinity of the anti-IgG4 antibody for nivolumab over pembrolizumab, greater stability, less cell migration, or that there is enhanced capacity for binding due to a greater induction of *PDCD*1 by cICB[371] (Figure S3.11).

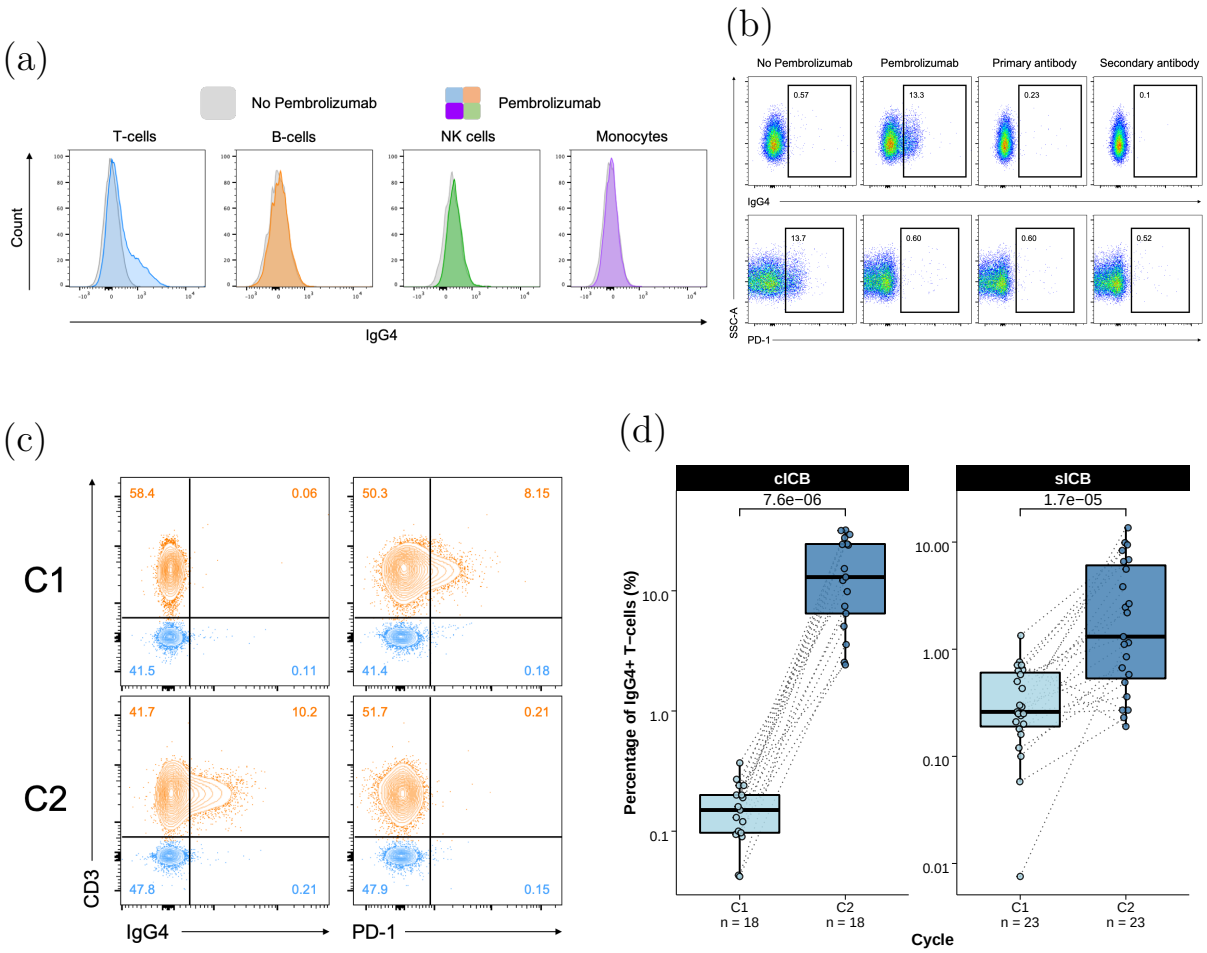


Figure 3.9 Loss of surface PD-1 in T-cells is related to ICB binding
a) Overlaid histograms represent IgG4 staining across different PBMC subsets ±pembrolizumab. Histograms in grey represent background IgG4 staining in the absence of pembrolizumab and histograms in colour represent pembrolizumab-treated samples. **b)** IgG4 and PD-1 staining in T-cells in untreated and pembrolizumab-treated samples including background primary and secondary antibody controls. **c)** Flow cytometry gating of IgG4 and PD-1 in T-cells in a representative paired C1/C2 sample. **d)** Comparison of surface IgG4 on T-cells in paired C1/C2 samples by treatment type (n=18 cICB, n=23 sICB). Statistics were calculated using paired Wilcoxon signed-rank tests.

3.2.1.4 ICB induces T-cell activation within conventional subsets

PD-1 expression, along with markers of activation and proliferation, was quantified in further flow cytometry panels. This confirmed successful PD-1 blockade in T-cells at

C2, as demonstrated by a reduction in PD-1 staining (Figure 3.10a), but also an increase in CD38$^+$ HLADR$^+$ (Figure 3.10b) and Ki67$^+$ T-cells (Figure 3.10c), indicative of T-cell activation, proliferation and response to ICB. Corresponding changes were found for both CD4$^+$ and CD8$^+$ T-cells (Figures S3.12a, S3.12b, S3.12c, S3.12d, S3.12e, S3.12f). Interestingly, PD-1 depletion and induction of CD38$^+$ HLADR$^+$ and Ki67$^+$ T-cells were more profound following cICB treatment compared to sICB and may signify the higher level of activation following cICB as previously described[371,547] (Figures 3.10d, 3.10e, 3.10f, S3.11). The greater loss in PD-1 following cICB also corroborates the previous flow cytometry data which demonstrated enhanced IgG4 binding after cICB (Figure S3.11).

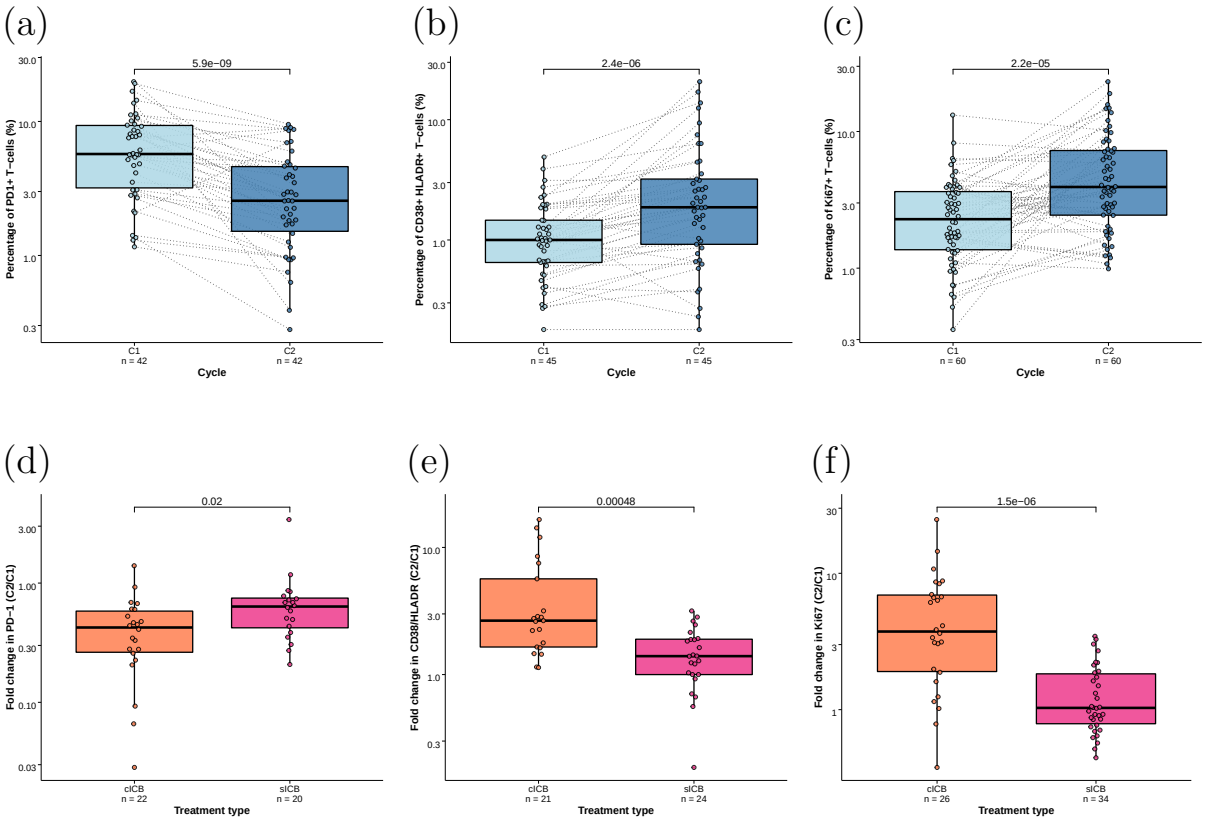


Figure 3.10 cICB induces greater activation in T-cells than sICB
Expression of surface **a)** PD-1, **b)** CD38/HLADR and **c)** Ki67, identified by flow cytometry, was compared between paired C1/C2 samples (n=42-60). Statistics were generated using paired Wilcoxon signed-rank tests. The fold change in **d)** PD-1, **e)** CD38/HLADR and **f)** Ki67 expression at C2 was then compared between sICB-treated (n=20-34) and cICB-treated (n=21-26) samples. Statistics were generated using unpaired Wilcoxon signed-rank tests.

PD-1 and CD38/HLADR expression were visualised by individual T-cell subset and compared between paired C1/C2 samples. Surprisingly, PD-1 and CD38/HLADR expression was highest in unconventional T-cells, including double positive (DP) CD4$^+$ CD8$^+$ T-cells, MAIT cells, iNKT cells and γδ T-cells (Figures 3.11a, 3.11b). DP T-cells are composed of the highest proportion of invariant T-cells as compared to CD4$^+$, CD8$^+$ and double negative CD4$^-$ CD8$^-$ T-cells (Figure S3.13). With an average of 28.34% of DP T-cells expressing either a MAIT, iNKT or γδ TCR, DP T-cells can as a result be considered more unconventional. Interestingly, a patient with PD-1 deficiency was

previously reported as having impaired IFN-γ production specifically by MAIT and Vδ2 T-cells and may highlight the importance of PD-1 in unconventional T-cell function[548]. The elevated expression of PD-1 and CD38/HLADR therefore posed unconventional T-cells as potential major targets of ICB. However, PD-1 loss and T-cell activation was only observed in conventional T-cell subsets and not for DP T-cells, MAIT cells, iNKT cells or γδ T-cells (Figures 3.11c, 3.11d) and may in fact imply that PD-1 has a distinct function in these subsets, representing a less attractive target.

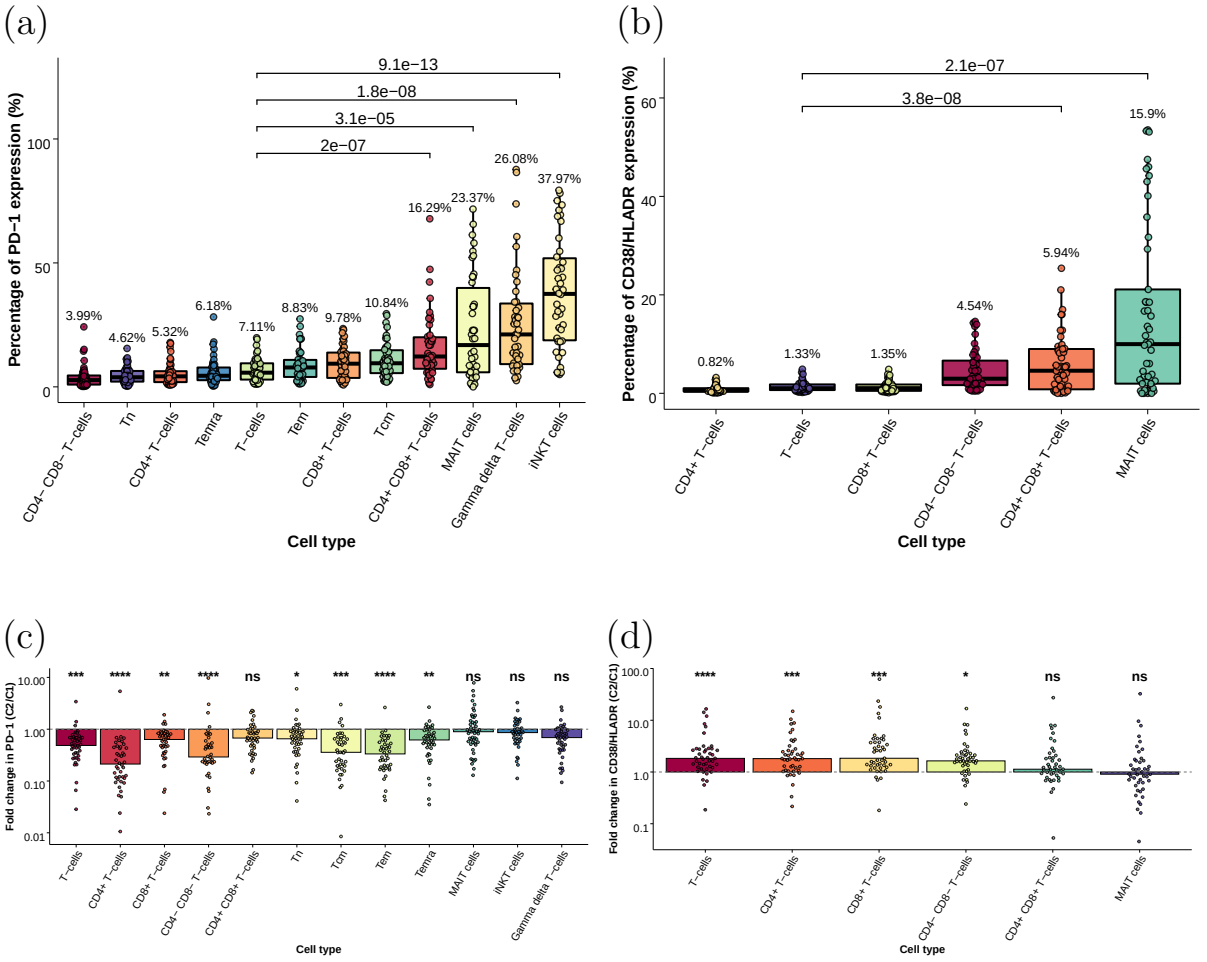


Figure 3.11 ICB activation is limited to conventional T-cell subsets
Flow cytometry expression of surface **a)** PD-1 (n=42) and **b)** CD38/HLADR (n=49) is shown for T-cell subtypes in pretreated samples in ascending order of expression, with average expression displayed above each bar plot. Statistics were generated using paired Wilcoxon signed-rank tests. Fold change in surface expression of **c)** PD-1 and **d)** CD38/HLADR post-ICB treatment is compared between different T-cell types. The level of significance of the change in PD-1 or CD38/HLADR between paired C1/C2 samples is displayed above each bar. Statistics were generated using paired Wilcoxon signed-rank tests and adjusted using Bonferroni correction. Adjusted p > 0.05 (ns), $p \leq 0.05$ (*), $p \leq 0.01$ (**), $p \leq 0.001$ (***), $p \leq 0.0001$ (****). *Tn = Naïve T-cell; Tcm = Central memory T-cell; Tem = Effector memory T-cell; Temra = Effector memory T-cell reexpressing CD45RA.*

3.2.2 Characterising the effect of melanoma on the CD8$^+$ T-cell transcriptome

3.2.2.1 Age, sex and library RNA input contribute to RNAseq data variation

Owing to efficient PD-1 blockade and subsequent activation observed in T-cells following ICB treatment, RNAseq was performed on CD8$^+$ T-cell samples to investigate the effects of ICB on the CD8$^+$ T-cell transcriptome. CD8$^+$ T-cells were isolated as previously mentioned (see section 2.2.4) and lysed prior to RNA extraction. RNAseq libraries were generated yielding 504 high quality CD8$^+$ T-cell transcriptomes (Figure 3.12). This included 70 healthy donors and 190 unique patients composed of 143 paired C1/C2 samples as well as several other longitudinal time-points.

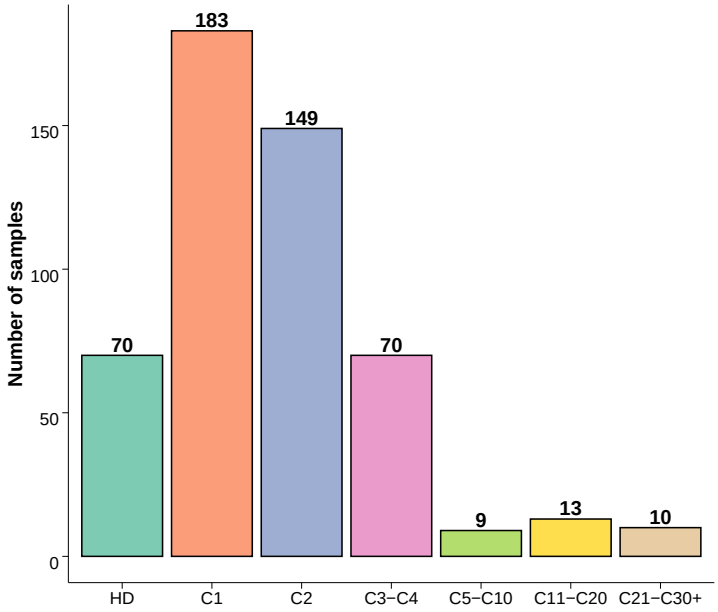


Figure 3.12 CD8$^+$ T-cell RNAseq sample summary
Bar chart depicting the number of CD8$^+$ T-cell transcriptomes successfully sequenced including healthy donors and melanoma patients. Sample number is displayed above each bar. *HD = healthy donor.*

*DESeq*2 was used to remove lowly expressed genes ($\leq$10 gene count), normalise gene counts for library size and analyse gene expression. PCA was performed on normalised gene counts to identify PCs associated with confounding factors that could subsequently be normalised in a *DESeq*2 design argument. A Scree plot demonstrates the contribution of PCs to the data variance and here demonstrates that the top five PCs combined accounted for 54% of the total explained data variance (Figure 3.13).

Typically, the first few PCs in any dataset correlate with RNA quality and concentration. Total RNA input (ng) into libraries, which is reflective of both RNA concentration and ultimately sequencing breadth, is an important contributor to variance in RNAseq data. Age and sex have also previously been associated with altered T-cell phenotype, senescence, subset composition as well as immune checkpoint expression[540–544,546,549,550] and may therefore also contribute to the data variation.

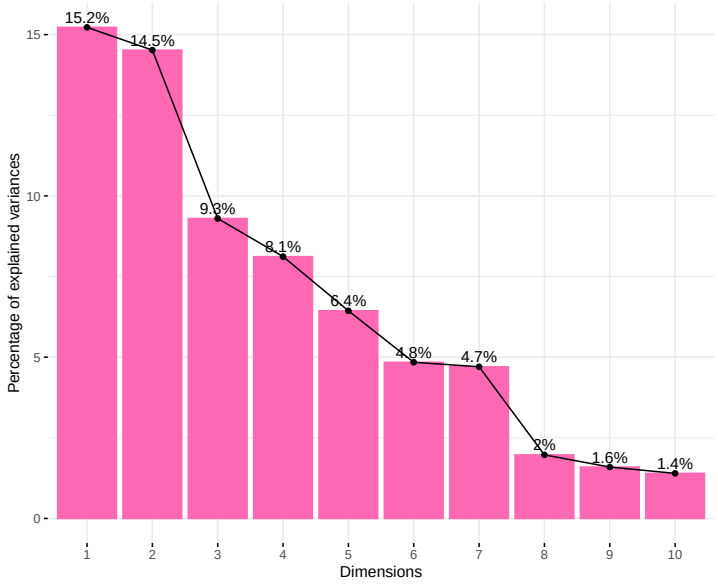


Figure 3.13 Scree plot of early CD8$^+$ T-cell principal components
Scree plot showing the contribution of each of the top ten principal components (dimensions) to the overall explained data variance with the percentage of data contribution displayed above each bar.

Library RNA input, age and sex were compared to the top 20 PCs. This uncovered profound correlations of these factors with several early PCs and hence contributed to a large proportion of the explained data variance (Figure 3.14). Accordingly, library RNA input, age and sex were controlled for in *DESeq*2 design arguments for unpaired tests.

3.2.2.2 T-cells are more proliferative in melanoma

In order to understand the effect of cancer on CD8$^+$ T-cell expression, 70 healthy control and 167 untreated patient (C1) CD8$^+$ T-cell transcriptomes were compared using *DESeq*2 analysis (Figure 3.15a). Any patient receiving adjuvant ICB treatment was removed from analysis as patients did not have metastatic disease. This revealed differential expression of 3,218 genes (1,499 enriched in MM patients, 1,719 overexpressed in healthy donors) after controlling for age, sex, library RNA input and sequencing batch.

Interestingly, the top gene upregulated in patient CD8$^+$ T-cells was *CXCL13*, a chemokine responsible for B-cell recruitment into lymphoid tissue dependent on binding to its cognate receptor CXCR5. CXCL13 production is associated with improved survival in patients receiving ICB[261,364,365,450,451] and is the most highly expressed chemokine by tumour-infiltrating PD-1$^+$ cells[452]. This highlights the importance of CXCL13 in ICB responses which may be due to its involvement in the development of TLS's which are thought to modulate antitumour responses, B-cell and T-cell activation as well as germinal centre activity[366,445–447,449].

Pathway analysis was performed on genes significantly upregulated in MM patients using Gene Ontological Biological Processes (GOBP) pathways and demonstrated a common role of these genes in T-cell division and proliferation pathways including "chromosome segregation", "nuclear division" and "DNA replication" (Figure 3.15b). This may be as a result of cancer recognition which induces chronic immune cell activation and high cell turnover.

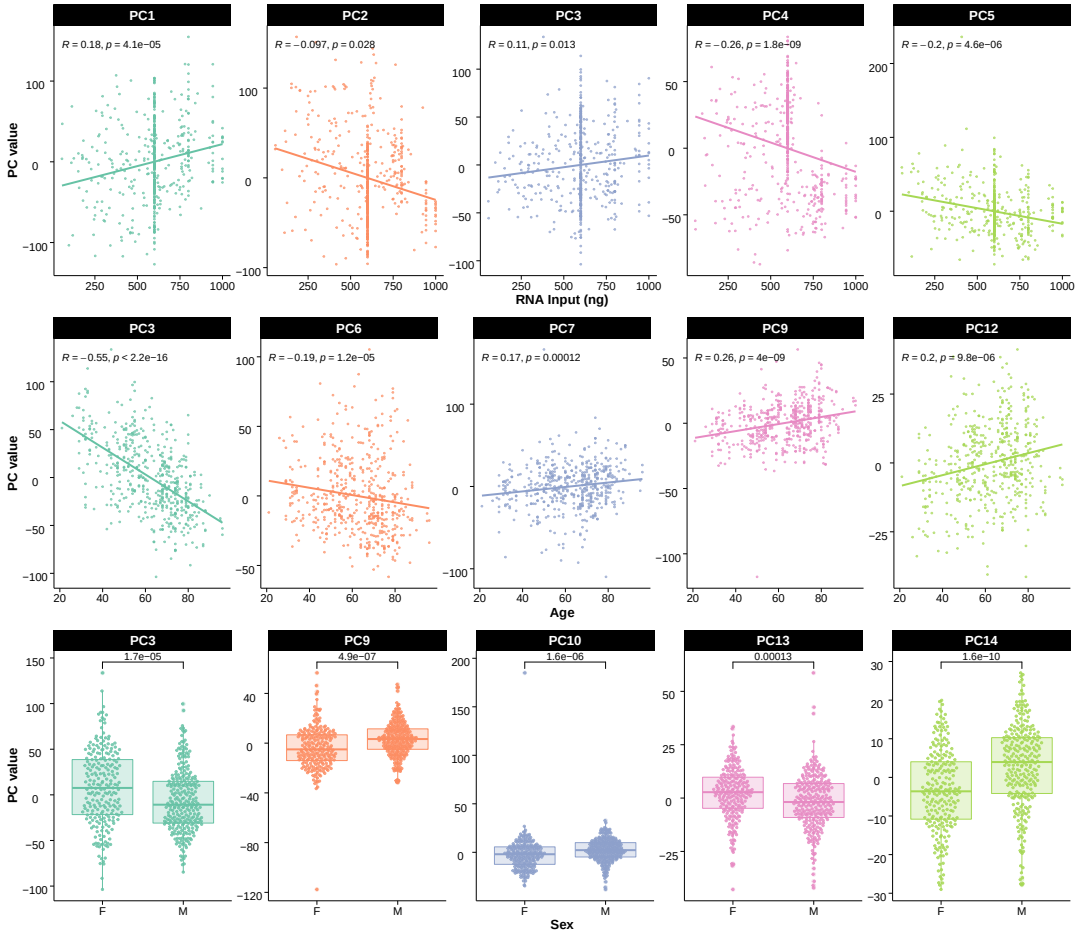


Figure 3.14 Early principal components correlate with library RNA input, age and sex
The top five most significantly correlated principal components (PCs) are compared to library RNA input (ng), age and sex (n=504). Statistics were calculated using Spearman's rank correlation coefficient for correlation analysis or unpaired Wilcoxon signed-rank tests for sex-based differences. *F = female*, *M = male*.

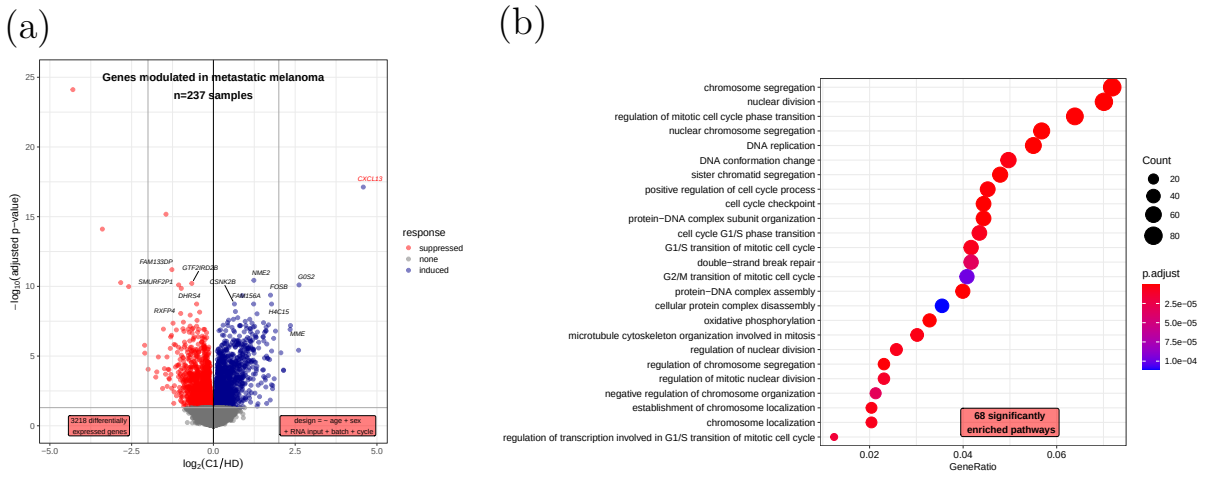


Figure 3.15

Figure 3.15 (Previous page) Differential CD8$^+$ T-cell expression in metastatic melanoma CD8$^+$ T-cell expression was compared between 70 healthy donors (HD) and 167 untreated MM patients (C1) using $DESeq2$, controlling for age, sex, library RNA input and sequencing batch. **a)** Volcano plot depicting genes differentially expressed between healthy donors and untreated MM patients (C1). Genes significantly enriched in MM patients are in blue and those significantly enriched in healthy donors are in red. The $\log_2$ fold change of each gene is visualised on the x-axis with the significance of this difference displayed on the y-axis. The number of significantly differentially expressed genes as well as the $DESeq2$ design formula are displayed in red boxes. Statistics were calculated using the negative binomial distribution and adjusted for multiple testing using the Benjamini-Hochberg procedure on $DESeq2$. *CXCL13* is highlighted in red. **b)** Pathway enrichment of genes upregulated in MM patients identified using GOBP. The number of significantly enriched pathways is displayed in a red box in the bottom right.

3.2.2.3 CMV infection is associated with distinct CD8$^+$ T-cell expression

Taking the relationship of CMV serostatus with T-cell composition into account (Figures 3.3a, 3.3b, 3.4a, 3.4b, 3.5a, 3.5b, 3.6), the effect of CMV infection on CD8$^+$ T-cell expression was examined using $DESeq2$, controlling for age, sex, library RNA input, cancer status and sequencing batch. 5,014 genes were discovered to be differentially expressed between CMV$^-$ (n=77) and CMV$^+$ (n=76) individuals with 2,654 genes induced in CMV$^+$ patients and 2,360 genes downregulated (Figure 3.16a). Pathway analysis of genes upregulated in CMV$^+$ individuals revealed an enrichment of genes in "T-cell activation", "antigen processing and presentation", "cellular response to interferon-gamma" and "regulation of defence response to virus by host" using GOBP pathways (Figure 3.16b).

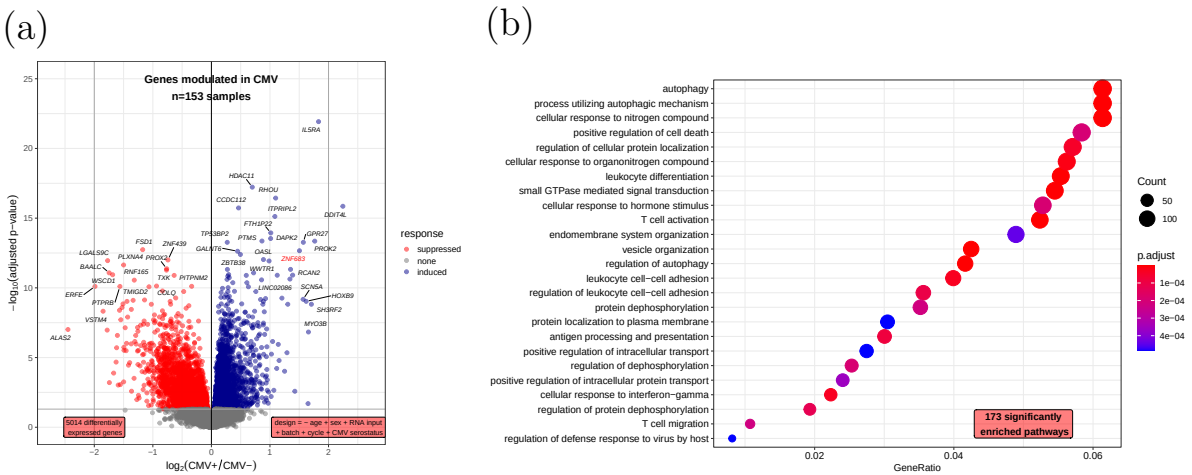


Figure 3.16

Figure 3.16 (Previous page) CMV infection alters $CD8^+$ T-cell expression
a) Volcano plot depicting genes differentially expressed between CMV^- (n=77) and CMV^+ (n=76) individuals. Genes significantly enriched in CMV^+ patients are in blue and those significantly downregulated are in red. The $\log_2$ fold change of each gene is visualised on the x-axis with the significance of this difference displayed on the y-axis. The number of significantly differentially expressed genes as well as the $DESeq2$ design formula are displayed in red boxes. Statistics were calculated using the negative binomial distribution and adjusted for multiple testing using the Benjamini-Hochberg procedure on $DESeq2$. *ZNF683* is highlighted in red. **b)** Pathway analysis of genes upregulated in CMV^+ individuals using GOBP pathways. The total number of significantly enriched pathways is displayed in a red box in the bottom right.

Interestingly, one of the most significantly enriched genes in CMV^+ individuals was *ZNF683* (HOBIT) which is highly expressed by CMV-specific $CD8^+$ T-cells, but not by EBV-specific or Influenza-specific T-cells[551–554]. Expression of HOBIT is also found to be important for IFN-γ and GZMB production as well as maintaining cytotoxic function and inducing tissue residency[552,555,556].

CMV was also found to induce differential expression in NK cells (data not shown), although many more genes were differentially expressed and to a higher magnitude of difference in $CD8^+$ T-cells.

3.2.2.4 CMV serostatus doesn't influence the differential expression observed between healthy donor and melanoma patient $CD8^+$ T-cells

Owing to the profound impact of CMV infection on the $CD8^+$ T-cell transcriptome and the association with age, differential gene expression analysis between healthy donors and MM patients was repeated after controlling for CMV. However, few healthy donor samples had been CMV tested and so it was not possible to control for CMV serostatus directly. As a result, a CMV expression score was generated for all $CD8^+$ T-cell samples and controlled for in the $DESeq2$ design argument. This score was generated by calculating the geometric mean of the top 50 genes upregulated in CMV^+ individuals as identified in Figure 3.16a. This score was then compared between tested samples and was found to be significantly predictive of CMV serostatus (Figure 3.17a). Further samples were CMV tested for a validation cohort. After calculating the CMV expression score for these samples, using the same genes as before, CMV^+ patients were found to have significantly higher scores, thus validating this approach (Figure 3.17b). Healthy donor and C1 samples were subsequently compared again controlling for this score. Despite controlling for this CMV score, a similar number of differentially expressed genes (DEGs) were identified as before when CMV score was not controlled for (CMV score uncontrolled n=3,218, CMV score controlled n=3,281) (Figure 3.17c). Overall, CMV did not seem to be responsible for the differences in $CD8^+$ T-cell expression between healthy controls and MM patients. Importantly, *CXCL13* remained more highly expressed by patients. Furthermore, the CMV expression score was found to be predictive of CMV serostatus and was thus used as a substitute for serostatus for further analyses.

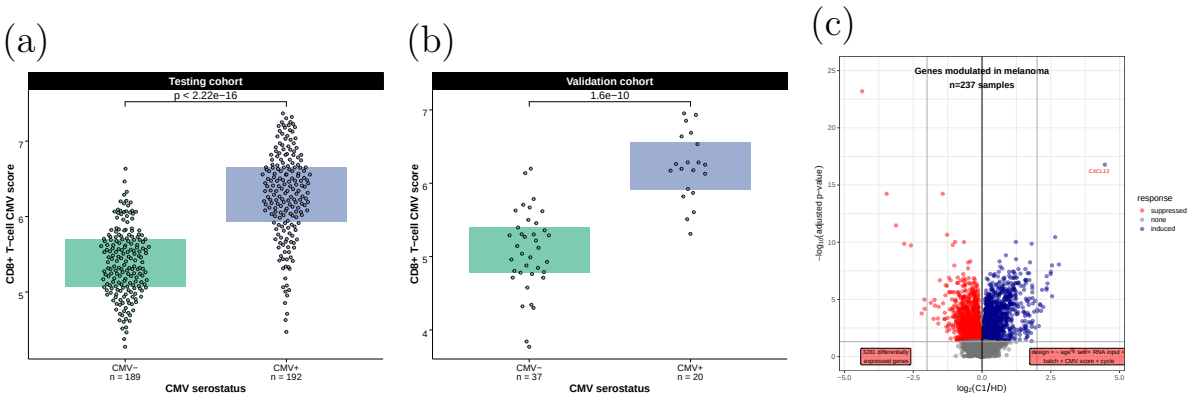


Figure 3.17 CMV does not contribute to the differential expression of CD8$^+$ T-cells observed in melanoma
CMV scores were generated for all CD8$^+$ T-cell samples by calculating the geometric mean of the top 50 genes induced during CMV infection. Deconvoluted CMV score was compared between CMV-tested individuals in the **a)** testing cohort (CMV$^-$ n=189, CMV$^+$ n=192) and **b)** validation cohort (CMV$^-$ n=37, CMV$^+$ n=20). Statistics were calculated using "lm(CD8$^+$ T-cell CMV score $\sim$ CMV serostatus + age + cancer status + library RNA input, data)" **c)** Healthy donor (HD, n=70) and untreated patient (C1, n=167) samples were compared after controlling for age, sex, library RNA input, sequencing batch and CMV score. The number of differentially expressed genes is displayed in a red box in the bottom left with the $DESeq2$ design argument in a red box in the bottom right. Gene enrichment is portrayed on the x-axis and significance on the y-axis. Genes significantly upregulated or downregulated in MM patients are blue or red respectively. Statistics were calculated using the negative binomial distribution and adjusted for multiple testing using the Benjamini-Hochberg procedure on $DESeq2$. *CXCL13* is highlighted in red.

3.2.3 Describing the CD8$^+$ T-cell ICB transcriptomic response

3.2.3.1 CD8$^+$ T-cells have the strongest response to ICB

Bulk RNAseq was also performed on CD14$^+$ monocyte, CD19$^+$ B-cell, CD4$^+$ naïve T-cell, CD4$^+$ memory T-cell and NK cell samples (Table 2.3). PCA of normalised gene counts revealed tight clustering of CD8$^+$ T-cells with CD4$^+$ naïve T-cells, CD4$^+$ memory T-cells and NK cells, with CD14$^+$ and CD19$^+$ cells clustering distinctly (Figure S3.14).

To compare the expression of ICB targets *CTLA4* and *PDCD1* between different PBMC cell types, gene counts were normalised for library size and gene skewing using $DESeq2$. In concordance with previous PBMC flow cytometry data (Figure 3.8a), normalised expression data revealed that lymphocytes expressed the most *CTLA4* and *PDCD1* and that CD14$^+$ monocytes expressed very little (Figures 3.18a, 3.18b). T-cells, regardless of CD4/CD8 expression, had the highest normalised gene counts for both *CTLA4* and *PDCD1*, followed by CD19$^+$ B-cells and NK cells. High expression of ICB targets in T-cells is in keeping with the assumption that T-cells have a higher capacity for immune checkpoint blocker binding.

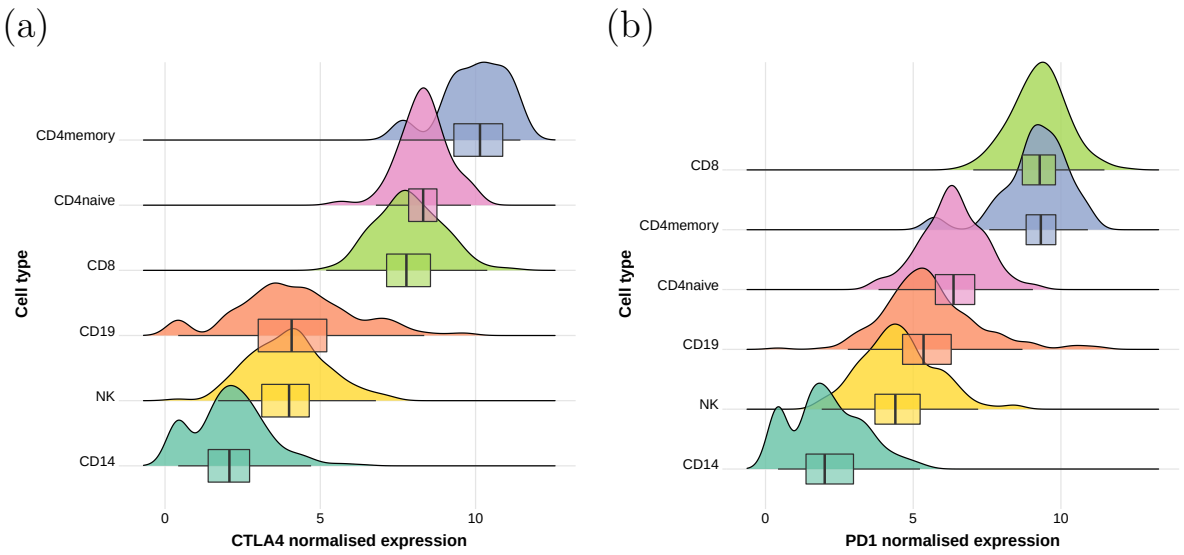


Figure 3.18 T-cells express the highest levels of *CTLA4* and *PDCD1*
PBMC bulk RNAseq gene counts were normalised using $DESeq2$ and used to compare expression of ICB target genes. Normalised **a)** *CTLA4* and **b)** *PDCD1* expression is compared between different PBMC cell types, shown in order of expression (n=504 CD8$^+$ T-cells, n=308 CD19$^+$ B-cells, n=284 CD14$^+$ monocytes, n=174 NK cells, n=69 CD4$^+$ naïve T-cells, n=26 CD4$^+$ memory T-cells).

To elucidate the mechanism of action of ICB, differential expression was calculated between paired C1/C2 samples per PBMC subset using $DESeq2$, controlling for patient ID to ensure a paired comparison. However, due to low sample numbers, CD4$^+$ naïve and CD4$^+$ memory T-cell samples were excluded from subsequent analyses. As library RNA input was found to significantly correlate with several early PCs in all PBMC cell types (Figures 3.14, S3.15), library RNA input was also controlled for in $DESeq2$ design arguments for all cell subsets. Due to differences in sample numbers for each cell type, and thus statistical power, data was subsampled to the minimum sample number collected for any cell subset per treatment type (n=19 sICB, n=26 cICB). Patients with nonmetastatic disease who were treated with adjuvant sICB were removed to avoid differences in response between metastatic and nonmetastatic disease. The number of DEGs, including the number of induced and suppressed genes, was calculated using $DESeq2$ and performed 100 times taking the average number of DEGs for all iterations. Analysis was performed by ICB treatment type owing to the differential activation previously observed in T-cells and differential regulation of CD19$^+$ B-cell count between treatment types (Figures 3.10d, 3.10e, 3.10f, S3.3a, S3.3b, S3.11).

Supporting the previous finding that PD-1 is most profoundly blocked in T-cells (Figure 3.8b), the greatest number of DEGs was discovered in CD8$^+$ T-cells regardless of ICB treatment type (Figures 3.19a, 3.19b). Interestingly, the order of differential expression varied between the remaining subsets. Differential expression was not observed at all following sICB treatment in CD19$^+$ B-cell samples. However, CD19$^+$ B-cells had the second most DEGs following cICB treatment, after CD8$^+$ T-cells, which may be reflective of the changes in circulating B-cell count, uniquely observed following cICB treatment (Figures S3.3a, S3.3b) and is discussed in Chapter four.

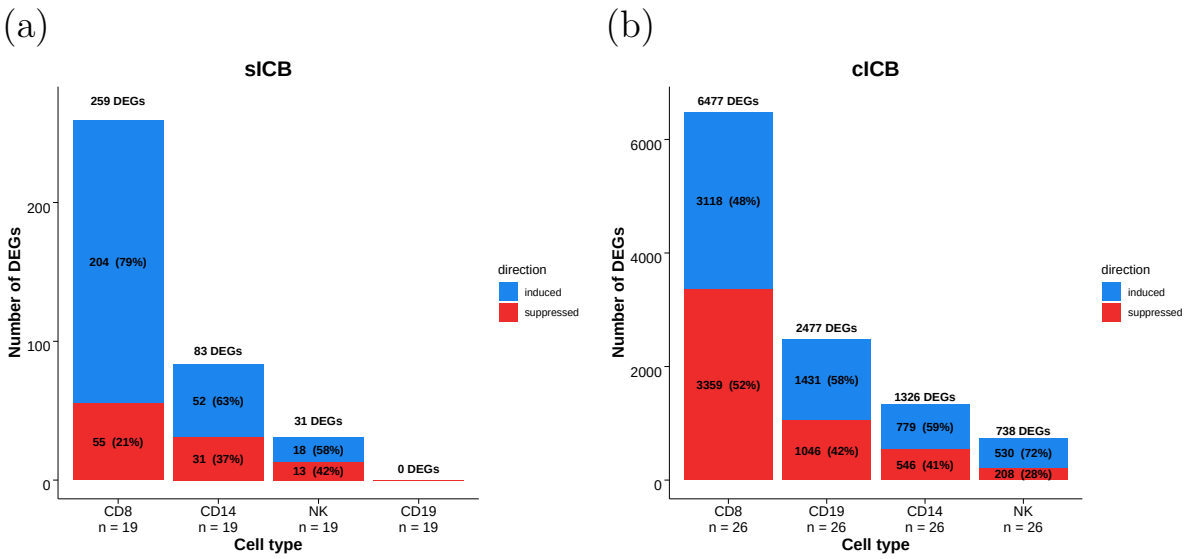


Figure 3.19 CD8$^+$ T-cells have the greatest transcriptomic response to ICB
Bar plots depicting the average number of differentially expressed genes per cell type in descending order in response to ICB after subsampling to equivalent sample numbers following either **a)** sICB (n=19) or **b)** cICB (n=26) treatment. Bars are split into induced (blue) and suppressed (red) genes following treatment showing the number of induced/suppressed genes and percentage of all differentially expressed genes that they represent. The total number of differentially expressed genes is displayed on top of each bar.

3.2.3.2 CD8$^+$ T-cells become activated and proliferate in response to ICB

With the strongest differential expression observed in CD8$^+$ T-cells, CD8$^+$ T-cell gene expression was investigated more closely and compared between paired C1/C2 samples (Figure 3.20a). 9,325 genes were found to be differentially expressed when controlling for both patient ID and library RNA input. Notably, an increase in cell cycle-associated genes including cell division cycle proteins (*CDC20*, *CDC45*, *CDC6*), cyclins (*CCNB2*, *CCNA2*, *CCNE1*), kinesin-like proteins (*KIF20A*, *KIF4A*, *KIF23*), centrosomal proteins (*CEP55*, *CEP68*, *CEP126*) as well as markers of proliferation (*MKI67*) was observed. Intriguingly, one of the most significantly induced genes, and one of the few cytokines differentially expressed, was *CXCL13*. *CXCL13* was found to be highly expressed in melanoma (Figure 3.15a), activated CD8$^+$ T-cells and PD-1^{hi} TILs[261,348,376,451–454], further demonstrating its importance in cancer.

Accordingly, pathway analysis of significantly upregulated genes using GOBP pathways revealed an enrichment within cell division pathways, including "regulation of mitotic cell cycle phase transition", "chromosome segregation" and "cell cycle G2/M phase transition" (Figure 3.20b). Furthermore, significantly upregulated genes were enriched in "mitochondrial gene expression", "mitochondrial translation" and "oxidative phosphorylation" pathways which may reflect the greater mitochondrial and metabolic activity required for cell activation and proliferation[557,558].

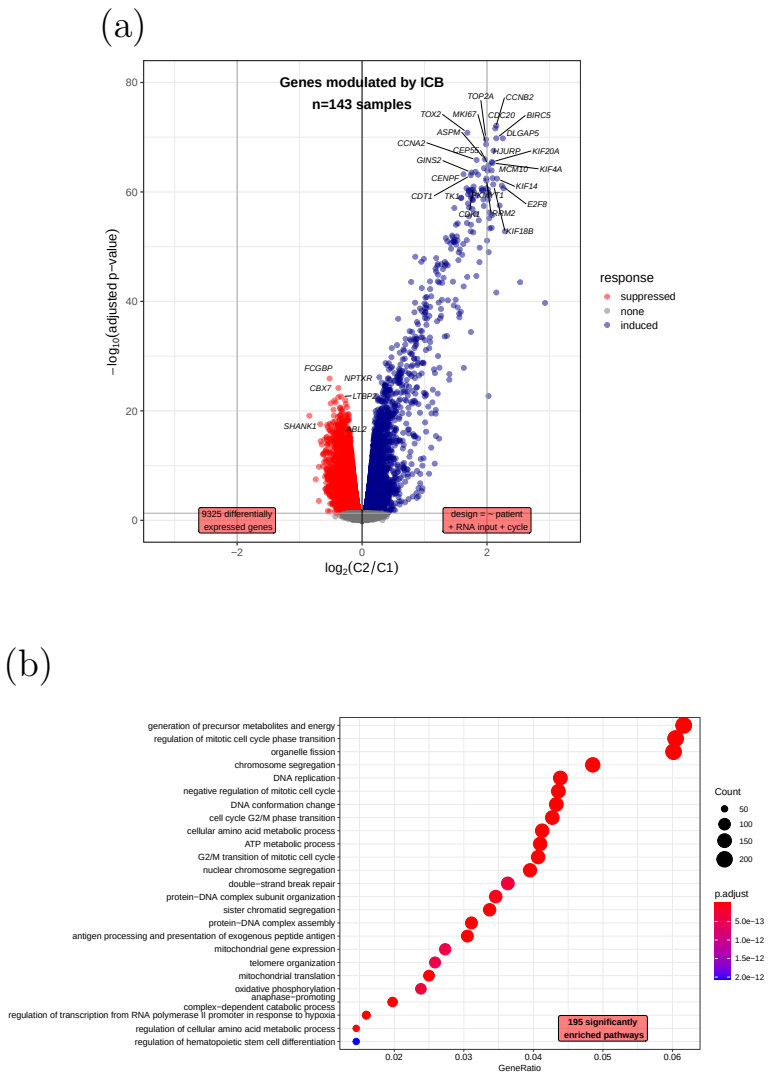


Figure 3.20 Induction of cell cycle-associated genes by CD8$^+$ T-cells at C2
a) Volcano plot visualising differential expression of CD8$^+$ T-cells in response to ICB in paired C1/C2 samples (n=143) after controlling for patient ID and library RNA input. Genes significantly enriched at C2 are in blue and those significantly downregulated are in red. The $\log_2$ fold change of each gene is visualised on the x-axis with the significance of this difference displayed on the y-axis. The number of significantly differentially expressed genes as well as the $DESeq2$ design formula are displayed in red boxes. Statistics were calculated using the negative binomial distribution and adjusted for multiple testing using the Benjamini-Hochberg procedure on $DESeq2$. **b)** Pathway enrichment analysis using the GOBP database reveals shared function of genes induced in response to ICB treatment. The number of significantly enriched pathways is displayed in a red box in the bottom right.

Although CD8$^+$ T-cells were found to be profoundly activated after ICB treatment, with increased expression of exhaustion markers *CTLA4*, *PDCD1*, *LAG3* and *HAVCR2*, no difference was observed in response to PMA/Ionomycin stimulation regardless of treatment status (Figures 3.21a, 3.21b, S3.16a, S3.16b). More specifically, no differences in upregulation of CD69, GZMB, IFN-γ or TNF-α were observed after culture with PMA/Ionomycin for 24 hours between paired C1/C2 samples. As a result, T-cells maintain the ability to respond to activating stimuli despite prior activation by ICB.

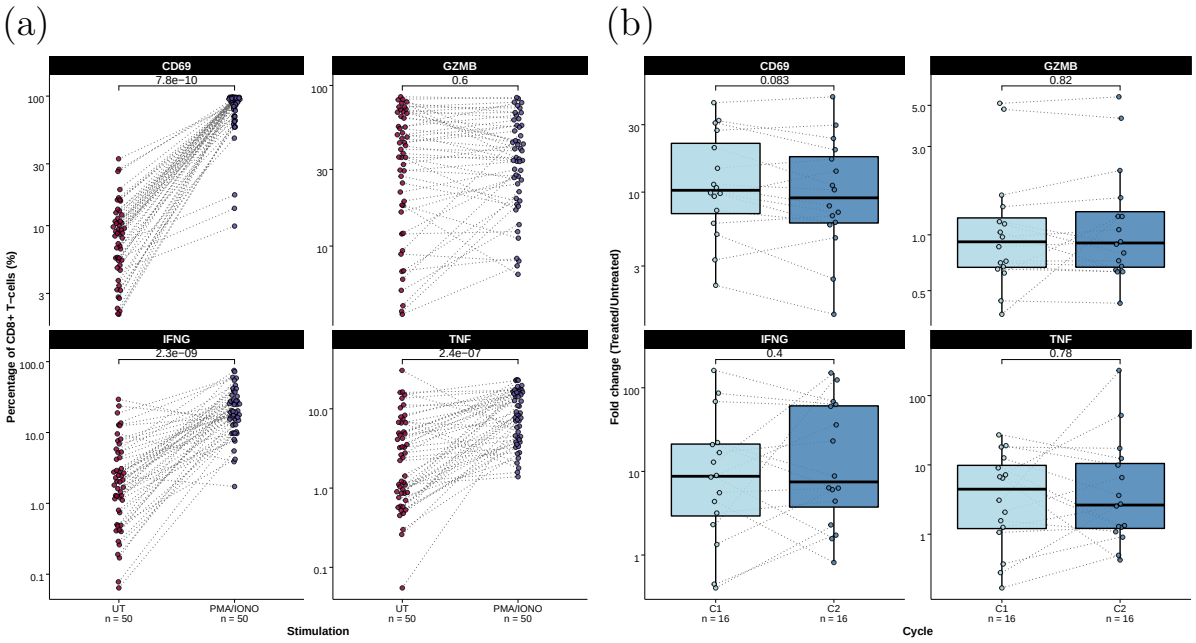


Figure 3.21 ICB has no effect on the CD8$^+$ T-cell response to stimulation
Paired C1/C2 PBMC samples were treated with PMA/Ionomycin (PMA/IONO) for 24 hours prior to flow cytometry analysis of CD8$^+$ T-cells. **a)** Paired untreated (UT) and PMA/IONO-treated samples (n=50) are compared for expression of activation markers and cytokine production. **b)** Induction of these markers is compared between paired C1/C2 samples (n=16). Statistics were calculated using paired Wilcoxon signed-rank tests.

3.2.3.3 cICB has larger effects on CD8$^+$ T-cell expression than sICB

Due to the differences observed in CD8$^+$ T-cell activation between sICB and cICB treatments (Figures 3.10d, 3.10e, 3.10f, S3.11), differential expression was examined between paired C1/C2 samples separately for each treatment type (n=59 sICB, n=77 cICB), after removing any patients treated with adjuvant sICB (Figures 3.22a, 3.22b). This revealed differential expression of 1,314 and 10,955 genes following sICB and cICB treatments respectively. To account for sample size, cICB analysis was performed again after subsampling to 59 samples to ensure equivalent statistical power between sICB-treated and cICB-treated samples. This was repeated 100 times, recording the total number of DEGs for each iteration, and taking the average. Despite using this subsampling approach, cICB still resulted in more DEGs on average (n=9,950) compared to sICB-treated samples (n=1,314) (Figure 3.22c). After comparing the magnitude of induction and suppression of significant DEGs between sICB-treated and cICB-treated samples, it was found that very few genes were only significantly differentially expressed after sICB (Figure 3.22d). In fact, all DEGs were modulated in the same direction for both treatments, but almost always to a higher magnitude following cICB treatment. This signifies that sICB and cICB have similar effects, but addition of CTLA-4 blockade augments stimulation. Interestingly, *CXCL13* was induced to a higher magnitude after cICB treatment compared to sICB treatment and may be driving the loss in circulating B-cells after cICB and explain the lack of transcriptomic response after sICB (Figures S3.3b, 3.19a).

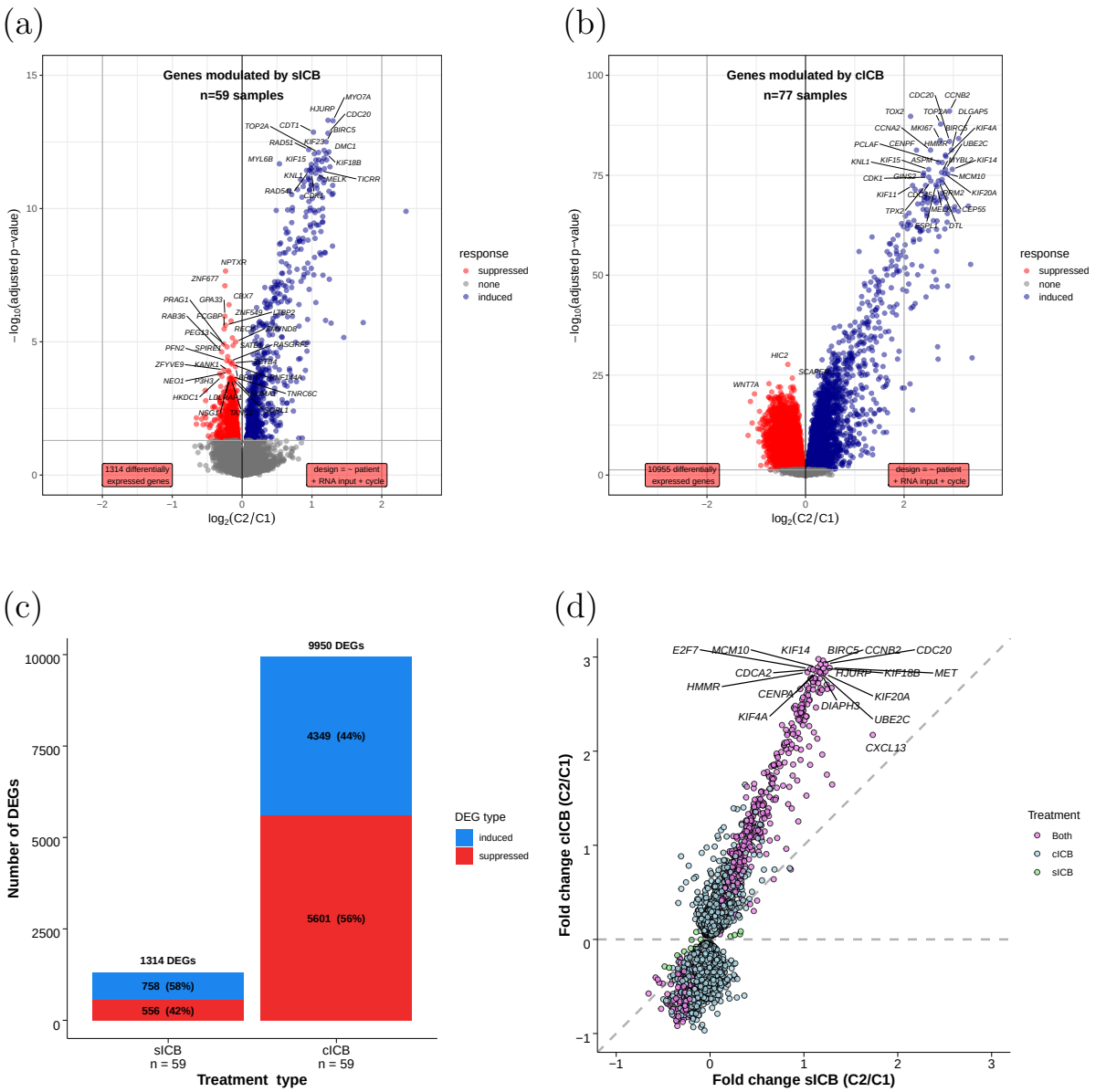


Figure 3.22 cICB induces similar genes to sICB, but to a higher magnitude
Volcano plots of paired C1/C2 samples treated with either **a)** sICB (n=59) or **b)** cICB (n=77). Genes significantly enriched at C2 are in blue and those significantly downregulated are in red. The $\log_2$ fold change of each gene is visualised on the x-axis with the significance of this difference displayed on the y-axis. The number of significantly differentially expressed genes as well as the $DESeq2$ design formula are displayed in red boxes. Statistics were calculated using the negative binomial distribution and adjusted for multiple testing using the Benjamini-Hochberg procedure on $DESeq2$. **c)** Bar chart showing the average number of differentially expressed genes derived from subsampled data (n=59). The number of induced and suppressed genes are also highlighted in blue and red respectively along with the percentage of total differentially expressed genes that they represent. **d)** Differential expression is compared between sICB-treated and cICB-treated samples looking at significant differentially expressed genes and highlighting those genes which are only significantly differentially expressed after sICB in green, after cICB in blue or differentially expressed after both treatments in pink (n=59 sICB, n=77 cICB).

3.2.3.4 *TOX2*, *MKI67* and ICB binding are important for the CD8$^+$ T-cell ICB response

To determine the drivers of CD8$^+$ T-cell ICB response, paired C1/C2 CD8$^+$ transcriptomes were compared after controlling for individual normalised CD8$^+$ T-cell gene counts. This was performed as a loop, controlling for one CD8$^+$ T-cell gene at a time in order to determine the contribution or association of expression of each gene to the overall ICB response. This was quantified as the total number of DEGs identified. Controlling for T-cell genes rarely resulted in an increase in DEGs identified and means that few are suppressive to ICB response (Figure 3.23). However, many genes were associated with a reduced number of DEGs when controlled for, implying that either these genes normally contribute directly to ICB response or that they at least correlate with ICB response. Notably, *TOX2* was the only gene in CD8$^+$ T-cells to completely abrogate differential expression when controlled for, and may therefore be the driver of ICB response. The second most influential T-cell gene in controlling T-cell ICB response was *MKI67*, with only two DEGs detected after controlling for expression, which may signify that T-cell proliferation is also crucial for ICB response. Supporting this, other cell cycle-associated genes were found to massively reduce the number of DEGs identified when controlled for including *KIF23*, *CCNB2* and *KIF18B*.

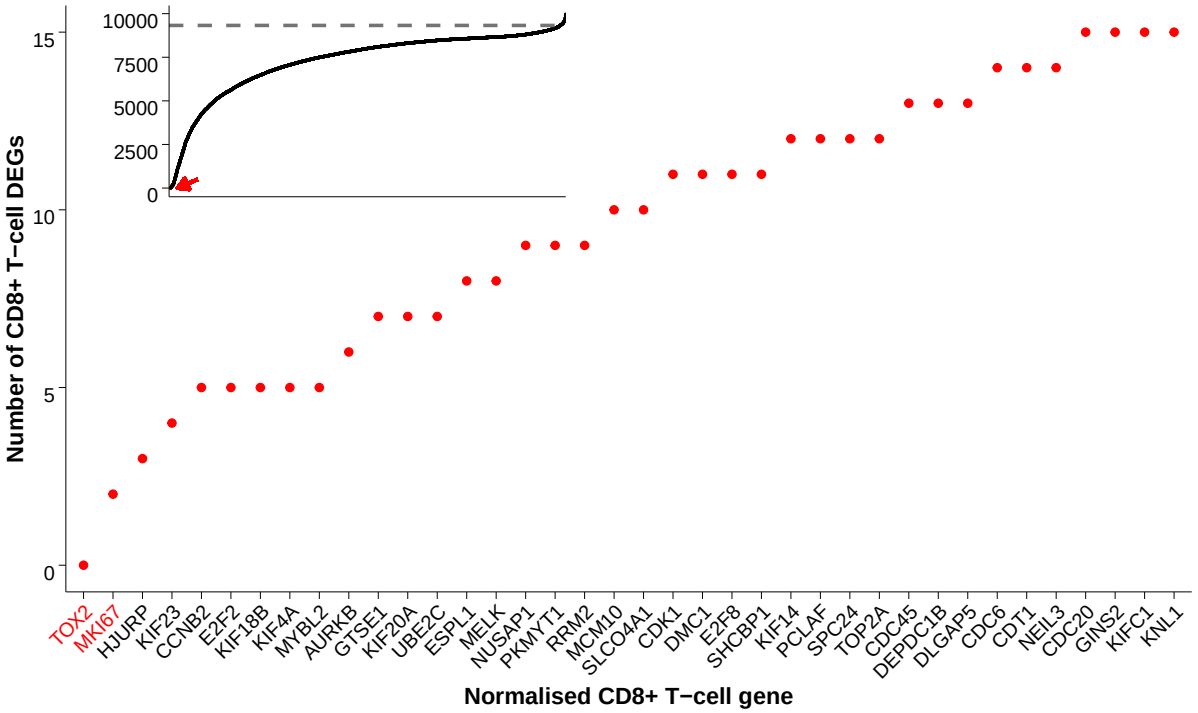


Figure 3.23 Expression of CD8$^+$ T-cell *TOX2* and *MKI67* is associated with CD8$^+$ T-cell ICB response

Sigmoid curves of the top CD8$^+$ T-cell genes associated with dampening CD8$^+$ T-cell response with a sigmoid curve of all genes overlaid. The arrow and points in red represent the magnified plot. *DESeq2* was used to compare paired C1/C2 CD8$^+$ T-cell transcriptomes (n=143) after controlling for patient ID, library RNA input and individual normalised CD8$^+$ T-cell gene counts as shown on the x-axis. The number of resulting DEGs is shown on the y-axis. *TOX2* and *MKI67* genes are highlighted in red.

To understand if the CD8$^+$ T-cell response to ICB was dependent on direct immune checkpoint blocker binding, response was compared to the induction in percentage of IgG4$^+$ CD8$^+$ T-cells, acting as a surrogate for immune checkpoint blocker binding. ICB response was quantified by generating a CD8$^+$ T-cell ICB activation score by calculating the geometric mean of the top 50 genes induced after ICB in CD8$^+$ T-cells. This revealed a strong correlation between the fold changes in IgG4$^+$ CD8$^+$ T-cells and CD8$^+$ ICB activation score at C2 (Figure 3.24).

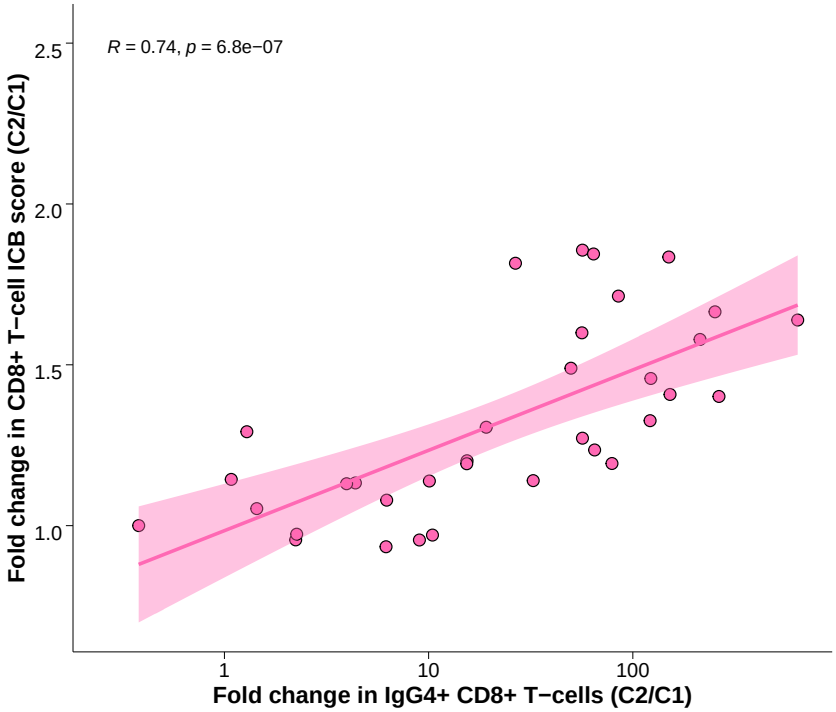


Figure 3.24 Direct ICB binding correlates with CD8$^+$ T-cell ICB response
Comparison of IgG4$^+$ CD8$^+$ T-cell induction at C2 with fold change in CD8$^+$ T-cell ICB activation score (n=41). Statistics were calculated using Spearman's rank correlation coefficient.

3.2.3.5 CD8$^+$ T-cell ICB activation drives response in other cell types

With only T-cells capable of binding pembrolizumab (Figure 3.9a), having a detectable reduction in surface PD-1 (Figure 3.8b) and experiencing the greatest differential expression (Figures 3.19a, 3.19b), T-cells represented the most likely target of immune checkpoint blocker binding. As a result, CD8$^+$ T-cells may be responsible for activation in other cell types.

Due to the profound effects of ICB on CD8$^+$ T-cells, as well as the importance of CD8$^+$ T-cell *TOX2* and *MKI67* for response, paired C1/C2 samples for all PBMC cell types were compared, controlling for either CD8$^+$ T-cell ICB score, normalised CD8$^+$ T-cell *TOX2*/*MKI67* gene count or the percentage of IgG4$^+$ CD8$^+$ T-cells (Figure 3.25). Although controlling for CD8$^+$ T-cell ICB score in CD8$^+$ T-cells didn't completely eliminate differential expression, it massively reduced the number of resulting DEGs. However, controlling for CD8$^+$ T-cell ICB score in all other cell types, namely CD14$^+$ monocytes, CD19$^+$ B-cells and NK cells, completely removed any effect of ICB on differential expression. This was also true when controlling for normalised CD8$^+$ T-cell *TOX2*/*MKI67* gene counts and IgG4 binding.

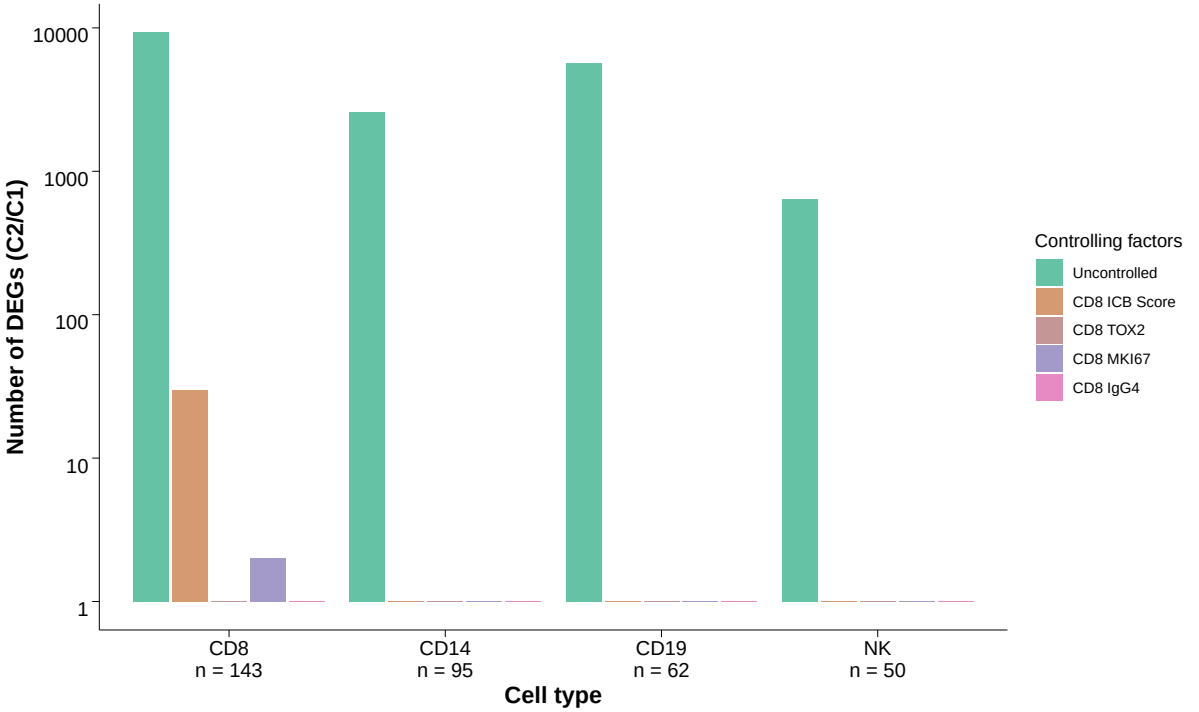


Figure 3.25 CD8$^+$ T-cell ICB response is important for activation in other cell types
Differential expression was determined for CD8$^+$ T-cells (n=143), CD14$^+$ monocytes (n=95), CD19$^+$ B-cells (n=62) and NK cells (n=50) comparing paired C1/C2 samples and controlling for patient ID, library RNA input as well as either CD8$^+$ T-cell ICB score, normalised CD8$^+$ T-cell *TOX2*/*MKI67* gene counts or IgG4$^+$ CD8$^+$ T-cell percentage using $DESeq2$. The PBMC subset compared is on the x-axis with the number of resulting DEGs on the y-axis. Green bars represent the number of DEGs identified without controlling for CD8$^+$ T-cell metrics.

Whether CD8$^+$ T-cell ICB response is merely correlative with response in other cell types or is actually essential remained to be determined. To investigate this further, differential expression analysis was performed for paired C1/C2 CD8$^+$ T-cell samples, controlling for ICB scores generated for other PBMC types, to see if it would remove all differential expression as CD8$^+$ T-cell ICB score did in other PBMC subsets (Figure 3.25). Although controlling for PBMC ICB scores in CD8$^+$ T-cell C1/C2 sample comparisons did significantly reduce the number of DEGs identified, no PBMC ICB score completely removed differential expression (Figure 3.26). This suggests that if you correct for the CD8$^+$ T-cell response to ICB, there are no other independent effects on other cell types. However, when you control for the ICB score for other PBMC types, there is minimal effect on the CD8$^+$ T-cell ICB response and hence CD14$^+$ monocyte, CD19$^+$ B-cell and NK cell ICB responses may be secondary to CD8$^+$ T-cell responses.

However, examination of the genes that reduced the number of CD8$^+$ T-cell DEGs in CD14$^+$ monocytes, CD19$^+$ B-cells and NK cells revealed that interferon-associated genes, including guanylate-binding proteins (GBPs) and *STAT1*, were consistently observed among the top genes in dampening CD8$^+$ T-cell ICB response (Figures 3.27a, 3.27b, 3.27c). This may reflect that the cells become activated in response to T-cell interferon signals induced at C2[210,559,560].

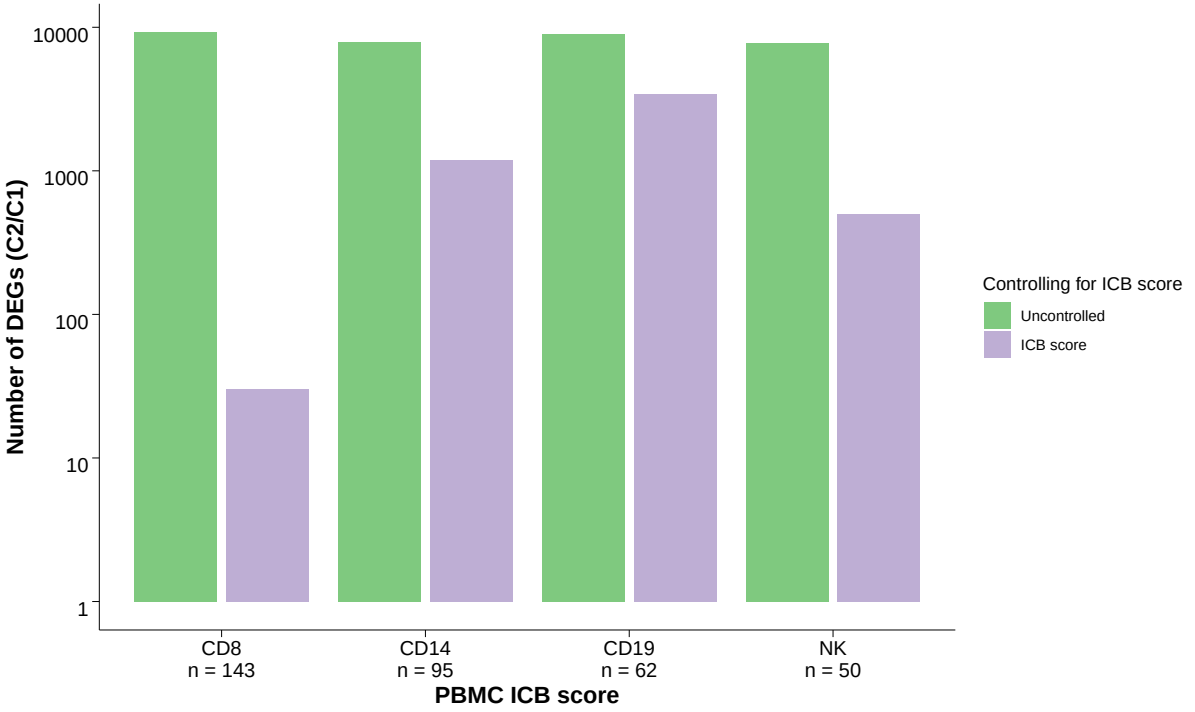


Figure 3.26 CD8$^+$ T-cell ICB response is not dependent on activation in other subsets
$DESeq2$ was used to compare expression in paired C1/C2 CD8$^+$ T-cell samples, controlling for patient ID and library RNA input as well as either CD8$^+$ T-cell (n=143), CD14$^+$ monocyte (n=95), CD19$^+$ B-cell (n=62) or NK cell (n=50) ICB activation scores. The PBMC ICB activation score controlled for is represented by the x-axis with the number of DEGs identified on the y-axis. Green bars represent the number of DEGs without controlling for ICB score and purple bars signify the number of DEGs after controlling for ICB score.

After comparing the genes upregulated at C2 between different PBMC cell subsets, 248 genes were found to be overexpressed in common and were visualised using $UpSetR$[561] (Figure 3.28). Shared upregulated genes included interferon-associated genes such as *GBP1*, *GBP2*, *GBP4*, *GBP1P1*, *STAT1*, *IFI6*, *IFI27*, *IFI35*, *IFIT3*, *IFITM3*, *IRF1* and *ISG15*. Strikingly, expression of GBPs and *STAT1* by PBMC subsets was found to correlate with CD8$^+$ T-cell ICB response (Figures 3.27a, 3.27b, 3.27c) and may represent genes driving PBMC cell activation in response to CD8$^+$ T-cell activation.

Further demonstrating the importance of CD8$^+$ T-cells in ICB response, 3,125 genes were found to be uniquely induced by CD8$^+$ T-cells (Figure 3.28).

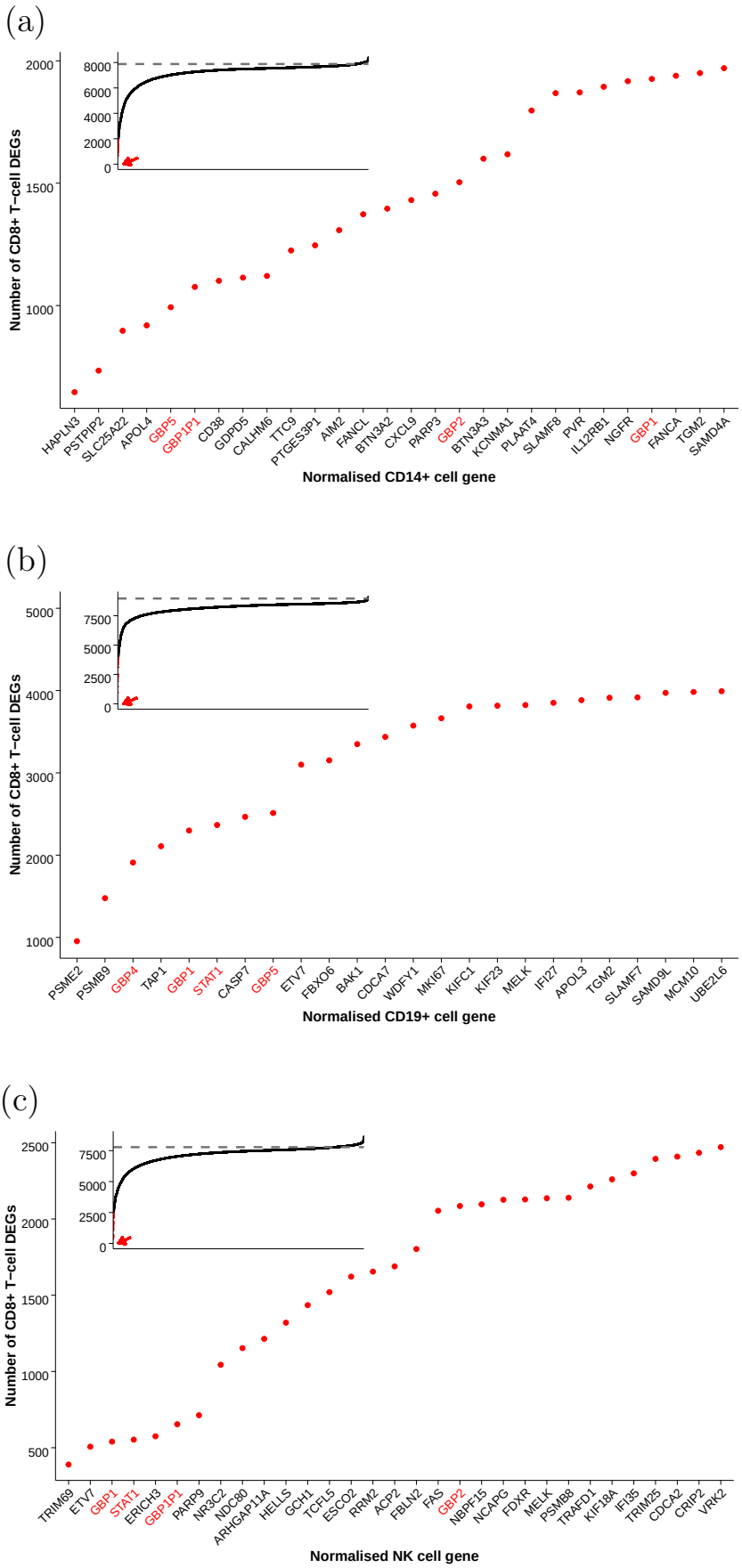

(a)
Number of CD8+ T−cell DEGs
Normalised CD14+ cell gene
HAPLN3 PSTPIP2 SLC25A22 APOL4 GBP5 GBP1P1 CD38 GDPD5 CALHM6 TTC9 PTGES3P1 AIM2 FANCL BTN3A2 CXCL9 PARP3 GBP2 BTN3A3 KCNMA1 PLAAT4 SLAMF8 PVR IL12RB1 NGFR GBP1 FANCA TGM2 SAMD4A
(b)
Number of CD8+ T−cell DEGs
Normalised CD19+ cell gene
PSME2 PSMB9 GBP4 TAP1 GBP1 STAT1 CASP7 GBP5 ETV7 FBXO6 BAK1 CDCA7 WDFY1 MKI67 KIFC1 KIF23 MELK IFI27 APOL3 TGM2 SLAMF7 SAMD9L MCM10 UBE2L6
(c)
Number of CD8+ T−cell DEGs
Normalised NK cell gene
TRIM69 ETV7 GBP1 STAT1 ERICH3 GBP1P1 PARP9 NR3C2 NDC80 ARHGAP11A HELLS GCH1 TCF15 ESCO2 RRM2 ACP2 FBLN2 FAS GBP2 NBPF15 NCAPG FDXR MELK PSMB8 TRAFD1 KIF18A IFI35 TRIM25 CDCA2 CRIP2 VRK2

Figure 3.27

Figure 3.27 (Previous page) CD14$^+$ monocyte, CD19$^+$ B-cell and NK cell expression of interferon-stimulated genes associates with the CD8$^+$ T-cell ICB response
Sigmoid curves of the top PBMC genes associated with dampening CD8$^+$ T-cell response with sigmoid curves of all genes overlaid. Arrows and points in red represent the magnified plots. $DESeq2$ was used to compare paired C1/C2 CD8$^+$ T-cell transcriptomes after controlling for patient ID, library RNA input and individual normalised **a)** CD14$^+$ monocyte (n=95), **b)** CD19$^+$ B-cell (n=62) or **c)** NK cell (n=50) normalised gene counts as shown on the x-axis. The number of resulting DEGs is shown on the y-axis. Interferon-associated genes are highlighted in red.

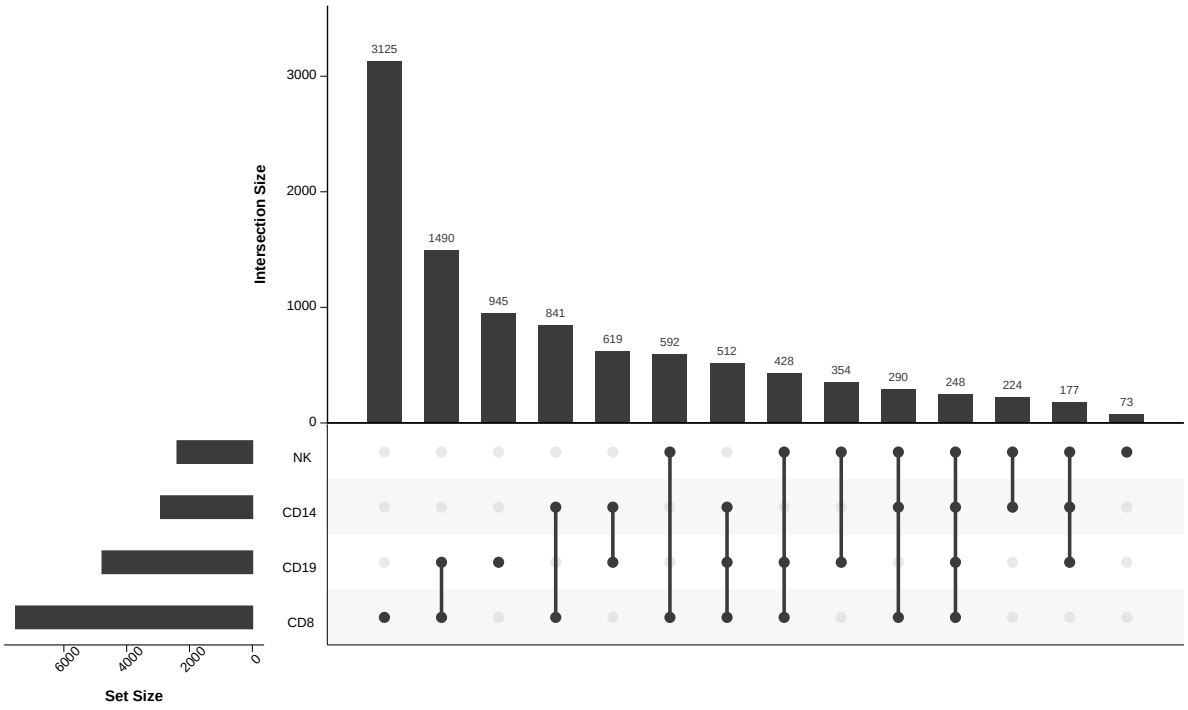


Figure 3.28 Comparison of genes upregulated at C2 between different PBMC subsets
Upset overlap plot demonstrating the number of genes upregulated either uniquely or in common with other cell types. The number of upregulated genes is displayed above each bar with points linking PBMC cell types for shared genes.

3.3 Conclusions

This chapter aimed to investigate the effect of ICB on the peripheral immune compartment in MM patients treated with either sICB or cICB, as well as identifying the major target of ICB using a mixture of transcriptomic and protein-based experimental approaches.

First, flow cytometry analysis of PBMC subsets revealed a loss in B-cells after cICB treatment, but not in any other cell types regardless of treatment type and CMV serostatus. Previous data have also described this loss in peripheral B-cells, but do not find it after single agent anti-CTLA-4 or anti-PD-1 treatment. This implies that B-cell depletion may be a result of stronger activation induced by targeting both CTLA-4 and PD-1 simultaneously[371,458,547].

Comparison of CMV^- and CMV^+ individuals revealed distinct T-cell composition including an enrichment of Temras with CMV which has previously been described[474,476–482]. Although T-cell composition was strongly associated with CMV serostatus, CMV did not determine the PBMC response to ICB.

Interestingly, T-cell surface PD-1 was not detectable following ICB treatment. This reduction was accompanied by an increase in IgG4 binding on $CD8^+$ T-cells and may therefore act as a surrogate for pembrolizumab/nivolumab binding. Additionally, an increase in activation (CD38/HLADR) and proliferation (Ki67) was detected in T-cells. Changes in these parameters were limited to conventional T-cells and were not observed for double positive $CD4^+$ $CD8^+$ T-cells, MAIT cells, iNKT cells or γδ T-cells. Interestingly, PD-1 blockade, activation and proliferation were markedly more induced after cICB treatment compared to sICB, and may represent greater immune stimulation with the inclusion of CTLA-4 targeting as previously demonstrated[371,547].

Normalised gene counts from bulk RNAseq PBMC data identified T-cells as expressing the highest levels of immune checkpoints *CTLA4* and *PDCD1* compared to non-T-cell PBMC subsets. Furthermore, data from flow cytometry suggests that not only do T-cells express the most PD-1, but they also experience significant PD-1 blockade and direct ICB binding. This further implicated T-cells as the predominant target of ICB binding. Comparison of paired C1/C2 PBMC transcriptomes identified $CD8^+$ T-cells as having the most DEGs out of all tested PBMC cell subsets after subsampling to ensure matched statistical power. $CD4^+$ T-cells were excluded from analysis due to insufficient sample size, but may also bind directly to ICB due to evidence of PD-1 blockade and activation from flow cytometry data.

Next, data derived from bulk RNAseq of PBMC samples was used to compare healthy donor and MM patient $CD8^+$ T-cell expression, but also to examine the effects of ICB. Differential expression analysis revealed a high proliferative state of $CD8^+$ T-cells[219,224] as well as increased expression of *CXCL13* in melanoma compared to healthy controls, which was further increased following ICB treatment. CXCL13 has roles in B-cell recruitment into lymphoid tissue as well as TLS development and subsequent germinal centre activity[449]. *CXCL13* induction may therefore be responsible for the changes observed in B-cell populations. Differences between healthy donor and MM patient $CD8^+$ transcriptomes were irrespective of CMV serostatus, despite the profound effect of CMV on $CD8^+$ T-cell expression.

Although both sICB and cICB treatment arms induced a high level of activation, cICB had more profound regulatory effects. Most genes were either uniquely induced by cICB or to a higher magnitude than sICB, supporting previously published data[371,547].

Interestingly, an increase in $CD8^+$ T-cell ICB response score was found to strongly correlate with $IgG4^+$ $CD8^+$ T-cells and signifies that $CD8^+$ T-cells respond as a result of direct ICB binding. With a higher level of $IgG4^+$ $CD8^+$ T-cells detected after cICB, binding of ICB may be more stable than for sICB and result in greater activation and expression changes.

Strikingly, *CXCL13* was found to be further upregulated after ICB treatment regardless of treatment type. However, *CXCL13* was found to be induced to a higher magnitude following cICB treatment than sICB treatment which may explain the differences in B-cell count and expression observed after cICB, but not sICB treatment[458]. Despite the high level of activation observed after ICB treatment, the response of $CD8^+$ T-cells to additional activating stimuli was not further modulated by treatment, with posttreatment samples still able to become activated to the same level as pretreatment samples. Whilst other inhibitory immune checkpoint proteins were induced at C2, including *LAG3* and *HAVCR2*, this didn't appear to affect further T-cell stimulation with T-cells maintaining the ability to respond to PMA/Ionomycin.

TOX2 and *MKI67* were found to be the most central $CD8^+$ T-cell genes in regulating the response of $CD8^+$ T-cells to ICB treatment. Controlling for $CD8^+$ T-cell *TOX2* completely removed any effect of ICB, with an absence of differential expression, highlighting its role as a driver of $CD8^+$ T-cell responses. Even though *TOX2* has previously been associated with imposing $CD8^+$ T-cell exhaustion[562], it can be postulated that due to its relationship with $CD8^+$ T-cell ICB response, it may in fact be associated with activation. Additionally, *TOX2* has been found to be highly expressed within mitotic $CD8^+$ T-cells in MM patients[208] and may instead represent a marker of proliferation.

Whilst controlling for *MKI67* and cell cycle-associated genes massively reduced the impact of ICB on expression, it did not completely remove all effects of ICB on $CD8^+$ T-cell expression. Although the association of *TOX2* and *MKI67* with $CD8^+$ T-cell ICB response may just be correlative, controlling for their expression removed any effects of ICB on expression in other PBMC cell subsets. Conversely, controlling for non-T-cell ICB activation scores in $CD8^+$ T-cells did not remove differential expression and may therefore imply that $CD8^+$ T-cell ICB response is essential for activation in all cell types and may be governed by direct ICB binding.

Even though non-T-cell ICB activation scores were not crucial for $CD8^+$ T-cell ICB response, interferon-associated genes, including the guanylyl binding protein family and *STAT1*, were found to be most strongly correlated with $CD8^+$ T-cell differential expression. Expression of these genes may be induced in response to increased T-cell interferon production observed after ICB[210,559,560] and may be essential for non-T-cell response to ICB. Interestingly, these genes were found to be upregulated by all PBMC cell types, supporting a role for these proteins in eliciting downstream ICB effects.

3.4 Supporting Information

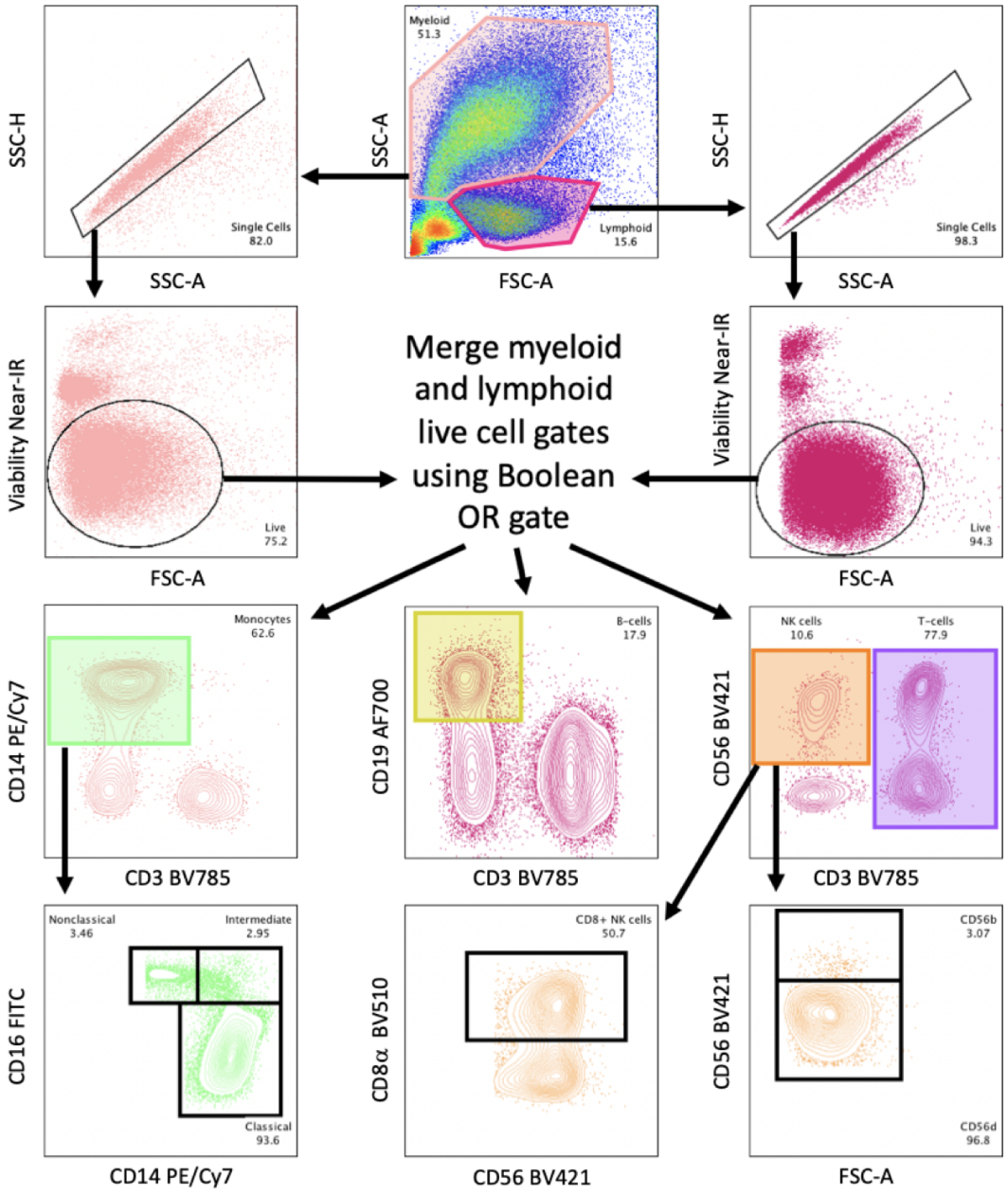


Figure S3.1 Panel B1 flow cytometry gating strategy of PBMC subsets
Flow cytometry was performed on 134 samples including 57 paired C1/C2 samples. Firstly, lymphoid (dark pink) and myeloid cells (light pink) were gated based on FSC-A/SSC-A and were processed separately due to differences in size and autofluorescence. Multiplets were removed based on SSC-A/SSC-H gating prior to dead cell depletion, selecting live/dead cell marker negative cells. Live lymphoid and myeloid cells were then combined using a Boolean OR gate on FlowJo to detect total percentage of PBMCs for each cell type. $CD14^{+}$ $CD3^{-}$ cells were gated as monocytes (green), $CD19^{+}$ $CD3^{-}$ cells as B-cells (yellow), $CD56^{+}$ $CD3^{-}$ as NK cells (orange) and $CD56^{\pm}$ $CD3^{+}$ cells as T-cells (purple). Monocytes were further gated into classical ($CD14^{+}$ $CD16^{-}$), intermediate ($CD14^{+}$ $CD16^{+}$) or nonclassical ($CD14^{lo}$ $CD16^{+}$) subsets based on CD14/CD16 expression. NK cells were further subdivided based on staining for CD8 as well as CD56 and separated into $CD8^{+}$, $CD56^{bright}$ (CD56b) and $CD56^{dim}$ (CD56d) populations. PD-1 gating was performed for all PBMC subsets. B-cells were also gated based on CD21 expression into $CD21^{hi}$ and $CD21^{lo}$ B-cell subsets.

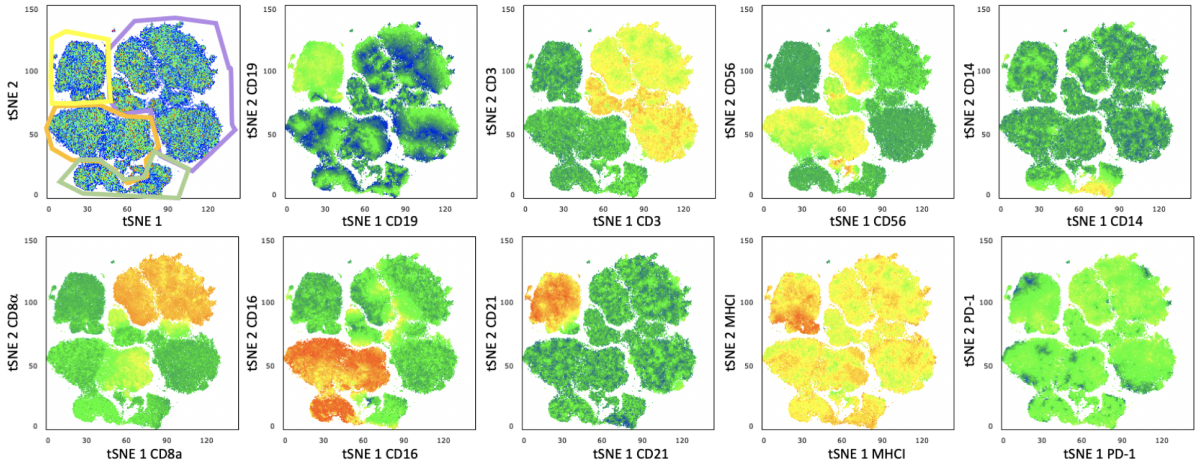


Figure S3.2 tSNE of panel B1 PBMC flow cytometry data
FlowJo was used to create a tSNE after subsampling to the same number of cells per sample for one batch (n=17). PBMC subsets are encircled in the first plot using previous colour codes (Monocytes=green, T-cells=purple, NK cells=orange, B-cells=yellow) with shade referring to cell density. Cells in other plots are coloured based on the heatmap statistic for a different marker per plot as labelled on the axes.

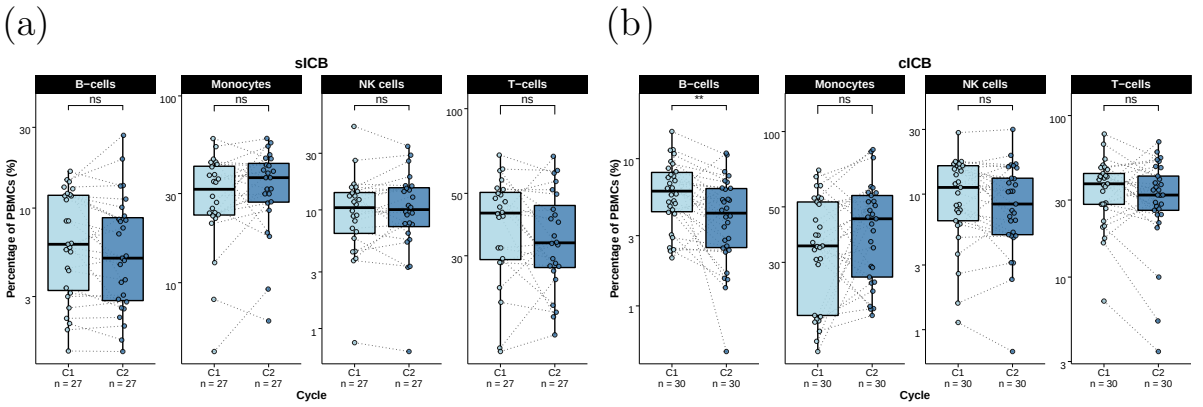


Figure S3.3 B-cells are depleted after cICB
Box plots comparing PBMC percentages between paired C1/C2 samples following either **a)** sICB (n=27) or **b)** cICB (n=30) treatment. Statistics were calculated using paired Wilcoxon signed-rank tests and adjusted using Bonferroni correction. Adjusted p > 0.05 (ns), $p \leq 0.05$ (*), $p \leq 0.01$ (**), $p \leq 0.001$ (***), $p \leq 0.0001$ (****).

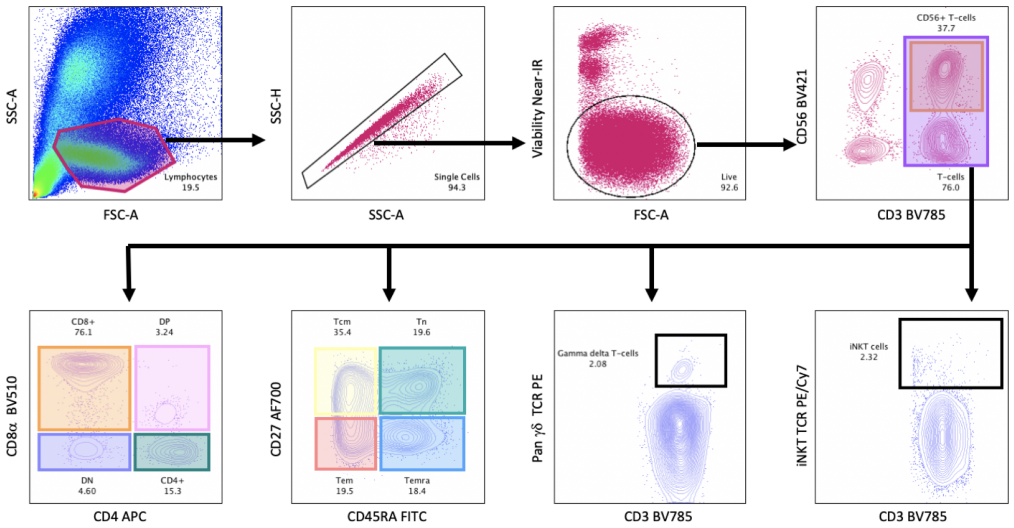


Figure S3.4 Panel T2 flow cytometry gating strategy of T-cells
Flow cytometry gating of 138 PBMC samples was performed to investigate T-cell phenotypes with gating shown in representative plots. First, lymphocytes (dark pink) were selected based on FSC-A/SSC-A prior to multiplet depletion using SSC-A/SSC-H and dead cell exclusion, only keeping cells negative for the live/dead cell marker. $CD56^{\pm}$ $CD3^{+}$ cells were identified as T-cells (purple) and gated based on CD4/CD8 expression or CD45RA/CD27 expression, classifying cells as either $CD4^{+}$ $CD8^{-}$, $CD4^{-}$ $CD8^{+}$, $CD4^{-}$ $CD8^{-}$ double negative (DN) or $CD4^{+}$ $CD8^{+}$ double positive (DP) T-cells or $CD45RA^{+}$ $CD27^{+}$ naïve (Tn), $CD45RA^{-}$ $CD27^{+}$ central memory (Tcm), $CD45RA^{-}$ $CD27^{-}$ effector memory (Tem) or $CD45RA^{+}$ $CD27^{-}$ effector memory cells reexpressing CD45RA (Temra). In addition, iNKT and γδ T-cells were detected based on expression of either iNKT-associated TRAV10-TRAJ18 or pan γδ T-cell receptors. PD-1 gating was also performed for all T-cell subsets.

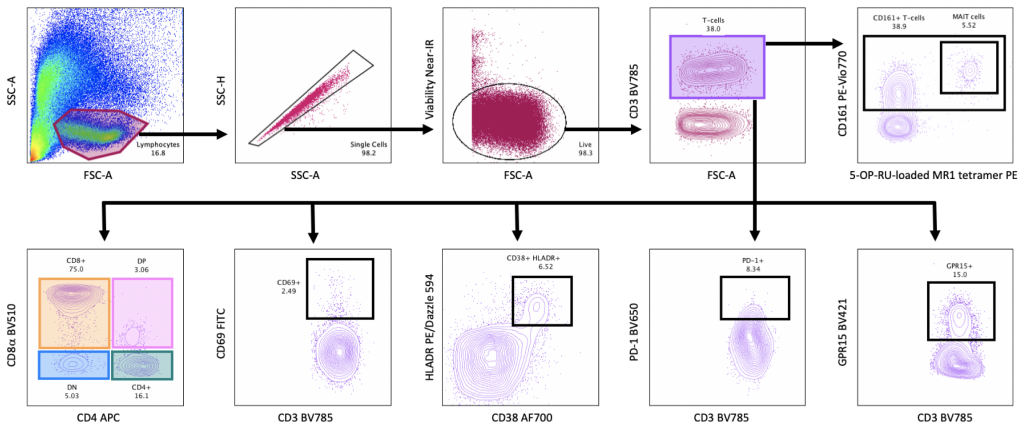


Figure S3.5 Panel M3 flow cytometry gating strategy of T-cells
Flow cytometry was performed on 132 PBMC samples to investigate markers of activation in T-cells and MAIT cells with gating shown in representative plots. First, lymphocytes (dark pink) were selected based on FSC-A/SSC-A prior to multiplet depletion using SSC-A/SSC-H and dead cell exclusion, only keeping cells negative for the live/dead cell marker. T-cells were isolated based on CD3 positivity. MAIT cells were identified as 5-OP-RU-loaded MR1 $tetramer^{+}$ $CD161^{+}$ T-cells. MAIT cells were further gated based on CD4/CD8 expression, classifying MAIT cells as either $CD4^{+}$ $CD8^{-}$, $CD4^{-}$ $CD8^{+}$, $CD4^{-}$ $CD8^{-}$ double negative (DN) or $CD4^{+}$ $CD8^{+}$ double positive (DP) MAIT cells. In addition, expression of CD69, double positive CD38/HLADR, PD-1 and GPR15 was quantified for both MAIT cells and T-cells.

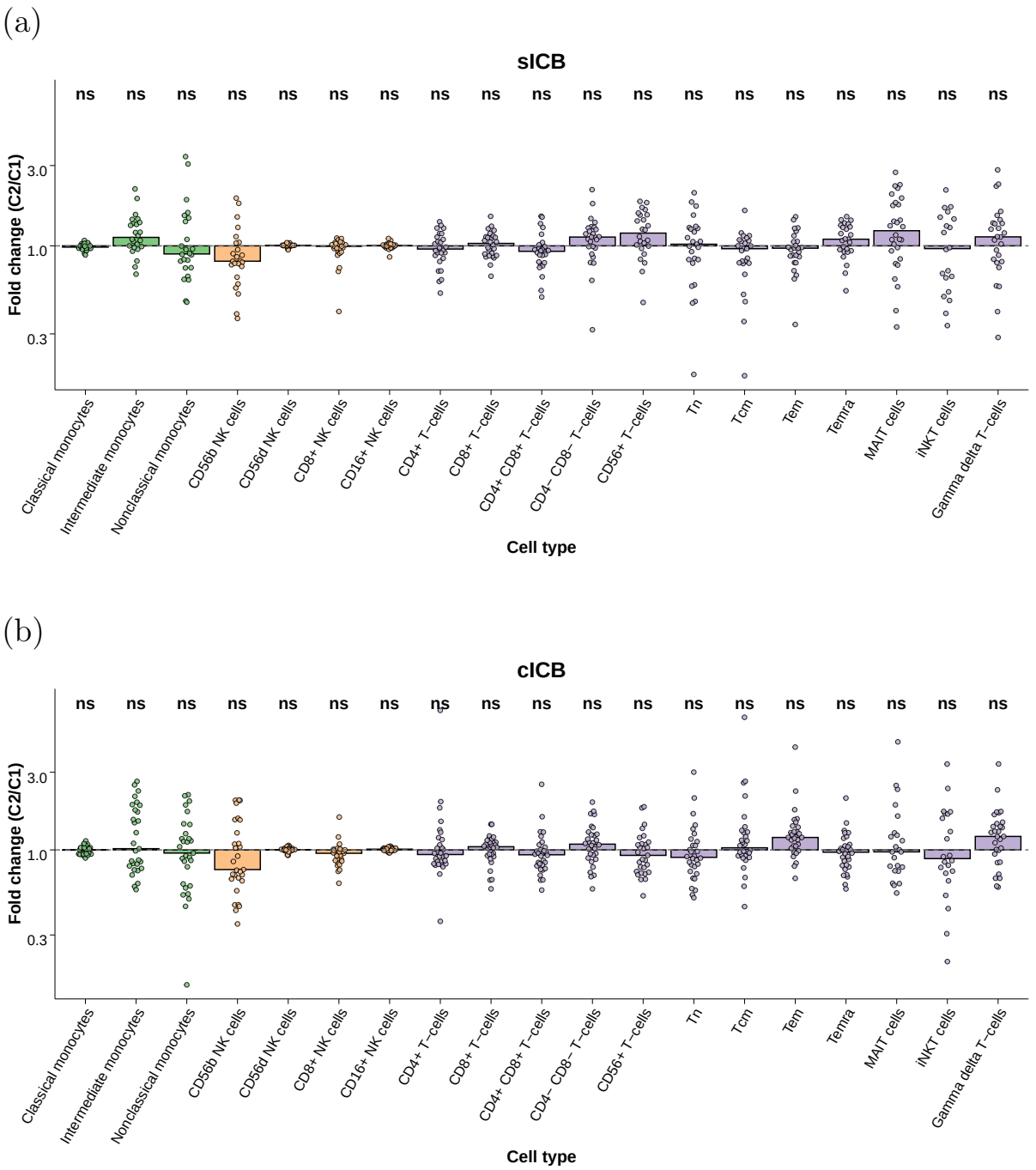


Figure S3.6 No changes observed in non-B-cell subsets at C2 regardless of treatment type
Bar plots showing fold change in cell subset proportion from C1 to C2 following either **a)** sICB (n=20-24) or **b)** cICB (n=22-29) treatment with the level of significance displayed above each bar. Statistics were calculated using paired Wilcoxon signed-rank tests and adjusted using Bonferroni correction. Adjusted p $>$ 0.05 (ns), $p \leq 0.05$ (*), $p \leq 0.01$ (**), $p \leq 0.001$ (***), $p \leq 0.0001$ (****). *CD56b = CD56^{bright}, CD56d = CD56^{dim}, Tn = Naïve T-cells, Tcm = Central memory T-cells, Tem = Effector memory T-cells, Temra = Effector memory T-cells reexpressing CD45RA.*

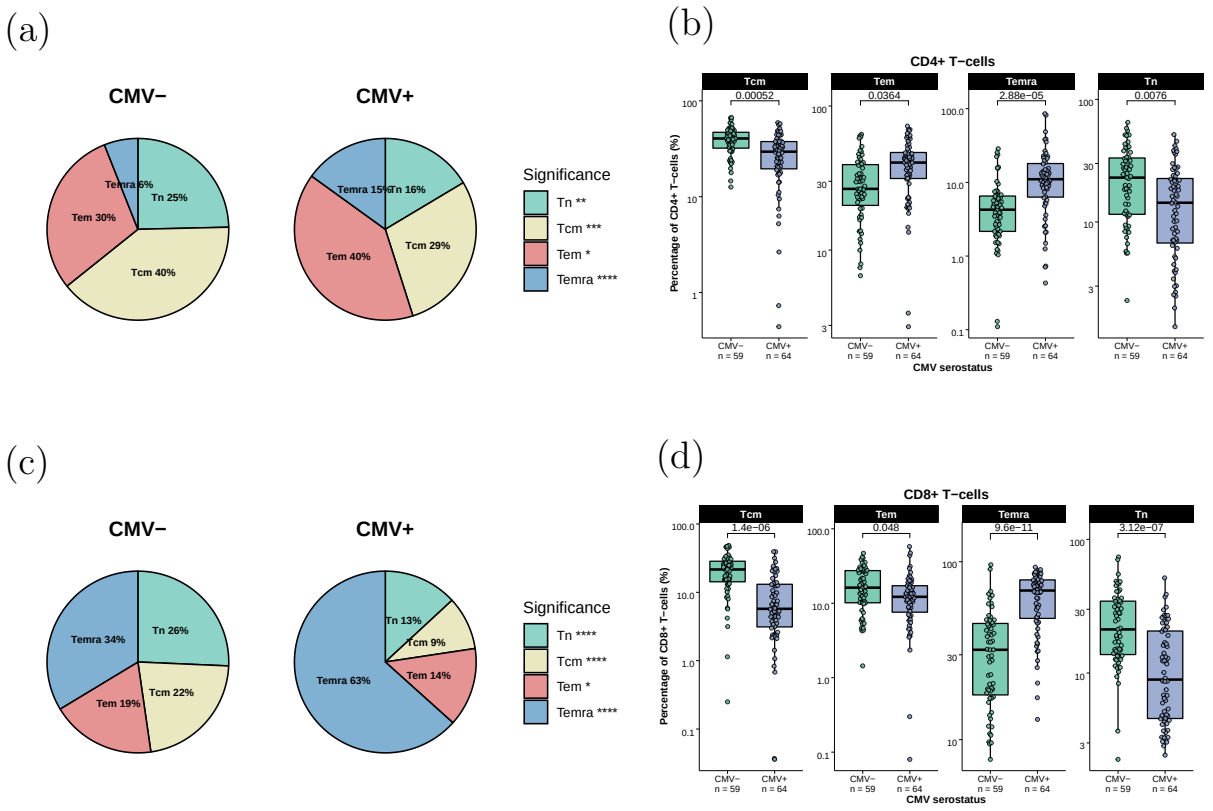


Figure S3.7 CMV inflates the Temra population for both $CD4^+$ and $CD8^+$ T-cells
Flow cytometry data of **a,b)** $CD4^+$ and **c,d)** $CD8^+$ T-cell differentiation subset composition is compared between CMV^- (n=59) and CMV^+ (n=64) samples after controlling for age and are visualised by **a,c)** pie chart or **b,d)** box plot. Average subset percentage is highlighted per pie chart. Statistics were calculated using "lm(T-cell subset percentage $\sim$ CMV serostatus + age, data)" and adjusted using Bonferroni correction. Adjusted p > 0.05 (ns), $p \leq 0.05$ (*), $p \leq 0.01$ (**), $p \leq 0.001$ (***), $p \leq 0.0001$ (****). *Tn = Naïve T-cells, Tcm = Central memory T-cells, Tem = Effector memory T-cells, Temra = Effector memory T-cells reexpressing CD45RA.*

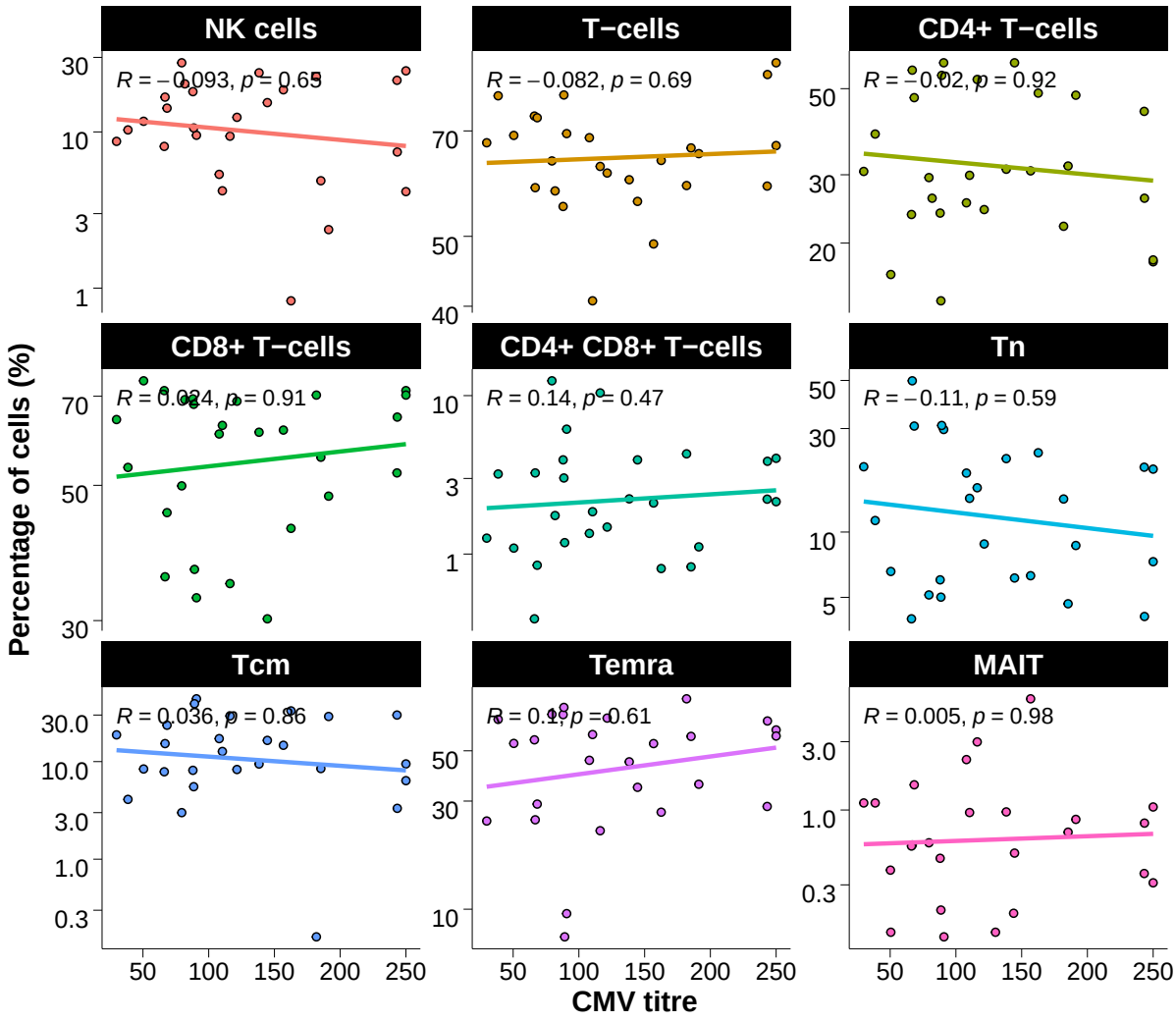


Figure S3.8 PBMC subsets associated with CMV do not correlate with anti-CMV IgG antibody titre

PBMC subsets associating with CMV serostatus were correlated with anti-CMV IgG antibody titre (n=26-27). Statistics were calculated using Spearman's rank correlation coefficient. *Tn = Naïve T-cells, Tcm = Central memory T-cells, Tem = Effector memory T-cells, Temra = Effector memory T-cells reexpressing CD45RA.*

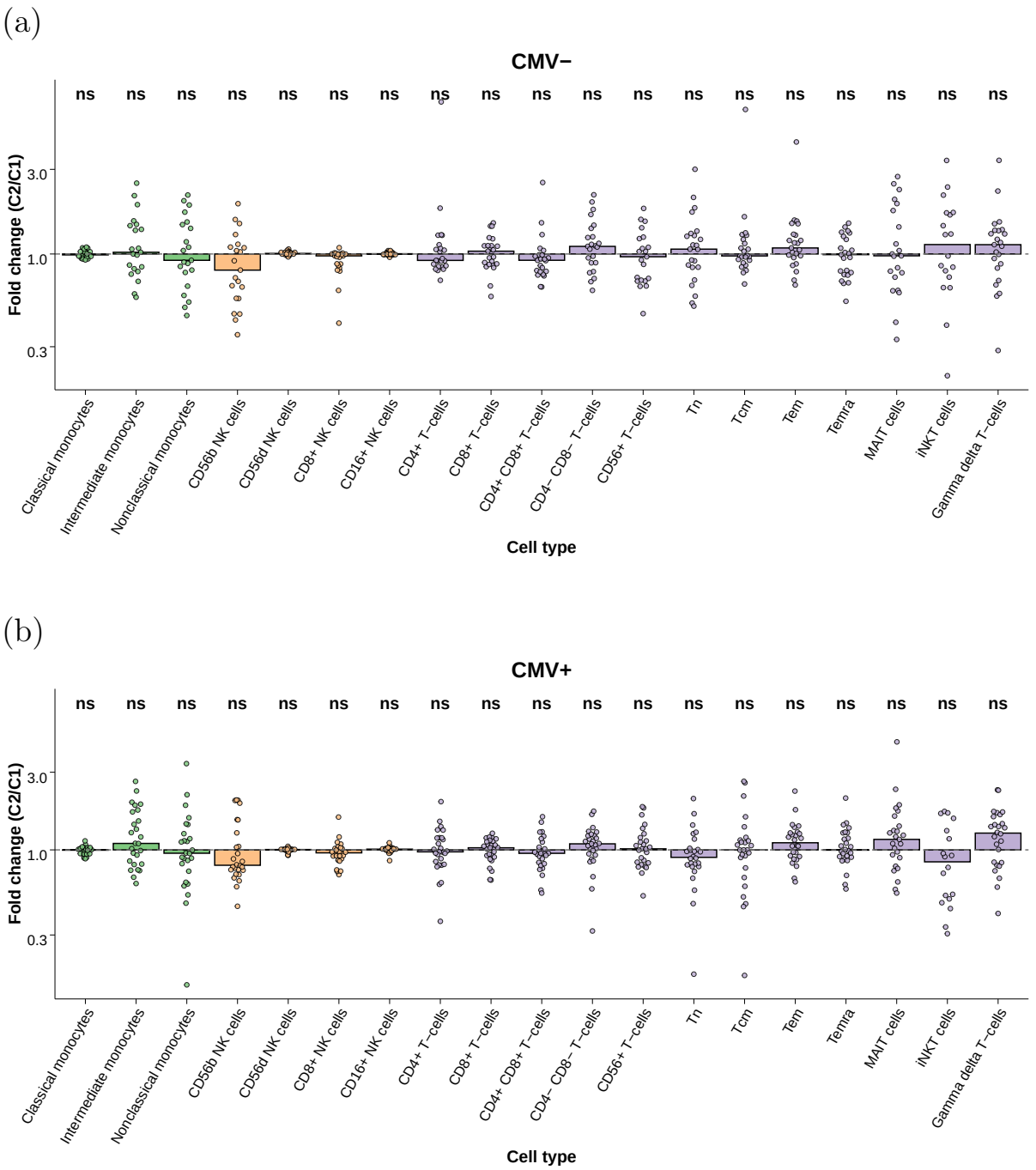
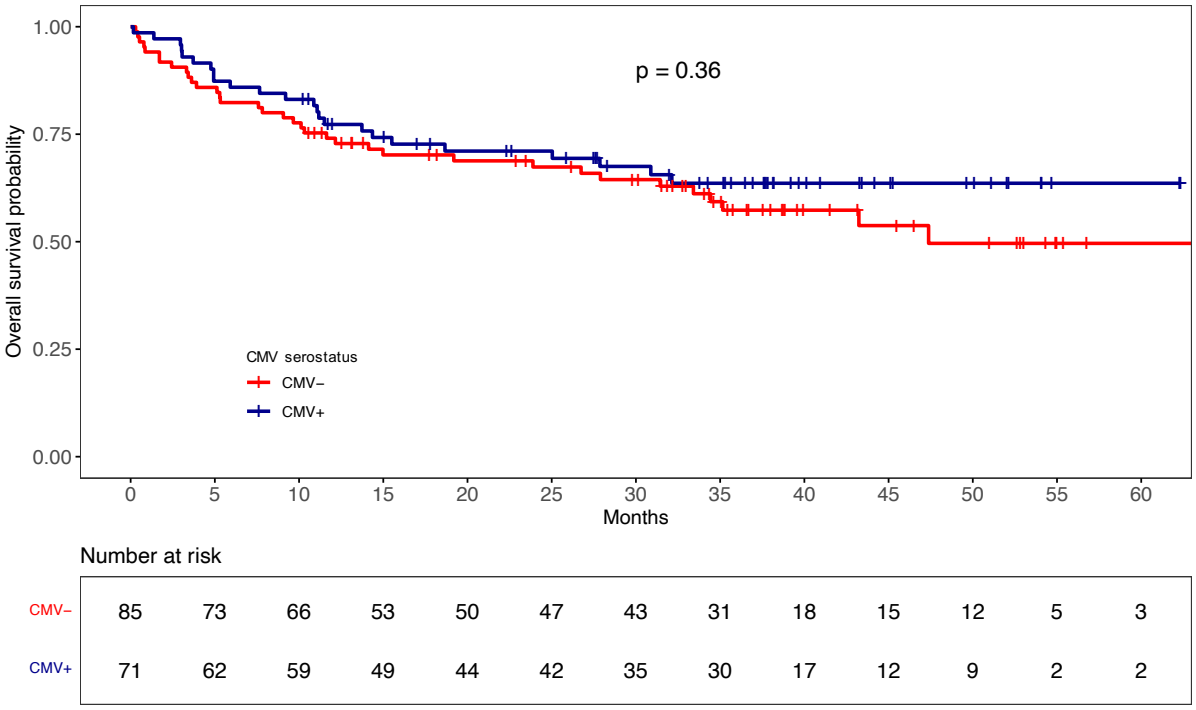


Figure S3.9 CMV has no effect on subset changes in response to ICB
Cell subset fold change was calculated between paired C1/C2 samples and plotted for each subset for **a)** CMV$^-$ (n=19-24) or **b)** CMV$^+$ (n=18-26) patients. The level of significance for each subset is displayed above each bar. Statistics were calculated using paired Wilcoxon signed-rank tests and adjusted using Bonferroni correction. Adjusted p > 0.05 (ns), $p \leq 0.05$ (*), $p \leq 0.01$ (**), $p \leq 0.001$ (***), $p \leq 0.0001$ (****). *CD56b = CD56^{bright}, CD56d = CD56^{dim}, Tn = Naïve T-cells, Tcm = Central memory T-cells, Tem = Effector memory T-cells, Temra = Effector memory T-cells reexpressing CD45RA.*

(a)



(b)

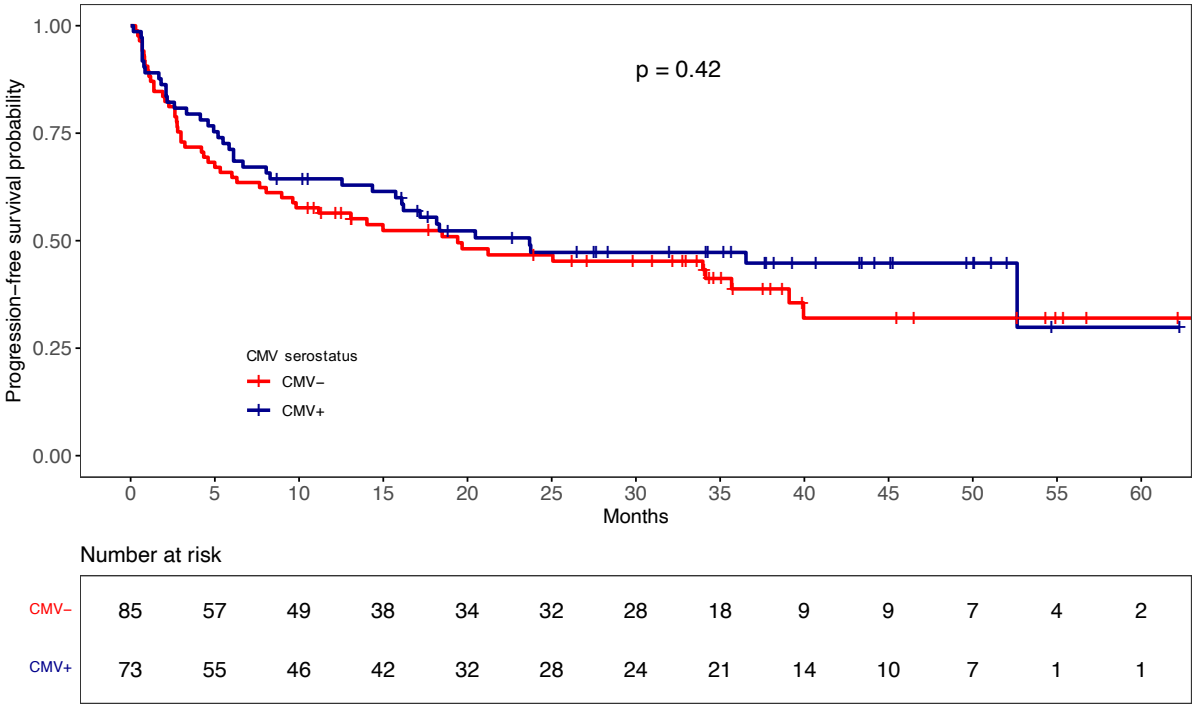


Figure S3.10 CMV does not associate with clinical outcome
Kaplan Meier plots showing any differences in **a)** overall survival (n=156) or **b)** progression-free survival (n=158) between CMV^{-} and CMV^{+} patients.

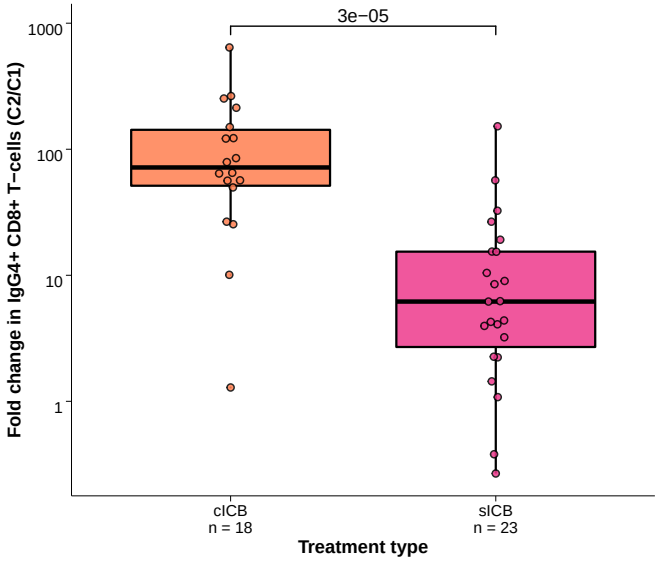


Figure S3.11 More IgG4 detected on CD8$^+$ T-cells following cICB
Fold change in IgG4 binding to CD8$^+$ T-cells at C2 is compared between sICB-treated (n=23) and cICB-treated (n=18) samples. Statistics were calculated using an unpaired Wilcoxon signed-rank test.

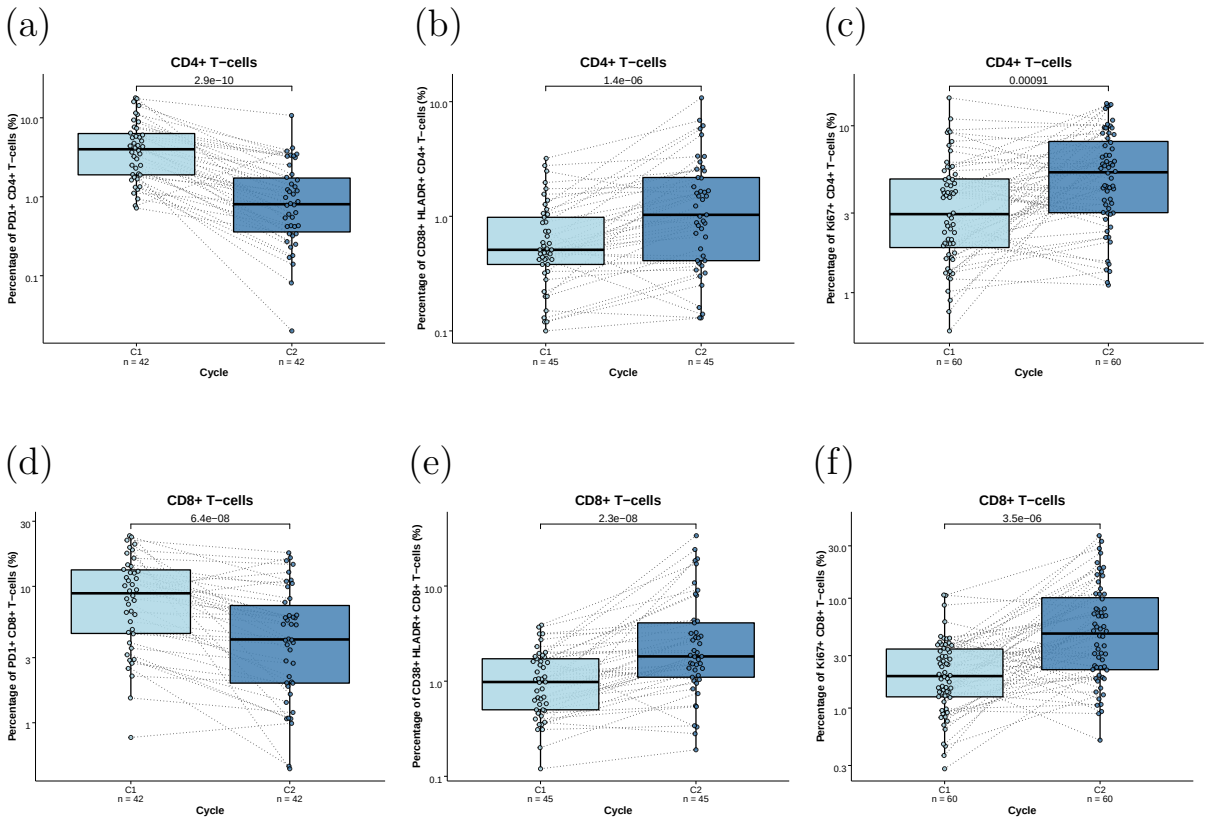


Figure S3.12 Both CD4$^+$ and CD8$^+$T-cells become activated in response to ICB
Expression of **a,d)** PD-1, **b,e)** CD38/HLADR and **c,f)** Ki67, identified by flow cytometry, was compared between paired C1/C2 samples (n=42-60) in **a,b,c)** CD4$^+$ and **d,e,f)** CD8$^+$ T-cells. Statistics were calculated using paired Wilcoxon signed-rank tests.

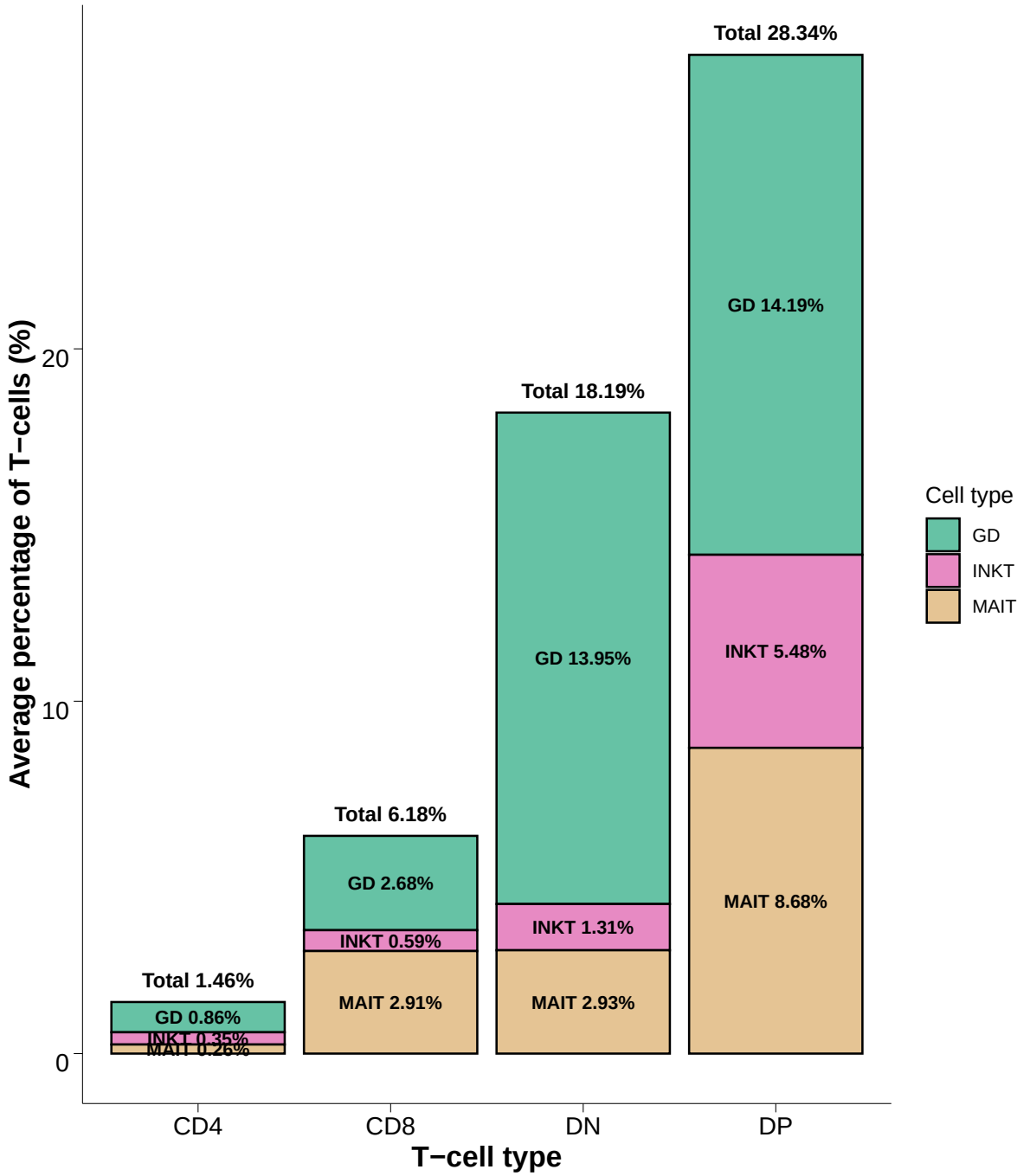


Figure S3.13 Double positive $CD4^+$ $CD8^+$ T-cells are enriched for unconventional T-cells
Bar plots comparing the average percentage of T-cells composed of unconventional T-cells including MAIT, iNKT and γδ T-cells between $CD4^+$ $CD8^-$, $CD4^-$ $CD8^+$, double negative (DN) $CD4^-$ $CD8^-$ and double positive (DP) $CD4^+$ $CD8^+$ T-cells (n=104-136). Total percentage of T-cells that express a MAIT, iNKT or γδ T-cell receptor are displayed above each bar as well as for each cell type.

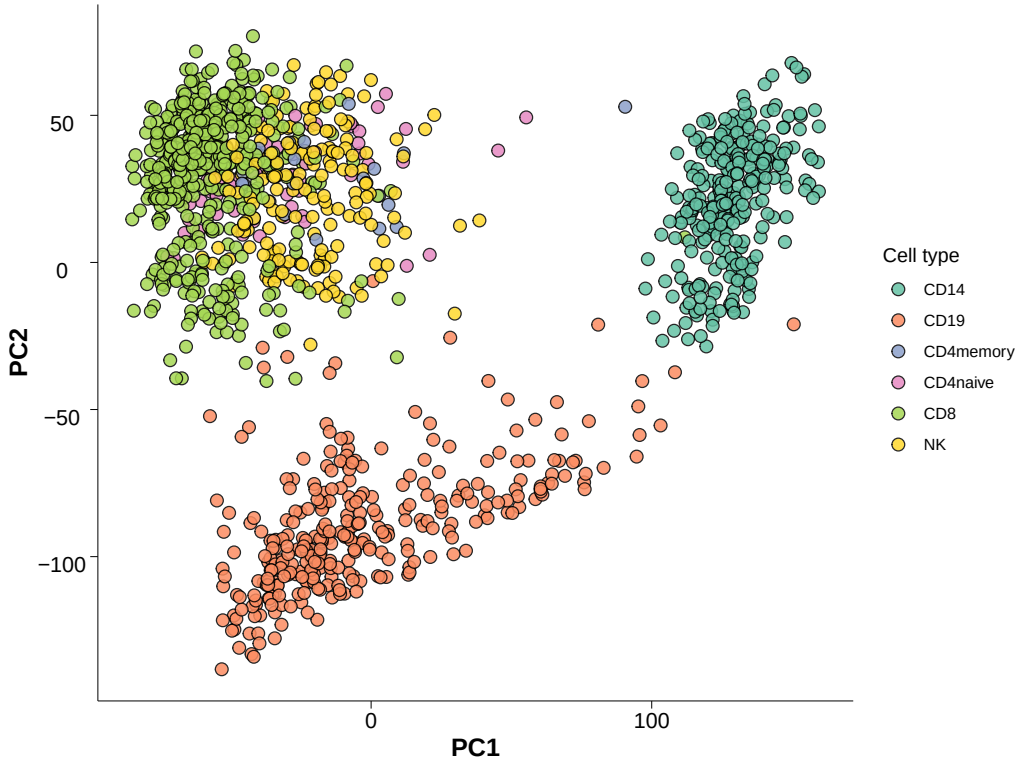


Figure S3.14 Principal component analysis of PBMC RNAseq samples
Principal component analysis was performed on normalised gene counts for all PBMC samples (n=504 CD8$^+$ T-cells, n=308 CD19$^+$ B-cells, n=284 CD14$^+$ monocytes, n=174 NK cells, n=69 CD4$^+$ naïve T-cells, n=26 CD4$^+$ memory T-cells) with the first two principal components (PCs) visualised.

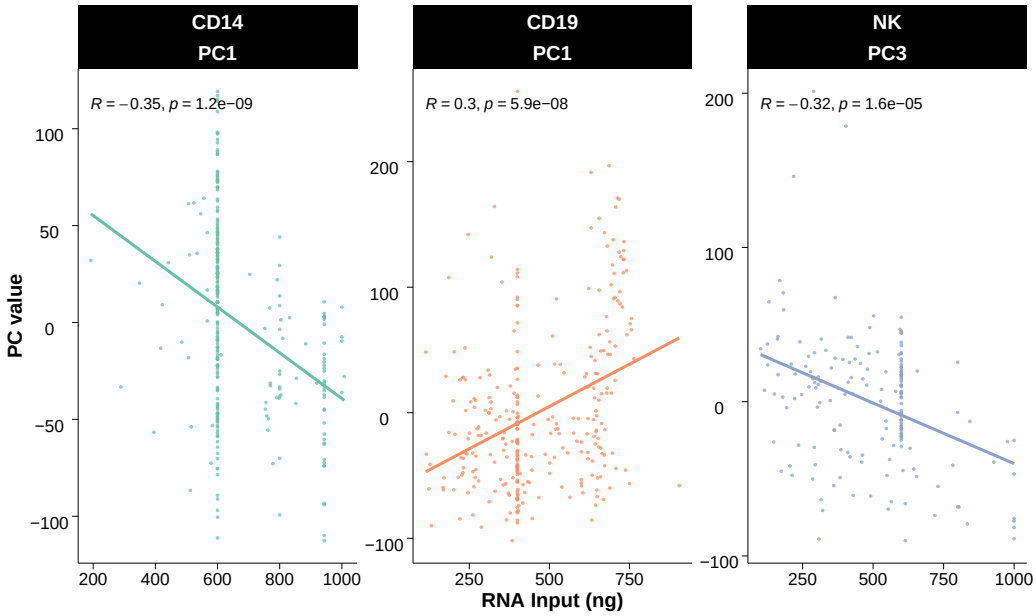


Figure S3.15 Library RNA input associates with early principal components for all PBMC types
Library RNA input (ng) for CD14$^+$ monocyte (n=284), CD19$^+$ B-cell (n=308) and NK cell (n=174) bulk RNAseq libraries was compared to early principal component (PC) values. Statistics were calculated using Spearman's rank correlation coefficient.

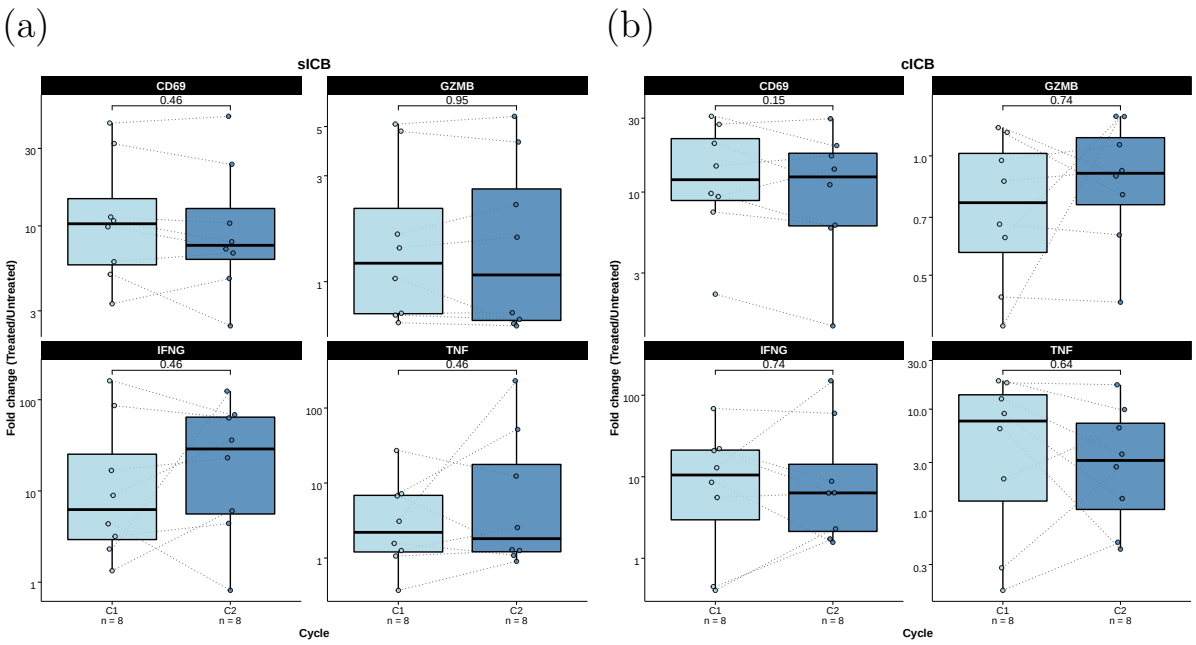


Figure S3.16 T-cell response to stimulation is unaffected by ICB regardless of treatment type Induction of T-cell CD69, GZMB, IFNG and TNF in response to PMA/Ionomycin (PMA/IONO) was compared between paired C1/C2 samples after **a)** sICB (n=8) and **b)** cICB (n=8). Statistics were calculated using paired Wilcoxon signed-rank tests.

3.5 Author Contributions

Chelsea A. Taylor, Orion Tong, Alba Verge de los Aires, Isar Nassiri, Elise A. Mahé, Sara Danielli, Piyush K. Sharma, Robert A. Watson, Rosalin A. Cooper

C.A.T, O.T, A.V.A, E.A.M, S.D, P.K.S, R.A.W and R.A.C were all involved in blood collection and processing; C.A.T, E.A.M, A.V.A and S.D extracted RNA; C.A.T and A.V.A generated and pooled bulk cDNA libraries for RNA sequencing; I.N performed upstream RNA sequencing analysis including read alignment and quality control; C.A.T performed flow cytometry with help from O.T and A.V.A; O.T performed Ki67 and IgG4 staining along with pembrolizumab culture; John Radcliffe hospital laboratories performed ELISA analysis of anti-CMV IgG antibodies to determine CMV serostatus.

Chapter 4

B-cells

4.1 Summary

4.1.1 Background

B-cells predominantly contribute to humoral immunity and form part of the adaptive immune response, owing to expression of the hypervariable BCR. Whilst extensive studies have been carried out assessing the impact of ICB on T-cells, the effect on B-cells is much less understood.

Griss *et al.* (2019) describe the importance of B-cells in antitumour responses such as inducing T-cell infiltration, driven by plasmablast-induced chemokines, and sustaining melanoma-targeted inflammation[433]. Helmink *et al.* (2020) go on to describe the crucial role of TLS's in clinical outcome following ICB treatment[366]. They find that both an increased number and proportion of B-cells in the tumour, as well as a higher density of TLS's, associates with enhanced survival following ICB treatment[366]. Whilst these data indicate an essential role of B-cells in mediating ICB response and downstream T-cell effector function within the tumour, the importance of peripheral B-cells in ICB response is unclear.

Das *et al.* (2018) investigate the effect of ICB on peripheral B-cells and compare differential effects of sICB (anti-CTLA-4 or anti-PD-1) therapy as well as cICB (anti-CTLA-4/anti-PD-1)[458]. Here, they uncover a profound loss in circulating B-cells with a concomitant increase in $CD21^{lo}$ B-cells and plasmablasts[458]. These effects are limited to cICB treatment and associate with development of irAEs[458].

Dissecting peripheral B-cell responses to ICB may therefore discern predictive markers of clinical outcome. Using an agnostic transcriptomic and cytometric assessment of B-cell ICB response across a large cohort of MM patients, this chapter identifies dynamic changes in peripheral B-cell proportion, phenotype subset composition and expression following ICB treatment, which associate with $CD8^{+}$ T-cell activation and clinical outcome.

This chapter combines transcriptomic and protein-based experimental approaches, encompassing bulk and single cell RNAseq data as well as flow cytometry and ELISA analyses. Data is used to describe differences within the peripheral B-cell compartment in MM patients as compared to healthy donors as well as any changes induced by ICB treatment and between different treatment arms.

4.1.2 Aims

- What is the effect of metastatic melanoma on peripheral B-cells?
- How are circulating B-cells affected by ICB treatment and to what extent is this treatment specific?
- Are any changes in B-cells related to the $CD8^+$ T-cell ICB response?
- Can we use these features to predict clinical outcomes in patients?

4.1.3 Experimental Approach

Both PBMCs and isolated $CD19^+$ B-cells, $CD8^+$ T-cells, $CD14^+$ monocytes, NK cells, $CD4^+$ naïve T-cells and $CD4^+$ memory T-cells were collected from healthy donors (n=295) as well as from nonmetastatic (n=10) and MM (n=190) patients. Patient samples were harvested immediately prior to ICB treatment and include samples at baseline (d0, C1) as well as over the course of treatment, with cycle number referring to the cycle of ICB the patient was about to receive.

Flow cytometry analysis of frozen MM patient PBMCs quantified B-cell percentage, subset composition and activation. This included untreated C1 samples (d0) as well as corresponding C2 (d21) and C4 (d63) samples. This allowed for dissection of B-cell fluctuations in proportion, differentiation and activation status post-ICB treatment.

308 high quality $CD19^+$ B-cell transcriptomes were generated using $CD19^+$ MACS-sorted cells and subsequent polyA mRNA library preparation. $DESeq2$[495] facilitated analysis of differential gene expression between different conditions after normalising for appropriate confounding variables. Similar data was also available for $CD8^+$ T-cells, $CD14^+$ monocytes and NK cells which allowed for testing intercell interactions.

Single cell RNAseq data, derived from $CD19^+$ B-cells, was used to identify gene expression at a more granular level and allowed subsequent subset deconvolution from bulk RNAseq data. Imputed subset scores allowed for comparison between paired C1/C2 samples to detect changes following ICB as well as identifying any associations with clinical outcome.

Plasma CXCL10 and CXCL13 were quantified by ELISA and subsequently correlated with transcriptomic and flow cytometry data, allowing inference of B-cell/T-cell migration and germinal centre activity.

4.2 Results

4.2.1 Phenotypic changes in B-cells following ICB treatment

4.2.1.1 Dynamic changes in B-cell percentage and subset composition following cICB

PBMC proportions including B-cells, NK cells, T-cells and monocytes were determined using flow cytometry data (Figure S3.1). Whilst no significant changes were observed in NK cells, T-cells or monocytes (Figure 3.1b), B-cells, as identified by CD19 expression, were found to be profoundly depleted after ICB treatment at C2 (Figure 4.1a). Dissecting this effect further demonstrated that B-cell loss at C2 was specific to cICB treatment and not observed following sICB therapy despite a similar number of samples (n=27 sICB, n=30 cICB) (Figures 4.1b, 4.1c). This decline was independent

of CMV serostatus (Figures 3.7a, 3.7b). However, this depletion was only transient as no significant changes in B-cell percentage were detected at C4 (n=17) (Figure 4.1d) regardless of treatment type (data not shown). Although, any changes may not be detectable due to low statistical power.

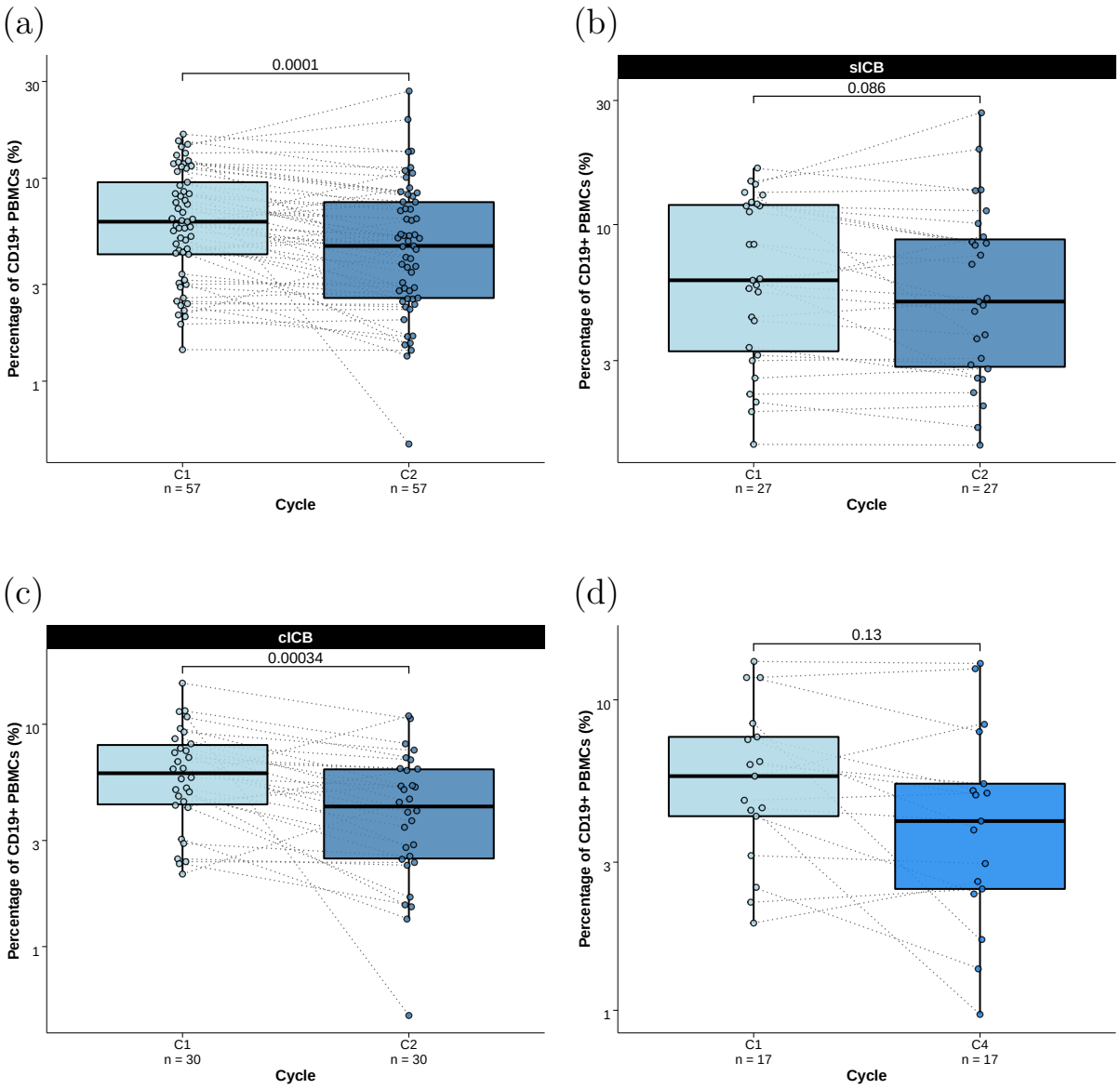


Figure 4.1 cICB induces B-cell lymphopenia
Flow cytometry was performed on paired C1/C2 samples as well as paired C1/C4 samples to quantify the percentage of CD19$^+$ B-cells. **a)** CD19$^+$ B-cell percentages are compared between paired C1/C2 samples (n=57). Samples were then stratified by treatment type comparing paired C1/C2 samples following **b)** sICB (n=27) and **c)** cICB (n=30) treatment. **d)** CD19$^+$ B-cell percentage was also compared between paired C1/C4 samples (n=17). Statistics were calculated using paired Wilcoxon signed-rank tests.

Strikingly, a low B-cell percentage was found to confer enhanced survival at C1 and C2 (Figures 4.2a, 4.2b) regardless of treatment type (data not shown). This may indicate an immunosuppressive role for B-cells or alternatively, that migration to the tumour or

TLS, and hence depletion in the periphery, is favourable.

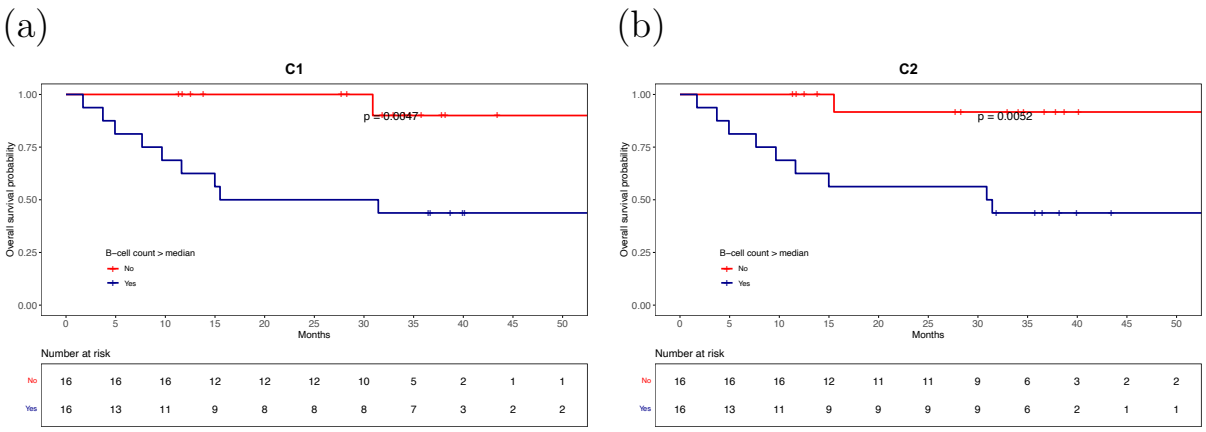


Figure 4.2 Patients with low B-cell percentage have longer survival
Kaplan-Meier curves show the association of B-cell percentage at **a)** C1 (n=32) **b)** and C2 (n=32) with overall survival after dichotomising patients into those above and below median B-cell percentage.

Further flow cytometry was performed on 46 patients receiving cICB using a distinct anti-CD19 clone and fluorochrome conjugate to detect B-cells (panel B5) (Figure S4.1). The depletion in peripheral B-cell percentage was validated by inferring $CD19^+$ B-cell percentage in these 46 patients (Figure S4.2a), including in 23 novel patients (Figure 4.3a). In total, a profound reduction in B-cells was observed after cICB in 53 distinct patients after combining data from both flow cytometry panels (Figure S4.2b).

To better understand this B-cell reduction, markers of subset composition and activation were included in the antibody staining panel (panel B5) for 37 patients treated with cICB (Figure S4.1). Canonical markers of established B-cell subsets, including IgD, CD27, CD38, CD24 and CD138, were included in the panel. Cells were then grouped into transitional B-cells (Tr, $CD24^{hi}$ $CD38^{hi}$), naïve B-cells (Bn, $CD27^-$ IgD^+), memory B-cells (Bmem, $CD27^+$, unswitched memory (USM) IgD^+, switched memory (SM) IgD^-), double negative B-cells (DN, IgD^- $CD27^-$) and antibody-secreting cells (ASCs, $CD27^{hi}$ $CD38^{hi}$, plasmablasts $CD138^-$, plasma cells $CD138^+$) (Figures 4.3b, S4.1, S4.3, S4.4a). Just one treatment cycle of cICB induced dynamic changes in the B-cell compartment including a reduction in Bmem cells, specifically USMs, with a concomitant increase in ASCs (Figure 4.3c), regardless of CMV serostatus (data not shown). The loss in $CD19^+$ B-cells may therefore reflect enhanced differentiation into ASCs which downregulate CD19 expression (Figure 4.3d). This CD19 downregulation may contribute to the B-cell decline that is observed following cICB treatment. Although no difference in B-cell CD19 median fluorescence intensity (MFI) was observed, a reduction in CD19 MFI was detected within ASCs and may indicate enhanced differentiation (Figure S4.4b). Despite the loss of CD19-expressing cells, a reduction in B-cells still held true when including $CD19^{lo/-}$ B-cells, predominantly comprising ASCs, in the percentage as defined by $lineage^-$ ($CD3^-$ $CD56^-$ $CD16^-$) $CD19^{\pm}$ $CD27^{hi}$ lymphocytes (Figures S4.1, S4.4c). This means that enhanced ASC differentiation, and ultimately CD19 downregulation, is not the sole reason for the B-cell depletion that is observed and that B-cells may also be lost through other mechanisms.

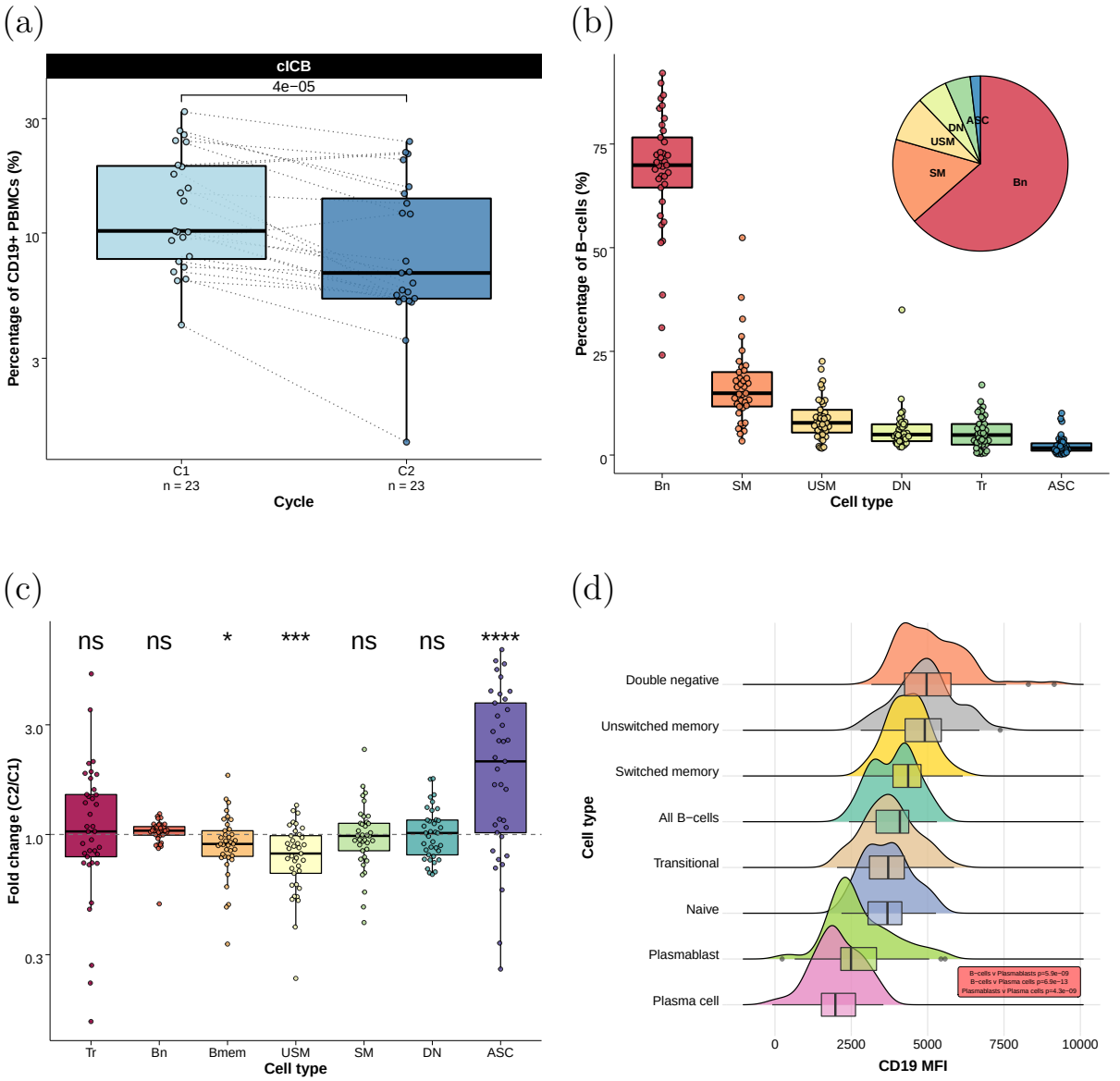


Figure 4.3 cICB promotes ASC differentiation

Flow cytometry analysis of 37 paired C1/C2 cICB samples shows the effect of ICB on a subset-specific basis. **a)** $CD19^+$ B-cell percentage is compared between paired C1/C2 cICB samples (n=23) in a validation cohort. **b)** B-cell subset proportions are compared and shown in order of expression (n=74). **c)** Box plots showing fold change per B-cell subset calculated as the fold induction per subset from C1 to C2 (n=37). **d)** CD19 MFI by B-cell subset (n=74) with statistical comparisons displayed in a red box. Statistics were calculated using paired Wilcoxon signed-rank tests and adjusted using Bonferroni correction. p > 0.05 (ns), $p \leq 0.05$ (*), $p \leq 0.01$ (**), $p \leq 0.001$ (***), $p \leq 0.0001$ (****). *Tr = transitional B-cells, Bn = naïve B-cells, Bmem = memory B-cells, USM = unswitched memory B-cells, SM = switched memory B-cells, DN = double negative IgD$^-$ CD27$^-$ B-cells, ASCs = antibody-secreting cells.*

4.2.1.2 cICB induces potent B-cell activation

Activation markers CD11c and CD71 were found to be upregulated at C2 post-cICB, as well as an enrichment of $CD21^{lo}$ cells (Figure 4.4a). $CD21^{hi}$ B-cells form the majority of B-cells, whereas CD21 is downregulated upon activation and is associated with chronic activation and BCR clonality[458]. In keeping with this, no difference in $CD21^{hi}$ B-cell proportion was observed following cICB. Expression of all activation molecules cocorrelated with the exception of $CD21^{hi}$ B-cells which inversely correlated with all activation markers as expected (Figure 4.4b).

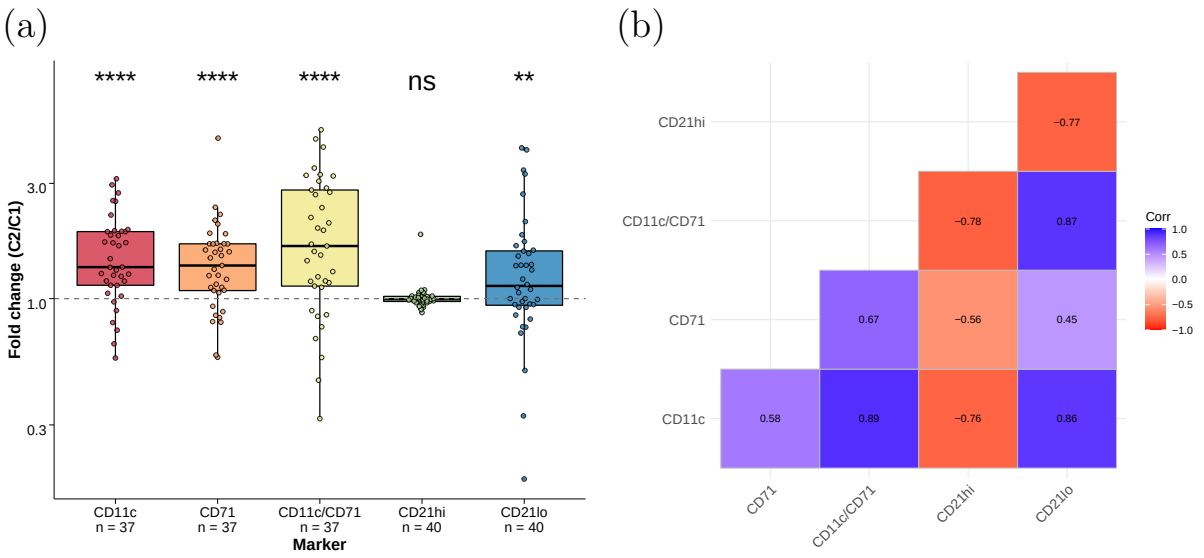


Figure 4.4 cICB upregulates markers of B-cell activation
Flow cytometry data from paired C1/C2 cICB samples provides information on B-cell activation. **a)** Fold change in percentage of B-cells expressing activation markers from C1 to C2 after cICB treatment (n=37-40). Statistics were calculated using paired Wilcoxon signed-rank tests and adjusted using Bonferroni correction. **b)** B-cell activation marker cocorrelation table (n=74-102). Statistics were calculated using Spearman's rank correlation coefficient. Colour refers to direction of association with shading representing Spearman correlation coefficient value. Coefficient values are only shown for significant associations. p > 0.05 (ns), $p \leq 0.05$ (*), $p \leq 0.01$ (**), $p \leq 0.001$ (***), $p \leq 0.0001$ (****). *CD11c/CD71 = $CD11c^+$ $CD71^+$ double positive cells.*

4.2.1.3 B-cell loss is associated with changes in B-cell subsets and activation

B-cell characteristics including subset proportion and expression of activation markers were correlated with B-cell percentage to look for determinants of B-cell loss. Changes in B-cell percentage, following one cycle of cICB, were correlated with corresponding changes in B-cell subset composition and expression of activation markers. B-cell depletion was found to correlate with induction of Bmems (both USMs and SMs), ASCs and activation markers (CD11c/CD71) (Figure 4.5). Although not quite reaching statistical significance, B-cell loss was associated with a reduction in Bn cells. This further demonstrates that the changes observed in B-cell percentage post-cICB are at least in part due to enhanced B-cell differentiation and activation.

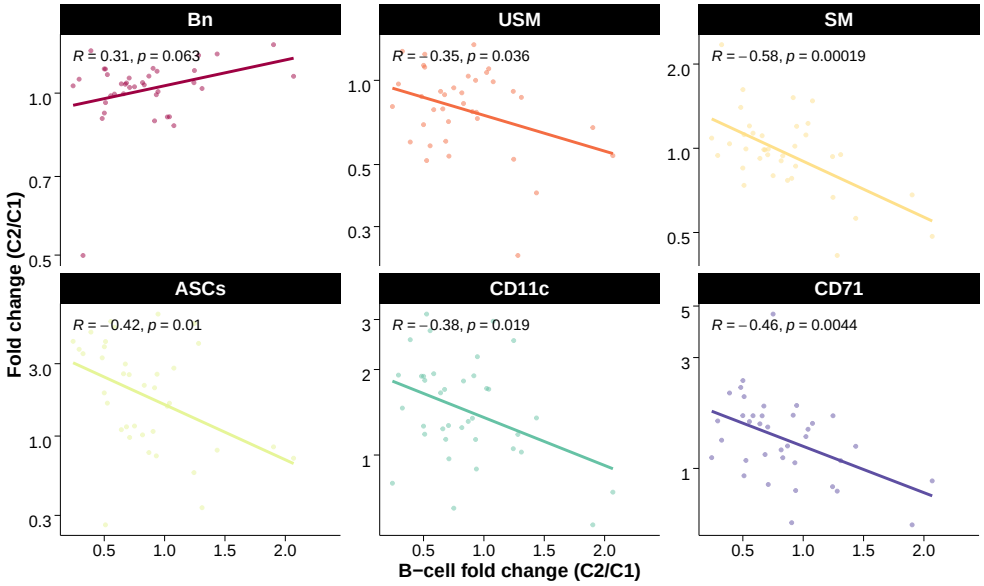


Figure 4.5 B-cell decline correlates with B-cell differentiation and activation
Fold changes in B-cell subsets as well as activation were correlated with B-cell loss at C2 (C2/C1) in paired cICB samples (n=30-37). Statistics were calculated using Spearman's rank correlation coefficient. *Bn = naïve B-cells, USM = unswitched memory B-cells, SM = switched memory B-cells, ASCs = antibody-secreting cells.*

4.2.2 Dissecting the effects of melanoma and ICB on the peripheral B-cell transcriptome

4.2.2.1 Age, sex and library RNA input contribute to RNAseq data variation

B-cells were isolated from peripheral blood, taken from 95 unique MM patients and 96 healthy donors, and submitted for RNAseq analysis (see section 2.3). MM samples included 65 paired C1/C2 samples, 29 paired C1/C4 samples as well as various other longitudinal time-points (Figure 4.6).

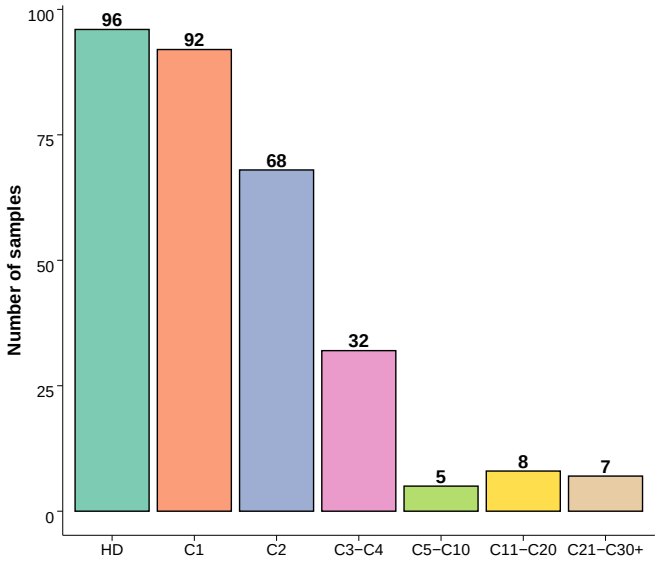


Figure 4.6

Figure 4.6 (Previous page) B-cell RNAseq sample summary
Bar chart depicting the number of CD19$^+$ B-cell transcriptomes successfully sequenced for healthy donors and MM patients by ICB treatment cycle. *HD = Healthy donor.*

*DESeq*2 was used to normalise data, as described earlier (see sections 2.3.1.5), and showed that the first five PCs display more than 61% of the total explained data variance combined (Figure 4.7a). B-cell subset composition, antibody production, CSR and BCR diversity have previously been shown to fluctuate over time, correlating with age[563,564], and may ultimately in part explain the observed data variation. Flow cytometry data of B-cells demonstrated an enrichment of B-cells in females compared to males in baseline C1 samples (Figure 4.7b). Sex-biased effects have previously been reported with differences in B-cell count and humoral immunity which are likely multifactorial[565–568].

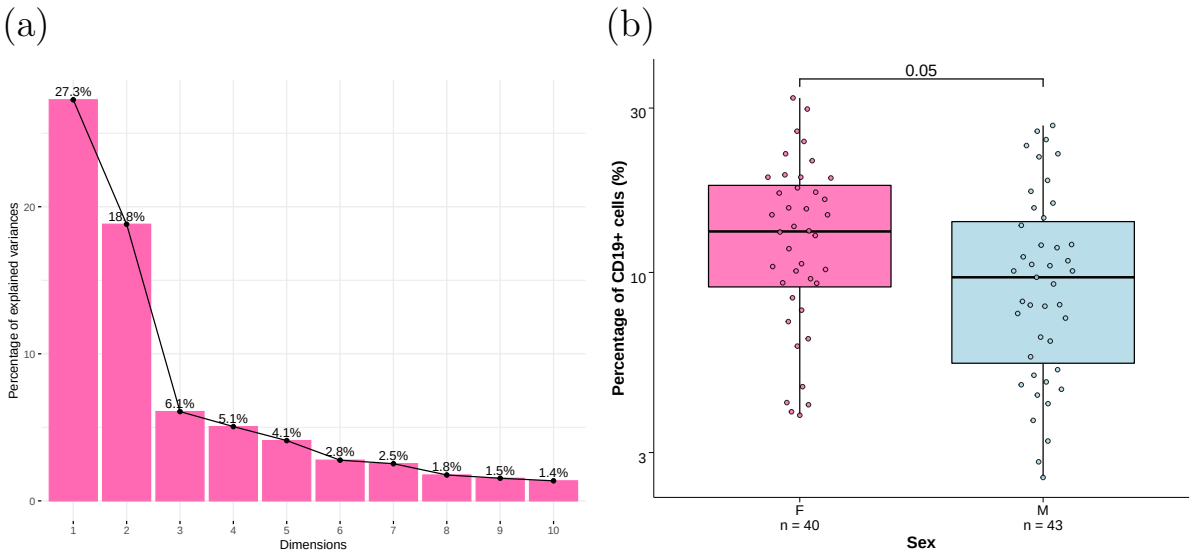


Figure 4.7 Scree plot of early CD19$^+$ B-cell principal components and association with sex
a) Scree plot showing the contribution of each of the top ten principal components (dimensions) to the overall explained data variance with the percentage of data contribution displayed above each bar. **b)** Flow cytometry data of CD19$^+$ B-cell percentage in untreated C1 samples comparing male (M, n=43) and female (F, n=40) donors. Statistics were generated using an unpaired Wilcoxon signed-rank test.

To identify contributors to the data variance, library RNA input, age and sex were, as a result, correlated with PC values. The top five PCs significantly correlating with library RNA input, age and sex are shown in Figure 4.8. Due to the profound correlations detected, library RNA input, age and sex were controlled for in *DESeq*2 design arguments for unpaired tests.

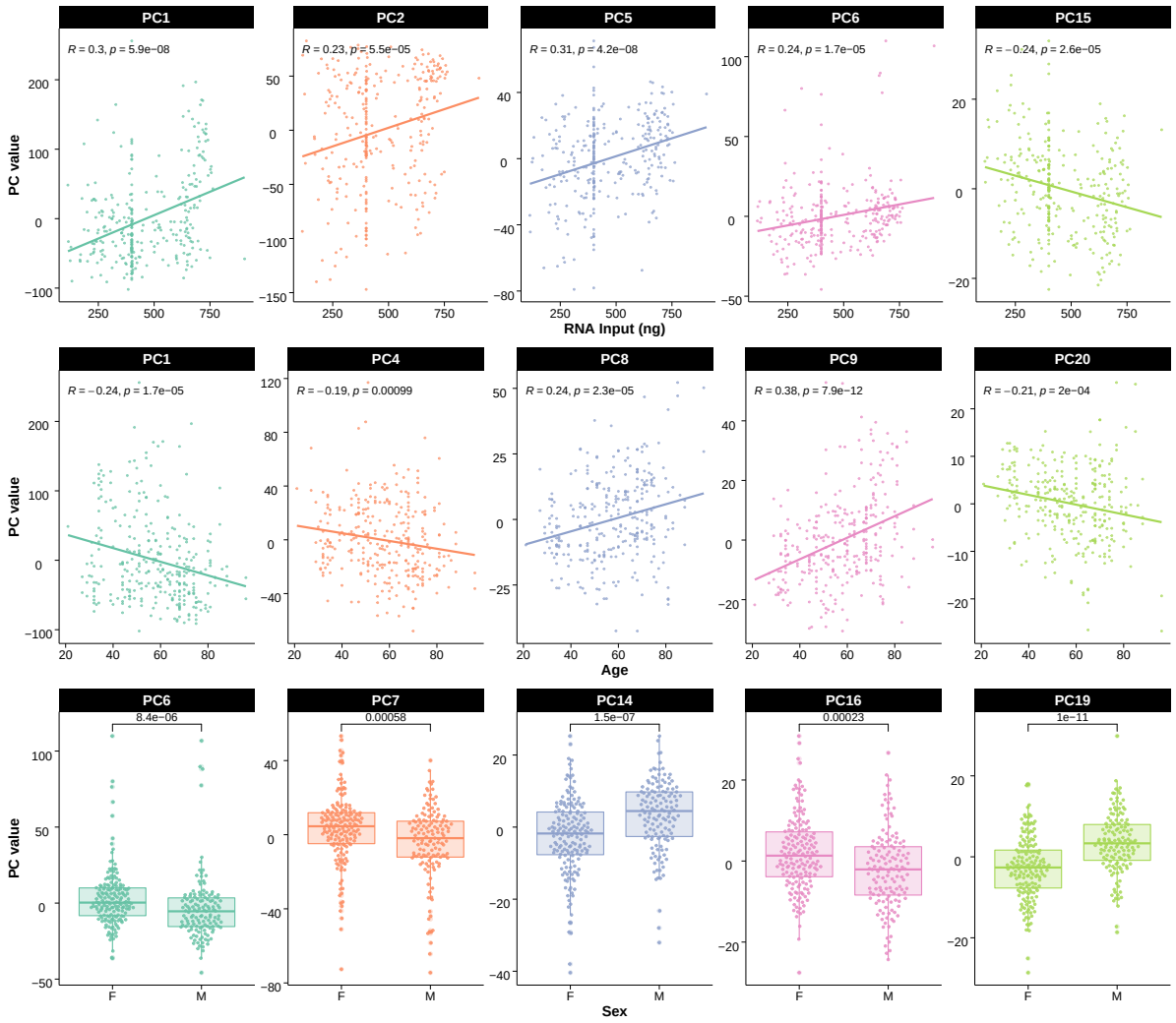


Figure 4.8 Early CD19$^+$ B-cell principal components correlate with library RNA input, age and sex The most significant correlations of principal components (PCs) with library RNA input (ng), age and sex are shown (n=308). Statistics were calculated using Spearman's rank correlation coefficient for correlation analysis or unpaired Wilcoxon signed-rank tests for sex comparisons. *F = female, M = male*.

4.2.2.2 Peripheral B-cells are highly activated in melanoma

Prior to exploring gene expression changes secondary to ICB treatment, I wished to assess the effect of MM. 96 healthy donor and 92 C1 MM patient CD19$^+$ B-cell transcriptomes were successfully sequenced which allowed for comparison between healthy and cancerous states. After controlling for sequencing batch, library RNA input, age and sex, 8,634 DEGs were found between healthy control and MM patient samples after adjusting for multiple testing (n=4,101 enriched in healthy donors, n=4,533 enriched in MM patients) (Figure 4.9a). CMV serostatus did not appear to affect CD19$^+$ B-cell expression (data not shown) and was thus not controlled for in any further comparisons.

Genes significantly elevated in patients were run through pathway analysis using GOBP pathways. This revealed a significant enrichment of genes upregulated in MM within 71 pathways after adjusting for multiple testing. Specifically, upregulated genes were found enriched within B-cell activation pathways including "B-cell activation",

"immunoglobulin production" and "B-cell receptor signalling" pathways (Figure 4.9b). These data clearly demonstrate a hyperactivated state in melanoma, possibly owing to tumour surveillance mechanisms and subsequent tumour recognition and response.

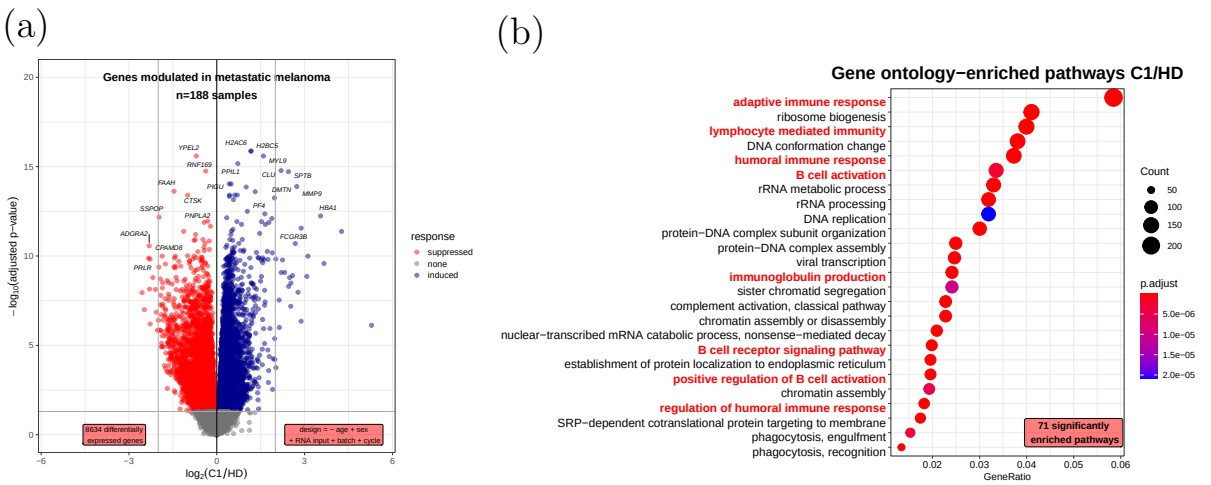


Figure 4.9 Peripheral B-cells are activated in melanoma
188 CD19$^+$ B-cell transcriptomes were analysed using $DESeq2$ comparing healthy donors (HD, n=96) and untreated MM patients (C1, n=92). The design argument included age, sex and library RNA input as well as sequencing batch to control for confounding factors. **a)** Volcano plot comparing CD19$^+$ B-cell expression between healthy donors and C1 samples. Genes significantly enriched in MM patients are in blue and those significantly enriched in healthy donors are in red. The $\log_2$ fold change of each gene is visualised on the x-axis with the significance of this difference displayed on the y-axis. The number of significantly differentially expressed genes as well as the $DESeq2$ design formula are displayed in red boxes. Statistics were calculated using the negative binomial distribution and adjusted for multiple testing using the Benjamini-Hochberg procedure on $DESeq2$. **b)** Pathway enrichment of genes upregulated in patients identified using GOBP pathways. The number of significantly enriched pathways is displayed in a red box in the bottom right. The top 25 significantly enriched pathways are displayed with B-cell associated pathways highlighted in red.

4.2.2.3 cICB induces transient transcriptomic changes in B-cells at C2

In order to further appreciate the changes observed in peripheral B-cells following ICB, B-cell gene expression was compared before and after ICB treatment. 65 paired C1/C2 transcriptomes were contrasted after controlling for library RNA input and patient ID to ensure a paired analysis. 4,298 genes were detected as being significantly differentially expressed post-ICB after accounting for multiple testing (2,340 induced, 1,958 suppressed) (Figure 4.10a). However, in light of previous findings (Figures 4.1b, 4.1c), data was also stratified by treatment type. This highlighted differences in treatment type with significant DEGs only detectable after cICB stimulation (n=45, 4,473 DEGs, 2,441 upregulated, 2,032 downregulated) (Figures 4.10b, 4.10c). The top induced genes primarily comprised GBPs including *GBP1P1*, *GBP1*, *GBP2*, *GBP3*, *GBP4* and *GBP5*. These interferon-inducible GTPases are important for inflammasome activation and may be induced by T-cell and NK cell-derived IFN-γ which is secreted in response to ICB stimulation[208,371] as hypothesised in Chapter three.

Supporting this notion, further IFN-γ-induced genes were found to be upregulated

including *STAT1*, *IL12RB1*, *JAK2* and *CXCL10*. Notably, *CXCL10*, a CXCR3 ligand, is upregulated in response to cICB and associates with a good prognosis[228,547,569]. ELISA analysis of plasma samples indeed revealed higher circulating levels at C2 following cICB treatment (Figure 4.10d). Studies have demonstrated that CXCL10 is predominantly induced by macrophages[569], but perhaps B-cells also contribute to this crucial CXCL10 gradient. Interestingly, induction of CXCL10 in the plasma was found to inversely correlate with the percentage of T-cells in the periphery (Figure S4.5) and may suggest that CXCR3$^+$ T-cells migrate towards these CXCL10 gradients into the tumour.

In addition to upregulation of IFN-γ-induced genes, *SLAMF7*, a notorious plasma cell marker, was found to be profoundly upregulated following cICB (Figure 4.10c). This further suggests that cICB accelerates B-cell differentiation into ASCs.

Genes upregulated in response to cICB treatment at C2 were analysed for pathway enrichment using GOBP pathways. Interestingly, induced genes were enriched in 345 pathways including "leukocyte differentiation", "positive regulation of cell migration", "positive regulation of cytokine production" and "antigen processing and presentation" (Figure 4.10e). This may signify the enhanced differentiation observed in flow cytometry data (Figure 4.3c) and suggests that B-cell decline may be due to B-cell migration to other tissues.

To assess durability of effect, paired C1/C4 cICB samples were compared using the same design argument. While most expression differences had resolved by this time, seven genes remained significantly differentially expressed, including exhaustion-associated markers *LAG3* and *CTLA4*, potentially limiting any further response to treatment (Figure 4.10f).

4.2.3 Deconvoluting B-cell subset scores from bulk RNAseq data

4.2.3.1 Defining peripheral B-cell clusters

Due to the limited statistical power of flow cytometry, single cell RNAseq was performed using the 10x Chromium v1 platform to gain a better appreciation of B-cell subset expression. This can ultimately be used to interpret bulk RNAseq data through subset deconvolution to infer subset composition and hence monitor changes over the course of ICB treatment.

CD19$^+$ B-cells were isolated from fresh peripheral blood derived from three healthy donors and one untreated C1 MM patient. Gene count tables were read into R and incorporated into a Seurat object using "*CreateSeuratObject(counts = counts table, min.cells = 3, min.features = 200)*" on Seurat[518–521] as described in section 2.3.3.4. Low quality cells were subsequently removed using the appropriate filters including the unique number of genes expressed, RNA content as well as expression of mitochondrial-associated genes, all of which associate with cell death and cell multiplets (Figure 4.11). A maximum of 15% was accepted for carriage of mitochrondrial genes. Typically, lower thresholds are implemented, but B-cells are known to carry a greater number of mitochondria, particularly after B-cell activation where mitochondrial function is crucial for differentiation, antibody secretion, CSR and SHM[522,523]. A total of 3,529 cells (2,684 healthy donors, 845 C1) were carried forward for subsequent analyses.

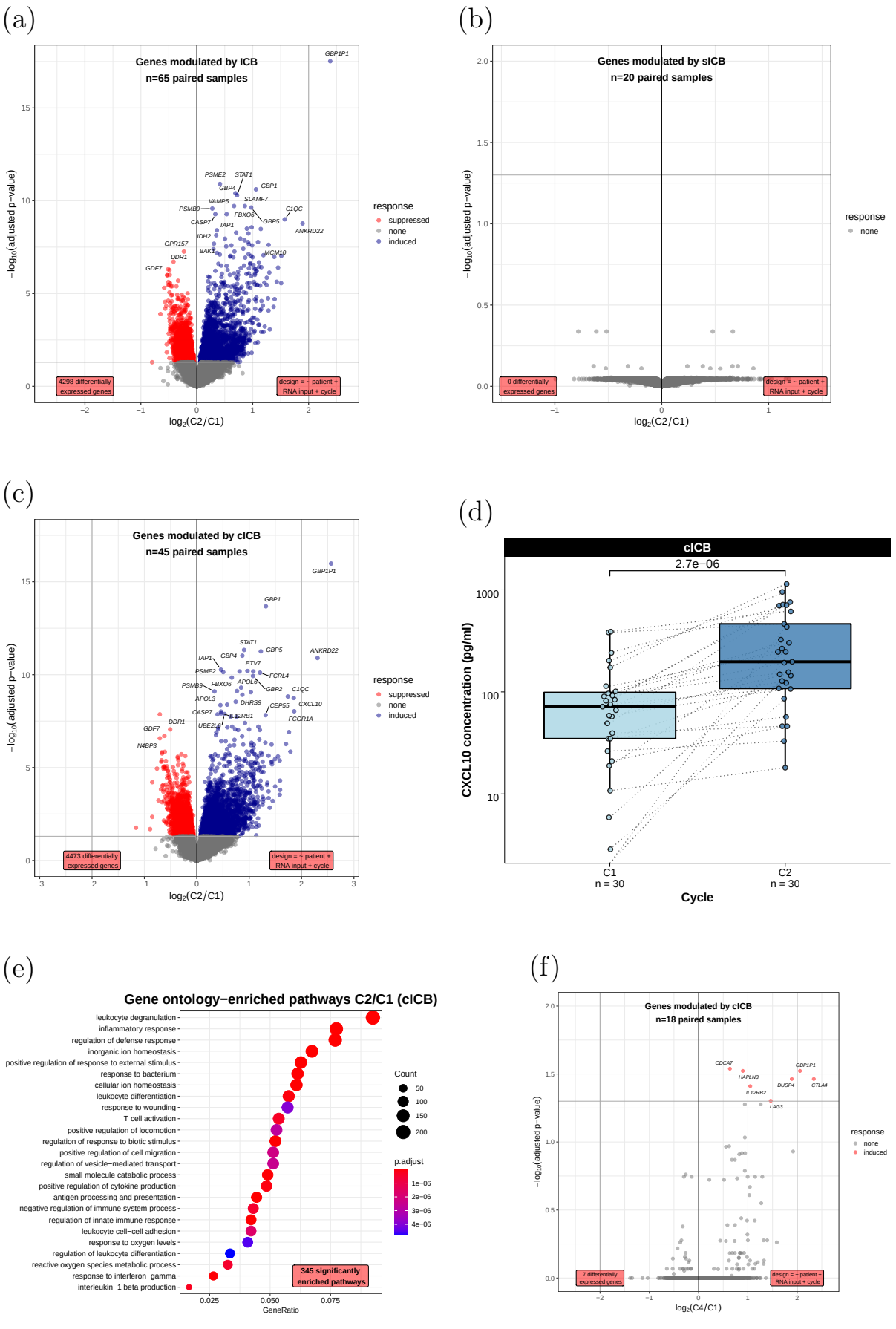

(a)
Genes modulated by ICB
n=65 paired samples
4298 differentially expressed genes
design = ~ patient + RNA input + cycle
response
suppressed
none
induced
(b)
Genes modulated by sICB
n=20 paired samples
0 differentially expressed genes
response
none
(c)
Genes modulated by cICB
n=45 paired samples
4473 differentially expressed genes
(d)
cICB
2.7e−06
CXCL10 concentration (pg/ml)
C1
n = 30
C2
n = 30
Cycle
(e)
Gene ontology−enriched pathways C2/C1 (cICB)
leukocyte degranulation
inflammatory response
regulation of defense response
inorganic ion homeostasis
positive regulation of response to external stimulus
response to bacterium
cellular ion homeostasis
leukocyte differentiation
response to wounding
T cell activation
positive regulation of locomotion
regulation of response to biotic stimulus
positive regulation of cell migration
regulation of vesicle−mediated transport
small molecule catabolic process
positive regulation of cytokine production
antigen processing and presentation
negative regulation of immune system process
regulation of innate immune response
leukocyte cell−cell adhesion
response to oxygen levels
regulation of leukocyte differentiation
reactive oxygen species metabolic process
response to interferon−gamma
interleukin−1 beta production
345 significantly enriched pathways
GeneRatio
Count
p.adjust
(f)
Genes modulated by cICB
n=18 paired samples
7 differentially expressed genes

Figure 4.10

Figure 4.10 (Previous page) cICB induces expression changes in peripheral B-cells
Paired C1/C2 samples and C1/C4 samples were compared for gene expression using $DESeq2$. Patient ID and library RNA input were included as controls in the design argument. Differential expression is visualised by volcano plot comparing **a)** paired C1/C2 samples (n=65), **b)** paired C1/C2 samples following sICB treatment (n=20) and **c)** paired C1/C2 samples treated with cICB (n=45). **d)** Circulating plasma CXCL10, as quantified by ELISA, is compared between paired C1/C2 samples following cICB (n=30). Statistics were calculated using a paired Wilcoxon signed-rank test. **e)** Pathway enrichment analysis using the GOBP database reveals significantly enriched pathways of induced genes at C2 following cICB treatment. **f)** Volcano plot showing differential expression between paired C1/C4 samples following cICB treatment (n=18). **a,b,c,f)** For volcano plots, genes significantly enriched at C2/C4 are in blue and those significantly downregulated are in red. The $\log_2$ fold change of each gene is visualised on the x-axis with the significance of this difference displayed on the y-axis. The number of significantly differentially expressed genes as well as the $DESeq2$ design formula are displayed in red boxes. Statistics were calculated using the negative binomial distribution and adjusted for multiple testing using the Benjamini-Hochberg procedure on $DESeq2$.

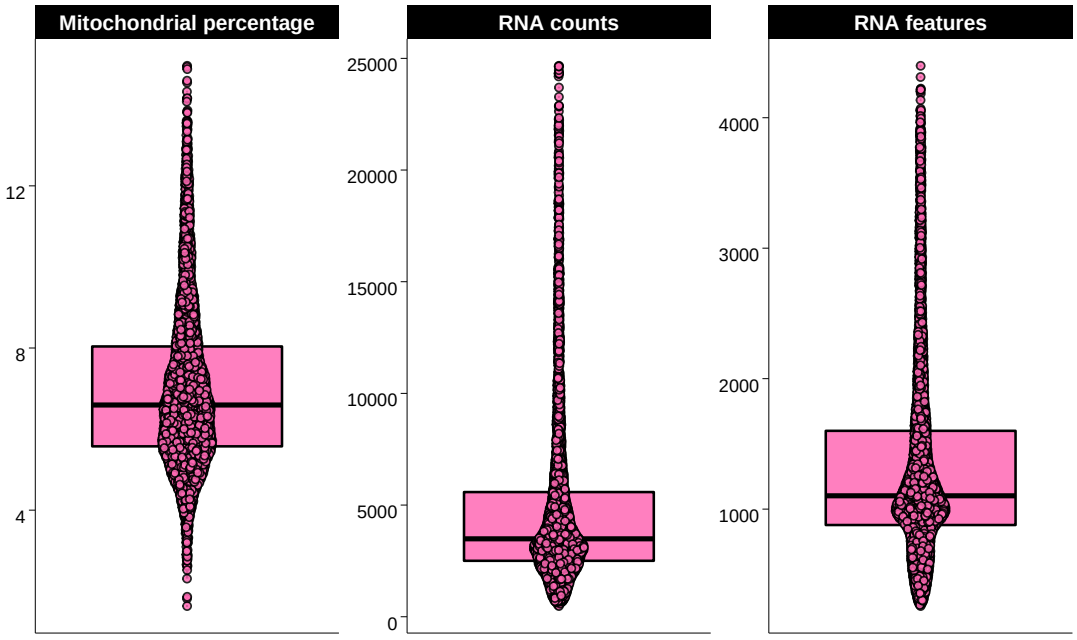


Figure 4.11 Single cell feature summary
3,529 CD19$^+$ cells passed quality control after filtering for mitochondrial percentage of genes (left), RNA counts (middle) and number of RNA features (right). Mitochondrial percentage represents the percentage of all genes that are mitochondrial-associated, RNA counts refers to the number of reads per cell and RNA features signifies the number of unique genes detected per cell.

Clustering of filtered B-cells was performed using Seurat[518–521]. Principal component analysis was performed to identify the PCs contributing to the data variability and therefore which were most important for capturing the majority of the total data variance. Significantly contributing PCs were included in UMAP analysis which was implemented to reduce dimensionality of the data for subsequent visualisation. The PCs to be included in such analysis were determined by elbow and Jack Straw plots (Figures 4.12a, 4.12b). The elbow plot visualises the impact of each PC on the standard deviation of the data. Once the PCs stop having a large impact on the data variance, the line levels off as an 'elbow'. This plateau occurs for this data at PC17. By comparison, JackStraw analysis

calculates the significance of each PC. Data is randomly subsampled and a PCA score is calculated per gene. This is compared to the observed PC scores, hence correlating all genes and PCs. The JackStraw plot combines QQ plots to visualise the p-value distribution for all genes per PC, alongside a uniform distribution. Significant PC p-value distributions are skewed to the left away from the null distribution. An overall p-value is determined per PC signifying an enrichment of genes with significant p-values. Whilst this approach reveals that the top 20 PCs are significant, there is a drop-off in magnitude of significance from PC17 to PC18. As a result, it was determined that the first 17 PCs contribute the majority of the data variation and should therefore be included in downstream UMAP analysis.

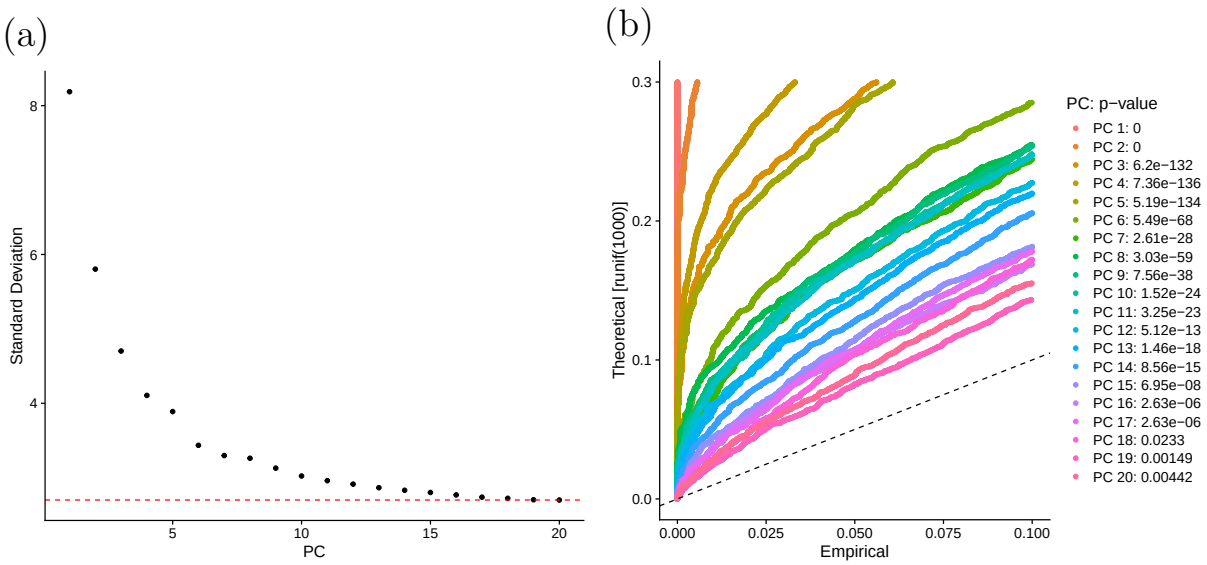


Figure 4.12 Determining the optimal number of principal components for analysis
a) The contribution of the top 20 principal components (PCs) to the data variance are displayed by elbow plot. A horizontal red, dashed line shows the point at which the curve plateaus. **b)** The significance of the contribution of each PC is visualised by Jack Straw plot with a dashed, black line representing the null distribution.

A further parameter to determine for UMAP analysis was resolution, referring to the granularity of the data and the number of subsequent clusters identified. Optimal resolution was determined using *Clustree*[524] which visualises the impact of resolution on the number of clusters generated and the number of cells within those clusters (Figure 4.13). Upon inspection, a resolution of 1.5 was identified as optimal for minimal cell shuffling between clusters and relative stability in cluster number with a comparable number of subsets observed at higher resolutions.

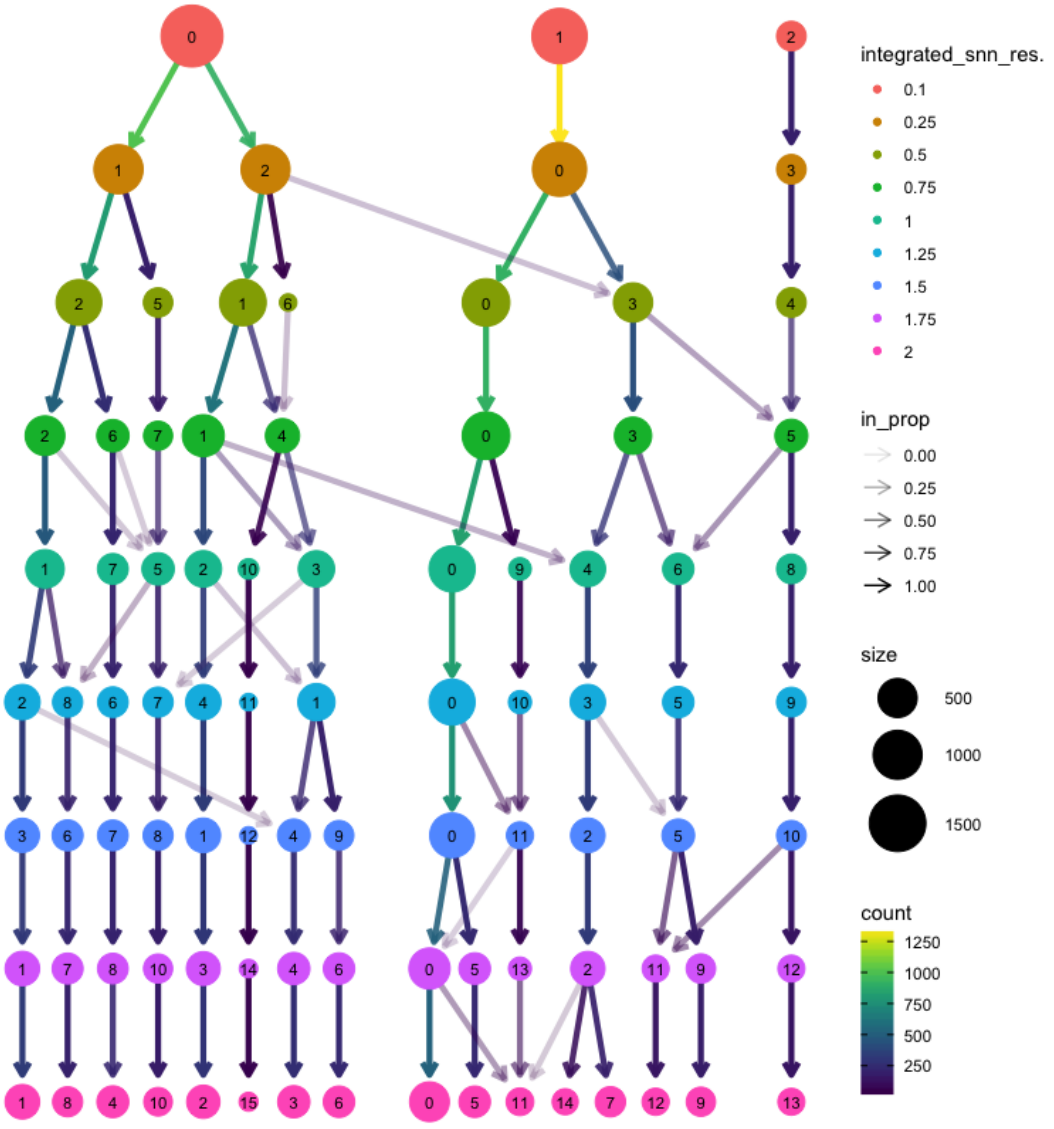


Figure 4.13 Determining optimal resolution using Clustree analysis
Optimal resolution for clustering was determined using *Clustree*. Each circle represents a unique subset identified by Seurat. Circle colour refers to the resolution implemented in analysis and size refers to the number of cells contained in that cluster at that resolution level. As the tree branches out, the resolution applied increases. As the resolution rises, the number of subsets identified is increased with arrows showing the direction of cell shuttling between clusters at different resolutions. Arrow colour represents the number of cells shuttling and shading refers to the proportion of that cluster changing. *integrated_snn_res. = resolution, in_prop = proportion of subset.*

Applying these metrics to UMAP analysis generated a total of 13 clusters (0-12) (Figure 4.14a) with a representation of all clusters in both healthy donors and the MM patient, although of varying magnitudes (Figure S4.6a). This is an obvious overclustering that is rectified by aligning to previously described subset data and combining similar Seurat subsets accordingly. Scores were generated per cell based on alignment with PBMC profiles derived from the Monaco Immune Dataset[527] using *SingleR*[570] (Figures 4.14b, 4.14c).

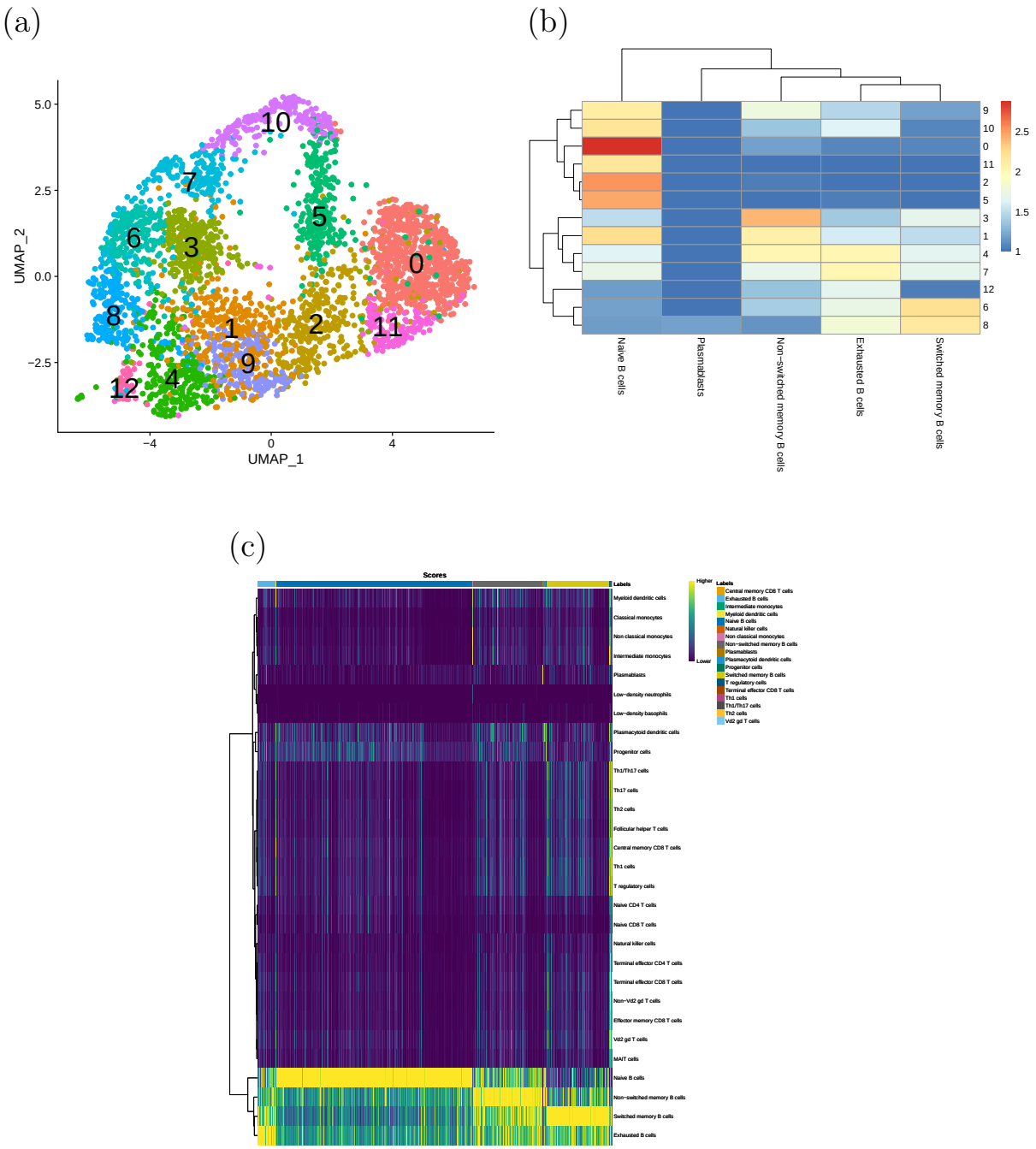


Figure 4.14 CD19^{+} B-cell Seurat cluster annotations
Final clustering analysis using 17 principal components and a resolution of 1.5. **a)** UMAP analysis reveals 13 unique Seurat clusters (0-12) (n=3,529 cells). **b)** Heatmap shows Seurat cluster scores per B-cell subset identified in the Monaco Immune dataset. Red indicates high enrichment and blue, low enrichment. **c)** Heatmap showing alignment of all cells to all PBMC subsets detected in the Monaco Immune dataset using *SingleR*. Yellow represents high enrichment and blue, low enrichment.

Taken together, Seurat cluster scores and expression of canonical B-cell markers (Figure S4.6b) allowed combination of Seurat clusters to generate a total of four final clusters including naïve (Bn), unswitched memory (USM), switched memory (SM) and antibody-secreting cells (ASCs) (Figure 4.15).

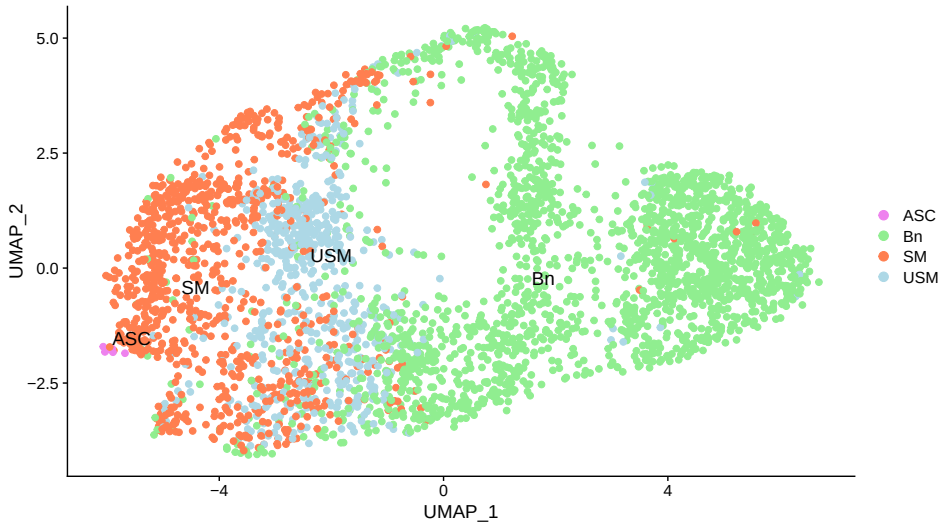


Figure 4.15 Final CD19$^+$ B-cell cluster annotations
3,529 CD19$^+$ B-cells were annotated using *SingleR* and the Monaco Immune Dataset as a reference. Seurat clusters were combined using cluster enrichment scores to generate final annotations which are visualised by UMAP. *Bn = naïve B-cell, USM = unswitched memory B-cell, SM = switched memory B-cell, ASC = antibody-secreting cell.*

4.2.3.2 Generating subset scores from bulk RNAseq data

Seurat function "*FindAllMarkers()*" was applied to the data to identify significantly differentially enriched genes per subset. A score per subset was deconvoluted from bulk CD19$^+$ B-cell RNAseq data by calculating the geometric mean of the top 20 genes enriched per subset. This score was validated by comparison of imputed ASC score with flow cytometry ASC percentages (Figure 4.16).

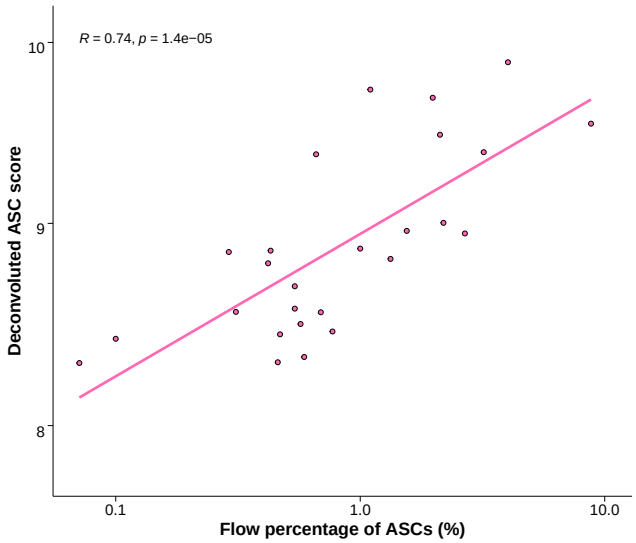


Figure 4.16 Validating CD19$^+$ B-cell subset deconvolution from bulk RNAseq data
Deconvoluted subset scores from CD19$^+$ bulk RNAseq samples were compared to flow cytometry annotated subsets by correlating ASC scores with flow cytometry ASC percentages as an example (n=74). Statistics were calculated using Spearman's rank correlation coefficient.

Imputed subset scores were compared between paired C1/C2 samples by treatment type (Figures 4.17a, 4.17b). This revealed an increase in ASC score at C2 following cICB treatment, but not sICB, supporting findings from the flow cytometry data (Figure 4.3c). However, no changes in any other subset were observed. Deconvoluted B-cell subset scores were also compared between healthy donors and MM patients, as well as between CMV^- and CMV^+ patients, however, no differences were observed (data not shown).

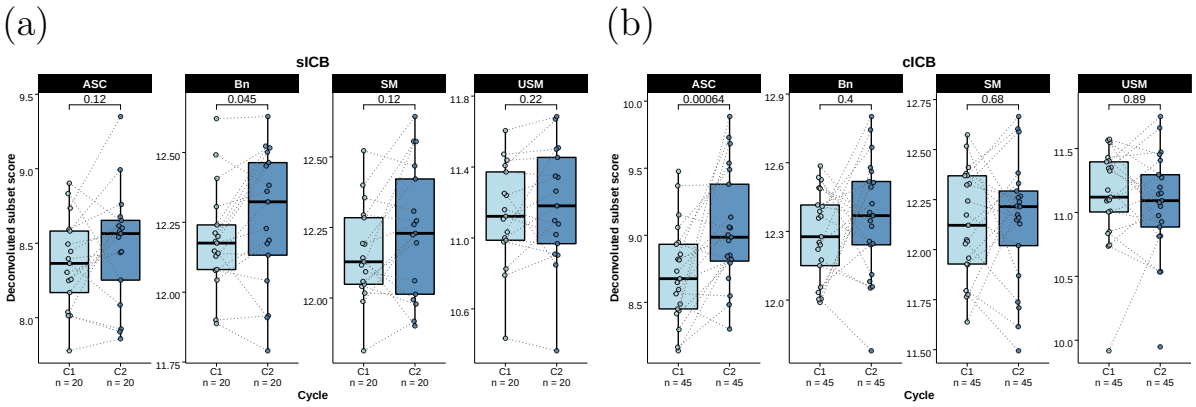


Figure 4.17 Deconvoluted $CD19^+$ B-cell subset scores show an increase in ASC score following cICB treatment
Imputed $CD19^+$ B-cell subset scores were compared between paired C1/C2 samples following **a)** sICB (n=20) and **b)** cICB (n=45) treatment. Statistics were calculated using paired Wilcoxon signed-rank tests.

Owing to the low number of ASCs identified, likely due to the use of CD19 magnetic-labelled bead selection, analysis was repeated using publicly available single cell datasets of whole B-cells[359,410,525]. Indeed, many more ASCs were captured using this approach (Figure 4.18).

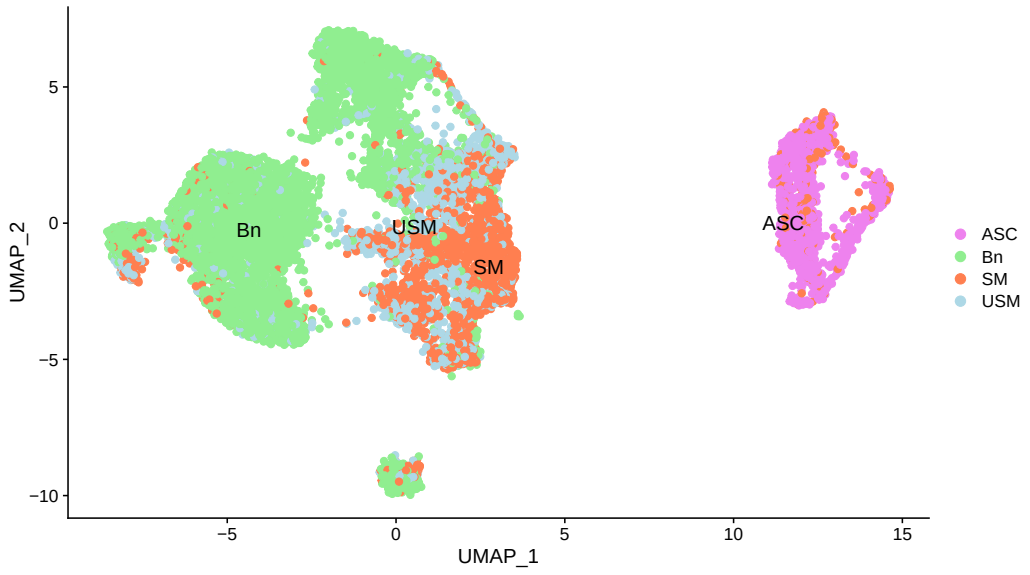


Figure 4.18

Figure 4.18 (Previous page) Subset annotation from public single cell B-cell datasets
Final UMAP clustering of annotated subsets (n=12,206 cells) from public B-cell single cell RNAseq datasets[359,410,525]. *Bn = naïve B-cell, USM = unswitched memory B-cell, SM = switched memory B-cell, ASC = antibody-secreting cell.*

To ensure consistency in ASC annotation, individual online datasets of B-cells were aligned to Monaco Immune data subsets using *SingleR* in a similar manner as before. With a greater number of ASCs identified, ASC deconvolution of bulk CD19$^+$ B-cell samples was likely more reliable. Nevertheless, deconvolution similarly demonstrated a profound enrichment in ASCs following cICB, not observed with sICB, for all datasets (Figures 4.19a, 4.19b).

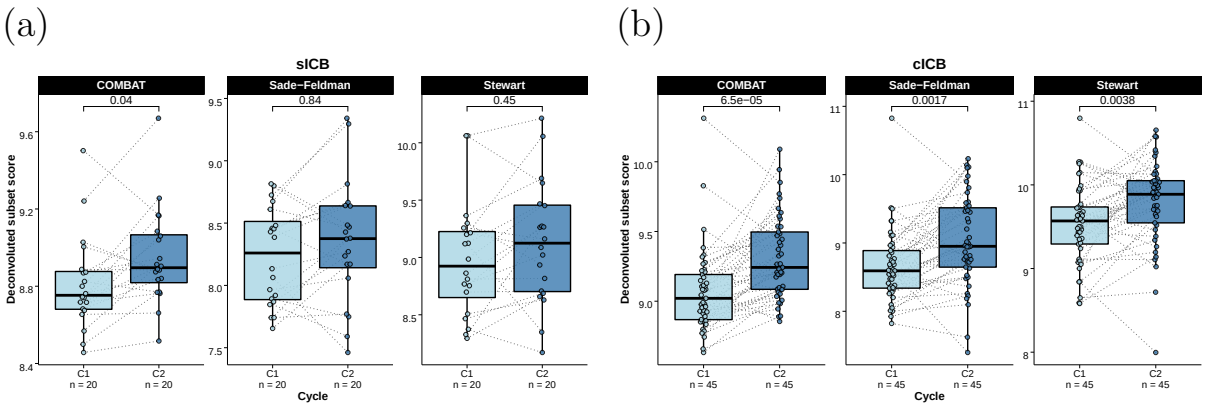


Figure 4.19 ASC scores generated using online datasets are increased following cICB
ASC scores were calculated using markers of ASCs generated using public data[359,410,525] to deconvolute bulk CD19$^+$ B-cell RNAseq samples. ASC score is compared between paired C1/C2 samples following **a)** sICB (n=20) or **b)** cICB (n=45). Statistics were calculated using paired Wilcoxon signed-rank tests.

Strikingly, induction of ASC score at C2 was found to associate with longer OS (Figure 4.20) and may explain why patients treated with cICB typically experience enhanced clinical benefit[143,203].

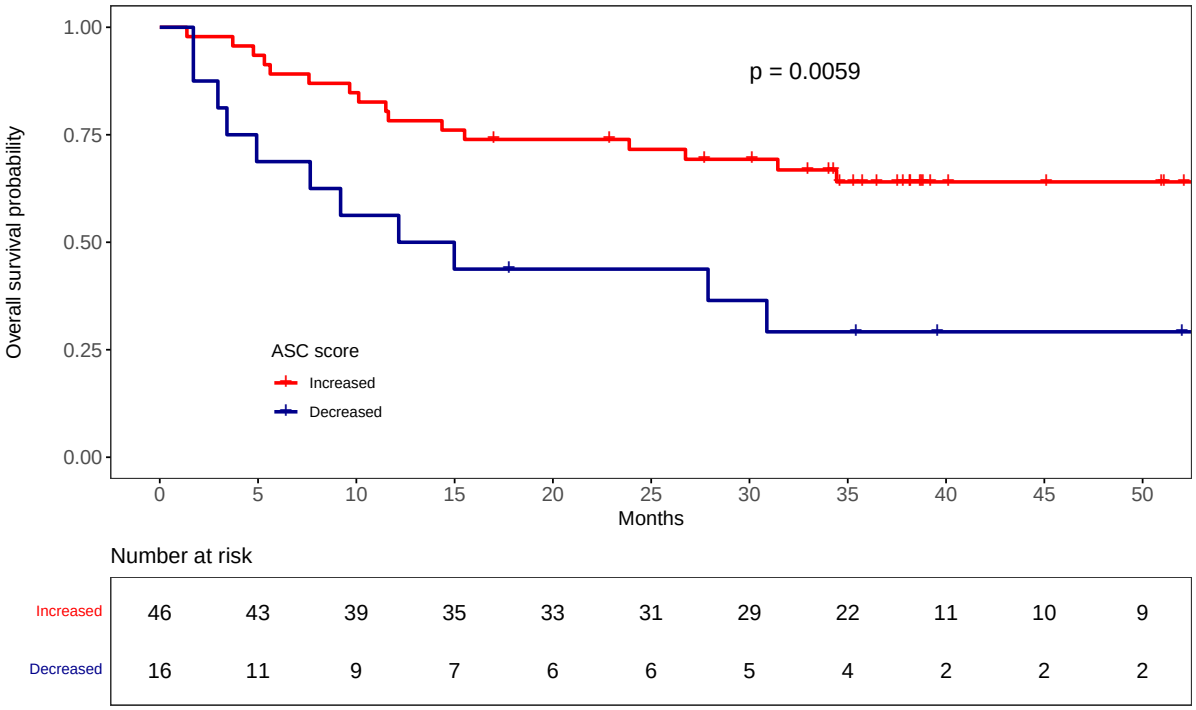


Figure 4.20 ASC induction prolongs survival
Kaplan-Meier curve shows the association of ASC score with overall survival (n=62) after dichotomising patients into those who increase or decrease ASC score at C2.

4.2.4 Contribution of monocytes, T-cells and NK cells to the B-cell ICB response

4.2.4.1 $CD8^+$ T-cell activation confers B-cell response to cICB

To investigate if the B-cell ICB response is dependent on other PBMC cell types, specifically $CD8^+$ T-cells, $CD19^+$ B-cell ICB response score was correlated with ICB response scores from $CD8^+$ T-cells, $CD14^+$ monocytes and NK cells. These response scores were calculated as the geometric mean of the top 50 induced genes following ICB per cell type. B-cell ICB response score strongly correlated with ICB response scores for all PBMC subsets. However, these correlations were only observed for cICB-treated samples, and not sICB-treated (Figure 4.21a). As cICB has previously been demonstrated to have similar, but greater effects than sICB on $CD8^+$ T-cells (Figures 3.10d, 3.10e, 3.10f, S3.11, 3.22c, 3.22d)[371,547], one may speculate that B-cell ICB response relies on the magnitude of activation in other PBMC subsets and that PBMC activation is not strong enough to induce a profound B-cell response following sICB.

To ascertain if B-cells respond to ICB directly or, indeed, indirectly through other PBMC subsets, baseline lymphocyte surface PD-1 expression was compared to $CD19^+$ B-cell cICB response scores (Figure 4.21b). Although no correlation was observed between induction of B-cell cICB score and baseline B-cell or NK cell PD-1 expression, a higher expression of T-cell PD-1 at C1 associated with a greater B-cell response to cICB. This suggests that B-cell PD-1 expression doesn't necessarily determine cICB response and therefore may mean that B-cells are not directly targeted by ICB, but rather respond as a result of $CD8^+$ T-cell activation as suggested in Chapter three. A higher expression of PD-1 in $CD8^+$ T-cells may make the T-cell more targetable by ICB and thus give the

cell a higher capacity for response and subsequent B-cell activation.

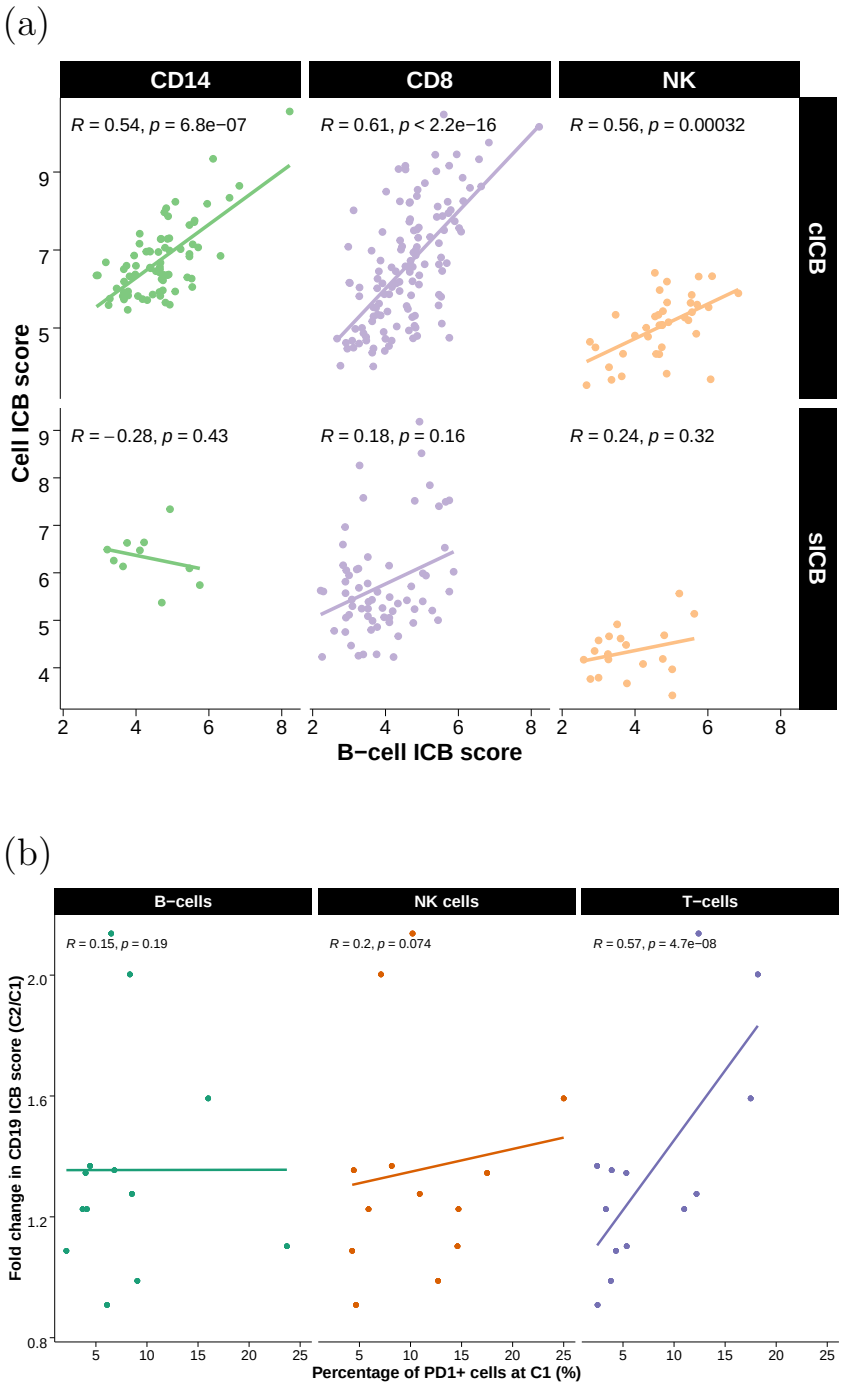


Figure 4.21 Baseline T-cell PD-1 expression associates with B-cell ICB response
a) B-cell ICB score is correlated with ICB scores derived from CD14$^+$ monocytes (n=10 sICB, n=64 cICB), CD8$^+$ T-cells (n=38 sICB, n=86 cICB) and NK cells (n=14 sICB, n=32 cICB) and faceted by treatment type. **b)** PBMC surface PD-1 expression at C1 is compared to the B-cell ICB response, quantified as the fold change in ICB score (C2/C1) in patients treated with cICB (n=13). Statistics were calculated using Spearman's rank correlation coefficient.

Chapter three described the importance of CD8$^+$ T-cell ICB response for responses

in other cell types including B-cells. However, this is investigated in more detail here. Firstly, any B-cell gene which resulted in dampened B-cell cICB response when controlled for identified the gene as being important for driving the cICB response in B-cells. Analysis revealed that B-cell expression of interferon-associated genes, including GBPs, *STAT1* and *CXCL10*, were strong determinants of response, so much so, that controlling expression of either *GBP4* or *STAT1* removed any significant differential expression (Figure 4.22). This was in addition to *SLAMF7* which is strongly expressed by plasma cells. This further suggests that B-cell differentiation and response to IFN-γ may be critical for eliciting B-cell cICB responses.

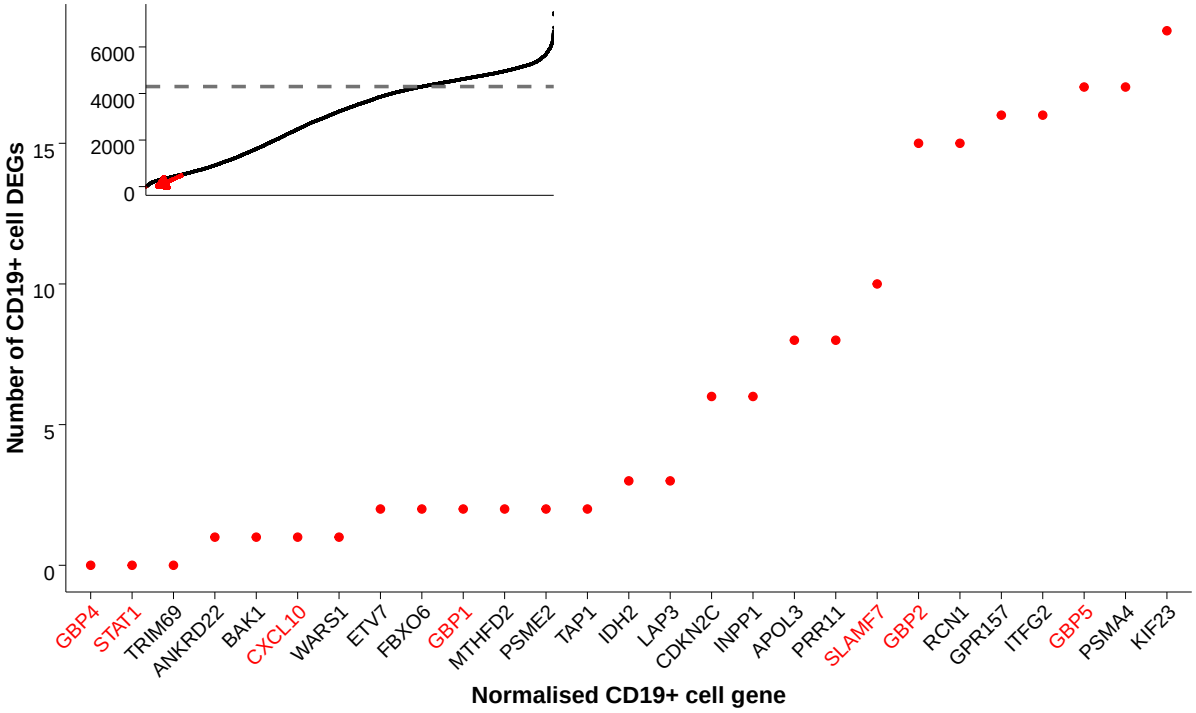


Figure 4.22 B-cell expression of interferon-associated genes correlates with cICB response
Sigmoid curve of the top CD19$^+$ B-cell genes associated with dampening CD19$^+$ B-cell cICB response when controlled for with a sigmoid curve of all genes overlaid. The arrow and points in red represent the magnified plot. *DESeq2* was used to compare paired C1/C2 CD19$^+$ B-cell transcriptomes following cICB (n=45) after controlling for patient ID, library RNA input and individual normalised CD19$^+$ B-cell gene counts as shown on the x-axis. The number of resulting DEGs is shown on the y-axis. Interferon-associated genes and *SLAMF7* are highlighted in red.

To determine if CD8$^+$ T-cell activation is important for B-cell cICB response, *DESeq2* analysis of paired C1/C2 cICB CD19$^+$ B-cell samples was performed again, but this time normalising for individual CD8$^+$ T-cell genes. Each gene was separately included in the design argument to identify any CD8$^+$ T-cell genes which govern B-cell cICB response. This analysis was looped for all CD8$^+$ T-cell genes acting as an *in silico* CRISPR. Interestingly, normalising some CD8$^+$ T-cell genes completely abrogated any effect of cICB on CD19$^+$ B-cells resulting in an absence of DEGs (Figure 4.23). This included *CD38* which has previously been reported to be induced post-ICB treatment (Figure S3.12e)[219,224,371]. Although normalisation of CD8$^+$ T-cell *MKI67* did not completely remove the effects of ICB on CD19$^+$ B-cells, it significantly reduced the magnitude of ICB response.

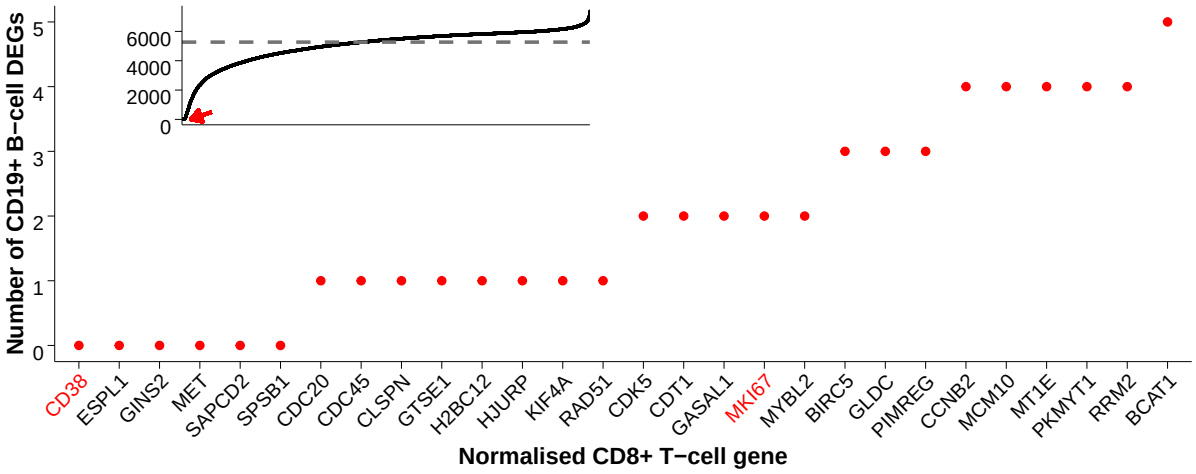


Figure 4.23 CD8$^+$ T-cell gene expression determines B-cell cICB response
Sigmoid curve of the top CD8$^+$ T-cell genes associated with dampening CD19$^+$ B-cell cICB response when controlled for with sigmoid curve of all genes overlaid. The arrow and points in red represent the magnified plot. *DESeq2* was used to compare paired C1/C2 CD19$^+$ B-cell transcriptomes following cICB controlling for patient ID, library RNA input and individual normalised CD8$^+$ T-cell (n=45) gene counts as shown on the x-axis. The number of resulting DEGs is shown on the y-axis. *CD38* and *MKI67* genes are highlighted in red.

As CD38 was included in the T-cell flow cytometry activation panel (panel M3), the impact of CD8$^+$ T-cell CD38 expression on cICB B-cell changes was investigated (Figure 4.24). Interestingly, induction of CD38 by CD8$^+$ T-cells after cICB predicted B-cell changes following cICB at C2 including B-cell activation (CD21^{lo} B-cell percentage), ASC enrichment and USM loss. However, CD38 induction did not correlate with the observed peripheral B-cell depletion.

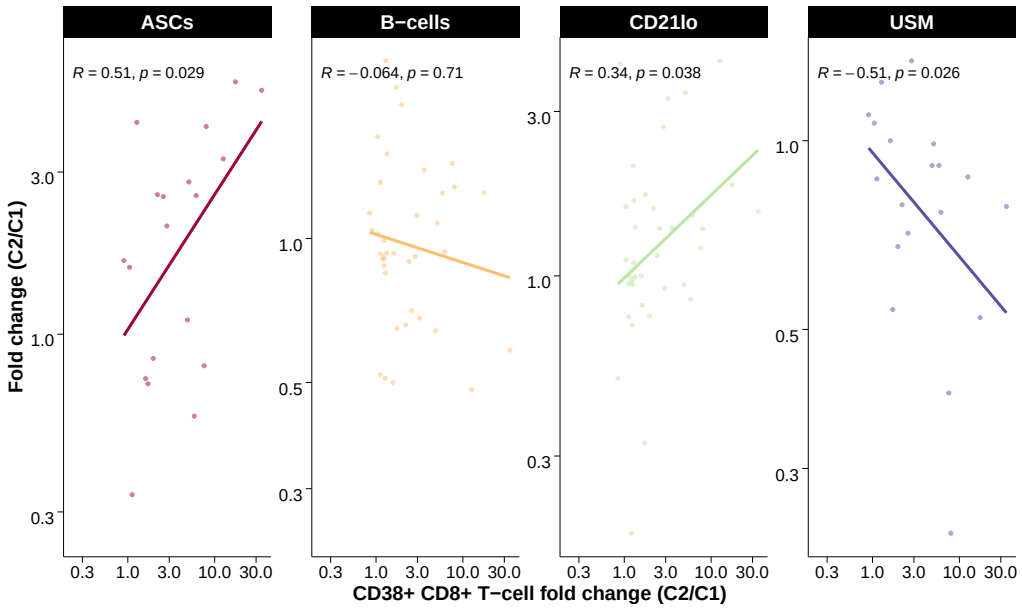


Figure 4.24 CD8$^+$ T-cell activation associates with B-cell cICB response
Induction of CD38 in CD8$^+$ T-cells following cICB treatment is compared to fold changes in B-cell percentage, subset proportion and activation using flow cytometry data (n=19-37). Statistics were generated using Spearman's rank correlation coefficient.

PBMC ICB response scores were also compared to B-cell and ASC percentages to see if magnitude in response associated with B-cell changes (Figures 4.25a, 4.25b). B-cell ICB score inversely correlated with B-cell percentage, but positively correlated with induction of ASCs, potentially signifying the transition into CD19$^{lo/-}$ ASCs. Although CD8$^+$ T-cell and NK cell ICB scores correlated with ASC induction, no correlation was found with peripheral B-cell percentage.

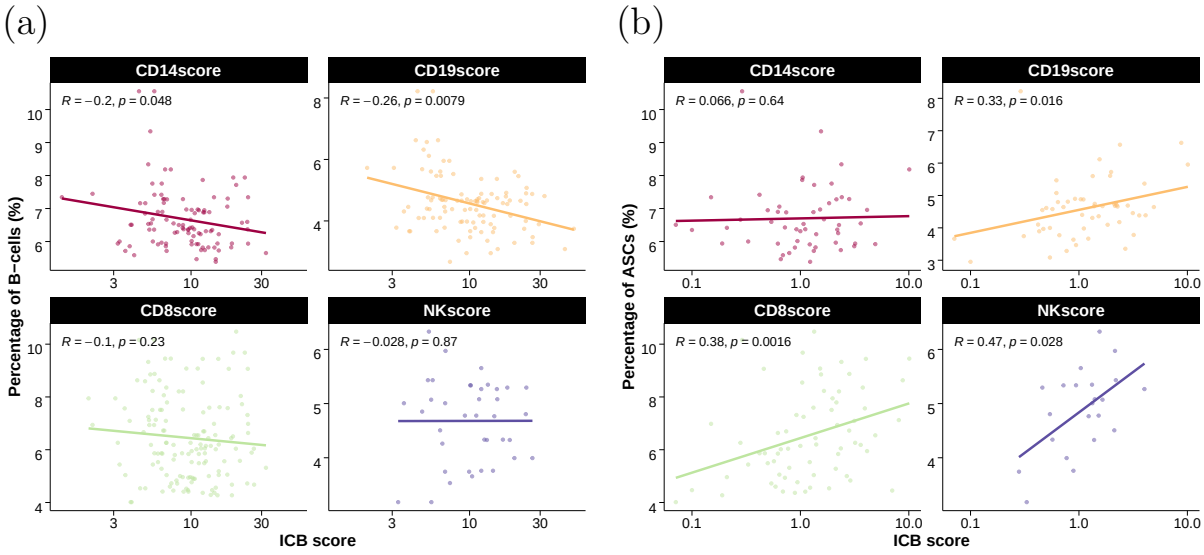


Figure 4.25 B-cell ICB score correlates with B-cell loss and ASC induction
PBMC ICB scores derived from CD14$^+$ monocytes, CD19$^+$ B-cells, CD8$^+$ T-cells and NK cells in MM patients treated with cICB were compared to **a)** B-cell (n=60-184) and **b)** ASC (n=22-84) percentages. Statistics were generated using Spearman's rank correlation coefficient.

4.2.4.2 CD8$^+$ T-cell induction of *CXCL13* predicts B-cell changes to cICB

Owing to the B-cell depletion and ASC induction observed, along with enrichment of cICB-induced genes within migratory and differentiation pathways (Figures 4.1a, 4.3c, 4.10e), the impact of *CXCL13* induction on B-cell changes was investigated. CXCL13 is a B-cell chemoattractant directing CXCR5-expressing B-cells into lymphoid tissue and organising them into B-cell follicles. CXCL13 levels strongly correlate with germinal centre activity[449] and thus reflect greater levels of SHM, CSR and plasma cell differentiation. Given that CD8$^+$ T-cell *CXCL13* expression associates with an enhanced B-cell response to cICB (discovered using *in silico* CRISPR), the contribution of CXCL13 to B-cell changes was investigated. Normalised *CXCL13* counts from CD19$^+$ B-cell, CD8$^+$ T-cell, CD14$^+$ monocyte, NK cell, CD4$^+$ naïve T-cell and CD4$^+$ memory T-cell transcriptomes revealed that T-cells, particularly CD4$^+$ memory T-cells and CD8$^+$ T-cells, express the highest levels of *CXCL13* (Figure 4.26a). Comparing expression in healthy donors and untreated MM patients revealed that CD19$^+$ B-cells and CD8$^+$ T-cells upregulate *CXCL13* in melanoma (Figure 4.26b), as already previously shown for CD8$^+$ T-cells (Figure 3.15a). Strikingly, when looking at the genes upregulated by CD8$^+$ T-cells in melanoma, *CXCL13* was unveiled as the most significantly enriched gene (Figure 3.15a). This potentially highlights the importance of CXCL13 in melanoma and the role it plays in germinal centre reactions[449] as well as TLS generation[366]. TLS's

surround tumours and may contribute to enhanced antigen presentation *in situ*, ASC differentiation, BCR diversity and ultimately may aid tumour surveillance mechanisms[366].

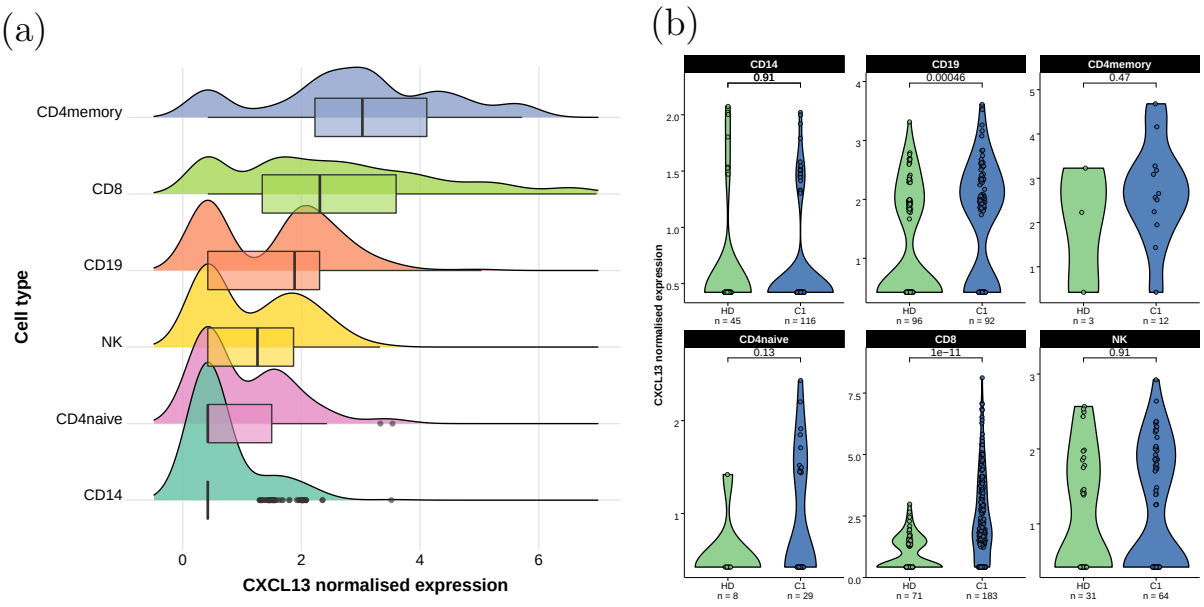


Figure 4.26 *CXCL13* is induced by CD8$^+$ T-cells in melanoma
a) Normalised *CXCL13* gene counts were compared between different PBMC cell types (n=504 CD8$^+$ T-cells, n=308 CD19$^+$ B-cells, n=284 CD14$^+$ monocytes, n=174 NK cells, n=69 CD4$^+$ naïve T-cells, n=26 CD4$^+$ memory T-cells) and are shown in order of expression. **b)** Healthy donors (HD, n=3-96) and C1 samples (n=12-183) were compared for expression of *CXCL13* for each PBMC subset. Statistics were calculated using "lm(Normalised CXCL13 gene count ~ cancer status + CD8$^+$ T-cell CMV score + age + library RNA input, data)".

Normalised *CXCL13* expression was also compared between paired C1/C2 ICB samples for all PBMC cell types (Figure 4.27a). CD8$^+$ T-cells were the only subset found to strongly upregulate *CXCL13* post-ICB following either sICB or cICB treatment (Figure 4.27b).

Circulating CXCL13 from patient plasma was quantified by ELISA analysis to confirm if similar findings were observed at the protein level. Although CXCL13 was induced by both sICB and cICB treatments, the increase was more significant for cICB-treated samples (Figure 4.27c), although this may be related to statistical power. This may explain why B-cell changes are predominantly confined to cICB treatment due to enhanced CXCL13 production which induces B-cell migration to lymphoid tissues and increases ASCs that arise as a result of increased germinal centre activity.

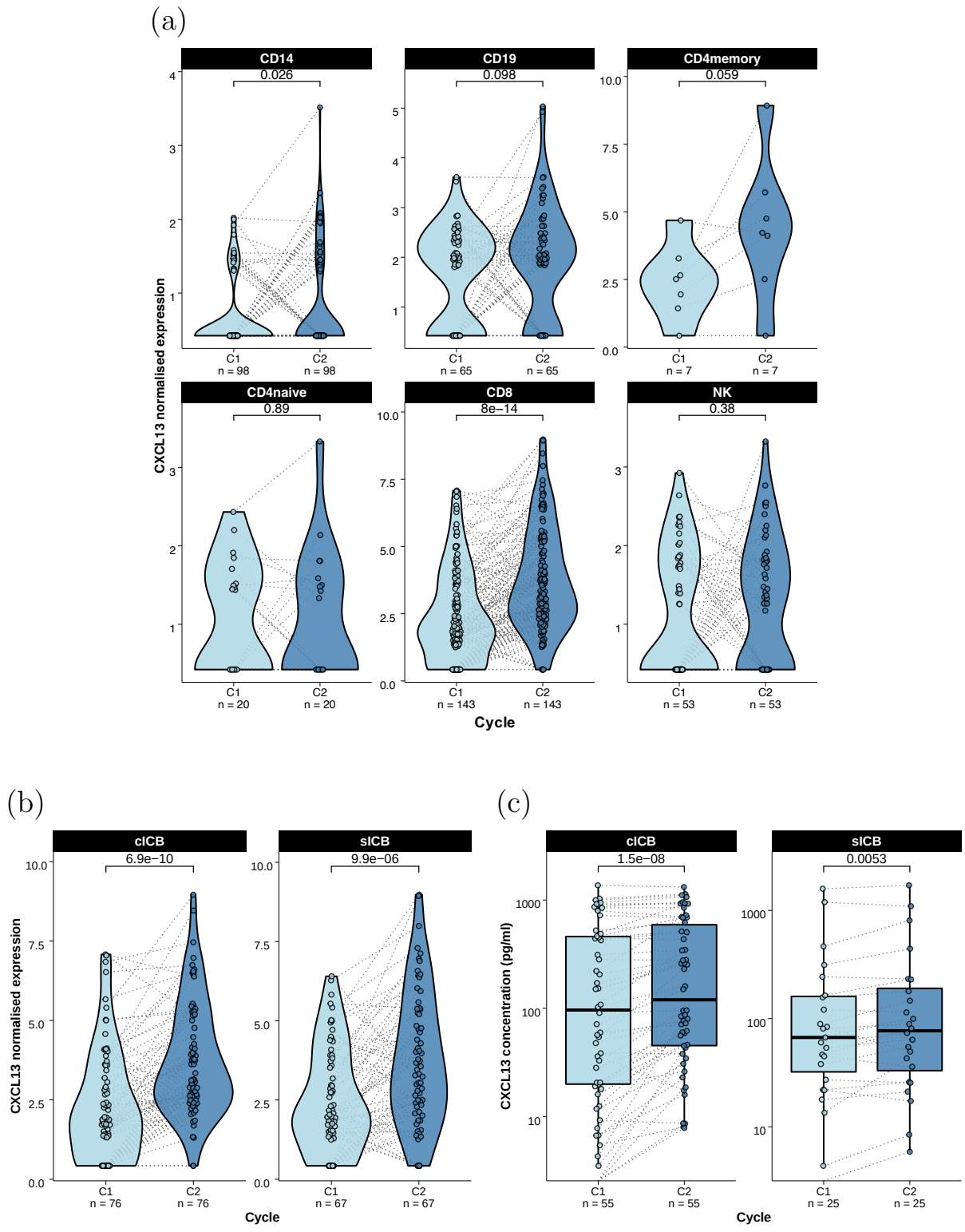


Figure 4.27 CD8$^+$ T-cells induce *CXCL13* at C2
a) Violin plots showing normalised *CXCL13* expression comparing paired C1/C2 samples (n=7-143) across different PBMC cell subsets as well as **b)** CD8$^+$ T-cells by treatment type (n=76 cICB, n=67 sICB). **c)** Circulating plasma CXCL13, quantified by ELISA, is compared between paired C1/C2 samples and faceted by ICB treatment type (n=55 cICB, n=25 sICB). Statistics were generated using paired Wilcoxon signed-rank tests.

Strikingly, induction of CD8$^+$ T-cell *CXCL13* and plasma CXCL13 was strongly correlated with the B-cell decline and induction of ASCs observed at C2 following cICB (Figures 4.28a, 4.28b). This is likely a result of increased migration to lymphoid tissue and differentiation into activated, switched CD19$^{lo/-}$ ASCs. This results in a two-pronged reduction in count due to migration to TLS's out of the blood as well as CD19 downregulation during differentiation into ASCs. It also explains the changes in subset composition, including a rise in ASCs and a loss of USM, as well as increased cell activation.

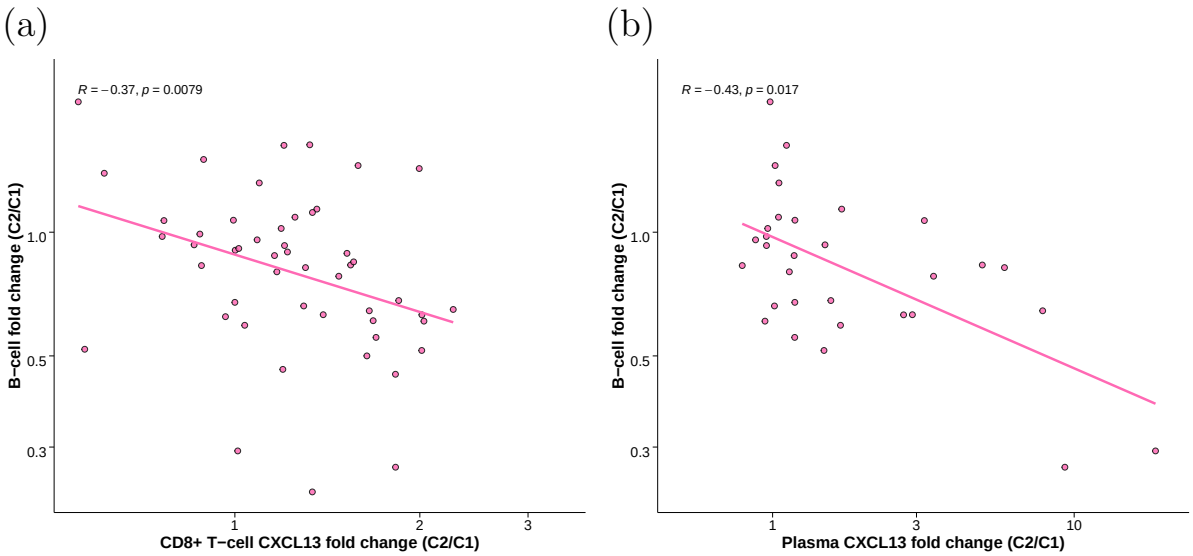


Figure 4.28 CXCL13 correlates with the peripheral B-cell depletion observed after cICB Induction of **a)** CD8$^+$ T-cell transcriptomic *CXCL13* (n=49) and **b)** plasma CXCL13 (n=44) after one cycle of cICB is compared to fold changes in circulating CD19$^+$ B-cell percentage. Statistics were generated using Spearman's rank correlation coefficient.

Whilst CXCL13 has previously been found to be upregulated following ICB and associated with enhanced survival[261,343,363–365,376,449–451], CD8$^+$ T-cell *CXCL13* was not found to associate with survival in this cohort (data not shown). However, MM patients with higher levels of plasma CXCL13 were found to have enhanced survival following sICB (data not shown). This wasn't the case for cICB treatment and may be explained by the high induction of CXCL13 by cICB in all patients and hence little variation between nonresponding and responding patients.

4.3 Conclusions

This chapter sought to explore the contribution of peripheral B-cells to the ICB response in a large cohort of MM patients on either sICB or cICB treatment arms, combining data obtained from flow cytometry, bulk RNAseq, single cell RNAseq and ELISA analyses.

Flow cytometry analysis of peripheral B-cells revealed a depletion in circulating B-cell percentage following one cycle of ICB treatment (C2). This loss was specific to cICB treatment and resolved by the fourth cycle of treatment. Similar observations have previously been made, identifying a reduction in circulating B-cell count following cICB treatment, but not after either anti-CTLA4 or anti-PD-1 treatment in isolation[458]. This indicates that the heightened response of B-cells to cICB treatment, compared to sICB, is likely due to the combined activation and not due to the specific actions of either anti-CTLA-4 or anti-PD-1 blockade individually. This mirrors what is seen in $CD8^+$ T-cells whereby cICB induces the same set of genes, but to a higher magnitude than sICB because of the increased level of activation[371,547].

Also in accordance with previous findings, an elevation in plasmablasts/plasma cells (ASCs) and chronically activated $CD21^{lo}$ cells was observed[458]. However, the data presented here also identifies novel findings including a reduction in USMs as well as an increase in B-cell activation (CD11c, CD71). This chapter also suggests that the loss in B-cells after cICB may be a combination of enhanced B-cell differentiation into $CD19^{lo/-}$ ASCs and B-cell migration into lymphoid tissue.

Bulk RNAseq analysis of $CD19^+$ B-cells from healthy donors and untreated C1 MM patients revealed a hyperactivated state in melanoma with enhanced cell division. The same is also observed when comparing paired C1/C2 samples. However, differential expression in response to ICB is uniquely observed following cICB therapy and almost completely resolves by C4, further supporting the previous findings that the effects of cICB are limited to early time-points.

Single cell RNAseq analysis identified four key subsets of peripheral B-cells including Bns, USMs, SMs and ASCs. This data allowed for subset deconvolution from bulk RNAseq data by generating a subset score, utilising the top 20 enriched genes per subset. Deconvoluted subset scores confirmed an enrichment of ASCs following cICB that was not observed after sICB therapy. Deconvoluted scores were also generated using public online datasets, further validating the enrichment in ASCs uniquely following cICB treatment[359,410,525]. However, most interestingly, an increase in ASC score at C2 was found to be predictive of favourable outcome.

This study has also uniquely assessed B-cell-PBMC interactions to better understand the dynamic changes that occur in B-cells in response to cICB. Firstly, ICB response scores were generated for all available PBMC subsets ($CD19^+$ B-cells, $CD8^+$ T-cells, $CD14^+$ monocytes and NK cells) by calculating geometric mean scores for the top 50 induced genes per subset in response to ICB. Interestingly, B-cell ICB score only correlated with PBMC ICB scores post-cICB which may be due to the magnitude of effect previously demonstrated to be higher post-cICB than sICB[371,547]. This meant that either patient magnitude of response was consistent regardless of cell type or that the degree of B-cell response was dependent on other cell types. In accordance with this, baseline B-cell PD-1 expression, using flow cytometry data, was compared to B-cell cICB score to give an indication whether B-cells could respond directly to cICB as higher PD-1 expression is anticipated to bind more ICB and ultimately result in a greater response.

Surprisingly, C1 B-cell PD-1 expression did not determine cICB responsiveness. However, a higher baseline expression of PD-1 on $CD8^+$ T-cells conferred a stronger B-cell cICB response, highlighting the importance of T-cell ICB activation for B-cell response.

Following on from this, the contribution of T-cell gene expression, using data obtained from bulk RNAseq analysis, on the B-cell cICB response was investigated. Controlling for specific individual $CD8^+$ T-cell genes completely abrogated or significantly diminished the number of B-cell DEGs post-cICB. Genes of interest included *CD38*, *MKI67* and *CXCL13*. In support of these data, induction of CD38 by $CD8^+$ T-cells, using flow cytometry data, was found to associate with B-cell changes post-cICB. However, induction did not correlate with the observed B-cell depletion indicating a contribution of additional elements.

Although $CD8^+$ T-cells seemed to be responsible for B-cell cICB response, the magnitude of $CD8^+$ T-cell activation, using ICB response scores, did not profoundly predict B-cell changes, suggesting that specific genes may be responsible and not global $CD8^+$ T-cell activation. One such gene profoundly induced by $CD8^+$ T-cells and controlling B-cell transcriptomic response was *CXCL13*. Recent publications have highlighted the importance of the B-cell attractant in the formation of TLS's[449]. Both CXCL13 level and TLS density are increased post-cICB, predicting beneficial survival outcomes[261,363–366,376,435,445,447,450,451]. Transcriptomic analysis of *CXCL13* revealed enhanced expression by $CD8^+$ T-cells in melanoma, likely representing the generation of TLS's necessary for tumour surveillance and lymphocyte function. Analogous with this finding, PD-1^+ sorted tumour-infiltrating lymphocytes were found to secrete very high levels of CXCL13, higher than any other cytokine tested[452]. Furthermore, $CXCL13^+$ $CD8^+$ T-cells have been associated with B-cell recruitment to the tumour, as well as neoantigen load[453], and therefore perhaps act as an indicator of tumour immunogenicity, known to be associated with improved outcome.

CXCL13 was further upregulated by $CD8^+$ T-cells following ICB stimulation. This corresponded with an increase in circulating plasma CXCL13 protein post-ICB. Induction of $CD8^+$ T-cell *CXCL13* and plasma CXCL13 predicted B-cell changes, including B-cell loss, which was not observed when comparing $CD8^+$ T-cell induction of CD38 or $CD8^+$ T-cell ICB score in which a stronger upregulation of *CXCL13* was associated with a greater B-cell loss. This potentially reflects the increased trafficking of B-cells from the peripheral blood into the lymphatics where they enter into subsequent germinal centre reactions, hence reducing the percentage of circulating $CD19^+$ B-cells. Here, B-cells would become activated and differentiate into ASCs.

The impact of CMV on B-cell changes was also explored, although no such association or effect on expression was detected.

4.4 Supporting Information

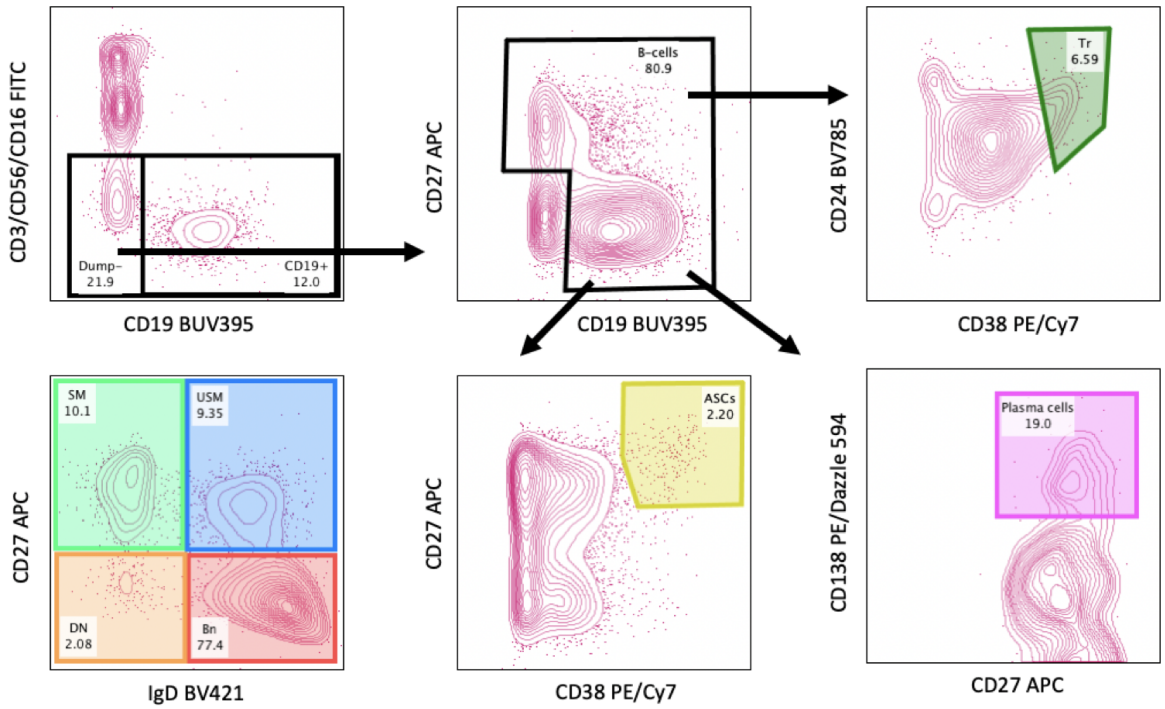


Figure S4.1 Panel B5 B-cell subset flow gating strategy
Lymphocytes were selected as before based on FSC-A/SSC-A prior to singlet selection using SSC-A and SSC-H gates and dead cell depletion using live/dead cell marker exclusion (Figures S3.1, S3.4, S3.5). $CD19^{+}$ B-cells were then gated based on absence of CD3/CD56/CD16, but expression of CD19. As ASCs may express low to undetectable levels of CD19, whole B-cells were selected from $dump^{-}$ cells ($CD3^{-}$ $CD56^{-}$ $CD16^{-}$), keeping both $CD19^{-}$ and $CD19^{+}$ cells. B-cells were then isolated by keeping either $CD19^{+}$ cells or $CD27^{hi}$ cells, representing ASCs. Transitional B-cells (Tr) were identified by high expression of both CD24 and CD38. Naïve B-cells (Bn) were detected as IgD^{+} $CD27^{-}$ cells. Memory B-cells were identified by CD27 positivity and were further subsetted into unswitched memory (USM) and switched memory (SM) B-cells based on IgD expression (USM IgD^{+}, SM IgD^{-}). Double negative (DN) B-cells were gated as IgD^{-} $CD27^{-}$ B-cells. ASCs were gated as $CD27^{hi}$ $CD38^{hi}$ cells. Specifically, plasma cells were identified by CD138 expression. B-cell activation was determined by CD11c and CD71 expression (not shown).

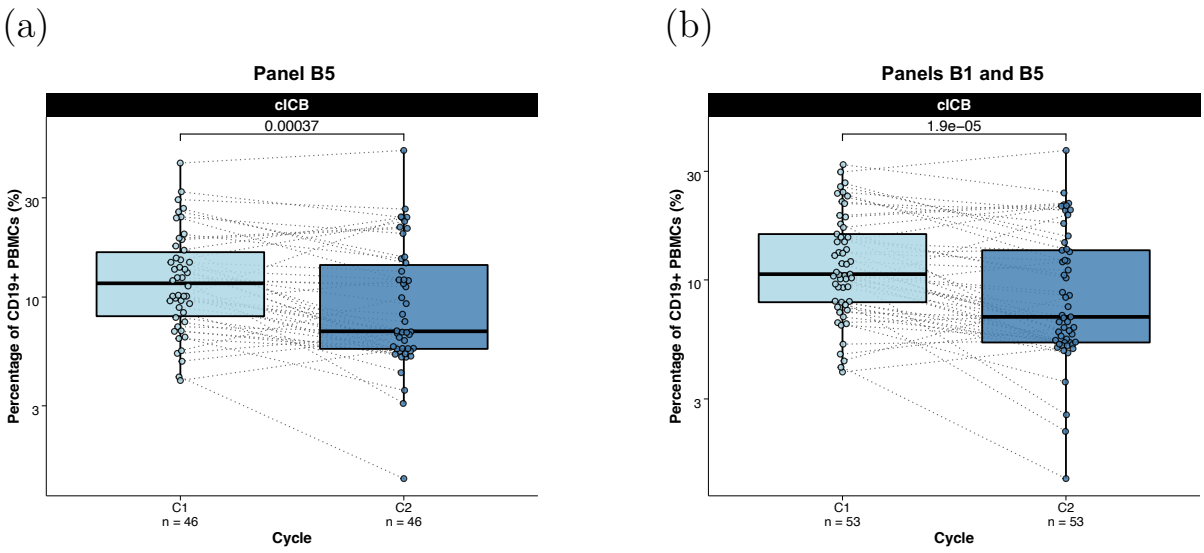


Figure S4.2 cICB causes B-cell depletion in the periphery
a) Peripheral CD19$^+$ cell percentage post-cICB in 46 paired C1/C2 cICB samples using antibody panel B5. **b)** B-cell percentages are compared between paired C1/C2 cICB samples (n=53) from both antibody panels B1 and B5. Statistics were generated using paired Wilcoxon signed-rank tests.

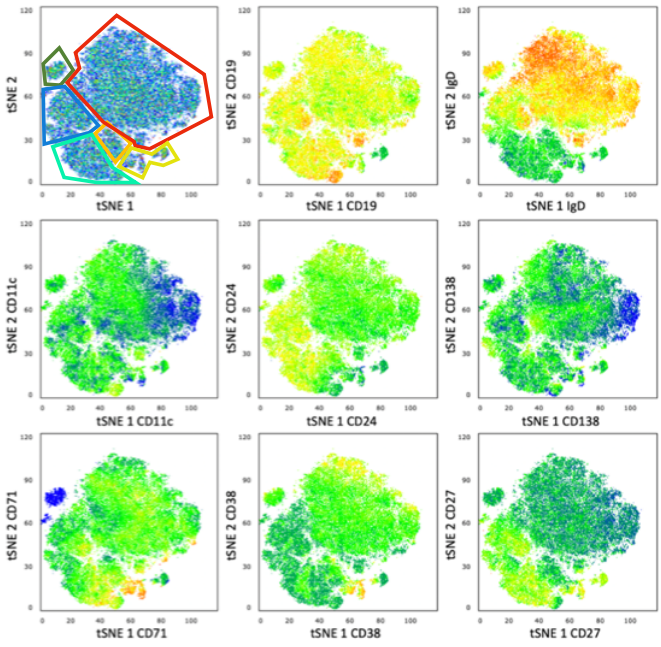


Figure S4.3 B-cell tSNE clustering of panel B5 flow cytometry data
tSNE analysis was performed on all B-cells from the panel, downsampling to the lowest number of cells out of all batches and then subsampled further to the lowest number of cells for each batch for equal sample representation. Each point represents a cell with markers coloured according to expression level, high=orange, low=blue. Each identified subset is encircled in the top left plot. *Red = naïve B-cells, dark green = transitional B-cells, blue = unswitched memory B-cells, light green = switched memory B-cells, yellow = antibody-secreting cells, orange = double negative IgD$^-$ CD27$^-$ B-cells*. Cells in other plots are coloured based on the heatmap statistic for a different marker per plot as labelled on the axes.

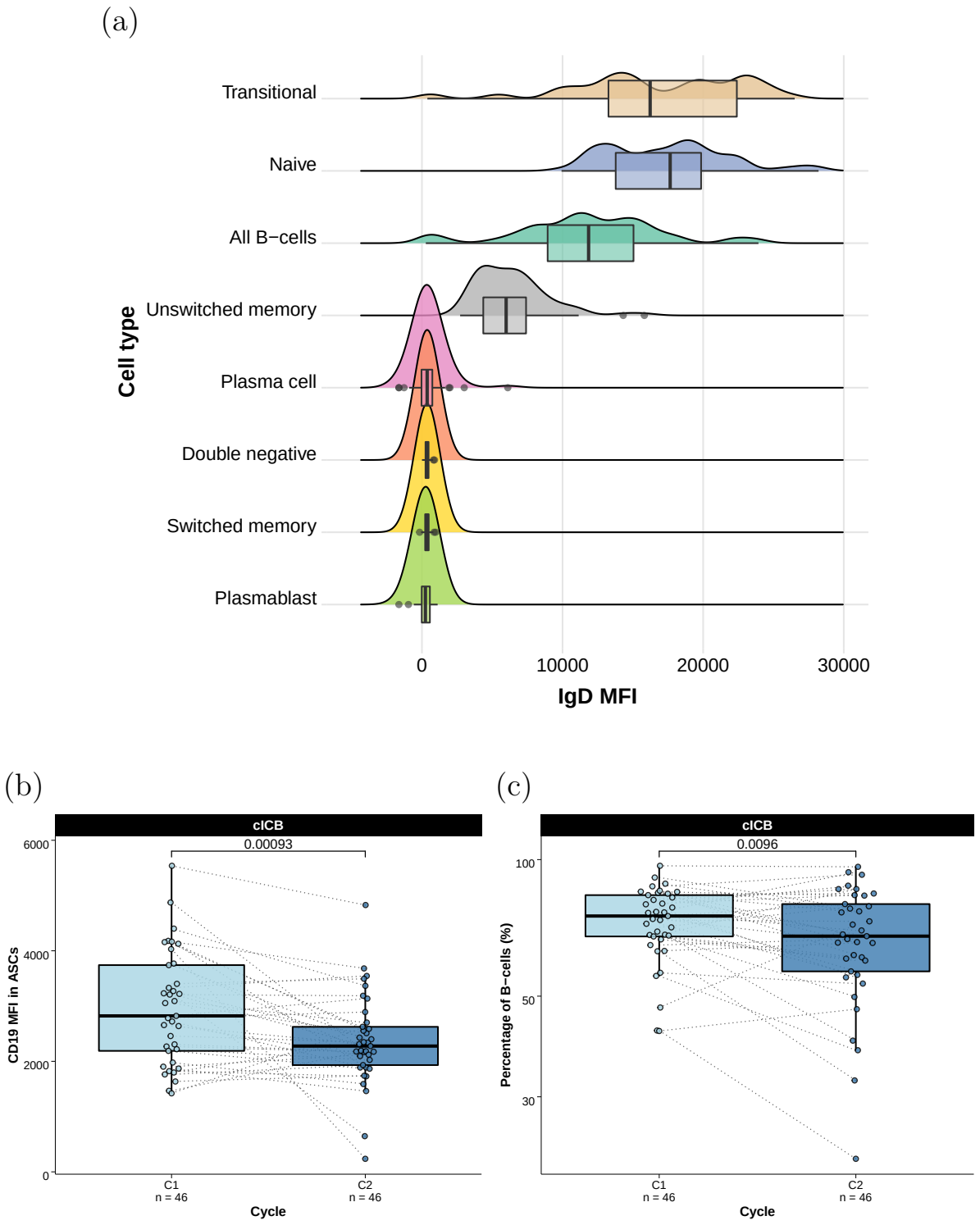


Figure S4.4 Antibody panel B5 identifies B-cell subsets and validates peripheral B-cell depletion B-cell subset and marker expression in paired C1/C2 cICB samples. **a)** IgD MFI by B-cell subset in order of expression (n=74). **b)** ASC CD19 MFI is compared between paired C1/C2 cICB samples (n=46). **c)** Percentage of all B-cells (CD19$^{\pm}$) by flow cytometry in paired C1/C2 cICB samples (n=46). Statistics were generated using paired Wilcoxon signed-rank tests.

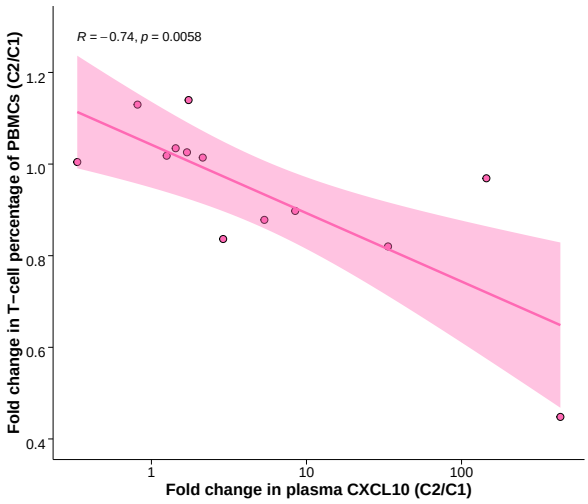


Figure S4.5 Induction of CXCL10 at C2 following cICB associates with peripheral T-cell depletion Comparison between the induction of plasma CXCL10 and the fold change in percentage of peripheral T-cells at C2 (n=13). Statistics were calculated using Spearman's rank correlation coefficient.

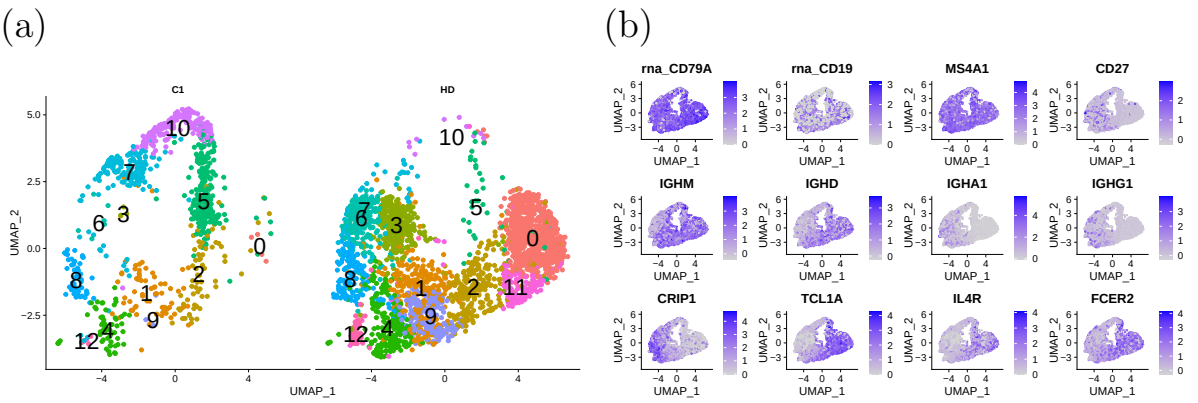


Figure S4.6 Single cell B-cell clusters and marker expression
a) All identified Seurat clusters are present in healthy donors and cancer (n=3,529 cells, n=3 healthy donors, n=1 C1 MM patient). **b)** UMAP clustering of B-cells coloured by canonical B-cell markers. *HD = healthy donor, MS4A1 = CD20, FCER2 = CD23.*

4.5 Author Contributions

Chelsea A. Taylor, Alba Verge de los Aires, Isar Nassiri, Elise A. Mahé, Sara Danielli, Rosalin A. Cooper, Orion Tong, Piyush K. Sharma, Robert A. Watson

C.A.T, E.A.M, A.V.A, S.D, O.T, P.K.S, R.A.W and R.A.C were all involved in blood collection and processing; C.A.T, E.A.M, S.D and A.V.A extracted RNA; C.A.T and A.V.A generated and pooled cDNA libraries for sequencing; C.A.T and R.A.C performed 10x single cell experiments and library preparation; I.N performed upstream RNA analysis; C.A.T performed flow cytometry analysis; C.A.T performed CXCL10 and CXCL13 ELISA analysis; John Radcliffe hospital laboratories performed ELISA analysis of anti-CMV IgG antibodies to determine CMV serostatus.

Chapter 5

Adaptive immune cell repertoires

5.1 Summary

5.1.1 Background

Both B-cells and T-cells form part of the adaptive immune system owing to expression of highly variable adaptive immune receptors and generation of immunological memory. The high specificity of these BCRs and TCRs is essential for efficient antigen detection whilst avoiding the development of autoimmunity. With profound changes detected in both $CD19^+$ B-cell and $CD8^+$ T-cell transcriptomes following ICB treatment, any alterations in corresponding BCR and TCR repertoires were subsequently investigated.

Although most studies have concentrated on tumour-associated BCR and TCR repertoires or surrounding TLS's[252,264,320,364,366,374,375,430,445,448], peripheral BCR and TCR repertoires can also provide insight into tumour ICB responses[208,250,370,371,377–380] in which peripheral T-cell clones are thought to repopulate the tumour after treatment[381]. Additionally, tumour-specific and tumour-associated TCR clones can be found within the periphery and typically adopt an effector-like phenotype[250,252,348,369,370,372,381,571]. Persistence of these tumour-reactive clones in the blood at later time-points associates with overall ICB response[454].

Despite ICB not directly affecting thymic output[250], treatment is associated with TCR diversification in both the blood and tumour, likely due to enhanced cell survival and differentiation, which associates with ICB response in several cohorts[250–252,264,363,370,379–381]. However, this is not consistently observed with some studies reporting associations of TCR convergence, clonality and stability with survival[374,377,378]. Thus, the true effect of ICB on TCR diversity remains to be determined.

CMV infection typically results in prominent changes within circulating T-cells, including terminal differentiation, exhaustion as well as inhibiting immune function, and is also thought to contribute to TCR clonality[479,480,572]. However, the effect of CMV on the ICB response is yet to be fully elucidated and may limit the extent of TCR diversification.

With the majority of studies being limited to conventional TCR clones, the impact of ICB treatment on unconventional T-cells is unclear. However, MAIT cells, an unconventional type of T-cell defined by carriage of *TRAV1-2* with *TRAJ12/TRAJ20/TRAJ33*, are shown to respond to ICB with upregulation of effector molecules including cytotoxic granzymes, *NKG7* and *IFNG* following ICB treatment[425]. In addition, a high percentage of MAIT cells is reported to be predictive of clinical

outcome following ICB treatment and may ultimately be important in eliciting ICB action[425–427]. Similarly, γδ T-cells have a restricted TCR repertoire, but associate with unfavourable clinical outcome following ICB treatment[351,391].

Whilst most studies focus on tumour-associated BCR and TCR repertoires, the impact of ICB on circulating BCR and TCR repertoires and the extent to which these changes correlate with associated transcriptomes and cell phenotypes is unclear. Furthermore, most studies that have explored circulating BCR and TCR repertoires have been limited to IGH and TRB chains, conventional T-cell clones and early ICB time-points without considering the impact on other chains, unconventional T-cells, durability of effect or the impact of CMV infection.

In this chapter, I first explore the relationship between peripheral BCR and TCR repertoires before identifying any effects of CMV infection. I then proceed to investigate the impact of melanoma on BCR and TCR profiles after normalising for any effects of CMV. Next, I establish any effects of ICB treatment on BCR and TCR repertoires, including for unconventional T-cells, assess durability of effect by tracking these changes at later time-points and discern if any of these effects are related to CMV serostatus. Finally, I monitor changes in clonal composition in response to ICB treatment and use BCR/TCR usage and online databases to identify expanding and involuting clones.

5.1.2 Aims

- What is the relationship between BCR and TCR repertoires?
- How are BCR and TCR repertoires altered in melanoma and CMV infection?
- How does ICB treatment affect peripheral BCR/TCR repertoires and clonality?
- Are any of these effects dependent on treatment type or CMV serostatus?
- What is the effect of ICB treatment on unconventional T-cell subsets?
- Can we use features of the BCR and TCR repertoires to predict clinical outcome?

5.1.3 Experimental Approach

504 $CD8^+$ T-cell and 308 $CD19^+$ B-cell high quality transcriptomes were generated from 260 (n=70 healthy donors, n=190 MM patients) and 191 (n=96 healthy donors, n=95 MM patients) individuals respectively. Fastq reads were aligned to BCR/TCR genes and annotated into different clonotypes based on BCR/TCR nucleotide sequence using *MiXCR*[503,504]. Outputs were then validated by comparison with qPCR of expanding and stable TCR clones or with flow cytometry analysis of MAIT cells, with established TCR usage, or ASCs.

Clonal metrics were compared between BCR and TCR repertoires, CMV^- and CMV^+ individuals, healthy donor and MM patients or between patients before and after ICB treatment. This included total clone number, average clonal proportion, Shannon diversity and Gini index, all of which were calculated using subsampled transcriptomes to control for differences in sequencing depth. BCR/TCR usage, including subsequently identified unconventional T-cell counts and CSR, were also compared between different samples. Additionally, BCR SHM rate was compared, taken as the average number of bases differing from reference genes as calculated by *MiXCR*. BCR and TCR clonal dynamics were assessed across the course of ICB treatment with significantly expanding and involuting clones identified using BCR/TCR usage or online datasets[511–514].

Finally, unconventional T-cell function was assessed through flow cytometry, cell stimulation and cytotoxicity assays.

5.2 Results

5.2.1 Comparison between peripheral BCR and TCR repertoires

5.2.1.1 Summary of BCR and TCR repertoires

Raw fastq files from 504 $CD8^+$ T-cell and 308 $CD19^+$ B-cell samples (Figures 3.12, 4.6) were aligned to reference BCR and TCR genes and assembled into corresponding clonotypes using *MiXCR*[503,504]. Contaminating BCR/TCR clones represented a minority of reads (Figure S5.1a, S5.1b) and were subsequently removed. BCR and TCR clones were identified by unique BCR/TCR nucleotide sequence with clonal information summarised in Tables 5.1 and 5.2 respectively.

Chain	Average number of reads per sample	Average number of clones per sample	Total number of unique clones	Total number of unique CDR3 nucleotide sequences	Total number of unique CDR3 amino acid sequences
All	108744	27829	7066587	6598910	5573754
IGH	50066	15724	4793057	4699509	4541110
IGK	33292	7046	1263362	1023619	485530
IGL	25386	5059	1010170	875784	547144

Table 5.1 BCR clonal summary for $CD19^+$ B-cell samples
Table of BCR clonal information for 308 $CD19^+$ B-cell samples for all clones or per BCR chain.

Chain	Average number of reads per sample	Average number of clones per sample	Total number of unique clones	Total number of unique CDR3 nucleotide sequences	Total number of unique CDR3 amino acid sequences
All	13035	3368	1459959	1440323	1211064
TRA	4199	1202	487632	479469	377056
TRB	7553	1918	883737	873834	769176
TRG	1157	221	76852	75431	53855
TRD	99	19	7906	7786	7631

Table 5.2 TCR clonal summary for $CD8^+$ T-cell samples
Table of TCR clonal information for 504 $CD8^+$ T-cell samples for all clones or per TCR chain.

On average, a greater proportion of BCR reads were detected per $CD19^+$ B-cell sample (0.66% ±0.56) compared to TCR reads in $CD8^+$ T-cell samples (0.038% ±0.024) regardless of sequencing batch (Figure S5.2a). This reflects the higher level of expression of BCR detected per B-cell compared to the level of TCR per T-cell that is observed in single cell datasets[208] (Figure S5.2b). B-cells express a high level of BCR, especially following CSR and by ASCs, which is important for antibody secretion (Figure S5.3). This is in contrast to T-cells which only express TCR at the surface and instead internalise and downregulate TCR in response to activation and subsequent PD-1 upregulation[178].

BCR and TCR clones of average amino acid lengths 15 and 14 respectively were selected and summarised by logo plot (Figure 5.1a, 5.1b). Almost all BCR and TCR

clone CDR3 regions began with a cysteine residue and ended with either a phenylalanine or a tryptophan residue (in the case of IGH clones) and were most variable in the central portion. As a result, any clone not commencing with a cysteine or ending with a phenylalanine/tryptophan residue was removed from subsequent analyses.

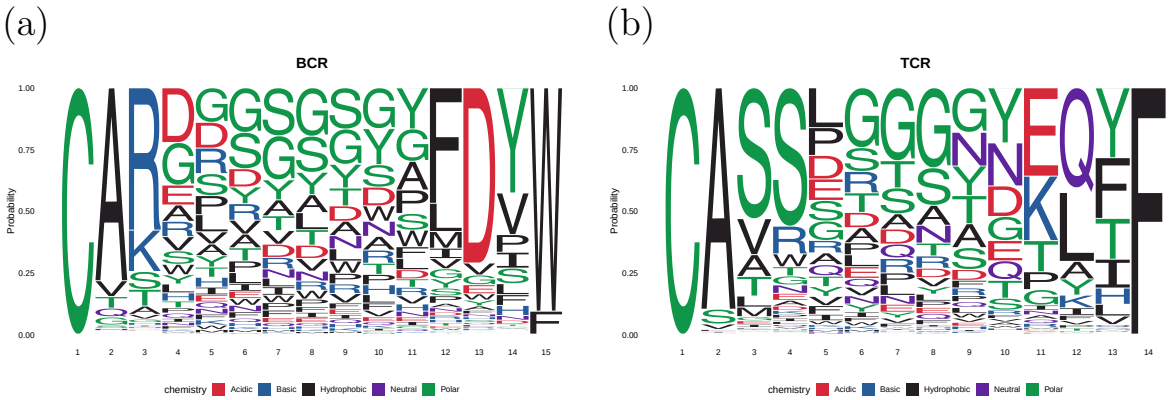


Figure 5.1 Summarised BCR/TCR CDR3 amino acid sequences
a) BCR (n=308) and **b)** TCR (n=504) CDR3 amino acid sequences of lengths 15 and 14 residues respectively are summarised by logo plot including the probability of expressing each residue at each position. Individual residues are coloured by amino acid chemistry and are displayed in sequential order.

5.2.1.2 *MiXCR* validation

MiXCR TCR alignment was validated for CD8$^+$ T-cell samples by comparing *MiXCR* imputed clonal expansion from C1 to C2 with that detected by qPCR. TCR primers were designed to capture large clones for both TRA and TRB chains including for clones either stable or expanding at C2. Detection of these clones by qPCR confirmed that stable clones had little change in expression at C2, but that expanding clones were highly enriched (Figure 5.2a). Clonal changes at C2 as detected by *MiXCR* and qPCR were very strongly correlated, hence verifying *MiXCR* alignment of TCR clones (Figure 5.2b). In addition, MAIT cell percentage, as identified by calculating the percentage of TRA reads that expressed MAIT cell-associated *TRAV1-2* recombined with *TRAJ12/TRAJ20/TRAJ33*, strongly correlated with percentages derived from flow cytometry data, further demonstrating the reliability of *MiXCR* TCR alignment (Figure 5.2c).

Assuming that most ASCs have undergone CSR, *MiXCR* BCR alignment was verified through the correlation of IGHC usage with paired flow cytometry ASC percentage (Figure 5.3). This demonstrated a profound inverse correlation of unswitched isotypes IgM and IgD with ASCs and a concomitant association with switched heavy chain constants IgG and IgA. No association was found between ASC percentage and IgG4/IgE usage, but this may be due to low expression. CD19$^+$ B-cell IGHC usage similarly correlated with flow cytometry plasma cell percentage as identified by CD138 expression (Figure S5.4).

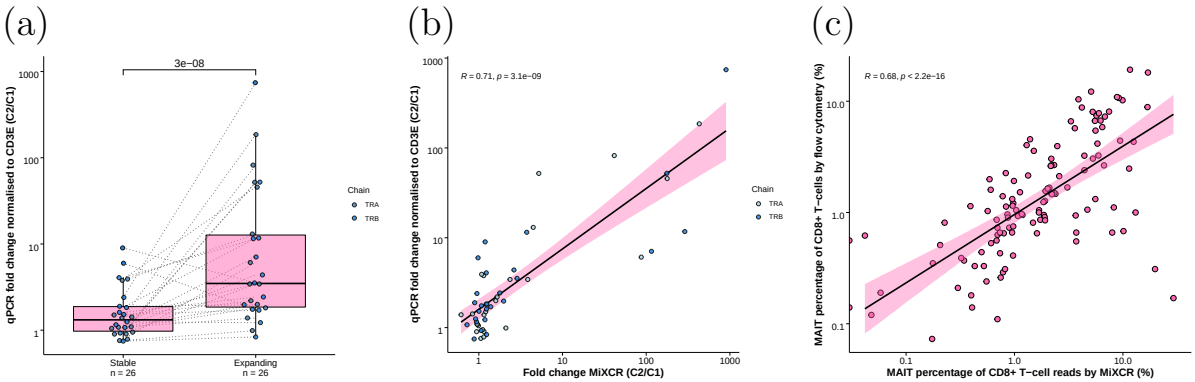


Figure 5.2 $MiXCR$-aligned TCR data corresponds with qPCR and flow cytometry analyses
qPCR analysis was performed on 13 paired C1/C2 patient samples including stable and expanding TRA and TRB clones. **a)** Clonal change at C2 was detected by qPCR after normalisation to CD3E and is compared between expanding and nonexpanding TRA and TRB clones (n=26 stable clones, n=26 expanding clones). Statistics were calculated using a paired Wilcoxon signed-rank test. **b)** Fold changes in stable and expanding TRA and TRB clones at C2 are compared between qPCR and $MiXCR$ detection methods (n=52). **c)** Correlation of flow cytometry CD8$^+$ MAIT cell and $MiXCR$-deconvoluted CD8$^+$ MAIT cell percentages (n=121). Statistics were calculated using Spearman's rank correlation coefficient.

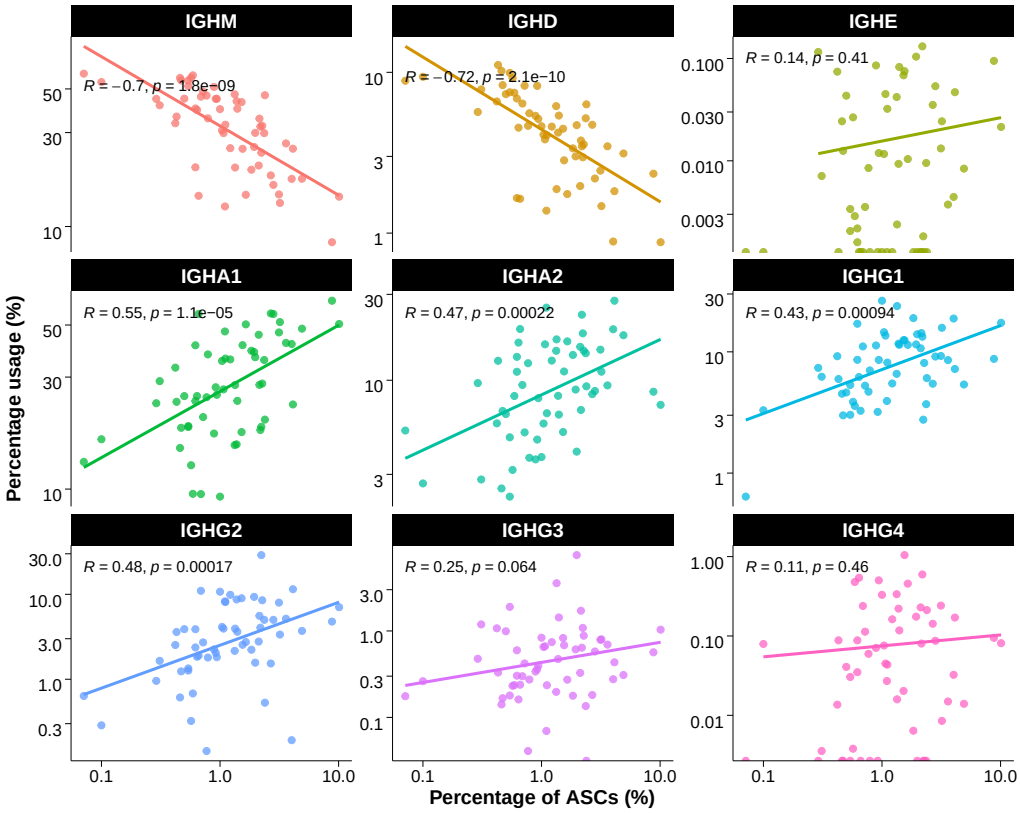


Figure 5.3 $MiXCR$ IGHC alignment correlates with flow cytometry ASC percentage
Antibody-secreting cell (ASC) percentage was identified by flow cytometry and correlated with $MiXCR$-aligned IGHC clone usage by unique isotype (n=57). Statistics were calculated using Spearman's rank correlation coefficient.

5.2.1.3 The BCR repertoire is more diverse than the TCR repertoire

In order to compare BCR and TCR metrics, 192 paired $CD19^+$ B-cell and $CD8^+$ T-cell samples were randomly subsampled to the lowest number of reads observed in a sample (n=1,496 reads) to control for differences in sequencing depth. Various parameters including the total number of clones detected, average clone size by percentage of repertoire, Shannon diversity and Gini index were calculated after subsampling. Analysis was repeated 1,000 times taking the average from these 1,000 iterations for each metric. Paired BCR/TCR metrics were compared after normalising for library RNA input which contributes to sequencing breadth, the percentage of fastq reads aligning to BCR/TCR genes and hence, the average number of reads identified per clone (Figures S5.5a, S5.5b).

After adopting this approach, almost twice the number of clones were detected on average per $CD19^+$ B-cell sample (1235 ±181) compared to $CD8^+$ T-cell samples (675 ±262) (Figure 5.4a). Accordingly, B-cell clones were half the size of $CD8^+$ T-cell clones, accounting for an average of 0.09% (±0.04) and 0.18% (±0.09) of the total repertoire respectively (Figure 5.4b). Subsequently, this resulted in greater clonal richness and less clonal unevenness, as quantified by Shannon diversity (BCR 6.89 ±0.71; TCR 5.54 ±0.90) and Gini index (BCR 0.16 ±0.12; TCR 0.50 ±0.16) respectively (Figures 5.4c, 5.4d).

After separating BCR and TCR clones into different clonal size categories using subsampled data (n=1,496 reads), the majority of BCR and TCR clones were found to represent 0-0.1% of BCR and TCR repertoires respectively (Figure 5.5a). However, a significantly higher proportion of TCR clones were identified as large (≥0.1%) compared to BCR clones (Figure 5.5b). In keeping with BCR clones being smaller, even the largest BCR clone still represented a significantly smaller proportion of the repertoire compared to the top TCR clone (Figure S5.6). Whilst the average clonal proportion rapidly grew with the inclusion of an increasing number of the top TCR clones, the clonal proportion of the top BCR clones only gradually increased with an increasing number of clones. This was until inclusion of the top 500 clones at which point the average clonal proportion rapidly increased.

In order to further understand the differences in diversity of adaptive immune receptors, BCR and TCR synonymy was calculated. This was quantified as the difference in number of unique CDR3 clones by nucleotide and amino acid sequences and expressed as a percentage of total identified clones. Although twice the number of BCR clones were identified on average compared to TCR clones (Figure 5.4a), a larger proportion of these BCR clones (10.7% ±1.2) were synonymous in comparison with TCR clones (1.1% ±0.5) (Figure 5.6a). This means that many more BCR clones are redundant with distinct nucleotide sequences producing identical clones by amino acid sequence. This may be as a result of SHM which hypermutates BCRs in germinal centre reactions and generates several similar clones which only differ by a few bases, but still produce identical amino acid sequences.

Analysis was also repeated by individual BCR chain and revealed that whilst high synonymy was observed for IGK (26.0% ±3.6) and IGL (16.6% ±3.3) chains, most IGH clones were nonsynonymous (1.5% ±1.3) (Figure 5.6b). This may refer to the greater diversity observed within heavy chains compared to light chains, calculated after subsampling to the same number of reads (n=1,028) (Figures S5.7a, S5.7b), as well as the CSR that occurs exclusively in IGH chains. Analysis by TCR chain demonstrated that TRA and TRG chains were more synonymous (TRA 1.5% ±0.8; TRG 1.8% ±1.3) than TRB (0.6% ±0.4) and TRD (0.3% ±1.4) chains (Figure 5.6c). However, these differences

were not as profound as between BCR chains. Whilst the low synonymy observed for TRD clones may be dictated by the low number of TRD clones detected, low synonymy in the TRB chain may represent the highest combination of gene segments and increased junctional diversity. However, after subsampling to the same number of reads (n=100), TRA still represented the most diverse TCR chain (Figures S5.7c, S5.7d).

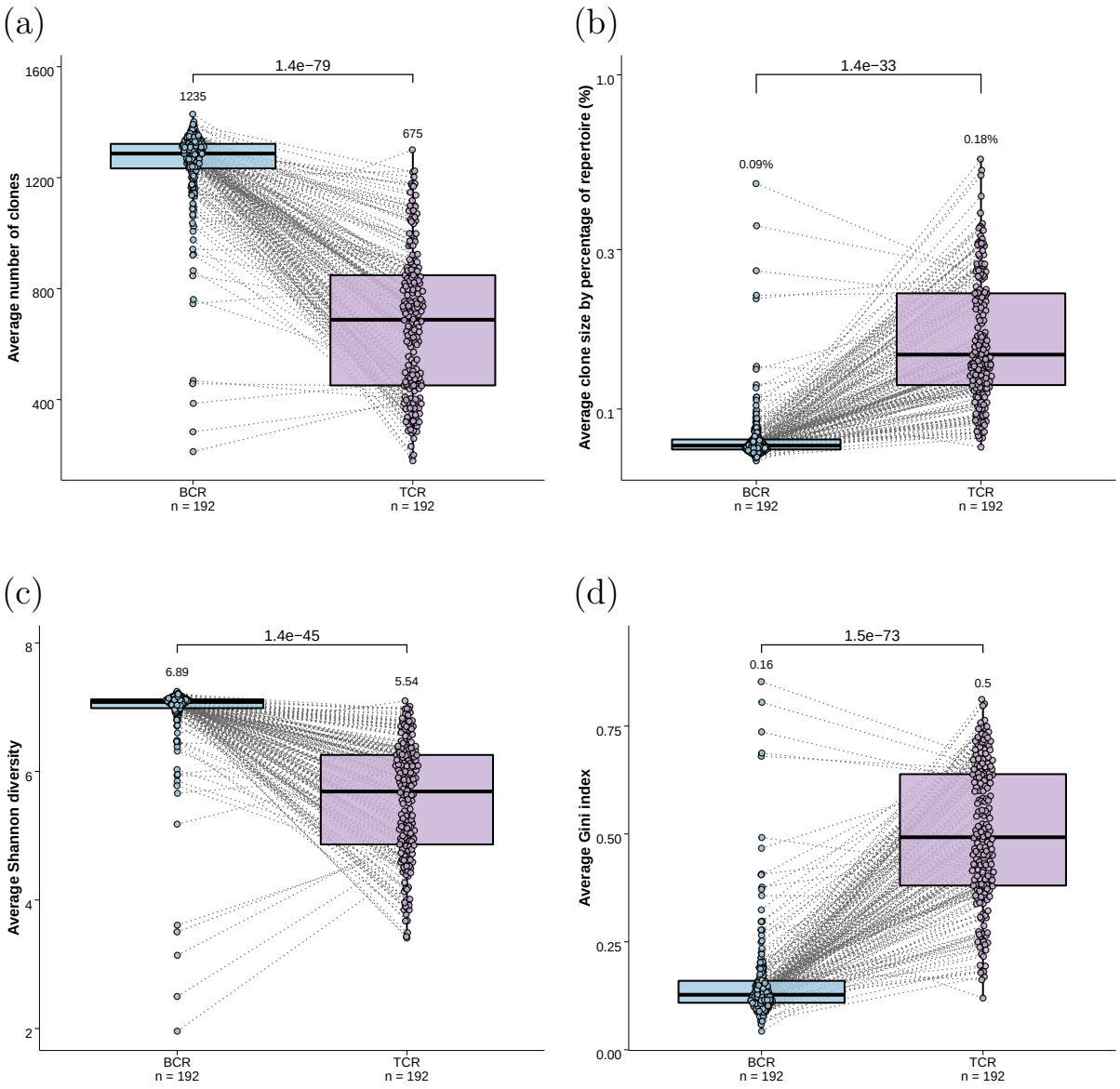


Figure 5.4 The BCR repertoire displays greater diversity than the CD8$^+$ T-cell TCR repertoire Comparison of the average **a)** number of clones, **b)** clone proportion, **c)** Shannon diversity and **d)** Gini index between 192 paired BCR and TCR repertoires. Average values were calculated from 1,000 iterations, using data subsampled to 1,496 reads per sample, and are displayed above each box plot. Statistics were calculated using lm(Shannon diversity/Gini index $\sim$ BCR/TCR + library RNA input, data).

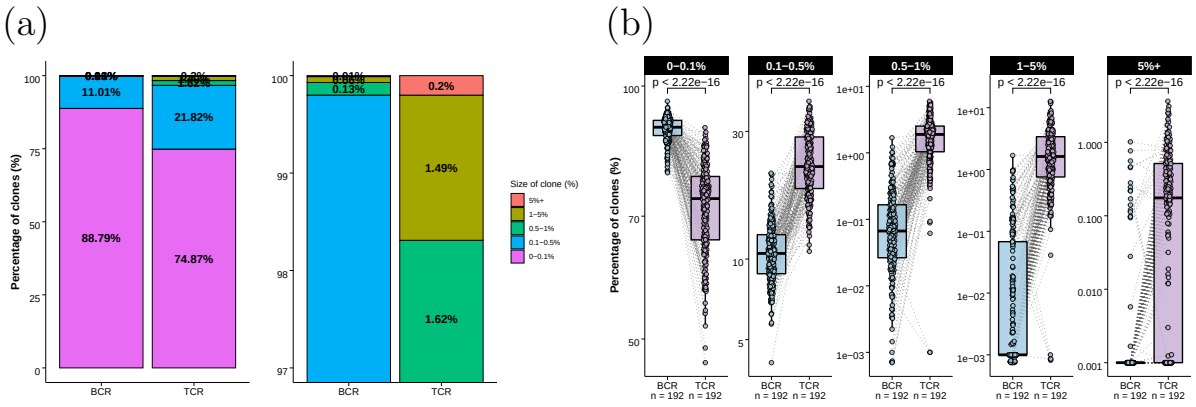


Figure 5.5 The TCR repertoire is made up of more large clones than the BCR repertoire
The number of clones of varying size is compared between paired subsampled BCR and TCR repertoires (n=192 samples, n=1,496 reads). **a)** Bar plots displaying the average percentage of clones that are identified per size bracket compare BCR and TCR repertoires with mean repertoire percentage displayed per bar for all sizes (left). A magnified view is included to visualise larger clone brackets (right). **b)** Box plots depicting clone repertoire percentages after subsampling and comparing paired BCR/TCR repertoires per clonal size bracket. Statistics were generated using lm(Percentage of clones ∼ BCR/TCR + library RNA input, data).

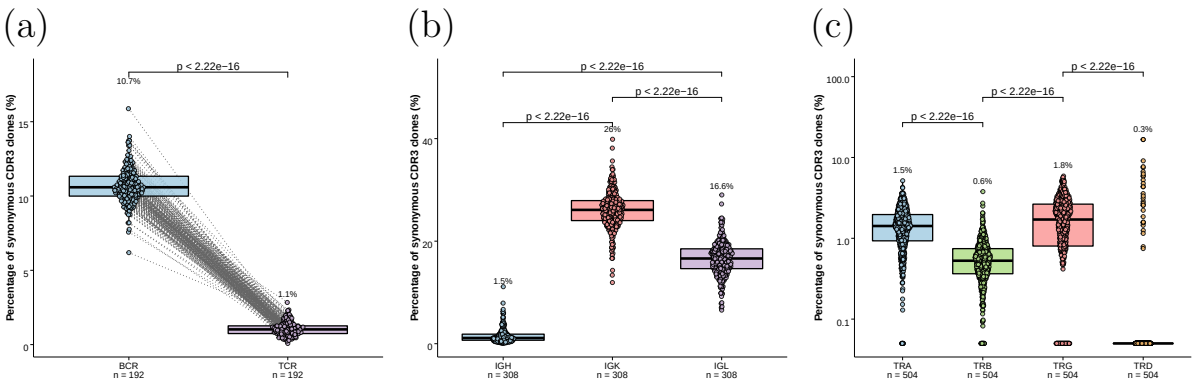


Figure 5.6 BCR clones are more synonymous than TCR clones
Clone synonymy was calculated for BCR and TCR clones by quantifying the percentage of CDR3 nucleotide sequences that result in expression of redundant CDR3 amino acid clones. Average synonymy is compared between **a)** paired CD19$^+$ B-cell and CD8$^+$ T-cell samples (n=192) as well as between distinct **b)** BCR (n=308) and **c)** TCR (n=504) chains. Average percentages are displayed above each box plot. Statistics were generated using paired Wilcoxon signed-rank tests.

Perhaps reflective of the greater diversity observed within the BCR repertoire and the capacity for binding native antigen, BCR CDR3 segments were almost three nucleotides longer on average than TCR CDR3 segments (BCR 44.6 ±1.1 nucleotides, TCR 42.2 ±0.5 nucleotides), encoding an extra amino acid (Figure 5.7a).

Next, the average number of mutations per BCR and TCR clone were detected by *MiXCR* after comparison with reference genes. These mutations included base substitutions, insertions and deletions. A higher number of mutations on average

were detected in BCR clones compared to TCR clones, representative of junctional diversity and SHM, and may also contribute to the increased diversity of BCRs (Figure 5.7b). Mutations were enriched within V genes in both BCR and TCR clones (Figures S5.8a, S5.8b). A higher mutation rate was observed within BCR light chains and within TRB/TRD TCR chains compared to BCR heavy chains and TRA/TRG chains respectively (Figures S5.8c, S5.8d). Furthermore, a higher mutation rate was observed in switched IGHC clones (IgG/IgA/IgE) compared to unswitched (IgM/IgD), demonstrating the association between CSR and SHM, both of which occur in germinal centre reactions (Figure S5.8e).

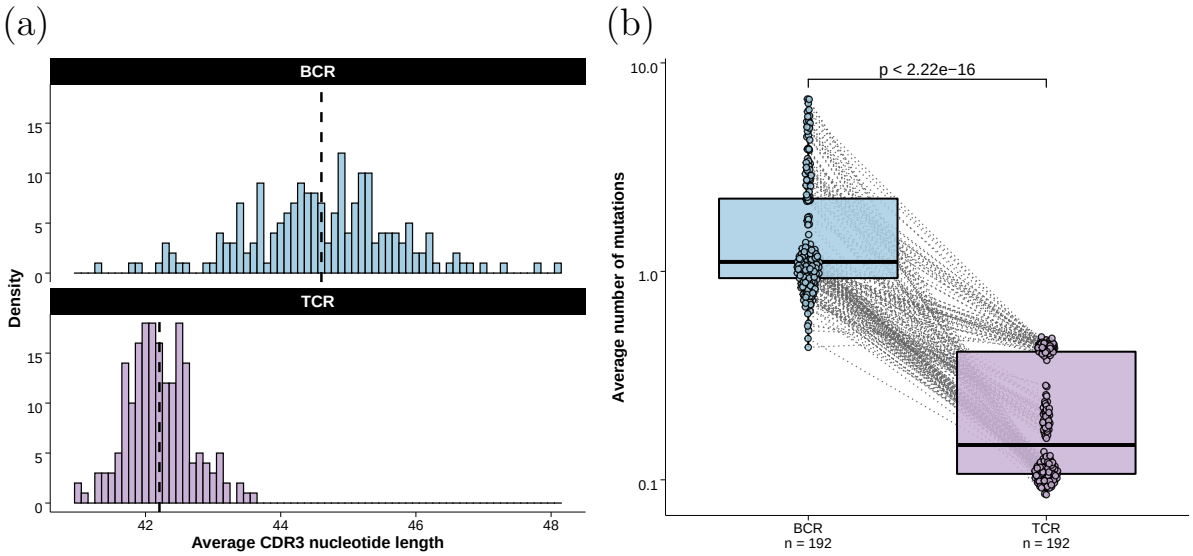


Figure 5.7 BCR clones have longer CDR3 nucleotide sequences and more mutations than TCR clones

a) Histograms of average CDR3 length by nucleotide sequence for BCR (top, n=192) and TCR (bottom, n=192) clones. A dashed line represents the average CDR3 length. **b)** Box plots showing the average number of mutations detected per BCR and TCR clone in paired samples (n=192). Statistics were calculated using a paired Wilcoxon signed-rank test.

5.2.2 CMV has profound effects on the CD8$^+$ T-cell TCR repertoire

5.2.2.1 CMV infection reduces TCR diversity

In order to appreciate the effect of melanoma and ICB treatment on BCR/TCR repertoires, any effects of CMV serostatus were first elucidated by looking at CMV-tested healthy donor and untreated patient (C1) samples. BCR and TCR metrics were compared between CMV$^-$ (n=50 BCR; n=83 TCR) and CMV$^+$ (n=43 BCR; n=78 TCR) individuals after controlling for age, library RNA input and cancer status.

Although no differences were observed in average number and size of BCR clones after subsampling, CMV was found to significantly reduce the number of TCR clones identified (CMV$^-$ 826 ±226; CMV$^+$ 554 ±238) and ultimately resulted in enlarged clones, represented as average clonal percentage of all subsampled TCR reads (CMV$^-$ 0.14% ±0.07; CMV$^+$ 0.22% ±0.10) (Figures 5.8a, 5.8b, 5.8c, 5.8d).

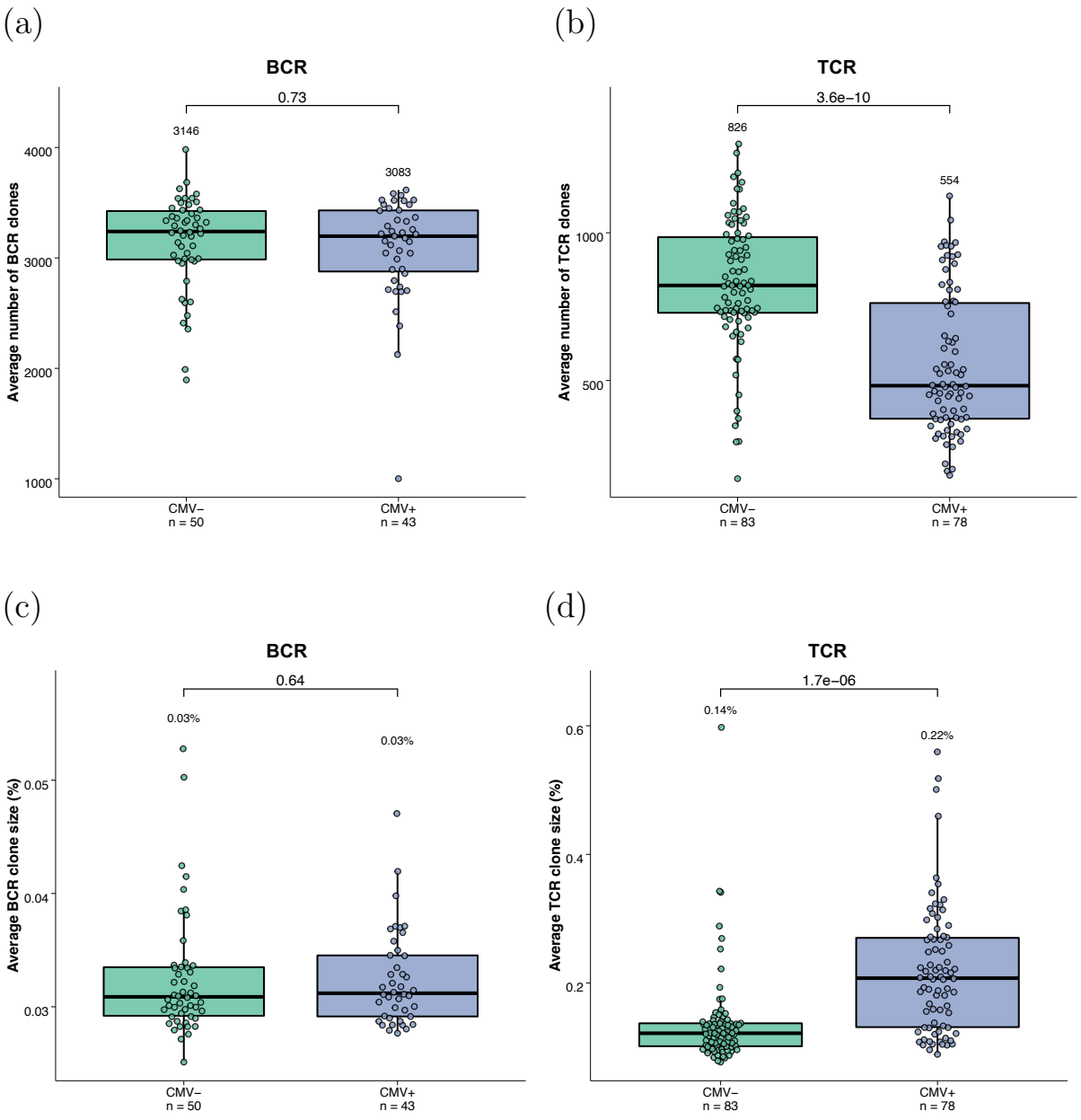


Figure 5.8 CMV serostatus associates with enlarged TCR clones
$CD19^+$ B-cell (CMV^- n=50, CMV^+ n=43) and $CD8^+$ T-cell (CMV^- n=83, CMV^+ n=78) samples were subsampled to 4,471 and 1,496 reads respectively, calculating the average number of clones and relative clonal size taken from 1,000 iterations. Box plots show the average number of **a)** BCR and **b)** TCR clones detected and average clonal percentage of **c)** BCR and **d)** TCR repertoires. Average values are displayed above each box plot. Statistics were calculated using "lm(metric ∼ CMV serostatus + library RNA input + age + cancer status, data)".

In keeping with the similarity in BCR clone number and size between CMV$^-$ and CMV$^+$ individuals, no differences in BCR Shannon diversity or Gini index were detected (Figure 5.9a). However, in accordance with the disparity in number of TCR clones and average clonal proportion, CD8$^+$ T-cells were found to be more clonal in CMV$^+$ individuals compared to CMV$^-$ individuals, with a lower Shannon diversity and a higher Gini index observed for most TCR chains (Figure 5.9b).

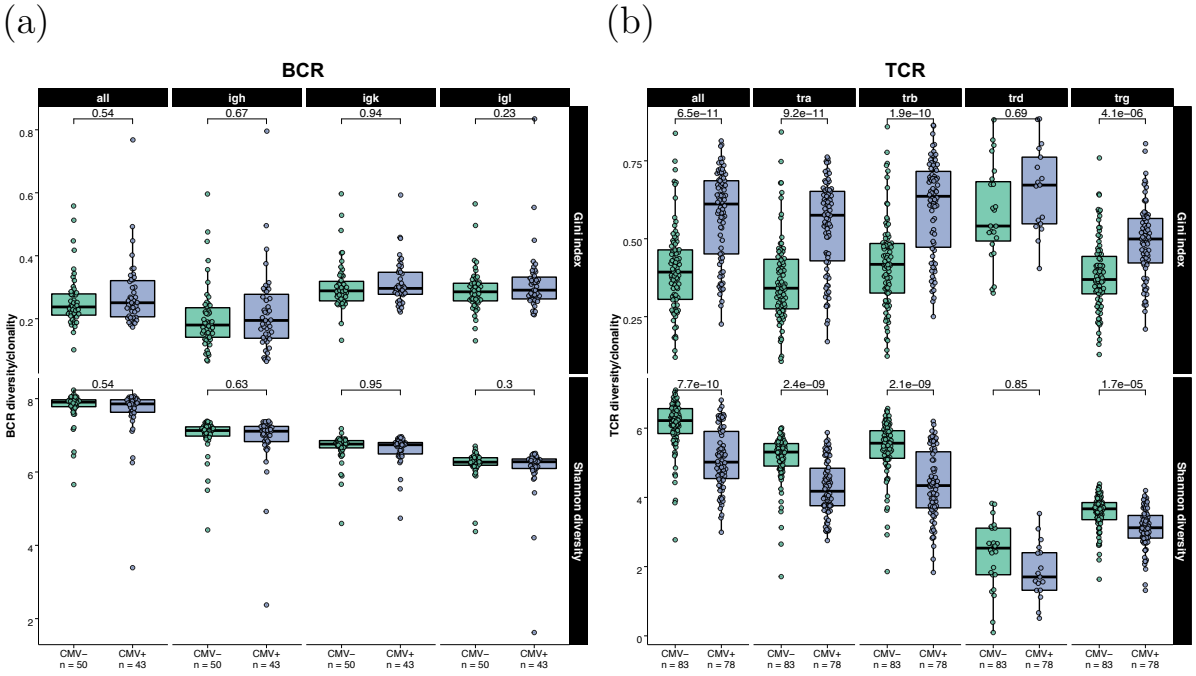


Figure 5.9 CD8$^+$ T-cells are more clonal in CMV$^+$ individuals
CD19$^+$ B-cell (CMV$^-$ n=50, CMV$^+$ n=43) and CD8$^+$ T-cell (CMV$^-$ n=83, CMV$^+$ n=78) samples were subsampled to 4,471 and 1,496 reads respectively, calculating the average Shannon diversity and Gini index across 1,000 iterations. Average Shannon diversity and Gini index were calculated for **a)** BCR and **b)** TCR samples and compared between CMV$^-$ and CMV$^+$ individuals. Statistics were calculated using "lm(Shannon diversity/Gini index $\sim$ CMV serostatus + library RNA input + age + cancer status, data)".

Furthermore, no differences were observed in BCR clone composition by clonal size (Figure 5.10a, 5.10b). Conversely, less small (0-0.1%) TCR clones were found in CMV$^+$ patients, with an increased number of larger clones which occurred at clone sizes $\geq$0.5% (Figures 5.10a, 5.10c).

5.2.2.2 Peripheral MAIT cells are depleted in CMV$^+$ individuals

BCR and TCR chain expression were compared between CMV$^-$ and CMV$^+$ individuals using *MiXCR* gene counts and employing *DESeq*2 differential analysis, after controlling for age, library RNA input, sequencing batch and cancer status. Unsurprisingly, BCR chain expression, together with light chain usage and CSR, taken as IGHC usage, were unaffected (Figures 5.11a, S5.9, S5.10a, S5.10b) as was BCR mutation rate (Figure S5.11).

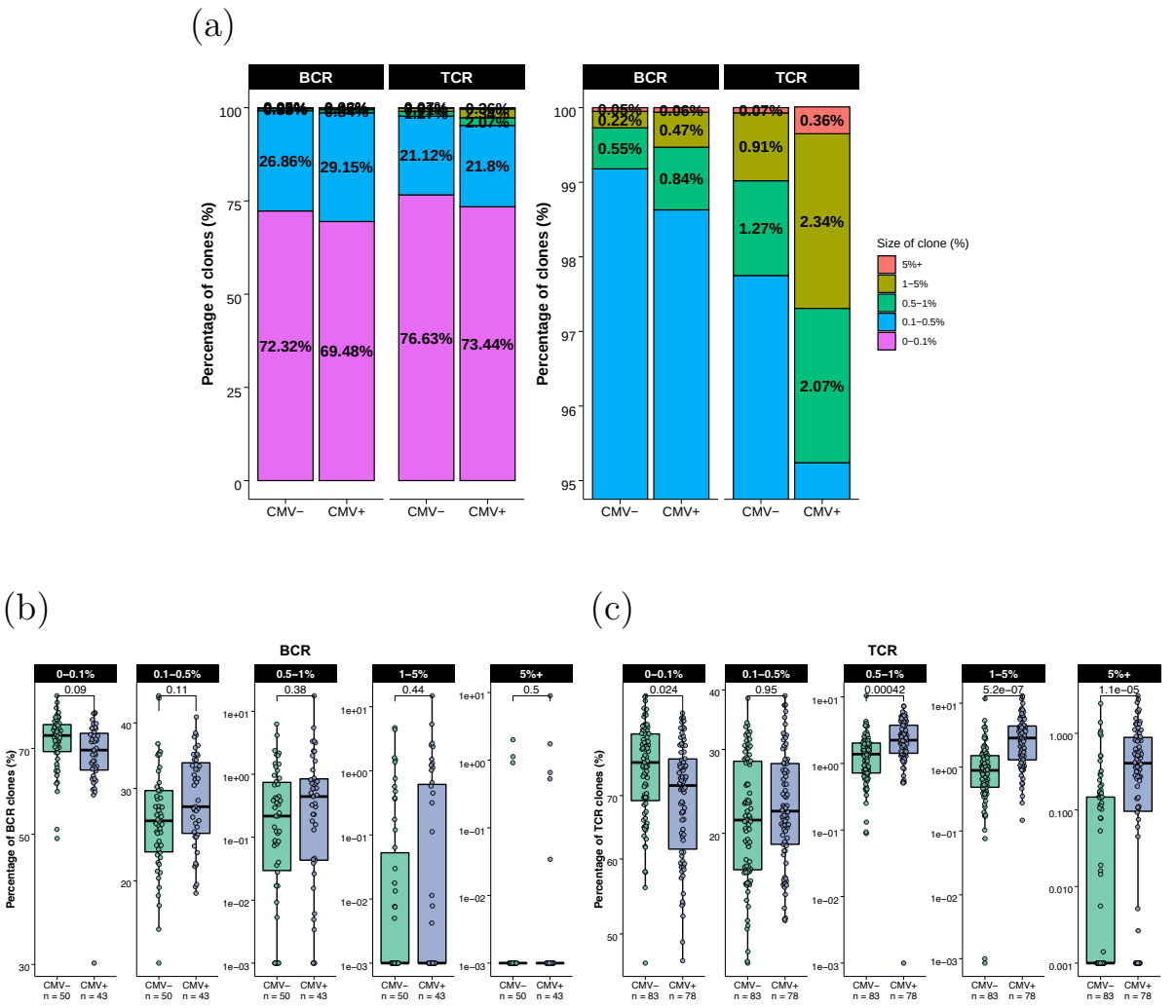


Figure 5.10 CMV$^+$ individuals have more large T-cell clones
The percentage of clones at a range of clone sizes is compared between CMV$^-$ and CMV$^+$ individuals for BCR (CMV$^-$ n=50, CMV$^+$ n=43) and TCR (CMV$^-$ n=83, CMV$^+$ n=78) samples after subsampling to 4,471 and 1,496 reads respectively. Bar plots show the average percentage of **a)** BCR and TCR clones for all clone size brackets (left) and are magnified to visualise larger clone ranges (right). Averages are displayed per bar plot. Raw clone percentages at each clone size are compared between CMV$^-$ and CMV$^+$ individuals for **b)** BCR and **c)** TCR samples. Statistics were calculated using "lm(Percentage of clones ~ CMV serostatus + age + library RNA input + cancer status, data)".

Conversely, several TCR genes were found to be differentially expressed between CMV$^-$ and CMV$^+$ individuals (Figure 5.11b). This included downregulation of MAIT cell-associated genes *TRAV1-2*, *TRAJ33* and *TRBV6-4* in CMV$^+$ individuals. To validate this downregulation, unconventional T-cell percentages were generated after subsampling to the same number of TCR (1,496) or TRA (487) reads per sample for γδ T-cells and MAIT/iNKT cells respectively. The average percentages from 1,000 iterations was subsequently used. In support of the flow cytometry data from Chapter three (Figure 3.6), no differences in iNKT cells or γδ T-cells were observed between CMV$^-$ and CMV$^+$ individuals. However, a profound depletion in MAIT cells was detected by both total TRA read count and proportion of TRA clones after controlling for age, library RNA

input and cancer status (Figures 5.12a, 5.12b).

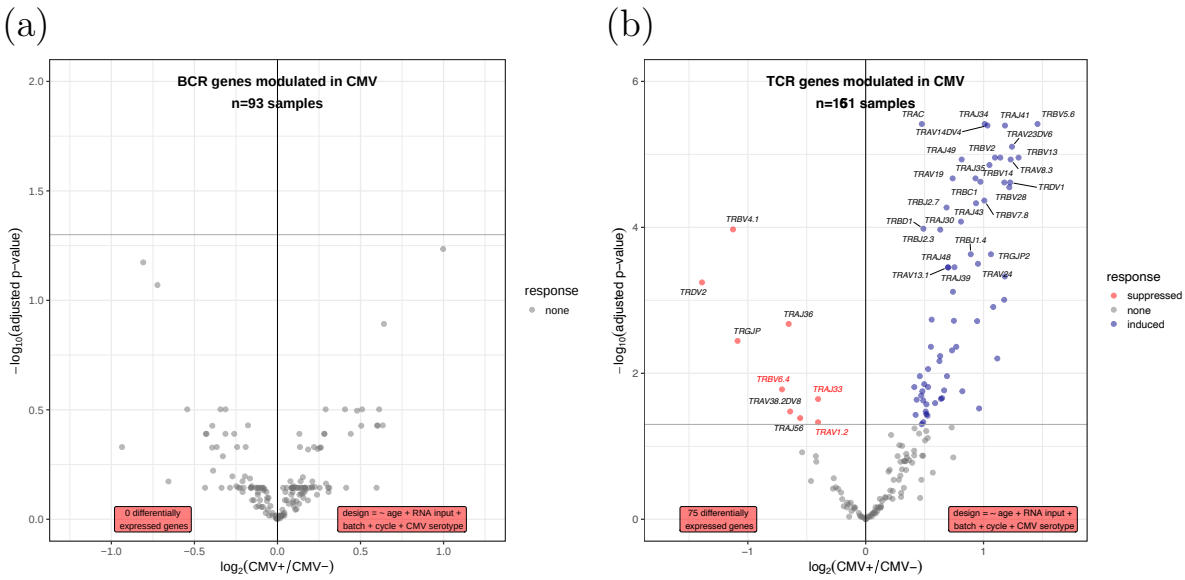


Figure 5.11 CMV infection induces differential TCR usage
$DESeq2$ was used to compare expression of normalised **a)** BCR and **b)** TCR gene counts between CMV$^-$ (n=50 BCR, n=83 TCR) and CMV$^+$ (n=43 BCR, n=78 TCR) individuals. Genes significantly enriched in CMV$^+$ patients are in blue and those significantly depleted in CMV$^+$ patients are in red. The $\log_2$ fold change of each gene is visualised on the x-axis with the significance of this difference displayed on the y-axis. The number of significant DEGs as well as the $DESeq2$ design formula are displayed in red boxes. MAIT cell-associated TCR genes are highlighted in red. Statistics were calculated using the negative binomial distribution and adjusted for multiple testing using the Benjamini-Hochberg procedure on $DESeq2$.

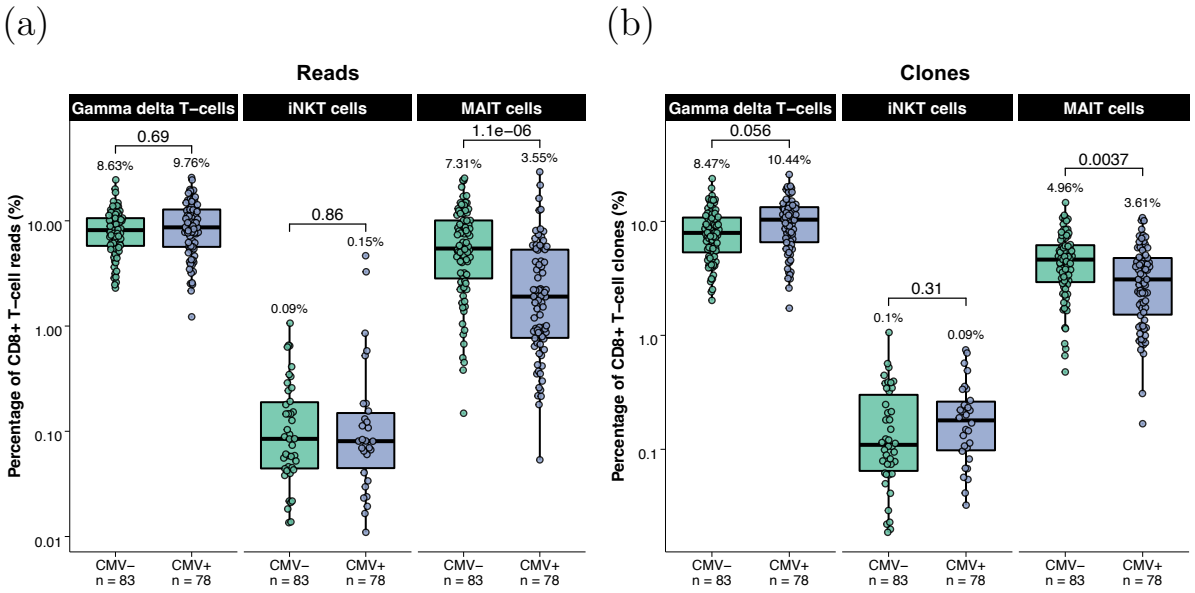


Figure 5.12

Figure 5.12 (Previous page) Peripheral MAIT cells are depleted in CMV$^+$ individuals
Unconventional T-cell percentages were calculated after subsampling to 1,496 reads and taking the average from 1,000 iterations. Subsequent unconventional T-cell percentages are compared between CMV$^-$ (n=83) and CMV$^+$ (n=78) individuals and were calculated as either the percentage of CD8$^+$ T-cell **a)** reads or **b)** unique clones expressing relevant TCR genes. Average percentages are displayed above each box plot. Statistics were calculated using "lm($\log_{10}$(Unconventional T-cell count) $\sim$ CMV serostatus + age + library RNA input + cancer status, data)"

With a reduction in peripheral MAIT cell proportion detected in CMV$^+$ individuals, Shannon diversity and Gini indexes were calculated from either MAIT cell or γδ T-cell clones after subsampling to 100 reads and taking the average from 1,000 iterations. With iNKT clones not detectable for many samples after subsampling, iNKT diversity and clonality were not investigated further. After controlling for age, library RNA input and cancer status, both MAIT and γδ T-cell Shannon diversity were found to be reduced in CMV$^+$ individuals, albeit much more significantly for γδ T-cells (Figure 5.13a). This reduction was associated with a higher Gini index for γδ T-cells, but not MAIT cells (Figure 5.13b). This suggests that MAIT cells are lost globally, irrespective of clone, because despite reduction in MAIT cell percentage and diversity with CMV seropositivity, no differences in clonal evenness were detected. On the other hand, with such profound differences in γδ T-cell Shannon diversity and Gini index, but no changes in cell proportion (Figures 3.6, 5.12a, 5.12b), CMV might affect γδ T-cell clones unequally either by maintaining or expanding specific clones. The differential usage of TRG/TRD genes observed in CMV (Figure 5.11b) therefore supports this hypothesis. Whilst the major TRDV gene in the periphery, *TRDV2*, was found to be depleted in CMV$^+$ patients, *TRDV1* was overexpressed and may be more enriched within CMV-reactive clones (Figure 5.11b). γδ T-cell expansion has previously been demonstrated during CMV infection with capacity for direct anti-CMV activity[150,573–575]. This enrichment was predominantly observed within immunosuppressed individuals and was accompanied by enhanced cell activation, oligoclonality and TRDV1 usage, hence supporting the findings made here[150,573–575].

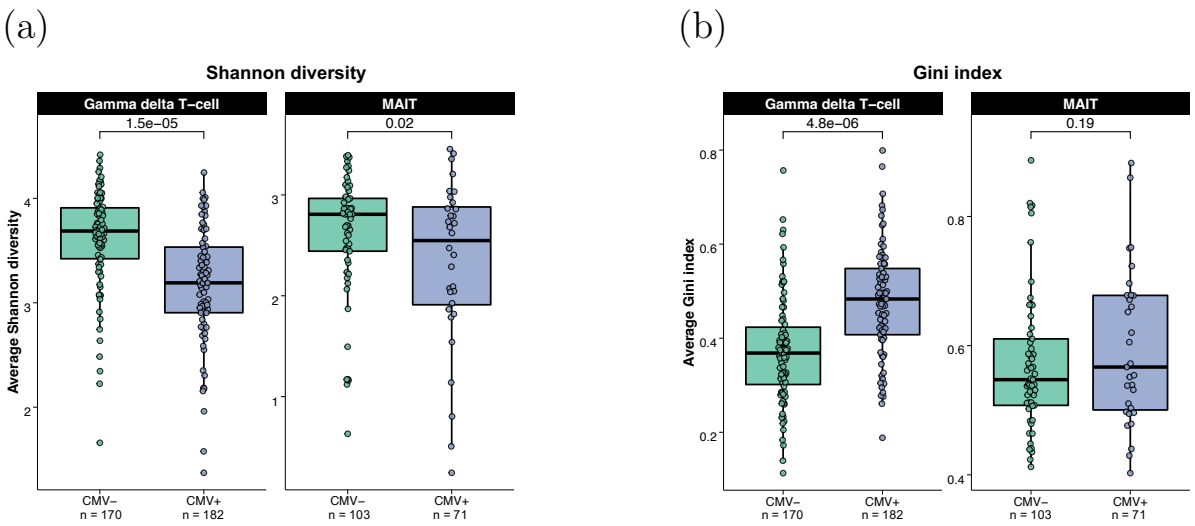


Figure 5.13

Figure 5.13 (Previous page) CMV increases γδ T-cell clonal unevenness
a) Shannon diversity and **b)** Gini indexes were calculated for γδ T-cell (left) and MAIT cell (right) clones, after subsampling to 100 reads and calculating the average from 1,000 iterations, and compared between CMV^- (n=103 MAIT; n=170 γδ T-cell) and CMV^+ (n=71 MAIT; n=182 γδ T-cell) individuals. Statistics were calculated using "lm(Shannon diversity/Gini index ∼ CMV serostatus + age + library RNA input + cancer status, data)".

5.2.2.3 MAIT cells are depleted in SARS-CoV-2 infection

MAIT cells are sensitive to viral infection and are depleted in the periphery during SARS-CoV-2 infection[409,410]. Single cell RNAseq data was performed by the COMBAT consortium[410] on 60 whole blood samples, collected from age-matched healthy donors and patients with active SARS-CoV-2 infection, including patients with mild (CM), severe (CS) and critical (CC) disease. Samples were used to look for similarities in unconventional T-cells between SARS-CoV-2 and CMV infection. Single cell RNAseq yielded a total of 218,596 T-cells (n=3,306 on average per sample) with accompanying V(D)J information (Figure 5.14a). MAIT cells were identified by recombination of *TRAV1-2* with *TRAJ12/TRAJ20/TRAJ33* and were found to be lost in patients exhibiting SARS-CoV-2 infection after controlling for age, regardless of disease severity (Figure 5.14b). It has been suggested that MAIT cells localise to the site of infection during active disease and become highly activated in those with CC disease[409,410]. Although few significant differences in TCR usage were detected between healthy donors and SARS-CoV-2 patients, expression of MAIT cell-associated *TRAV1-2* and *TRAJ33* were profoundly downregulated in patients, regardless of disease severity, after controlling for age (Figure 5.14c)[410].

Shannon diversity and Gini index were calculated for MAIT cells after subsampling to 15 cells and calculating the average from 1,000 iterations. Despite not quite reaching statistical significance (p=0.059), MAIT cell diversity was found to be reduced in patients with SARS-CoV-2, but with no differences in Gini index observed (Figures 5.14d, 5.14e). These observations reflect the CMV data, demonstrating a reduction in peripheral MAIT cell proportion and diversity, but no increase in clonality, likely representing global MAIT cell loss.

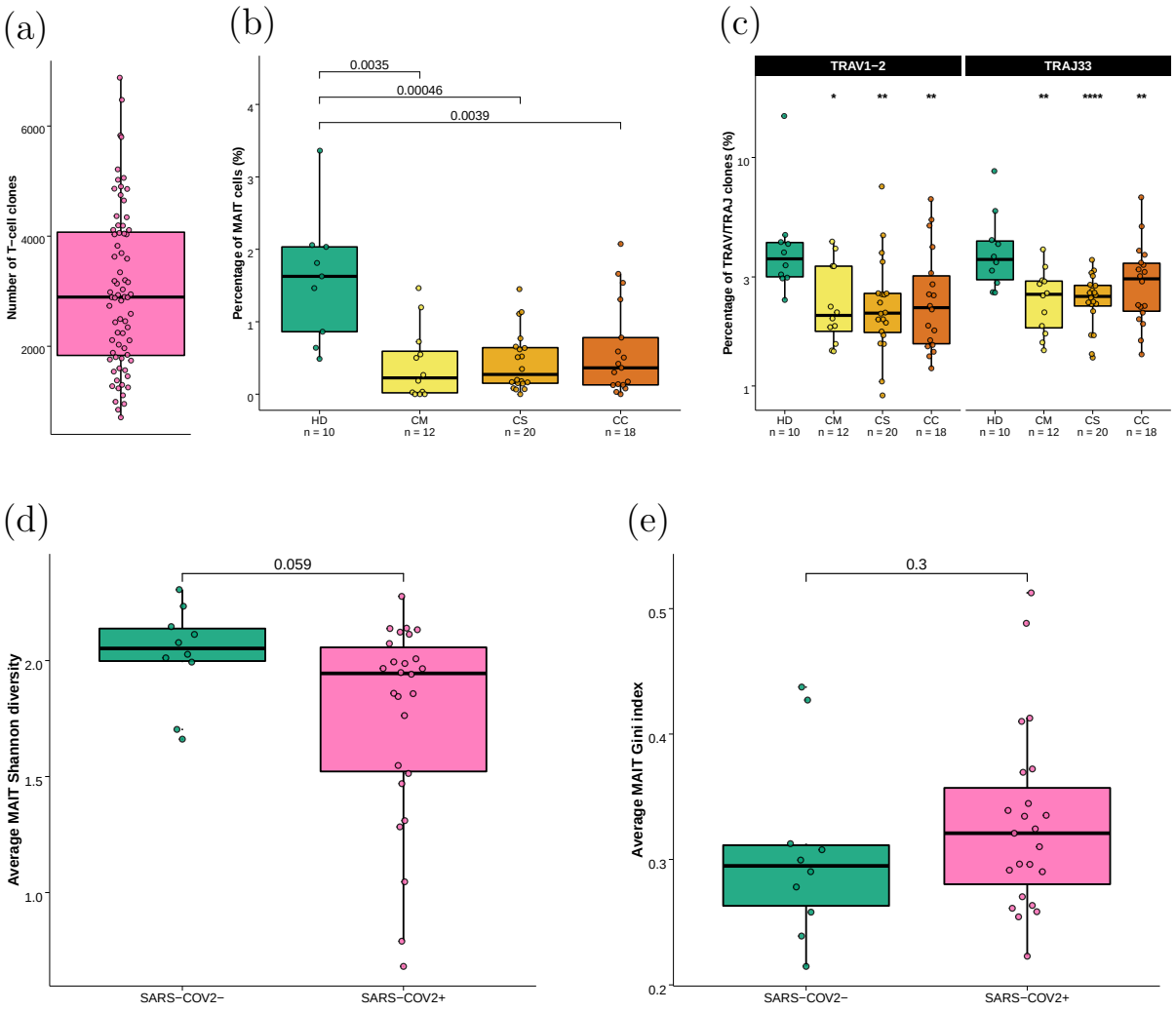


Figure 5.14 Peripheral MAIT cells are depleted in SARS-CoV-2 infection
Single cell RNAseq was performed on 60 whole blood samples including age-matched healthy donors (HD, n=10) and patients with SARS-CoV-2 of varying disease severity (n=12 COVID mild (CM), n=20 COVID severe (CS), n=18 COVID critical (CC)). **a)** Box plot showing the number of successfully sequenced TCR clones. **b)** Comparison of MAIT cell percentage between healthy donors and SARS-CoV-2 patients. **c)** *TRAV1-2* and *TRAJ33* usage is compared between healthy donors and SARS-CoV-2 patients. MAIT cells were subsampled to 15 cells calculating the average **d)** Shannon diversity and **e)** Gini index across 1,000 iterations and are compared between patients with and without active SARS-CoV-2 infection. Statistics were calculated using "lm(metric $\sim$ COVID status + age, data)". p>0.05 (ns), $p \leq 0.05$ (*), $p \leq 0.01$ (**), $p \leq 0.001$ (***), $p \leq 0.0001$ (****).

5.2.2.4 MAIT cells associate with TCR diversity

In accordance with the flow cytometry data which shows an association of CMV infection with PBMC composition and T-cell differentiation (Figures 3.3b, 3.4b, 3.5b), $CD8^+$ MAIT cell percentage was similarly found to inversely correlate with T-cell, $CD8^+$ T-cell and $CD8^+$ Temra cell percentages (Figure 5.15). However, MAIT cell percentage positively associated with NK cell count, $CD4^+$ T-cells and $CD8^+$ Tn, Tcm and Tem subset proportions.

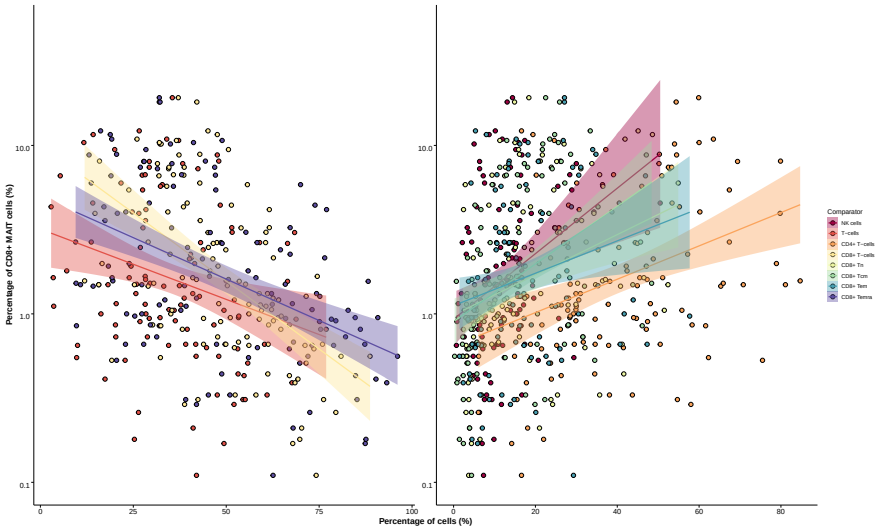


Figure 5.15 CD8$^+$ MAIT cell percentage associates with NK cells and T-cell differentiation
CD8$^+$ MAIT cell percentage was correlated with PBMC percentages and CD8$^+$ T-cell differentiation subset proportions derived from flow cytometry data (n=137). Correlations are separated based on direction of association (negative correlations left, positive correlations right). *Tn = Naïve T-cells, Tcm = Central memory T-cells, Tem = Effector memory T-cells, Temra = Effector memory T-cells reexpressing CD45RA.*

With such striking correlations found between CD8$^+$ MAIT cells and CMV infection, the association between unconventional T-cell counts, overall Shannon diversity and Gini index was investigated (Figures 5.16a, 5.16b). It is perhaps unsurprising that γδ T-cell percentage is negatively correlated with TCR Shannon diversity and associated with greater clonal unevenness given the significantly lower diversity demonstrated by TRG and TRD chains (Figures S5.7c, S5.7d). On the other hand, despite expressing highly invariant TCRs, both iNKT and MAIT cells were positively associated with TCR Shannon diversity and inversely correlated with Gini index, but most significantly for MAIT cells (Figures 5.16a, 5.16b).

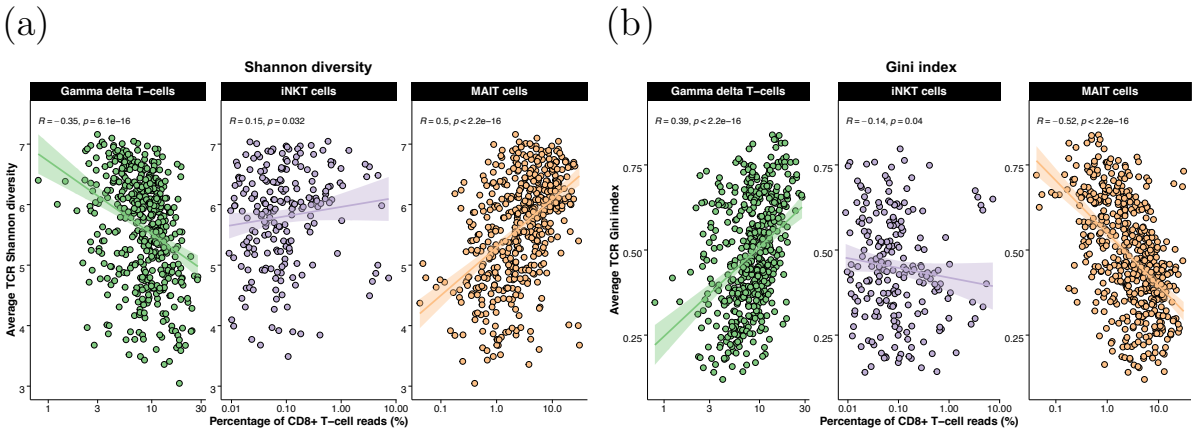


Figure 5.16 Unconventional T-cells associate with TCR diversity and clonal unevenness
Unconventional CD8$^+$ T-cell percentages (n=504) are compared to overall TCR **a)** Shannon diversity and **b)** Gini index generated from subsampled data (1,496 reads). Statistics were calculated using Spearman's rank correlation coefficient.

5.2.2.5 MAIT cell-associated genes are downregulated in CD8$^+$ T-cells in CMV$^+$ patients

CD8$^+$ T-cell genes associated with MAIT cell and γδ T-cell percentages were identified using *DESeq2* after controlling for age, library RNA input, cancer status, days on treatment and CMV score. 4,680 and 6,056 genes were associated with MAIT cell and γδ T-cell percentages respectively (Figures 5.17a, 5.17b). This included MAIT and γδ T-cell associated TCR genes as well as established MAIT cell-associated genes *RORC* (RORγT) and *KLRB1* (CD161). While the most strongly γδ T-cell associated genes were predominantly composed of *TRG* and *TRD* genes, many of the most significantly enriched MAIT cell genes comprised non-TCR genes. These included *LTK*, *SLC4A10*, *ME1*, *IL23R* and *NCR3* previously demonstrated to be associated with MAIT cells in RNAseq datasets[208,425,576–579]. Interestingly, *TRGV9* and *TRDV2* were the strongest associated V-gene segments associated with γδ T-cells, indicative of the preponderance of Vγ9Vδ2 T-cells in the periphery.

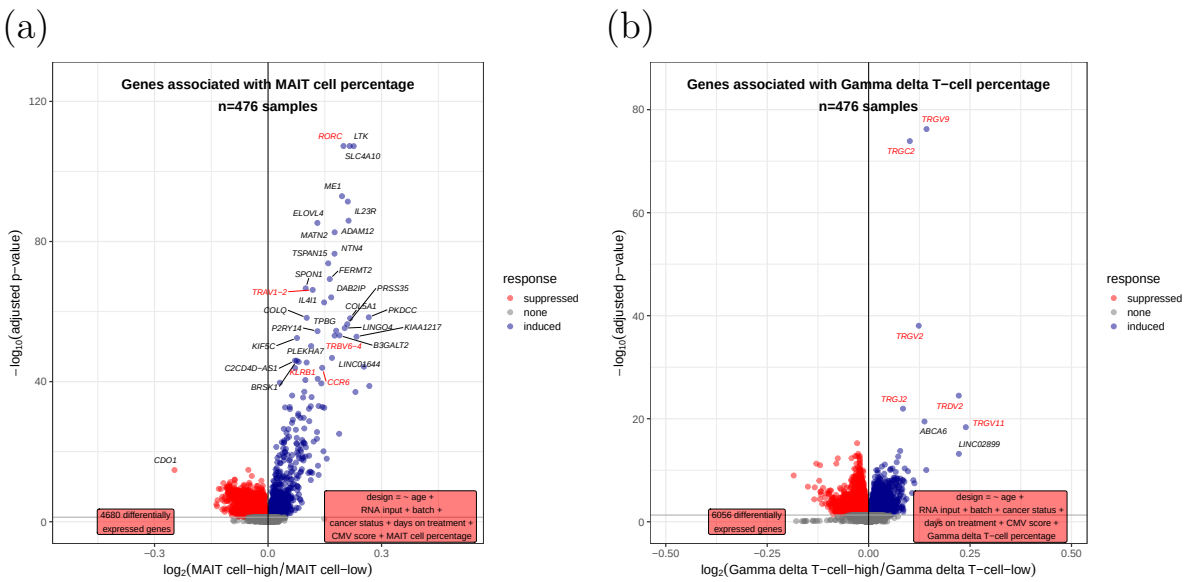


Figure 5.17 CD8$^+$ T-cell genes associated with MAIT and γδ T-cells
DESeq2 was performed on CD8$^+$ T-cell samples (n=476) identifying genes associated with **a)** MAIT and **b)** γδ T-cell percentages. Genes significantly associated with MAIT or γδ T-cell percentages are in blue and those significantly inversely correlated are in red. The $\log_2$ fold change of each gene is visualised on the x-axis with the significance of this difference displayed on the y-axis. The number of significantly differentially expressed genes as well as the *DESeq2* design formula are displayed in red boxes. Genes previously associated with MAIT or γδ T-cells are highlighted in red. Statistics were calculated using the negative binomial distribution and adjusted for multiple testing using the Benjamini-Hochberg procedure on *DESeq2*.

In addition to TCR usage, association of MAIT and γδ T-cells with CMV was also performed by gene expression. MAIT and γδ T-cell scores were generated for CD8$^+$ T-cell samples by calculating the geometric mean of the top 100 most significantly enriched genes. MAIT and γδ T-cell scores were found to significantly correlate with MAIT and γδ T-cell percentages as identified by TCR usage (Figures 5.18a, 5.18b). Enrichment of the top 100 MAIT and γδ T-cell-associated genes within CMV DEGs

was determined using $fgsea$[502]. This revealed that MAIT cell-associated genes were significantly enriched within lower rank genes, accompanied by a lower t-statistic, and hence associated with downregulation in CMV$^+$ individuals (Figure 5.18c). No significant enrichment was observed for γδ T-cell-associated genes (Figure 5.18d), supporting the finding that CMV specifically decreases MAIT cells whilst leaving the γδ T-cell proportion unaffected (Figures 3.6, 5.11b, 5.12a, 5.12b).

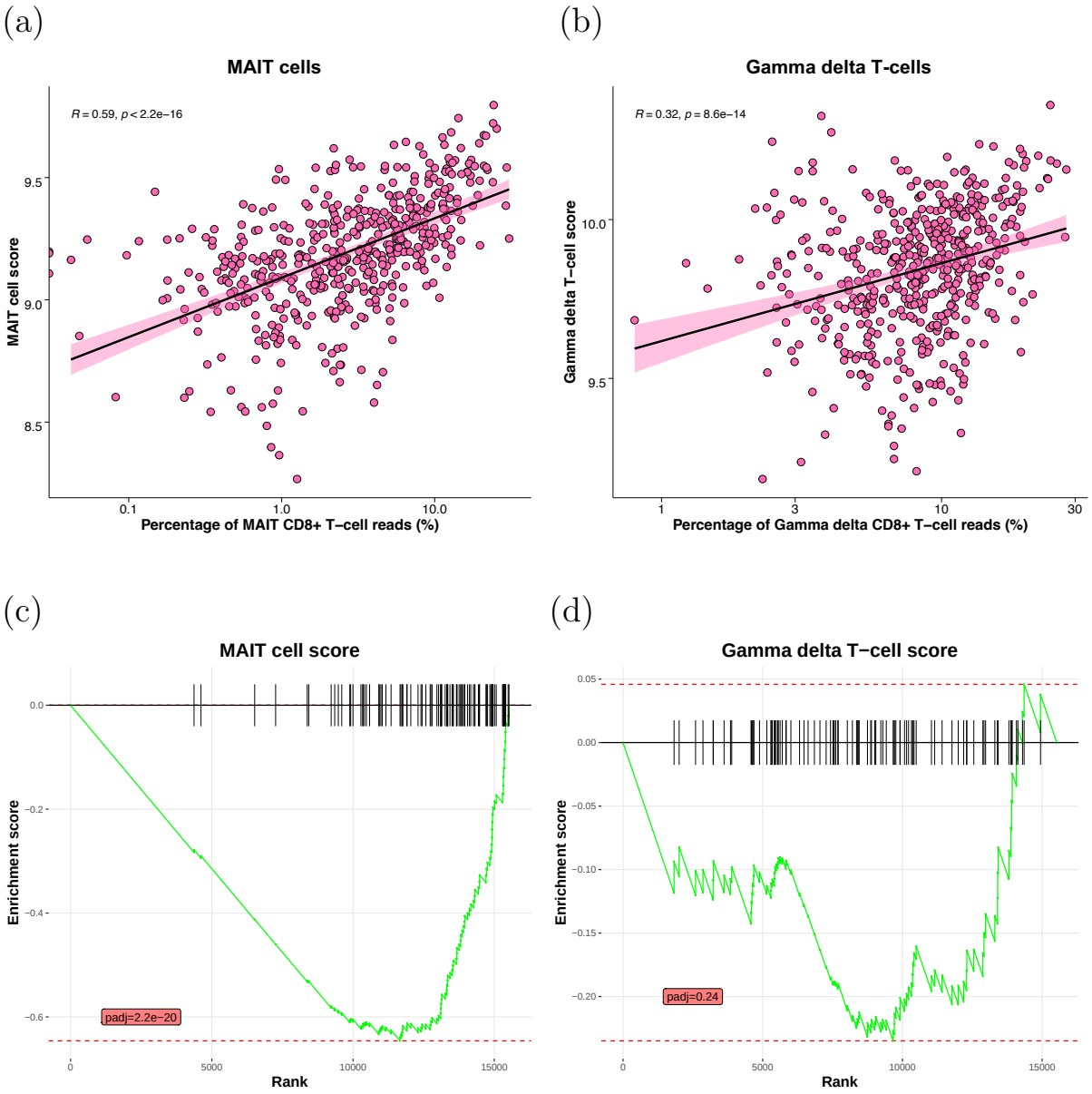


Figure 5.18 MAIT cell-associated genes are downregulated in CMV$^+$ individuals
a) MAIT and **b)** γδ T-cell percentages by TCR usage are correlated against MAIT and γδ T-cell scores generated from the top 100 most significantly enriched genes from CD8$^+$ T-cell transcriptomes (n=504). Statistics were calculated using Spearman's rank correlation coefficient. Barcode plots show enrichment of the top 100 most significantly associated **c)** MAIT cell and **d)** γδ T-cell genes amongst high or low ranked genes identified between CMV$^-$ (n=77) and CMV$^+$ (n=76) individuals. Adjusted p-values for the enrichment are displayed in red boxes.

5.2.2.6 MAIT cell activation associates with cytotoxicity score in CMV$^+$ individuals

Due to the profound inverse correlation of MAIT cells with CMV infection and the association of CMV with CD8$^+$ T-cell cytotoxicity score (data not shown), MAIT cell proportion was compared to CD8$^+$ T-cell cytotoxicity score. Accordingly, MAIT cell percentage was found to inversely correlate with cytotoxicity score (Figure 5.19). Similarly, iNKT cell percentage was also found to negatively correlate with cytotoxicity score. However, γδ T-cell percentage was strongly associated with cytotoxicity score which might be reflective of the higher clonality (Figure 5.16b) or greater percentage of Temras observed in patients with high γδ T-cell proportions[474–478,482].

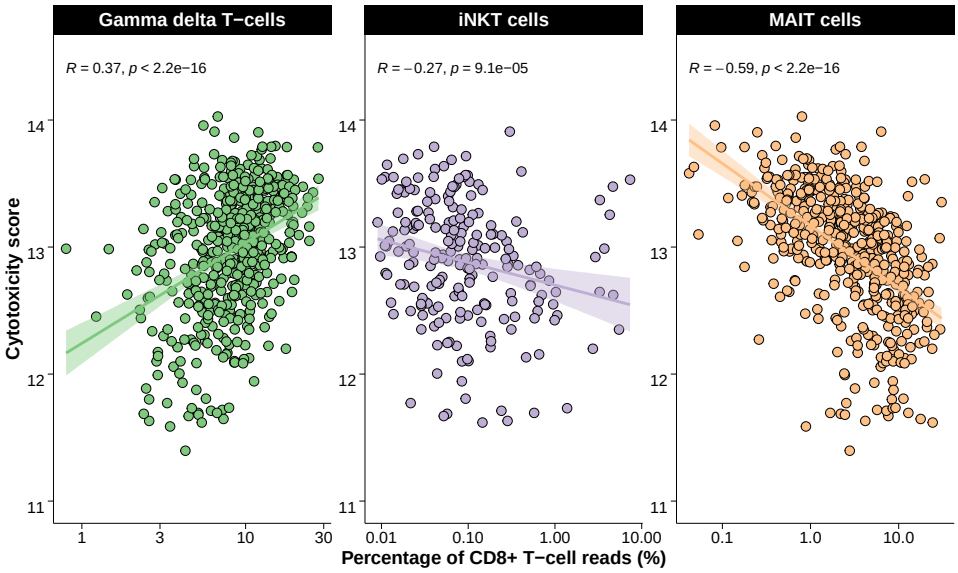


Figure 5.19 Unconventional T-cells associate with overall CD8$^+$ T-cell cytotoxicity score
MAIT, iNKT and γδ T-cell percentages (n=504) were calculated as the percentage of CD8$^+$ T-cell reads aligning to the relevant TCR genes. These percentages are correlated with CD8$^+$ T-cell cytotoxicity score which was calculated as the geometric mean of the top 50 genes associated with *IFNG* expression[208]. Statistics were calculated using Spearman's rank correlation coefficient.

Interestingly, MAIT cell activation, including expression of CD69, CD38/HLADR and PD-1, inversely correlated with circulating MAIT cell percentage, whilst MFI of 5-OP-RU-loaded MR1 tetramer and CD161 positively associated (Figure 5.20a). To understand the significance of MAIT cell TCR/CD161 downregulation, PBMC samples were cultured with MAIT cell-specific ligand 5-OP-RU, MAIT cell-activating cytokines IL-12 and IL-18, or PMA/Ionomycin which bypass TCR signalling through protein kinase C activation. Comparison of surface MAIT cell-associated TRAV1-2 and coreceptor CD161 expression between stimulated samples and UT controls confirmed that TCR-dependent activation downregulated the expression of both genes. The same change in expression was not observed after cytokine stimulation, implying that TCR/CD161 downregulation represents MAIT cell TCR activation (Figures S5.12a, S5.12b). Accordingly, MAIT cell TCR and CD161 MFI inversely correlated with markers of MAIT cell activation (Figure S5.13). Although MAIT cell activation negatively correlated with MAIT cell percentage, activation was found to correlate with CD8$^+$ T-cell cytotoxicity score (Figure 5.20b).

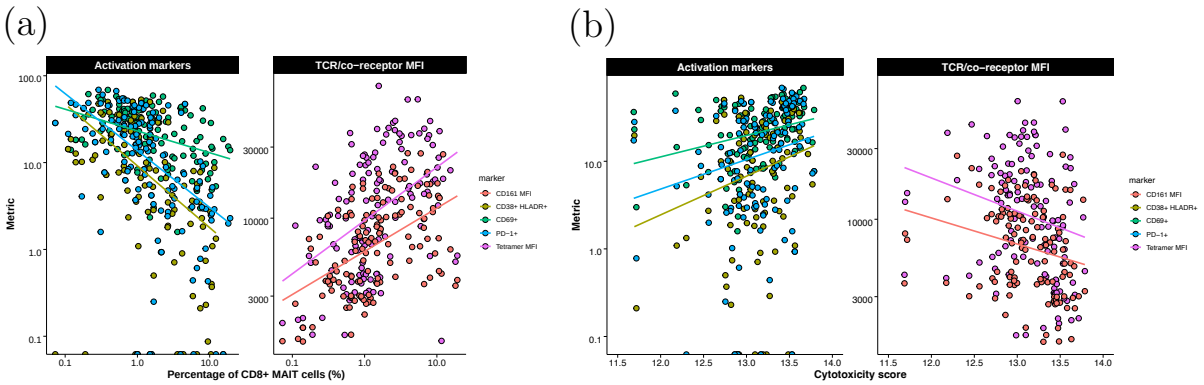


Figure 5.20 MAIT cell activation correlates with overall CD8$^+$ T-cell cytotoxicity score
Flow cytometry data of MAIT cell activation markers (n=114-132) is compared to **a)** CD8$^+$ MAIT cell percentage and **b)** CD8$^+$ T-cell cytotoxicity score, calculated as the geometric mean of the top 50 genes associated with *IFNG* expression[208].

With CMV$^+$ individuals having a diminished MAIT cell population, MAIT cell activation was compared between different CMV serostatuses. MAIT cells were found to be more activated in CMV$^+$ individuals including CD38/HLADR and PD-1 upregulation, but downregulation of both TCR and CD161 (Figure 5.21). Despite increased MAIT cell activation in CMV$^+$ individuals, CMV serostatus had no further effect on the response to both TCR-dependent and TCR-independent stimuli (Figure S5.14).

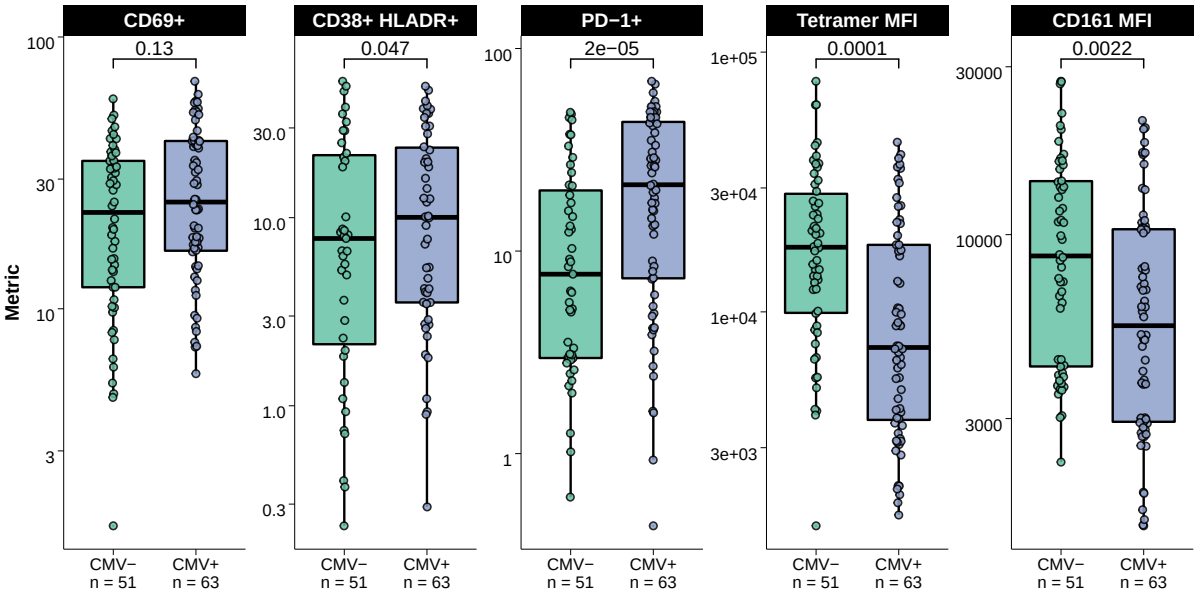


Figure 5.21 MAIT cells are more activated in CMV$^+$ individuals
Expression of MAIT cell activation markers derived from flow cytometry data is compared between CMV$^-$ (n=51) and CMV$^+$ (n=63) patients. Statistics were calculated using "lm(Metric $\sim$ CMV serostatus + age, data)".

MAIT cell activation, as quantified by expression of CD69, CD38/HLADR and PD-1, consistently associated with a lower MAIT cell percentage regardless of CMV serostatus

and may mean that expression of these markers in MAIT cells sensitises them to cell death, migration or TCR/CD161 downregulation. However, the absence of association between TCR/CD161 MFI and MAIT cell percentage in CMV$^-$ patients suggests greater heterogeneity in activated states (Figure 5.22a). Similarly, MAIT cell activation and TCR/CD161 MFI only associated with cytotoxicity score in CMV infected individuals (Figure 5.22b). TCR/CD161 downregulation is limited to TCR-dependent activation (Figures S5.12a, S5.12b) and so the association with CMV serostatus may suggest that MAIT cells are able to detect antigen during CMV infection, although this needs to be formally tested. These differences may imply variable states of activation or increased MAIT cell transcriptional heterogeneity in CMV$^-$ patients, whereas, all are shifted to activation in CMV$^+$ patients.

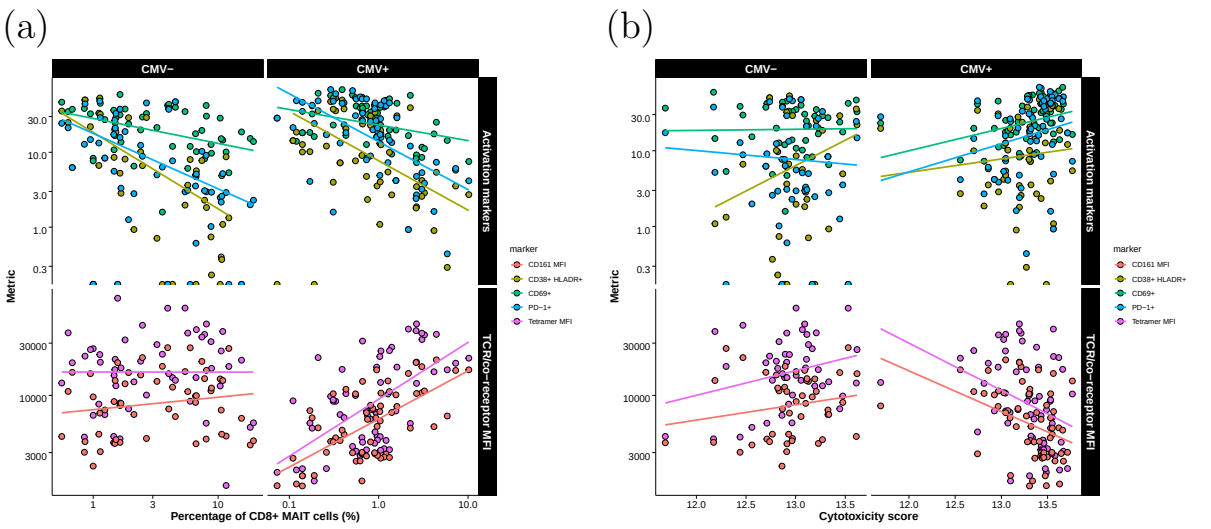


Figure 5.22 The association of MAIT cell activation with MAIT cell percentage and CD8$^+$ T-cell cytotoxicity score is dependent on CMV serostatus
Expression of MAIT cell activation markers is correlated with **a)** MAIT cell percentage or **b)** overall CD8$^+$ T-cell cytotoxicity score by CMV serostatus (n=114-132).

5.2.2.7 CMV-associated features correlate with CMV-specific clone proportion

TCR clones were aligned to previously identified CMV-specific clones using VDJdb[511,512] (reliability score >0) or to CMV-associated clones using McPAS[513] or TBAdb[514] according to TCR chain. Only complete database TCR clones beginning with a cysteine and ending with a phenylalanine residue were kept for analysis. Indeed, a higher percentage of the TCR repertoire was accounted for by CMV clones in CMV$^+$ individuals compared to CMV$^-$ regardless of TCR chain and was similarly increased when separating by HLA type (Figure 5.23a, 5.23b, S5.15a, S5.15b). Interestingly, CMV clones are present within CMV$^-$ individuals which may indicate that they are expressed regardless of infection state, that they reflect their broad specificity or may represent seroconversion. Alternatively, this may suggest that there is a disconnect with serostatus with some patients able to clear virus, yet their TCR shows evidence of prior exposure.

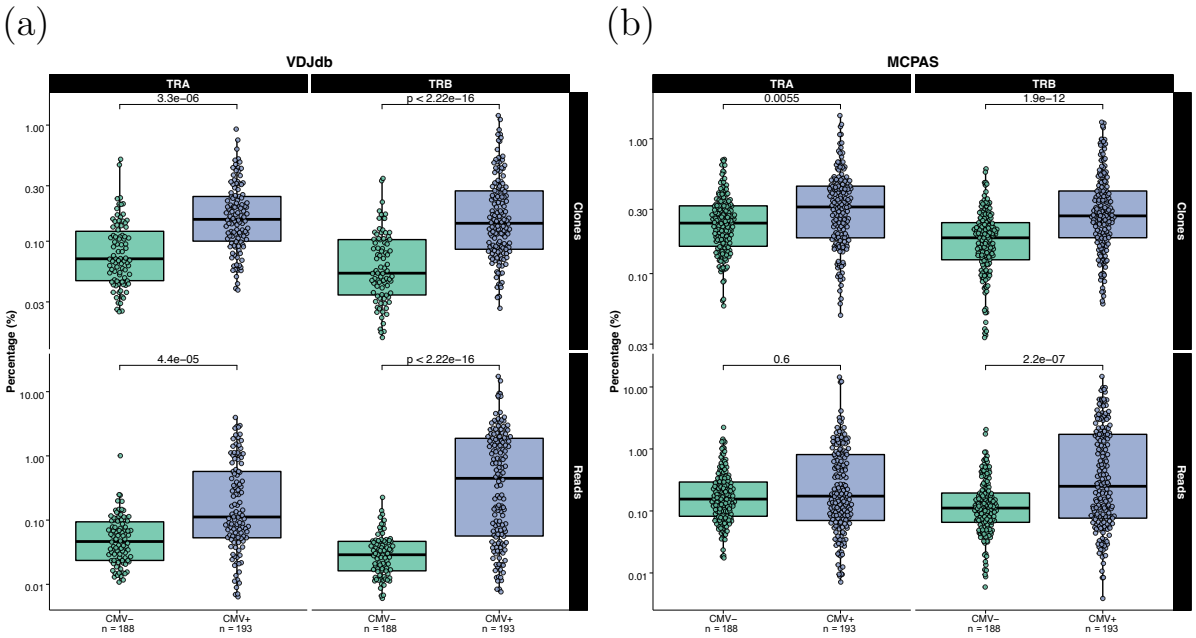


Figure 5.23 CMV-specific and CMV-associated clones are found more highly expressed by CMV$^+$ patients
The combined percentage of CMV-specific clones derived from **a)** VDJdb or CMV-associated clones from **b)** McPAS out of all clones or reads is compared between CMV$^-$ (n=188) and CMV$^+$ (n=193) individuals by TCR gene. Statistics were generated using unpaired Wilcoxon signed-rank tests.

Factors identified to associate with CMV were then compared to the percentage of clones represented by HLA-A*01 and HLA-A*02-restricted CMV-specific VDJdb clones within CMV$^+$ patients who carry HLA-A*01 and/or HLA-A*02 genes. Unsurprisingly, patient age and anti-CMV IgG titre were found to correlate with CMV clone burden (Figure 5.24). This was in addition to CMV score, calculated as the geometric mean of the top 50 CD8$^+$ T-cell genes associated with CMV infection (Figure 3.16), as well as the percentage of CD8$^+$ T-cells and γδ T-cell Gini index. Conversely, CMV clone percentage negatively correlated with CD8$^+$ MAIT cell percentage, as calculated by flow cytometry or RNAseq, and γδ T-cell Shannon diversity. The impact of CMV infection can therefore be observed within both the CD8$^+$ T-cell transcriptome and TCR repertoire, including in unconventional T-cells, with effects heightened by age and CMV immune response, as indicated by anti-CMV IgG titre.

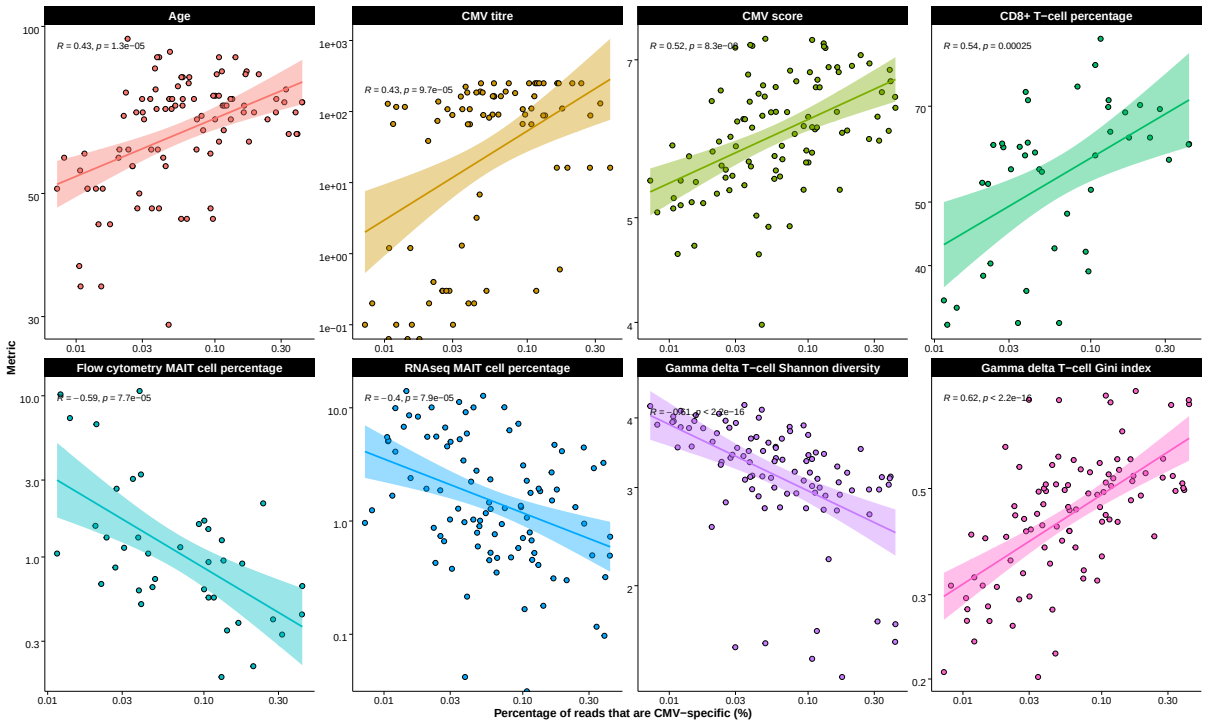


Figure 5.24 Carriage of CMV-specific clones correlates with CMV-associated factors
The percentage of TCR clones composed of HLA-A*01/HLA-A*02-restricted VDJdb CMV-specific clones is correlated with factors associated with CMV infection in HLA-A*01/HLA-A*02-expressing patients (n=39-97). Statistics were calculated using Spearman's rank correlation coefficient.

5.2.3 Melanoma-associated BCR/TCR profiles

5.2.3.1 No effect of melanoma on overall BCR and TCR clonality

Due to the profound differences observed in expression between healthy donors and MM patients in both $CD19^+$ B-cell and $CD8^+$ T-cell samples, it was postulated that similar changes might occur in corresponding BCR/TCR repertoires. Owing to the extensive contribution of CMV to the peripheral TCR repertoire, including effects on the number of clones, clonal size, diversity, TCR usage, MAIT cell proportion and γδ T-cell diversity indexes, CMV serostatus was controlled in comparisons of the TCR repertoire between healthy donors and MM patients, using imputed sample CMV scores obtained from expression data (Figure 3.16a). In keeping with the transcriptomic data, no such correlations of CMV with the BCR repertoire were observed (data not shown). As a result, CMV was not controlled for in BCR repertoire comparisons.

Firstly, the average number and size of BCR and TCR clones were determined after subsampling (n=4,471 BCR reads; n=1,496 TCR reads) and taking the average from 1,000 iterations. However, no differences in clone count or size were detected between healthy donor and MM patient samples after controlling for age, library RNA input as well as CMV score for T-cells (Figures 5.25a, 5.25b, 5.25c, 5.25d). Although no differences in the proportion of BCR clones by size were observed between healthy donors and MM patients, a higher percentage of large TCR clones (0.1-0.5%) were detected in patients after normalising for age, library RNA input and CMV score (Figures S5.16a, S5.16b). However, no differences were observed in Shannon diversity or Gini indexes for BCR and TCR repertoires regardless of chain (Figures S5.17a, S5.17b).

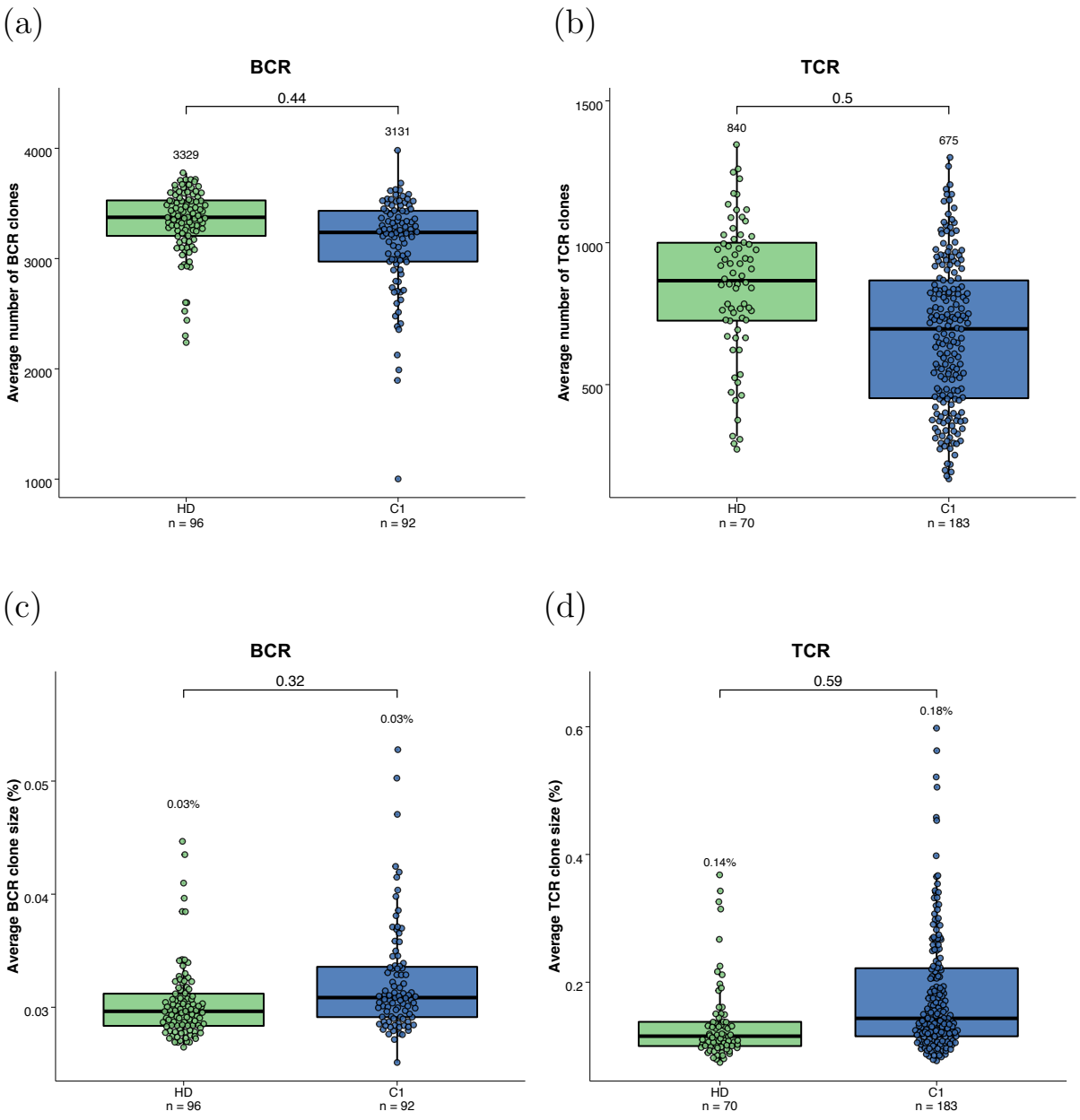


Figure 5.25 No difference in BCR/TCR clone number or size in melanoma patients
BCR (n=96 healthy donors, 92 C1) and TCR (n=70 healthy donors, 183 C1) samples were subsampled to 4,471 and 1,496 reads respectively calculating the average number of clones and clone percentage taken from 1,000 iterations. The average number of clones detected for **a)** BCR and **b)** TCR samples as well as the average clonal size of **c)** BCR and **d)** TCR clones as the percentage of the repertoire were compared between healthy donors (HD) and untreated MM patients (C1). Averages are displayed above each box plot. Statistics were calculated using "lm(metric $\sim$ cancer status + age + library RNA input, data)" for BCR samples and "lm(metric $\sim$ cancer status + age + library RNA input + CMV score, data)" for TCR samples.

5.2.3.2 Switched BCR clones are larger in melanoma

Although no differences in clonal number, size and diversity were detected for either BCR or TCR clones in melanoma, BCR and TCR usage were compared between healthy

donors and untreated MM patients (C1) using *DESeq2*. After controlling for age, library RNA input and sequencing batch, 18 BCR genes were found to be significantly differentially expressed. This included isotype determining genes *IGHG1*, *IGHG2* and *IGHA2*, which were upregulated in MM patients, and unswitched isotype gene *IGHD*, which was reduced in MM patients (Figure 5.26). However, no differences in light chain usage were found (Figure S5.18).

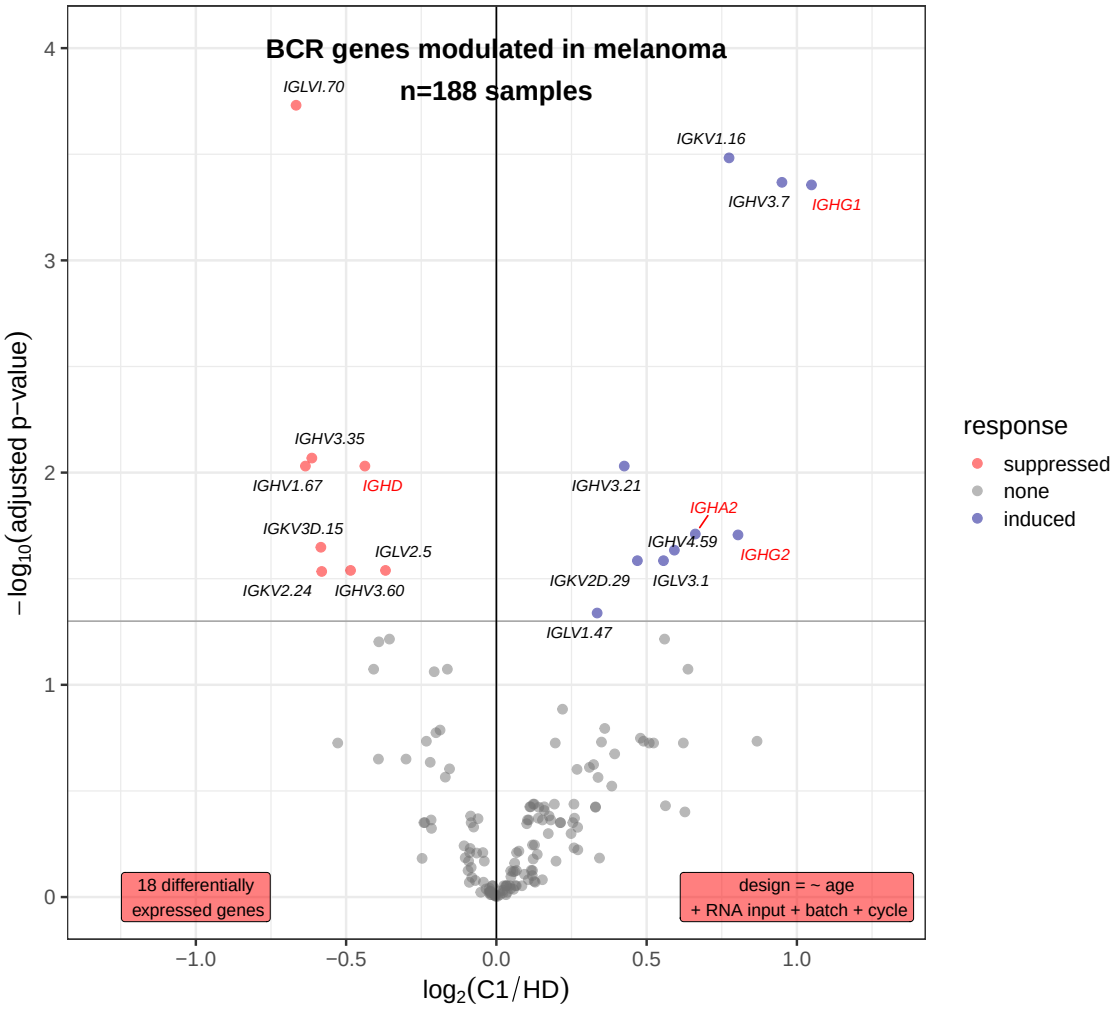


Figure 5.26 Differential BCR usage in melanoma patients
Volcano plot depicting differentially expressed BCR genes between healthy donors (HD, n=96) and untreated MM patients (C1, n=92). Genes significantly enriched in MM patients are in blue and those significantly enriched in HDs are in red. The $\log_2$ fold change of each gene is visualised on the x-axis with the significance of this difference displayed on the y-axis. The number of significantly differentially expressed genes as well as the *DESeq2* design formula are displayed in red boxes. IGHC genes are highlighted in red. Statistics were calculated using the negative binomial distribution and adjusted for multiple testing using the Benjamini-Hochberg procedure on *DESeq2*.

Antibody isotype usage was investigated further, but this time looking at IGHC usage instead of overall expression. Expressed as the percentage of IGHC clones, few differences were observed in CSR between healthy donors and MM patients, except for *IGHG2* and *IGHD* which were overrepresented and depleted in MM patients respectively (Figures 5.27a, 5.27b). However, by instead quantifying IGHC usage as the percentage of

IGHC reads, several differences in healthy donors and patients were observed, including a reduction in unswitched isotypes IGHM and IGHD and a concomitant increase in IGHA2, IGHG1 and IGHG2 in keeping with the differential expression analysis (Figures 5.27c, 5.27d). This may indicate that although there is little difference in CSR, as measured by IGHC clonal usage, switched clones may be expanded in MM patients. However, no differences in mutation rate were observed between healthy donors and MM patients (Figure S5.19).

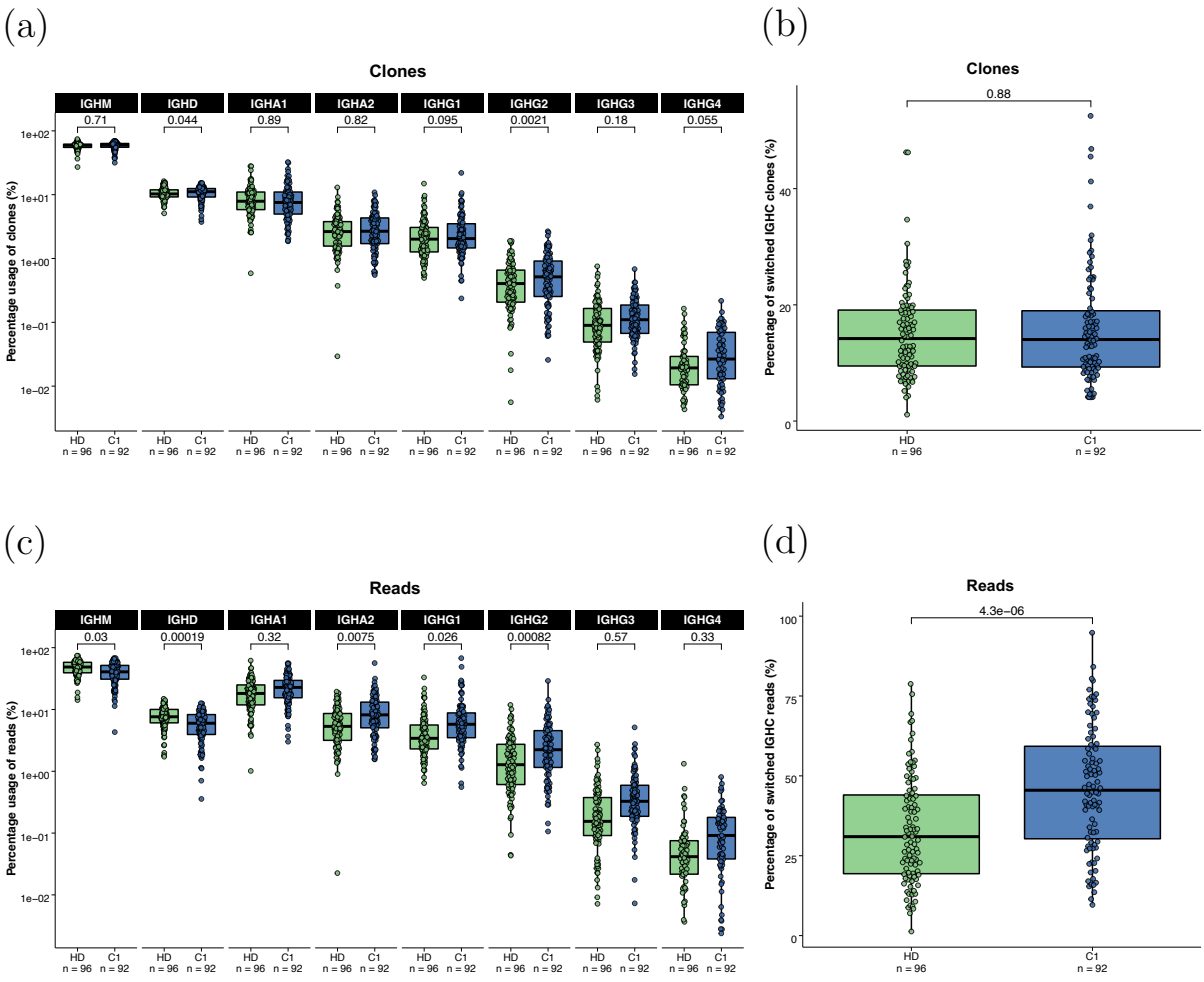


Figure 5.27 Switched BCR clones are larger in melanoma patients
IGHC usage is calculated as the percentage of all IGHC **a,b)** clones or **c,d)** reads either by **a,c)** individual isotype or **b,d)** combined switched isotypes (IgA, IgG, IgE). IGHC usage is compared between healthy donors (HD, n=96) and untreated MM patient samples (C1, n=92). Statistics were calculated using "lm(IGHC usage $\sim$ cancer status + age + library RNA input, data)".

5.2.3.3 Melanoma induces differential TCR usage

*DESeq*2 was used to compare TCR usage between healthy donors and MM patients after controlling for age, library RNA input, sequencing batch and CMV score. This revealed 26 TCR genes to be differentially expressed between healthy donors and MM patients (Figure 5.28). Accordingly, no differences in unconventional T-cell proportions

were observed (Figure S5.20a, S5.20b). TCR genes enriched in melanoma patients may be important for antigen recognition and represent large melanoma-associated clones or may reflect biases in HLA status. Although beyond the scope of this thesis, the importance of these genes in melanoma recognition warrants further investigation.

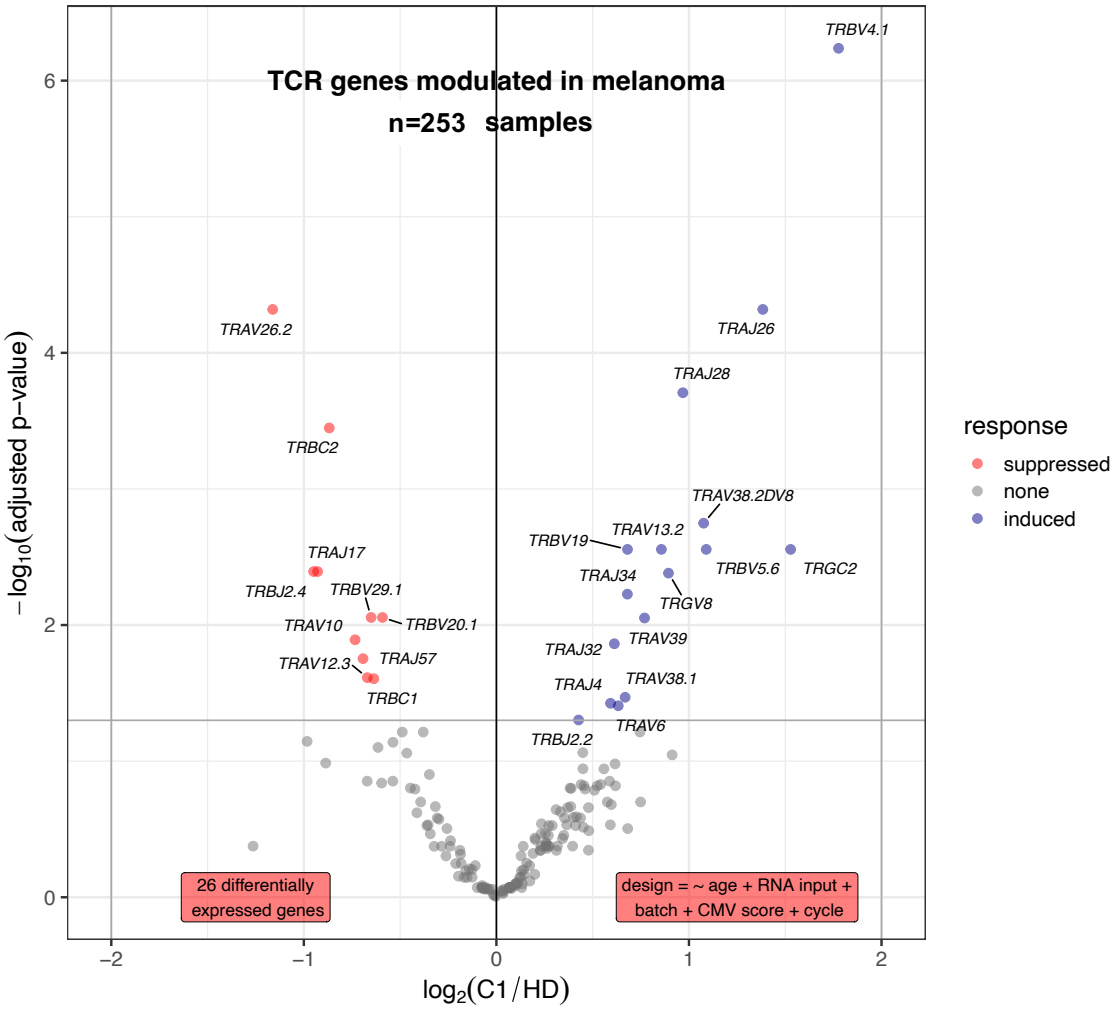


Figure 5.28 Differential TCR usage in melanoma patients
Volcano plot depicting differentially expressed TCR genes between healthy donors (HD, n=70) and untreated MM patients (C1, n=183). Genes significantly enriched in MM patients are in blue and those significantly enriched in healthy donors are in red. The $\log_2$ fold change of each gene is visualised on the x-axis with the significance of this difference displayed on the y-axis. The number of significantly differentially expressed genes as well as the $DESeq2$ design formula are displayed in red boxes. Statistics were calculated using the negative binomial distribution and adjusted for multiple testing using the Benjamini-Hochberg procedure on $DESeq2$.

5.2.4 The effect of ICB treatment on BCR and TCR repertoires

5.2.4.1 ICB treatment has no effect on overall BCR and TCR diversity

Next, effects of ICB treatment on BCR and TCR repertoires were investigated. Firstly, the average number of clones and average corresponding clonal sizes detected after subsampling were compared between paired C1/C2 and C1/C4 samples. However,

no significant differences were found in either BCR or TCR repertoires at either time-point (Figures 5.29a, 5.29b, 5.29c, 5.29d, S5.21a, S5.21b, S5.21c, S5.21d) regardless of treatment type (data not shown). Additionally, no differences were observed between paired C1/C2 or C1/C4 samples by clone size, Shannon diversity or Gini index (Figures S5.22a, S5.22b, S5.22c, S5.22d, S5.23a, S5.23b, S5.23c, S5.23d).

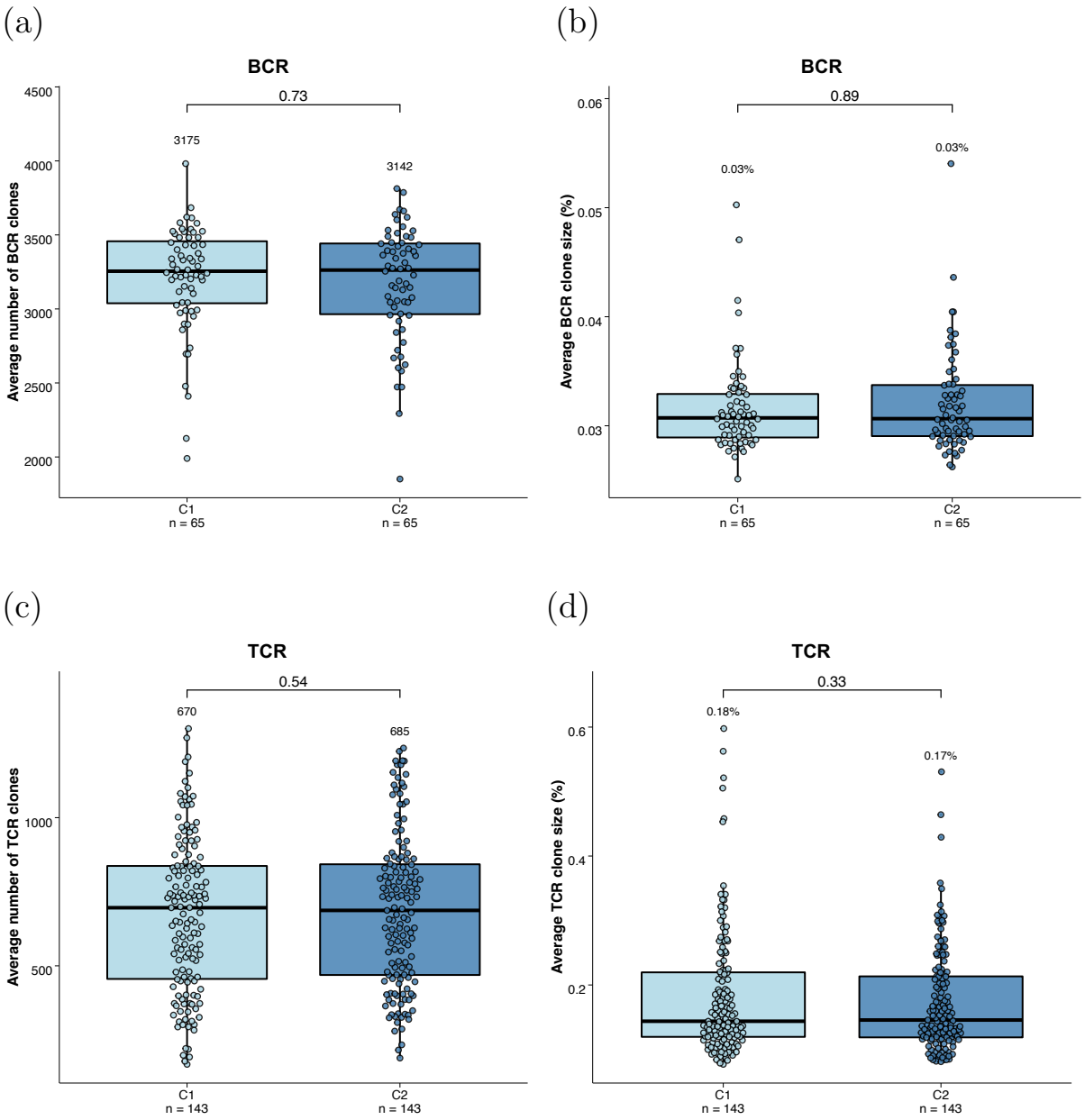


Figure 5.29 BCR and TCR average clone number and size are unaffected by ICB treatment
Data was subsampled to 4,471 and 1,496 reads for BCR (n=65) and TCR (n=143) samples respectively calculating the average **a,c)** number of clones and the **b,d)** percentage of the repertoire that **a,b)** BCR and **c,d)** TCR clones represent on average after 1,000 iterations. Average values are displayed above each box plot. Statistics were calculated using "lm(metric $\sim$ cycle + library RNA input, data)".

Although no differences were detected in BCR or TCR diversity after treatment,

a lower TCR Gini index at C4 was found to associate with prolonged OS and PFS after excluding any nonmetastatic patients (Figures 5.30a, 5.30b). Furthermore, patients with a low percentage of hyperexpanded clones constituting ≥5% of the repertoire were also found to have superior outcomes at C4 (Figures 5.30c, 5.30d). Whilst overall TCR diversity was unassociated with survival outcomes, these findings highlight the importance of clonal evenness in ICB response. Similarly, survival has previously been linked to TCR clones of a specific size[371]. Despite association of TCR Gini index and survival outcomes, no such correlations were found for any BCR metric (data not shown).

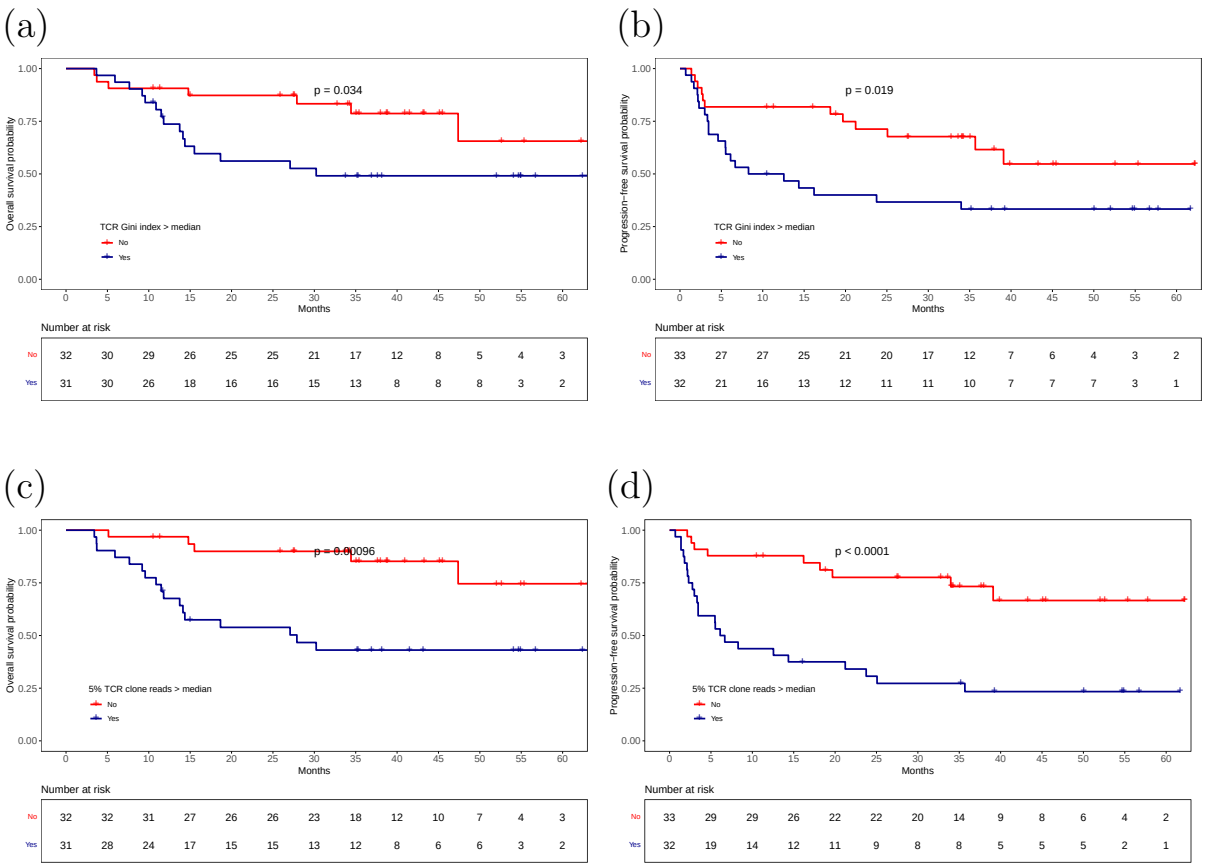


Figure 5.30 Patients with low TCR clonality at C4 have favourable outcomes
Patients were dichotomised into those with a TCR Gini index or percentage of ≥5% clone reads above or below the median at C4 (n=63-65). Patients who fall below the median are in red and those above are in blue. Kaplan Meier plots depict the differences in **a,c)** overall survival or **b,d)** progression-free survival between MM patients with low or high **a,b)** $CD8^+$ T-cell TCR Gini index or **c,d)** percentage of reads taken up by clones accounting for ≥5% of total clones, both calculated after subsampling to 1,496 reads per sample.

5.2.4.2 cICB induces CSR and SHM in BCR clones

BCR gene expression was compared between paired C1/C2 samples using *DESeq2* after controlling for patient ID and library RNA input to ensure a paired analysis whilst controlling for sequencing breadth. Although no differentially expressed BCR genes were detected after sICB, 18 genes were found to be significantly differentially enriched after cICB. This included increased expression of switched IGHC genes *IGHA1*,

IGHG1, *IGHG3* and *IGHE* at C2, but a reduction in unswitched *IGHM* and *IGHD* isotypes (Figures 5.31a, 5.31b). However, no such changes were observed at later cycles of treatment regardless of treatment type (data not shown).

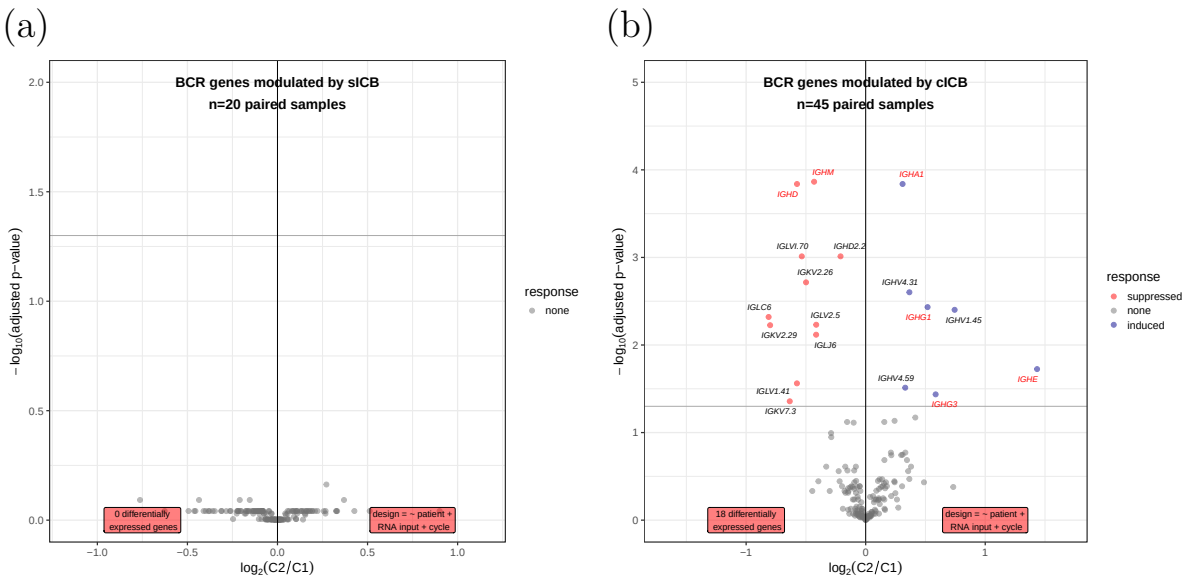


Figure 5.31 cICB induces differential BCR gene expression
$DESeq2$ was used to compare normalised BCR gene counts between paired C1/C2 samples following either **a)** sICB (n=20) or **b)** cICB (n=45) treatment. Genes significantly upregulated at C2 are in blue and those significantly depleted are in red. The $\log_2$ fold change of each gene is visualised on the x-axis with the significance of this difference displayed on the y-axis. The number of significantly differentially expressed genes as well as the $DESeq2$ design formula are displayed in red boxes. IGHC genes are highlighted in red. Statistics were calculated using the negative binomial distribution and adjusted for multiple testing using the Benjamini-Hochberg procedure on $DESeq2$.

Although no changes were observed in light chain usage following ICB treatment (Figures S5.24a, S5.24b), an increase in CSR at C2, taken as IGHC usage, was detected specifically following cICB treatment (Figures 5.32a, 5.32b, 5.32c, 5.32d). A loss in unswitched isotypes *IGHM* and *IGHD*, but a gain in all switched isotypes, except *IGHG4*, was observed after cICB either by clones or by reads. This implies that cICB induces CSR as well as expansion of these switched clones. Accordingly, the induction of switched clones at C2 was greater following cICB treatment than sICB (Figure S5.25a, S5.25b). However, once again, no differences were observed at C4, irrespective of ICB treatment type (Figures S5.26a, S5.26b). The percentage of switched IGH reads was tracked across the course of ICB treatment by days since ICB treatment commenced and revealed that although no effect was observed following sICB treatment at any time-point, patients treated with cICB experienced an initial increase which soon resolved at later time-points, highlighting the transient effect of CSR in the periphery (Figure 5.32e).

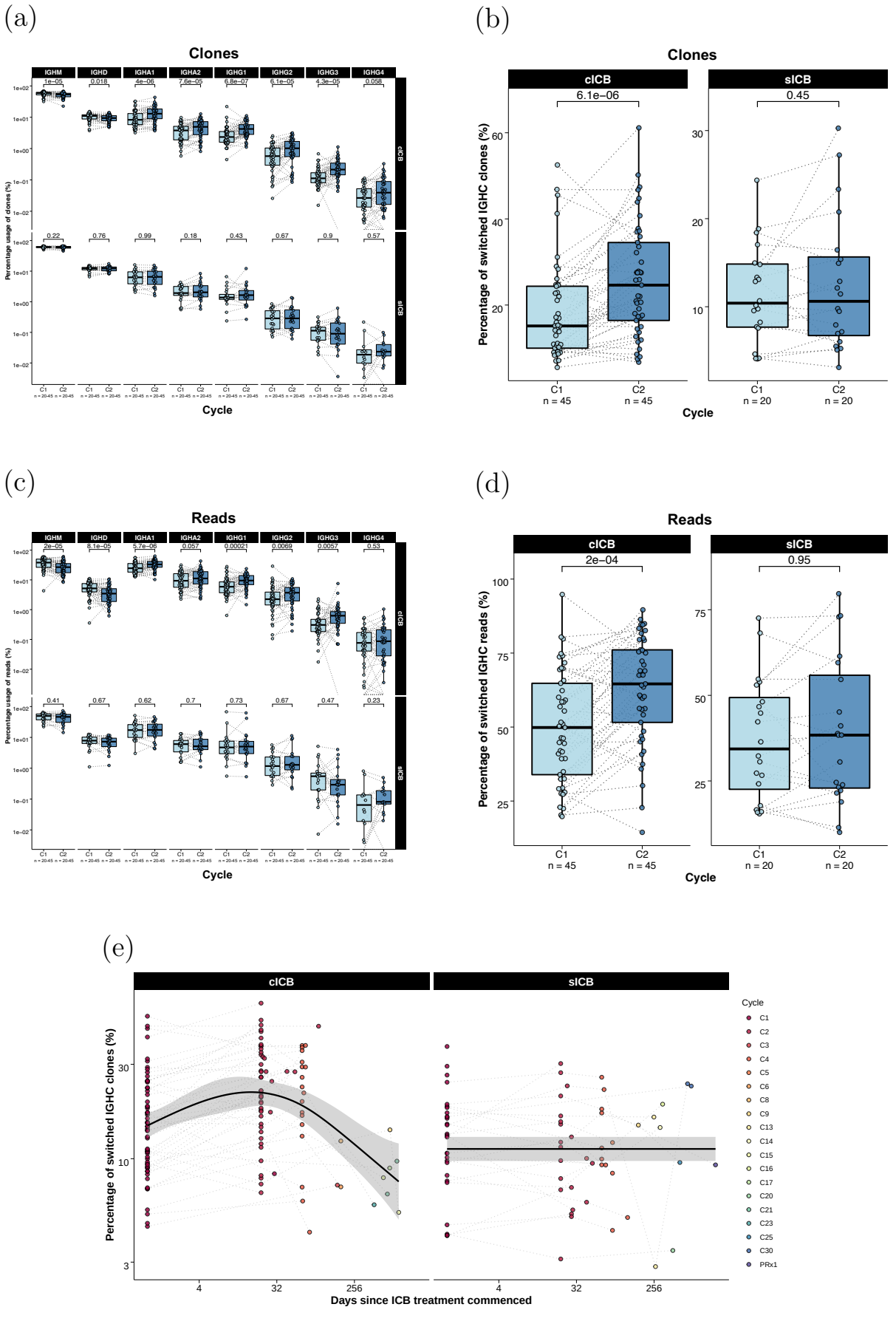

(a)
Clones
IGHM
IGHD
IGHA1
IGHA2
IGHG1
IGHG2
IGHG3
IGHG4
cICB
sICB
Percentage usage of clones (%)
Cycle
(b)
Clones
cICB
sICB
6.1e−06
0.45
Percentage of switched IGHC clones (%)
C1
n = 45
C2
n = 45
C1
n = 20
C2
n = 20
Cycle
(c)
Reads
Percentage usage of reads (%)
Cycle
(d)
Reads
2e−04
0.95
Percentage of switched IGHC reads (%)
Cycle
(e)
Percentage of switched IGHC clones (%)
Days since ICB treatment commenced
Cycle
C1
C2
C3
C4
C5
C6
C8
C9
C13
C14
C15
C16
C17
C20
C21
C23
C25
C30
PRx1

Figure 5.32

Figure 5.32 (Previous page) Increased CSR is observed at C2 following cICB treatment
Usage of individual IGHC genes by percentage of IGH **a)** clones or **c)** reads is compared between paired C1/C2 samples by ICB treatment (n=20 sICB, n=45 cICB). The combined percentage of switched **b)** clones or **d)** reads (IgG/IgA/IgE) is compared between paired C1/C2 samples by treatment type. Statistics were generated using paired Wilcoxon signed-rank tests. **e)** The percentage of switched IGH clones is tracked across the course of ICB by treatment type with points coloured by treatment cycle. *PRx1 = Sample collected after cessation of ICB treatment.*

On account of the increase in ASCs and CSR observed after cICB, likely arising from enhanced germinal centre reactions, BCR mutation rate was also examined. This revealed an increase in average mutation number per BCR clone at C2 after cICB treatment which was not observed following sICB (Figure 5.33a). This held true for all BCR chains (Figure S5.27). However, no changes in mutation rate were detected after either treatment at C4 (Figure 5.33b).

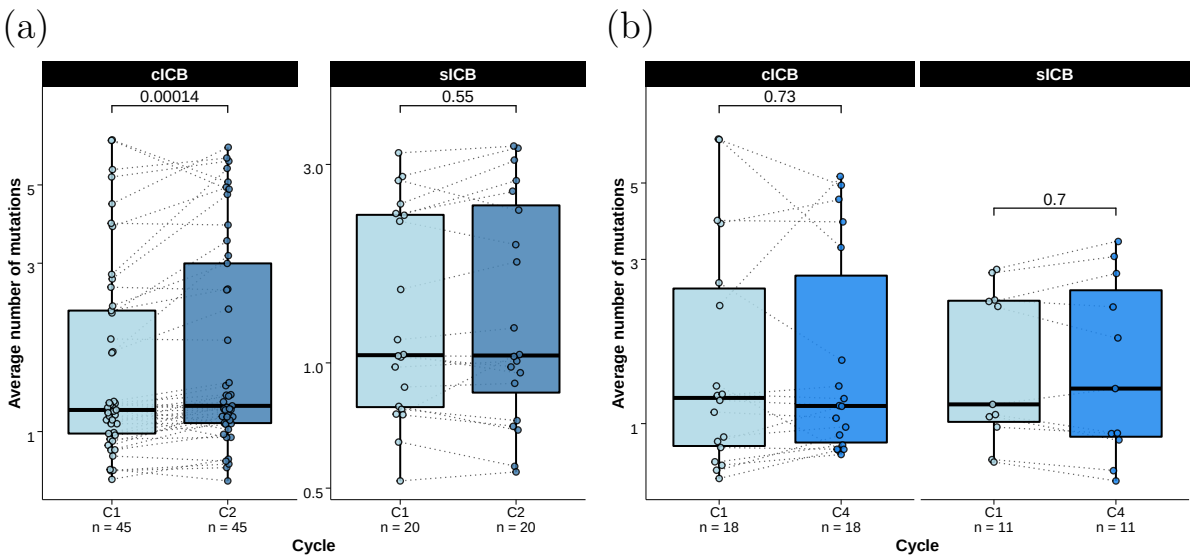


Figure 5.33 cICB increases the BCR mutation rate at C2
The average number of mutations identified per BCR clone is compared between paired **a)** C1/C2 (n=20 sICB, n=45 cICB) and **b)** C1/C4 (n=11 sICB, n=18 cICB) samples by ICB treatment type. Statistics were generated using paired Wilcoxon signed-rank tests.

The induction of switched BCR reads at C2 was found to correlate with the increase in ASCs, BCR mutation rate and CD19$^+$ B-cell ICB response score (Figure 5.34). Interestingly, this increase was also associated with the CD8$^+$ T-cell ICB response score, *MKI67* expression and the loss in T-cell PD-1. Although no association was found between the induction of switched BCR reads and CD8$^+$ T-cell *TOX2* expression, a positive association was found by instead comparing with the induction of switched BCR clones rather than reads (data not shown). Surprisingly, however, the induction of CD8$^+$ T-cell *CXCL13* or plasma CXCL13 was not associated regardless of treatment type.

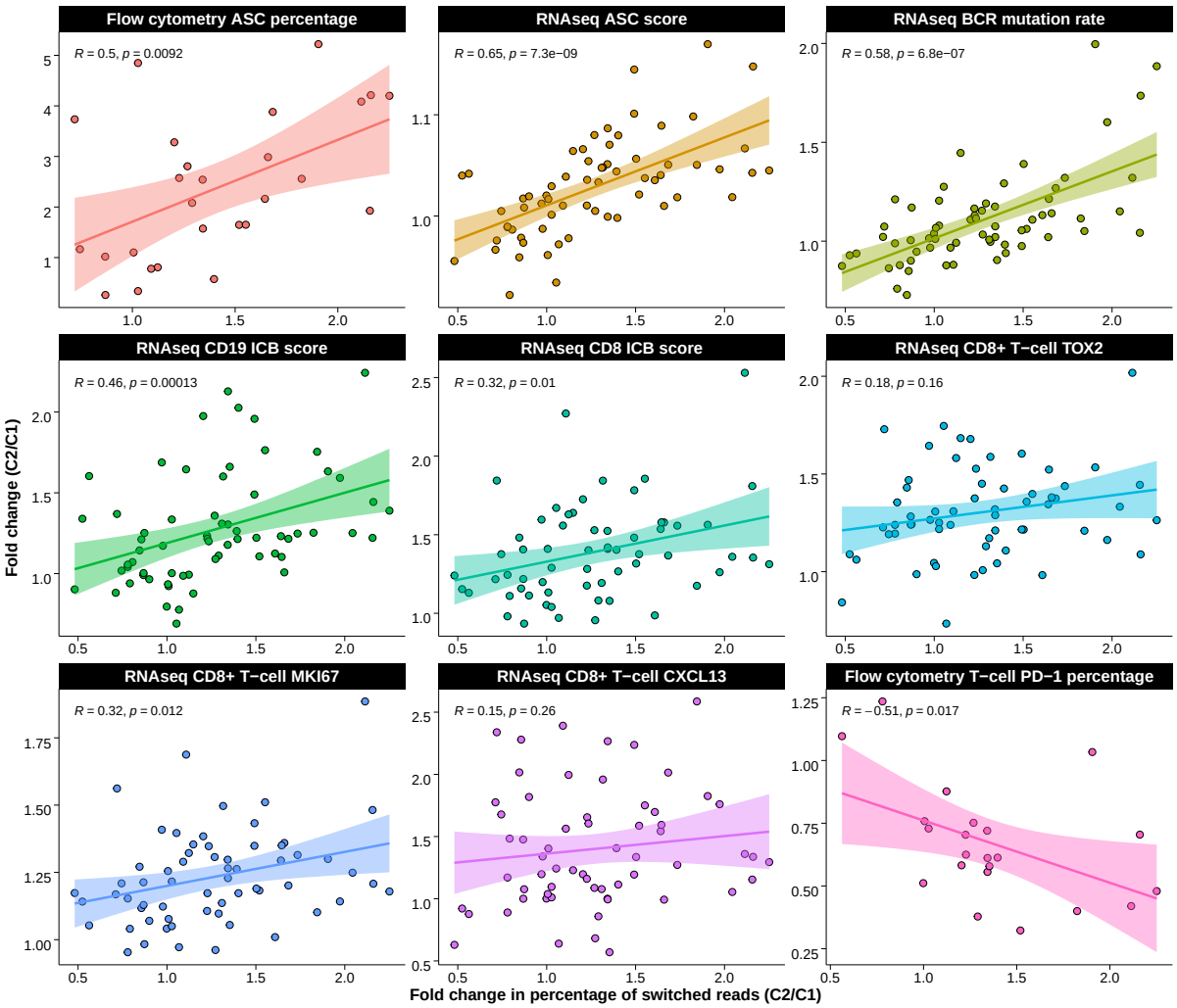


Figure 5.34 ICB-induced CSR associates with the CD8$^+$ T-cell ICB response
The induction in CSR, taken as the fold change in percentage of switched IGH reads (C2/C1), is compared to the fold change in BCR mutation rate, flow cytometry cell percentages and ICB response scores (n=27-62). Statistics were calculated using Spearman's rank correlation coefficient.

5.2.4.3 cICB induces a loss in circulating MAIT cells

Differential gene expression analysis was also performed for TCR genes to investigate the effect of ICB. In a similar fashion to BCR gene expression, no differences were observed following sICB, but 12 genes were found to be significantly differentially regulated following cICB (Figures 5.35a, 5.35b). Strikingly, the most significantly downregulated genes included MAIT cell-associated *TRAV1-2*, *TRAJ33* and *TRBV6-4*. Although *TRAV1-2* and *TRBV6-4* remained depleted at C4, downregulation of *TRAV1-2*, *TRAJ33* and *TRBV6-4* had nearly entirely resolved at later time-points (C10$^+$), but this may be a result of low statistical power (Figures S5.28a, S5.28b).

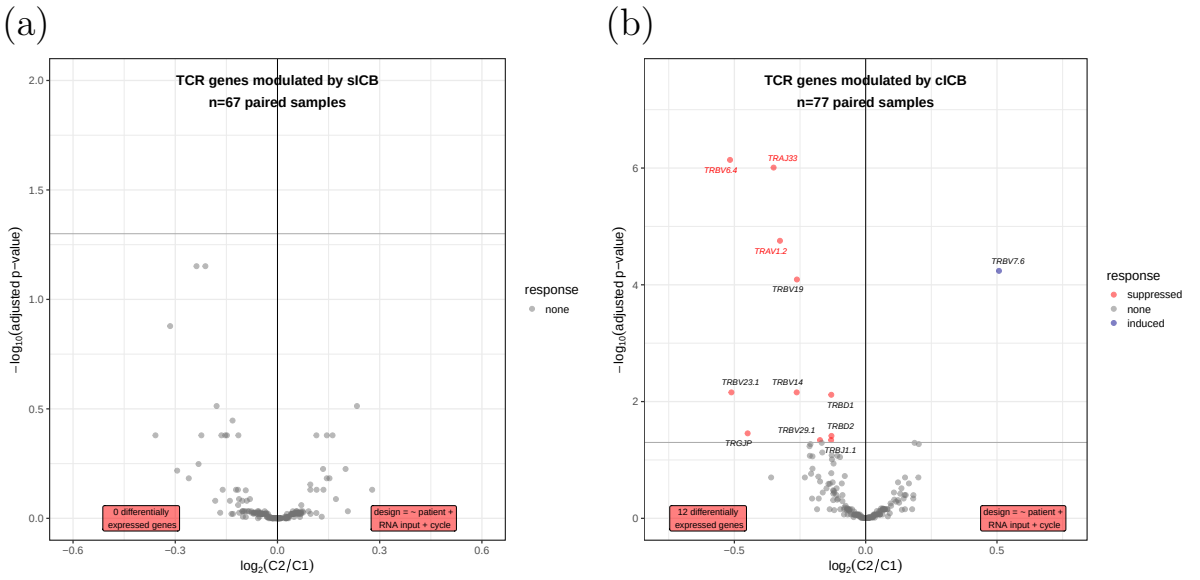


Figure 5.35 MAIT cell-associated TCR genes are downregulated following cICB treatment
$DESeq2$ was used to compare normalised TCR gene counts between paired C1/C2 samples following **a)** sICB (n=67) and **b)** cICB (n=77) treatment. Genes significantly upregulated at C2 are in blue and those significantly depleted are in red. The $\log_2$ fold change of each gene is visualised on the x-axis with the significance of this difference displayed on the y-axis. The number of significantly differentially expressed genes as well as the $DESeq2$ design formula are displayed in red boxes. MAIT cell-associated TCR genes are highlighted in red. Statistics were calculated using the negative binomial distribution and adjusted for multiple testing using the Benjamini-Hochberg procedure on $DESeq2$.

MAIT cell percentage, as identified by the percentage of TRA reads aligning to known MAIT cell TRA genes, was found to be significantly reduced at C2 exclusively after cICB treatment (Figure 5.36a). Although not quite reaching statistical significance, MAIT cell percentage remained depleted at C4 after cICB treatment, but not sICB (Figure S5.29a). However, as MAIT cell-associated *TRAJ12* and *TRAJ20* were not found to be significantly differentially expressed, MAIT cell percentage was recalculated as the percentage of TRA reads with carriage of *TRAV1-2* and *TRAJ33*, hence excluding any MAIT cells expressing *TRAJ12* or *TRAJ20*. Comparison between paired C1/C2 or C1/C4 samples revealed a more significant depletion of *TRAJ33*-expressing MAIT cells as opposed to MAIT cells as a whole (Figures 5.36b, S5.29b). No such changes were observed in flow cytometry data and may be explained by low statistical power or the use of 5-OP-RU-labelled MR1 tetramers, which capture all MAIT cells, not limited to those expressing TRAJ33 and TRBV6-4. Furthermore, previous studies have demonstrated that 5-OP-RU-labelled MR1 tetramer-sorted T-cells or MR1-restricted T-cells, in general, are not entirely composed of canonical MAIT cell TCRs and often contain atypical TCRs[428,580,581]. The percentage of TCR reads made up of TRAJ33$^+$ MAIT cell clones was also tracked longitudinally by treatment type and revealed a continuous depletion after cICB that did not resolve in time (Figure 5.36c). However, no changes were detected after sICB treatment.

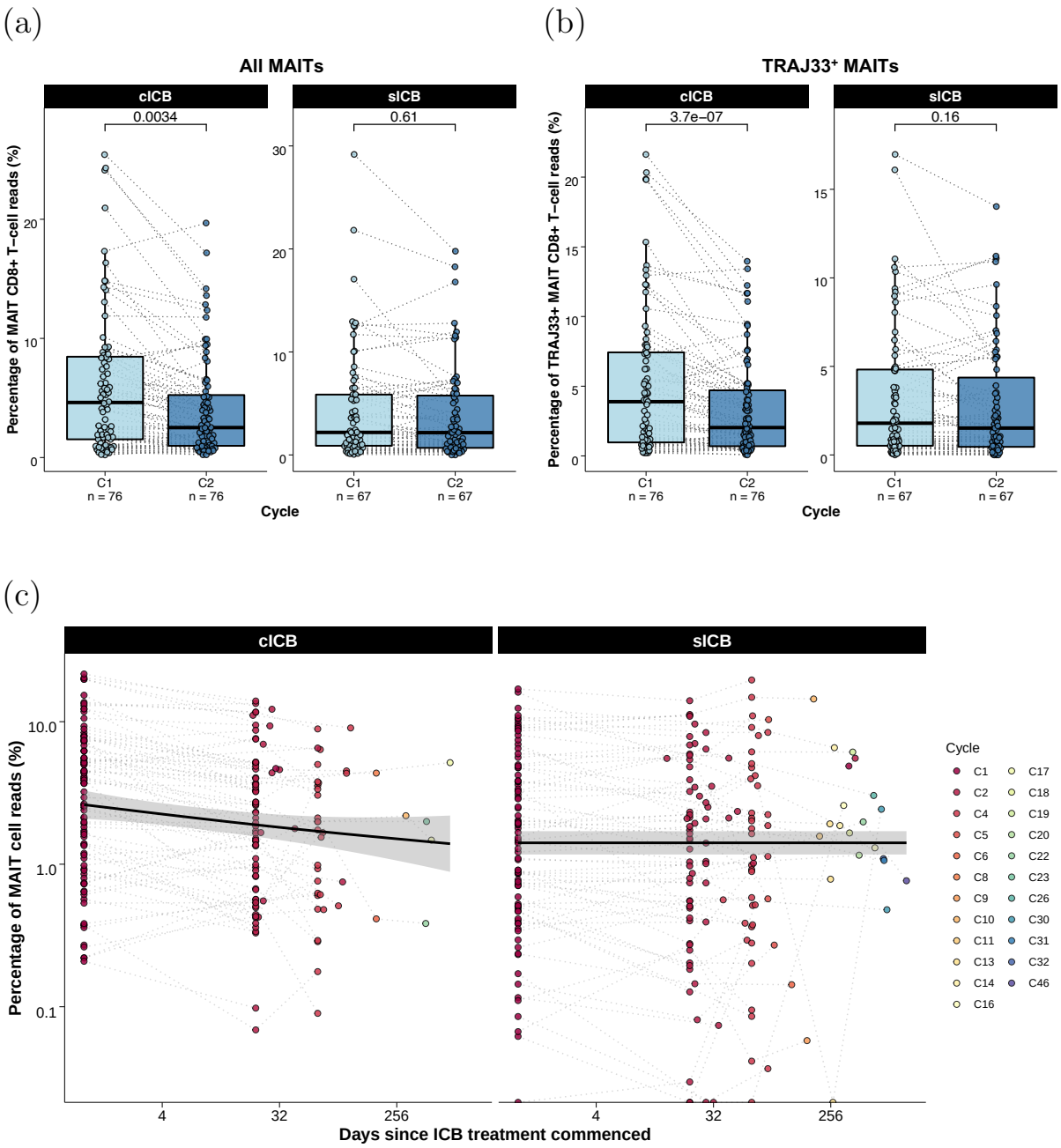


Figure 5.36 MAIT cells are depleted following cICB treatment
The average percentage of TRA reads expressing MAIT cell-associated *TRAV1-2* with **a)** either *TRAJ12/TRAJ20/TRAJ33* or **b)** specifically *TRAJ33* is compared between paired C1/C2 samples by ICB treatment type (n=67 sICB, n=76 cICB). Statistics were generated using paired Wilcoxon signed-rank tests. **c)** The percentage of TRAJ33$^+$ MAIT cell reads is tracked over the course of ICB by treatment type (n=224 sICB, n=209 cICB) with points coloured by ICB treatment cycle.

Surprisingly, the loss in MAIT cells after cICB was found to be specific to CMV$^-$ patients (Figures S5.29c, S5.29d). This may be explained by the depletion in MAIT cells that is observed in CMV$^+$ patients (Figure 3.6, 5.12a, 5.12b) and thus any effect of cICB treatment in MAIT cell reduction may be limited. Accordingly, no difference in MAIT cell activation was observed following ICB treatment (data not shown). Despite the decline in MAIT cells observed following cICB, no change in MAIT cell Shannon diversity or Gini index was observed between C1/C2 samples, regardless of CMV serostatus (data not shown), after subsampling to 100 MAIT cell reads per sample (Figures S5.30a, S5.30b). This may represent that the MAIT cell population comprises viral/activation sensitive and insensitive cells.

To support these findings, MAIT cell gene enrichment analysis was performed on differentially expressed CD8$^+$ T-cell genes following cICB treatment using MAIT cell-associated genes (Figure 5.17a). This revealed that MAIT cell-associated genes were significantly enriched in genes downregulated after cICB (Figure 5.37a). The same analysis was also performed for γδ-associated genes to determine the specificity of this depletion and confirmed that γδ-associated genes (Figure 5.17b) were not enriched within cICB DEGs (Figure 5.37b). This validated that the reduction in MAIT cells observed after cICB is not necessarily due to TCR downregulation since MAIT cell gene expression was also depleted. Despite the profound loss in circulating MAIT cells following cICB, ICB treatment had no effect on the response of MAIT cells to activating TCR-dependent/independent stimuli (Figure S5.31).

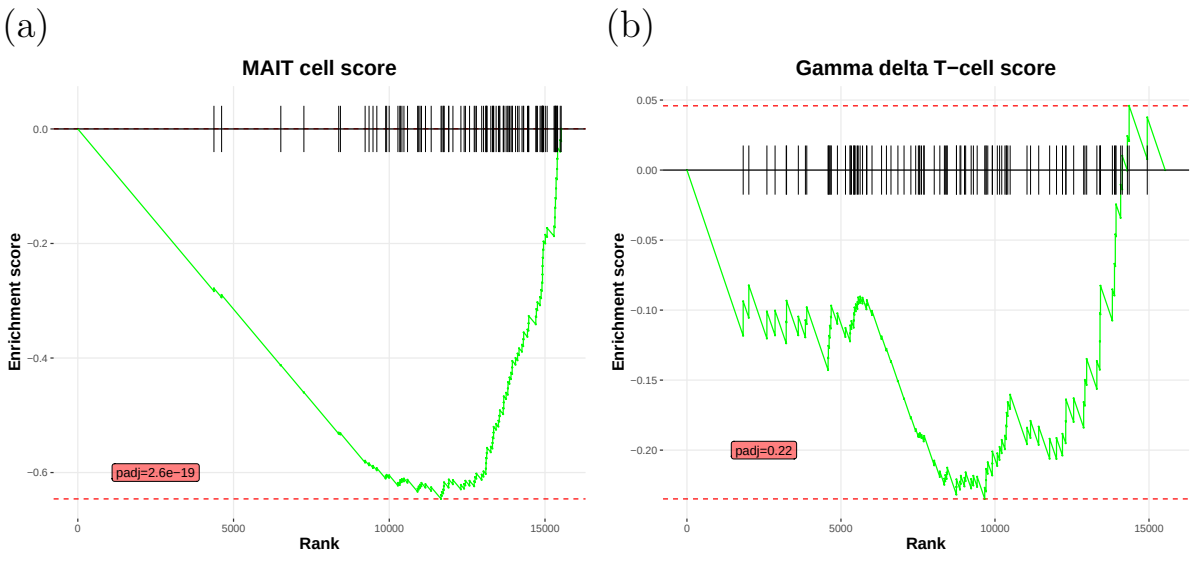


Figure 5.37 MAIT cell-associated genes are downregulated after cICB treatment
Barcode plots show enrichment of the top 100 most significantly associated **a)** MAIT cell and **b)** γδ T-cell genes amongst high or low ranked genes identified between paired cICB-treated C1/C2 CD8$^+$ T-cell samples (n=77). Adjusted p-values for the enrichment are displayed in red boxes.

Separately, owing to the upregulation of CXCR3 ligands by monocytes and B-cells at C2 and the loss of T-cells in response to CXCL10 upregulation (Figures 4.10c, 4.10d, S4.5), the effect of CXCL10 upregulation was compared to MAIT cell loss. Interestingly, a higher plasma concentration of CXCL10 in patients receiving cICB was associated with a reduced MAIT cell percentage (Figure 5.38). However, no such association was detected for patients receiving sICB treatment and may explain why a reduction in MAIT cells is only observed following cICB.

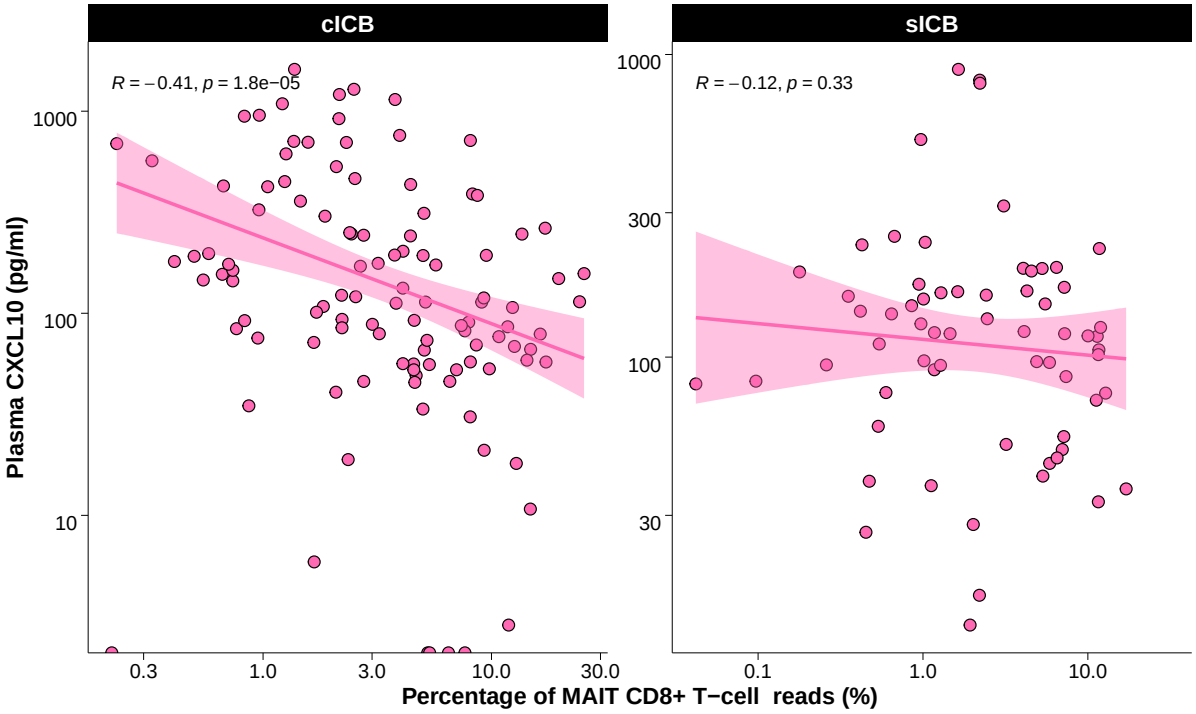


Figure 5.38 MAIT cell percentage inversely correlates with plasma CXCL10
MAIT cell percentage of CD8$^+$ T-cell reads is compared against plasma CXCL10 and faceted by ICB treatment type (n=245 cICB, n=267 sICB). Statistics were calculated using Spearman's rank correlation coefficient.

Although TRAJ33$^+$ MAIT cell loss was not found to be associated with PD-1 loss or IgG4 binding in CD8$^+$ T-cells, surrogates for ICB binding, TRAJ33$^+$ MAIT cell loss was found to significantly negatively correlate with CD8$^+$ T-cell ICB response score, *TOX2* and *MKI67* normalised gene counts (Figure 5.39). Whilst IgG4 binding is important for resultant CD8$^+$ T-cell ICB response, CD8$^+$ T-cell ICB score represents the endpoint of ICB response and may be more informative. Additionally, CD8$^+$ T-cell normalised expression of *TOX2* and *MKI67* were also proven to be highly predictive of CD8$^+$ T-cell ICB response. Interestingly, no association of any metric of B-cell ICB response, including B-cell percentage, CSR, ASC score and CD19$^+$ B-cell ICB response score, was found to associate with TRAJ33$^+$ MAIT cell loss at C2 following ICB treatment (Figure 5.39).

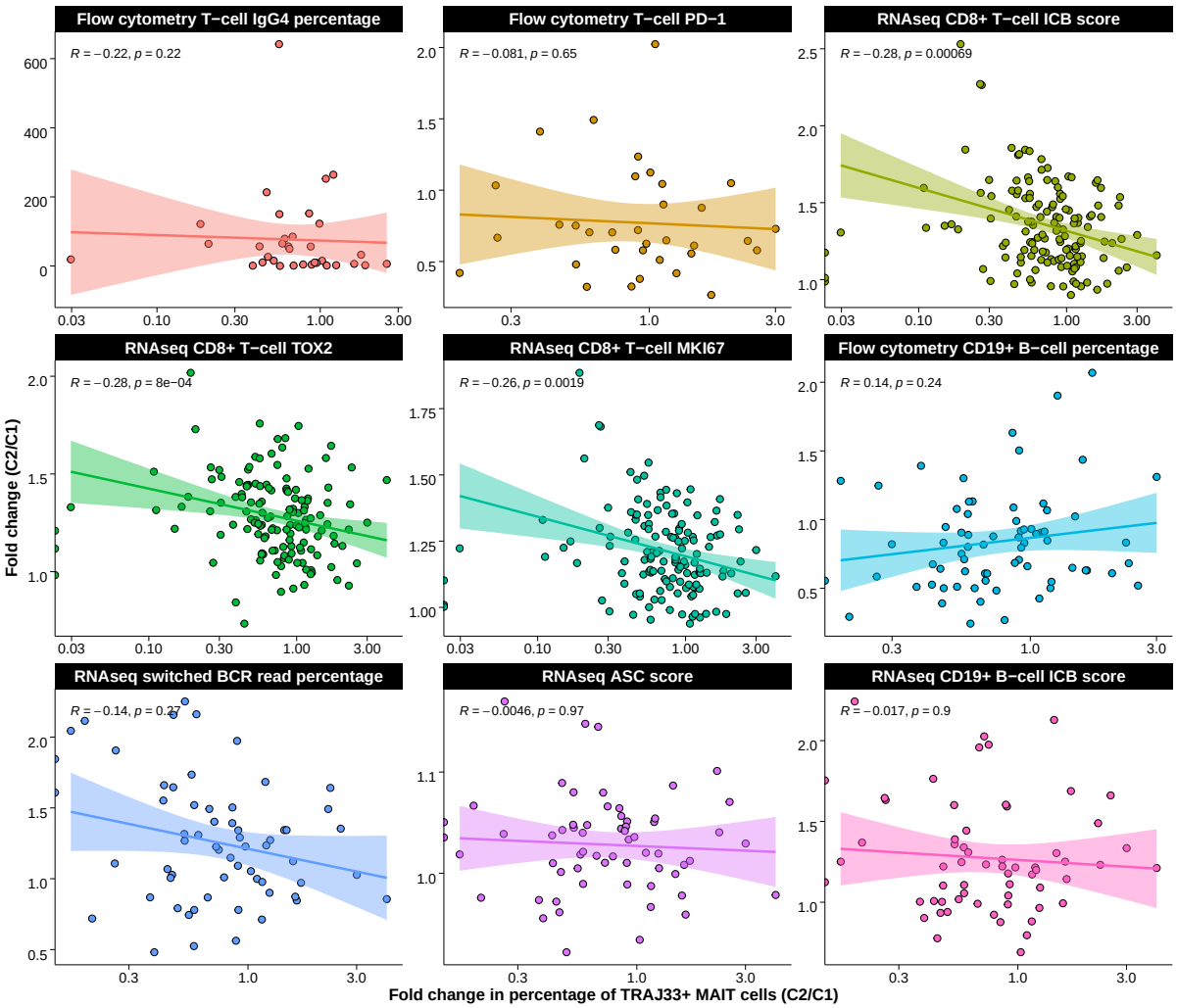


Figure 5.39 TRAJ33$^+$ MAIT cell loss associates with CD8$^+$ T-cell ICB response, but not CD19$^+$ B-cell ICB response
The fold change in percentage of TRA reads aligning to TRAJ33$^+$ MAIT cells at C2 (C2/C1) is compared to the fold change in other metrics known to change with ICB treatment (n=34-143). Statistics were calculated using Spearman's rank correlation coefficient.

5.2.4.4 MAIT cells demonstrate cytotoxicity against melanoma cell lines

With MAIT cell activation strongly correlating with CD8$^+$ T-cell cytotoxicity score (Figure 5.20b), it was hypothesised that activated MAIT cells may have the capacity for melanoma-directed lysis. MAIT cell loss, which negatively correlates with MAIT cell activation and may signify migration to the tumour, was found to inversely correlate with an induction in CD8$^+$ T-cell cytotoxicity score (Figure 5.40). This negative correlation was more striking following cICB treatment and may show that a reduction in circulating MAIT cells, but an increase in activation, may improve cytotoxic potential.

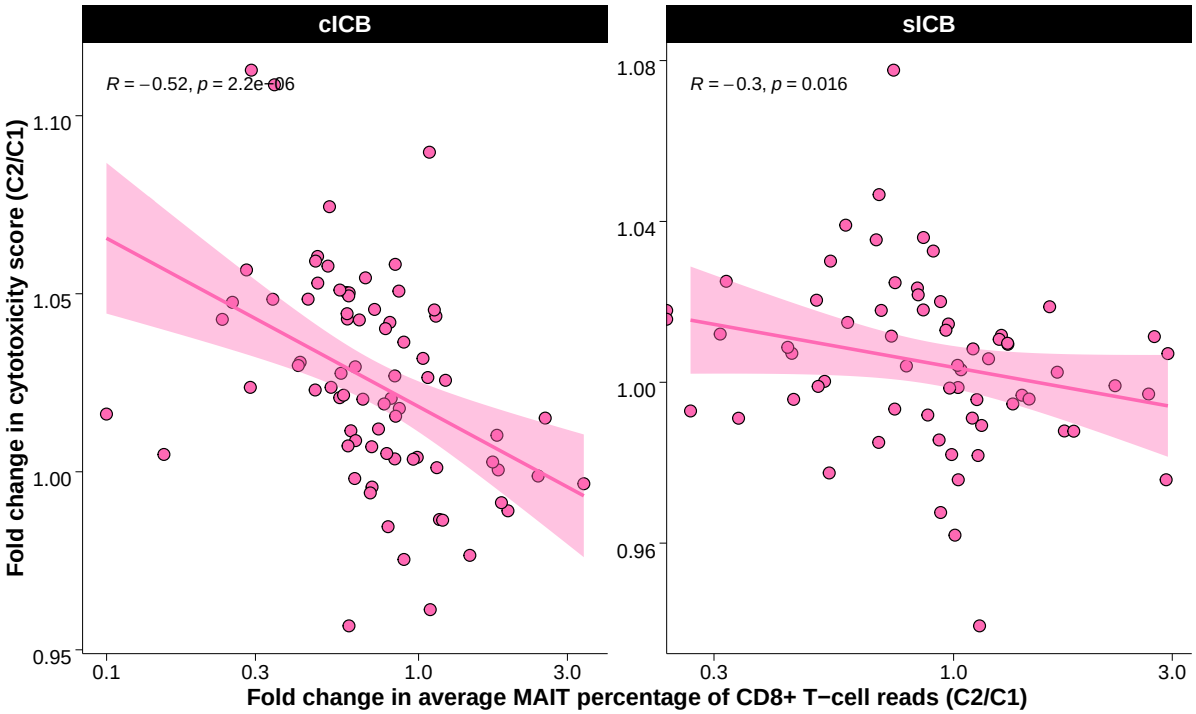


Figure 5.40 MAIT cell loss associates with an increase in cytotoxicity score at C2
The fold change in percentage of MAIT CD8$^+$ T-cell reads (C2/C1) is compared to the fold change in CD8$^+$ T-cell cytotoxicity score (C2/C1) by ICB treatment type (n=67 sICB, n=77 cICB) after subsampling to 1,496 reads and taking the average from 1,000 iterations. Statistics were calculated using Spearman's rank correlation coefficient.

MAIT cells have previously been demonstrated to elicit direct lysis of bacteria as well as indirectly of virally-infected cells through IL-12, IL-18 and type I IFN activity[404]. Treatment of cancer cell lines with MAIT cell-specific 5-OP-RU has been shown to enable MAIT cells to efficiently eliminate cancer cells through MR1[424,582]. Yet, whether MAIT cells can eliminate melanoma in the absence of known MAIT ligands remains unknown.

To investigate if MAIT cells have cytotoxic potential against melanoma cell lines, frozen PBMCs were thawed and resuspended in warmed R10 media. Cells were then stained with PE-conjugated 5-OP-RU-loaded tetramer followed by incubation with anti-PE microbeads. Next, samples were applied to magnetic columns isolating MAIT cell-depleted PBMC samples from flow throughs and MAIT cells from cells magnetically labelled. Unstained PBMC samples were also passed through the column and served as controls. PBMCs, MAIT cell-depleted PBMCs and isolated MAIT cells were then cocultured with a variety of melanoma cell lines for five days at a 1:1 effector:target ratio.

MAIT cells were found to induce tumour-directed cytotoxicity independently of other PBMC subsets (Figure 5.41). Strikingly, removal of MAIT cells from PBMC samples was associated with a reduction in cytotoxicity compared to PBMC controls, highlighting a potentially important role of MAIT cells in tumour lysis. This cytotoxicity is not thought to be a result of alloreactivity and HLA mismatch as MAIT cells are MHC-independent.

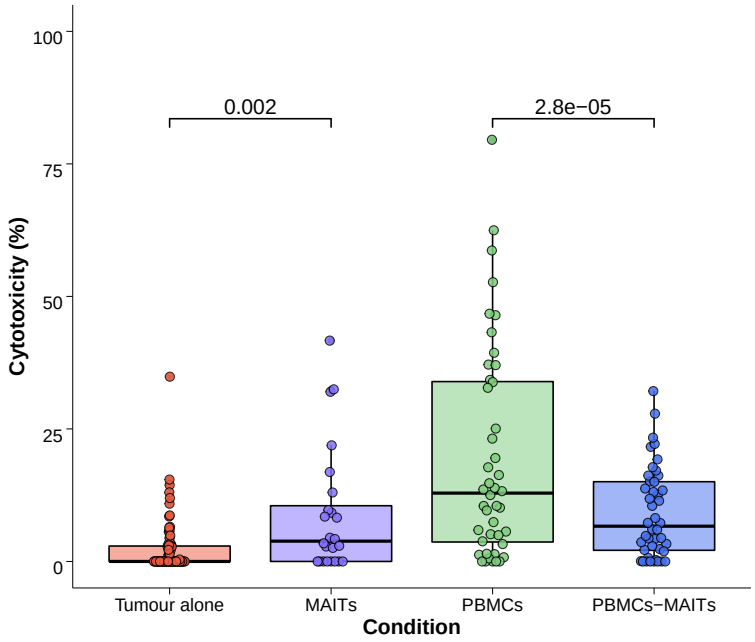


Figure 5.41 MAIT cells demonstrate antimelanoma cytotoxicity
PBMCs, MAIT cell-depleted PBMCs (PBMCs-MAITs) and MAIT cells were cocultured with 12 melanoma cell lines at an effector:target ratio of 1:1 for five days (n=2-4 samples). Cytotoxicity was detected by MTT assay as the percentage of melanoma cells lost after coincubation. Tumour alone controls represent any background melanoma cell death observed in the absence of T-cells or PBMCs. Statistics were calculated using an unpaired or paired Wilcoxon signed-rank test for tumour alone/MAIT cell and PBMC/MAIT cell-depleted PBMC comparisons respectively.

Although significant melanoma cell lysis was observed after culture with MAIT cells and PBMCs, the level of cytotoxicity was limited. As a result, PBMC culture was further optimised by using anti-CD2/anti-CD3/anti-CD28 T-cell expander beads prior to coculture to increase T-cell survival, proliferation and activation. PBMC samples were cultured with IL-2 ±anti-CD2/anti-CD3/anti-CD28 at varying concentrations (2µl, 5µl, 10µl, 20µl beads per million PBMCs/ml) and left to expand for a week at 37°C in a humidified atmosphere of 5% CO_2 to outgrow the beads. Cells were washed to remove any cytokines induced as a result of activation and put through a magnetic column to remove any remaining anti-CD2/anti-CD3/anti-CD28 beads and were cocultured with melanoma cell lines for five days at an effector:target ratio of 1:1. PBMCs cultured with IL-2 in the absence of beads were found to kill at a similar level as before (Figures 5.41, 5.42a). However, the addition of beads massively improved cytotoxicity and demonstrated the ability of MM patient PBMCs to kill all 12 melanoma cell lines (Figures 5.42a, S5.32). Despite profound T-cell expansion and activation, very little nonspecific toxicity was observed after culture with primary melanocyte cells (Figure 5.42b). With little difference between the lowest and highest concentration, beads were subsequently used at the lower concentration of 2µl/1x10^6 PBMCs/ml.

Prior to MTT assay, PBMCs were removed from cocultures, taking care not to remove any tumour, and were processed for flow cytometry analysis. Interestingly, MAIT cell production of cytolytic cytokines including GZMB, IFN-γ and TNF-α was associated with overall cytotoxicity, which was not observed for other PBMC subsets including non-MAIT T-cells (data not shown), thus implicating a role for MAIT cells in tumour cell lysis (Figure 5.43).

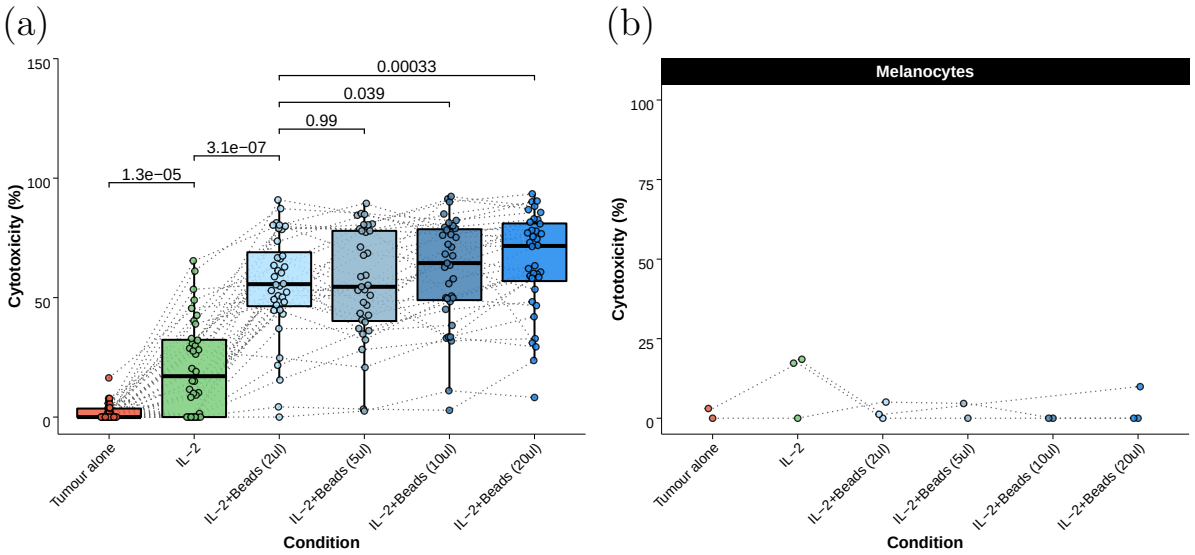


Figure 5.42 Culture with T-cell expander beads improves melanoma-specific cytotoxicity
PBMC samples (n=3) were expanded for seven days with varying concentrations of anti-CD2/anti-CD3/anti-CD28 T-cell expander beads (2µl, 5µl, 10µl, 20µl beads/1x10^6 PBMCs/ml) or IL-2 alone as a control. Expanded T-cells were then cultured with either **a)** melanoma cell lines (n=12) or **b)** primary melanocytes. Cytotoxicity is a measure of melanoma cell death detected by MTT assay and quantified as the percentage reduction in melanoma cells. Tumour alone controls demonstrate background melanoma cell death in the absence of PBMCs. Statistics were calculated using an unpaired Wilcoxon signed-rank test for comparisons with tumour alone or using paired Wilcoxon signed-rank test for comparisons with other conditions.

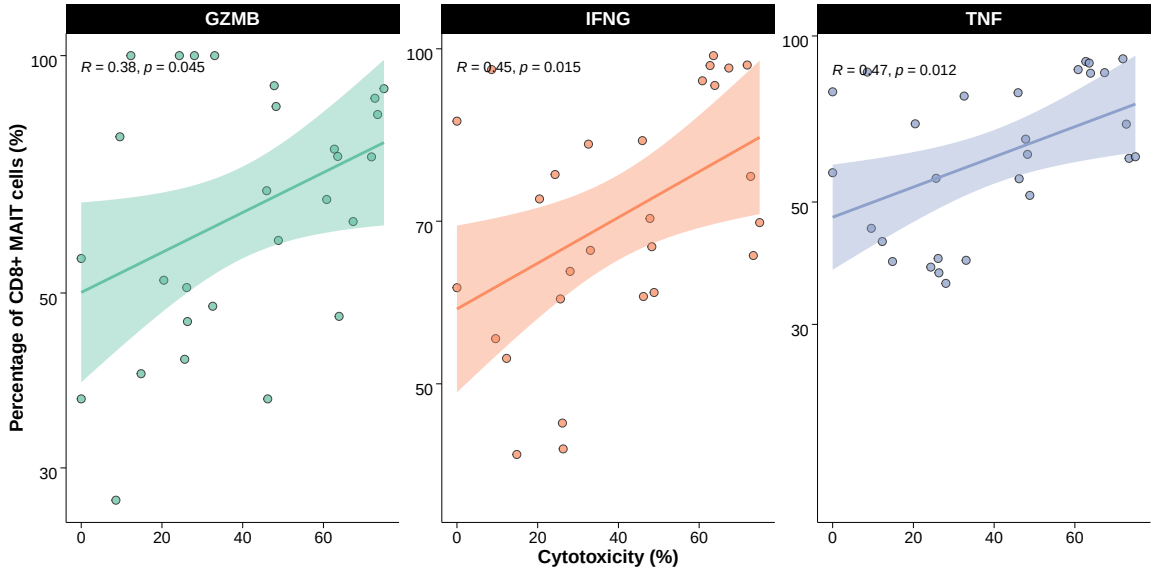


Figure 5.43 Expression of cytolytic MAIT cytokines associates with melanoma cytotoxicity
PBMC samples cultured with 2µl anti-CD2/anti-CD3/anti-CD28 T-cell expander beads/1x10^6 PBMCs/ml from several cocultures (n=33) were processed for flow cytometry analysis. Expression of MAIT cell effector cytokines is compared to observed cytotoxicity determined by MTT assay as the percentage reduction in melanoma cells. Statistics were calculated using Pearson correlation coefficient.

Next, melanoma-specific cytotoxicity was compared between paired $CD8^+$, MAIT and γδ T-cell samples. Following PBMC culture with IL-2 and anti-CD2/anti-CD3/anti-CD28 beads (2µl beads per million PBMCs/ml) for seven days, MAIT cells were isolated as previously mentioned. γδ T-cells were isolated by incubating PBMCs with a PE-labelled pan-γδ TCR antibody prior to incubation with anti-PE beads and subsequent isolation. PBMCs were incubated with CD8 microbeads to isolate $CD8^+$ T-cells (see section 2.2.4). Separated $CD8^+$, MAIT and γδ T-cells were then cultured with melanoma cell lines at an effector:target ratio of 1:1 for five days. Despite MAIT cells inversely correlating with $CD8^+$ T-cell cytotoxicity score and γδ T-cells correlating (Figure 5.19), no difference in killing was observed (Figure 5.44a). $CD8^+$ T-cell cytotoxicity score strongly correlates with Temra populations, CMV infection and TCR clonality, perhaps being more representative of chronic T-cell activation and clonal expansion. This may explain why MAIT cell percentage does not correlate with $CD8^+$ T-cell cytotoxicity score yet having the capacity for direct melanoma lysis.

The mechanism by which MAIT cells are able to elicit such cytotoxicity was further investigated through MR1 blockade in melanoma cell lines to determine if melanoma recognition is TCR dependent. Blockade of either MHCI or MR1 was found to reduce PBMC cytotoxicity (Figure 5.44b). However, blockade of either receptor did not completely abrogate killing, likely as a result of compensatory mechanisms by other PBMC cells. Despite a reduction in cytotoxicity observed following tumour MR1 blockade in PBMC cocultures, the same effect was not observed in isolated MAIT cell-tumour cocultures, although a trend was observed (Figure 5.44c). This may be due to low statistical power or subsequent blockade of other MR1-restricted non-MAIT cells that are present within PBMC cocultures. However, addition of MAIT cell inhibitory ligand Ac-6-FP did significantly impede cytotoxicity. This further demonstrates that MAIT cell activation is important for tumour cell lysis, although this may not be mediated through the TCR. These data indicate that while melanoma-directed lysis is partially dependent on MR1 (Figure 5.44b), it is not essential and may instead be mediated through TCR-independent cytokine stimulation in MAIT cells. To verify this, MAIT cells were cultured with a combination of IL-12, IL-15 and IL-18, cytokines known to elicit MAIT cell activation through TCR-independent mechanisms. Although addition of these cytokines had no effect on melanoma death when added to melanoma cell lines in isolation (data not shown), a significant increase in cytotoxicity was observed upon addition of these cytokines in the presence of MAIT cells (Figure 5.44c). After combining data from all MAIT cell-tumour cocultures, MAIT cells were found to have broad reactivity against most tested melanoma cell lines and may therefore have an important role in antitumour and ICB responses (Figure S5.33).

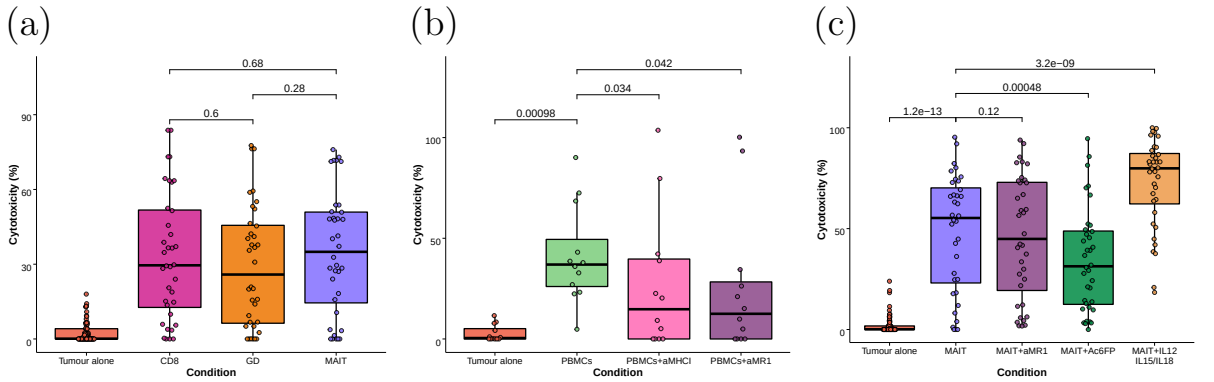


Figure 5.44 MAIT cells contribute to antimelanoma cytotoxicity
a) Isolated CD8$^+$, MAIT and γδ T-cells were cultured with 12 melanoma cell lines at an effector:target ratio of 1:1 for five days with cytotoxicity determined by WST-8 assay. Cytotoxicity, quantified as the percentage of melanoma cell death, is compared between CD8$^+$, MAIT and γδ T-cell cocultures (n=12 melanoma cell lines, n=3 samples). **b)** PBMCs were cultured with untreated (UT) or anti-MHCI/anti-MR1 (aMHCI/aMR1) pretreated melanoma cell lines (n=3 melanoma cell lines, n=3 samples) at an effector:target ratio of 1:1 for five days using a WST-8 assay to quantify cytotoxicity. **c)** Isolated MAIT cells were cultured with 12 melanoma cell lines ±MAIT cell inhibitor Ac-6-FP (MAIT+Ac6FP), ±IL-12/IL-15/IL-18 (MAIT+IL12/IL15/IL18) or with anti-MR1-treated melanoma cell lines (MAIT+aMR1) at an effector:target ratio of 1:1 for five days. Tumour alone controls represent background melanoma cell death in the absence of T-cells or PBMCs. Statistics were calculated using paired Wilcoxon signed-rank tests or an unpaired Wilcoxon signed-rank test for comparisons with tumour alone. *GD = Gamma delta T-cell.*

Although MAIT cell loss at C2 did not associate with OS or PFS (data not shown), MAIT cell depletion at C4 following sICB was found to associate with shorter OS and PFS (Figures 5.45a, 5.45b). The same effect is not observed at C4 after cICB treatment and may be because MAIT cells are already depleted in response to cICB unlike sICB where there may be greater variation in response. Even though MAIT cell loss was only associated with OS and PFS following sICB treatment, a high MAIT cell percentage at C4 was associated with longer OS and PFS for all samples (Figures 5.45c, 5.45d). This mirrors observations made by other studies which find that patients with a high MAIT cell percentage associates with favourable outcomes[426,427]. This suggests that either maintaining peripheral populations of MAIT cells is important for eliciting ICB response or that loss is associated with chronic activation and ultimately an absence of response to ICB treatment. Surprisingly, patients with a low MAIT cell Shannon diversity, calculated after subsampling to 100 MAIT cell reads, were found to associate with prolonged OS and PFS (Figures 5.45e, 5.45f). Accordingly, a high MAIT cell Gini index was found to associate with longer PFS (data not shown). However, analysis was limited to samples with at least 100 MAIT cell reads. One may infer that it is instead the maintenance of certain MAIT cell clones that determines ICB response, although this should be investigated further.

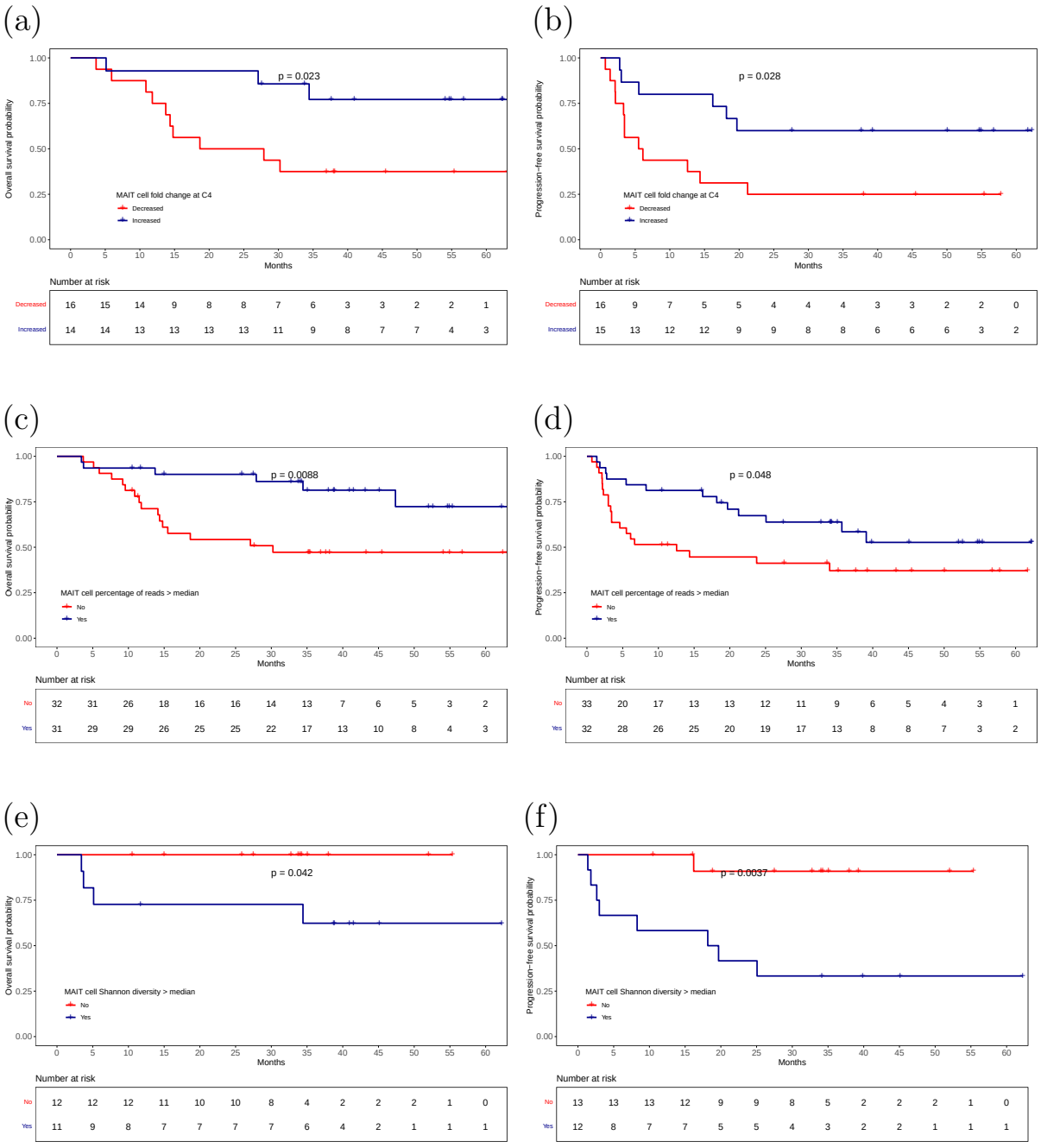


Figure 5.45 Maintenance of peripheral MAIT cell populations at C4 associates with survival Kaplan Meier plots showing any differences in survival between **a,b)** MM patients with an increase or decrease in MAIT cell percentage of TRA reads at C4 after sICB (n=30-31), **c,d)** MM patients above and below the median MAIT cell percentage of TRA reads at C4 following sICB or cICB (n=63-65) or **e,f)** MM patients with a MAIT cell Shannon diversity above and below the median at C4 after sICB or cICB (n=23-25) by **a,c,e)** overall survival or **b,d,f)** progression-free survival. Patients above the median are represented by a blue line and those below by a red line.

5.2.5 Clonal dynamics

5.2.5.1 Large clones at baseline persist following ICB treatment

Although no changes were observed in BCR clone number and size after ICB treatment, BCR clones were found to be more switched following cICB which resolved at later time-points. Similarly, no changes in TCR clone number and size were detected between paired C1/C2 and C1/C4 samples, however, a depletion in MAIT cells was observed following cICB treatment. These data suggest a role for ICB in modulating clonal expansion and deletion in specific B-cell and $CD8^+$ T-cell populations. To ascertain if ICB had such effects, BCR and TCR clones were tracked across ICB treatment, monitoring changes in proportion. TCR clones were also annotated with publicly available datasets where possible.

BCR and TCR clones present at baseline (C1), as identified by CDR3 nucleotide sequence, were tracked over the course of treatment. Strikingly, only an average of 11.06% (±4.26%) and 21.15% (±8.84%) of baseline BCR and TCR clones respectively were still present after one cycle of ICB treatment, although a similar percentage was maintained at later time-points (Figure 5.46). These findings were consistent even when identifying clones by CDR3 amino acid sequence (Figure S5.34).

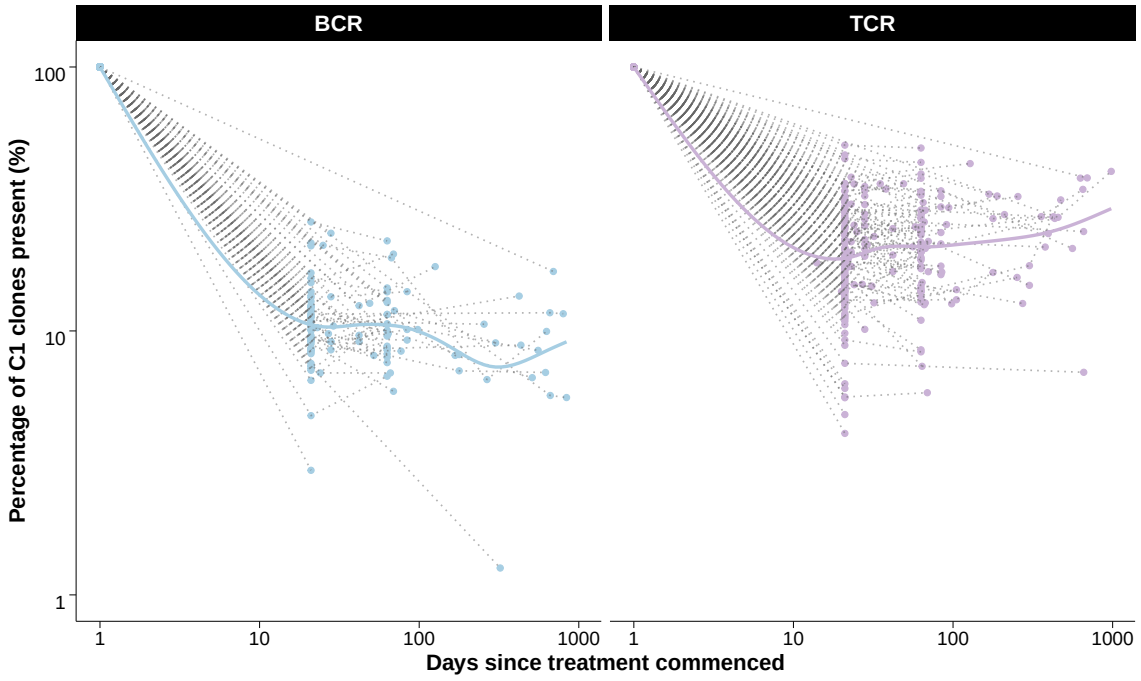


Figure 5.46 The majority of baseline BCR and TCR clones by CDR3 nucleotide sequence are lost following ICB treatment
The percentage of baseline (C1) clones present per sample is tracked longitudinally looking at the days since ICB treatment commenced for BCR (n=212) and TCR (n=434) clones as identified by CDR3 nucleotide sequence.

However, almost all large clones at baseline (C1) persisted, taken as clones representing 0.1% and 0.5% of BCR and TCR reads respectively, selected based on the proportion of reads present at these sizes (Figures 5.5a, 5.5b) and previous literature[371] (Figure 5.47). This suggests that while no difference was observed in clone number or diversity, clonal replacement does take place.

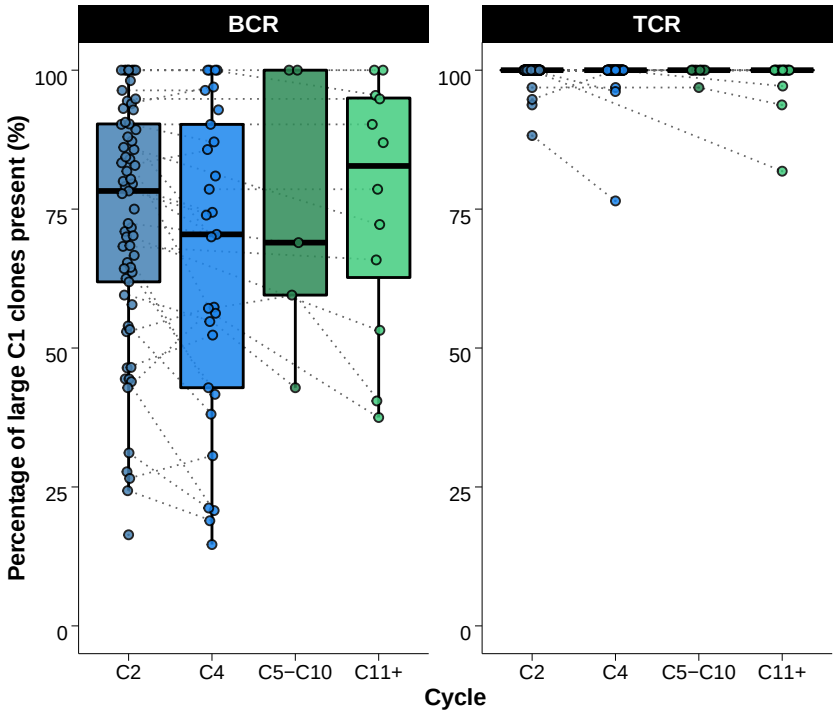


Figure 5.47 Most large clones at baseline persist after ICB treatment
Box plots showing the percentage of baseline (C1) large BCR (n=120) and TCR (n=251) clones, taken as ≥0.1% of BCR reads or ≥0.5% of TCR reads, present at various cycles.

5.2.5.2 Greater clonal changes are observed following cICB treatment

Changes in clonal proportion from C1 to C2 were calculated using Fisher's exact tests per unique clone and adjusted using Bonferroni correction to detect any significant changes in enrichment. Clonal changes were markedly different between patients with some exhibiting overall clonal stability and others displaying marked changes (Figures 5.48a, 5.48b, 5.48c, 5.48d). Due to the higher number of BCR clones detected, which were of a smaller size, greater changes were detected in the BCR repertoire than the TCR repertoire at either C2 or C4 (Figures 5.48e, 5.48f). After adjusting for the number of clones identified, BCR light chain clones were found to be more differentially expressed than heavy chain clones (Figure S5.35a, S5.35b). However, TCR clones varied at a similar rate regardless of chain with the exception of TRD chain clones which is likely due to low expression.

Peripheral blood samples were also collected from an age-matched healthy donor at two different time-points three weeks apart, mirroring the time between ICB treatments, to determine normal variation in such a time frame. This revealed that although hardly any changes occurred in the TCR repertoire, more fluctuations were observed in the BCR repertoire (Figures S5.36a, S5.36b). Although the changes that occurred in the healthy donor TCR repertoire were much less than in patients following ICB treatment, changes in the BCR repertoire were similar to some patients (Figure S5.37). This implies that changes in the TCR repertoire induced by ICB are above background variation, but many of the changes that occur in the BCR repertoire may be a result of typical background fluctuation. This background data is, however, limited to one patient and should be collected for further healthy donors.

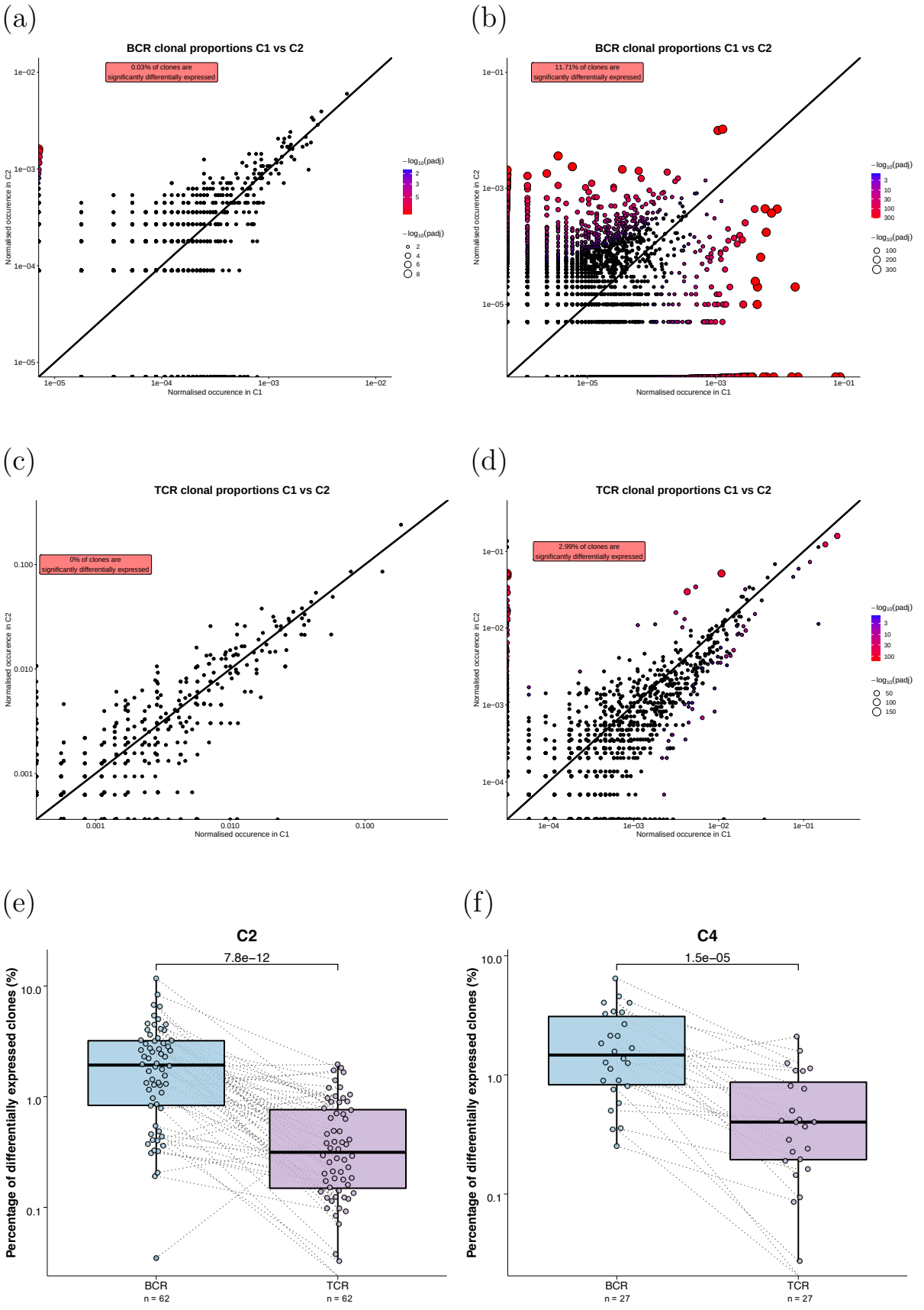

(a)
BCR clonal proportions C1 vs C2
0.03% of clones are significantly differentially expressed
Normalised occurence in C2
Normalised occurence in C1
(b)
BCR clonal proportions C1 vs C2
11.71% of clones are significantly differentially expressed
Normalised occurence in C2
Normalised occurence in C1
(c)
TCR clonal proportions C1 vs C2
0% of clones are significantly differentially expressed
Normalised occurence in C2
Normalised occurence in C1
(d)
TCR clonal proportions C1 vs C2
2.99% of clones are significantly differentially expressed
Normalised occurence in C2
Normalised occurence in C1
(e)
C2
7.8e−12
Percentage of differentially expressed clones (%)
BCR
n = 62
TCR
n = 62
(f)
C4
1.5e−05
Percentage of differentially expressed clones (%)
BCR
n = 27
TCR
n = 27

Figure 5.48

Figure 5.48 (Previous page) ICB induces changes in BCR and TCR clone proportions
Comparison of clone proportions between paired C1/C2 samples for **a,b)** BCR and **c,d)** TCR clones in representative patients displaying **a,c)** few or **b,d)** many clonal changes. Significantly expanding and involuting clones are coloured with point shading and size referring to the adjusted p-value of the differential enrichment. The percentage of clones that are significantly differentially expressed is displayed in red boxes. Statistics were calculated using Fisher's exact tests and adjusted using Bonferroni correction. The percentage of differentially expressed clones at **e)** C2 (n=62) and **f)** C4 (n=27) is compared between paired BCR and TCR samples. Statistics were calculated using paired Wilcoxon signed-rank tests.

The percentage of clones significantly differentially expressed at C2 was greater after cICB than sICB treatment and may reflect the greater changes observed in CSR/SHM and MAIT cells in BCR and TCR repertoires respectively (Figures 5.49a, 5.49b). This difference is even more significant at C4 for TCR clones, however, does not reach significance for BCR clones at C4 (Figures S5.38a, S5.38b).

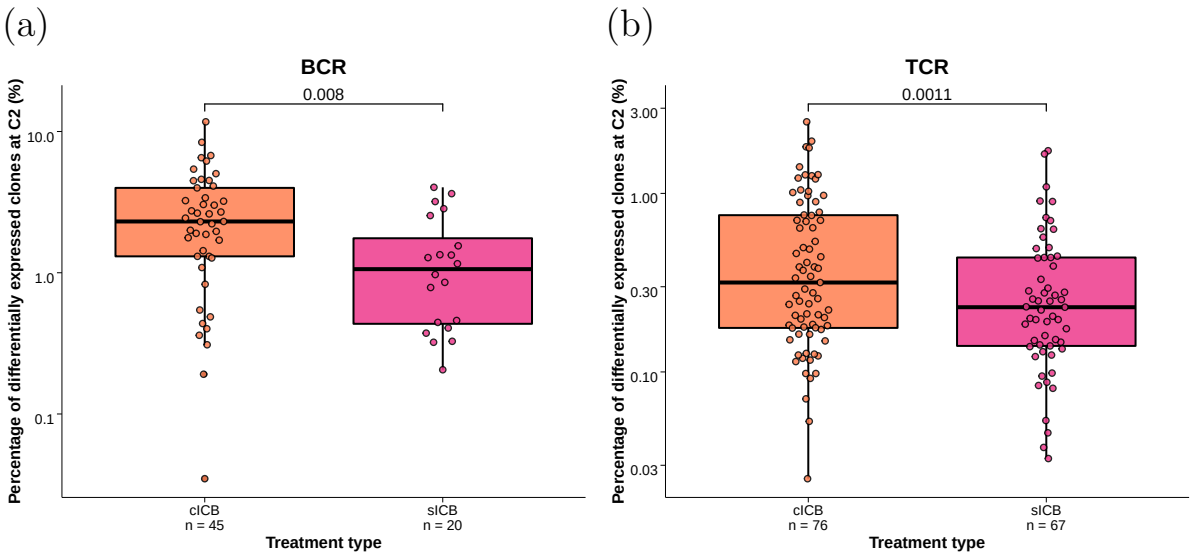


Figure 5.49 cICB induces more clonal changes in BCR and TCR clones than sICB treatment
The percentage of differentially expressed **a)** BCR and **b)** TCR clones at C2 is compared between sICB (n=20 BCR, n=67 TCR) and cICB (n=45 BCR, n=76 TCR) treatments. Statistics were calculated using unpaired Wilcoxon signed-rank tests.

Interestingly, MM patients with a higher percentage of TCR clones that emerge at C2 than the median were found to have longer OS and PFS (Figures 5.50a, 5.50b). Although overall TCR Shannon diversity did not correlate with OS or PFS at C2, the association of novel clones implies that TCR diversification, taken as clonal replacement, is important for ICB response. This supports the previous findings that low clonality, as measured by Gini index and percentage of reads accounting for $\geq$5% of the repertoire at C4, is associated with enhanced survival (Figures 5.30a, 5.30b, 5.30c, 5.30d). As opposed to overall Shannon diversity being important in ICB response, it is maybe the emergence of these novel clones and loss of hyperexpanded clones that is essential. No such associations have been found for BCR clones on account of the prominent diversity

and clonal replacement that is observed.

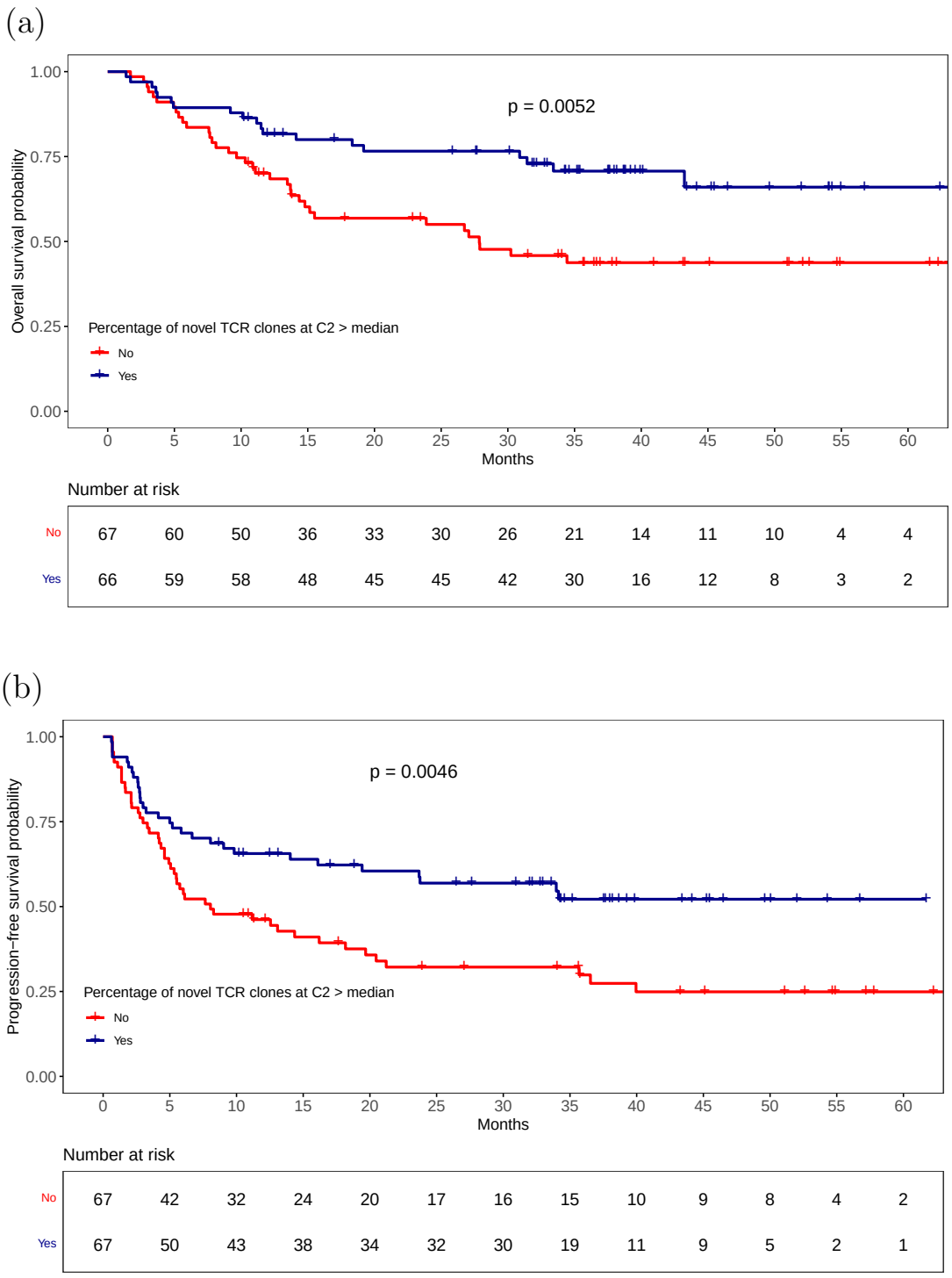
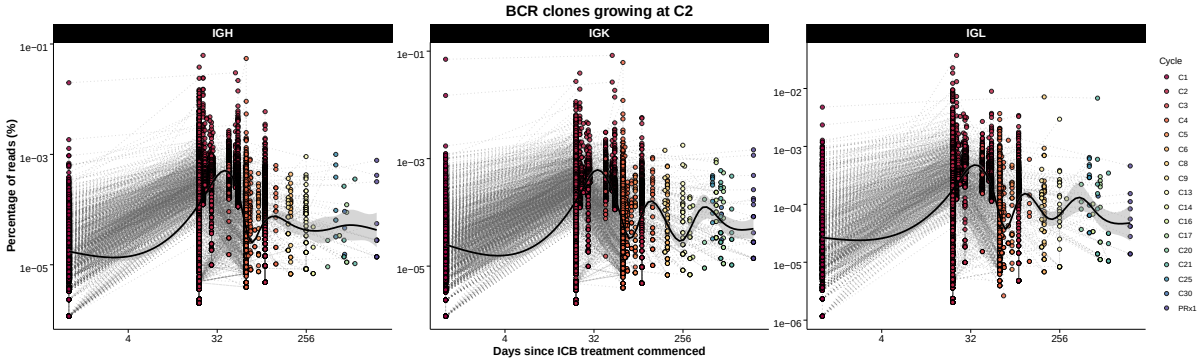


Figure 5.50 Patients with a higher level of novel TCR clones at C2 have enhanced survival Kaplan Meier curves showing the effect of the percentage of novel TCR clones at C2 on **a)** overall survival (n=133) or **b)** progression-free survival (n=134). Patients are dichotomised into those with a percentage of emergent clones above and below the median. Patients above the median are represented by a blue line and those below by a red line.

5.2.5.3 BCR clonal expansion resolves at later time-points

BCR clones significantly expanded at C2 were tracked across the course of treatment and were found to decrease at later time-points regardless of chain (Figure 5.51a). Owing to the profound diversity observed in the BCR repertoire, clonal expansion at C2 may therefore represent intersample variation. As a result, analysis was repeated for BCR clones significantly expanded at C4 to determine if these clones were only expanded at C4 or if they gradually increased up to this point. Indeed, clones expanding at C4 were also found to be elevated at C2 suggesting that these expanded clones are genuinely expanded and not just as a result of sample diversity (Figure 5.51b). Although reduced at later time-points, expanding BCR clones persisted even after cessation of treatment. Similarly, clonal depletion resolved at later time-points (Figures S5.39a, S5.39b).

(a)



(b)

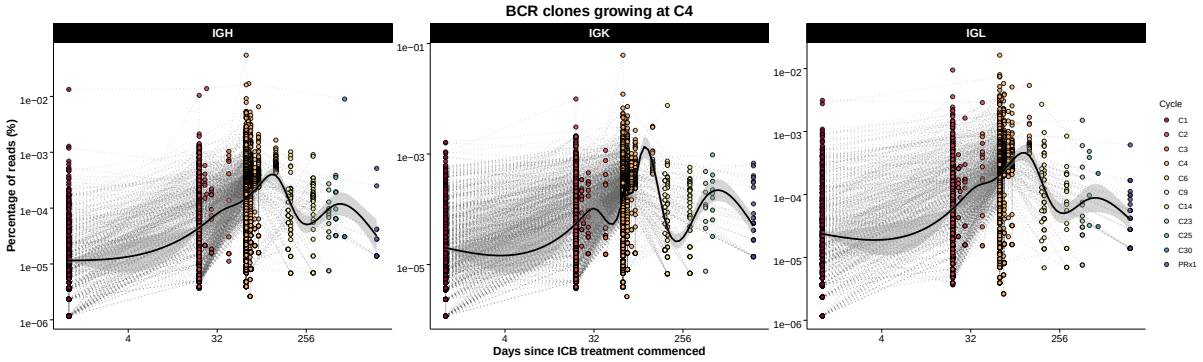


Figure 5.51 Significantly expanding BCR clones are reduced at later time-points
The percentage of reads accounted for by significantly expanding BCR clones at **a)** C2 (n=65) and **b)** C4 (n=29) by chain is tracked longitudinally per expanding clone by days since ICB treatment commenced. Samples are coloured by ICB treatment cycle. *PRx1 = Sample collected after cessation of ICB treatment.*

5.2.5.4 Expanding BCR clones are predominantly switched

BCR usage was then compared between significantly expanded and nonexpanded BCR clones at C2 or C4 (Figures 5.52a, 5.52b). Whilst unswitched IGHC isotypes were

significantly enriched in nonexpanding clones, switched IGHC genes were overexpressed by expanding clones. This suggests that BCR clones expanding at either C2 or C4 are more switched, which may be as a result of increased ASCs, CSR or proliferation of switched clones. Expanding clones at C2 or C4 also displayed a higher mutation rate than nonexpanding clones (Figures 5.52c, 5.52d).

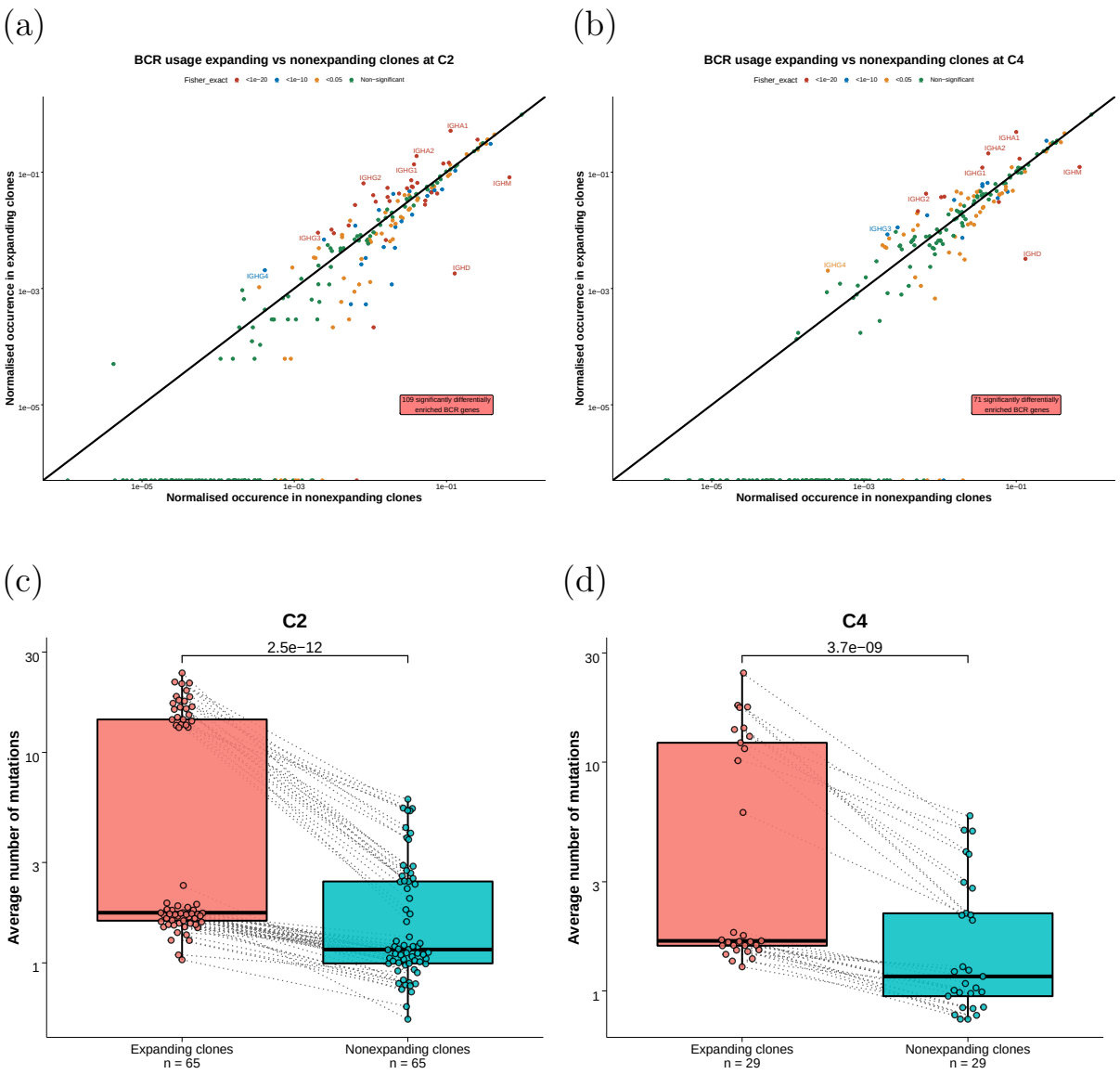


Figure 5.52 Expanding BCR clones are predominantly switched and highly mutated
BCR usage is compared between significantly expanding and nonexpanding clones at **a)** C2 (n=65) and **b)** C4 (n=29). Statistics were calculated using Fisher's exact tests and adjusted using Bonferroni correction. BCR genes are coloured by the significance of the enrichment with IGHC genes labelled. The number of significantly differentially enriched BCR genes is displayed in a red box. The average number of mutations per BCR clone is compared between significantly expanding and nonexpanding BCR clones at **c)** C2 (n=65) and **d)** C4 (n=29). Statistics were calculated using paired Wilcoxon signed-rank tests.

Supporting the notion that ICB increases CSR, the vast majority of novel IGH clones at C2 were found to be switched (Figure 5.53a). Surprisingly, this was observed following both sICB and cICB treatments despite no significant increase in CSR following sICB treatment. Persistent BCR clones that were found in both C1 and C2 samples were found to be predominantly switched suggesting that most persistent clones were already switched and that many of the novel clones may arise due to CSR (Figure 5.53b). In support of this, almost all large persisting clones ($\geq$0.1% of BCR reads) at C2 were found to be switched. This proportion was significantly lower in smaller persistent clones (<0.1% of BCR reads) (Figure 5.53c). However, no such differences were found at C4 (Figures S5.40a, S5.40b). This suggests that both sICB and cICB similarly induce CSR, but due to stronger effects of cICB on clonal expansion (Figure 5.49a), is more apparent after cICB. However, these effects were transient and normalised by C4. With an increase in tumour-associated TLS's[363,366,430] and CXCL13 (Figures 4.27a, 4.27b, 4.27c) observed in response to ICB treatment, this may indicate that these relevant switched clones migrate to the tumour site. Therefore, any changes observed in the periphery following ICB are transient.

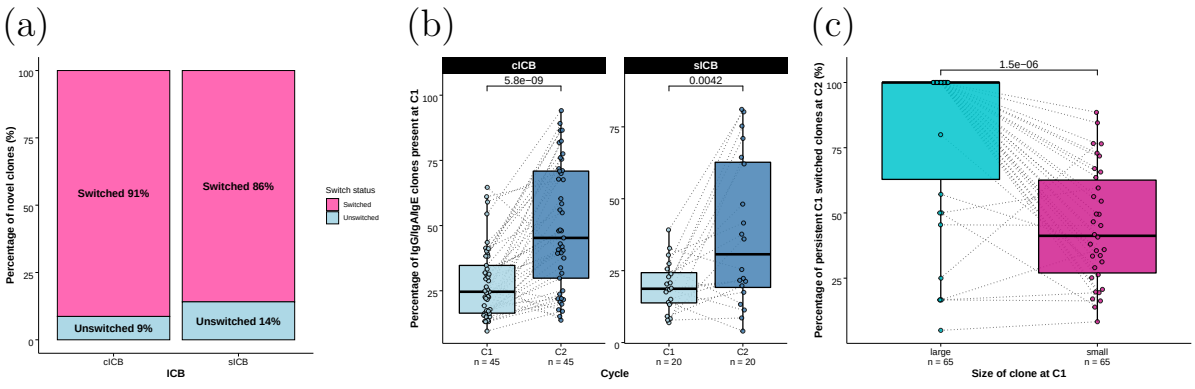
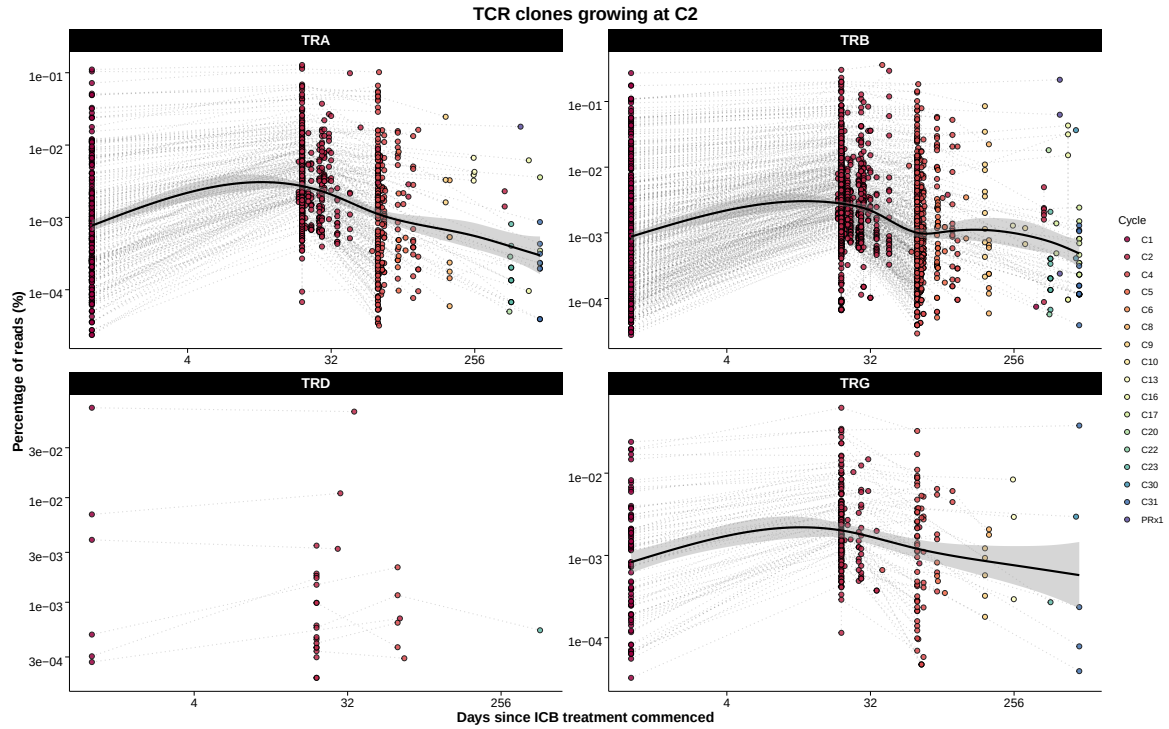


Figure 5.53 Most novel BCR clones at C2 are switched
a) Bar plots showing the percentage of novel BCR clones at C2 (n=20 sICB, n=45 cICB) that are unswitched (IgM/IgD) or switched (IgG/IgA/IgE) by treatment type. **b)** Box plots showing the percentage of reads that are switched in BCR clones present in paired C1/C2 samples by treatment type (n=20 sICB, n=45 cICB). **c)** The percentage of switched IGH clones is compared between small (<0.1% of BCR repertoire) and large ($\geq$0.1% of BCR repertoire) persistent baseline (C1) BCR clones found at C2 (n=65). Statistics were calculated using paired Wilcoxon signed-rank tests.

5.2.5.5 TCR clonal expansion resolves at later time-points

Analysis was repeated for TCR clones and similarly revealed that TCR clones expanding at C2 and C4 decrease at later time-points regardless of chain, but nevertheless, do persist (Figures 5.54a, 5.54b). Similarly, significantly involuting TCR clones were found to return to similar levels observed pretreatment (Figures S5.41a, S5.41b).

(a)



(b)

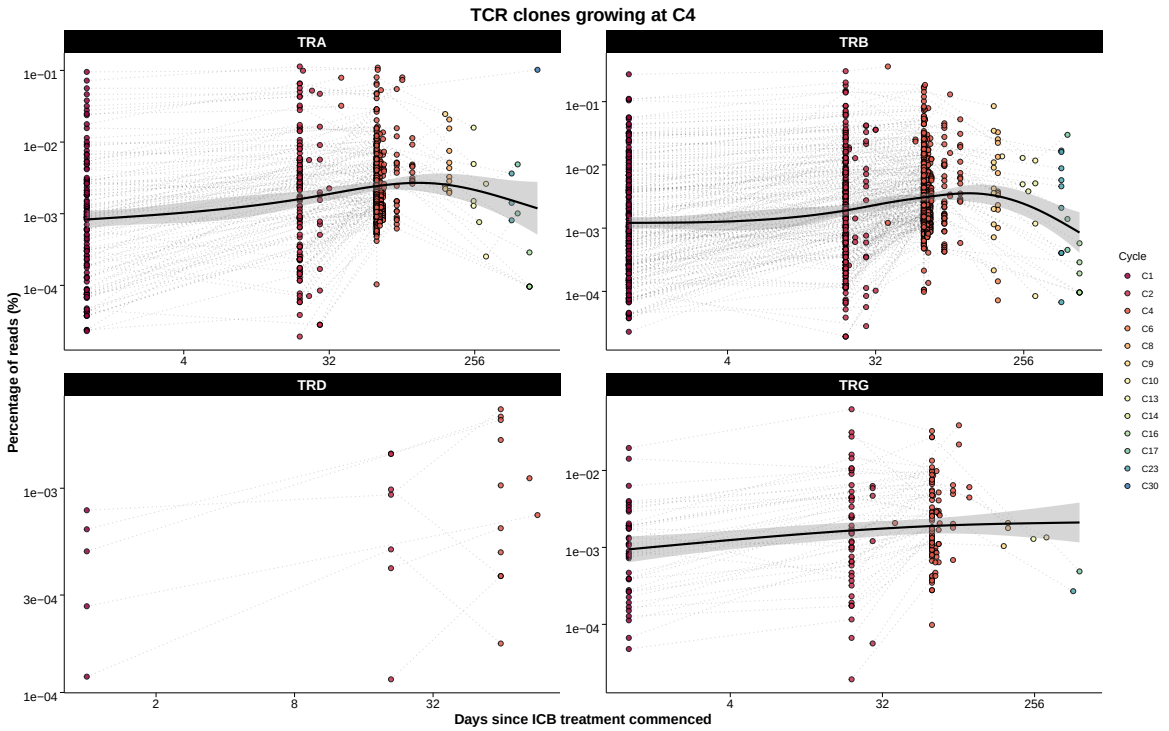


Figure 5.54 Significantly expanding TCR clones are reduced at later time-points
The percentage of reads accounted for by significantly expanding TCR clones at **a)** C2 (n=130) and **b)** C4 (n=58) by chain is tracked longitudinally per expanding clone by days since ICB treatment commenced. Samples are coloured by ICB treatment cycle. *PRx1 = Sample collected after cessation of ICB treatment.*

5.2.5.6 MAIT cells are enriched in involuting clones after cICB

Differential TCR usage was also calculated between expanding and nonexpanding clones at C2/C4. Although several DEGs were detected, the magnitude of difference between expanding and nonexpanding clones was small (Figures 5.55a, 5.55b). Expanding clones were enriched for *TRAV17*, *TRAV19*, *TRBV28* and *TRBJ2-1* consistently at C2 or C4 which may be important for melanoma recognition. Nevertheless, no association of any of these genes were found with survival (data not shown).

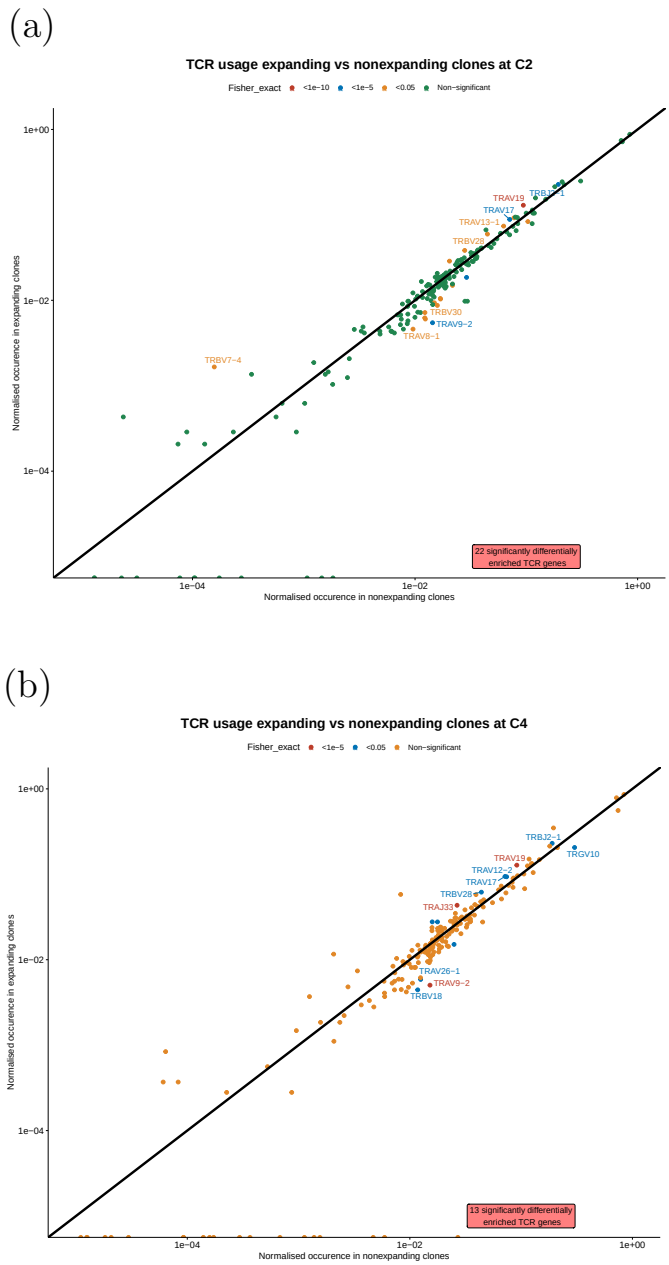


Figure 5.55 Differential TCR usage of expanding clones
TCR usage is compared between significantly expanding and nonexpanding clones at **a)** C2 (n=130) and **b)** C4 (n=58). TCR genes are coloured by the significance of the enrichment with the number of significantly differentially enriched TCR genes displayed in a red box. Statistics were calculated using Fisher's exact tests and adjusted using Bonferroni correction.

In order to support previous observations of MAIT cell reduction following cICB treatment, the percentage enrichment of MAIT cells within significantly expanding and involuting TCR clones at C2 and C4 was compared (Figures 5.56a, 5.56b). Analysis revealed that MAIT cells were significantly more enriched within involuting clones than expanding, but only after cICB treatment. Accordingly, hardly any MAIT cells were found to be significantly expanded at either C2 or C4.

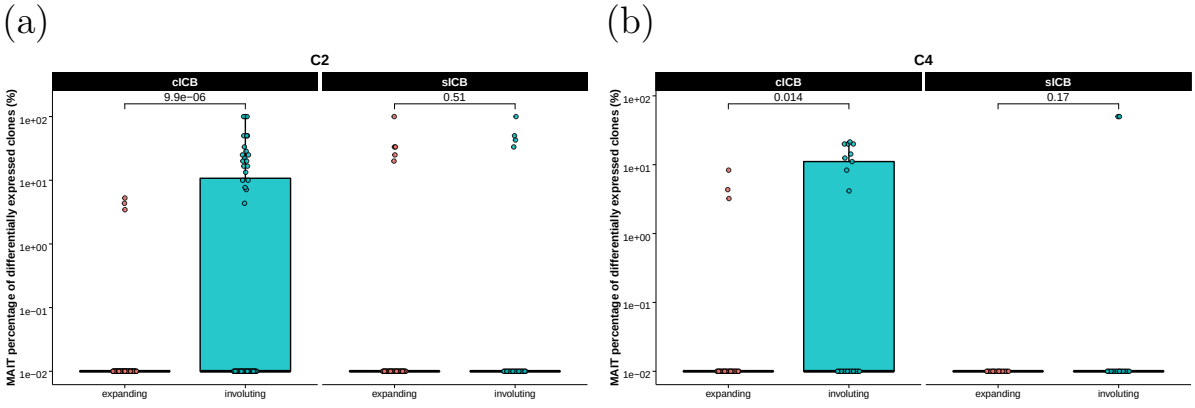


Figure 5.56 MAIT cell clones are enriched in involuting TCR clones following cICB
TCR clones significantly expanding and involuting at C2 and C4 were identified after performing Fisher's exact test per clone for all samples and Bonferroni correction. The percentage of MAIT cell clones within significantly expanding or involuting clones is compared between paired **a)** C1/C2 (n=120-130) and **b)** C1/C4 (n=54-58) samples by treatment type. Statistics were calculated using paired Wilcoxon signed-rank tests.

In order to further help identify any significantly expanded or involuted TCR clones, clones were aligned to those with previously identified antigen specificity including for cancer-specific and CMV-specific clones using VDJdb (reliability score >0)[511,512]. However, neither enrichment of cancer-restricted nor CMV-restricted clones was found to differ between significantly expanding and involuting clones or with survival (data not shown).

Clones identified as cancer-reactive or CMV-reactive were compared between paired C1/C2 and C1/C4 samples as well as tracked across the course of ICB treatment. However, hardly any differences were detected, with little variation observed across treatment (Figures 5.57a, 5.57b, 5.57c, 5.57d), regardless of treatment type and clinical outcome (data not shown). Furthermore, cancer-specific and CMV-specific clones were found to be more significantly enriched within large persistent TCR clones at C2 ($\geq$0.5% of TCR reads) compared to smaller persistent clones (<0.5% of TCR reads) (Figures 5.57e, 5.57f) and may explain why negligible changes are observed with treatment and why a greater number of large clones associate with survival[371].

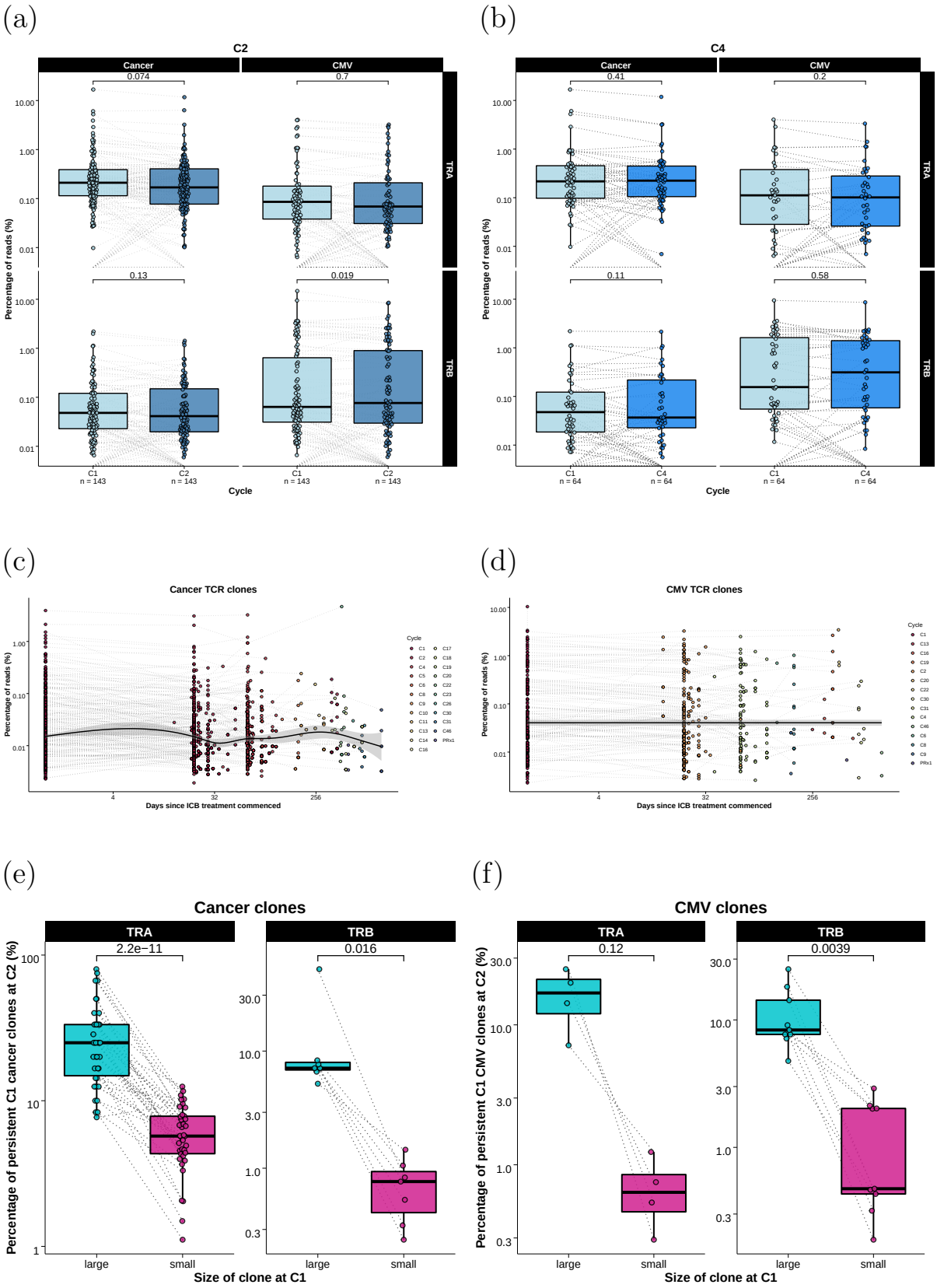

(a)
C2
Cancer
CMV
0.074
0.7
0.13
0.019
TRA
TRB
Percentage of reads (%)
Cycle
(b)
C4
0.41
0.2
0.11
0.58
(c)
Cancer TCR clones
Days since ICB treatment commenced
(d)
CMV TCR clones
(e)
Cancer clones
2.2e−11
0.016
Percentage of persistent C1 cancer clones at C2 (%)
large
small
Size of clone at C1
(f)
CMV clones
0.12
0.0039
Percentage of persistent C1 CMV clones at C2 (%)

Figure 5.57

Figure 5.57 (Previous page) Cancer-specific and CMV-specific clones are unaffected by ICB and persist as large clones
Cancer-specific and CMV-specific TCR clones were identified using VDJdb with percentage of reads compared between paired **a)** C1/C2 (n=143) and **b)** C1/C4 (n=64) by TCR chain. **c)** Cancer-specific and **d)** CMV-specific clones are also tracked across ICB treatment by days since treatment commenced with points coloured by treatment cycle. Cancer-specific and CMV-specific TCR clones shared between paired C1/C2 samples were selected and grouped into either large ($\geq$0.5% of TCR repertoire) or small ($<$0.5% of TCR repertoire) clones. Enrichment of **e)** cancer-specific and **f)** CMV-specific clones is compared between persistent small and large clones in paired samples by TCR chain. Statistics were calculated using paired Wilcoxon signed-rank tests. *PRx1 = Sample collected after cessation of ICB treatment.*

5.2.5.7 BCR changes in response to ICB may be secondary to CD8$^+$ T-cell changes

Given that the ICB response of CD19$^+$ B-cells may be secondary to CD8$^+$ T-cells, factors related to B-cells and CD8$^+$ T-cells were compared (Figure 5.58). Interestingly, several CD19$^+$ B-cell changes were associated with CD8$^+$ T-cell changes in response to ICB. The CD8$^+$ T-cell ICB response score, calculated as the geometric mean of the top 50 genes induced by ICB (Figure 3.20a), was found to correlate with USM loss and B-cell induction of IFN-associated genes (*GBP/STAT1* expression). However, the CD8$^+$ T-cell ICB response score also associated with BCR CSR and ASC score. Furthermore, expression of CD8$^+$ T-cell *TOX2*, found to be significantly associated with CD8$^+$ T-cell ICB response, was discovered to correlate with BCR clone expansion, B-cell activation and expression of IFN-associated genes. CD8$^+$ T-cell *MKI67* expression was additionally associated with USM loss, ASC and overall CD19$^+$ B-cell ICB response scores. Finally, an increase in CD8$^+$ T-cell cytotoxicity score was associated with B-cell and USM depletion at C2, as well as an induction of B-cell IFN-associated genes.

These data, along with findings from Chapters three and four, highlight potentially important B-cell/T-cell interactions that may help elucidate the mechanism of action of ICB.

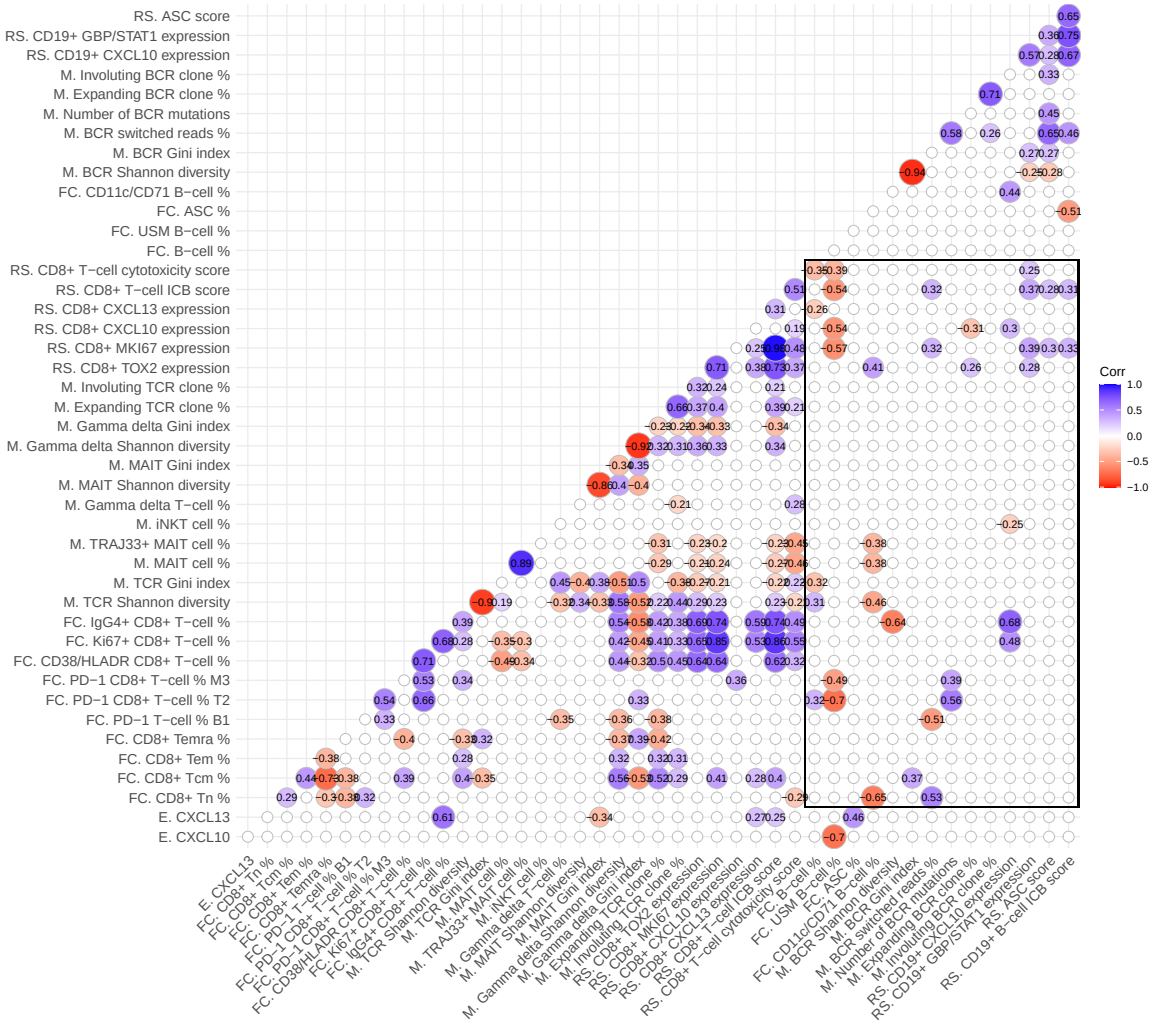


Figure 5.58 B-cell and CD8$^+$ T-cell ICB responses are linked
Fold changes in various B-cell and CD8$^+$ T-cell metrics at C2 (C2/C1) are compared. Metrics derived from flow cytometry, RNAseq, MiXCR or ELISA analyses are labelled with "FC.", "RS.", "M.", and "E." respectively. Correlation coefficient values are displayed per correlation with circle size and shading according to size of coefficient. Coefficients are only displayed for statistically significant correlations. B-cell/T-cell correlations are contained within a rectangle. Statistics were calculated using Spearman's rank correlation coefficient for correlation analysis.

5.3 Conclusions

In this chapter, I investigated the effects of CMV, melanoma and ICB on peripheral BCR and TCR repertoires. Additionally, I explored how ICB-induced changes were correlated between B-cells and T-cells as well as with transcriptomic and phenotypic changes previously identified in Chapters three and four.

Before investigating the effects of ICB, any impact of CMV infection on peripheral BCR and TCR repertoires was first established. Although no effect of CMV was detected for any incorporated BCR metric, CMV seropositivity resulted in extensive TCR changes. These included enhanced TCR clonality with a reduced number of TCR clones detected, TCR inflation (especially clones $\geq$0.5% of the TCR repertoire), low clonal richness and high clonal unevenness. This was accompanied by shifts in the unconventional T-cell pool including MAIT cell depletion and increased γδ clonal unevenness.

The γδ T-cell response to CMV has already been fairly well described. Although γδ T-cell expansion has previously been reported during CMV infection, most studies have been limited to acute CMV infection with short follow-up times and have been focused on immunosuppressed individuals[150,573,574]. However, owing to the age and cancer status of individuals within this cohort, CMV infection is likely chronic in which any γδ T-cell expansion may have since subsided. Despite γδ T-cell clonal expansion being detected by other studies, similar observations have been made in this cohort including increased γδ T-cell clonality and TRDV1 bias[150,573,574], thus, long-lasting effects of CMV may include γδ T-cell clonal unevenness and TRDV1 expansion.

MAIT cells have previously been demonstrated to respond to a host of viral infections including dengue, influenza, hepatitis B, hepatitis C, HIV and SARS-CoV-2, exhibiting a loss in count in the periphery with enhanced activation[404–417]. This MAIT cell loss was often associated with migration to sites of infection before returning to normal levels after disease resolution[409,411]. Although MAIT cells cannot recognise viruses directly through TCR/MR1 presentation, they are able to respond to viral infections independently of the TCR through monocyte-derived cytokines including IL-18 and type I IFNs[404].

The loss in circulating MAIT cells in CMV$^+$ individuals in this cohort was identified not only by TCR usage, but also by associated gene expression. CD8$^+$ T-cell genes found to be significantly associated with MAIT cell percentage were not limited to canonical MAIT cell markers and included genes previously found to be highly expressed by MAIT cells including *LTK*, *SLC4A10*, *ME1*, *IL23R* and *NCR3*[208,425,576–579]. This concurrent reduction in MAIT cell gene expression score suggests that a loss in MAIT cell TCR clones is not necessarily due to TCR downregulation and may in fact signify MAIT cell death in response to chronic activation or migration to sites of infection, such as is observed with Influenza and SARS-CoV-2 infections[409,411].

MAIT cells were also found to be highly activated within CMV$^+$ individuals and to have internalised TCR and CD161. With MAIT cell TCR and CD161 downregulation only observed in response to direct TCR ligation, the loss in MAIT cells may be induced by direct recognition of CMV antigen and supports the notion that MAIT cells may be able to sense CMV. The association between CMV infection and peripheral MAIT cell loss and activation has not been previously described and is a novel and significant discovery.

Next, the impact of melanoma on circulating BCR and TCR repertoires was investigated through comparison with healthy donors. Due to the profound effect of CMV on the TCR repertoire, CD8$^+$ T-cell CMV-associated expression score was controlled to

reduce any impact of CMV. Whilst melanoma appeared to have large effects on both BCR and TCR samples, including reduced clonal richness and enhanced clonal unevenness, no significant differences were detected between healthy donors and untreated MM patients after controlling for age as well as CMV score for $CD8^+$ T-cell samples. Any differences may therefore be as a result of the differences in CMV serostatus and age observed between healthy donors (45 ± 11) and melanoma patients (64 ± 14).

Despite no differences in BCR or TCR clonality being observed between healthy donors and melanoma patients, switched BCR clones were found to be significantly larger in patients, after controlling for the effects of age, and may represent expanded melanoma-specific SM or ASCs. However, no differences in CSR or mutation rates were observed. Similarly, several TCR genes were found to be significantly differentially expressed between healthy donors and melanoma patients, however, the significance of this remains to be understood. Perhaps this skewing of TCR genes is related to expanded melanoma-specific clones or HLA bias. The importance of these genes in melanoma recognition should be investigated in future work.

ICB had no detectable effect on BCR or TCR diversity. Furthermore, ICB has no effect on thymic activity and cannot increase clonal output, hence limiting any effects to preexisting clones[250]. Although no changes in global diversity were observed, several emergent BCR and TCR clones were detected following treatment and may result from increased survival and differentiation mediated by treatment. Interestingly, MM patients with a high level of novel TCR clones emerging post-ICB treatment experienced enhanced survival compared to those with a low number of novel clones. In concordance with this, low TCR clonality was found to have superior outcomes to those with high clonality. The emergence of novel clones and loss in hyperexpanded clones may facilitate enhanced antitumour responses through tumour repopulation and enhanced tumour recognition[381]. In support of this, BCR and TCR clones found to be expanded following ICB treatment were observed to resolve to baseline levels at later time-points and may suggest that expanded clones migrate to the tumour site. Accordingly, enhanced B-cell and T-cell tumour infiltration has been shown to be beneficial for ICB response[278,295,320,331,363]. Surprisingly, cancer-specific TCR clones, as identified using online databases, were not found to be enriched in these expanding clones or within responding patients.

Increased CSR and mutation rate is observed exclusively following cICB treatment within BCR clones and associates with the increase in ASCs. However, novel BCR clones were also detected after sICB treatment which were, likewise, almost entirely switched and suggest that sICB can indeed induce CSR and SHM, but effects were limited to a few clones and thus any changes were undetectable. This is likely due to weaker activation imposed on B-cells by sICB and not necessarily due to the action of CTLA-4 blockade in cICB as no effect of anti-CTLA4 sICB treatment was found on B-cell differentiation or activation in other studies[458]. Additionally, sICB was found to induce less changes in clonal composition than cICB treatment. With expanding BCR clones representing the majority of switched and mutated clones, any increase in CSR and SHM induced by sICB may be limited to a few clones.

Interestingly, this increase in CSR was found to associate with the $CD8^+$ T-cell ICB response, proliferation and PD-1 blocking within $CD8^+$ T-cells. This supports the notion that $CD8^+$ T-cell ICB responses may not only determine $CD19^+$ B-cell transcriptomic and phenotypic responses, but also BCR response. Although this was hypothesised to be through induction of CXCL13 after ICB, no such correlations were observed within this cohort. However, CXCL13 was found to associate with B-cell loss and concurrent

induction of ASCs, so this study may be underpowered. Profound CSR was observed immediately following cICB treatment which resolved by later time-points. This may be reflective of migration to the tumour or surrounding TLS's which has previously been demonstrated following ICB treatment[363,366,430].

Only cICB was found to have any effect on TCR usage. This included downregulation of MAIT cell-associated TCRs which was sustained at later time-points. Furthermore, MAIT cells were found to be enriched within significantly involuting TCR clones following cICB treatment. Likewise, MAIT cell expression score was found to be depleted after cICB treatment, likely representing actual MAIT cell loss and not just TCR downregulation.

Interestingly, MAIT cells have previously been reported to respond directly to ICB including upregulation of effector molecules[425] and have been demonstrated to elicit antimelanoma activity in this cohort. Melanoma-directed cytotoxicity was independent of other PBMC subsets and MR1/TCR interaction. However, cytotoxicity could be enhanced by IL-12/IL-15/IL-18 stimulation. Antimelanoma cytotoxicity initiated by MAIT cells may function in a manner similar to viral infections in which MAIT cells elicit melanoma cell lysis in response to inflammatory cytokines[404]. With MAIT cells found to mediate direct antimelanoma cell lysis and respond to ICB, with increased expression of effector molecules, MAIT cell loss observed in this cohort may symbolise chronic MAIT cell activation and ultimately activation-induced cell death or migration to the tumour site. Normalisation of MAIT cells following ICB treatment was found to be associated with prolonged survival in accordance with other studies and thus MAIT cells may represent important mediators of ICB response[425–427].

Nevertheless, MAIT cell loss was found to strongly correlate with $CD8^+$ T-cell ICB response and activation. The same was not observed for $CD19^+$ B-cell ICB response and suggests that whilst $CD8^+$ T-cell response is important for $CD19^+$ B-cells, the $CD8^+$ T-cell ICB response is independent of $CD19^+$ B-cells.

5.4 Supporting Information

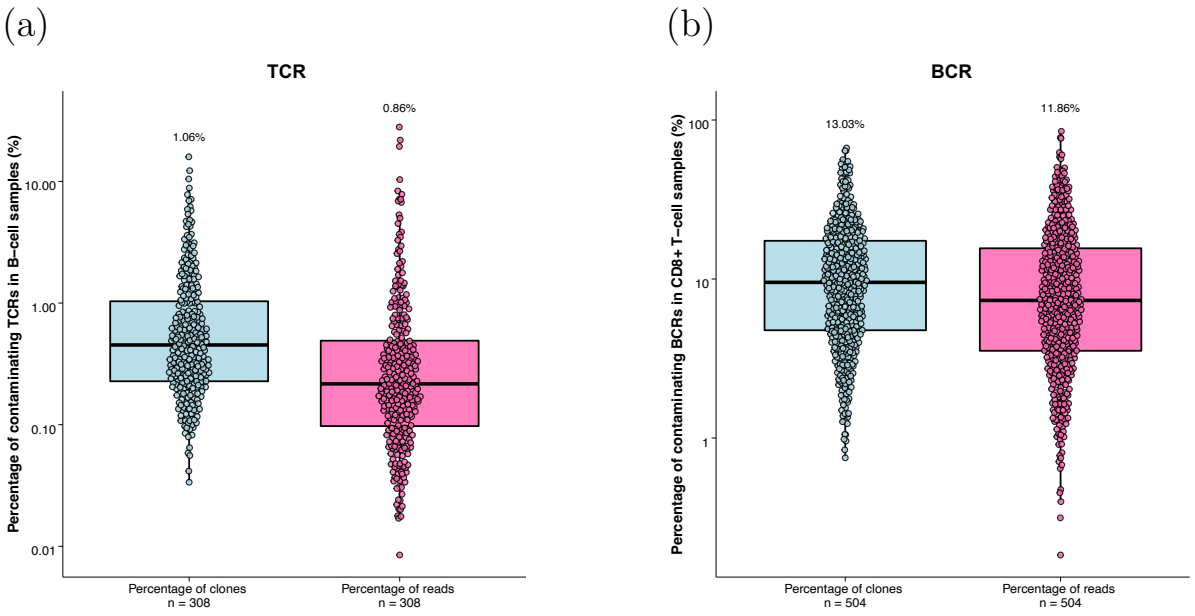


Figure S5.1 BCR/TCR contamination is minimal
Box plots depicting the percentage of **a)** contaminating TCR reads/clones in B-cell samples (n=308) or **b)** contaminating BCR reads/clones in CD8$^+$ T-cell samples (n=504). Average percentage is displayed above each box plot.

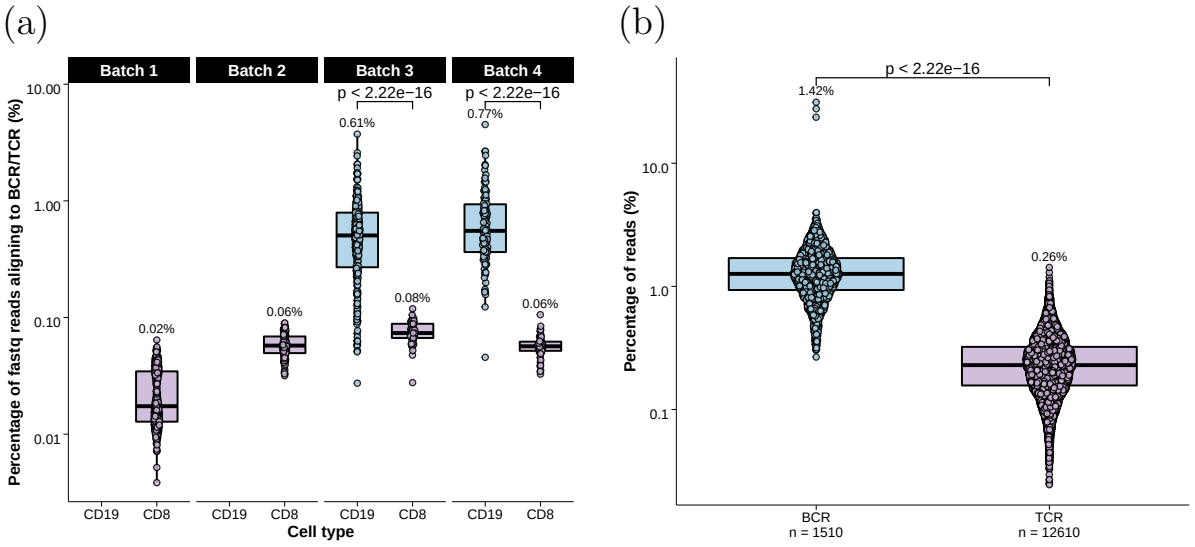


Figure S5.2 The BCR is expressed more highly than the TCR
a) Percentage of bulk RNAseq fastq reads aligning to BCR or TCR reads using $MiXCR$ per (n=308) or CD8$^+$ T-cell (n=504) transcriptome respectively by sequencing batch. **b)** Expression of BCR (n=1,510) and TCR (n=12,610) per cell calculated as the percentage of total reads that align to BCR or TCR respectively using single cell RNAseq data[208]. Average percentages are displayed above each box plot. Statistics were calculated using unpaired Wilcoxon signed-rank tests.

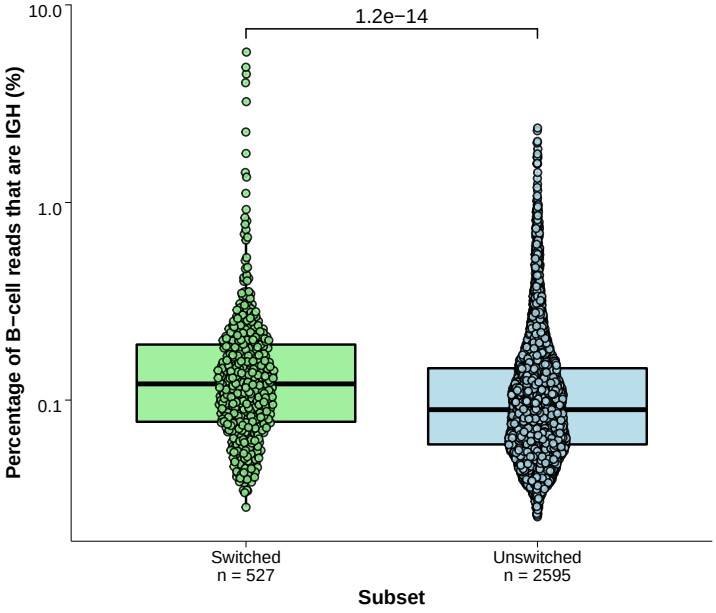


Figure S5.3 Switched BCR clones express a higher level of BCR
Box plots comparing the percentage of the total reads that are constituted of BCR heavy chains between unswitched (IgM/IgD, n=2,595) and switched (IgG/IgA/IgE, n=527) BCR clones using single cell RNAseq data. Statistics were generated using an unpaired Wilcoxon signed-rank test.

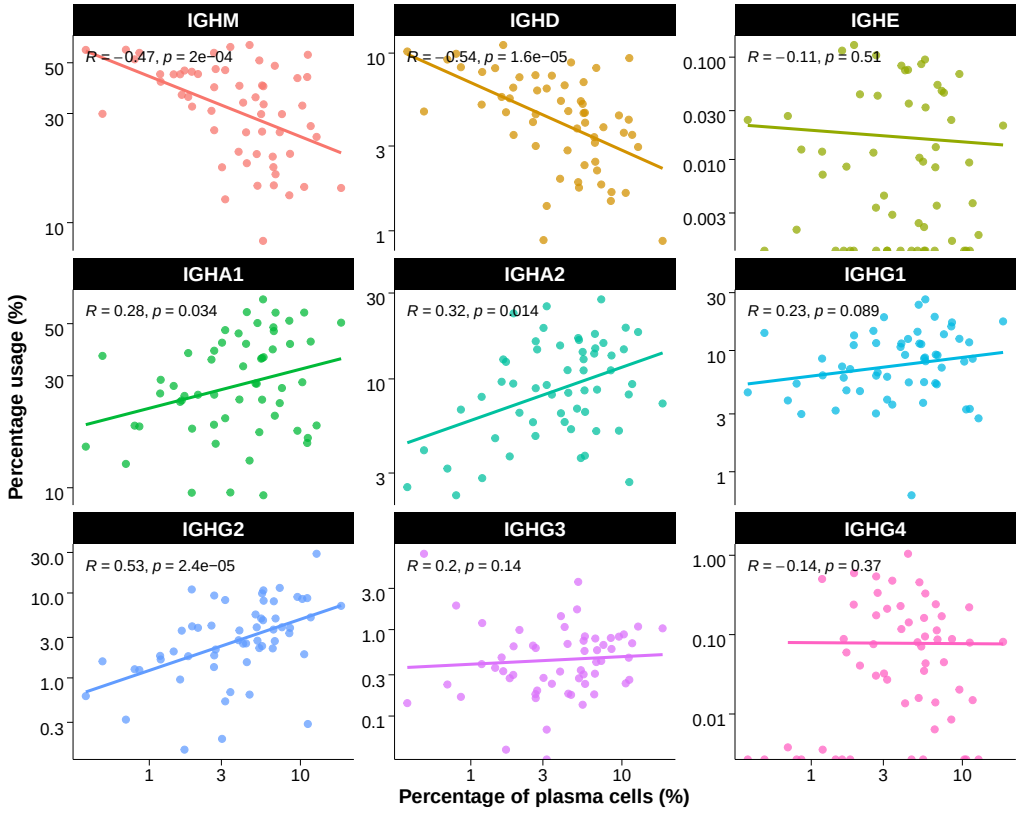


Figure S5.4 $MiXCR$ IGHC alignment correlates with flow cytometry plasma cell percentage
Plasma cell percentage was identified by flow cytometry as CD138$^+$ B-cells and is correlated with $MiXCR$-aligned IGHC usage by unique isotype (n=57). Statistics were calculated using Spearman's rank correlation coefficient.

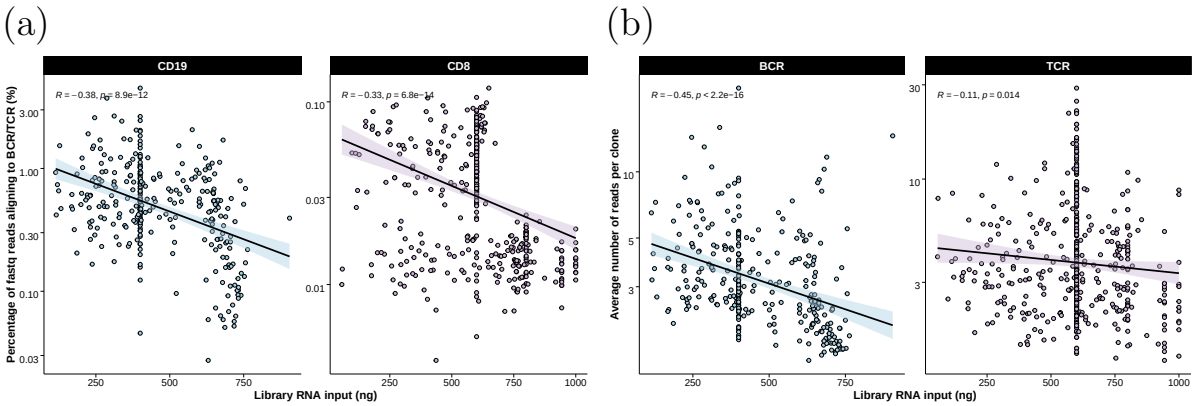


Figure S5.5 Library RNA input associates with the number of BCR and TCR reads detected
The amount of RNA (ng) used for bulk RNAseq library generation derived from CD19$^+$ B-cell (n=308) and CD8$^+$ T-cell (n=504) samples is compared with the **a)** percentage of fastq reads aligning to BCR (left) or TCR (right) genes and with **b)** the average number of reads identified per BCR (left) or TCR (right) clone. Statistics were calculated using Spearman's rank correlation coefficient.

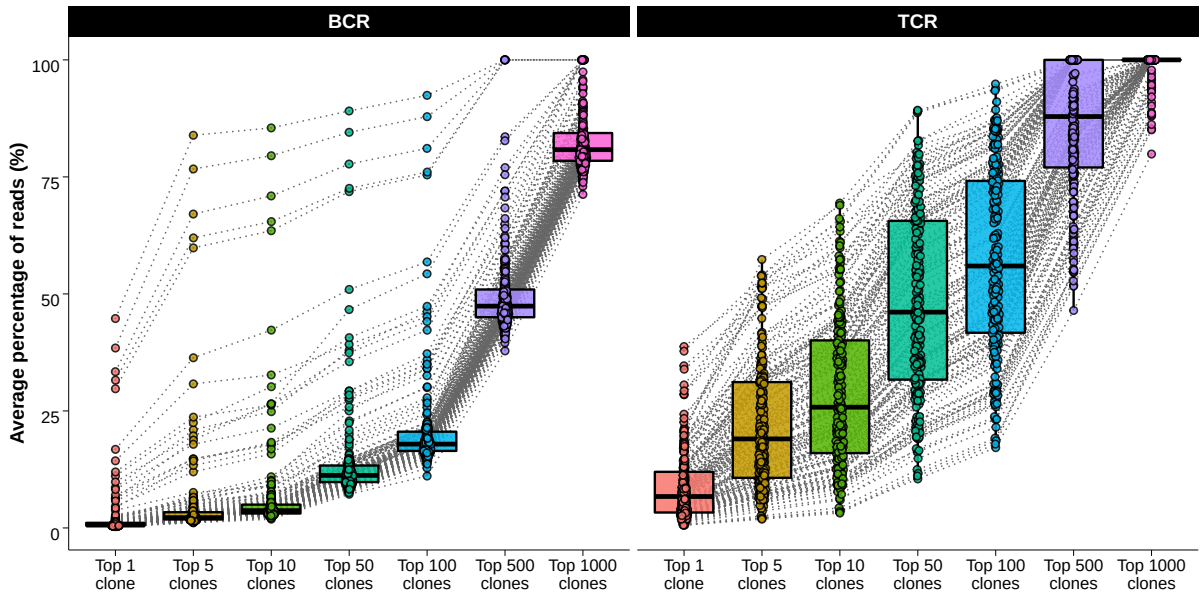


Figure S5.6 The top BCR clones constitute a lower proportion of the repertoire than the top TCR clones
Data was subsampled to 1,496 reads calculating the percentage of the repertoire that an increasing number of the top clones represented for paired BCR (left) and TCR (left) samples (n=192) and taking the average from 1,000 iterations.

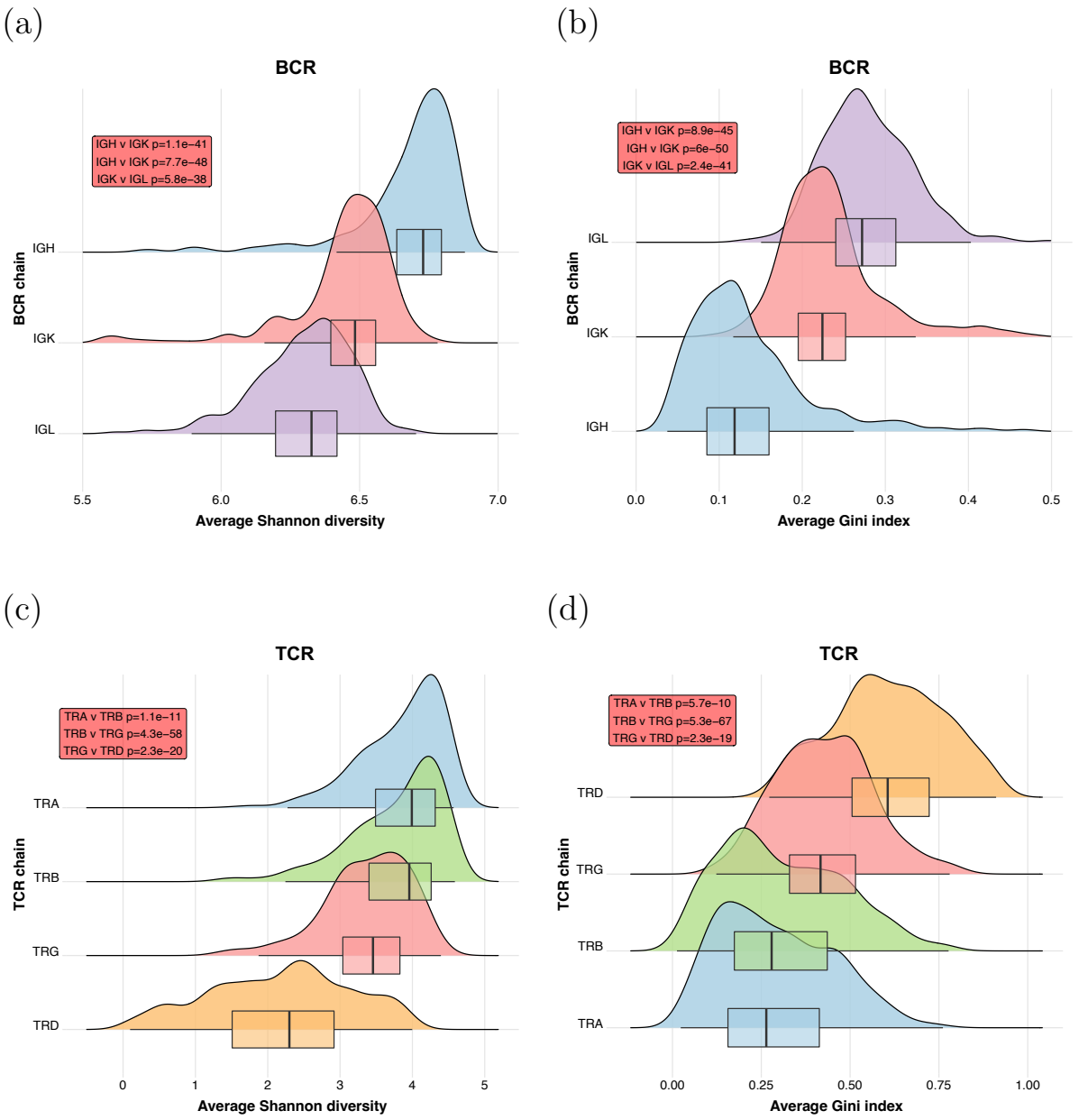


Figure S5.7 Interchain variation in BCR and TCR diversity
CD19$^+$ B-cell (n=308) and CD8$^+$ T-cell (n=504) samples were subsampled to 1,028 and 100 reads per chain respectively. **a,c)** Shannon diversity and **b,d)** Gini index were calculated for **a,b)** BCR and **c,d)** TCR transcriptomes taking the average from 1,000 iterations. Statistics were calculated using paired Wilcoxon signed-rank tests and are displayed in red boxes.

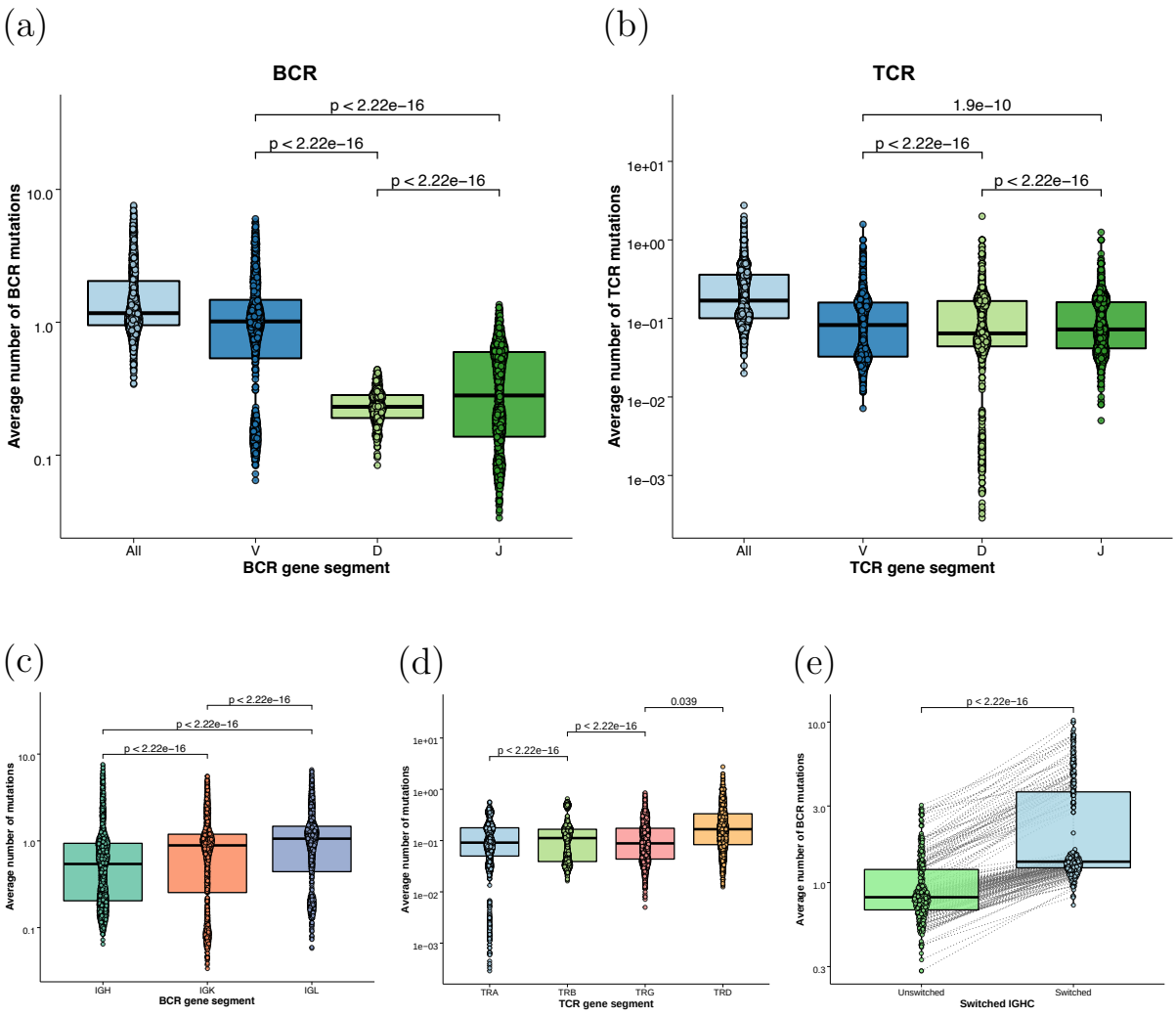


Figure S5.8 BCR and TCR mutations are differentially enriched by gene segment, chain and isotype Box plots displaying the average number of mutations detected per V(D)J gene segment for **a)** BCR (n=308) and **b)** TCR (n=504) clones as well as by individual **c)** BCR and **d)** TCR chains. **e)** The average number of mutations per clone is compared between unswitched (IgM/IgD) and switched (IgG/IgA/IgE) BCR clones (n=308). Statistics were generated using paired Wilcoxon signed-rank tests.

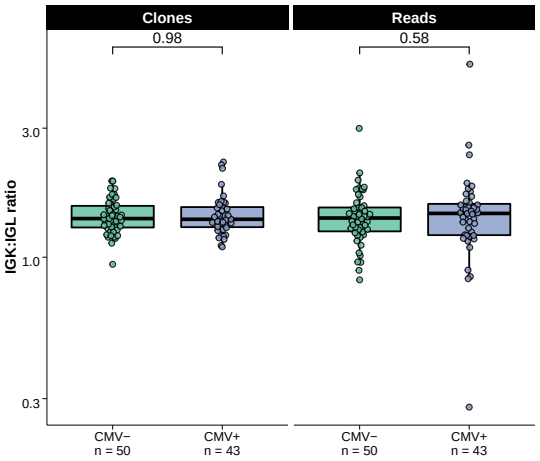


Figure S5.9 BCR light chain usage is unaffected in CMV$^+$ patients
The ratio of IGK:IGL clones (left) or reads (right) is compared between CMV$^-$ (n=50) and CMV$^+$ individuals (n=43). Statistics were calculated using lm(IGK:IGL ratio $\sim$ CMV serostatus + age + library RNA input, data).

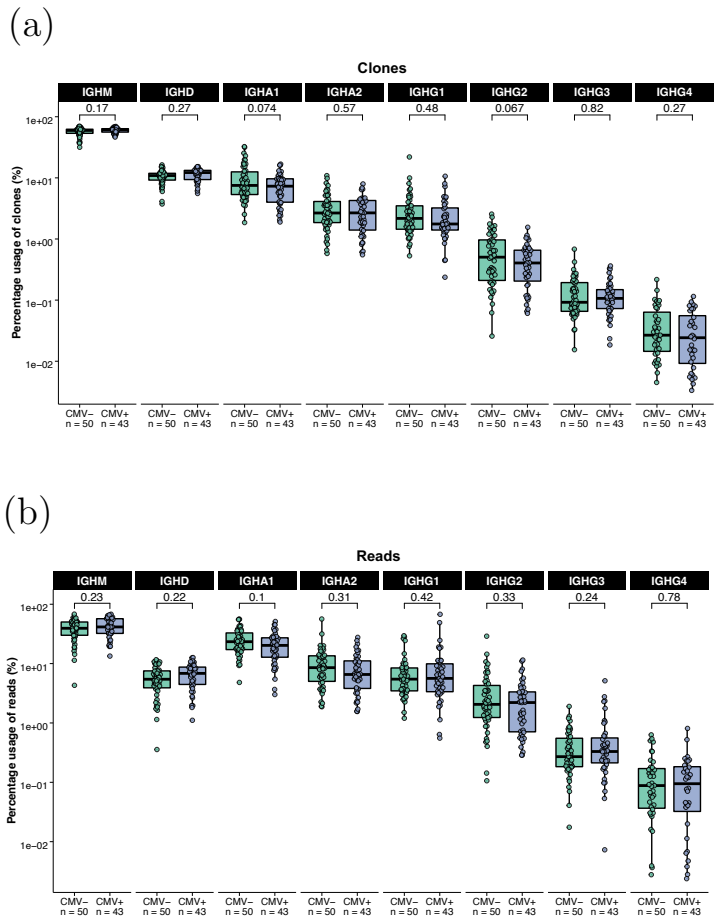


Figure S5.10 CMV infection has no effect on IGHC usage
IGHC usage, taken as the percentage of IGH **a)** clones or **b)** reads expressing each isotype, is compared between CMV$^-$ (n=50) and CMV$^+$ (n=43) patients. Statistics were calculated using lm(IGHC usage $\sim$ CMV serostatus + age + library RNA input, data).

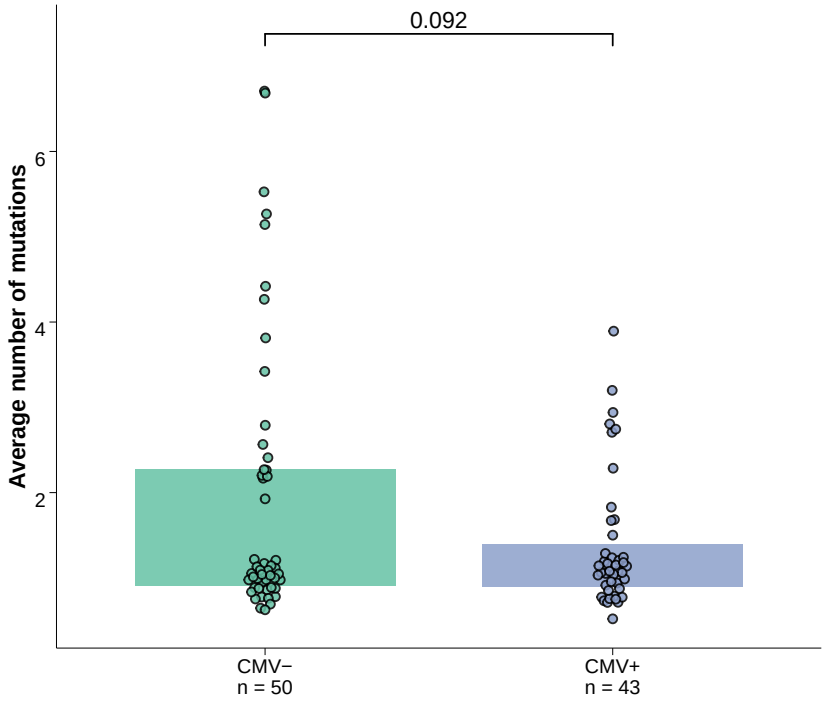


Figure S5.11 CMV has no impact on BCR mutation rate
Box plots comparing the average number of mutations detected per BCR clone between CMV$^-$ (n=50) and CMV$^+$ (n=43) patients. Statistics were calculated using lm(Number of mutations $\sim$ CMV serostatus + age + library RNA input, data).

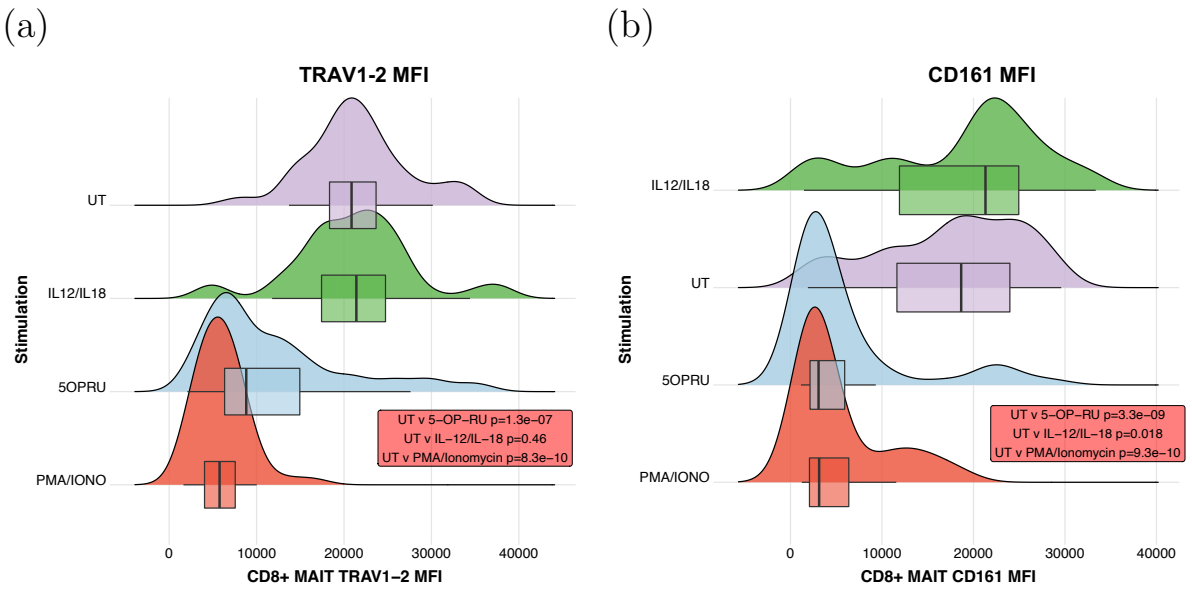


Figure S5.12 MAIT cell TCR and CD161 are downregulated in response to TCR-mediated activation
PBMC samples (n=50) were cultured with 5-OP-RU (5OPRU), IL-12 and IL-18 (IL12/IL18), or PMA/Ionomycin (PMA/IONO) for 24 hours. CD8$^+$ MAIT cell **a)** TRAV1-2 MFI or **b)** CD161 MFI are compared between stimulated samples and untreated (UT) controls. Statistics were generated using paired Wilcoxon signed-rank tests and are displayed in a red box.

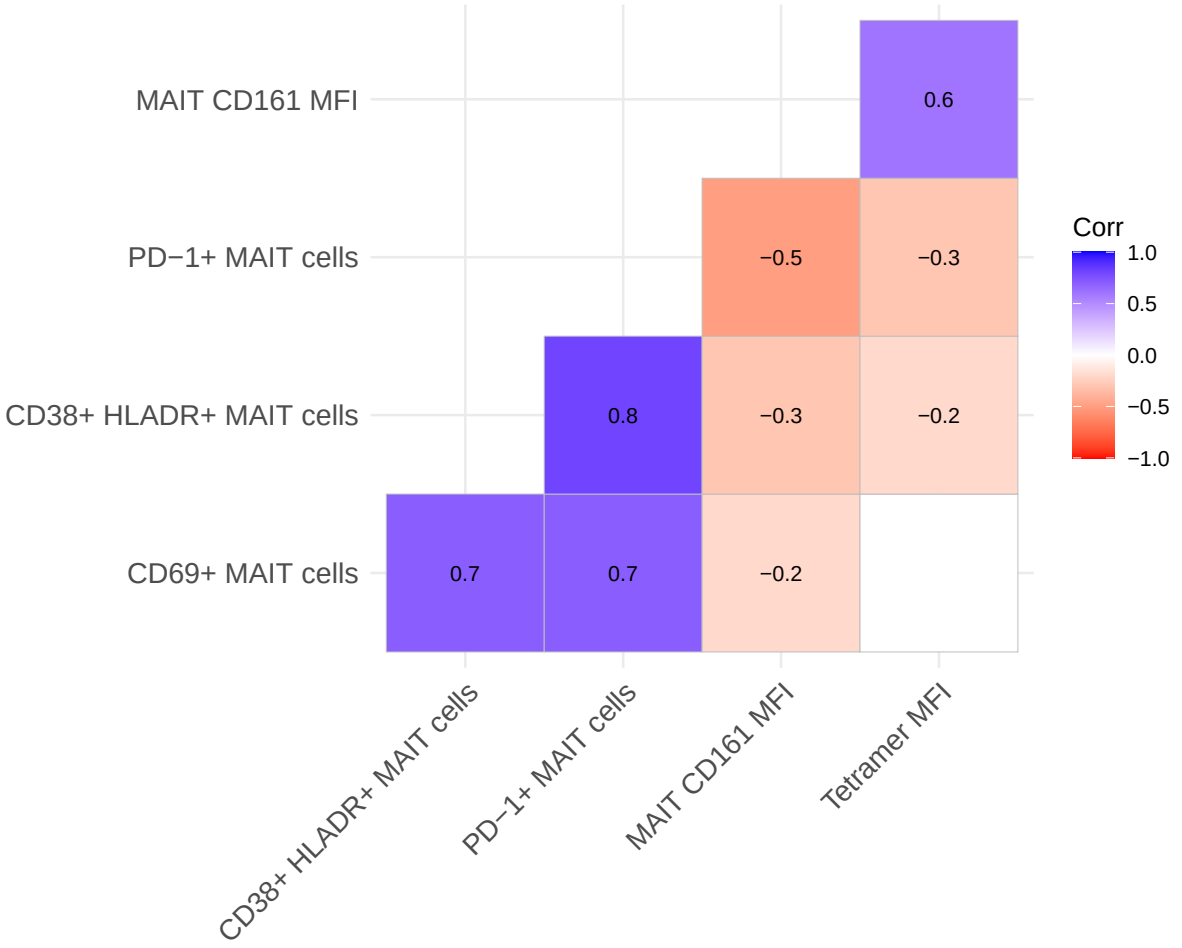


Figure S5.13 MAIT cell TCR and CD161 downregulation associate with activation
Correlogram of MAIT cell activation markers using flow cytometry data (n=114). Correlation coefficient values are displayed per correlation with shading according to size of coefficient. Coefficients are only displayed for statistically significant correlations. Statistics were calculated using Spearman's rank correlation coefficient for correlation analysis.

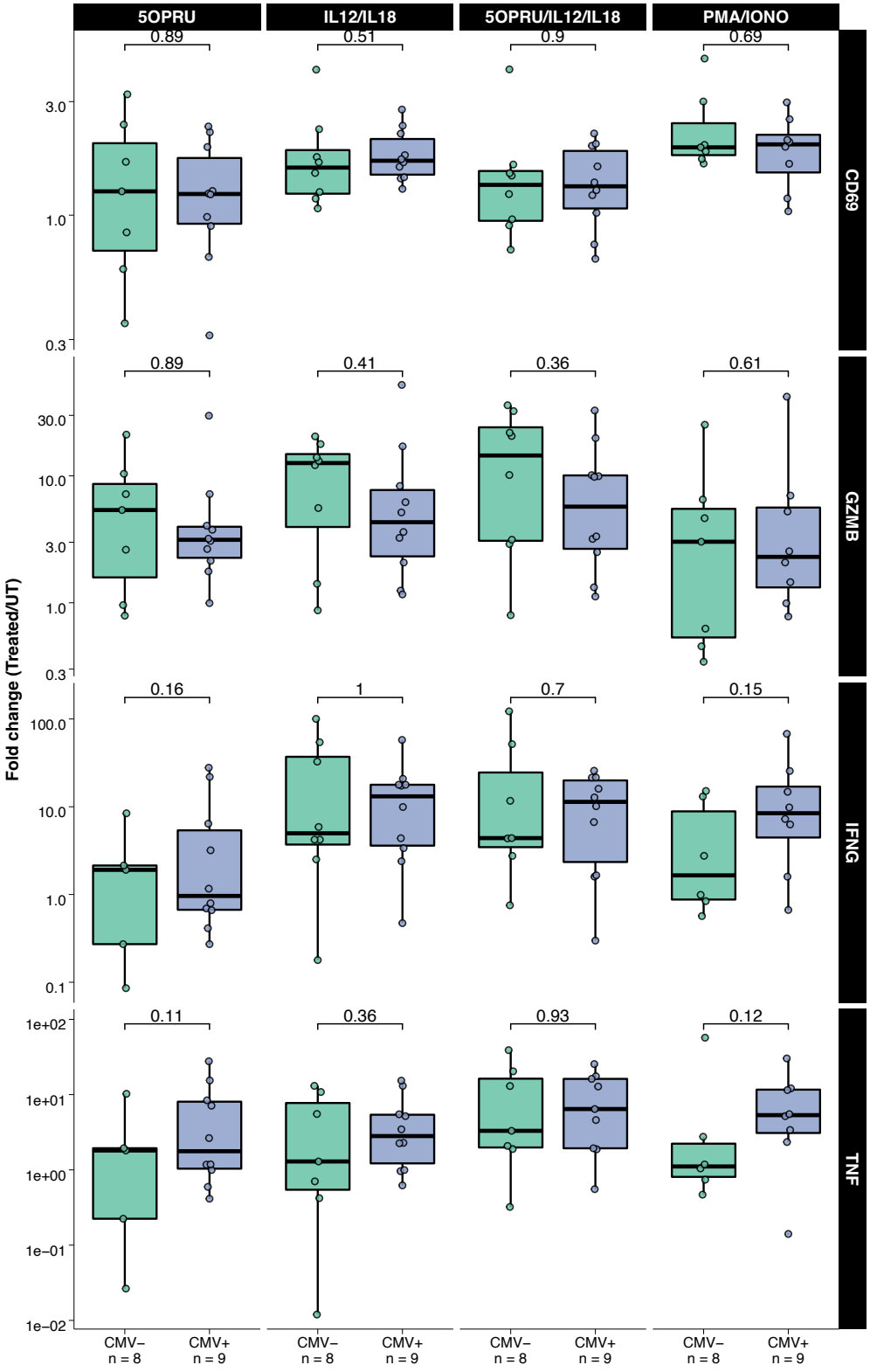


Figure S5.14 CMV has no effect on MAIT cell response to stimulation
PBMC samples were treated with a range of activating stimuli for 24 hours prior to flow cytometry analysis of $CD8^+$ MAIT cell activation and effector markers. Box plots compare the induction of these markers (treated/untreated) between CMV^- (n=8) and CMV^+ (n=9) MM patients (C1) following stimulation with either 5-OP-RU (5OPRU), IL-12/IL-18 (IL12/IL18), 5-OP-RU/IL-12/IL-18 (5OPRU/IL12/IL18), or PMA/Ionomycin (PMA/IONO). These markers include CD69, granzyme B (GZMB), IFN-γ (IFNG) and TNF-α (TNF). Statistics were calculated using lm(Metric fold change ~ CMV serostatus + age, data).

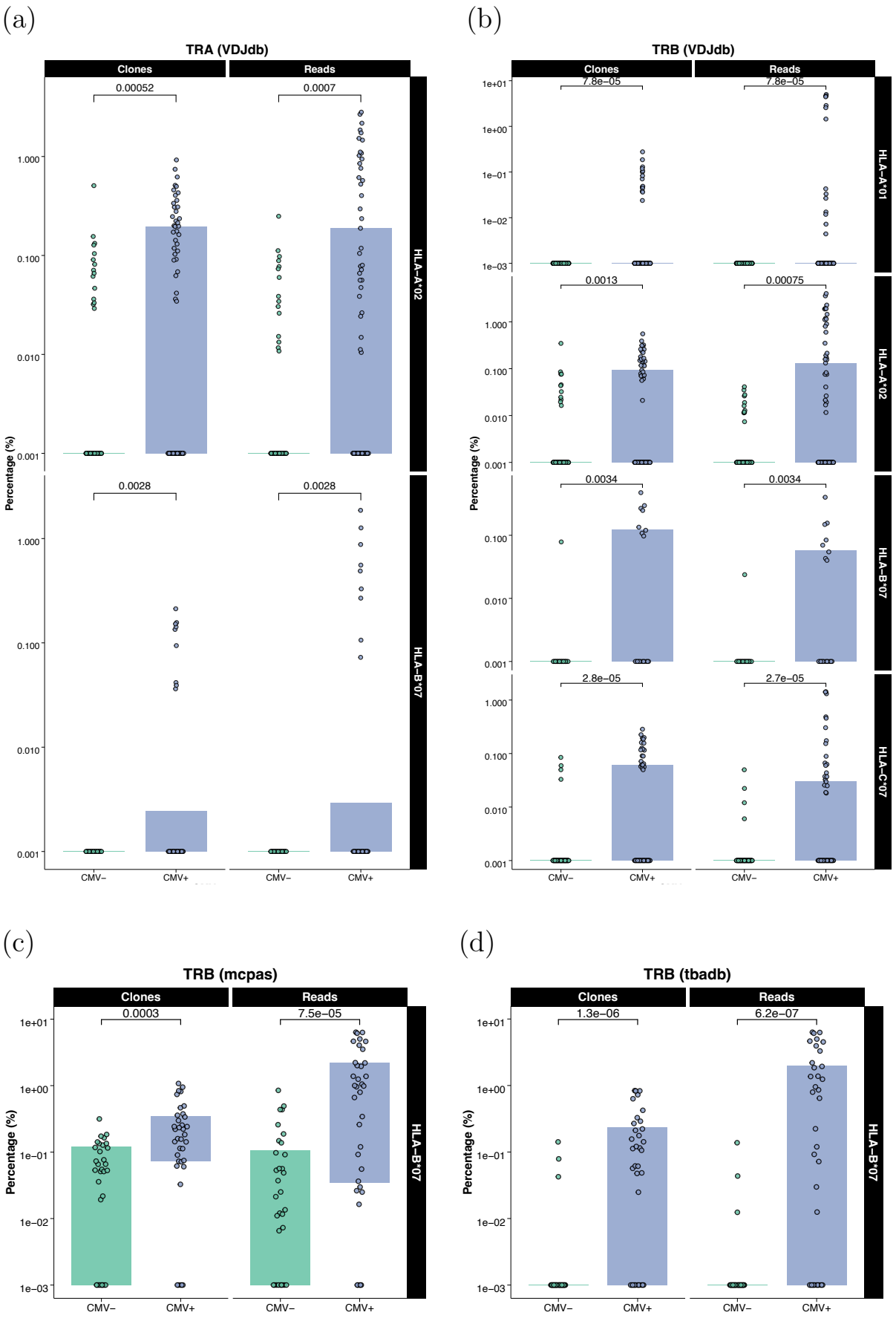

(a)
TRA (VDJdb)
Clones
Reads
0.00052
0.0007
0.0028
0.0028
HLA−A*02
HLA−B*07
Percentage (%)
CMV−
CMV+
(b)
TRB (VDJdb)
7.8e−05
7.8e−05
0.0013
0.00075
0.0034
0.0034
2.8e−05
2.7e−05
HLA−A*01
HLA−A*02
HLA−B*07
HLA−C*07
(c)
TRB (mcpas)
0.0003
7.5e−05
(d)
TRB (tbadb)
1.3e−06
6.2e−07

Figure S5.15

Figure S5.15 (Previous page) CMV-specific and CMV-associated clones are more highly expressed by CMV$^+$ patients according to HLA type
The percentage of VDJdb, McPAS and TBAdb CMV-specific or CMV-associated clones was calculated per TCR repertoire by either the total number of unique clones (left) or reads (right) for VDJdb **a)** TRA and **b)** TRB clones as well as **c)** McPAS TRB and **d)** TBAdb TRB clones by HLA type. Statistics were calculated using unpaired Wilcoxon signed-rank tests.

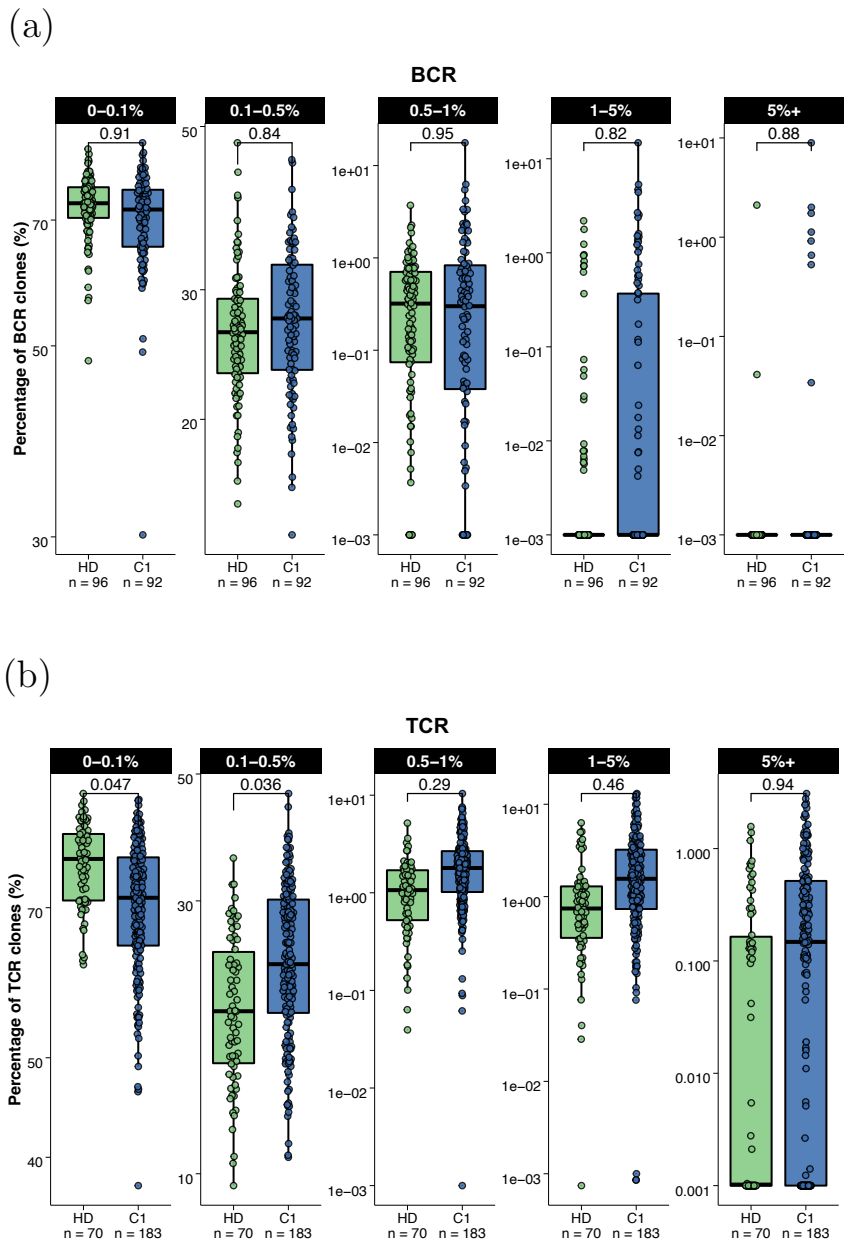


Figure S5.16 More TCR clones of size 0.1-0.5% are found in melanoma
Data was subsampled to 4,471 and 1,496 reads for BCR and TCR samples respectively. Box plots comparing the percentage of **a)** BCR (n=96 healthy donors, n=92 C1) and **b)** TCR (n=70 healthy donors, n=183 C1) clones of each clone size range between healthy donors (HD) and untreated MM patients (C1). Statistics were calculated using "lm(Clone size percentage $\sim$ cancer status + age + library RNA input, data)" for BCR samples and "lm(Clone size percentage $\sim$ cancer status + age + library RNA input + CMV score, data)" for TCR samples.

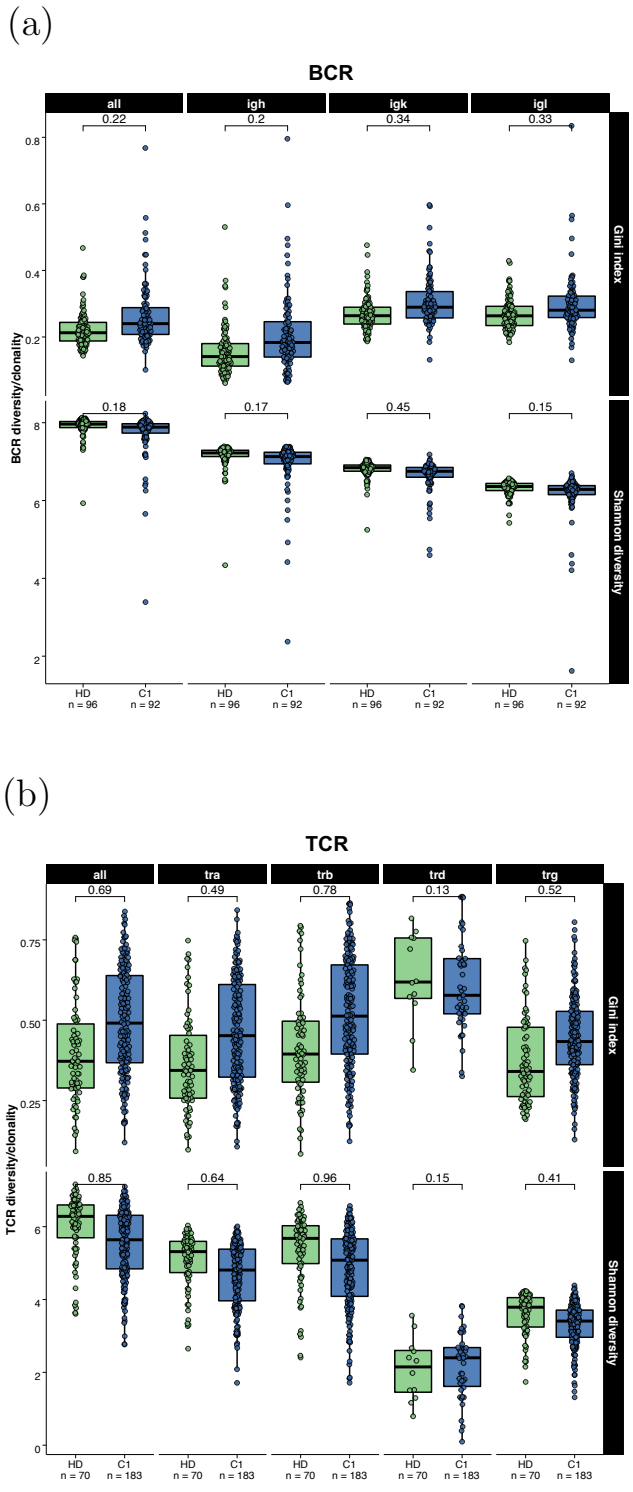


Figure S5.17 No differences are observed in BCR or TCR diversity indexes between healthy donors and melanoma patients

Average Shannon diversity and Gini index were calculated by taking the average of 1,000 iterations from subsampled data (n=4,471 reads for BCR samples, n=1,496 reads for TCR samples) and are compared between healthy donors (HD) and untreated patient samples (C1) for **a)** BCR (n=96 HD, n=92 C1) and **b)** TCR (n=70 HD, n=183 C1) samples. Statistics were calculated using lm(Shannon diversity/Gini index $\sim$ cancer status + age + library RNA input, data) for BCR comparisons or lm(Shannon diversity/Gini index $\sim$ cancer status + age + library RNA input + CMV score, data) for TCR comparisons.

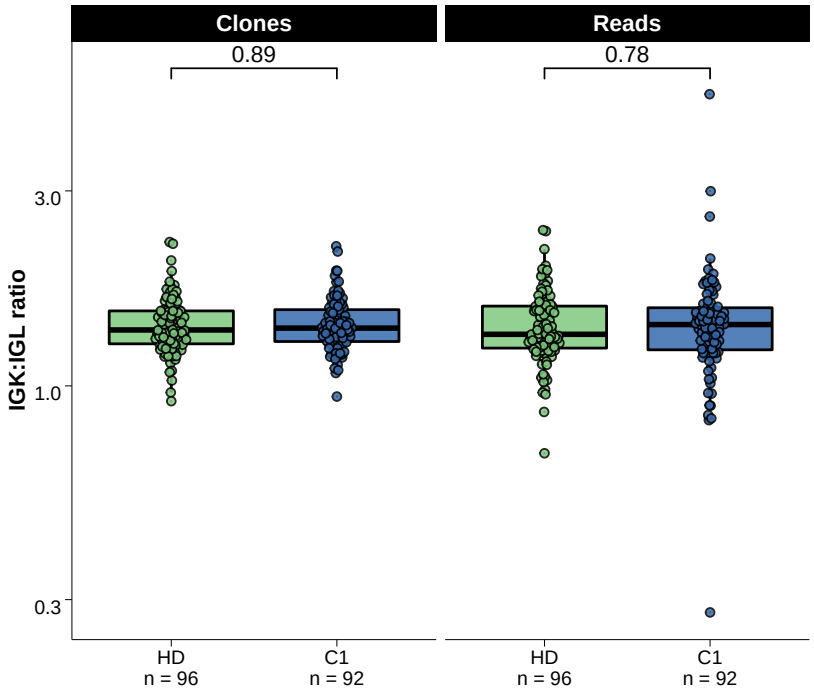


Figure S5.18 BCR light chain usage is unaffected in melanoma
BCR light chain usage, taken as the ratio of IGK:IGL clones (left) or reads (right), is compared between healthy donors (HD, n=96) and untreated MM patients (C1, n=92). Statistics were calculated using "lm(IGK:IGL ratio $\sim$ cancer status + age + library RNA input, data)".

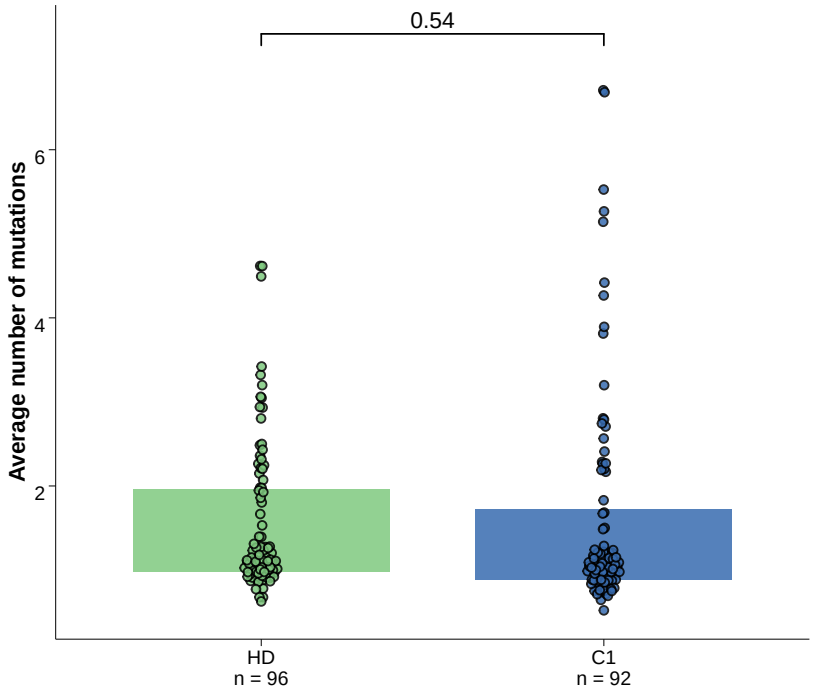


Figure S5.19 Melanoma has no effect on BCR mutation rate
The average number of mutations per BCR clone is compared between healthy donors (HD, n=96) and untreated MM patients (C1, n=92). Statistics were calculated using "lm(Average number of BCR mutations $\sim$ cancer status + age + library RNA input, data)".

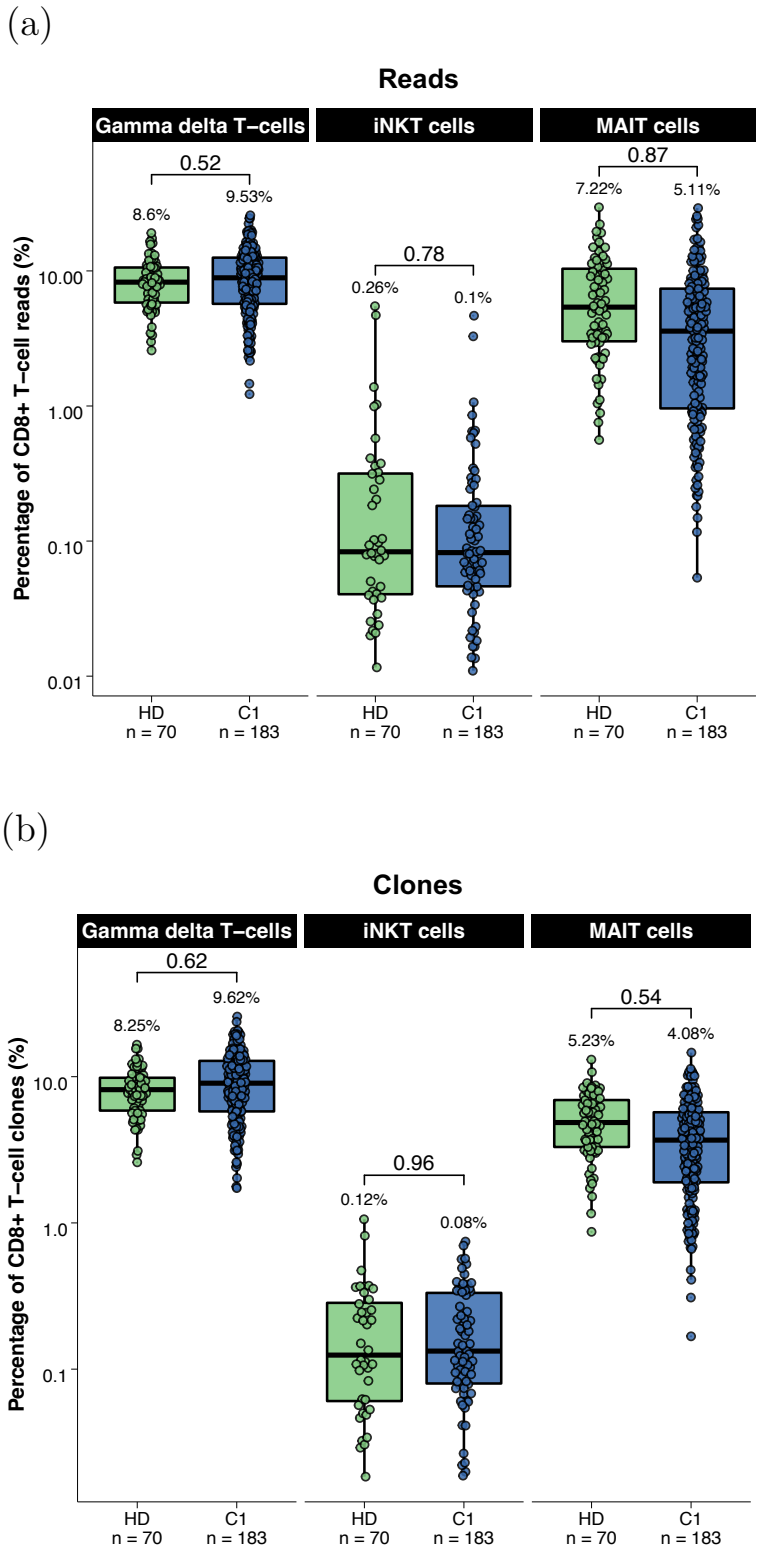


Figure S5.20 No differences in unconventional T-cell composition are observed in melanoma Unconventional T-cell proportions are compared between healthy donors (HD, n=70) and untreated MM patients (C1, n=183) calculated as either the percentage of $CD8^+$ T-cell **a)** reads or **b)** unique clones that express unconventional TCRs. Average unconventional T-cell percentages are displayed above each box plot. Statistics were calculated using lm($\log_{10}$(Unconventional T-cell percentage) $\sim$ cancer status + age + library RNA input + CMV score, data).

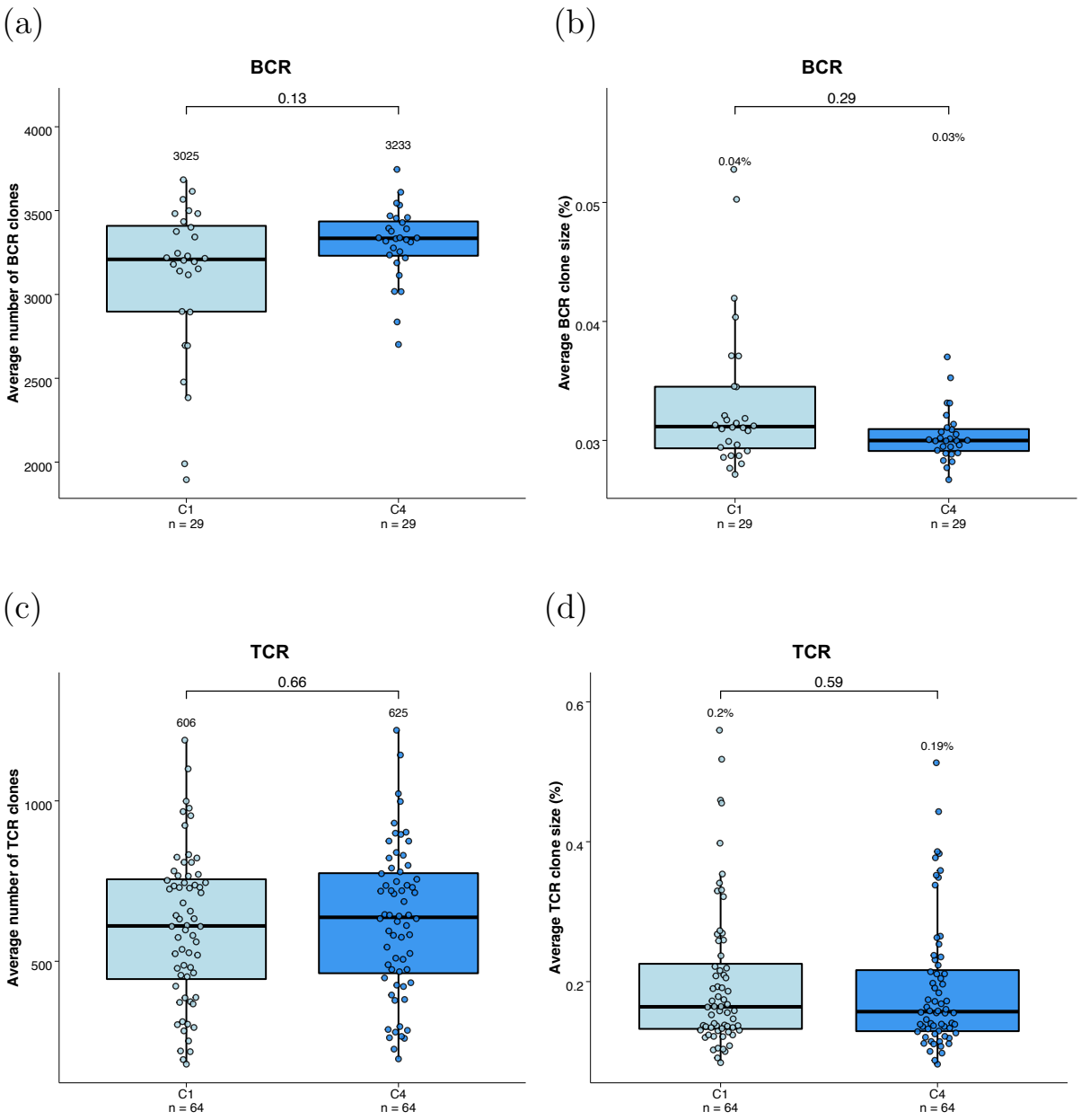


Figure S5.21 ICB has no effect on BCR and TCR clone number and size at C4
Data was subsampled to 4,471 and 1,496 reads for BCR (n=29) and TCR (n=64) samples respectively calculating the average **a,c)** number of clones and the **b,d)** percentage of the repertoire that **a,b)** BCR and **c,d)** TCR clones represent on average after 1,000 iterations. Average values are displayed above each box plot. Statistics were calculated using "lm(metric $\sim$ cycle + library RNA input, data)".

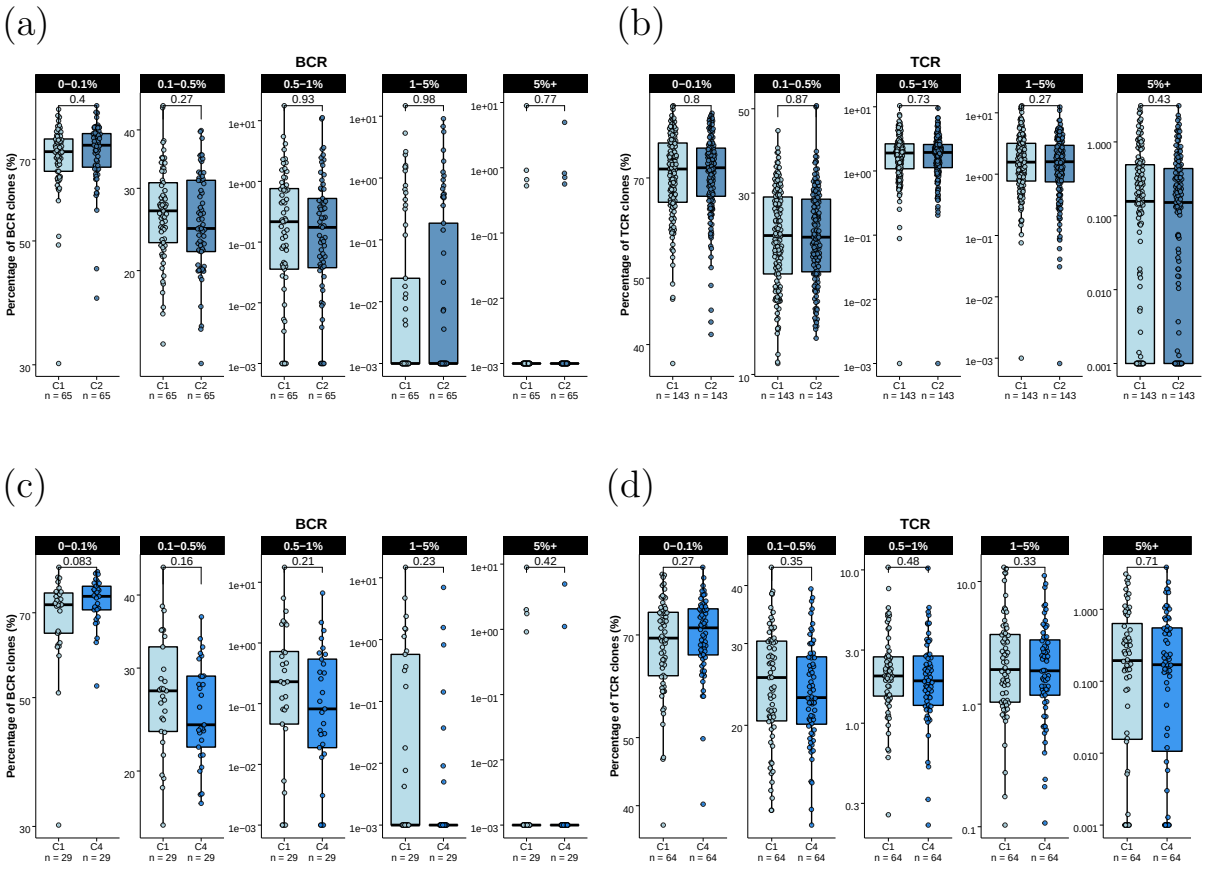


Figure S5.22 ICB has no effect on BCR or TCR clone proportion regardless of size
BCR and TCR data was subsampled to 4,471 and 1,496 reads respectively before calculating the proportion of clones at various sizes. The proportion of **a,c)** BCR (n=65 C1/C2, n=29 C1/C4) and **b,d)** TCR (n=143 C1/C2, n=64 C1/C4) clones by clonal proportion of repertoire is compared between paired **a,b)** C1/C2 or **c,d)** C1/C4 samples. Statistics were calculated using "lm(metric $\sim$ cycle + library RNA input, data)".

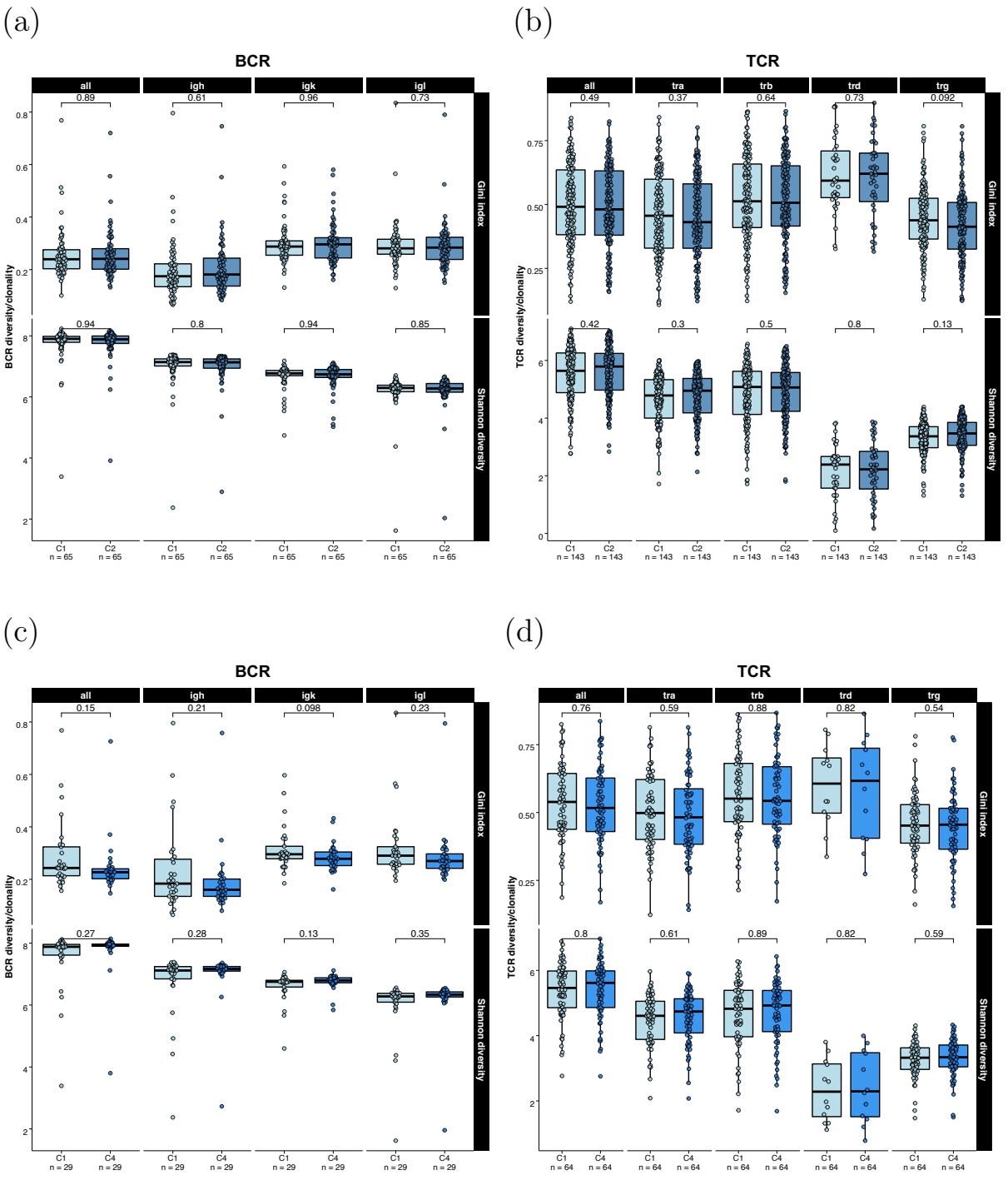


Figure S5.23 No differences in BCR or TCR diversity indexes are detected after ICB treatment Average Shannon diversity and Gini index were calculated from subsampled data (n=4,471 reads for BCR samples, n=1,496 reads for TCR samples) taking the average from 1,000 iterations and are compared between paired C1/C2 samples for **a)** BCR (n=65) and **b)** TCR (n=143) samples or between paired C1/C4 samples for **c)** BCR (n=29) and **d)** TCR (n=64) samples by chain. Statistics were calculated using lm(Shannon diversity/Gini index $\sim$ cycle + library RNA input, data).

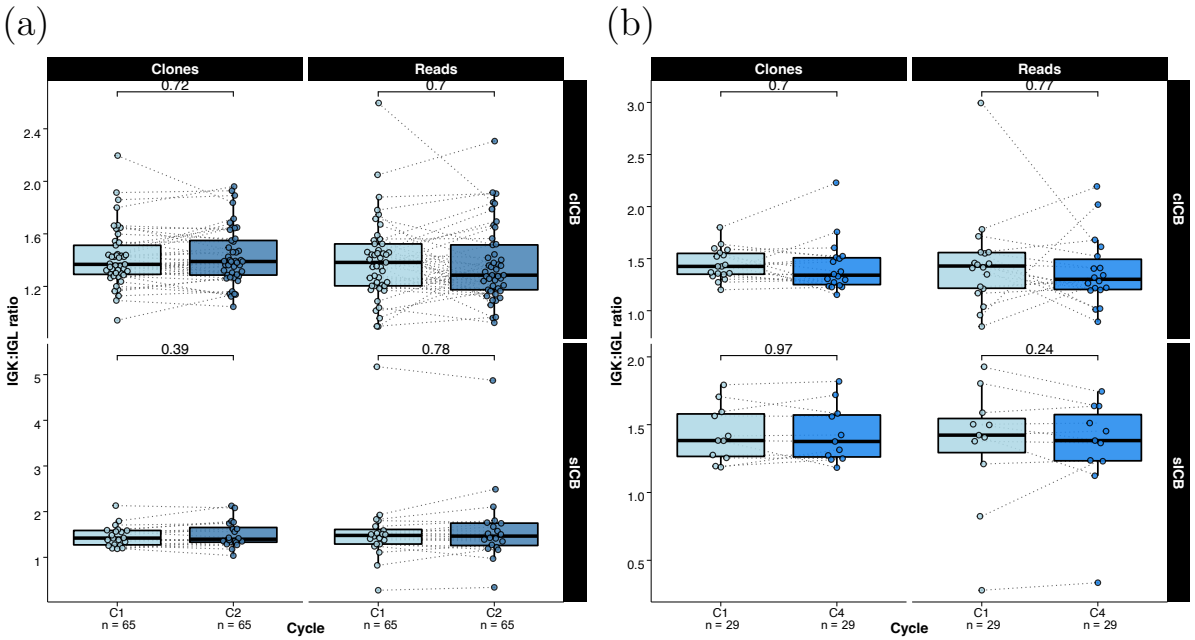


Figure S5.24 ICB treatment has no effect on BCR light chain usage
BCR light chain usage, calculated as the ratio of IGK:IGL clones (left) or reads (right) is compared between paired **a)** C1/C2 (n=65) or **b)** C1/C4 (n=29) samples by treatment type. Statistics were calculated using paired Wilcoxon signed-rank tests.

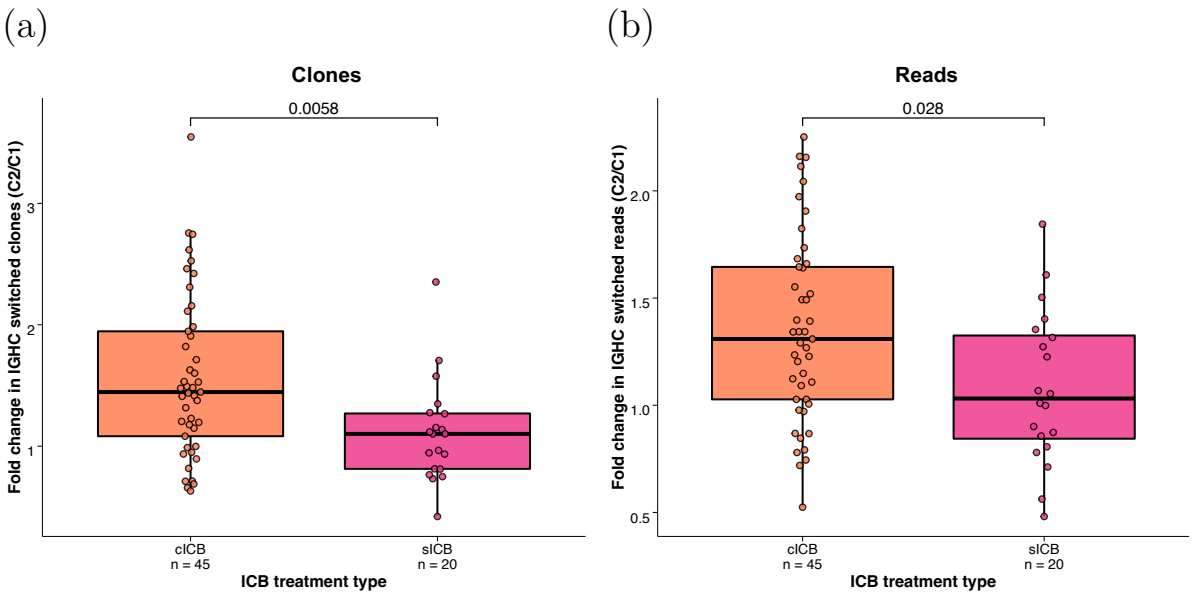


Figure S5.25 A higher induction of switched BCR clones is observed following cICB treatment
The fold change in switched IGHC (IgG/IgA/IgE) **a)** clones or **b)** reads at C2 (C2/C1) is compared between patients treated with sICB (n=20) or cICB (n=45). Statistics were calculated using unpaired Wilcoxon signed-rank tests.

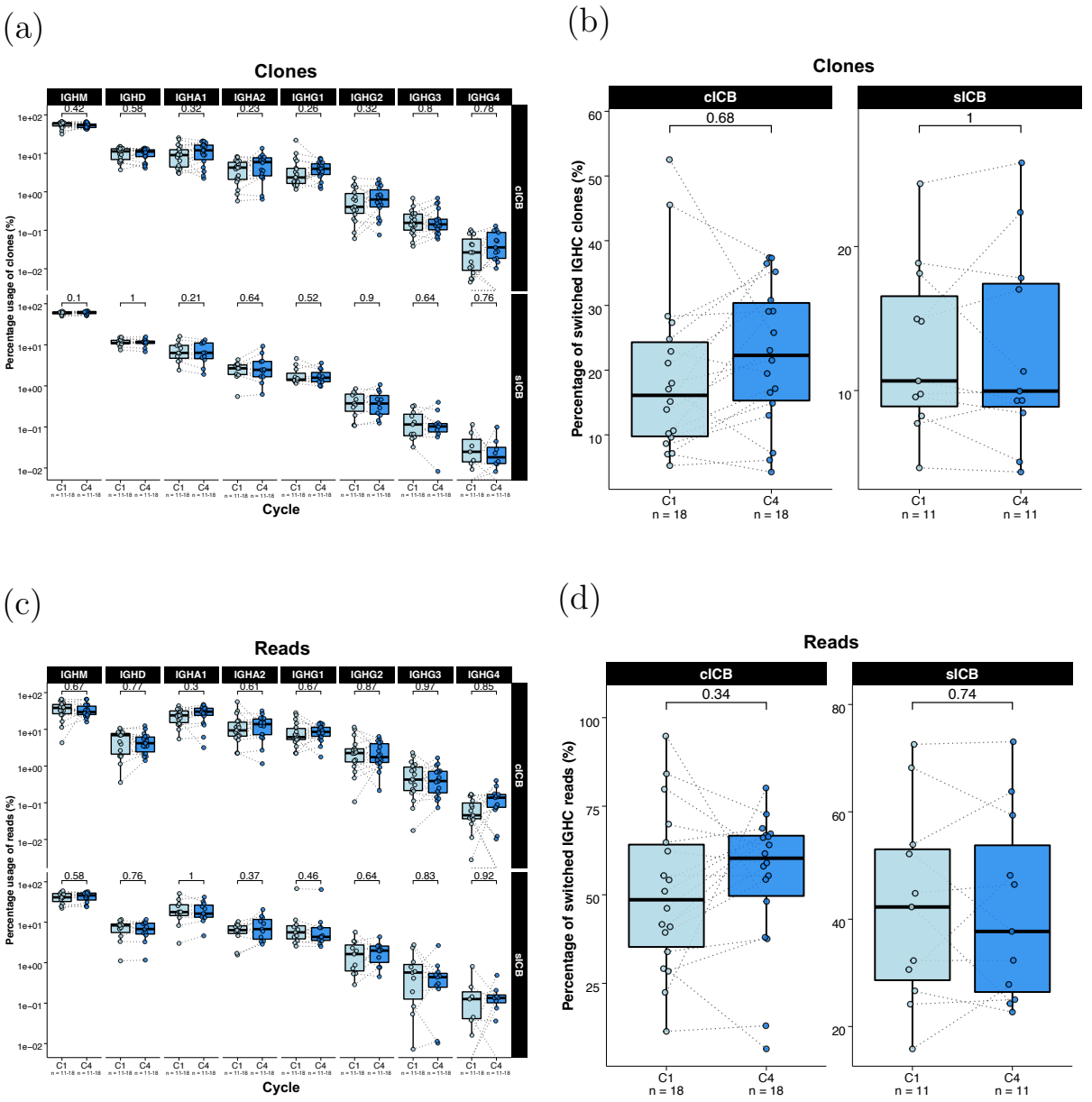


Figure S5.26 Changes in IGHC usage resolve by C4
Usage of individual IGHC genes by percentage of IGH **a)** clones or **c)** reads is compared between paired C1/C4 samples by ICB treatment (n=11 sICB, n=18 cICB). The combined percentage of switched **b)** clones or **d)** reads (IgG/IgA/IgE) is compared between paired C1/C4 samples by treatment type. Statistics were calculated using paired Wilcoxon signed-rank tests.

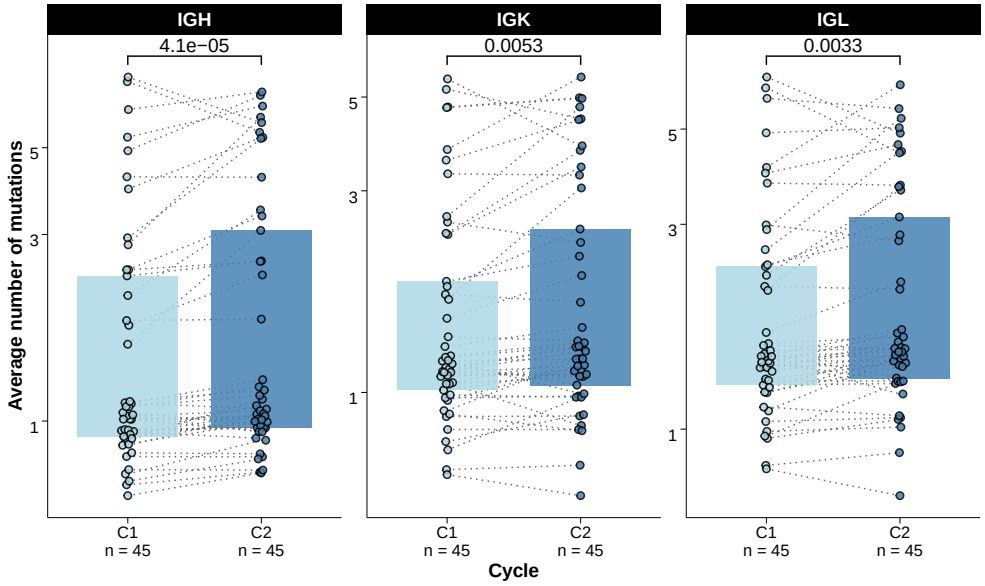


Figure S5.27 ICB increases the mutation rate in BCR clones regardless of chain
The average number of mutations in BCR clones is compared between paired C1/C2 samples (n=45) following cICB treatment by chain. Statistics were calculated using paired Wilcoxon signed-rank tests.

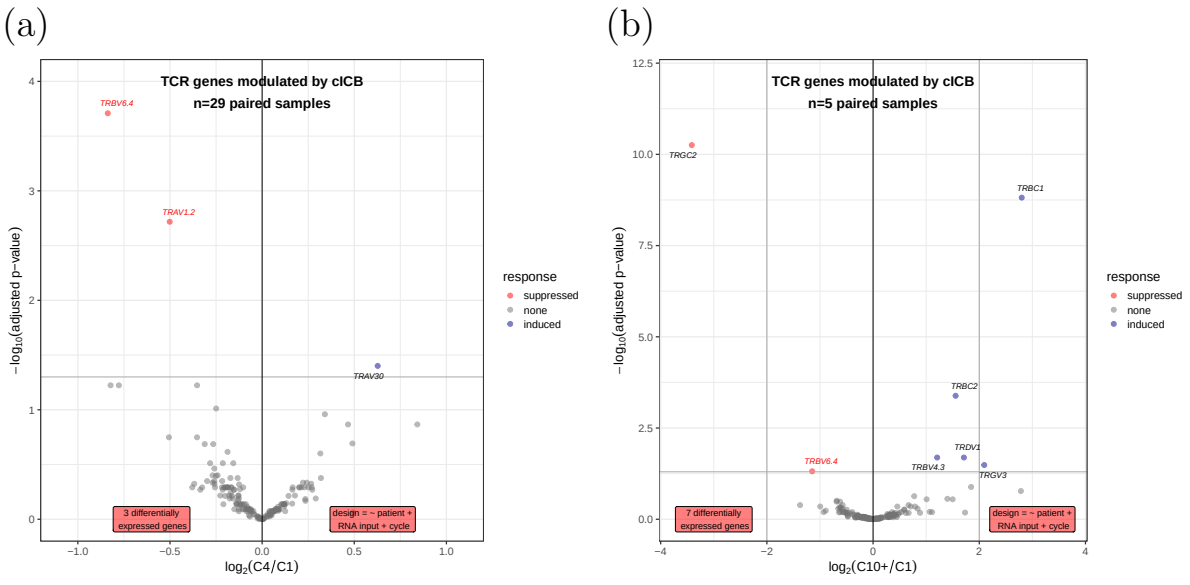


Figure S5.28 MAIT cell-associated TCR genes remain depleted at C4, but resolve by later time-points following cICB treatment
TCR expression was compared between paired cICB-treated **a)** C1/C4 (n=29) or **b)** C1/C10$^+$ (n=5) samples using $DESeq2$. Genes significantly upregulated after ICB treatment are in blue and those significantly depleted are in red. The $\log_2$ fold change of each gene is visualised on the x-axis with the significance of this difference displayed on the y-axis. The number of significantly differentially expressed genes as well as the $DESeq2$ design formula are displayed in red boxes. MAIT cell-associated TCR genes are highlighted in red. Statistics were calculated using the negative binomial distribution and adjusted for multiple testing using the Benjamini-Hochberg procedure on $DESeq2$.

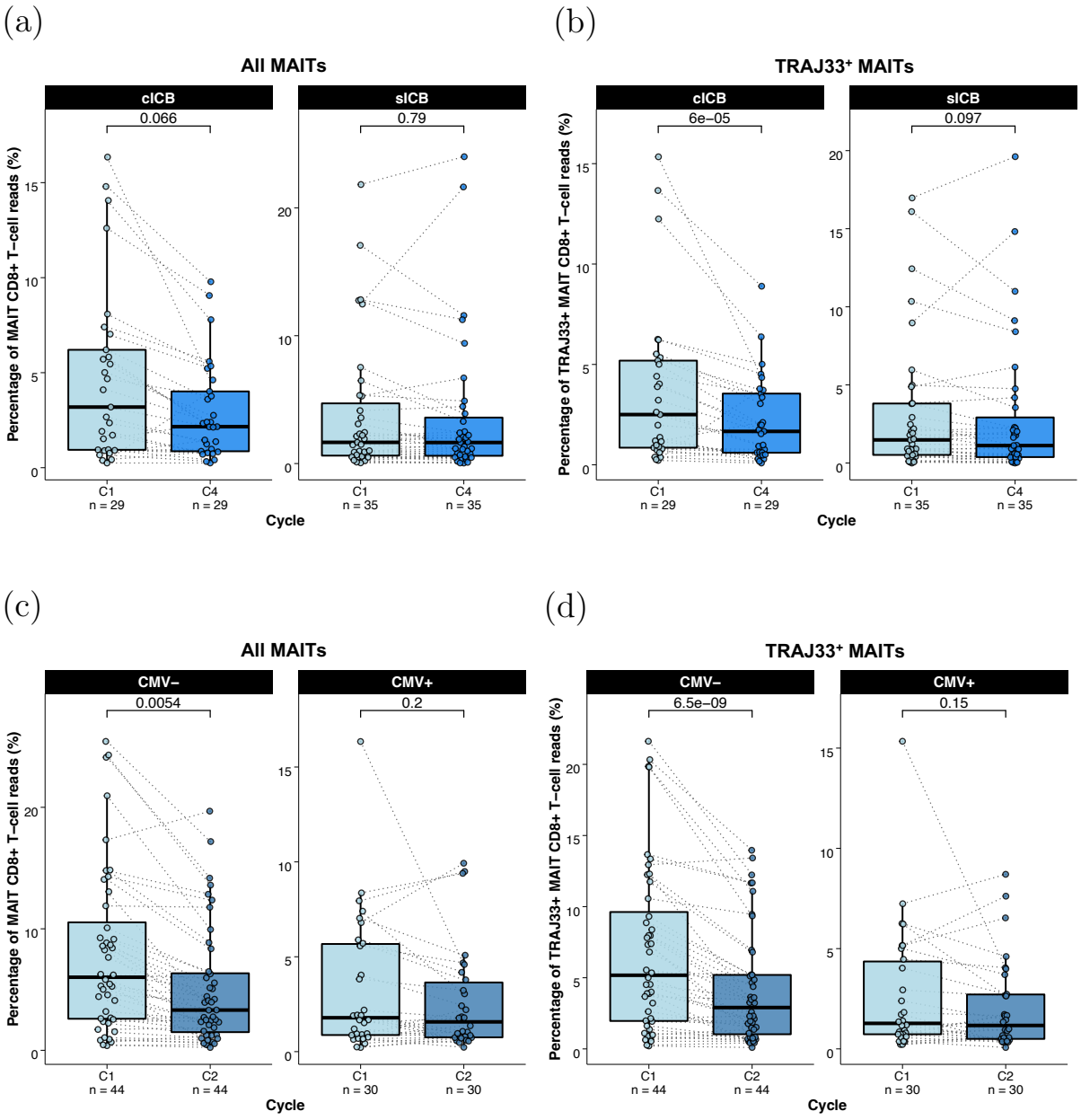


Figure S5.29 cICB maintains MAIT cell depletion at C4 with MAIT cell loss restricted to CMV$^-$ patients

MAIT cell percentage of CD8$^+$ T-cell TRA reads as identified by expression of *TRAV1-2* with **a)** *TRAJ12/TRAJ20/TRAJ33* or **b)** specifically *TRAJ33* is compared between paired C1/C4 samples by treatment type (n=29 cICB, n=35 sICB). Analysis is repeated for cICB-treated C1/C2 samples for **c)** all MAIT cells or **d)** TRAJ33-bearing MAIT cells by CMV serostatus (n=44 CMV$^-$, n=30 CMV$^+$). Statistics were calculated using paired Wilcoxon signed-rank tests.

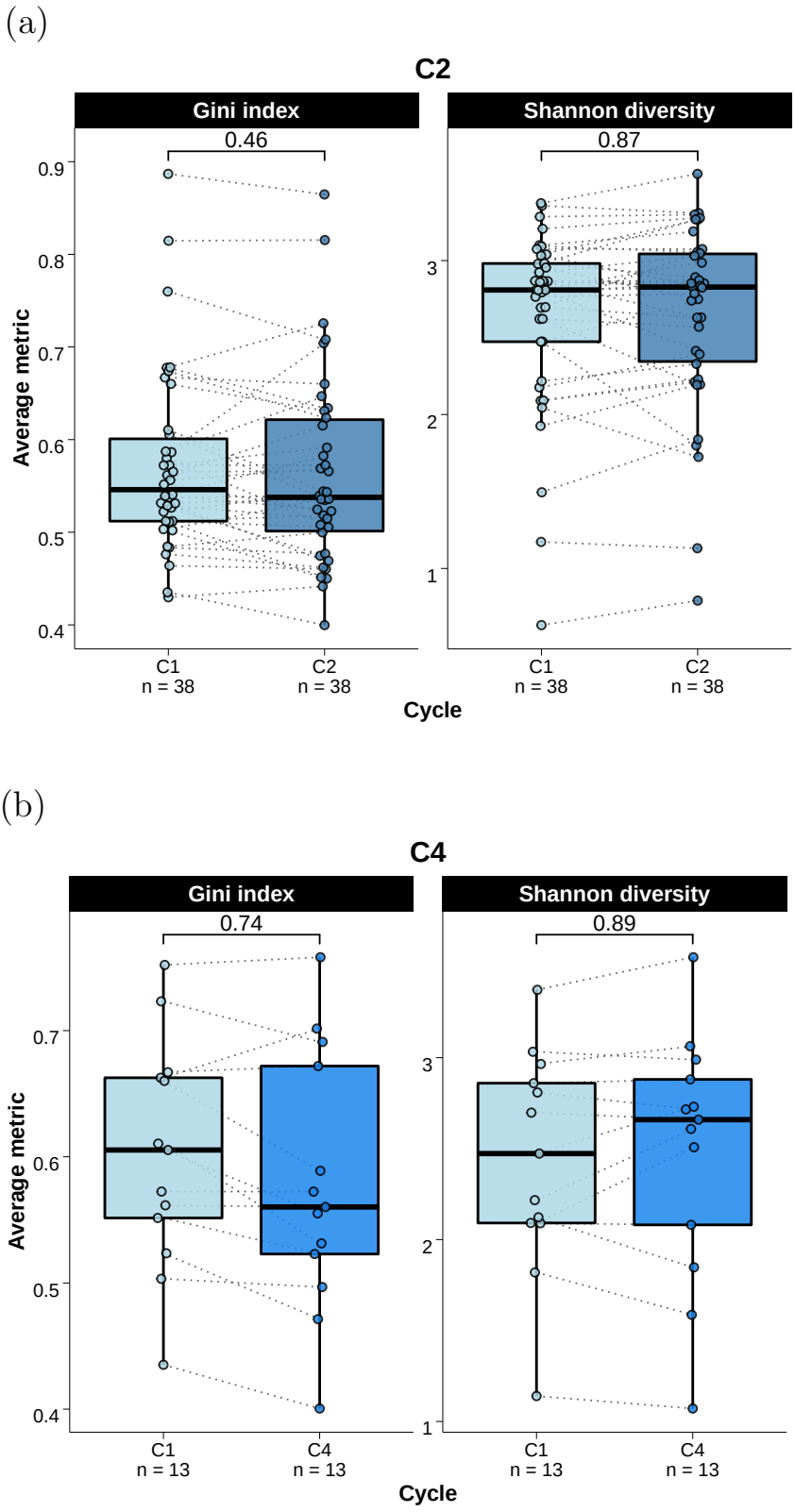


Figure S5.30 cICB has no effect on MAIT cell diversity indexes
MAIT cell Shannon diversity and Gini index were calculated after subsampling to 100 MAIT cell reads per sample and are compared between **a)** paired C1/C2 (n=38) and **b)** C1/C4 (n=13) samples receiving cICB treatment. Statistics were calculated using lm(Shannon diversity/Gini index ~ cycle + library RNA input, data).

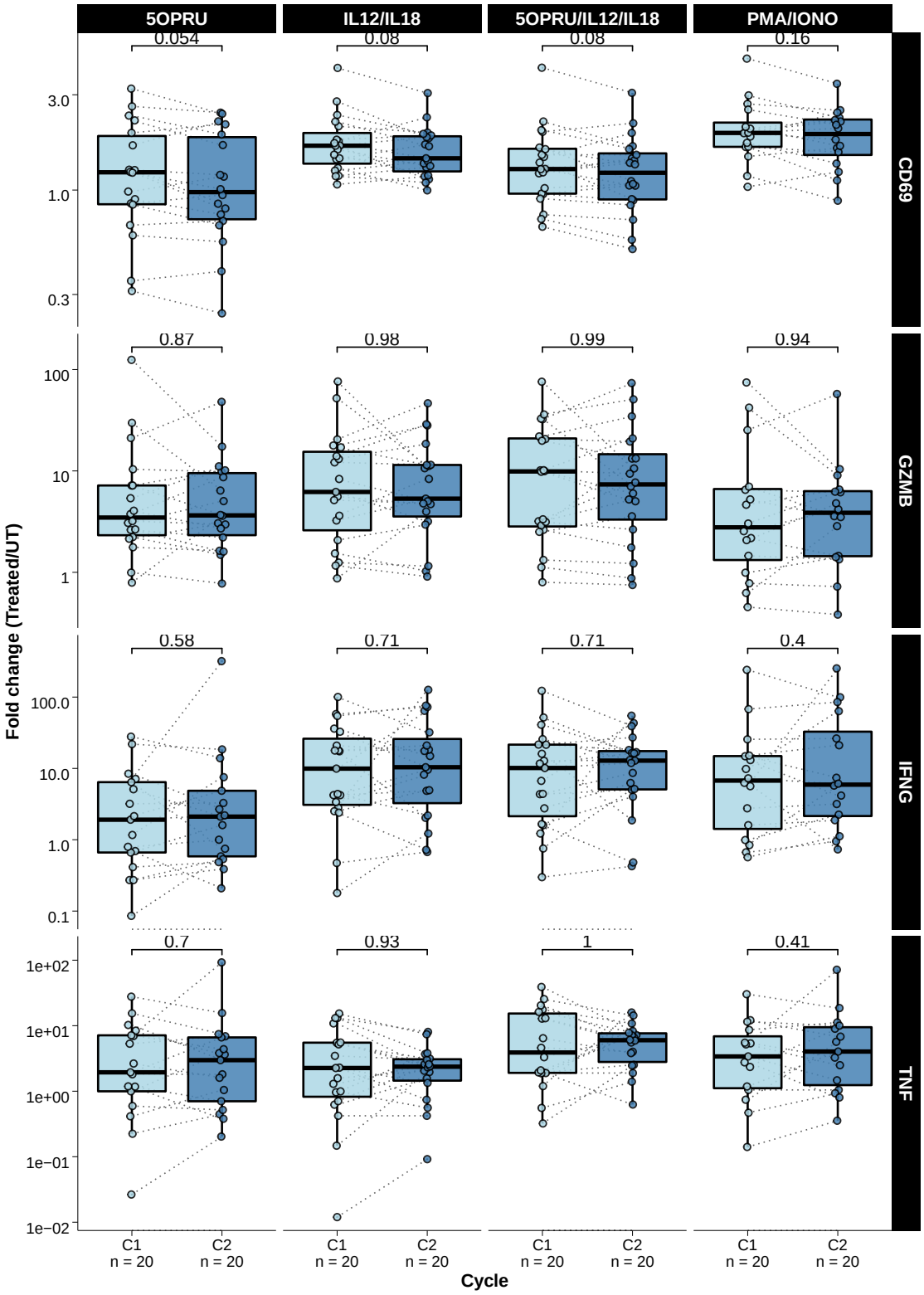


Figure S5.31 ICB treatment has no effect on the MAIT cell response to stimulation
PBMC samples were treated with a range of activating stimuli for 24 hours prior to flow cytometry analysis of $CD8^+$ MAIT cell activation and effector markers. Box plots compare the induction of these markers (treated/untreated) between paired C1 and C2 samples (n=20) following stimulation with either 5-OP-RU (5OPRU), IL-12/IL-18 (IL12/IL18), 5-OP-RU/IL-12/IL-18 (5OPRU/IL12/IL18), or PMA/Ionomycin (PMA/IONO). These markers include CD69, granzyme B (GZMB), IFN-γ (IFNG) and TNF-α (TNF). Statistics were calculated using paired Wilcoxon signed-rank tests. *UT = untreated*.

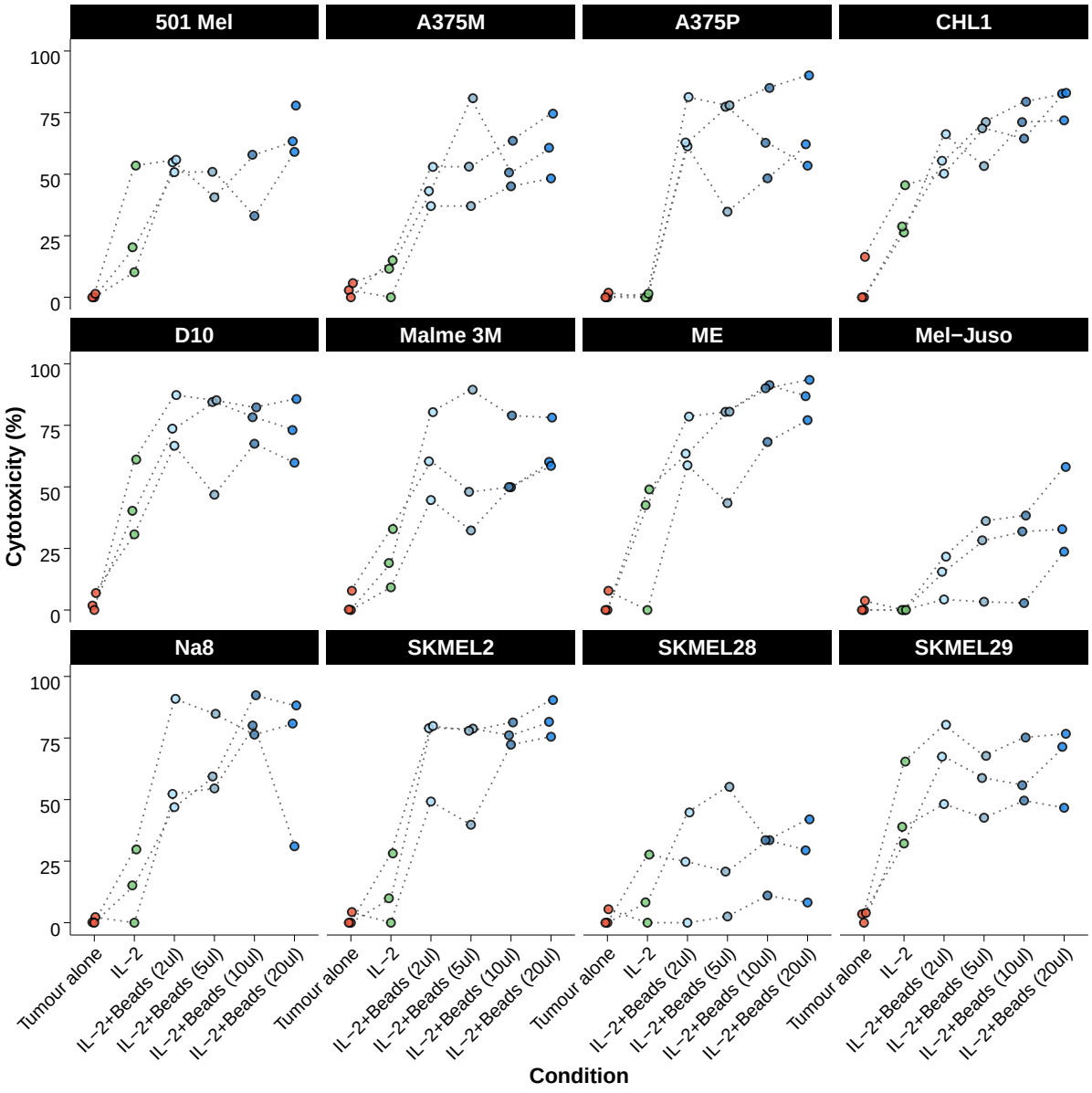


Figure S5.32 Expanded T-cells have broad cytotoxicity against melanoma cell lines
PBMCs (n=3) were expanded for seven days using varying concentrations of anti-CD2/anti-CD3/anti-CD28 beads (2µl, 5µl, 10µl, 20µl beads/1x10^6 PBMCs/ml) and cultured with 12 melanoma cell lines at an effector:target ratio of 1:1 for five days. Cytotoxicity was determined by MTT assay as the percentage reduction in melanoma cells. Tumour alone samples represent background melanoma cell death in the absence of PBMCs.

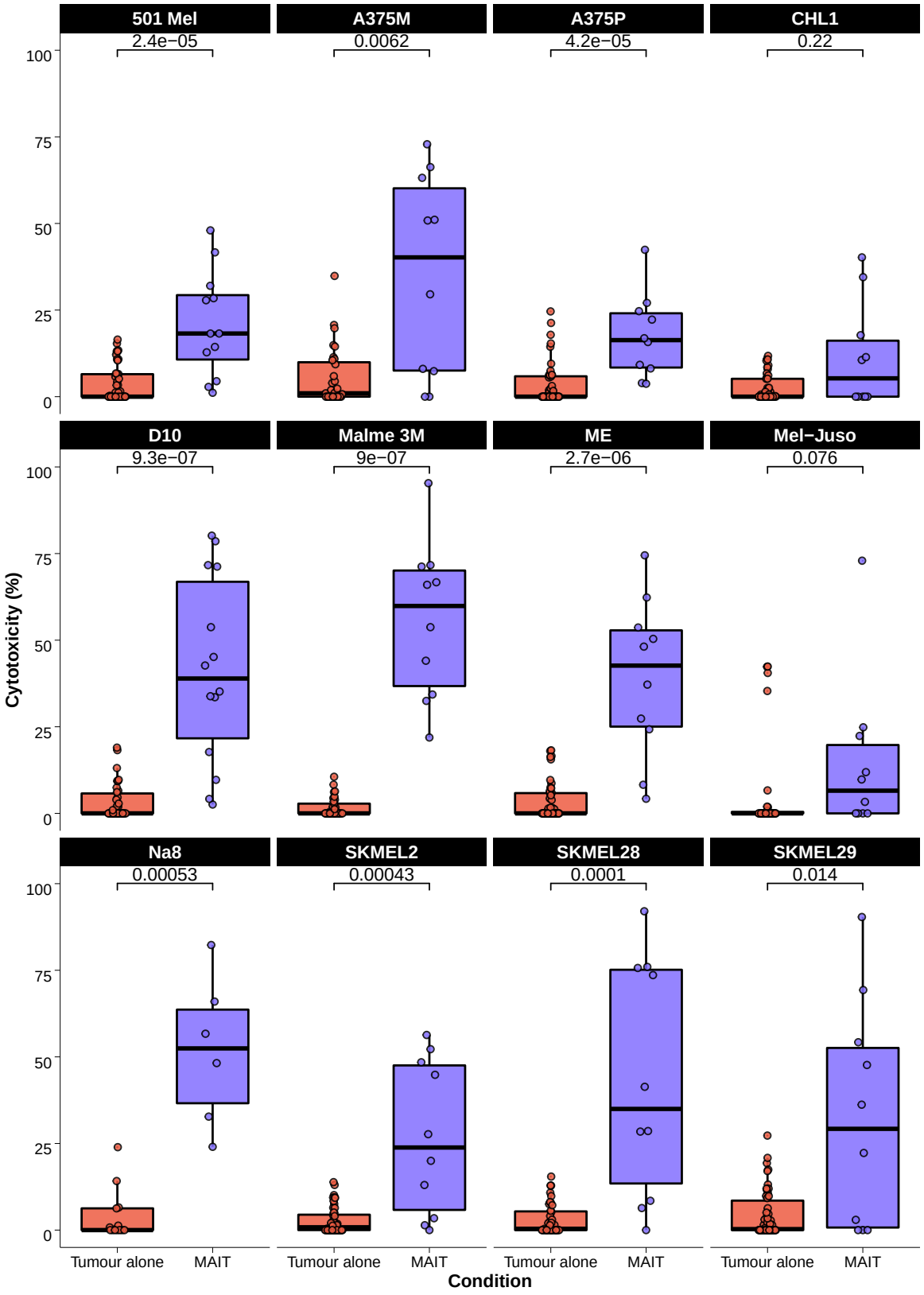


Figure S5.33 MAIT cells have antimelanoma cytotoxic potential against a variety of melanoma cell lines

MAIT cells (n=6-10) were cultured with 12 melanoma cell lines at an effector:target ratio of 1:1 for five days. Cytotoxicity was determined by either MTT or WST-8 assay as the percentage reduction in melanoma cells. Tumour alone controls serve as background melanoma cell death in the absence of MAIT cells. Statistics were calculated using unpaired Wilcoxon signed-rank tests.

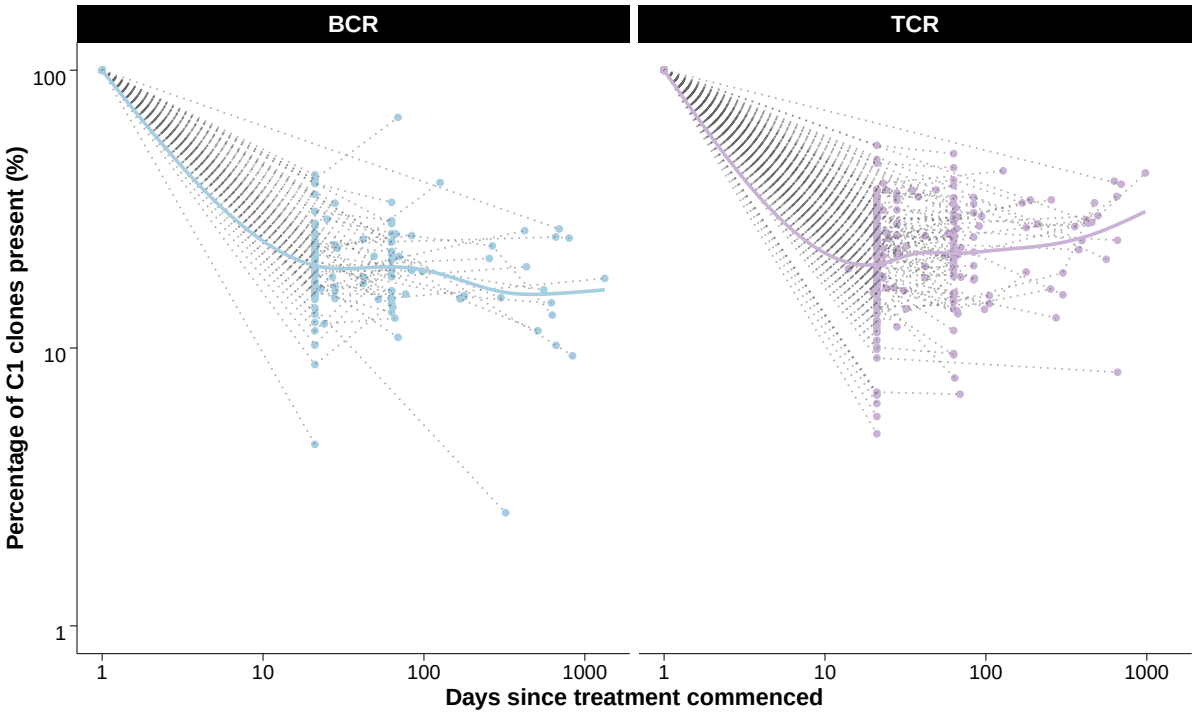


Figure S5.34 The majority of baseline BCR and TCR clones by CDR3 amino acid sequence are lost following ICB treatment
The percentage of baseline (C1) clones present per sample is tracked longitudinally looking at the days since ICB treatment commenced for BCR (n=212) and TCR (n=434) clones as identified by CDR3 amino acid sequence.

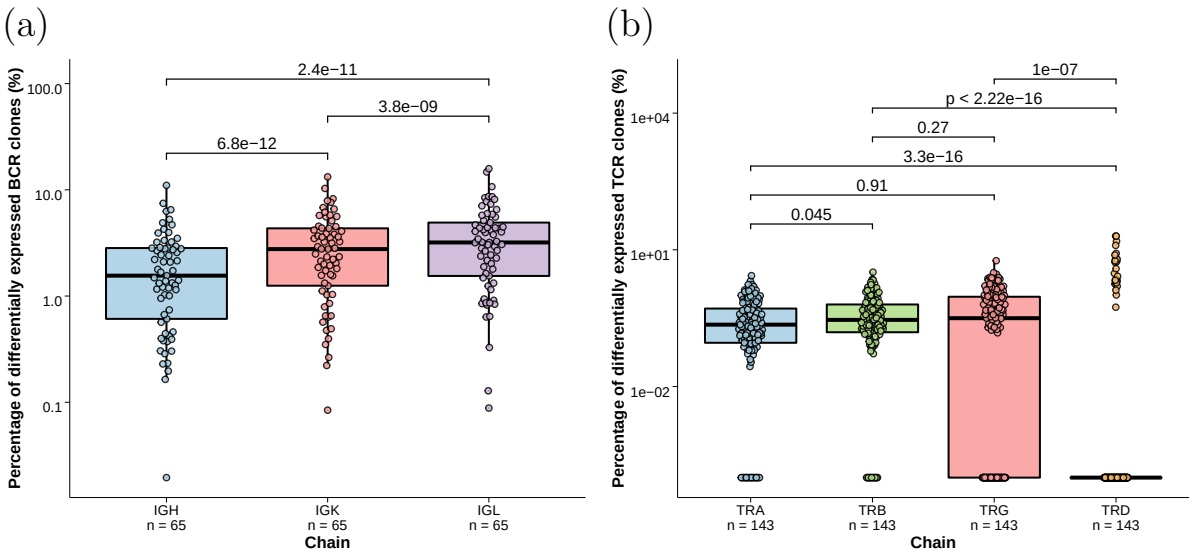


Figure S5.35 ICB induces greater changes in BCR light chain clones
The percentage of **a)** BCR (n=65) and **b)** TCR (n=143) clones significantly expanding or involuting at C2 is compared between different chains. Statistics were calculated using paired Wilcoxon signed-rank tests.

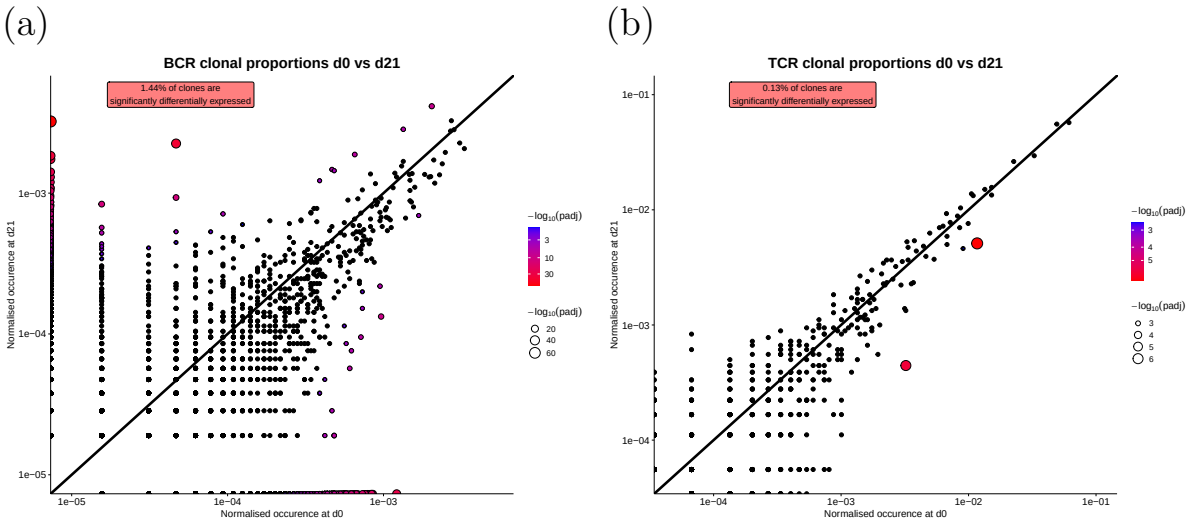


Figure S5.36 The healthy donor TCR repertoire remains largely stable over the course of three weeks

Two samples of peripheral blood were collected from a healthy donor three weeks apart to match the time between ICB treatment cycles with **a)** BCR and **b)** TCR clonal proportions compared between these time-points. Clonal proportion at d0 (x-axis) is compared to clonal proportion at d21 (y-axis) for all clones. Significantly expanding and involuting clones are coloured with point shading and size referring to the adjusted p-value of the differential enrichment. The percentage of clones significantly differentially expressed is displayed in red boxes. Statistics were calculated using Fisher's exact tests and adjusted using Bonferroni correction.

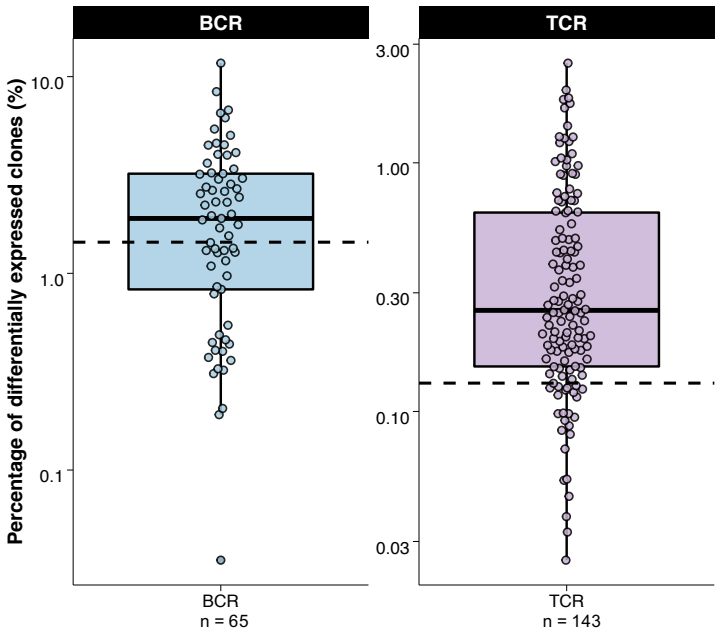


Figure S5.37 Clonal changes in the TCR repertoire following ICB treatment exceed background fluctuations

Box plots showing the percentage of significantly differentially expressed BCR (n=65) and TCR (n=143) clones at C2. The percentage of significantly differentially expressed BCR and TCR clones observed after three weeks from the healthy donor is represented as a dashed line.

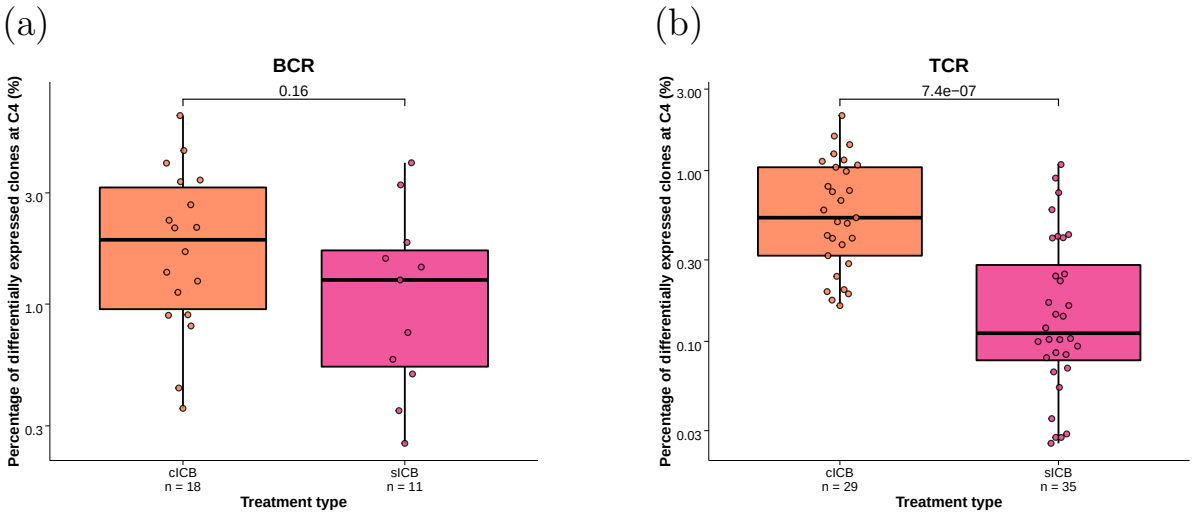


Figure S5.38 cICB induces greater clonal changes in the TCR repertoire than sICB at C4
The percentage of significantly differentially enriched clones at C4 is compared between sICB and cICB treatments for **a)** BCR (n=11 sICB, n=18 cICB) and **b)** TCR (n=35 sICB, n=29 cICB) repertoires. Statistics were calculated using unpaired Wilcoxon signed-rank tests.

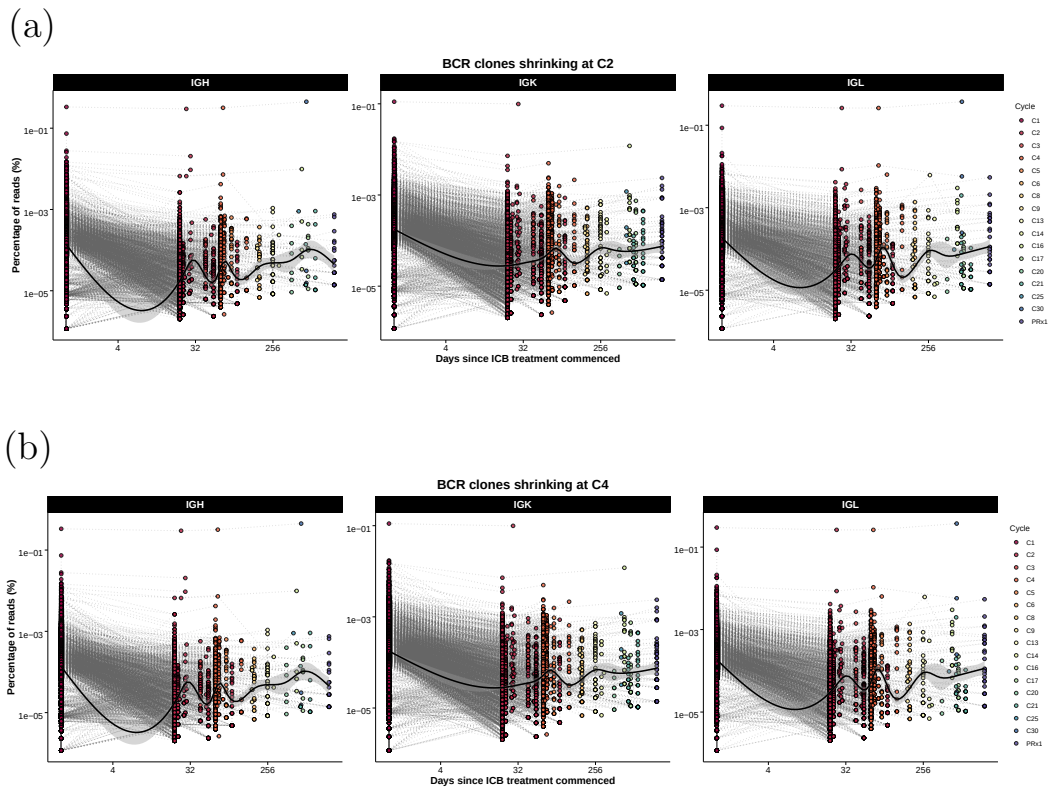


Figure S5.39 Significantly involuted BCR clones after ICB treatment resolve at later time-points
The percentage of reads accounted for by significantly involuting BCR clones at **a)** C2 (n=65) and **b)** C4 (n=29) by chain is tracked longitudinally per involuting clone by days since ICB treatment commenced. Samples are coloured by ICB treatment cycle. *PRx1 = Sample collected after cessation of ICB treatment.*

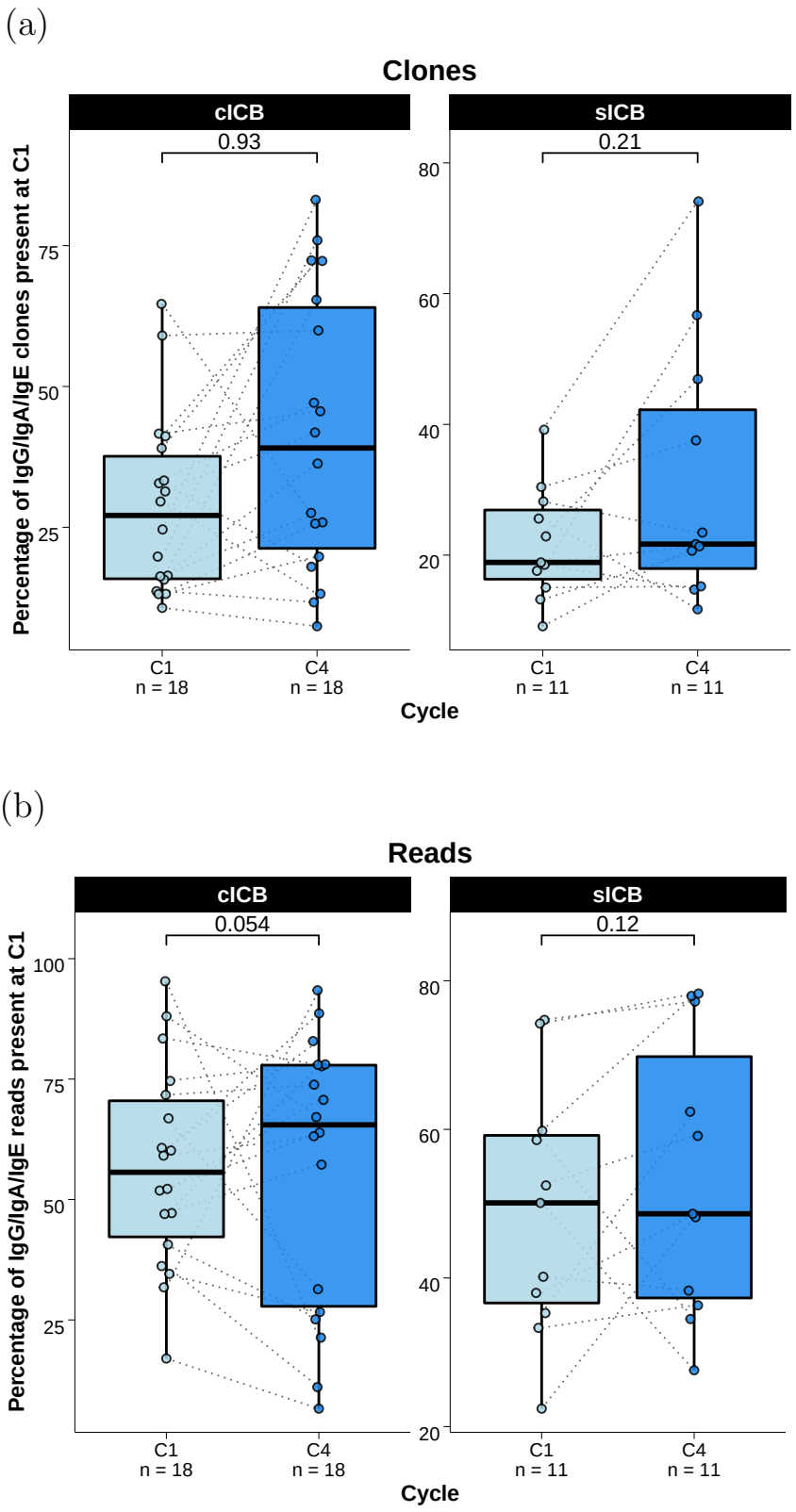
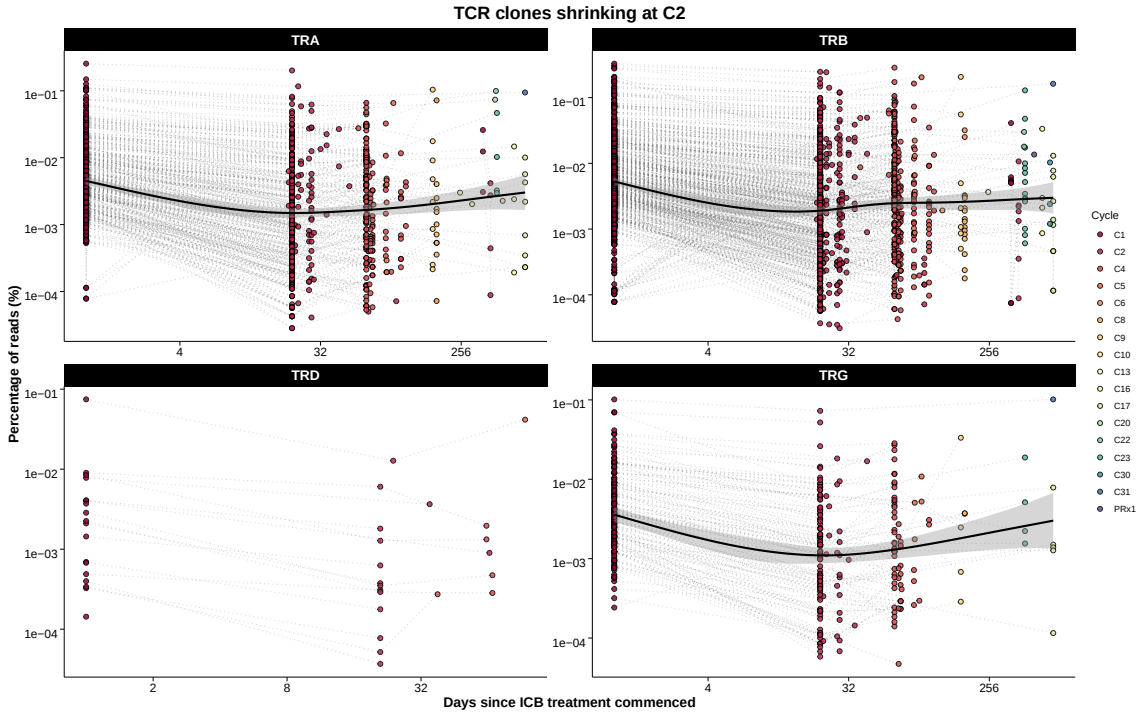


Figure S5.40 No difference is observed in CSR in clones persisting at C4
Box plots showing the percentage of switched (IgG/IgA/IgE) IGH **a)** clones and **b)** reads that are present at both C1 and C4 by ICB treatment type (n=11 sICB, n=18 cICB). Statistics were calculated using paired Wilcoxon signed-rank tests.

(a)



(b)

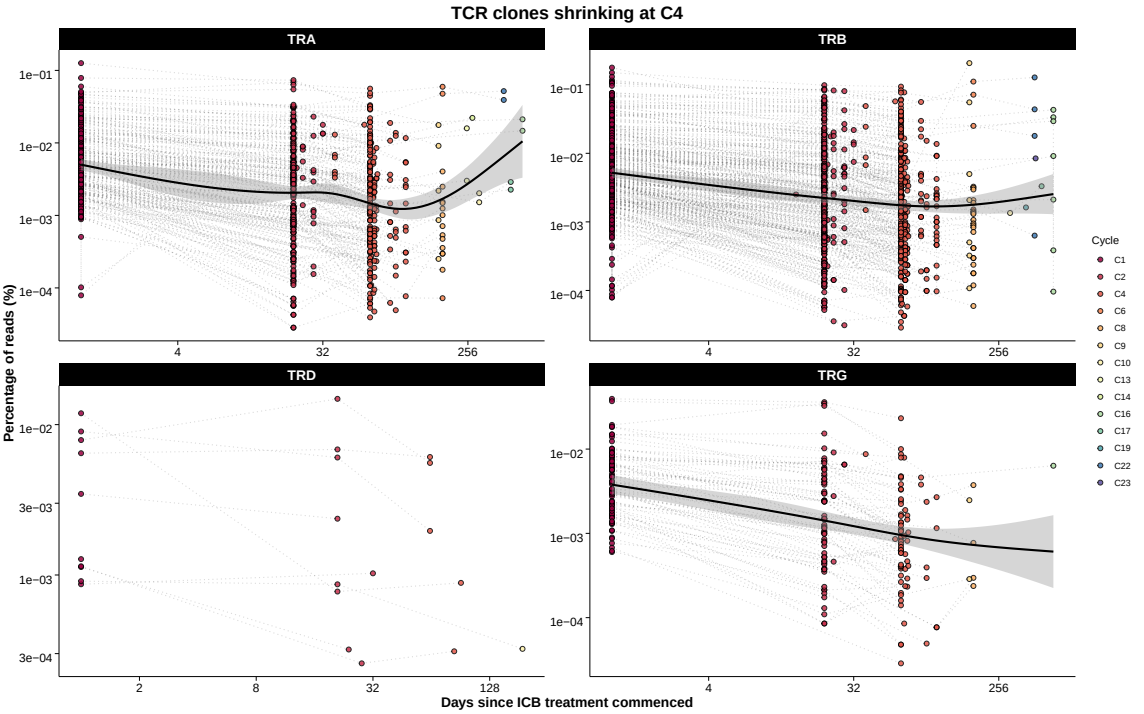


Figure S5.41 Significantly involuted TCR clones after ICB treatment resolve at later time-points The percentage of reads accounted for by significantly involuting TCR clones at **a)** C2 (n=120) and **b)** C4 (n=54) by chain is tracked longitudinally per involuting clone by days since ICB treatment commenced. Samples are coloured by ICB treatment cycle. *PRx1 = Sample collected after cessation of ICB treatment.*

5.5 Author Contributions

Chelsea A. Taylor, Alba Verge de los Aires, Isar Nassiri, Orion Tong, Robert A. Watson, Elise A. Mahé, Sara Danielli, Rosalin A. Cooper, Piyush K. Sharma, Christina Ye, COMBAT consortium

C.A.T, E.A.M, A.V.A, S.D, O.T, P.K.S, R.A.W and R.A.C were all involved in blood collection and processing; C.A.T, E.A.M, A.V.A and S.D extracted RNA; C.A.T and A.V.A generated and pooled bulk cDNA libraries for sequencing; I.N was responsible for upstream RNA analysis of the melanoma cohort; C.A.T performed all downstream BCR, TCR and transcriptomic analysis; C.A.T carried out qPCR reactions; John Radcliffe hospital generated anti-CMV IgG ELISA data to determine individual CMV serostatus; C.C collected samples, performed 10x single cell RNAseq, upstream bioinformatic analysis and annotated clusters of COMBAT single cell data; C.A.T analysed MAIT cells using COMBAT single cell data; C.A.T performed all cell culture assays and killing assays; C.A.T performed flow cytometry; O.T generated flow cytometry data for IgG4 and Ki67; C.A.T generated CXCL10 and CXCL13 ELISA data; R.A.W and C.Y collected clinical outcome data for all patients.

Chapter 6

Discussion

In this thesis, I make novel observations about the effects of CMV, metastatic melanoma and ICB treatment on peripheral immunity as well as identify predictive markers of clinical outcome in response to treatment. Here, I summarise these findings and discuss them in relation to the existing literature and also identify any future work that should be performed in order to further substantiate these data.

6.1 CMV

Firstly, I examined any effects of CMV on peripheral immunity which might affect the capacity for ICB response.

CMV infection was found to polarise PBMC composition in which CMV^+ individuals had a depleted NK cell population, but an expanded T-cell pool. However, no effects of CMV were detected in peripheral monocytes or B-cells including subset composition, markers of activation, transcriptomic expression and the BCR repertoire. It is surprising that almost no effects of CMV were detected in B-cells despite evidence of B-cell recognition through production of CMV-specific antibodies as well as increased B-cell count, clonality and mutation rate[477,583]. However, these reported changes were subtle and largely age-dependent, so may not be observed in this cohort due to the heterogeneity in age or even potentially due to viral latency. Nevertheless, the effect of CMV was still apparent within NK cells and T-cells which might serve as better surrogates for infection, especially due to the importance of both cell types in the control of viral infections.

Significant changes were also observed within the T-cell compartment including an increase in the CD8:CD4 ratio, an enlarged Temra population as well as a reduction in MAIT cells after controlling for age. This supports previous data which demonstrates an expansion of $CD8^+$ T-cells which are more differentiated and less naïve in CMV^+ individuals[474,477–481]. However, the accelerated loss in MAIT cells in CMV infection is over and above that observed with age[540–542]. This MAIT cell decline during CMV infection represents a novel finding and has not been previously reported.

Whilst a reduction in circulating MAIT cells was observed, MAIT cells were found to be more activated, potentially signifying a direct response of MAIT cells to CMV infection. This is likely to be mediated through signalling of proinflammatory cytokines inducing migration to distal sites where they become highly activated as is observed in SARS-CoV-2 infection[404,409,410]. Despite this increased level of MAIT cell activation, CMV did not affect the response of MAIT cells to activating TCR-dependent or TCR-independent stimuli.

These changes were also accompanied by differential expression of NK cells and $CD8^+$ T-cells in CMV. However, the effect of CMV was markedly higher in $CD8^+$ T-cells. Pathway analysis revealed that genes upregulated in CMV^+ patient $CD8^+$ T-cells were associated with T-cell activation, differentiation, antigen presentation and response to IFN-γ, suggestive of a direct response to CMV infection. Interestingly, one of the top genes found to be associated with CMV was *ZNF683* (HOBIT). HOBIT has previously been shown to be overexpressed in CMV-specific T-cells and associates with IFN-γ production and effector function[551–555] and thus may serve as a surrogate marker for the effects of CMV on $CD8^+$ T-cells. By calculating a CMV gene expression score per $CD8^+$ T-cell sample, a CMV-associated signature was identified which strongly correlated with CMV seropositivity in both exploratory and validation cohorts, regardless of age and cancer status. As a result, this CMV expression signature may find utility in predicting CMV serostatus and monitoring immune responses to infection. Collectively, these data identify $CD8^+$ T-cells as not only a major target of CMV-induced changes, but also as a predictive marker of serostatus. However, to further validate this CMV-associated gene signature, single cell analysis should be performed to identify expression of either known CMV-reactive TCR clones or tetramer-sorted CMV-specific T-cell clones and confirm if these cells also have this expression pattern.

Although no differences were detected within the BCR repertoire, CMV was found to significantly modulate the $CD8^+$ T-cell TCR repertoire. This included a reduction in the number of TCR clones detected and consequently, significantly larger clones on average compared to CMV^- individuals. Correspondingly, these changes were associated with a loss in clonal richness, but an increase in clonal unevenness. This supports previous findings which demonstrate a loss in TCR diversity, but a gain in clonality in CMV infection[371,475,572]. Such inflated clones may be CMV-specific and warrant further investigation.

Despite the impact of CMV infection on $CD8^+$ T-cells, changes induced by melanoma or ICB treatment were unaffected by CMV score. This is, however, with the exception of MAIT cell changes. Likely as a result of the significant clonal expansion observed within CMV^+ patients, TCR usage was found to vary between CMV^- and CMV^+ individuals. Although many of these CMV-associated genes may be enriched within CMV-specific clones, MAIT cell-associated genes were found to be depleted in CMV^+ individuals. By correlating MAIT cell percentage with $CD8^+$ T-cell expression, a MAIT cell gene expression score was generated by calculating the average expression of genes found to be significantly associated with MAIT cells. Supporting the reduction in MAIT TCR usage, MAIT cell expression score was also found to be significantly depleted within CMV^+ patients which suggested that MAIT cells were indeed reduced in CMV and this was not necessarily solely due to TCR downregulation. In addition, although no difference was found in MAIT cell clonality, a reduction in MAIT cell diversity was observed in CMV. This is suggestive of global MAIT cell loss, not confined to specific clones, and reflects observations previously made in SARS-CoV-2 infection[410]. The impact of CMV infection on MAIT cells thus limited any observations that could be made in MAIT cells following ICB treatment. However, the mechanism by which CMV depletes MAIT cells is not understood and should be investigated further to see if MAIT cells die, or indeed, migrate to distal sites during infection.

Surprisingly, although no effect of CMV on circulating γδ T-cell percentage or γδ T-cell expression score was found, γδ T-cell diversity was discovered to be significantly depleted in CMV^+ individuals with a concurrent increase in clonality. This may demonstrate that

whilst no changes in γδ T-cell proportion are observed, CMV may cause expansion of specific γδ T-cell clones as evidenced by the differences in γδ TCR usage. Previous studies describe a profound effect of CMV in increasing γδ T-cell numbers which is attributed to CMV recognition[573–575,584]. However, this expansion may be limited in melanoma patients and specific to certain γδ T-cell subsets as seen within the differential TCR usage that is observed. Nevertheless, previous data has similarly shown that γδ T-cells are more oligoclonal and biased towards TRDV1 usage in CMV[573–575,584], supporting the observations made in this cohort.

On top of correlations with CMV serostatus and CMV gene expression score, $CD8^+$ T-cell proportion, MAIT cell depletion and γδ T-cell clonality all correlated with the percentage of CMV-specific clones as identified using clones from the VDJdb database[511,512]. This highlights the importance of CMV in determining $CD8^+$ T-cell composition, particularly for T-cell differentiation and unconventional T-cells. Although CMV was not found to further regulate melanoma and ICB responses in $CD8^+$ T-cells, CMV serostatus should still be taken into consideration, especially for investigations into MAIT cells.

6.2 Metastatic melanoma

I then proceeded to explore any effects of melanoma on $CD8^+$ T-cells and $CD19^+$ B-cells by comparison with healthy donors. Subsequently, I determined how these changes were further regulated following ICB.

Interestingly, expression of both $CD8^+$ T-cells and $CD19^+$ B-cells was found to be significantly altered in MM patients as compared to healthy donors after controlling for the effects of age and CMV serostatus. Whilst MM-associated gene expression in $CD8^+$ T-cells was found to be significantly enriched within cell division pathways, MM-enriched genes in $CD19^+$ B-cells were associated with activation, humoral response and BCR signalling pathways. Both of these observations suggested a direct response to cancer.

CXCL13, known for its B-cell recruiting properties, was found to be upregulated by both $CD8^+$ T-cells and $CD19^+$ B-cells in MM patients. Strikingly, *CXCL13* was found to be the most significantly upregulated $CD8^+$ T-cell gene in melanoma and thus may highlight an important role for B-cell recruitment in T-cell antitumour responses. In accordance with this, CXCL13 has previously been shown to be highly expressed by $PD\text{-}1^{hi}$ TILs as well as by expanding TCR clones and to recruit B-cells to the tumour site where they are able to stimulate tumour-specific T-cell responses[261,348,366,376,451–454,456]. In addition to the clinical benefit of CXCL13 production and TLS formation that is shown following ICB treatment[261,364,365,430,435,445–448,451], these data highlight an important role for B-cells and hence the extent of recruitment to these sites may be crucial.

In addition to gene expression, the effect of melanoma on BCR and TCR repertoires was explored. Despite having distinct expression profiles in MM patients, hardly any effects of melanoma were observed within BCR and TCR repertoires. Specifically, BCR and TCR clone number, clone size, diversity and clonality were unaffected after controlling for age in BCR samples and for both age and CMV serostatus in $CD8^+$ T-cell TCR samples. However, several differences were observed in BCR and TCR usage which might reflect enrichment of specific genes within cancer-specific clones. Surprisingly, despite the profound induction of *CXCL13* by $CD8^+$ T-cells, no differences were detected in BCR clone CSR or SHM. Nevertheless, switched BCR clones were found to be more expanded

and may represent melanoma-reactive clones and the enrichment within BCR signalling and immunoglobulin production pathways that was observed.

However, expression and repertoire changes were distinct from the effects observed following ICB treatment with the exception of *CXCL13* and $CD8^+$ T-cell division which were further enhanced by ICB.

6.3 ICB

Finally, any effects of ICB on peripheral immune cells and subsequent associations with clinical outcome were explored.

Firstly, data derived from RNAseq and flow cytometry analysis revealed that T-cells expressed the highest levels of both CTLA-4 and PD-1 as compared to other PBMC subsets. T-cells thus represented the most likely target of ICB. Although no differences were observed in T-cell proportion or composition using flow cytometry data, detection of surface PD-1 was significantly reduced in T-cells following ICB. Indeed, this loss in surface PD-1 detection was specific to T-cells and was found to be as a result of efficient PD-1 blockade as detected by the presence of $IgG4^+$ and pembrolizumab-bound $CD8^+$ T-cells. Interestingly, a greater induction of $IgG4^+$ $CD8^+$ T-cells was observed following cICB compared to sICB and may be explained by differences in anti-IgG4 antibody affinity for pembrolizumab and nivolumab or indicate that as cICB induces *PDCD1* to a higher level than sICB, there is enhanced capacity for ICB binding. This may ultimately explain the greater magnitude of $CD8^+$ T-cell response to cICB as compared to sICB[371,547].

In addition to the loss in surface PD-1, flow cytometry data demonstrated that both $CD4^+$ and $CD8^+$ T-cells were significantly activated and proliferative owing to upregulation of CD38/HLADR and Ki67. This activation and PD-1 suppression were identified for all conventional T-cell subsets regardless of treatment type and CMV serostatus. However, such changes were markedly more increased following cICB treatment compared to sICB therapy. This was also reflected within the RNAseq data which demonstrated greater changes in expression following cICB. Although a very similar gene set was regulated by sICB and cICB, a higher number of genes were differentially expressed by cICB and to a greater magnitude, supporting previous findings[371,547].

As this data implicated T-cells as the direct target of ICB, the effect of ICB on gene expression was compared between different PBMC subsets. Due to lack of samples, $CD4^+$ T-cells were not investigated further. After subsampling to equivalent sample number per cell type, $CD8^+$ T-cells were found to have the most profound response to ICB compared to other cell subsets, incurring the highest number of DEGs. Pathway analysis revealed an enrichment of upregulated genes within cell division pathways, corresponding with the flow cytometry data which demonstrated an upregulation of Ki67. Despite this profound activation and proliferation, the response of $CD8^+$ T-cells to activating stimuli was not affected and thus $CD8^+$ T-cells retained their capacity to respond. Due to the similar changes observed in activation and PD-1 suppression in $CD4^+$ T-cells shown in this study, amongst others[209–213,384], it is likely that $CD4^+$ T-cells also mount a strong response. However, this cohort was underpowered to make any such observations and thus the effect of ICB on $CD4^+$ T-cells and the contribution to non-T-cell ICB responses should be explored in future studies.

For each cell type, an ICB response score was generated by calculating the average expression of the top 50 most significantly upregulated genes at C2. Interestingly, the

increase in $CD8^+$ T-cell ICB response score was correlated with the induction of $IgG4^+$ $CD8^+$ T-cells. Strikingly, any effect of ICB on $CD8^+$ T-cell expression completely disappeared after controlling for IgG4 binding and may suggest that the response of $CD8^+$ T-cells is directly determined by the extent of ICB binding. This was also the case when normalising for either $IgG4^+$ $CD8^+$ T-cells or $CD8^+$ T-cell ICB response score in other cell types, further demonstrating the relevance of $CD8^+$ T-cell ICB responses for $CD19^+$ B-cell, $CD14^+$ monocyte and NK cell responses. Furthermore, the importance of direct ICB binding in determining $CD8^+$ T-cell ICB response may explain differences observed in the magnitude of response between sICB and cICB treatments, with cICB found to induce a greater level of ICB binding.

To determine potential driver genes of this response, differential expression analysis was reperformed for $CD8^+$ T-cells following ICB, but controlling for one individual $CD8^+$ T-cell gene at a time. The effect of ICB on $CD8^+$ T-cells was only completely abrogated after controlling for $CD8^+$ T-cell expression of *TOX2*. Expression of *TOX2*, along with family member *TOX*, has previously been found to induce an exhausted like state in T-cells[562]. However, in a similar manner to PD-1, which is considered a marker of both activation and exhaustion, *TOX2* may also signify profound activation and hence ICB response. Expression of *MKI67* was also important in determining $CD8^+$ T-cell ICB response, suggesting the relevance of $CD8^+$ T-cell proliferation. Controlling for expression of $CD8^+$ T-cell *TOX2* or *MKI67* similarly removed any effect of ICB on $CD19^+$ B-cells, $CD14^+$ monocytes and NK cells and may directly determine responses in these cells.

Whilst $CD8^+$ T-cell ICB response score, IgG4 binding and expression of *TOX2* and *MKI67* may just be correlative with response in other cell types, controlling for $CD19^+$ B-cell, $CD14^+$ monocyte or NK cell ICB response scores had much less impact on $CD8^+$ T-cell differential expression. Hence, non-T-cell responses may be secondary to $CD8^+$ T-cell response and not the other way around. However, the importance of $CD8^+$ T-cells should be further demonstrated in *in vitro* studies by assessing if $CD19^+$ B-cells, $CD14^+$ monocytes and NK cells are responsive to ICB in the absence of $CD8^+$ T-cells. Even though, non-T-cells were shown to be incapable of binding pembrolizumab, further flow cytometry should be performed to determine if non-T-cells can bind other immune checkpoint blockers directly, namely nivolumab and ipilimumab, and therefore if they are truly reliant on downstream $CD8^+$ T-cell ICB responses or if they can indeed respond to ICB directly themselves.

Although no single gene expressed by non-T-cell subsets eliminated the response of $CD8^+$ T-cells to ICB, several were found to significantly reduce the impact. These genes were typically composed of IFN-γ response genes including GBPs, *STAT1* and *CXCL10*. This may indicate that non-T-cells respond to ICB indirectly through T-cell IFN-γ production which is upregulated following ICB. Thus, this highlights a potential mechanism by which non-T-cell subset responses are secondary to $CD8^+$ T-cell ICB response. However, this has not been formally proven and future studies should investigate the effect of ICB on non-T-cell subsets after blocking IFN-γ.

In addition to changes in expression, any effect of ICB on PBMC subset composition was also investigated using flow cytometry data. However, out of all PBMC subsets, only B-cell proportion and subset composition were found to be significantly modulated. Specifically, B-cells were found to be transiently depleted following cICB treatment, but not sICB, regardless of CMV serostatus. This is similarly described in a separate study which finds that B-cell changes are only detected following cICB and not after sICB anti-CTLA-4 or anti-PD-1[458]. This is of particular interest because B-cell changes are

therefore not due to inclusion of an anti-CTLA-4 antibody specifically, but rather as a result of increased activation by blocking both CTLA-4 and PD-1 simultaneously[458]. However, any effects were lost by C4. Interestingly, a low B-cell proportion was associated with enhanced OS and PFS both prior to and following ICB treatment. B-cell accumulation at tumour sites and surrounding TLS's is associated with favourable outcomes[99,252,320,334,359,365,366,391,429–437] and may explain why B-cells are depleted in the periphery in responding patients. This B-cell depletion was accompanied by activation and a loss in USMs, but an increase in ASCs as previously demonstrated[458]. As ASCs downregulate CD19 during differentiation, this may partially account for the loss in circulating $CD19^+$ B-cells. Accordingly, increases in ASCs and activation, but loss of USMs associated with B-cell depletion.

Next, the $CD19^+$ B-cell transcriptomic response to ICB was investigated. Similarly to the effects observed in B-cell proportion and subset composition, genes were only found to be differentially expressed after cICB and not sICB. However, these transcriptomic effects were only transient and had subsided by C4. Pathway analysis demonstrated an enrichment of significantly upregulated genes in cell migration, differentiation and IFN-γ response pathways. Interestingly, IFN-γ-inducible *CXCL10* was found to be strongly upregulated by B-cells following cICB treatment and was accompanied by elevated CXCL10 within patient plasma. *CXCL10* was also upregulated, along with fellow CXCR3 ligands *CXCL9* and *CXCL11*, by $CD14^+$ monocytes. CXCL10 is important in T-cell ICB response, owing to high expression of CXCR3 by T-cells, and stimulates proliferation, expression of effector cytokines and T-cell priming through enhanced interaction with DCs[228,569]. Significantly, expression of CXCR3 ligands associate with clinical outcome[67,176,223,227,228,261,320,343,365–367]. Although $CD8^+$ T-cells are the major determinant of ICB response, perhaps $CD19^+$ B-cells and $CD14^+$ monocytes also contribute to $CD8^+$ T-cell responses through production of CXCR3 ligands which induce $CD8^+$ T-cell migration to the tumour and increase effector function.

Due to the limited power of the flow cytometry data, subset composition was deconvoluted from bulk RNAseq data. This was performed using genes found to be correlated with individual $CD19^+$ B-cell subsets from single cell RNAseq data. ASC score was found to be uniquely increased following cICB and not sICB, thus supporting findings from flow cytometry. Importantly, induction of this ASC score associated with prolonged OS and PFS, highlighting a putative role of ASCs in antitumour responses. Previously, ASC tumour infiltration has been found to subsequently enhance T-cell infiltration through production of T-cell attracting chemokines (CCL3, CCL4 and CCL5) and thus may contribute directly to T-cell antitumour responses[433].

Further substantiating the importance of $CD8^+$ T-cells in eliciting downstream $CD19^+$ B-cell responses, baseline expression of PD-1 in $CD8^+$ T-cells, and hence the capacity for ICB binding, was found to associate with $CD19^+$ B-cell response. After controlling for individual $CD8^+$ T-cell genes in $CD19^+$ B-cell C1/C2 comparisons, expression of $CD8^+$ T-cell *CD38* and *MKI67* were also found to associate with $CD19^+$ B-cell ICB response. This was in addition to the importance of $CD8^+$ T-cell ICB response score, IgG4 binding and expression of *TOX2* and *MKI67* that had already been identified as associates of $CD19^+$ B-cell responses. Induction of $CD38^+$ $CD8^+$ T-cells, identified using flow cytometry data, was also found to correlate with B-cell changes including USM depletion, activation and induction of ASCs. However, no such association was found with B-cell lymphopenia. Similarly, although $CD8^+$ T-cell ICB score was found to correlate with ASC induction, no such correlation was found with B-cell depletion.

Owing to the enrichment of $CD19^+$ B-cell ICB-upregulated genes in migratory and chemotaxis pathways and elevated expression of *CXCL13* in MM patient $CD8^+$ T-cells, which is further enhanced by ICB, CXCL13 was investigated. Strikingly, *CXCL13* was found to be one of the most significantly upregulated genes in $CD8^+$ T-cells following ICB. Induction of CXCL13 was also observed within patient plasma after ICB. However, with regards to transcriptomic and protein expression, CXCL13 was more highly induced following cICB. Interestingly, not only did increased levels of CXCL13 associate with ASC induction, but also the B-cell depletion that is observed following ICB treatment. Although expression of $CD8^+$ T-cell *CXCL13* did not associate with survival, high levels of plasma CXCL13 were found to associate with prolonged OS following sICB. This is not observed following cICB, but this may be due to the profound induction of CXCL13 in all patients and hence a negligible difference in variation.

Finally, any effects of ICB on BCR and TCR repertoires were investigated. Despite profound differences in $CD8^+$ T-cell and $CD19^+$ B-cell expression and phenotype, no differences were observed in BCR or TCR diversity. However, low TCR clonality, along with a higher induction of novel TCR clones, was found to associate with prolonged OS. This may be due to the importance of peripheral $CD8^+$ T-cell clones for replenishing tumour cell populations[372,381] with TCR diversity determining the capacity for tumour recognition. Although not consistently observed between different studies, previous data highlights a possible role for peripheral TCR diversity in predicting clinical outcome to ICB treatment[250,251,363,379].

In accordance with changes in B-cell expression and phenotype, no differences in CSR or SHM were observed after sICB, but were strongly induced after cICB. However, these changes were transient and disappeared by C4. This increased level of CSR associated with ASC induction, mutation rate as well as $CD8^+$ T-cell metrics including ICB response score, induction of Ki67 and PD-1 blockade. However, increased CSR and SHM may not be detectable for sICB due to the reduced impact that is observed in clonal composition compared to cICB and limitations in statistical power. In support of this, most novel and expanding clones at C2 were found to be switched and highly mutated regardless of ICB treatment. This suggests that there is indeed increased germinal centre activity following ICB for both sICB and cICB, although this is limited to just a few clones in sICB and is thus not detectable.

In order to better understand the effects of ICB on specific B-cell subsets, single cell RNAseq analysis should be performed on whole B-cells, so as to ensure inclusion of $CD19^{lo/-}$ ASCs. This would allow detection of the most responsive subsets to ICB as well as enable the identification of B-cell differentiation trajectory and track specific clones during this differentiation as has previously been used for $CD8^+$ T-cells[208]. Additionally, to further understand B-cell changes to ICB, the number and activity of TLS's should be explored to see if this determines the B-cell depletion that is observed in the periphery, owing to B-cell recruitment and hence migration out of the periphery. This would also ascertain if TLS's contribute to the increased B-cell differentiation, activation, SHM, CSR and plasma CXCL13 observed following cICB and ultimately any association with clinical outcome.

Similarly, TCR usage only differed following cICB. This included downregulation of MAIT cell TCR genes which remained depleted at later time-points. Additionally, MAIT cell gene expression score was also depleted following cICB, but was only detectable in CMV^- patients. This is likely as a result of the depletion that is already observed within CMV^+ patients which hence limits any further decline in cell numbers. However, a high

MAIT cell proportion was found to associate with longer OS and may be due to the ability to maintain a high level of MAIT cells. This MAIT cell depletion associated with $CD8^+$ T-cell ICB response score, *TOX2* and *MKI67* expression. Understanding the role of MAIT cells in clinical benefit is important and may explain why MAIT cells are so activated in MM patients even before ICB treatment has begun.

Although MAIT cells were found to be depleted at C2 and inversely correlated with $CD8^+$ T-cell cytotoxicity expression score, they were able to efficiently kill melanoma cell lines in which production of MAIT cell effector cytokines directly correlated with overall cytotoxicity. This was independent of MR1, yet was enhanced by IL-12, IL-15 and IL-18 and thus MAIT cells may respond to cancer through proinflammatory cytokines. However, experiments should be reperformed using blocking antibodies against IL-12/IL-15/IL-18 and type I IFNs to identify the dependency of MAIT cell cytotoxicity. While the depletion in MAIT cells observed after ICB may be due to hyperactivation and subsequent activation-induced cell death, the ability of MAIT cells to kill cancer cell lines[541] may highlight a role in antitumour responses in which MAIT cells migrate to the tumour. Additionally, MAIT cells retained the ability to respond to both TCR-dependent and TCR-independent stimuli after ICB which may indicate that they are still functional and not in fact dying. Furthermore, $CD8^+$ T-cell cytotoxicity score is most likely just a marker of effector $CD8^+$ T-cells[208] and thus it may not be surprising that MAIT cells negatively correlate and should still be considered as capable of inducing antitumour responses. However, whether ICB contributes to enhanced MAIT cell antitumour responses is not known and should be investigated.

Although flow cytometry data showed that unconventional T-cells expressed higher levels of CD38/HLADR and PD-1 compared to conventional T-cell subsets, no change in CD38/HLADR or PD-1 expression was observed following ICB treatment and may represent a lack of response to ICB in a conventional manner. Nevertheless, MAIT cells have previously been demonstrated to respond to ICB[425]. This may mean that unconventional T-cells respond distinctly to ICB or even die due to a preexisting hyperactivated state which when targeted by ICB induces activation-induced cell death. However, further studies should investigate whether unconventional T-cells are indeed targeted by ICB directly and whether they are able to respond and migrate to the tumour or if they in fact die.

6.4 Summary of ICB mechanism of action

Although the mechanism of action of ICB on tumour-associated and peripheral T-cells has been extensively studied, the interplay with other cell subsets in the periphery is unclear. In this section, I describe a possible mechanism by which ICB exerts its effects on peripheral immune cells, not limited to T-cell subsets.

As demonstrated by flow cytometry data, ICB has been shown to target $CD8^+$ T-cells directly and induce sufficient PD-1 blockade. This binding was found to associate with $CD8^+$ T-cell activation and proliferation, identified using both flow cytometry and RNAseq data, and to be essential for expression changes. However, $CD8^+$ T-cell ICB binding was also found to be crucial for non-T-cell ICB responses. Genes upregulated in all sequenced PBMC subsets included IFN-γ response genes such as *GBPs* and *STAT1*. These same genes were found to be the most strongly correlated with $CD8^+$ T-cell ICB response and thus may indicate a direct response of non-T-cells to the IFN-γ induced by

$CD8^+$ T-cells.

Interestingly, CXCR3 ligands *CXCL9*, *CXCL10* and *CXCL11* were all found to be massively upregulated by $CD14^+$ monocytes as well as *CXCL10* by $CD19^+$ B-cells. CXCL10 is essential for governing $CD8^+$ T-cell proliferation and cytotoxicity[228] and may be involved in $CD8^+$ T-cell migration to the tumour. Strikingly, one of the top genes induced by $CD8^+$ T-cells is *CXCL13* which is important for B-cell recruitment to the tumour and surrounding TLS's[453]. Both CXCL10 and CXCL13 proteins were also detected at higher levels within the circulation following ICB treatment. Therefore, one can speculate that elevated CXCL10 production induces $CD8^+$ T-cell migration into the tumour which in turn, produces CXCL13 and attracts B-cells to the tumour site and adjacent TLS's. Accordingly, the induction of CXCL13 was found to associate with an induction of ASCs, CSR and SHM and therefore suggests that $CD19^+$ B-cells have undergone differentiation and germinal centre reactions within lymphoid tissue. Although the increase in ASC differentiation is associated with CD19 downregulation, migration of $CD19^+$ B-cells to distal lymphoid tissue may also explain this observed B-cell lymphopenia.

Although profound $CD8^+$ T-cell activation and PD-1 blockade is observed following ICB treatment, the same effects are not detected in unconventional T-cells despite high expression of PD-1. This may highlight a different mechanism for ICB in unconventional T-cells. Whilst no effect of ICB was found within iNKT cells or γδ T-cells, MAIT cells were found to be depleted following cICB using either TCR usage or MAIT cell gene expression score. This may mean that MAIT cells die in response to ICB, owing to already high baseline levels of activation, including PD-1, which might make them a more attractive target. However, no such loss in surface MAIT cell PD-1 was observed after ICB. Despite MAIT cell depletion, remaining MAIT cells retained the ability to respond to both TCR-dependent and TCR-independent stimuli which one would expect to be reduced if undergoing cell death. Therefore, this loss may indicate that MAIT cells migrate to the tumour with other $CD8^+$ T-cells in which they have been found to negatively correlate with plasma CXCL10 production.

The findings from this thesis have been collated into one working model of the peripheral ICB response (Figure 6.1).

6.5 Concluding remarks

In conclusion, this thesis makes novel observations regarding the peripheral immune response to ICB and suggests a dynamic mechanism of cell interplay which is predominantly driven by $CD8^+$ T-cell responses. In addition, this study identifies several key predictors of clinical outcome. I also show that peripheral MAIT cells are reduced in CMV infection as well as after cICB treatment. I further demonstrate that MAIT cells can kill melanoma cells independently of other cell subsets. Finally, data from this thesis shows that B-cells are sensitive to cICB treatment. Notably, B-cells are found to decline in the periphery, increase differentiation into ASCs and undergo enhanced secondary antibody diversification in the form of CSR and SHM. Collectively, these data may be useful in determining patient prognosis and helping guide treatment selection for MM patients.

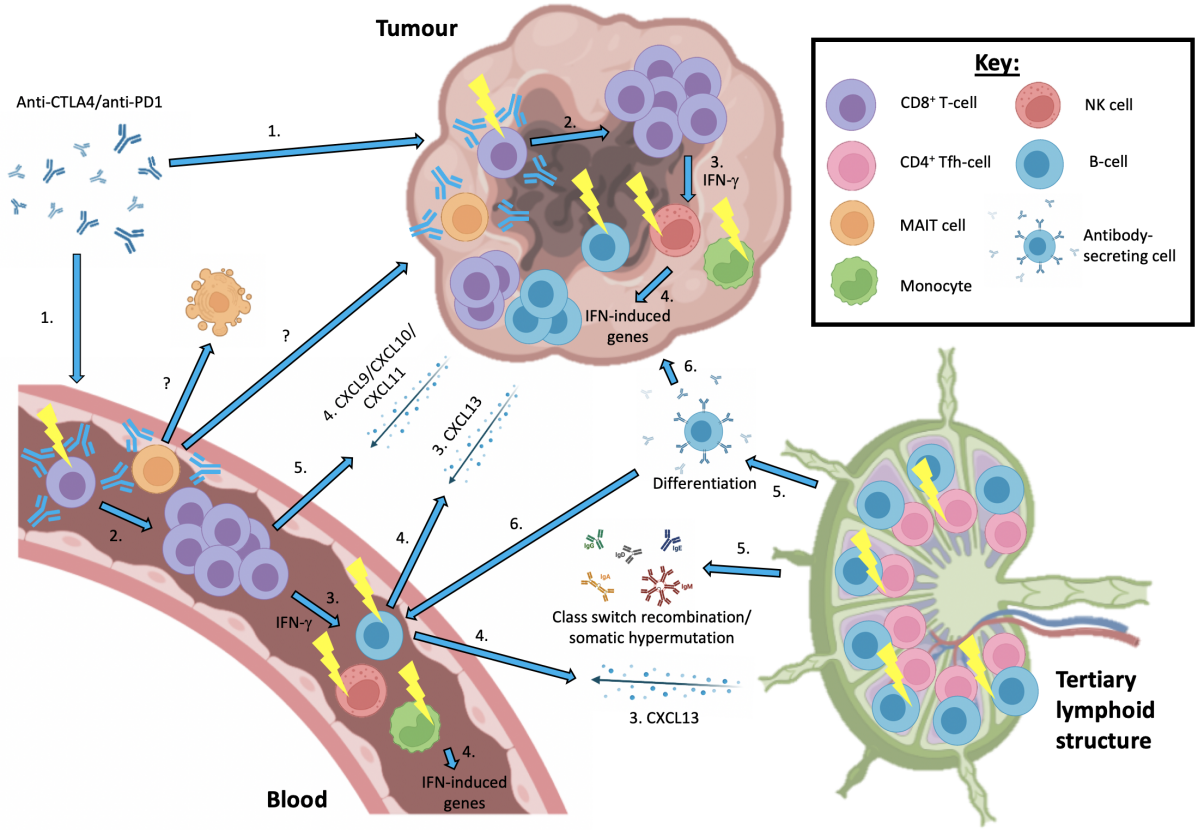


Figure 6.1 Working model of ICB response
Diagram which combines findings from this thesis to show a potential mechanism of action of ICB on peripheral immune cells. Unique cell types are differentiated by colour as indicated by the key.
1. ICB binds $CD8^+$ T-cells and potentially MAIT cells.
2. $CD8^+$ T-cells become activated and proliferate. However, the impact on MAIT cells is not clear. MAIT cells may either die as a result of activation or migrate to the tumour.
3. $CD8^+$ T-cells upregulate *IFNG* and *CXCL13*.
4. IFN-γ signalling induces responses in $CD19^+$ B-cells, $CD14^+$ monocytes and NK cells including production of interferon-associated genes (*GBPs* and *STAT1*) as well as CXCR3 ligands (*CXCL9*, *CXCL10* and *CXCL11*). CXCL13 also recruits $CD19^+$ B-cells to the tumour and TLS's.
5. $CXCR3^+$ $CD8^+$ T-cells migrate to the tumour in response to CXCL9/CXCL10/CXCL11 signals. CXCL13 and B-cell accumulation in TLS's increase germinal centre activity including differentiation into ASCs, CSR and SHM.
6. ASCs recirculate in the blood and migrate to the tumour and draining lymph nodes.
This figure was created with BioRender.com[585].

Bibliography

1. Cancer Research UK. *Melanoma skin cancer statistics* `https://www.cancerresearchuk.org/health-professional/cancer-statistics/statistics-by-cancer-type/melanoma-skin-cancer#heading-Six`.
2. Avril, M. Fotemustine compared with dacarbazine in patients with disseminated malignant melanoma: a phase III study. *J Clin Oncol* **22,** 1118–1125 (2004).
3. Bedikian, A. Bcl-2 antisense (oblimersen sodium) plus dacarbazine in patients with advanced melanoma: the Oblimersen Melanoma Study Group. *J Clin Oncol* **24,** 4738–4745 (2006).
4. Sileni, V. Phase II randomized study of dacarbazine, carmustine, cisplatin and tamoxifen versus dacarbazine alone in advanced melanoma patients. *Melanoma Res* **11,** 189–196 (2001).
5. Pak, B. Radiation resistance of human melanoma analysed by retroviral insertional mutagenesis reveals a possible role for dopachrome tautomerase. *Oncogene* **23,** 30–38 (2004).
6. Shahbazian, D. Radiation sensitivity and sensitization in melanoma. *Pigment Cell Melanoma Res* **26,** 928–930 (2013).
7. Lawrence, M. Mutational heterogeneity in cancer and the search for new cancer-associated genes. *Nature* **499,** 214–218 (2013).
8. Alexandrov, L. Signatures of mutational processes in human cancer. *Nature* **500,** 415–421 (2013).
9. Mitchell, D. The relative cytotoxicity of (6-4) photoproducts and cyclobutane dimers in mammalian cells. *Photochem Photobiol* **48,** 51–57 (1988).
10. Friedberg, E. *DNA Repair and Mutagenesis* (ASM Press, 2006).
11. Bradford, P. Cancer and neurologic degeneration in xeroderma pigmentosum: long term follow-up characterises the role of DNA repair. *J Med Genet* **48,** 168–176 (2011).
12. Tornaletti, S. Slow repair of pyrimidine dimers at p53 mutation hotspots in skin cancer. *Science* **263,** 1436–1438 (1994).
13. Brash, D. A role for sunlight in skin cancer: UV-induced p53 mutations in squamous cell carcinoma. *Proc Natl Acad Sci U S A* **88,** 10124–10128 (1991).
14. You, Y. Cyclobutane pyrimidine dimers are responsible for the vast majority of mutations induced by UVB irradiation in mammalian cells. *J Biol Chem* **276,** 44688–44694 (2001).
15. Kvam, E. Induction of oxidative DNA base damage in human skin cells by UV and near visible radiation. *Carcinogenesis* **18,** 2379–2384 (1997).

16. Zhang, X. Induction of 8-oxo-7,8-dihydro-2'-deoxyguanosine by ultraviolet radiation in calf thymus DNA and HeLa cells. *Photochem Photobiol* **65,** 119–124 (1997).

17. Douki, T. Oxidation of guanine in cellular DNA by solar UV radiation: biological role. *Photochem Photobiol* **70,** 184–190 (1999).

18. Arimoto-Kobayashi, S. Mutation, DNA strand cleavage and nitric oxide formation caused by N-nitrosoproline with sunlight: a possible mechanism of UVA carcinogenicity. *Carcinogenesis* **23,** 1537–1540 (2002).

19. Hockberger, P. Activation of flavin-containing oxidases underlies light-induced production of H2O2 in mammalian cells. *Proc Natl Acad Sci U S A* **96,** 6255–6260 (1999).

20. Dahle, J. Induction of delayed mutations and chromosomal instability in fibroblasts after UVA-, UVB-, and X-radiation. *Cancer Res* **63,** 1464–1469 (2003).

21. Hodis, E. A landscape of driver mutations in melanoma. *Cell* **150,** 251–263 (2012).

22. Gast, A. Somatic alterations in the melanoma genome: a high-resolution array-based comparative genomic hybridization study. *Genes Chromosomes Cancer* **49,** 733–745 (2010).

23. Jonsson, G. Genomic profiling of malignant melanoma using tiling-resolution arrayCGH. *Oncogene* **26,** 4738–4748 (2007).

24. Krauthammer, M. Exome sequencing identifies recurrent somatic RAC1 mutations in melanoma. *Nat Genet* **44,** 1006–1014 (2012).

25. Krauthammer, M. Exome sequencing identifies recurrent mutations in NF1 and RASopathy genes in sun-exposed melanomas. *Nat Genet* **47,** 996–1002 (2015).

26. Cohen, C. Mitogen-actived protein kinase activation is an early event in melanoma progression. *Clin Cancer Res* **8,** 3728–3733 (2002).

27. Davies, H. Mutations of the BRAF gene in human cancer. *Nature* **417,** 949–954 (2002).

28. Curtin, J. Distinct sets of genetic alterations in melanoma. *N Engl J Med* **353,** 2135–2147 (2005).

29. Curtin, J. Somatic activation of KIT in distinct subtypes of melanoma. *J Clin Oncol* **24,** 4340–4346 (2006).

30. Melamed, R. Genomic Characterization of Dysplastic Nevi Unveils Implications for Diagnosis of Melanoma. *J Invest Dermatol* **137,** 905–909 (2017).

31. Viros, A. Ultraviolet radiation accelerates BRAF-driven melanomagenesis by targeting TP53. *Nature* **511,** 478–482 (2014).

32. Chudnovsky, Y. Melanoma genetics and the development of rational therapeutics. *J Clin Invest* **115,** 813–824 (2005).

33. Nissan, M. Loss of NF1 in cutaneous melanoma is associated with RAS activation and MEK dependence. *Cancer Res* **74,** 2340–2350 (2014).

34. Jakob, J. NRAS mutation status is an independent prognostic factor in metastatic melanoma. *Cancer* **118,** 4014–4023 (2012).

35. Lee, J. Frequencies of BRAF and NRAS mutations are different in histological types and sites of origin of cutaneous melanoma: a meta-analysis. *Br J Dermatol* **164,** 776–784 (2011).

36. Polakis, P. Structural requirements for the interaction of p21ras with GAP, exchange factors, and its biological effector target. *J Biol Chem* **268,** 9157–9160 (1993).

37. Lovly, C. Routine multiplex mutational profiling of melanomas enables enrollment in genotype-driven therapeutic trials. *PLoS One* **7,** e35309 (2012).

38. Wan, P. Mechanism of activation of the RAF-ERK signaling pathway by oncogenic mutations of B-RAF. *Cell* **116,** 855–867 (2004).

39. Candido, S. Analysis of the B-RafV600E mutation in cutaneous melanoma patients with occupational sun exposure. *Oncol Rep* **31,** 1079–1082 (2014).

40. Ellerhorst, J. Clinical correlates of NRAS and BRAF mutations in primary human melanoma. *Clin Cancer Res* **17,** 229–235 (2011).

41. Amos, C. Genome-wide association study identifies novel loci predisposing to cutaneous melanoma. *Hum Mol Genet* **20,** 5012–5023 (2011).

42. Barrett, J. Genome-wide association study identifies three new melanoma susceptibility loci. *Nat Genet* **43,** 1108–1113 (2011).

43. Bishop, D. Genome-wide association study identifies three loci associated with melanoma risk. *Nat Genet* **41,** 920–925 (2009).

44. Brown, K. Common sequence variants on 20q11.22 confer melanoma susceptibility. *Nat Genet* **40,** 838–840 (2008).

45. Macgregor, S. Genome-wide association study identifies a new melanoma susceptibility locus at 1q21.3. *Nat Genet* **43,** 1114–1118 (2011).

46. Kanetsky, P. Population-based study of natural variation in the melanocortin-1 receptor gene and melanoma. *Cancer Res* **66,** 9330–9337 (2006).

47. Helgadottir, H. Germline CDKN2A Mutation Status and Survival in Familial Melanoma Cases. *J Natl Cancer Inst* **108** (2016).

48. Borg, A. High frequency of multiple melanomas and breast and pancreas carcinomas in CDKN2A mutation-positive melanoma families. *J Natl Cancer Inst* **92,** 1260–1266 (2000).

49. Van der Rhee, J. Clinical and histologic characteristics of malignant melanoma in families with a germline mutation in CDKN2A. *J Am Acad Dermatol* **65,** 281–288 (2011).

50. Puntervoll, H. Melanoma prone families with CDK4 germline mutation: phenotypic profile and associations with MC1R variants. *J Med Genet* **50,** 264–270 (2013).

51. Zuo, L. Germline mutations in the p16INK4a binding domain of CDK4 in familial melanoma. *Nat Genet* **12,** 97–99 (1996).

52. Horn, S. TERT promoter mutations in familial and sporadic melanoma. *Science* **339,** 959–961 (2013).

53. Sumner, W. Spontaneous regression of melanoma. *Cancer* **6,** 1040–1043 (1953).

54. Blessing, K. Histological regression in primary cutaneous melanoma: recognition, prevalence and significance. *Histopathology* **20,** 315–322 (1992).

55. Emanuel, P. Complete regression of primary malignant melanoma. *Am J Dermatopathol* **30,** 178–181 (2008).

56. Smith, J. Spontaneous regression of primary malignant melanomas with regional metastases. *Cancer* **18,** 1399–1415 (1965).

57. Bayer-Garner, I. The immunopathology of regression in benign lichenoid keratosis, keratoacanthoma and halo nevus. *Clin Med Res* **2,** 89–97 (2004).

58. Saleh, F. Primary melanoma tumour regression associated with an immune response to the tumour-associated antigen melan-A/MART-1. *Int J Cancer* **94,** 551–557 (2001).

59. Clark, W. Model predicting survival in stage I melanoma based on tumor progression. *J Natl Cancer Inst* **81,** 1893–1904 (1989).

60. Clemente, C. Prognostic value of tumor infiltrating lymphocytes in the vertical growth phase of primary cutaneous melanoma. *Cancer* **77,** 1303–1310 (1996).

61. Taylor, R. Tumor-infiltrating lymphocytes predict sentinel lymph node positivity in patients with cutaneous melanoma. *J Clin Oncol* **25,** 869–875 (2007).

62. Mandala, M. Clinical and histopathological risk factors to predict sentinel lymph node positivity, disease-free and overall survival in clinical stages I-II AJCC skin melanoma: outcome analysis from a single-institution prospectively collected database. *Eur J Cancer* **45,** 2537–2545 (2009).

63. Burton, A. Prognostic significance of tumor infiltrating lymphocytes in melanoma. *Am Surg* **77,** 188–192 (2011).

64. Azimi, F. Tumor-infiltrating lymphocyte grade is an independent predictor of sentinel lymph node status and survival in patients with cutaneous melanoma. *J Clin Oncol* **30,** 2678–2683 (2012).

65. Thomas, N. Tumor-infiltrating lymphocyte grade in primary melanomas is independently associated with melanoma-specific survival in the population-based genes, environment and melanoma study. *J Clin Oncol* **31,** 4252–4259 (2013).

66. Muul, L. Identification of specific cytolytic immune responses against autologous tumor in humans bearing malignant melanoma. *J Immunol* **138,** 989–995 (1987).

67. Van Braeckel-Budimir, N. Combinatorial immunotherapy induces tumor-infiltrating CD8 + T cells with distinct functional, migratory, and stem-like properties. *J Immunother Cancer* **9,** e003614 (2021).

68. Dunn, G. The three Es of cancer immunoediting. *Annu Rev Immunol* **22,** 329–360 (2004).

69. Yan, J. Human polymorphonuclear neutrophils specifically recognize and kill cancerous cells. *Oncoimmunology* **3,** e950163 (2014).

70. Zivkovic, M. Oxidative burst of neutrophils against melanoma B16-F10. *Cancer Lett* **246,** 100–108 (2007).

71. Gershkovitz, M. TRPM2 modulates neutrophil attraction to murine tumor cells by regulating CXCL2 expression. *Cancer Immunol Immunother* **68,** 33–43 (2019).

72. Schedel, F. Evidence and impact of neutrophil extracellular traps in malignant melanoma. *Pigment Cell Melanoma Res* **33,** 63–73 (2020).

73. Gale, R. Polymorphonuclear leukocytes in antibody-dependent cellular cytotoxicity. *J Immunol* **114,** 1047–1051 (1975).

74. Barker, E. Effect of a chimeric anti-ganglioside GD2 antibody on cell-mediated lysis of human neuroblastoma cells. *Cancer Res* **51,** 144–149 (1991).

75. Matlung, H. Neutrophils Kill Antibody-Opsonized Cancer Cells by Trogoptosis. *Cell Rep* **23,** 3946–3959 (2018).

76. Siders, W. Involvement of neutrophils and natural killer cells in the anti-tumor activity of alemtuzumab in xenograft tumor models. *Leuk Lymphoma* **51,** 1293–1304 (2010).

77. Hernandez-Ilizaliturri, F. Neutrophils Contribute to the Biological Antitumor Activity of Rituximab in a Non-Hodgkin's Lymphoma Severe Combined Immunodeficiency Mouse Model. *Clin Cancer Res* **9,** 5866–5873 (2003).

78. Albanesi, M. Neutrophils mediate antibody-induced antitumor effects in mice. *Blood* **122,** 3160–3164 (2013).

79. Gül, N. Macrophages eliminate circulating tumor cells after monoclonal antibody therapy. *J Clin Invest* **124,** 812–823 (2014).

80. Barrio, M. Human macrophages and dendritic cells can equally present MART-1 antigen to CD8(+) T cells after phagocytosis of gamma-irradiated melanoma cells. *PLoS One* **7,** e40311 (2012).

81. Muraoka, D. Antigen delivery targeted to tumor-associated macrophages overcomes tumor immune resistance. *J Clin Invest* **129,** 1278–1294 (2019).

82. Singhal, S. Human tumor-associated monocytes/macrophages and their regulation of T cell responses in early-stage lung cancer. *Sci Transl Med* **11,** eaat1500 (2019).

83. Ladányi, A. Density of DC-LAMP(+) mature dendritic cells in combination with activated T lymphocytes infiltrating primary cutaneous melanoma is a strong independent prognostic factor. *Cancer Immunol Immunother* **56,** 1459–1469 (2007).

84. Redondo, P. Immunologic escape and angiogenesis in human malignant melanoma. *J Am Acad Dermatol* **49,** 255–263 (2003).

85. Wu, X. Immune microenvironment profiles of tumor immune equilibrium and immune escape states of mouse sarcoma. *Cancer Lett* **340,** 124–133 (2013).

86. Hanahan, D. Hallmarks of Cancer: New Dimensions. *Cancer Discov* **12,** 31–46 (2022).

87. Seliger, B. Immune escape of melanoma: first evidence of structural alterations in two distinct components of the MHC class I antigen processing pathway. *Cancer Res* **61,** 8647–8650 (2001).

88. Cormier, J. Heterogeneous expression of melanoma-associated antigens and HLA-A2 in metastatic melanoma in vivo. *Int J Cancer* **75,** 517–524 (1998).

89. Maeurer, M. Tumor escape from immune recognition: lethal recurrent melanoma in a patient associated with downregulation of the peptide transporter protein TAP-1 and loss of expression of the immunodominant MART-1/Melan-A antigen. *J Clin Invest* **98,** 1633–1641 (1996).

90. Viguier, M. Utility of tumour-infiltrating CD25+FOXP3+ regulatory T cell evaluation in predicting local recurrence in vertical growth phase cutaneous melanoma. *J Immunol* **173,** 1444–1453 (2004).

91. Gray, C. Association of increased levels of heavy-chain ferritin with increased CD4+ CD25+ regulatory T-cell levels in patients with melanoma. *Clin Cancer Res* **9,** 2551–2559 (2003).

92. Miracco, C. Utility of tumour-infiltrating CD25+FOXP3+ regulatory T cell evaluation in predicting local recurrence in vertical growth phase cutaneous melanoma. *Oncol Rep* **18,** 1115–1122 (2007).

93. Klages, K. Selective depletion of Foxp3+ regulatory T cells improves effective therapeutic vaccination against established melanoma. *Cancer Res* **70,** 7788–7799 (2010).

94. Klarquist, J. Ccl22 Diverts T Regulatory Cells and Controls the Growth of Melanoma. *Cancer Res* **76,** 6230–6240 (2016).

95. Jiang, H. Elevated chronic inflammatory factors and myeloid-derived suppressor cells indicate poor prognosis in advanced melanoma patients. *Int J Cancer* **136,** 2352–2360 (2015).

96. Schlecker, E. Tumor-infiltrating monocytic myeloid-derived suppressor cells mediate CCR5-dependent recruitment of regulatory T cells favoring tumor growth. *J Immunol* **189,** 5602–5611 (2012).

97. Jordan, K. Myeloid-derived suppressor cells are associated with disease progression and decreased overall survival in advanced-stage melanoma patients. *Cancer Immunol Immunother* **62,** 1711–1722 (2013).

98. Falleni, M. M1 and M2 macrophages' clinicopathological significance in cutaneous melanoma. *Melanoma Res* **27,** 200–210 (2017).

99. Gentles, A. The prognostic landscape of genes and infiltrating immune cells across human cancers. *Nat Med* **21,** 938–945 (2015).

100. Muller-Hermelink, N. TNFR1 signaling and IFN-gamma signaling determine whether T cells induce tumor dormancy or promote multistage carcinogenesis. *Cancer Cell* **13,** 507–518 (2008).

101. Walunas, T. CTLA-4 can function as a negative regulator of T cell activation. *Immunity* **1,** 405–413 (1994).

102. Yu, X. The surface protein TIGIT suppresses T cell activation by promoting the generation of mature immunoregulatory dendritic cells. *Nat Immunol* **10,** 48–57 (2009).

103. Fourcade, J. CD8(+) T cells specific for tumor antigens can be rendered dysfunctional by the tumor microenvironment through upregulation of the inhibitory receptors BTLA and PD-1. *Cancer Res* **72,** 887–896 (2012).

104. Beavis, P. Blockade of A2A receptors potently suppresses the metastasis of CD73+ tumors. *Proc Natl Acad Sci U S A* **110,** 14711–14716 (2013).

105. Krummel, M. CD28 and CTLA-4 Have Opposing Effects on the Response of T ceils to Stimulation. *J Exp Med* **182,** 459–465 (1995).

106. Ahmadzadeh, M. Tumor antigen-specific CD8 T cells infiltrating the tumor express high levels of PD-1 and are functionally impaired. *Blood* **114,** 1537–1544 (2009).

107. Workman, C. The CD4-related molecule, LAG-3 (CD223), regulates the expansion of activated T cells. *Eur J Immunol* **33,** 970–979 (2003).

108. Workman, C. Lymphocyte activation gene-3 (CD223) regulates the size of the expanding T cell population following antigen activation in vivo. *J Immunol* **172,** 5450–5455 (2004).

109. Sabatos, C. Interaction of Tim-3 and Tim-3 ligand regulates T helper type 1 responses and induction of peripheral tolerance. *Nat Immunol* **4,** 1102–1110 (2003).

110. Sánchez-Fueyo, A. Tim-3 inhibits T helper type 1-mediated auto- and alloimmune responses and promotes immunological tolerance. *Nat Immunol* **4,** 1093–1101 (2003).

111. Boles, K. A novel molecular interaction for the adhesion of follicular CD4 T cells to follicular DC. *Eur J Immunol* **39,** 695–703 (2009).

112. Stanietsky, N. The interaction of TIGIT with PVR and PVRL2 inhibits human NK cell cytotoxicity. *Proc Natl Acad Sci U S A* **106,** 17858–17863 (2009).

113. Balch, C. Final version of 2009 AJCC melanoma staging and classification. *J Clin Oncol* **27,** 6199–6206 (2009).

114. Chapman, P. Improved survival with vemurafenib in melanoma with BRAF V600E mutation. *N Engl J Med* **364,** 2507–2516 (2011).

115. McArthur, G. Safety and efficacy of vemurafenib in BRAF(V600E) and BRAF(V600K) mutation-positive melanoma (BRIM-3): extended follow-up of a phase 3, randomised, open-label study. *N Engl J Med* **364,** 2507–2516 (2011).

116. Hauschild, A. Dabrafenib in BRAF-mutated metastatic melanoma: a multicentre, open-label, phase 3 randomised controlled trial. *Lancet* **380,** 358–365 (2012).

117. Flaherty, K. Improved survival with MEK inhibition in BRAF-mutated melanoma. *N Engl J Med* **367,** 107–114 (2012).

118. Wagenaar, T. Resistance to vemurafenib resulting from a novel mutation in the BRAFV600E kinase domain. *Pigment Cell Melanoma Res* **27,** 124–133 (2014).

119. Long, G. Increased MAPK reactivation in early resistance to dabrafenib/trametinib combination therapy of BRAF-mutant metastatic melanoma. *Nat Commun* **5,** 98–105 (2014).

120. Hoogstraat, M. Detailed imaging and genetic analysis reveal a secondary BRAF(L505H) resistance mutation and extensive intrapatient heterogeneity in metastatic BRAF mutant melanoma patients treated with vemurafenib. *Pigment Cell Melanoma Res* **28,** 318–323 (2015).

121. Louveau, B. A targeted genomic alteration analysis predicts survival of melanoma patients under BRAF inhibitors. *Oncotarget* **10,** 1669–1687 (2019).

122. Monsma, D. Melanoma patient derived xenografts acquire distinct Vemurafenib resistance mechanisms. *Am J Cancer Res* **5,** 1507–1518 (2015).

123. Rizos, H. BRAF inhibitor resistance mechanisms in metastatic melanoma: spectrum and clinical impact. *Clin Cancer Res* **20,** 1965–1977 (2014).

124. Van Allen, E. The genetic landscape of clinical resistance to RAF inhibition in metastatic melanoma. *Cancer Discov* **4,** 94–109 (2014).

125. Villanueva, J. Concurrent MEK2 mutation and BRAF amplification confer resistance to BRAF and MEK inhibitors in melanoma. *Cell Rep* **4,** 1090–1099 (2013).

126. Pupo, G. Clinical significance of intronic variants in BRAF inhibitor resistant melanomas with altered BRAF transcript splicing. *Biomark Res* **5** (2017).

127. Carlino, M. Preexisting MEK1P124 mutations diminish response to BRAF inhibitors in metastatic melanoma patients. *Clin Cancer Res* **21,** 98–105 (2015).

128. NICE. *Vemurafenib for treating locally advanced or metastatic BRAF V600 mutation-positive malignant melanoma* `https://www.nice.org.uk/guidance/ta269`.

129. NICE. *Dabrafenib for treating unresectable or metastatic BRAF V600 mutation-positive melanoma* `https://www.nice.org.uk/guidance/ta321`.

130. NICE. *Trametinib in combination with dabrafenib for treating unresectable or metastatic melanoma* `https://www.nice.org.uk/guidance/ta396`.

131. Rosenberg, S. Treatment of 283 consecutive patients with metastatic melanoma or renal cell cancer using high-dose bolus interleukin 2. *JAMA* **271,** 907–913 (1994).

132. Atkins, M. High-dose recombinant interleukin-2 therapy in patients with metastatic melanoma: long-term survival update. *Cancer J Sci Am* **6,** S11–14 (2000).

133. Bright, R. Clinical Response Rates From Interleukin-2 Therapy for Metastatic Melanoma Over 30 Years' Experience: A Meta-Analysis of 3312 Patients. *J Immunother* **40,** 21–30 (2017).

134. Kirkwood, J. High-dose interferon alfa-2b significantly prolongs relapse-free and overall survival compared with the GM2-KLH/QS-21 vaccine in patients with resected stage IIB-III melanoma: results of intergroup trial E1694/S9512/C509801. *J Immunol* **19,** 2370–2380 (2001).

135. Eggermont, M. Adjuvant therapy with pegylated interferon alfa-2b versus observation alone in resected stage III melanoma: final results of EORTC 18991, a randomised phase III trial. *Lancet* **372,** 117–126 (2008).

136. Eggermont, M. Long term follow up of the EORTC 18952 trial of adjuvant therapy in resected stage IIB-III cutaneous melanoma patients comparing intermediate doses of interferon-alpha-2b (IFN) with observation: Ulceration of primary is key determinant for IFN-sensitivity. *Eur J Cancer* **55,** 111–121 (2016).

137. Barrow, C. Tumor antigen expression in melanoma varies according to antigen and stage. *Clin Cancer Res* **12,** 764–771 (2006).

138. Rosenberg, S. Immunologic and therapeutic evaluation of a synthetic peptide vaccine for the treatment of patients with metastatic melanoma. *Nat Med* **4,** 321–327 (1998).

139. Rosenberg, S. Impact of cytokine administration on the generation of antitumor reactivity in patients with metastatic melanoma receiving a peptide vaccine. *J Immunol* **163,** 1690–1695 (1999).

140. Schwartzentruber, D. gp100 peptide vaccine and interleukin-2 in patients with advanced melanoma. *N Engl J Med* **364,** 2119–2127 (2011).

141. Cormier, J. Enhancement of cellular immunity in melanoma patients immunized with a peptide from MART-1/Melan A. *Cancer J Sci Am* **3,** 37–44 (1997).

142. Reynolds, S. Stimulation of CD8+ T cell responses to MAGE-3 and Melan A/MART-1 by immunization to a polyvalent melanoma vaccine. *Int J Cancer* **72,** 972–976 (1997).

143. Larkin, J. Five-Year Survival with Combined Nivolumab and Ipilimumab in Advanced Melanoma. *N Engl J Med* **381,** 1535–1546 (2019).

144. Brunet, J. A new member of the immunoglobulin superfamily–CTLA-4. *Nature* **328,** 267–270 (1987).

145. Tivol, E. Loss of CTLA-4 leads to massive lymphoproliferation and fatal multiorgan tissue destruction, revealing a critical negative regulatory role of CTLA-4. *Immunity* **3,** 541–547 (1995).

146. Waterhouse, P. Lymphoproliferative disorders with early lethality in mice deficient in Ctla-4. *Science* **270,** 985–988 (1995).

147. Leung, H. Cytotoxic T lymphocyte-associated molecule-4, a high-avidity receptor for CD80 and CD86, contains an intracellular localization motif in its cytoplasmic tail. *J Biol Chem* **270,** 25107–25114 (1995).

148. Alegre, M. Regulation of surface and intracellular expression of CTLA4 on mouse T cells. *J Immunol* **157,** 4762–4770 (1996).

149. Valk, E. T Cell Receptor-Interacting Molecule Acts as a Chaperone to Modulate Surface Expression of the CTLA-4 Coreceptor. *Immunity* **25,** 807–821 (2006).

150. Lafage-Pochitaloff, M. Human CD28 and CTLA-4 Ig superfamily genes are located on chromosome 2 at bands q33-q34. *Immunogenetics* **31,** 198–201 (1990).

151. Harper, K. CTLA-4 and CD28 activated lymphocyte molecules are closely related in both mouse and human as to sequence, message expression, gene structure, and chromosomal location. *J Immunol* **147,** 1037–1044 (1991).

152. Linsley, P. CTLA-4 is a second receptor for the B cell activation antigen B7. *J Exp Med* **174,** 561–569 (1991).

153. Collins, A. The interaction properties of costimulatory molecules revisited. *Immunity* **17,** 201–210 (2002).

154. Quereshi, O. Trans-endocytosis of CD80 and CD86: a molecular basis for the cell-extrinsic function of CTLA-4. *Science* **332,** 600–603 (2011).

155. Marengère, L. Regulation of T cell receptor signaling by tyrosine phosphatase SYP association with CTLA-4. *Science* **272,** 1170–1173 (1996).

156. Lee, K. Molecular basis of T cell inactivation by CTLA-4. *Science* **282,** 2263–2266 (1998).

157. Chuang, E. The CD28 and CTLA-4 receptors associate with the serine/threonine phosphatase PP2A. *Immunity* **13,** 313–322 (2000).

158. Olsson, C. CTLA-4 ligation suppresses CD28-induced NF-kappaB and AP-1 activity in mouse T cell blasts. *J Biol Chem* **274,** 14400–14405 (1999).

159. Fraser, J. CTLA4 ligation attenuates AP-1, NFAT and NF-ϰB activity in activated T cells. *Eur J Immunol* **29,** 838–844 (1999).

160. Read, S. Cytotoxic T lymphocyte-associated antigen 4 plays an essential role in the function of CD25(+)CD4(+) regulatory cells that control intestinal inflammation. *J Exp Med* **192,** 295–302 (2000).

161. Takahashi, T. Immunologic self-tolerance maintained by CD25(+)CD4(+) regulatory T cells constitutively expressing cytotoxic T lymphocyte-associated antigen 4. *J Exp Med* **192,** 303–310 (2000).

162. Read, S. Blockade of CTLA-4 on CD4+CD25+ regulatory T cells abrogates their function in vivo. *J Immunol* **177,** 4376–4383 (2006).

163. Zheng, S. TGF-β Requires CTLA-4 Early after T Cell Activation to Induce FoxP3 and Generate Adaptive CD4+CD25+ Regulatory Cells. *J Immunol* **176,** 3321–3329 (2006).

164. Wing, K. CTLA-4 control over Foxp3+ regulatory T cell function. *Science* **322,** 271–275 (2008).

165. Friedline, R. CD4+ regulatory T cells require CTLA-4 for the maintenance of systemic tolerance. *J Exp Med* **206,** 421–434 (2009).

166. Ishida, Y. Induced expression of PD-1, a novel member of the immunoglobulin gene superfamily, upon programmed cell death. *EMBO J* **11,** 3887–3895 (1992).

167. Nishimura, H. Development of lupus-like autoimmune diseases by disruption of the PD-1 gene encoding an ITIM motif-carrying immunoreceptor. *Immunity* **11,** 141–151 (1999).

168. Nishimura, H. Autoimmune dilated cardiomyopathy in PD-1 receptor-deficient mice. *Science* **291,** 319–322 (2001).

169. Okazaki, T. PD-1 immunoreceptor inhibits B cell receptor-mediated signaling by recruiting src homology 2-domain-containing tyrosine phosphatase 2 to phosphotyrosine. *Proc Natl Acad Sci U S A* **98,** 13866–13871 (2001).

170. Sheppard, K.-A. PD-1 inhibits T-cell receptor induced phosphorylation of the ZAP70/CD3zeta signalosome and downstream signaling to PKCtheta. *FEBS Lett* **574,** 37–41 (2004).

171. Hui, E. T cell costimulatory receptor CD28 is a primary target for PD-1-mediated inhibition. *Science* **355,** 1428–1433 (2017).

172. Freeman, G. Engagement of the PD-1 immunoinhibitory receptor by a novel B7 family member leads to negative regulation of lymphocyte activation. *J Exp Med* **192,** 1027–1034 (2000).

173. Latchman, Y. PD-L2 is a second ligand for PD-1 and inhibits T cell activation. *Nat Immunol* **2,** 261–268 (2001).

174. Dong, H. B7-H1, a third member of the B7 family, co-stimulates T-cell proliferation and interleukin-10 secretion. *Nat Med* **5,** 1365–1369 (1999).

175. Patsoukis, N. Selective effects of PD-1 on Akt and Ras pathways regulate molecular components of the cell cycle and inhibit T cell proliferation. *Sci Signal* **5,** ra46 (2012).

176. Mayoux, M. Dendritic cells dictate responses to PD-L1 blockade cancer immunotherapy. *Sci Transl Med* **12,** eaav7431 (2020).

177. Li, K. PD-1 suppresses TCR-CD8 cooperativity during T-cell antigen recognition. *Nat Commun* **12,** 2746 (2021).

178. Karwacz, K. PD-L1 co-stimulation contributes to ligand-induced T cell receptor down-modulation on CD8+ T cells. *EMBO Mol Med* **3,** 581–592 (2011).

179. Peng, Q. PD-L1 on dendritic cells attenuates T cell activation and regulates response to immune checkpoint blockade. *Nat Commun* **11,** 4835 (2020).

180. Prestipino, A. Oncogenic JAK2 V617F causes PD-L1 expression, mediating immune escape in myeloproliferative neoplasms. *Sci Transl Med* **10,** eaam7729 (2018).

181. Marzec, M. Oncogenic kinase NPM/ALK induces through STAT3 expression of immunosuppressive protein CD274 (PD-L1, B7-H1). *Proc Natl Acad Sci U S A.* **105,** 20852–20857 (2008).

182. Chung, Y. Sensitizing tumors to anti-PD-1 therapy by promoting NK and CD8+ T cells via pharmacological activation of FOXO3. *J Immunother Cancer* **9,** e002772 (2021).

183. Huang, L. Targeting STAT3 Abrogates Tim-3 Upregulation of Adaptive Resistance to PD-1 Blockade on Regulatory T Cells of Melanoma. *Front Immunol* **12** (2021).

184. Lastwika, K. Control of PD-L1 Expression by Oncogenic Activation of the AKT-mTOR Pathway in Non-Small Cell Lung Cancer. *Cancer Res* **76,** 227–238 (2016).

185. Shang, M. The folate cycle enzyme MTHFD2 induces cancer immune evasion through PD-L1 up-regulation. *Nat Commun* **12,** 1940 (2021).

186. Parsa, A. Loss of tumor suppressor PTEN function increases B7-H1 expression and immunoresistance in glioma. *Nat Med* **13,** 84–88 (2007).

187. Casey, S. MYC regulates the antitumor immune response through CD47 and PD-L1. *Science* **352,** 227–231 (2016).

188. Coelho, M. Oncogenic RAS Signaling Promotes Tumor Immunoresistance by Stabilizing PD-L1 mRNA. *Immunity* **47,** 1083–1099 (2017).

189. Zhao, Y. PD-L1:CD80 Cis-Heterodimer Triggers the Co-stimulatory Receptor CD28 While Repressing the Inhibitory PD-1 and CTLA-4 Pathways. *Immunity* **51,** 1059–1073 (2019).

190. Sugiura, D. Restriction of PD-1 function by cis-PD-L1/CD80 interactions is required for optimal T cell responses. *Science* **364,** 558–566 (2019).

191. Thompson, R. Costimulatory B7-H1 in renal cell carcinoma patients: Indicator of tumor aggressiveness and potential therapeutic target. *Proc Natl Acad Sci U S A* **101,** 17174–17179 (2004).

192. Thompson, R. Tumor B7-H1 is associated with poor prognosis in renal cell carcinoma patients with long-term follow-up. *Cancer Res* **66,** 3381–3385 (2006).

193. Ohigashi, Y. Clinical significance of programmed death-1 ligand-1 and programmed death-1 ligand-2 expression in human esophageal cancer. *Clin Cancer Res* **11,** 2947–2953 (2005).

194. Nakanishi, J. Overexpression of B7-H1 (PD-L1) significantly associates with tumor grade and postoperative prognosis in human urothelial cancers. *Cancer Immunol Immunother* **56,** 1173–1182 (2007).

195. Hamanishi, J. Programmed cell death 1 ligand 1 and tumor-infiltrating CD8+ T lymphocytes are prognostic factors of human ovarian cancer. *Proc Natl Acad Sci U S A* **104,** 3360–3365 (2007).

196. Nomi, T. Clinical significance and therapeutic potential of the programmed death-1 ligand/programmed death-1 pathway in human pancreatic cancer. *Clin Cancer Res* **13,** 2151–2157 (2007).

197. Van Allen, E. Genomic correlates of response to CTLA-4 blockade in metastatic melanoma. *Science* **350,** 207–211 (2015).

198. Hodi, F. Improved survival with ipilimumab in patients with metastatic melanoma. *N Engl J Med* **363,** 711–723 (2010).

199. Robert, C. Pembrolizumab versus Ipilimumab in Advanced Melanoma. *N Engl J Med* **372,** 2521–2532 (2015).

200. Weber, J. Nivolumab versus chemotherapy in patients with advanced melanoma who progressed after anti-CTLA-4 treatment (CheckMate 037): a randomised, controlled, open-label, phase 3 trial. *Lancet Oncol* **16,** 375–384 (2015).

201. Weber, J. Safety profile of nivolumab monotherapy: A pooled analysis of patients with advanced melanoma. *J Clin Oncol* **35,** 785–792 (2017).

202. Robert, C. Nivolumab in previously untreated melanoma without BRAF mutation. *N Engl J Med* **372,** 320–330 (2015).

203. Larkin, J. Combined Nivolumab and Ipilimumab or Monotherapy in Untreated Melanoma. *N Engl J Med* **373,** 23–34 (2015).

204. Hodi, F. Nivolumab plus ipilimumab or nivolumab alone versus ipilimumab alone in advanced melanoma (CheckMate 067): 4-year outcomes of a multicentre, randomised, phase 3 trial. *Lancet Oncol* **19,** 1480–1492 (2018).

205. Hodi, F. Combined nivolumab and ipilimumab versus ipilimumab alone in patients with advanced melanoma: 2-year overall survival outcomes in a multicentre, randomised, controlled, phase 2 trial. *Lancet Oncol* **17,** 1558–1568 (2016).

206. NICE. *Nivolumab in combination with ipilimumab for treating advanced melanoma* `https://www.nice.org.uk/guidance/ta400`.

207. Zhang, Y. Hijacking antibody-induced CTLA-4 lysosomal degradation for safer and more effective cancer immunotherapy. *Cell Res* **29,** 609–627 (2019).

208. Watson, R. Immune checkpoint blockade sensitivity and progression-free survival associates with baseline CD8 + T cell clone size and cytotoxicity. *Sci Immunol* **6,** eabj8825 (2021).

209. Carthon, B. Preoperative CTLA-4 blockade: Tolerability and immune monitoring in the setting of a presurgical clinical trial. *Clin Cancer Res* **16,** 2861–2871 (2010).

210. Chen, H. Anti-CTLA-4 therapy results in higher CD4+ ICOShi T cell frequency and IFN- levels in both nonmalignant and malignant prostate tissues. *Proc Natl Acad Sci U S A* **106,** 2729–2734 (2009).

211. Fan, X. Engagement of the ICOS pathway markedly enhances efficacy of CTLA-4 blockade in cancer immunotherapy. *J Exp Med* **211,** 715–725 (2014).

212. Wang, W. Biomarkers on melanoma patient T cells associated with ipilimumab treatment. *J Transl Med* **10** (2012).

213. Tang, D. Increased frequency of ICOS+ CD4 T cells as a pharmacodynamic biomarker for anti-CTLA-4 therapy. *Cancer Immunol Res* **1,** 229–234 (2013).

214. Romano, E. Ipilimumab-dependent cell-mediated cytotoxicity of regulatory T cells ex vivo by nonclassical monocytes in melanoma patients. *Proc Natl Acad Sci U S A* **112,** 6140–6145 (2015).

215. Vargas, F. Fc Effector Function Contributes to the Activity of Human Anti-CTLA-4 Antibodies. *Cancer Cell* **33,** 649–663 (2018).

216. Simpson, T. Fc-dependent depletion of tumor-infiltrating regulatory t cells co-defines the efficacy of anti-CTLA-4 therapy against melanoma. *J Exp Med* **210,** 1695–1710 (2013).

217. Bulliard, Y. Activating fc γ receptors contribute to the antitumor activities of immunoregulatory receptor-targeting antibodies. *J Exp Med* **210,** 1685–1693 (2013).

218. Schoonderwoerd, M. Targeting Endoglin-Expressing Regulatory T Cells in the Tumor Microenvironment Enhances the Effect of PD1 Checkpoint Inhibitor Immunotherapy. *Clin Cancer Res* **26,** 3831–3842 (2020).

219. Huang, A. T-cell invigoration to tumour burden ratio associated with anti-PD-1 response. *Nature* **545,** 60–65 (2017).

220. Park, J. Immune Checkpoint Inhibitor-induced Reinvigoration of Tumor-infiltrating CD8 + T Cells is Determined by Their Differentiation Status in Glioblastoma. *Cancer Immunol Immunother* **61,** 1019–1031 (2012).

221. Kumagai, S. The PD-1 expression balance between effector and regulatory T cells predicts the clinical efficacy of PD-1 blockade therapies. *Nat Immunol* **21,** 1346–1358 (2020).

222. Lowther, D. PD-1 marks dysfunctional regulatory T cells in malignant gliomas. *JCI Insight* **1,** e85935 (2016).

223. Oba, T. Overcoming primary and acquired resistance to anti-PD-L1 therapy by induction and activation of tumor-residing cDC1s. *Nat Commun* **11,** 5415 (2020).

224. Kamphorst, A. Proliferation of PD-1+ CD8 T cells in peripheral blood after PD-1-targeted therapy in lung cancer patients. *Proc Natl Acad Sci U S A* **114,** 4993–4998 (2017).

225. Waite, J. Tumor-targeted CD28 bispecific antibodies enhance the antitumor efficacy of PD-1 immunotherapy. *Sci Transl Med* **12,** eaba2325 (2020).

226. Morrison, A. Sufficiency of CD40 activation and immune checkpoint blockade for T cell priming and tumor immunity. *Proc Natl Acad Sci U S A* **117,** 8022–8031 (2020).

227. Williford, J. Recruitment of CD103+ dendritic cells via tumor-targeted chemokine delivery enhances efficacy of checkpoint inhibitor immunotherapy. *Sci Adv* **5,** eaay1357 (2019).

228. Chow, M. Intratumoral Activity of the CXCR3 Chemokine System Is Required for the Efficacy of Anti-PD-1 Therapy. *Immunity* **50,** 1498–1512 (2019).

229. Perez-Ruiz, E. Prophylactic TNF blockade uncouples efficacy and toxicity in dual CTLA-4 and PD-1 immunotherapy. *Nature* **569,** 428–432 (2019).

230. Valpione, S. Sex and interleukin-6 are prognostic factors for autoimmune toxicity following treatment with anti-CTLA4 blockade. *J Transl Med* **16,** 94 (2018).

231. Hu-Lieskovan, S. Tumor characteristics associated with benefit from pembrolizumab in advanced non–small cell lung cancer. *Clin Cancer Res* **25,** 5061–5068 (2019).

232. Ali, O. Characterization of nivolumab-associated skin reactions in patients with metastatic non-small cell lung cancer. *Oncoimmunology* **5,** e1231292 (2016).

233. Shimozaki, K. Multiple immune-related adverse events and anti-tumor efficacy: Real-world data on various solid tumors. *Cancer Manag Res* **12,** 4585–4593 (2020).

234. Giannicola, R. Early blood rise in auto-antibodies to nuclear and smooth muscle antigens is predictive of prolonged survival and autoimmunity in metastatic-non-small cell lung cancer patients treated with PD-1 immune-check point blockade by nivolumab. *Mol Clin Oncol* **11,** 81–90 (2019).

235. Queirolo, P. Association of CTLA-4 polymorphisms with improved overall survival in melanoma patients treated with CTLA-4 blockade: A pilot study. *Cancer Invest* **31,** 336–345 (2013).

236. Freeman-Keller, M. Nivolumab in resected and unresectable metastatic melanoma: Characteristics of immune-related adverse events and association with outcomes. *Clin Cancer Res* **3221,** 886–894 (2016).

237. Hua, C. Association of vitiligo with tumor response in patients with metastatic melanoma treated with pembrolizumab. *JAMA Dermatol* **152,** 45–51 (2016).

238. Nakamura, Y. Correlation between vitiligo occurrence and clinical benefit in advanced melanoma patients treated with nivolumab: A multi-institutional retrospective study. *J Dermatol* **44,** 117–122 (2017).

239. Haratani, K. Association of immune-related adverse events with nivolumab efficacy in non-small cell lung cancer. *JAMA Oncol* **4,** 374–378 (2018).

240. Hori, R. Real-World Outcomes and Prognostic Factors in Patients Receiving Nivolumab Therapy for Recurrent or Metastatic Head and Neck Carcinoma. *Cancers (Basel)* **11,** 1317 (2019).

241. Sarnaik, A. Extended dose ipilimumab with a peptide vaccine: Immune correlates associated with clinical benefit in patients with resected high-risk stage IIIc/IV melanoma. *Clin Cancer Res* **17,** 896–906 (2011).

242. Okada, N. Association Between Immune-Related Adverse Events and Clinical Efficacy in Patients with Melanoma Treated With Nivolumab: A Multicenter Retrospective Study. *Clin Ther* **41,** 59–67 (2019).

243. Diem, S. Pembrolizumab-triggered Uveitis: An Additional Surrogate Marker for Responders in Melanoma Immunotherapy? *J Immunother* **39,** 379–382 (2016).

244. Li, Y. Treatment-related adverse events and response rate to immune checkpoint inhibition. *J Int Med Res* **48,** 300060519886454 (2020).

245. Espana, S. Endocrine adverse events related to immune-oncology agents: Retrospective experience of a single institution. *Transl Lung Cancer Res* **9,** 103–110 (2020).

246. Rogado, J. Effect of excess weight and immune-related adverse events on the efficacy of cancer immunotherapy with anti-PD-1 antibodies. *Oncoimmunology* **9,** 1751548 (2020).

247. Khan, Z. Polygenic risk for skin autoimmunity impacts immune checkpoint blockade in bladder cancer. *Proc Natl Acad Sci U S A* **117,** 12288–12294 (2020).

248. Berner, F. Association of Checkpoint Inhibitor-Induced Toxic Effects with Shared Cancer and Tissue Antigens in Non-Small Cell Lung Cancer. *JAMA Oncol* **5,** 1043–1047 (2019).

249. Bakhru, P. Combination central tolerance and peripheral checkpoint blockade unleashes antimelanoma immunity. *JCI Insight* **2,** e93265 (2017).

250. Valpione, S. Immune awakening revealed by peripheral T cell dynamics after one cycle of immunotherapy. *Nat Cancer* **1,** 210–221 (2020).

251. Oh, D. Immune toxicities elicited by CTLA-4 blockade in cancer patients are associated with early diversification of the T-cell repertoire. *Cancer Res* **77,** 1322–1330 (2017).

252. Anagnostou, V. Integrative Tumor and Immune Cell Multi-omic Analyses Predict Response to Immune Checkpoint Blockade in Melanoma. *Cell Rep Med* **1,** 100139 (2020).

253. Rizvi, N. Cancer immunology. Mutational landscape determines sensitivity to PD-1 blockade in non-small cell lung cancer. *Science* **348,** 124–128 (2015).

254. Samstein, R. Tumor mutational load predicts survival after immunotherapy across multiple cancer types. *Nat Genet* **51,** 202–206 (2019).

255. Snyder, A. Genetic basis for clinical response to CTLA-4 blockade in melanoma. *N Engl J Med* **371,** 2189–2199 (2014).

256. Valero, C. Pretreatment neutrophil-to-lymphocyte ratio and mutational burden as biomarkers of tumor response to immune checkpoint inhibitors. *Nat Commun* **12,** 729 (2021).

257. Nabet, B. Noninvasive Early Identification of Therapeutic Benefit from Immune Checkpoint Inhibition. *Cell* **183,** 363–376 (2020).

258. Cristescu, R. Pan-tumor genomic biomarkers for PD-1 checkpoint blockade-based immunotherapy. *Science* **362,** eaar3593 (2018).

259. Hugo, W. Genomic and Transcriptomic Features of Response to Anti-PD-1 Therapy in Metastatic Melanoma. *Cell* **165,** 35–44 (2016).

260. Hellmann, M. Genomic Features of Response to Combination Immunotherapy in Patients with Advanced Non-Small-Cell Lung Cancer. *Cancer Cell* **33,** 843–852 (2018).

261. Litchfield, K. Meta-analysis of tumor- and T cell-intrinsic mechanisms of sensitization to checkpoint inhibition. *Cell* **184,** 596–614 (2021).

262. Liu, D. Integrative molecular and clinical modeling of clinical outcomes to PD1 blockade in patients with metastatic melanoma. *Nat Med* **25,** 1916–1927 (2019).

263. Miao, D. Genomic correlates of response to immune checkpoint blockade in microsatellite-stable solid tumors. *Nat Genet* **50,** 1271–1281 (2018).

264. Riaz, N. Tumor and Microenvironment Evolution during Immunotherapy with Nivolumab. *Cell* **171,** 934–949 (2017).

265. Richard, C. Exome Analysis Reveals Genomic Markers Associated with Better Efficacy of Nivolumab in Lung Cancer Patients. *Clin Cancer Res* **25,** 957–966 (2019).

266. Rooney, M. Molecular and genetic properties of tumors associated with local immune cytolytic activity. *Cell* **160,** 48–61 (2015).

267. Hellmann, M. Nivolumab plus Ipilimumab in Lung Cancer with a High Tumor Mutational Burden. *N Engl J Med* **378,** 2093–2104 (2018).

268. Kim, K. Predicting clinical benefit of immunotherapy by antigenic or functional mutations affecting tumour immunogenicity. *Nat Commun* **11,** 951 (2020).

269. McGranahan, N. Clonal neoantigens elicit T cell immunoreactivity and sensitivity to immune checkpoint blockade. *Science* **351,** 1463–1469 (2016).

270. Lo, J. Epitope spreading toward wild-type melanocyte-lineage antigens rescues suboptimal immune checkpoint blockade responses. *Sci Transl Med* **13,** eabd8636 (2021).

271. Lindeboom, R. The impact of nonsense-mediated mRNA decay on genetic disease, gene editing and cancer immunotherapy. *Nat Genet* **51,** 1645–1651 (2019).

272. Turajlic, S. Insertion-and-deletion-derived tumour-specific neoantigens and the immunogenic phenotype: a pan-cancer analysis. *Lancet Oncol* **18,** 1009–1021 (2017).

273. Mandal, R. Genetic diversity of tumors with mismatch repair deficiency influences anti-PD-1 immunotherapy response. *Science* **364,** 485–491 (2019).

274. Lu, T. Tumor neoantigenicity assessment with CSiN score incorporates clonality and immunogenicity to predict immunotherapy outcomes. *Sci Immunol* **5,** eaaz3199 (2020).

275. Gettinger, S. Impaired HLA class I antigen processing and presentation as a mechanism of acquired resistance to immune checkpoint inhibitors in lung cancer. *Cancer Discov* **7,** 1420–1435 (2017).

276. Sade-Feldman, M. Resistance to checkpoint blockade therapy through inactivation of antigen presentation. *Nat Commun* **8,** 1136 (2017).

277. Zaretsky, J. Mutations associated with acquired resistance to PD-1 blockade in melanoma. *N Engl J Med* **375,** 819–829 (2016).

278. Kawashima, S. TIGIT/CD155 axis mediates resistance to immunotherapy in patients with melanoma with the inflamed tumor microenvironment. *J Immunother Cancer* **9,** e003134 (2021).

279. Zhang, H. Homozygous deletion of the HLA-B gene as an acquired-resistance mechanism to nivolumab in a patient with lung adenocarcinoma: a case report. *Ann Transl Med* **9,** 1506 (2021).

280. Kalaora, S. Immunoproteasome expression is associated with better prognosis and response to checkpoint therapies in melanoma. *Nat Commun* **11,** 896 (2020).

281. Patel, S. Identification of essential genes for cancer immunotherapy. *Nature* **548,** 537–542 (2017).

282. Shin, D. Primary Resistance to PD-1 Blockade Mediated by JAK1/2 Mutations. *Cancer Discov* **7,** 188–201 (2017).

283. Liu, X. PBRM1 loss defines a nonimmunogenic tumor phenotype associated with checkpoint inhibitor resistance in renal carcinoma. *Nat Commun* **11,** 2135 (2020).

284. Green, M. Integrative analysis reveals selective 9p24.1 amplification, increased PD-1 ligand expression, and further induction via JAK2 in nodular sclerosing Hodgkin lymphoma and primary mediastinal large B-cell lymphoma. *Blood* **116,** 3268–3277 (2010).

285. Roemer, M. Major histocompatibility complex class II and programmed death ligand 1 expression predict outcome after programmed death 1 blockade in classic Hodgkin lymphoma. *J Clin Oncol* **36,** 942–950 (2018).

286. Manguso, R. In vivo CRISPR screening identifies Ptpn2 as a cancer immunotherapy target. *Nature* **547,** 413–418 (2017).

287. Chowell, D. Patient HLA class I genotype influences cancer response to checkpoint blockade immunotherapy. *Science* **359,** 582–587 (2018).

288. Chowell, D. Evolutionary divergence of HLA class I genotype impacts efficacy of cancer immunotherapy. *Nat Med* **25,** 1715–1720 (2019).

289. Naranbhai, V. HLA-A*03 and response to immune checkpoint blockade in cancer: an epidemiological biomarker study. *Lancet Oncol* **S1470-2045,** 582–589 (2021).

290. Holmgaard, R. Targeting myeloid-derived suppressor cells with colony stimulating factor-1 receptor blockade can reverse immune resistance to immunotherapy in indoleamine 2,3-dioxygenase-expressing tumors. *Nat Commun* **12,** 7005 (2021).

291. Holmgaard, R. Tumor-expressed IDO recruits and activates MDSCs in a Treg-dependent manner. *Cell Rep* **13,** 412–424 (2015).

292. Martens, A. Baseline peripheral blood biomarkers associated with clinical outcome of advanced melanoma patients treated with ipilimumab. *Clin Cancer Res* **22,** 2908–2918 (2016).

293. Ottonello, S. Association Between Response to Nivolumab Treatment and Peripheral Blood Lymphocyte Subsets in Patients With Non-small Cell Lung Cancer. *Front Immunol* **11,** 125 (2020).

294. Principe, N. Tumor Infiltrating Effector Memory Antigen-Specific CD8 + T Cells Predict Response to Immune Checkpoint Therapy. *Front Immunol* **11,** 584423 (2020).

295. Feng, M. Pharmacological inhibition of β-catenin/BCL9 interaction overcomes resistance to immune checkpoint blockades by modulating T reg cells. *Sci Adv* **5,** eaau5240 (2019).

296. DeStreel, G. Selective inhibition of TGF-β1 produced by GARP-expressing Tregs overcomes resistance to PD-1/PD-L1 blockade in cancer. *Nat Commun* **11,** 4545 (2020).

297. Iannone, R. Adenosine limits the therapeutic effectiveness of anti-CTLA4 mAb in a mouse melanoma model. *Am J Cancer Res* **4,** 172–181 (2014).

298. Di Pilato, M. Targeting the CBM complex causes T reg cells to prime tumours for immune checkpoint therapy. *Nature* **570,** 112–116 (2019).

299. Zappasodi, R. Non-conventional Inhibitory CD4+ Foxp3- PD-1hi T Cells as a Biomarker of Immune Checkpoint Blockade Activity. *Cancer Cell* **34,** 691 (2018).

300. Aslan, K. Heterogeneity of response to immune checkpoint blockade in hypermutated experimental gliomas. *Nat Commun* **11,** 931 (2020).

301. DeHenau, O. Overcoming resistance to checkpoint blockade therapy by targeting PI3Kγ in myeloid cells. *Nature* **539,** 443–447 (2016).

302. Strauss, L. Targeted deletion of PD-1 in myeloid cells induces antitumor immunity. *Sci Immunol* **5,** eaay1863 (2020).

303. Kitano, S. Computational algorithm-driven evaluation of monocytic myeloid-derived suppressor cell frequency for prediction of clinical outcomes. *Cancer Immunol Res* **2,** 812–821 (2014).

304. Koh, J. MDSC subtypes and CD39 expression on CD8 + T cells predict the efficacy of anti-PD-1 immunotherapy in patients with advanced NSCLC. *Eur J Immunol* **50,** 1810–1819 (2020).

305. Gebhardt, C. Myeloid cells and related chronic inflammatory factors as novel predictive markers in melanoma treatment with ipilimumab. *Clin Cancer Res* **21,** 5453–5459 (2015).

306. Raphael, I. TIGIT and PD-1 Immune Checkpoint Pathways Are Associated With Patient Outcome and Anti-Tumor Immunity in Glioblastoma. *Front Immunol* **12** (2021).

307. Flores-Toro, J. CCR2 inhibition reduces tumor myeloid cells and unmasks a checkpoint inhibitor effect to slow progression of resistant murine gliomas. *Proc Natl Acad Sci U S A* **117,** 1129–1138 (2020).

308. Singh, S. IL-1α Mediates Innate and Acquired Resistance to Immunotherapy in Melanoma. *J Immunol* **206,** 1966–1975 (2021).

309. Diskin, B. PD-L1 engagement on T cells promotes self-tolerance and suppression of neighboring macrophages and effector T cells in cancer. *Nat Immunol* **21,** 442–454 (2020).

310. Panni, R. Agonism of CD11b reprograms innate immunity to sensitize pancreatic cancer to immunotherapies. *Sci Transl Med* **11,** eaau9240 (2019).

311. Wei, Z. Boosting anti-PD-1 therapy with metformin-loaded macrophage-derived microparticles. *Nat Commun* **12,** 440 (2021).

312. De Hanau, D. Overcoming resistance to checkpoint blockade therapy by targeting PI3Kγ in myeloid cells. *Nature* **539,** 443–447 (2016).

313. Kridel, R. The prognostic impact of CD163-positive macrophages in follicular Lymphoma: A study from the BC cancer agency and the lymphoma study association. *Clin Cancer Res* **21,** 3428–3435 (2015).

314. Molgora, M. TREM2 Modulation Remodels the Tumor Myeloid Landscape Enhancing Anti-PD-1 Immunotherapy. *Cell* **182,** 886–900 (2020).

315. Alessi, V. Low peripheral blood derived neutrophil-to-lymphocyte ratio (dNLR) is associated with increased tumor T-cell infiltration and favorable outcomes to first-line pembrolizumab in non-small cell lung cancer. *J Immunother Cancer* **9,** e003536 (2021).

316. Hopkins, A. Development and Validation of a Prognostic Model for Patients with Advanced Lung Cancer Treated with the Immune Checkpoint Inhibitor Atezolizumab. *Clin Cancer Res* **26,** 3280–3286 (2020).

317. Petrova, M. Neutrophil to lymphocyte ratio as a potential predictive marker for treatment with pembrolizumab as a second line treatment in patients with non-small cell lung cancer. *Biosci Trends* **14,** 48–55 (2020).

318. Matsuki, T. Hematological predictive markers for recurrent or metastatic squamous cell carcinomas of the head and neck treated with nivolumab: A multicenter study of 88 patients. *Cancer Med* **9,** 5015–5024 (2020).

319. Cassidy, M. Neutrophil to Lymphocyte Ratio is Associated With Outcome During Ipilimumab Treatment. *EBioMedicine* **18,** 56–61 (2017).

320. Liu, X. The Prognosis and Immune Checkpoint Blockade Efficacy Prediction of Tumor-Infiltrating Immune Cells in Lung Cancer. *Front Cell Dev Biol* **9** (2021).

321. Dusselier, M. Neutrophil-to-lymphocyte ratio evolution is an independent predictor of early progression of second-line nivolumab-treated patients with advanced non-small-cell lung cancers. *PLoS One* **14,** e0219060 (2019).

322. Liu, J. Systemic immune-inflammation index, neutrophil-to-lymphocyte ratio, platelet-to-lymphocyte ratio can predict clinical outcomes in patients with metastatic non-small-cell lung cancer treated with nivolumab. *J Clin Lab Anal* **33,** e22964 (2019).

323. Passiglia, F. Efficacy of nivolumab in pre-treated non-small-cell lung cancer patients harbouring KRAS mutations. *Br J Cancer* **120,** 57–62 (2019).

324. Adachi, Y. Predictive factors for progression-free survival in non-small cell lung cancer patients receiving nivolumab based on performance status. *Cancer Med* **9,** 1383–1391 (2020).

325. Capone, M. Frequency of circulating CD8+CD73+T cells is associated with survival in nivolumab-treated melanoma patients. *J Transl Med* **18,** 121 (2020).

326. Schalper, K. Elevated serum interleukin-8 is associated with enhanced intratumor neutrophils and reduced clinical benefit of immune-checkpoint inhibitors. *Nat Med* **26,** 688–692 (2020).

327. Yuen, K. High systemic and tumor-associated IL-8 correlates with reduced clinical benefit of PD-L1 blockade. *Nat Med* **26,** 693–698 (2020).

328. Hardy-Werbin, M. Serum cytokine levels as predictive biomarkers of benefit from ipilimumab in small cell lung cancer. *Oncoimmunology* **8,** e1593810 (2019).

329. Hino, R. Tumor cell expression of programmed cell death-1 ligand 1 is a prognostic factor for malignant melanoma. *Cancer* **116,** 1757–1766 (2010).

330. Zhang, B. Predictive effect of PD-L1 expression for immune checkpoint inhibitor (PD-1/PD-L1 inhibitors) treatment for non-small cell lung cancer: A meta-analysis. *Int Immunopharmacol* **80,** 106214 (2020).

331. Amaria, R. Neoadjuvant immune checkpoint blockade in high-risk resectable melanoma. *Nat Med* **24,** 1649–1654 (2018).

332. Chang, C. The Prognostic Significance of PD1 and PDL1 Gene Expression in Lung Cancer: A Meta-Analysis. *Front Oncol* **11,** 759497 (2021).

333. Khattak, M. PD-L1 Expression on Circulating Tumor Cells May Be Predictive of Response to Pembrolizumab in Advanced Melanoma: Results from a Pilot Study. *Oncologist* **25,** 520–527 (2020).

334. Ku, G. Single-institution experience with ipilimumab in advanced melanoma patients in the compassionate use setting lymphocyte count after 2 doses correlates with survival. *Clin Cancer Res* **116,** 1767–1775 (2016).

335. Tumeh, P. PD-1 blockade induces responses by inhibiting adaptive immune resistance. *Nature* **515,** 568–571 (2014).

336. Davis, A. The role of PD-L1 expression as a predictive biomarker: an analysis of all US Food and Drug Administration (FDA) approvals of immune checkpoint inhibitors. *J Immunother Cancer* **7,** 278 (2019).

337. NICE. *Pembrolizumab for untreated PD-L1-positive metastatic non-small-cell lung cancer* `https://www.nice.org.uk/guidance/ta531`.

338. NICE. *Pembrolizumab for treating PD-L1-positive non-small-cell lung cancer after chemotherapy* `https://www.nice.org.uk/guidance/ta428`.

339. NICE. *Atezolizumab for untreated PD-L1-positive advanced urothelial cancer when cisplatin is unsuitable* `https://www.nice.org.uk/guidance/ta739`.

340. Jacquelot, N. Predictors of responses to immune checkpoint blockade in advanced melanoma. *Nat Commun* **8,** 592 (2017).

341. Motzer, R. Nivolumab versus Everolimus in Advanced Renal-Cell Carcinoma. *N Engl J Med* **373,** 1803–1813 (2015).

342. Wallis, C. Association between PD-L1 status and immune checkpoint inhibitor response in advanced malignancies: a systematic review and meta-analysis of overall survival data. *Jpn J Clin Oncol* **50,** 800–809 (2020).

343. Ayers, M. IFN-γ–related mRNA profile predicts clinical response to PD-1 blockade. *J Clin Invest* **127,** 2930–2940 (2017).

344. Powles, T. Clinical efficacy and biomarker analysis of neoadjuvant atezolizumab in operable urothelial carcinoma in the ABACUS trial. *Nat Med* **25,** 1706–1714 (2019).

345. Chow, L. Antitumor activity of pembrolizumab in biomarker-unselected patients with recurrent and/or metastatic head and neck squamous cell carcinoma: Results from the phase Ib KEYNOTE-012 expansion cohort. *J Clin Oncol* **34,** 3838–3845 (2016).

346. Horn, L. Nivolumab versus docetaxel in previously treated patients with advanced non-small-cell lung cancer: Two-year outcomes from two randomized, open-label, phase III Trials (CheckMate 017 and CheckMate 057). *J Clin Oncol* **35,** 3924–3933 (2017).

347. Mohan, N. Atezolizumab potentiates Tcell-mediated cytotoxicity and coordinates with FAK to suppress cell invasion and motility in PD-L1+ triple negative breast cancer cells. *Oncoimmunology* **8,** e1624128 (2019).

348. Balança, C. Dual Relief of T-lymphocyte Proliferation and Effector Function Underlies Response to PD-1 Blockade in Epithelial Malignancies. *Cancer Immunol Res* **8,** 869–882 (2020).

349. Andrews, L. Resistance to PD1 blockade in the absence of metalloprotease-mediated LAG3 shedding. *Sci Immunol* **5,** eabc2728 (2020).

350. Bai, A. NADH oxidase-dependent CD39 expression by CD8 + T cells modulates interferon gamma responses via generation of adenosine. *Nat Commun* **6,** 8819 (2015).

351. Krieg, C. High-dimensional single-cell analysis predicts response to anti-PD-1 immunotherapy. *Nat Med* **24,** 144–153 (2018).

352. Woods, D. Nivolumab and ipilimumab are associated with distinct immune landscape changes and response-associated immunophenotypes. *JCI Insight* **5,** e137066 (2020).

353. Kunert, A. CD45RA+ CCR7- CD8 T cells lacking co-stimulatory receptors demonstrate enhanced frequency in peripheral blood of NSCLC patients responding to nivolumab. *J Immunother Cancer* **7,** 149 (2019).

354. Inomata, M. Peripheral PD1-positive CD4 T-lymphocyte count can predict progression-free survival in patients with non-small cell lung cancer receiving immune checkpoint inhibitor. *Anticancer Res* **39,** 6887–6893 (2019).

355. Graves, M. Monitoring Patient Response to Pembrolizumab With Peripheral Blood Exhaustion Marker Profiles. *Front Med (Lausanne)* **6,** 113 (2019).

356. Genova, C. Correlation between B7-H4 and Survival of Non-Small-Cell Lung Cancer Patients Treated with Nivolumab. *J Clin Med* **8,** 1566 (2019).

357. Allard, B. Targeting CD73 enhances the antitumor activity of anti-PD-1 and anti-CTLA-4 mAbs. *Clin Cancer Res* **19,** 5626–5635 (2013).

358. Yang, M. Checkpoint molecules coordinately restrain hyperactivated effector T cells in the tumor microenvironment. *Oncoimmunology* **9,** 1708064 (2020).

359. Sade-Feldman, M. Defining T Cell States Associated with Response to Checkpoint Immunotherapy in Melanoma. *Cell* **175,** 998–1013 (2018).

360. Delyon, J. Experience in daily practice with ipilimumab for thetreatment of patients with metastatic melanoma: Anearly increase in lymphocyte and eosinophil countsis associated with improved survival. *Ann Oncol* **24,** 1697–1703 (2013).

361. Martens, A. Increases in absolute lymphocytes and circulating CD4+ and CD8+ T cells are associated with positive clinical outcome of melanoma patients treated with ipilimumab. *Clin Cancer Res* **22,** 4848–4858 (2016).

362. Blank, C. Neoadjuvant versus adjuvant ipilimumab plus nivolumab in macroscopic stage III melanoma. *Nat Med* **24,** 1655–1661 (2018).

363. Chalabi, M. Neoadjuvant immunotherapy leads to pathological responses in MMR-proficient and MMR-deficient early-stage colon cancers. *Nat Med* **26,** 566–576 (2020).

364. Gunderson, A. Germinal center reactions in tertiary lymphoid structures associate with neoantigen burden, humoral immunity and long-term survivorship in pancreatic cancer. *Oncoimmunology* **10,** 1900635 (2021).

365. Goswami, S. ARID1A mutation plus CXCL13 expression act as combinatorial biomarkers to predict responses to immune checkpoint therapy in mUCC. *Science Transl Med* **12** (2020).

366. Helmink, B. B cells and tertiary lymphoid structures promote immunotherapy response. *Nature* **577,** 549–555 (2020).

367. Ji, R. An immune-active tumor microenvironment favors clinical response to ipilimumab. *Cancer Immunol Immunother* **61,** 1019–1031 (2012).

368. Subrahmanyam, P. Distinct predictive biomarker candidates for response to anti-CTLA-4 and anti-PD-1 immunotherapy in melanoma patients. *J Immunother Cancer* **6,** 18 (2018).

369. Fehlings, M. Late-differentiated effector neoantigen-specific CD8+ T cells are enriched in non-small cell lung carcinoma patients responding to atezolizumab treatment. *J Immunother Cancer* **7,** 249 (2019).

370. Han, J. Resident and circulating memory T cells persist for years in melanoma patients with durable responses to immunotherapy. *Nat Cancer* **2,** 300–311 (2021).

371. Fairfax, B. Peripheral CD8+ T cell characteristics associated with durable responses to immune checkpoint blockade in patients with metastatic melanoma. *Nat Med* **26,** 193–199 (2020).

372. Wu, T. Peripheral T cell expansion predicts tumour infiltration and clinical response. *Nature* **579,** 274–278 (2020).

373. Arakawa, A. Clonality of CD4+ blood T cells predicts longer survival with CTLA4 or PD-1 checkpoint inhibition in advanced melanoma. *Front Immunol* **10,** 1336 (2019).

374. Roh, W. Integrated molecular analysis of tumor biopsies on sequential CTLA-4 and PD-1 blockade reveals markers of response and resistance. *Sci Transl Med* **9,** eaah3560 (2017).

375. Valpione, S. The T cell receptor repertoire of tumor infiltrating T cells is predictive and prognostic for cancer survival. *Nat Commun* **12,** 4098 (2021).

376. Bassez, A. A single-cell map of intratumoral changes during anti-PD1 treatment of patients with breast cancer. *Nat Med* **27,** 820–832 (2021).

377. Looney, T. TCR Convergence in Individuals Treated With Immune Checkpoint Inhibition for Cancer. *Front Immunol* **10,** 2985 (2020).

378. Poran, A. Combined TCR Repertoire Profiles and Blood Cell Phenotypes Predict Melanoma Patient Response to Personalized Neoantigen Therapy plus Anti-PD-1. *Cell Rep Med* **1,** 100141 (2020).

379. Postow, M. Peripheral T cell receptor diversity is associated with clinical outcomes following ipilimumab treatment in metastatic melanoma. *J Immunother Cancer* **3,** 23 (2015).

380. Cha, E. Improved survival with T cell clonotype stability after anti-CTLA-4 treatment in cancer patients. *Sci Transl Med* **6,** 238ra70 (2014).

381. Yost, K. Clonal replacement of tumor-specific T cells following PD-1 blockade. *Nature* **25,** 1251–1259 (2019).

382. Gutierrez-Arcelus, M. Lymphocyte innateness defined by transcriptional states reflects a balance between proliferation and effector functions. *Nat Commun* **10,** 687 (2019).

383. Zhou, X. A Pan-Cancer Analysis of CD161, a Potential New Immune Checkpoint. *Front Immunol* **12,** 688215 (2021).

384. Pirozyan, M. Pretreatment Innate Cell Populations and CD4 T Cells in Blood Are Associated With Response to Immune Checkpoint Blockade in Melanoma Patients. *Front Immunol* **11,** 372 (2020).

385. Di Marco Barros, R. Epithelia Use Butyrophilin-like Molecules to Shape Organ-Specific γδ T Cell Compartments. *Cell* **167,** 203–218 (2016).

386. Vavassori, S. Butyrophilin 3A1 binds phosphorylated antigens and stimulates human γδ T cells. *Nat Immunol* **14,** 908–916 (2013).

387. Decaup, E. Phosphoantigens and butyrophilin 3A1 induce similar intracellular activation signaling in human TCRVγ9+ γδ T lymphocytes. *Immunol Lett* **161,** 133–137 (2014).

388. Sandstrom, A. The Intracellular B30.2 Domain of Butyrophilin 3A1 Binds Phosphoantigens to Mediate Activation of Human Vγ9Vδ2 T Cells. *Immunity* **40,** 490–500 (2014).

389. Girardi, M. Regulation of cutaneous malignancy by gammadelta T cells. *Science* **294,** 605–609 (2001).

390. Wakita, D. Tumor-infiltrating IL-17-producing gammadelta T cells support the progression of tumor by promoting angiogenesis. *Eur J Immunol* **40,** 1927–1937 (2010).

391. Xiong, D. A gene expression signature of TREM2 hi macrophages and γδ T cells predicts immunotherapy response. *Nat Commun* **11,** 5084 (2020).

392. Ko, H. Immunosuppressive myeloid-derived suppressor cells can be converted into immunogenic APCs with the help of activated NKT cells: an alternative cell-based antitumor vaccine. *J Immunol* **182,** 1818–1828 (2009).

393. Porcelli, S. Analysis of T cell antigen receptor (TCR) expression by human peripheral blood CD4-8- alpha/beta T cells demonstrates preferential use of several V beta genes and an invariant TCR alpha chain. *J Exp Med* **178,** 1–16 (1993).

394. Tilloy, F. An invariant T cell receptor alpha chain defines a novel TAP-independent major histocompatibility complex class Ib-restricted alpha/beta T cell subpopulation in mammals. *J Exp Med* **189,** 1907–1921 (1999).

395. Treiner, E. Selection of evolutionarily conserved mucosal-associated invariant T cells by MR1. *Nature* **422,** 164–169 (2003).

396. Reantragoon, R. Antigen-loaded MR1 tetramers define T cell receptor heterogeneity in mucosal-associated invariant T cells. *J Exp Med* **210,** 2305–2320 (2013).

397. Gold, M. Human mucosal associated invariant T cells detect bacterially infected cells. *PLoS Biol* **8,** e1000407 (2010).

398. Le Bourhis, L. Antimicrobial activity of mucosal-associated invariant T cells. *Nat Immunol* **11,** 701–708 (2010).

399. Kurioka, A. Diverse Streptococcus pneumoniae Strains Drive a Mucosal-Associated Invariant T-Cell Response Through Major Histocompatibility Complex class I-Related Molecule-Dependent and Cytokine-Driven Pathways. *J Infect Dis* **217,** 988–999 (2018).

400. Kjer-Nielsen, L. MR1 presents microbial vitamin B metabolites to MAIT cells. *Nature* **491,** 717–723 (2012).

401. Soudais, C. In Vitro and In Vivo Analysis of the Gram-Negative Bacteria-Derived Riboflavin Precursor Derivatives Activating Mouse MAIT Cells. *J Immunol* **194,** 4641–4649 (2015).

402. Eckle, S. A molecular basis underpinning the T cell receptor heterogeneity of mucosal-associated invariant T cells. *J Exp Med* **211,** 1585–1600 (2014).

403. Corbett, A. T-cell activation by transitory neo-antigens derived from distinct microbial pathways. *Nature* **509,** 361–365 (2014).

404. Loh, L. Human mucosal-associated invariant T cells contribute to antiviral influenza immunity via IL-18-dependent activation. *Proc Natl Acad Sci U S A* **113,** 10133–10138 (2016).

405. Van Wilgenburg, B. MAIT cells are activated during human viral infections. *Nat Commun* **7** (2016).

406. Eberhard, J. Reduced CD161 + MAIT cell frequencies in HCV and HIV/HCV co-infection: Is the liver the heart of the matter? *J Hepatol* **65,** 1261–1263 (2016).

407. Hengst, J. Nonreversible MAIT cell-dysfunction in chronic hepatitis C virus infection despite successful interferon-free therapy. *Eur J Immunol* **46,** 2204–2210 (2016).

408. Spaan, M. Frequencies of Circulating MAIT Cells Are Diminished in Chronic HCV, HIV and HCV/HIV Co-Infection and Do Not Recover during Therapy. *PLoS One* **11,** e0159243 (2016).

409. Parrot, T. MAIT cell activation and dynamics associated with COVID-19 disease severity. *Sci Immunol* **5,** eabe1670 (2020).

410. Consortium, C.-1. M.-o. B. A. (A blood atlas of COVID-19 defines hallmarks of disease severity and specificity. *Cell* (2022).

411. Van Wilgenburg, B. MAIT cells contribute to protection against lethal influenza infection in vivo. *Nat Commun* **9,** 1 (2018).

412. Boeijen, L. Mucosal-Associated Invariant T Cells Are More Activated in Chronic Hepatitis B, but Not Depleted in Blood: Reversal by Antiviral Therapy. *J Infect Dis* **216,** 969–976 (2017).

413. Yong, Y. Hyper-Expression of PD-1 Is Associated with the Levels of Exhausted and Dysfunctional Phenotypes of Circulating CD161 ++ TCR iVα7.2 + Mucosal-Associated Invariant T Cells in Chronic Hepatitis B Virus Infection. *Front Immunol* **9** (2018).

414. Yong, Y. Decrease of CD69 levels on TCR Vα7.2 + CD4 + innate-like lymphocytes is associated with impaired cytotoxic functions in chronic hepatitis B virus-infected patients. *Innate Immun* **23,** 459–467 (2017).

415. Barathan, M. Peripheral loss of CD8(+) CD161(++) TCRVα7·2(+) mucosal-associated invariant T cells in chronic hepatitis C virus-infected patients. *Eur J Clin Invest* **46,** 170–180 (2016).

416. Beudeker, B. Mucosal-associated invariant T-cell frequency and function in blood and liver of HCV mono- and HCV/HIV co-infected patients with advanced fibrosis. *Liver Int* **38,** 458–468 (2018).

417. Bolte, F. Intra-Hepatic Depletion of Mucosal-Associated Invariant T Cells in Hepatitis C Virus-Induced Liver Inflammation. *Gastroenterology* **153,** 1392–1403 (2017).

418. Zabijak, L. Increased tumor infiltration by mucosal-associated invariant T cells correlates with poor survival in colorectal cancer patients. *Cancer Immunol Immunother* **64,** 1601–1608 (2015).

419. Won, E. Clinical relevance of circulating mucosal-associated invariant T cell levels and their anti-cancer activity in patients with mucosal-associated cancer. *Oncotarget* **7,** 76274–76290 (2016).

420. Sundström, P. Human Mucosa-Associated Invariant T Cells Accumulate in Colon Adenocarcinomas but Produce Reduced Amounts of IFN-γ. *J Immunol* **195,** 3472–3481 (2015).

421. Ling, L. Circulating and tumor-infiltrating mucosal associated invariant T (MAIT) cells in colorectal cancer patients. *Sci Rep* **6,** 20358 (2016).

422. Huang, W. Less circulating mucosal-associated invariant T cells in patients with cervical cancer. *Taiwan J Obstet Gynecol* **58,** 117–121 (2019).

423. Favreau, M. Both mucosal-associated invariant and natural killer T-cell deficiency in multiple myeloma can be countered by PD-1 inhibition. *Haematologica* **102,** e266–e270 (2017).

424. Gherardin, N. Enumeration, functional responses and cytotoxic capacity of MAIT cells in newly diagnosed and relapsed multiple myeloma. *Sci Rep* **8,** 4159 (2018).

425. Yao, T. Leveraging Public Single-Cell and Bulk Transcriptomic Datasets to Delineate MAIT Cell Roles and Phenotypic Characteristics in Human Malignancies. *Front Immunol* **11** (2020).

426. De Biasi, S. Circulating mucosal-associated invariant T cells identify patients responding to anti-PD-1 therapy. *Nat Commun* **12,** 1669 (2020).

427. Vorwald, V. Circulating CD8 + mucosal-associated invariant T cells correlate with improved treatment responses and overall survival in anti-PD-1-treated melanoma patients. *Clin Transl Immunology* **11,** e1367 (2022).

428. Crowther, M. Genome-wide CRISPR–Cas9 screening reveals ubiquitous T cell cancer targeting via the monomorphic MHC class I-related protein MR1. *Nat Immunol* **21,** 178–185 (2020).

429. Coronella, J. Evidence for an antigen-driven humoral immune response in medullary ductal breast cancer. *Cancer Res* **61,** 7889–7899 (2001).

430. Rodriguez, A. Immune mechanisms orchestrate tertiary lymphoid structures in tumors via cancer-associated fibroblasts. *Cell Rep* **36,** 109422 (2021).

431. Xia, L. Predictable Roles of Peripheral IgM Memory B Cells for the Responses to Anti-PD-1 Monotherapy Against Advanced Non-Small Cell Lung Cancer. *Front Immunol* **12,** 759217 (2021).

432. Milne, K. Systematic analysis of immune infiltrates in high-grade serous ovarian cancer reveals CD20, FoxP3 and TIA-1 as positive prognostic factors. *PLoS One* **4,** e6412 (2009).

433. Griss, J. B cells sustain inflammation and predict response to immune checkpoint blockade in human melanoma. *Nature Communications* **10,** 4186 (2019).

434. Selitsky, S. Prognostic value of B cells in cutaneous melanoma. *Genome Med* **11,** 36 (2019).

435. Cabrita, R. Tertiary lymphoid structures improve immunotherapy and survival in melanoma. *Nature* **577,** 561–565 (2020).

436. Erdag, G. Immunotype and immunohistologic characteristics of tumor-infiltrating immune cells are associated with clinical outcome in metastatic melanoma. *Cancer Res* **72,** 1070–1080 (2012).

437. Garg, K. Tumor-associated B cells in cutaneous primary melanoma and improved clinical outcome. *Hum Pathol* **54,** 157–164 (2016).

438. Damsky, W. B cell depletion or absence does not impede anti-tumor activity of PD-1 inhibitors. *J Immunother Cancer* **7,** 153 (2019).

439. De Jonge, K. Inflammatory B cells correlate with failure to checkpoint blockade in melanoma patients. *Oncoimmunology* **10,** 1873585 (2021).

440. Yuan, S. Pretreatment Peripheral B Cells Are Associated With Tumor Response to Anti-PD-1-Based Immunotherapy. *Front Immunol* **11,** 563653 (2020).

441. Gilbert, A. Monitoring the systemic human memory B cell compartment of melanoma patients for anti-tumor IgG antibodies. *PLoS One* **6,** e19330 (2011).

442. Fässler, M. Antibodies as biomarker candidates for response and survival to checkpoint inhibitors in melanoma patients. *J Immunother Cancer* **7,** 50 (2019).

443. Diem, S. Immunoglobulin G and Subclasses as Potential Biomarkers in Metastatic Melanoma Patients Starting Checkpoint Inhibitor Treatment. *J Immunother* **42,** 89–93 (2019).

444. Cipponi, A. Neogenesis of lymphoid structures and antibody responses occur in human melanoma metastases. *Cancer Res* **72,** 3997–4007 (2012).

445. Lynch, K. Heterogeneity in tertiary lymphoid structure B-cells correlates with patient survival in metastatic melanoma. *J Immunother Cancer* **9** (2021).

446. Ruffin, A. B cell signatures and tertiary lymphoid structures contribute to outcome in head and neck squamous cell carcinoma. *Nat Commun* **12,** 3349 (2021).

447. Petitprez, F. B cells are associated with survival and immunotherapy response in sarcoma. *Nature* **577,** 556–560 (2020).

448. Feng, H. Prognostic Significance of Gene Signature of Tertiary Lymphoid Structures in Patients With Lung Adenocarcinoma. *Front Oncol* **11** (2021).

449. Havenar-Daughton, C. CXCL13 is a plasma biomarker of germinal center activity. *Proc Natl Acad Sci U S A.* **113,** 2702–2707 (2016).

450. Groeneveld, C. Tertiary lymphoid structures marker CXCL13 is associated with better survival for patients with advanced-stage bladder cancer treated with immunotherapy. *Eur J Cancer* **118,** 181–189 (2021).

451. Yang, M. CXCL13 shapes immunoactive tumor microenvironment and enhances the efficacy of PD-1 checkpoint blockade in high-grade serous ovarian cancer. *J Immunother Cancer* **9** (2021).

452. Thommen, D. A transcriptionally and functionally distinct PD-1+ CD8+ T cell pool with predictive potential in nonsmall- cell lung cancer treated with PD-1 blockade. *Nat Med* **24,** 994–1004 (2018).

453. Workel, H. A Transcriptionally Distinct CXCL13+ CD103+ CD8+ T-cell Population Is Associated with B-cell Recruitment and Neoantigen Load in Human Cancer. *Cancer Immunol Res* **7,** 784–796 (2019).

454. Pai, J. Regional and clonal T cell dynamics at single cell resolution in immune checkpoint blockade. *bioRxiv* (2021).

455. Germain, C. Tertiary Lymphoid Structure-B Cells Narrow Regulatory T Cells Impact in Lung Cancer Patients. *Front Immunol* **12** (2021).

456. Wennhold, K. CD86 + Antigen-Presenting B Cells Are Increased in Cancer, Localize in Tertiary Lymphoid Structures, and Induce Specific T-cell Responses. *Cancer Immunol Res* **9,** 1098–1108 (2021).

457. Eschweiler, S. Intratumoral follicular regulatory T cells curtail anti-PD-1 treatment efficacy. *Nat Immunol* **22,** 1052–1063 (2021).

458. Das, R. Early B cell changes predict autoimmunity following combination immune checkpoint blockade. *Journal of Clinical Investigation* **128,** 715–720 (2018).

459. DeFarco, J. Non-progressing cancer patients have persistent B cell responses expressing shared antibody paratopes that target public tumor antigens. *Clin Immunol* **187,** 37–45 (2018).

460. Cannon, M. Review of cytomegalovirus seroprevalence and demographic characteristics associated with infection. *Rev Med Virol* **20,** 202–213 (2010).

461. Korndewal, M. Cytomegalovirus infection in the Netherlands: seroprevalence, risk factors, and implications. *J Clin Virol* **63,** 53–58 (2015).

462. Cannon, M. Congenital cytomegalovirus (CMV) epidemiology and awareness. *J Clin Virol* **46,** S6–10 (2009).

463. Bate, S. Cytomegalovirus seroprevalence in the United States: the national health and nutrition examination surveys, 1988-2004. *Clin Infect Dis* **50,** 1439–1447 (2010).

464. Dunn, W. Functional profiling of a human cytomegalovirus genome. *Proc Natl Acad Sci U S A* **100,** 14223–14228 (2003).

465. Welte, S. Selective intracellular retention of virally induced NKG2D ligands by the human cytomegalovirus UL16 glycoprotein. *Eur J Immunol* **33,** 194–203 (2003).

466. Fielding, C. Two novel human cytomegalovirus NK cell evasion functions target MICA for lysosomal degradation. *PLoS Pathog* **10,** e1004058 (2014).

467. Wang, E. Suppression of costimulation by human cytomegalovirus promotes evasion of cellular immune defenses. *Proc Natl Acad Sci U S A* **115,** 4998–5003 (2018).

468. Chaudhry, M. Cytomegalovirus inhibition of extrinsic apoptosis determines fitness and resistance to cytotoxic CD8 T cells. *Proc Natl Acad Sci U S A* **117,** 12961–12968 (2020).

469. Geljic, I. Cytomegalovirus protein m154 perturbs the adaptor protein-1 compartment mediating broad-spectrum immune evasion. *Elife* **9,** e50803 (2020).

470. Khan, S. A cytomegalovirus inhibitor of gamma interferon signaling controls immunoproteasome induction. *J Virol* **78,** 1831–1842 (2004).

471. Spencer, J. Potent immunosuppressive activities of cytomegalovirus-encoded interleukin-10. *J Virol* **76,** 1285–1292 (2002).

472. Jenkins, C. A novel viral transcript with homology to human interleukin-10 is expressed during latent human cytomegalovirus infection. *J Virol* **78,** 1440–1447 (2004).

473. Bantug, G. CD8+ T lymphocytes control murine cytomegalovirus replication in the central nervous system of newborn animals. *J Immunol* **181,** 2111–2123 (2008).

474. Zhang, W. CMV Status Drives Distinct Trajectories of CD4+ T Cell Differentiation. *Front Immunol* **12** (2021).

475. Hadrup, S. Longitudinal studies of clonally expanded CD8 T cells reveal a repertoire shrinkage predicting mortality and an increased number of dysfunctional cytomegalovirus-specific T cells in the very elderly. *J Immunol* **176,** 2645–2653 (2006).

476. Van der Heiden, M. Differential effects of Cytomegalovirus carriage on the immune phenotype of middle-aged males and females. *Sci Rep* **6** (2016).

477. Chidrawar, S. Cytomegalovirus-seropositivity has a profound influence on the magnitude of major lymphoid subsets within healthy individuals. *Clin Exp Immunol* **155,** 423–432 (2009).

478. Ouyang, Q. Large numbers of dysfunctional CD8+ T lymphocytes bearing receptors for a single dominant CMV epitope in the very old. *J Clin Immunol* **23,** 247–257 (2003).

479. Hassouneh, F. Differential Effect of Cytomegalovirus Infection with Age on the Expression of CD57, CD300a, and CD161 on T-Cell Subpopulations. *Front Immunol* **8** (2017).

480. Hassouneh, F. Functional Changes of T-Cell Subsets with Age and CMV Infection. *Int J Mol Sci* **22,** 9973 (2021).

481. Derhovanessian, E. Infection with cytomegalovirus but not herpes simplex virus induces the accumulation of late-differentiated CD4+ and CD8+ T-cells in humans. *J Gen Virol* **92,** 2746–2756 (2011).

482. Weltevrede, M. Cytomegalovirus persistence and T-cell immunosenescence in people aged fifty and older: A systematic review. *Exp Gerontol* **77,** 87–95 (2016).

483. Ouyang, Q. Age-associated accumulation of CMV-specific CD8+ T cells expressing the inhibitory killer cell lectin-like receptor G1 (KLRG1). *Exp Gerontol* **38,** 911–920 (2003).

484. Henze, J. RECIST 1.1, irRECIST 1.1, and mRECIST: How to Do. *Current Radiology Reports* **4** (2016).

485. NIH. *Common Terminology Criteria for Adverse Events (CTCAE) — Protocol Development* `https://ctep.cancer.gov/protocoldevelopment/electronic%5C_applications/ctc.htm#ctc%5C_40`.

486. Therneau, T. M. *A Package for Survival Analysis in R* R package version 3.2-13 (2021). `https://CRAN.R-project.org/package=survival`.

487. Kassambara, A., Kosinski, M. & Biecek, P. *survminer: Drawing Survival Curves using 'ggplot2'* R package version 0.4.9 (2021). `https://CRAN.R-project.org/package=survminer`.

488. Dardis, C. *survMisc: Miscellaneous Functions for Survival Data* R package version 0.5.5 (2018). `https://CRAN.R-project.org/package=survMisc`.

489. Kim, D. HISAT: a fast spliced aligner with low memory requirements. *Nat Methods* **12,** 357–360 (2015).

490. Kim, D. Graph-based genome alignment and genotyping with HISAT2 and HISAT-genotype. *Nat Biotechnol* **37,** 907–915 (2019).

491. Barnett, D. BamTools: a C++ API and toolkit for analyzing and managing BAM files. *Bioinformatics* **27,** 1691–1692 (2011).

492. Broad Institute. *Picard toolkit* `https://broadinstitute.github.io/picard/`. 2019.

493. Anders, S. HTSeq—a Python framework to work with high-throughput sequencing data. *Bioinformatics* **31,** 166–169 (2015).

494. Jun, G. Detecting and estimating contamination of human DNA samples in sequencing and array-based genotype data. *Am J Hum Genet* **91,** 839–848 (2012).

495. Love, M. Moderated estimation of fold change and dispersion for RNA-seq data with DESeq2. *Genome Biology* **15,** 550 (2014).

496. R Core Team. *R: A Language and Environment for Statistical Computing* R Foundation for Statistical Computing (Vienna, Austria, 2021). `https://www.R-project.org/`.

497. Mark, A. *mygene: Access MyGene.Info_ services* R package version 1.29.0 (2021).

498. Pruim, R. The mosaic Package: Helping Students to 'Think with Data' Using R. *The R Journal* **9,** 77–102. `https://journal.r-project.org/archive/2017/RJ-2017-024/index.html` (2017).

499. Wu, T. clusterProfiler 4.0: A universal enrichment tool for interpreting omics data. *Innovation (N Y)* **2,** 100141 (2021).

500. Yu, G. clusterProfiler: an R package for comparing biological themes among gene clusters. *OMICS* **16,** 284–287 (2012).

501. Carlson, M. *org.Hs.eg.db: Genome wide annotation for Human* R package version 3.8.2 (2019).

502. Korotkevich, G. Fast gene set enrichment analysis. *bioRxiv.* `http://biorxiv.org/content/early/2016/06/20/060012` (2019).

503. Bolotin, D. MiXCR: software for comprehensive adaptive immunity profiling. *Nature Methods* **12,** 380–381 (2014).

504. Bolotin, D. Antigen receptor repertoire profiling from RNA-seq data. *Nat Biotechnol* **35,** 908–911 (2017).

505. Wagih, O. *ggseqlogo: A 'ggplot2' Extension for Drawing Publication-Ready Sequence Logos* R package version 0.1 (2017). `https://CRAN.R-project.org/package=ggseqlogo`.

506. Wickham, H. Welcome to the tidyverse. *Journal of Open Source Software* **4,** 1686 (2019).

507. Dixon, P. VEGAN, a package of R functions for community ecology. *Journal of Vegetation Science* **14,** 927–930 (2003).

508. Oksanen, J. *vegan: Community Ecology Package* R package version 2.5-7 (2020). `https://CRAN.R-project.org/package=vegan`.

509. Vavrek, M. fossil: palaeoecological and palaeogeographical analysis tools. *Palaeontologia Electronica* **14.** R package version 0.4.0, 1T (2011).

510. Signorell, A. *DescTools: Tools for Descriptive Statistics* R package version 0.99.43 (2021). `https://cran.r-project.org/package=DescTools`.

511. Shugay, M. VDJdb: a curated database of T-cell receptor sequences with known antigen specificity. *Nucleic Acids Res* **46,** D419–D427 (2018).

512. Bagaev, D. VDJdb in 2019: database extension, new analysis infrastructure and a T-cell receptor motif compendium. *Nucleic Acids Res* **48,** D1057–D1062 (2020).

513. Tickotsky, N. McPAS-TCR: a manually curated catalogue of pathology-associated T cell receptor sequences. *Bioinformatics* **33,** 2924–2929 (2017).

514. Zhang, W. PIRD: Pan Immune Repertoire Database. *Bioinformatics* **36,** 897–903 (2020).

515. Zheng, G. Massively parallel digital transcriptional profiling of single cells. *Nat Commun* **8** (2017).

516. McCarty, D. Scater: pre-processing, quality control, normalization and visualization of single-cell RNA-seq data in R. *Bioinformatics* **33,** 1179–1186 (2017).

517. Lun, A. A step-by-step workflow for low-level analysis of single-cell RNA-seq data with Bioconductor. *F1000Res* **5** (2016).

518. Satija, R. Spatial reconstruction of single-cell gene expression data. *Nat Biotechnol* **33,** 495–502 (2015).

519. Butler, A. Integrating single-cell transcriptomic data across different conditions, technologies, and species. *Nat Biotechnol.* **36,** 411–420 (2018).

520. Stuart, T. Comprehensive Integration of Single-Cell Data. *Cell* **177,** 1888–1902. https://doi.org/10.1016/j.cell.2019.05.031 (2019).

521. Hao, Y. Integrated analysis of multimodal single-cell data. *Cell* **184,** 3573–3587. https://doi.org/10.1016/j.cell.2021.04.048 (2021).

522. Urbanczyk, S. Mitochondrial function is essential for humoral immunity by controlling flux of the TCA cycle, phosphatidic acid and mTOR activity in B cells. *BioRxiv* (2021).

523. Jang, K. Mitochondrial function provides instructive signals for activation-induced B-cell fates. *Nature Communications* **6** (2015).

524. Zappia, L. Clustering trees: a visualization for evaluating clusterings at multiple resolutions. *Gigascience* **7** (2018).

525. Stewart, A. Single-Cell Transcriptomic Analyses Define Distinct Peripheral B Cell Subsets and Discrete Development Pathways. *Front Immunol.* **12** (2021).

526. Aran, D. Reference-based analysis of lung single-cell sequencing reveals a transitional profibrotic macrophage. *Nat Immunol* **20,** 163–172 (2019).

527. Monaco, G. RNA-Seq Signatures Normalized by mRNA Abundance Allow Absolute Deconvolution of Human Immune Cell Types. *Cell Rep* **26,** 1627–1640 (2019).

528. van den Boogaart, K. G., Tolosana-Delgado, R. & Bren, M. *compositions: Compositional Data Analysis* R package version 2.0-2 (2021). https://CRAN.R-project.org/package=compositions.

529. Ye, J. Primer-BLAST: a tool to design target-specific primers for polymerase chain reaction. *BMC Bioinformatics* **13** (2012).

530. Kent, W. The human genome browser at UCSC. *Genome Res* **12,** 996–1006 (2002).

531. Gasteiger, E. ExPASy: The proteomics server for in-depth protein knowledge and analysis. *Nucleic Acids Res* **31,** 3784–3788 (2003).

532. Kaipe, H. *MAIT cells Methods and Protocols* (Springer US, 2020).

533. Dickinson, B. *FlowJo™ Software Version v10s.7.1* (2021).

534. Wickham, H. *ggplot2: Elegant Graphics for Data Analysis* ISBN: 978-3-319-24277-4. https://ggplot2.tidyverse.org (Springer-Verlag New York, 2016).

535. Kassambara, A. *ggpubr: 'ggplot2' Based Publication Ready Plots* https://CRAN.R-project.org/package=ggpubr.

536. Pfannenstiel, L. Immune-Checkpoint Blockade Opposes CD8 + T-cell Suppression in Human and Murine Cancer. *Cancer Immunol Res* **7,** 510–525 (2019).

537. Lindgren, A. CD8- natural killer cells are greatly enriched in the human gastrointestinal tract and have the capacity to respond to bacteria. *J Innate Immun* **2,** 294–302 (2010).

538. Penack, O. $CD56^{dim}$ $CD16^{neg}$ cells are responsible for natural cytotoxicity against tumor targets. *Leukemia* **19,** 835–840 (2005).

539. Jacobs, R. CD56^{bright} cells differ in their KIR repertoire and cytotoxic features from CD56^{dim} NK cells. *Eur J Immunol* **31,** 3121–3127 (2001).

540. Chen, P. Circulating Mucosal-Associated Invariant T Cells in a Large Cohort of Healthy Chinese Individuals From Newborn to Elderly. *Front Immunol* **10** (2019).

541. Gherardin, N. Human blood MAIT cell subsets defined using MR1 tetramers. *Immunol Cell Biol* **96,** 507–525 (2018).

542. Lee, O. Circulating mucosal-associated invariant T cell levels and their cytokine levels in healthy adults. *Exp Gerontol* **49,** 47–54 (2014).

543. Jing, Y. Aging is associated with a rapid decline in frequency, alterations in subset composition, and enhanced Th2 response in CD1d-restricted NKT cells from human peripheral blood. *Exp Gerontol* **42,** 719–732 (2007).

544. Peralbo, E. Decreased frequency and proliferative response of invariant Valpha24Vbeta11 natural killer T (iNKT) cells in healthy elderly. *Biogerontology* **7,** 483–492 (2006).

545. Stervbo, U. Age dependent differences in the kinetics of γδ T cells after influenza vaccination. *PLoS One* **12,** e0181161 (2017).

546. Van der Geest, K. Impact of Aging on the Frequency, Phenotype, and Function of CD161-Expressing T Cells. *Front Immunol* **9** (2018).

547. Das, R. Combination therapy with anti-CTLA-4 and anti-PD-1 leads to distinct immunologic changes in vivo. *J Immunol* **194,** 950–959 (2015).

548. Ogishi, M. Inherited PD-1 deficiency underlies tuberculosis and autoimmunity in a child. *Nat Med* **27,** 1646–1654 (2021).

549. Li, M. Age related human T cell subset evolution and senescence. *Immun Ageing* **16** (2019).

550. Reitsema, R. Effect of age and sex on immune checkpoint expression and kinetics in human T cells. *Immun Ageing* **17,** 32 (2020).

551. Braga, F. Blimp-1 homolog Hobit identifies effector-type lymphocytes in humans. *Eur J Immunol* **45,** 2945–2958 (2015).

552. Vieira Braga, F. Blimp-1 homolog Hobit identifies effector-type lymphocytes in humans. *Eur J Immunol* **45,** 2945–2958 (2015).

553. Hertoghs, K. Molecular profiling of cytomegalovirus-induced human CD8+ T cell differentiation. *J Clin Invest* **48,** 4077–4090 (2010).

554. Oja, A. The Transcription Factor Hobit Identifies Human Cytotoxic CD4 + T Cells. *Front Immunol* **8** (2017).

555. Kragten, N. Blimp-1 induces and Hobit maintains the cytotoxic mediator granzyme B in CD8 T cells. *Eur J Immunol* **48,** 1644–1662 (2018).

556. Mackay, L. Hobit and Blimp1 instruct a universal transcriptional program of tissue residency in lymphocytes. *Science* **352,** 459–463 (2016).

557. Akkaya, B. Increased Mitochondrial Biogenesis and Reactive Oxygen Species Production Accompany Prolonged CD4+ T Cell Activation. *J Immunol* **201,** 3294–3306 (2018).

558. Cao, Y. Metabolic reprogramming towards aerobic glycolysis correlates with greater proliferative ability and resistance to metabolic inhibition in CD8 versus CD4 T cells. *PLoS One* **9,** e104104 (2014).

559. Roberts, A. Ex vivo modelling of PD-1/PD-L1 immune checkpoint blockade under acute, chronic, and exhaustion-like conditions of T-cell stimulation. *Sci Rep* **11,** 4030 (2021).

560. Stecher, C. PD-1 Blockade Promotes Emerging Checkpoint Inhibitors in Enhancing T Cell Responses to Allogeneic Dendritic Cells. *Front Immunol* **8** (2017).

561. Conway, J. UpSetR: an R package for the visualization of intersecting sets and their properties. *Bioinformatics* **33,** 2938–2940 (2017).

562. Seo, H. TOX and TOX2 transcription factors cooperate with NR4A transcription factors to impose CD8 + T cell exhaustion. *Proc Natl Acad Sci U S A* **116,** 12410–12415 (2019).

563. Blanco, E. Age-associated distribution of normal B-cell and plasma cell subsets in peripheral blood. *J Allergy Clin Immunol* **141,** 2208–2219 (2018).

564. Gibson, K. B-cell diversity decreases in old age and is correlated with poor health status. *Aging cell* **8,** 18–25 (2009).

565. Abdullah, M. Gender effect on in vitro lymphocyte subset levels of healthy individuals. *Cell Immunology* **272,** 214–219 (2012).

566. Teixeira, D. Evaluation of lymphocyte levels in a random sample of 218 elderly individuals from São Paulo city. *Rev Bras Hematol Hemoter* **33,** 367–371 (2011).

567. Fan, H. Gender differences of B cell signature in healthy subjects underlie disparities in incidence and course of SLE related to estrogen. *J Immunol Res.* **2014** (2014).

568. Furman, D. Systems analysis of sex differences reveals an immunosuppressive role for testosterone in the response to influenza vaccination. *Proc Natl Acad Sci U S A.* **111,** 869–874 (2014).

569. House, I. Macrophage-Derived CXCL9 and CXCL10 Are Required for Antitumor Immune Responses Following Immune Checkpoint Blockade. *Clin Cancer Res* **26,** 487–504 (2020).

570. Aran, D. Reference-based analysis of lung single-cell sequencing reveals a transitional profibrotic macrophage. *Nat Immunol* **20,** 163–172 (2019).

571. Pauken, K. Single-cell analyses identify circulating anti-tumor CD8 T cells and markers for their enrichment. *J Exp Med* **218,** e20200920 (2021).

572. Krishna, C. Genetic and environmental determinants of human TCR repertoire diversity. *Immun Ageing* **17** (2020).

573. Dechanet, J. Implication of gammadelta T cells in the human immune response to cytomegalovirus. *J Clin Invest* **103,** 1437–1449 (1999).

574. Couzi, L. Gamma-delta T cell expansion is closely associated with cytomegalovirus infection in all solid organ transplant recipients. *Transpl Int* **24,** e40–2 (2011).

575. Vermijlen, D. Human cytomegalovirus elicits fetal gammadelta T cell responses in utero. *J Exp Med* **207,** 807–821 (2010).

576. Shi, J. Single-Cell Transcriptomic Profiling of MAIT Cells in Patients With COVID-19. *Front Immunol* **12,** 700152 (2021).

577. Park, D. Differences in the molecular signatures of mucosal-associated invariant T cells and conventional T cells. *Sci Rep* **9,** 7094 (2019).

578. Zheng, C. Landscape of Infiltrating T Cells in Liver Cancer Revealed by Single-Cell Sequencing. *Cell* **169,** 1342–1356 (2017).

579. Pomaznoy, M. Quantitative and Qualitative Perturbations of CD8 + MAITs in Healthy Mycobacterium tuberculosis-Infected Individuals. *Immunohorizons* **4,** 292–307 (2020).

580. Gherardin, N. Diversity of T Cells Restricted by the MHC Class I-Related Molecule MR1 Facilitates Differential Antigen Recognition. *Immunity* **44,** 32–45 (2016).

581. Koay, H. Diverse MR1-restricted T cells in mice and humans. *Nat Commun* **10,** 2243 (2019).

582. Petley, E. MAIT cells regulate NK cell-mediated tumor immunity. *Nat Commun* **12,** 4746 (2021).

583. Wang, C. Effects of Aging, Cytomegalovirus Infection, and EBV Infection on Human B Cell Repertoires. *J Immunol* **192,** 603–611 (2014).

584. Lafarge, X. Cytomegalovirus infection in transplant recipients resolves when circulating gammadelta T lymphocytes expand, suggesting a protective antiviral role. *J Infect Dis* **184,** 533–541 (2001).

585. BioRender. `https://biorender.com`.